Transactions of the ASME®

Journal of Engineering for Gas Turbines and Power

Published Quarterly by The American Society of Mechanical Engineers

VOLUME 124 • NUMBER 1 • JANUARY 2002

TECHNICAL PAPERS

Gas Turbines: Combustion and Fuels

Gas Turbines: Cycle Innovations

(**Contents continued on inside back cover**)

Editor
L. S. LANGSTON (2006)
Associate Editors
Advanced Energy Systems
G. REISTAD (2002)
Fuels and Combustion Technologies
S. GOLLAHALLI (2002)
Internal Combustion Engines
D. ASSANIS (2002)
Nuclear
R. DUFFY (2002)
Power
D. LOU (2002)
International Gas Turbine Institute
IGTI Review Chair
D. R. BALLAL (2000)
R. NATOLE (2001)
E. BENVENUTI (2002)
Combustion and Fuels
P. MALTE (2003)
Structures and Dynamics
N. ARAKERE (2004)
M. MIGNOLET (2002)

BOARD ON COMMUNICATIONS
Chair and Vice-President
OZDEN OCHOA

OFFICERS OF THE ASME
President, **W. A. WEIBLEN**
Executive Director, **D. L. BELDEN**
Treasurer, **R. E. NICKELL**

PUBLISHING STAFF
Managing Director, Engineering
THOMAS G. LOUGHLIN
Director, Technical Publishing
PHILIP DI VIETRO
Managing Editor, Technical Publishing
CYNTHIA B. CLARK
Managing Editor, Transactions
CORNELIA MONAHAN
Production Coordinator
JUDITH SIERANT
Production Assistant
MARISOL ANDINO

Transactions of the ASME, Journal of Engineering for Gas Turbines and Power (ISSN 0742-4795) is published quarterly (Jan., April, July, Oct.) by The American Society of Mechanical Engineers, Three Park Avenue, New York, NY 10016. Periodicals postage paid at New York, NY and additional mailing offices. POSTMASTER: Send address changes to Transactions of the ASME, Journal of Engineering for Gas Turbines and Power, c/o THE AMERICAN SOCIETY OF MECHANICAL ENGINEERS, 22 Law Drive, Box 2300, Fairfield, NJ 07007-2300.
CHANGES OF ADDRESS must be received at Society headquarters seven weeks before they are to be effective. Please send old label and new address.
STATEMENT from By-Laws. The Society shall not be responsible for statements or opinions advanced in papers or ... printed in its publications (B7.1, par. 3).
COPYRIGHT © 2002 by the American Society of Mechanical Engineers. For authorization to photocopy material for internal or personal use under circumstances not falling within the fair use provisions of the Copyright Act, contact the Copyright Clearance Center (CCC), 222 Rosewood Drive, Danvers, MA 01923, Tel: 978-750-8400, www.copyright.com.
INDEXED by Applied Mechanics Reviews and Engineering Information, Inc. Canadian Goods & Services Tax Registration #126148048

This journal is printed on acid-free paper, which exceeds the ANSI Z39.48-1992 specification for permanence of paper and library materials. ∞™
♲ 85% recycled content, including 10% post-consumer fibers.

Downloaded 03 Jun 2010 to 171.66.16.159. Redistribution subject to ASME license or copyright; see http://www.asme.org/terms/Terms_Use.cfm

(**Contents continued**)

Journal of Engineering for Gas Turbines and Power **JANUARY 2002**

Volume 124, Number 1

ANNOUNCEMENTS AND SPECIAL NOTES

Journal of Engineering for Gas Turbines and Power

Editorial

Greetings. It is my challenge, pleasure, and honor to be the new editor (July 1, 2001–June 30, 2006) of the Transactions of the ASME, *Journal of Engineering for Gas Turbines and Power*. Retiring Technical Editor Hal Nelson is advising me as I get started. I thank him and Ted Okiishi, Editor of our companion publication, *Journal of Turbomachinery*, for their help and continued support. Each issue of the Journal is put together in New York ASME headquarters by Production Coordinator Judy Sierant. The Editorial Assistant is Liz Langston (my wife) who will keep me on schedule. I look forward to working with and being advised by the Journal's experienced team of Associate Editors, and the leadership of ASME technical committees and divisions.

The *Journal of Engineering for Gas Turbines and Power* provides the means to solicit and publish reviewed technical papers on topics related to energy and power conversion. These topics include cycle thermodynamics, hydrocarbon and nuclear power generation, gas turbine technology, internal combustion engines, fuel cell systems, aircraft and aerospace propulsion and combined cycle and combined heat and power systems. Within ASME, the Journal serves as an archive for reviewed technical papers from the International Gas Turbine Institute and Society technical divisions which include Internal Combustion Engines, Fuels & Combustion Technologies, Nuclear Engineering, Advanced Energy Systems, and Power.

Robert Day, author of a well-known text on technical writing,[1] observes that editors have an impossible job, because of the attitude of some authors towards them. Day sums up his slightly satirical view with an assertion from an unnamed author: ''I expect the editor to accept all my papers, accept them as they are submitted, and publish them promptly. I also expect him to scrutinize all other papers with the utmost care, especially those of my competitors.'' Day then adds another author's comment on an editor's place in the scheme of things: ''Editors are, in my opinion, a low form of life—inferior to the viruses and only slightly above academic deans.'' (Having been a one-time interim dean, this author's opinion delights me, for as a new editor, my station in life has been elevated from that in the past.)

In all fairness, let me offer some support for an editor's opinion of authors with a quote from Samuel Johnson. In carrying out editorial duties for a London publication in the 1700s Johnson wrote to an author: ''Your manuscript is both good and original, but the part that is good is not original and the part that is original is not good.''

The work of and interplay between authors and editors has sustained the *Journal of Engineering for Gas Turbines and Power* for over 120 years. The Journal began as a collection of papers on energy conversion technology, in the first volume of the Transactions of the ASME, in 1880. Over the years the number of published papers increased each year so that in 1959, the Transactions were subdivided into five separate quarterly journals, one of which was called the *Journal of Engineering for Power* (Vol. 81, Series A, No. 1), later to have ''Gas Turbines'' added to the Journal title in 1983.

Table 1 Energy Converters

Date of First Working Device	
Steam engine	1769
Fuel cell	1839
Otto engine	1876
Steam turbine	1884
Diesel engine	1897
Gas turbine	1939

From its beginning in 1880 the Journal had an ASME staff editorial department. That changed in 1983 when the Journal got its first volunteer/member editor. Since then, the Journal has had the following editors:

Arthur Wennerstrom	1983–1988
George Serovy	1988–1993
Howard Julien	1993–1998
Harold Nelson	1998–2001

As one would expect, the general areas of energy conversion technology covered by Journal papers has changed since 1880. Papers before 1900 dealt mostly with steam power (e.g., ''Steam-Engine Efficiencies: The Ideal Engine Compared with the Real Engine,'' R. H. Thurston, Trans. ASME, 1891, Vol. XII, pp. 729–739. The author was ASME's first president). Technical papers on internal combustion aircraft engines first started to appear after 1915. At the present time, about 75 percent of the Journal's papers deal with gas turbine technology.

Table 1 lists a short history of significant energy conversion devices. One can see a reason for the present dominance of gas turbine papers in the Journal; the gas turbine is by far the ''youngest'' of the energy converters listed. Thus activity in gas turbine technology would be expected to be more intense than that of the more mature converters (such as steam engines).

In the past decade, a revolution of sorts has been happening with energy converters listed in the table. Steam and gas turbines have been brought together to form combined cycle plants with the highest of thermal efficiencies (~60 percent) ever. Their high efficiency and low cost are two of the underlying reasons for the deregulation of electric power generation worldwide. Thermal efficiencies and the cost of both Otto and Diesel engines are being greatly improved. ASME papers are being published, showing how fuel cell and gas turbine systems can be combined to get 70 percent thermal efficiencies and greater.

James Boswell, Editor Samuel Johnson's biographer (*Life of Johnson*, 1791) interviewed early British industrialist Matthew Boulton, cofounder of Boulton and Watt Company, manufacturer of the James Watt steam engine. Boulton's words to Boswell

---

[1] *How to Write & Publish a Scientific Paper*, 3rd Ed., Robert A. Day, Oryx Press, 1988.

were: ‘‘I sell here, Sir, what all the world desires to have—POWER.’’ As with many founding companies, Boulton and Watt no longer exists, but the world’s need for power—and power technology—continues to grow.

The next five years look very exciting for power technology and for the Journal, now in its 122nd year. As the new editor, I invite you to contribute as a writer, researcher, reviewer, session organizer or reader, to the *Journal of Engineering for Gas Turbines and Power*.

Lee S. Langston
Editor

Detailed Analysis of the Acoustic Mode Shapes of an Annular Combustion Chamber

G. Walz
W. Krebs
S. Hoffmann
H. Judith

Siemens AG KWU,
Wiesenstr. 35,
D-45466 Mülheim, Germany

To get a better understanding of the formation of thermoacoustic oscillations in an annular gas turbine combustor, an analysis of the acoustic eigenmodes has been conducted using the finite element method. The influence of different boundary conditions and a space-dependent velocity of sound has been investigated. The boundary conditions actually define the eigenfrequency spectrum. Hence, it is crucial to know, e.g., the burner impedance. In case of the combustion system without significant mixing air addition considered in this paper, the space-dependence of the velocity of sound is of minor importance for the eigenfrequency spectrum leading to a maximum deviation of only five percent in the eigenvalues. It is demonstrated that the efficiency of the numerical eigenvalue analysis can be improved by making use of symmetry, by splitting the problem into several steps with alternate boundary conditions, and by choosing the shift frequency ω_s *in the range of frequencies one is interested in.* [DOI: 10.1115/1.1396346]

1 Introduction

Ring combustors of gas turbines combine the advantages of a reduced requirement for cooling air due to their compact design and a homogeneous temperature distribution upstream of the turbine inlet. Together with lean premixed combustion, this offers the potential of significantly reducing NO_x emissions. Consequently, annular combustion chambers are often applied as a design feature of modern gas turbines such as the hybrid burner ring (HBR) combustor of the Siemens 3A series ([1]). In Fig. 1 a cross section of the V84.3A, the 60 Hz version, is shown.

Due to the ever-increasing reaction densities in modern gas turbine combustors, the risk of the formation of thermoacoustic oscillations also rises. These oscillations have been investigated in detail both experimentally and theoretically for single burner arrangements ([2–4]). However, little is known about their mode shapes and excitation in annular combustors. In order to achieve a better understanding of combustion oscillations in annular combustors and to assist the interpretation of dynamic pressure measurements on site, a detailed analysis of the acoustic modes within an annular combustor has been carried out.

The modal analysis has been performed both by application of analytical and finite element tools. In Section 2 the essentials of the theory of acoustic wave motion are introduced. The eigenmodes of a cylinder are studied in detail in Section 3. Using this simple model the main features of acoustic eigenmodes can be discussed on an analytical basis. Furthermore, the analytical solution serves as a benchmark for the finite element analysis. Since an analytical solution for annular combustion chambers is not available, their eigenmodes are analyzed numerically in Section 4.

2 Theory

Since the main flow inside gas turbine combustors is characterized by a Mach Number below 0.1, the effect of the mean flow on the transport of acoustic properties can be neglected. Hence, the acoustic wave motion can be determined solving the transport equation for the scalar velocity potential Φ [5]:

$$\frac{\partial^2\Phi}{\partial t^2}=\frac{1}{k\rho}\Delta\Phi. \tag{1}$$

The fluid is characterized by a compressibility "k" and density "ρ" which are assumed to be independent of space for simplicity. Measurable quantities are the acoustic pressure "p" and the acoustic velocity "v" which are related to Φ by

$$p=\rho\frac{\partial\Phi}{\partial t},\quad v=-\operatorname{grad}\Phi. \tag{2}$$

Both p and v also obey a wave equation of the type (1). The second equation of (2) shown is tantamount to curl $v=0$. The speed c of a sound wave is given by

$$c^2=\frac{1}{k\rho}. \tag{3}$$

Time and space variables are separated by assuming special solutions of the form $\Phi=A\exp(i\omega t)$, which are the "eigensolutions of the Laplacian Δ" at an "eigenfrequency ω." On the boundaries of the enclosed region "V" two conditions can be specified. For an open wall the velocity potential is set to zero ($\Phi=0=p$, Dirichlet type for Φ). At a rigid wall, the outer normal component of the acoustic velocity vector v_n is set to zero which means $\partial\Phi/\partial n=0=v_n$ (of Neumann type for Φ). With these boundary conditions only discrete values of ω are possible that can be arranged in an ascending order and referenced by an integer N, whereby N is the number of eigenfrequencies smaller than a fixed value ω_N.

It is well known that there is an infinite number of eigenfrequencies ω_N which are all real and positive (the lowest one$=0$ for Neumann-type boundary conditions). The "higher" eigenfrequencies approach

$$\omega_N\rightarrow c\left(\frac{N6\pi^2}{V}\right)^{1/3}\equiv N^{1/3}\omega_0,\quad \text{if}\quad N\rightarrow\infty. \tag{4}$$

In the following the proportionality factor ω_0 which represents a typical value for the eigenfrequencies of the combustor will be used to normalize all eigenfrequencies ω_N. The normalized eigenfrequencies are independent of the speed of sound and the combustor volume, especially in the limit of large N. It is revealed that all frequencies ω_N decrease if the volume is increased and N or the speed of sound is decreased.

Contributed by the International Gas Turbine Institute (IGTI) of THE AMERICAN SOCIETY OF MECHANICAL ENGINEERS for publication in the ASME JOURNAL OF ENGINEERING FOR GAS TURBINES AND POWER. Paper presented at the International Gas Turbine and Aeroengine Congress and Exhibition, Indianapolis, IN, June 7–10, 1999; ASME Paper 99-GT-113. Manuscript received by IGTI, October 1998; final revision received by the ASME Headquarters, March 1999. Associate Editor: D. Wisler.

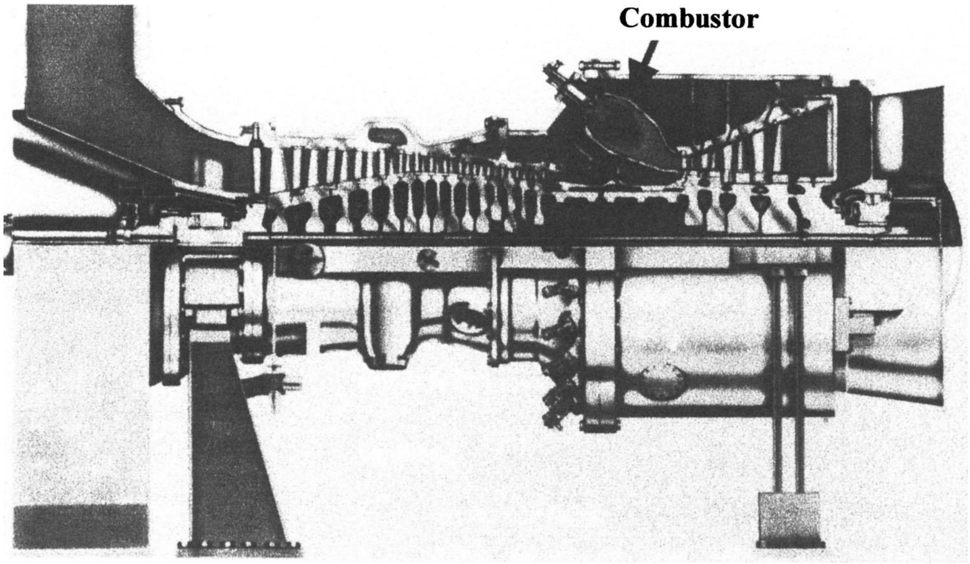

Fig. 1 Cross section of the V83.3A gas turbine

The eigenfunctions Φ_N corresponding to different eigenvalues ω_N are orthogonal, i.e.,

$$(\Phi_N,\Phi_M)\equiv\int_V \Phi_N\Phi_M dV=0,\quad N\neq M. \tag{5}$$

They can be selected to form a complete orthonormal set of functions. This means that every solution Φ of the acoustic wave equation (1) can be expanded in terms of the Φ_N:

$$\Phi=\sum_n (\Phi,\Phi_N)\Phi_N. \tag{6}$$

The eigenfunction Φ_1 corresponding to the lowest eigenfrequencies has no nodes (i.e., is nonzero everywhere). If there are $J>1$ eigenfunctions Φ_J with the same eigenvalue ω_N, the eigenmodes are called J-fold "degenerate." Degeneracy is always related to a type of symmetry.

The set of nodes of Φ_N, for $N\geqslant 2$, divide the region V into at least two subregions and at most, N subregions.

In the following section, as an example, the eigensolutions of a cylinder with different types of boundary conditions are investigated in detail.

3 Eigenmodes of a Cylindrical Ring Combustion Chamber

3.1 Analytical Solution. The geometry of a cylindrical ring is very similar to the annular combustion chamber thus demonstrating the main features of such eigenmodes. The main dimensions are its length L, its outer diameter r_a and its inner diameter r_i. On the other hand, the model is simple enough to have an analytical solution available by which it is possible to check the quality of the numerical analysis of the finite element method. Assuming rigid walls throughout the entire boundary, the eigenfunctions for a cylindrical coordinate system (r,φ,z) can be expressed in the form

$$\phi_{nlm}=Z_n(z)R_{lm}(r)\Psi_m(\varphi)e^{i\omega_{nlm}t}, \tag{7a}$$

i.e., as a product of an axial contribution $Z_n(z)$, a radial one $R_{lm}(r)$, a circumferential one $\Psi_m(\varphi)$, and of the time-dependent factor $\exp(i\omega_{nlm}t)$. The functions Z_n, R_{lm}, and Ψ_m are given by

$$Z_n(z)=\sqrt{\frac{2}{L}}\cos\left(n\frac{\pi}{L}z\right),$$

$$R_{lm}(r)=A_{lm}S_{lm}(r)$$

with the abbreviations

$$S_{lm}(r)=\left[J_m\left(a_{ml}\frac{r}{r_i}\right)-\frac{\dfrac{\partial J_m(a_{ml})}{\partial r}}{\dfrac{\partial Y_m(a_{ml})}{\partial r}}Y_m\left(a_{ml}\frac{r}{r_l}\right)\right]$$

and

$$A_{lm}=\left\{\frac{1}{2}r_a^2\left[1-\left(\frac{m}{a_{ml}\frac{r_a}{r_i}}\right)^2\right]S_{lm}^2\left(a_{ml}\frac{r_a}{r_i}\right)-\frac{1}{2}r_t^2\left[1-\left(\frac{m}{a_{ml}}\right)^2\right]S_{lm}^2(a_{ml})\right\}^{-1/2},$$

$$\Psi_m(\varphi)=\frac{1}{\sqrt{2\pi}}e^{im\varphi}. \tag{7b}$$

J_m and Y_m denote the Bessel functions of the first and second kind and of order m. The eigenmodes are characterized by the three integers $N\cong(nlm)$, with n representing the number of peaks in the axial, l their number in the radial, and m their number in the circumferential direction, respectively. Pure axial eigenmodes, e.g., have $l=m=0$ and $n\neq 0$. The a_{lm} are the infinite number of zeros of

$$\frac{\partial J_m(a_{lm})}{\partial r}\,\frac{\partial Y_m\left(a_{lm}\frac{r_a}{r_i}\right)}{\partial r}-\frac{\partial Y_m(a_{lm})}{2r}\,\frac{\partial J_m\left(a_{lm}\frac{r_a}{r_i}\right)}{\partial r}=0. \tag{8}$$

This equation ensures that the proper boundary condition $\partial\Phi/\partial n=0$ is satisfied at $r=r_i$, and $r=r_a$. Note that due to the choice of the constants, the Φ_{nlm} are orthogonal and normalized: $(\Phi_{nlm},\Phi_{n'l'm'})=\delta_{nn'}\delta_{ll'}\delta_{mm'}$.

The corresponding eigenfrequencies ω_{nlm} are

$$\omega_{nlm}=c\sqrt{\left(n\frac{\pi}{L}\right)^2+\left(\frac{a_{lm}}{r_i}\right)^2} \tag{9}$$

approaching in the limit of a thin cylinder ($r_i \rightarrow r_a$) and for $l \neq 0$ [3]

$$\omega_{nlm} \rightarrow c\sqrt{\left(n\frac{\pi}{L}\right)^2+\left(\frac{\pi l r_a}{(r_a-r_i)r_i}+\frac{4m^2+3}{8\pi l r_i^2}(r_a-r_i)\right)^2}.$$

Eigenmodes with circumferential contributions ($m \neq 0$) are twofold degenerate, because for integer values of m the following relations hold:

$$J_{-m}=(-1)^m J_m \quad \text{and} \quad Y_{-m}=(-1)^m Y_m.$$

Hence, Eq. (8) depends only on m^2. This is an immediate consequence of the circumferential symmetry of the cylinder and remains valid also in the annular combustion chamber.

Note that the eigenvalues and -functions strongly depend on geometry and on the respective boundary conditions. If the wall is open at $z=0$ ($p=0$), for example, the only changes in the eigenfunctions and the eigenfrequencies in Eq. (7) and (9) are

$$Z_n(z)=\sqrt{\frac{2}{L}}\sin\left(\left\{n+\frac{1}{2}\right\}\frac{\pi}{L}z\right)$$

$$\omega_{nlm}=c\sqrt{\left(\left\{n+\frac{1}{2}\right\}\frac{\pi}{L}\right)^2+\left(\frac{a_{lm}}{r_i}\right)^2}. \tag{10}$$

A further aspect which might have an influence on the eigenmodes and which will be investigated later in the numerical example, is a spatially distributed velocity of sound $c=c(r,\varphi,z)$ which is related to the local temperature and species in the combustion process. Consider as a typical example the cylinder where one-half ($0 \leqslant z \leqslant L/2$) has $c(r,\varphi,z)=2c_0$ and the other $c(r,\varphi,z)=c_0(L/2 \leqslant z \leqslant L)$. In this case an incoming longitudinal wave of type $\exp(ikz)$ is not only reflected at the end of the cylinder ($z=L$) but is also split half way down the cylinder (at $z=L/2$) into a transmitted and a reflected part. All these contributions superimpose to produce a standing wave in the entire cylinder. In this problem the eigenfrequencies are calculated assuming rigid walls across the entire boundary.

$$\omega_{nklm}=c\sqrt{\left(nf_k\frac{\pi}{L}\right)^2+\left(\frac{a_{lm}}{r_i}\right)^2} \tag{11}$$

with

$$f_0=0,\ f_1=0.3661,\ f_2=0.6339(k=0,1,2).$$

Note that additional eigenmodes in the z-direction arise whereas the modes in the radial and the circumferential directions are not affected.

3.2 Confirmation of the Analytical Results by Finite Element Analysis. For a validation of the finite element tool, the eigenmodes as given in Eqs. (7) to (10) for the cylindrical ring model of the combustion chamber have also been calculated numerically. The geometry parameters are chosen to represent the main dimensions of the annular combustion chamber. In Table 1 some of the eigenfrequencies including the related integers (nlm) and the ordering mode number N are presented. The entire boundary is assumed to be a rigid wall. The last three columns of the table include the analytical results (ω/ω_0 anal) for the eigenfrequencies evaluated from solving Eqs. (7) and (8), the results of the finite element analysis (ω/ω_0 finite element) and the error of the numerical values compared to the analytical ones, respectively. The numerical analysis is performed with the ABAQUS code [6] which iteratively extracts a certain number of eigenvalues closest to a prescribed shift frequency ω_s. The properties of the enclosed gas are characterized by its inverse compressibility $1/k$ and density ρ. As the frequencies are determined by the velocity of sound c only, it is convenient to take $\rho \equiv 1$ and $1/k=c^2$ (cf. Eqs. (3), (8), and (9)).

By variation of ω_s and of the number of frequencies to be calculated the complete spectrum of eigenvalues is covered. For the lowest eigenvalues the ω_s is chosen negative resulting in $\omega_1=0$.

Table 1 Selected eigenfrequencies of the cylinder model. The analytical solution is compared to the finite element results. The bold typed frequencies indicate modes with axial/radial (no hoop) contributions only.

n	(n l m)	ω/ω_0 anal	ω/ω_0 (Finite Element)	Error (Percent)
1	**00 0**	**0**	**0**	**0**
2	00 1	0.321	0.321	−0.005
3	00 1	0.321	0.321	−0.005
4	00 2	0.642	0.642	−0.002
5	00 2	0.642	0.642	−0.002
6	00 3	0.960	0.960	0.000
7	00 3	0.960	0.960	0.000
8	00 4	1.276	1.276	−0.002
9	00 4	1.276	1.276	−0.002
10	**10 0**	**1.342**	**1.343**	**−0.009**
11	10 1	1.380	1.380	−0.010
12	10 1	1.380	1.380	−0.010
13	10 2	1.488	1.488	−0.008
14	10 2	1.488	1.488	−0.008
15	00 5	1.588	1.588	−0.006
16	00 5	1.588	1.588	−0.006
17	10 3	1.650	1.650	−0.007
18	10 3	1.650	1.650	−0.007
19	10 4	1.852	1.852	−0.006
20	10 4	1.852	1.852	−0.006
21	00 6	1.896	1.897	−0.009
22	00 6	1.896	1.897	−0.011
23	10 5	2.079	2.080	−0.007
24	10 5	2.079	2.080	−0.007
25	00 7	2.200	2.201	−0.020
26	00 7	2.200	2.201	−0.018
27	10 6	2.323	2.324	−0.010
28	10 6	2.323	2.324	−0.010
29	**01 0**	**2.461**	**2.461**	**−0.011**
30	01 1	2.483	2.483	−0.010
…				
39	01 3	2.657	2.657	−0.010
40	**20 0**	**2.685**	**2.689**	**−0.160**
41	20 1	2.704	2.708	−0.158
…				
48	01 4	2.801	2.801	−0.010
49	**11 0**	**2.803**	**2.803**	**−0.011**
50	11 1	2.823	2.823	−0.011
…				
88	1011	3.631	3.635	−0.096
89	1011	3.631	3.635	−0.096
90	**21 0**	**3.642**	**3.645**	**−0.097**
91	21 1	3.657	3.660	−0.097
…				
119	**30 0**	**4.027**	**4.057**	**−0.742**
…				
183	**02 0**	**4.898**	**4.905**	**−0.159**
…				
250	02 7	5.411	5.469	−1.060

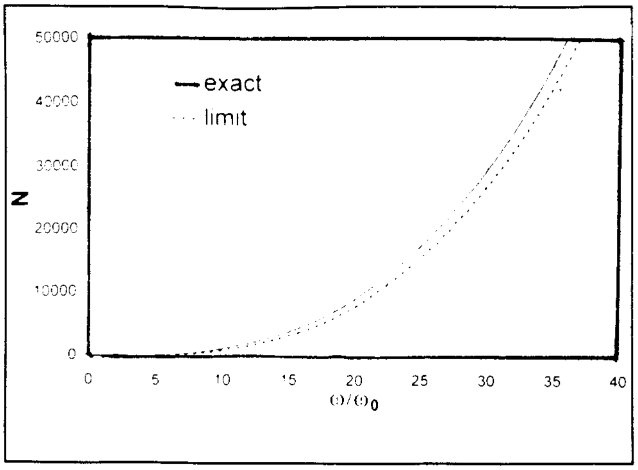

Fig. 2 Eigenfrequency spectrum of the cylinder model. The limit curve is given by $N=(\omega/\omega_0)^3$ (see Eq. (4)).

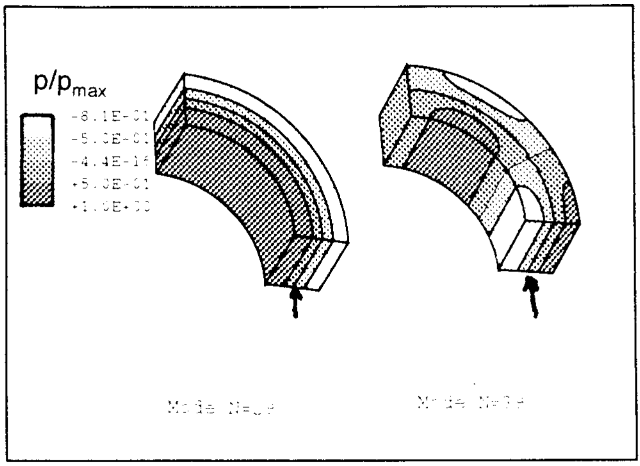

Fig. 3 Examples of eigenmodes of the cylinder model: mode $N=29$ (left) and $N=39$ (right). The eigenmodes are characterized by the normalized pressure distribution.

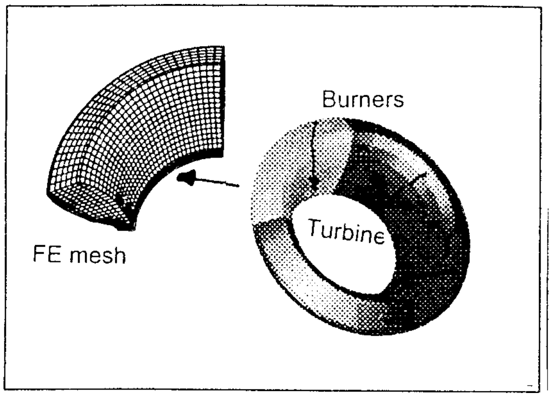

Fig. 4 Geometry and finite element model of the annual combustor

In order to increase the computational efficiency of the finite element analysis, including either reducing the computation time or increasing the accuracy with a more refined mesh, only one quarter of the cylinder is modeled. The entire spectrum of eigenvalues is then obtained by splitting the calculation into two steps with different boundary conditions (BC). The first step imposes a rigid "wall" at both circumferentially directed boundaries (*symmetrical BC*). The second step assumes an open "wall" at one of these boundaries and a rigid "wall" at the other (*asymmetrical BC*). As a consequence, the aforementioned circumferential degeneracy is removed and every eigenfrequency is calculated only once. The "asymmetrical step" provides modes with circumferential contributions that are known to be twofold degenerate. The "symmetrical step," however, provides all kinds of modes. Their degeneracy can be only assessed by considering the pressure distribution. The nondegenerate eigenmodes are readily revealed within the finite element scheme by a third analysis with a two dimensional axisymmetric model providing the pure axial/radial modes (with $m \neq 0$) exclusively. In the case of the simple cylinder, it is not necessary to apply this procedure. However, it will be required for more complex domains such as realistic annular combustors.

The mesh used in the analysis of the cylinder ring consists of 375 isoparametric 20-node brick elements resulting in a total of 2076 pressure degrees-of-freedom. The agreement of numerical and analytical results is excellent, the maximum error is 1 percent. The discrepancy between analytical and numerical values in-

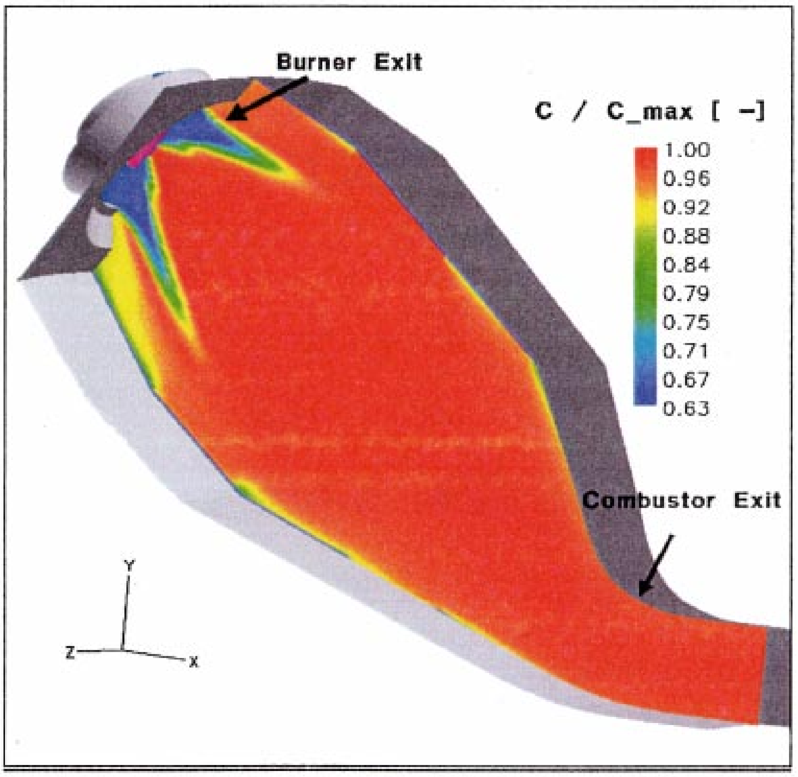

Fig. 5 Distribution of the speed of sound normalized to its maximum value c_0 in the $z=0$ m plane (CFD calculation ([7]))

Table 2 Eigenfrequencies of an annular gas turbine combustion chamber according to problems I, II, and III (see text), and, for comparison, to the cylinder model of Section 3. The bold typed frequencies indicate modes with axial/radial (no hoop) contributions only.

$(N)_l$	Problem I	Problem II	Problem III	Problem IV
1	**0**	**0**	**0.56**	**0**
2	0.32	0.32	0.65	0.32
4	0.63	0.63	0.87	0.64
6	0.94	0.93	1.14	0.96
8	1.24	1.22	1.42	1.28
10	**1.35**	**1.34**	**1.53**	**1.34**
11	1.39	1.38	1.57	1.38
13	1.53	1.51	1.68	1.49
15	1.53	1.52	1.70	1.59
17	1.72	1.72	1.86	1.65
19	1.81	1.78	1.98	1.85
21	1.97	1.96	2.09	1.90
23	2.09	2.05	2.24	2.08
25	2.24	2.24	2.35	2.20
27	**2.34**	2.31	**2.36**	2.32
28	2.36	**2.31**	2.37	**2.46**
30	2.36	2.33	2.43	2.48
32	**2.41**	**2.37**	**2.48**	2.50
33	2.43	2.39	2.50	2.55
35	2.43	2.39	2.51	2.58
37	2.49	2.46	2.52	2.66
39	2.52	2.48	2.58	**2.68**
41	2.54	2.52	2.62	2.70
43	2.60	2.56	2.63	2.76
45	2.63	2.59	2.70	2.79
47	2.67	2.60	2.76	**2.80**
49	2.77	2.75	2.78	2.80
51	2.81	2.76	2.86	2.82
53	2.82	2.81	2.90	2.84
55	2.89	2.82	2.94	2.85
57	2.97	2.91	3.01	2.88
59	3.00	2.97	3.06	2.97
61	3.10	3.06	3.12	2.98
63	3.15	3.09	3.18	2.98
65	3.19	3.09	**3.23**	3.09
67	3.20	**3.20**	3.24	3.10
69	**3.26**	3.21	3.25	3.11
70	3.28	3.21	3.25	3.11
72	3.33	3.26	3.29	3.18
74	3.38	3.28	3.32	3.27
76	3.40	3.29	3.36	3.29
78	3.40	3.34	3.45	3.37
80	3.41	3.36	3.47	3.37
82	**3.43**	**3.41**	**3.54**	3.41
83	3.45	3.43	3.54	3.45
85	3.47	3.44	3.55	3.47
87	3.50	3.47	3.55	3.63
89	3.51	3.48	3.58	**3.64**
91	3.58	3.51	3.60	3.66
93	3.62	3.56	3.60	3.66
95	3.64	3.56	3.68	3.66
97	3.65	3.57	3.69	3.67
99	3.66	3.61	3.75	3.67
101	3.69	3.68	3.75	3.70
103	3.75	3.73	3.79	3.78
105	3.80	3.75	3.79	3.88
107	3.83	3.76	3.82	3.88
109	3.86	3.81	3.92	3.90
111	3.91	3.82	3.93	3.90
113	3.92	3.84	3.93	3.93
115	3.98	3.90	4.00	3.94
117	4.00	3.99	4.06	4.01
119	4.04	4.00	4.09	4.03
121	4.10	4.02	4.10	4.04
123	4.17	4.03	4.12	4.08
125	4.17	4.07	4.14	4.09
127	4.17	4.10	4.24	4.14
129	4.19	4.18	**4.25**	4.15
131	**4.27**	**4.22**	4.26	4.16
132	4.29	4.23	4.28	4.16
134	4.32	4.24	4.30	4.21
136	4.33	4.27	4.33	4.22
138	4.35	4.28	4.34	4.22
140	4.39	4.31	4.36	4.31
142	4.39	4.31	4.39	4.33
144	4.40	4.33	4.41	4.34
146	4.42	4.35	4.44	4.41
148	4.43	4.40	4.44	4.43
150	4.47	**4.42**	4.52	4.45
152	**4.50**	4.42	4.55	4.49
153	4.51	4.43	4.56	4.50
155	4.55	4.46	4.58	4.54
157	4.58	4.51	**4.59**	4.54
159	4.61	4.52	4.61	4.59

creases with mode number N, as the spectrum gets denser. In principle, these errors can be further reduced with a more refined mesh, a properly chosen shift frequency and with increasing the number of iteration vectors in the analysis. Figure 2 depicts the complete spectrum of eigenfrequencies versus mode number N in the range $0<\omega/\omega_0<10$. The dashed line represents the limit curve in Eq. (4). Still higher frequencies ($N \geqslant 10^6$) must be used before the actual curve is smoothed out and approaches its limit.

In Fig. 3 two examples of a related pressure distribution are given: $N=29$, $(nlm)=(010)$, $\omega/\omega_0=2.461$ and $N=39$, $(nlm)=(013)$, $\omega/\omega_0=2.657$.

Note that the pressure values are normalized so that the maximum is 1. Mode 29 includes a standing wave with the shape of a sine function extending in radial direction. The set of nodes ($p=0$) is indicated by the arrows. It divides the original cylinder into two concentric parts of nearly equal thickness. The higher the numbers (nlm) the more peaks will occur in the eigensolution and the more complicated the set of nodes will be as indicated by mode 39 having one sine in the radial and three in the circumferential direction.

With a space-dependent velocity of sound $c=c(\mathbf{x})$, similar results are obtained: In particular, the eigenfrequencies given by the analytical expression (9) are reproduced by finite element analysis with the same high accuracy. The spatial dependence is technically taken into account by a prescribed temperature field $T(x)$ with temperature-dependent material parameters $1/k=1/k(T(x))$.

In conclusion, finite element analysis provides the complete eigenspectrum of acoustic wave motion with rather high precision, in particular, for the low frequencies that are sufficiently distinct. For circumferentially symmetric geometries, the efficiency of the calculation can be increased by making use of symmetry and by splitting the calculation into several independent steps with proper boundary conditions at the cut.

Most of these results remain valid for the more complex cone shaped geometry of the annular combustion chamber to be studied in the next chapter, of which an analytical solution is no longer available.

4 Eigenmodes of an Inclined Annular Combustion Chamber

In Fig. 4 the geometry of an annular gasturbine combustor, typical for the $V\times 4.3A$ gas turbine family, together with the finite element discretization of a quarter of it is shown. The mesh consists of 4800 isoparametric 20-node brick elements including about 22,400 degrees-of-freedom.

With this geometry fixed, the following types of analysis have been performed:

Analysis	**I**	**II**	**III**
Velocity of sound	$c_0=\text{const}$	$c=c(x)$ (see Fig. 5)	$c=c(x)$ (see Fig. 5)
Boundary condition at burner inlets	$\partial\Phi/\partial n=0$ (rigid)	$\partial\Phi/\partial n=0$ (rigid)	$\Phi=0$ (open)

Rigid walls ($\partial\Phi/\partial n=0$) are assumed at all other boundaries. The burner outlets are represented by six holes and the centers placed at equal distance in the middle of the surface adjacent to the burners.

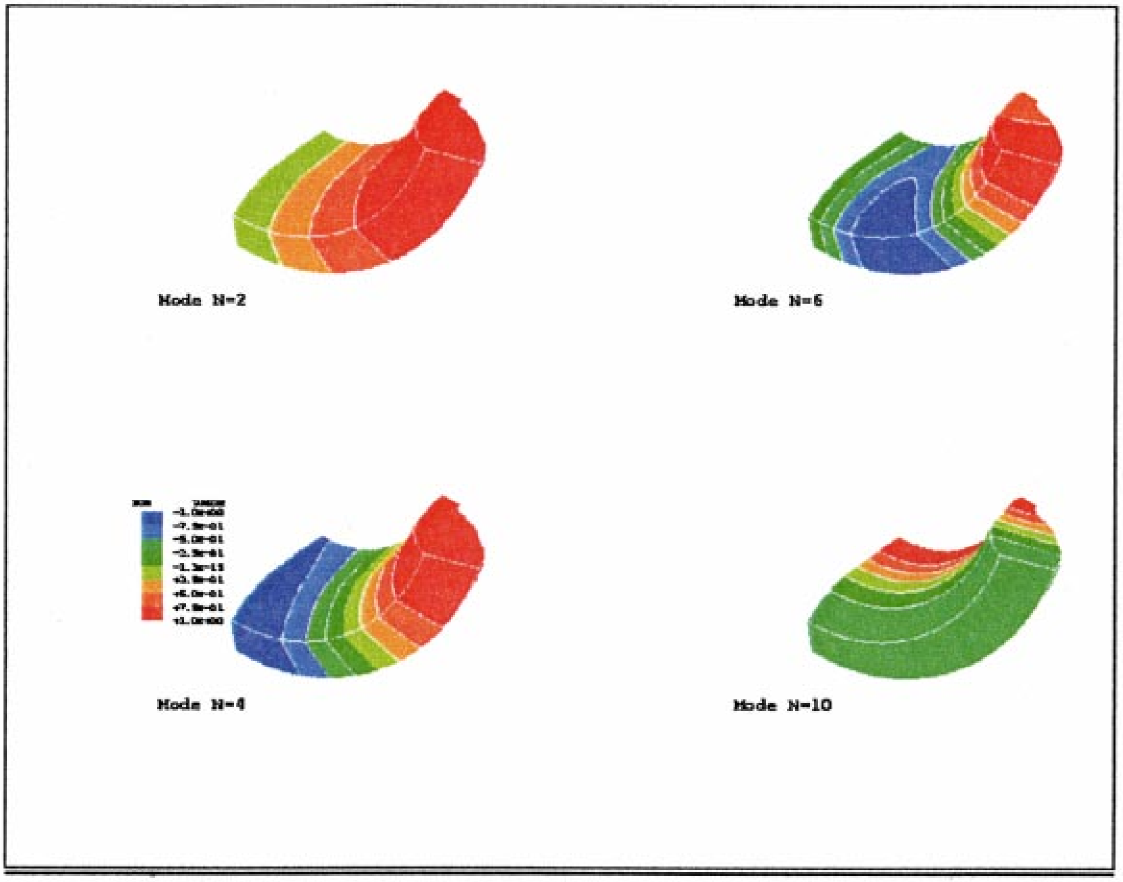

Fig. 6 Selected eigenmodes of the annular combustor with boundary conditions of Problem II. The pictures show the normalized pressure distribution.

The spatial distribution of the velocity of sound $c(x)/c_0$ is given in Fig. 5. c_0 is the maximum speed of sound in the combustion chamber. $c(x)$ is calculated from the temperature field and the distribution of species concentration taken from a CFD analysis of the combustion process [7]. The distribution of the speed of sound $c(x)$ is quite similar to the temperature distribution. It is nearly constant $c(x)=c_0$ downstream of the flame front which covers most of the combustion chamber. Values $c(x)$ less than c_0 are observed upstream of the flame front in the immediate vicinity of the burner outlets and near the wall, where cooling air is added. In the inner recirculation zone, values greater than c_0 are calculated.

In Table 2 the eigenfrequencies for Problems I, II, and III are listed. The values are again normalized by $\omega_0=c_0(6\pi^2/V)^{1/3}$. As before, the nondegenerate modes are marked as bold characters. To avoid repetitions, the degenerate modes are mentioned only once, resulting in steps of 2 of the mode number N in the list. For comparison the cylinder solution of the preceding section with rigid walls assumed at all boundaries is also given.

As the annular combustion chamber has the shape of a cone, the axial and radial directions mix and the integers (nl) have no meaning anymore. Nevertheless, the low eigenfrequencies $\omega<2\omega_0$ for Problems I, II, and the cylinder model are in good agreement and show distinct gaps. For higher values of ω/ω_0 the eigenfrequencies become blurred, and minor differences in the mode shape occur in these three problems. For example, the third axial/radial mode is assigned to $N=27$ in Problem I and the cylinder problem, but it is assigned to $N=28$ in Problem II. Hence, in Table 2 the numbers N only refer to Problem I. The effect of the space-dependent velocity of sound $c(x)$ in Fig. 5 is about 5 percent for the entire spectrum. In Fig. 6 four examples of pressure distributions corresponding to Problem II are shown. The locations of pressure nodes are indicated by the interface areas between the two green colors. Modes 2 and 4 are the lowest circumferential dominated modes, mode 10 is the lowest mode without any circumferential contribution. Mode 6 is a typical mixed mode.

Problems I, II and the cylinder problem have equally formulated boundary conditions of Neumann type on all boundaries, whereas for Problem III at the circular holes of the burner inlets a Dirichlet-type boundary condition has been prescribed. Hence, the lowest eigenfrequency is greater than zero and the spectrum is completely different to the other three, as already becomes evident looking at formulas (9) and (10). Figure 7 confirms this showing some simpler mode shapes. The lowest eigenfrequency corresponds to a half-sine primarily in axial direction. Mode 2 and 3 are the lowest modes showing distinct circumferential contributions. Mode 6 has dominant axial-/radial contributions and corresponds to mode 10 in the preceding example.

5 Conclusion

An analysis of the acoustic wave motion of an annular gasturbine combustor has been performed.

The quality of the analysis has been verified using a cylinder ring, which is a simple geometry with an analytical solution. It is demonstrated that the entire acoustic spectrum can be calculated by finite element analysis with rather high accuracy for the lower frequencies that are sufficiently far apart from each other. The efficiency of the numerical eigenvalue analysis can be improved by making use of symmetry, by splitting the problem into several steps with alternate boundary conditions, and by choosing the

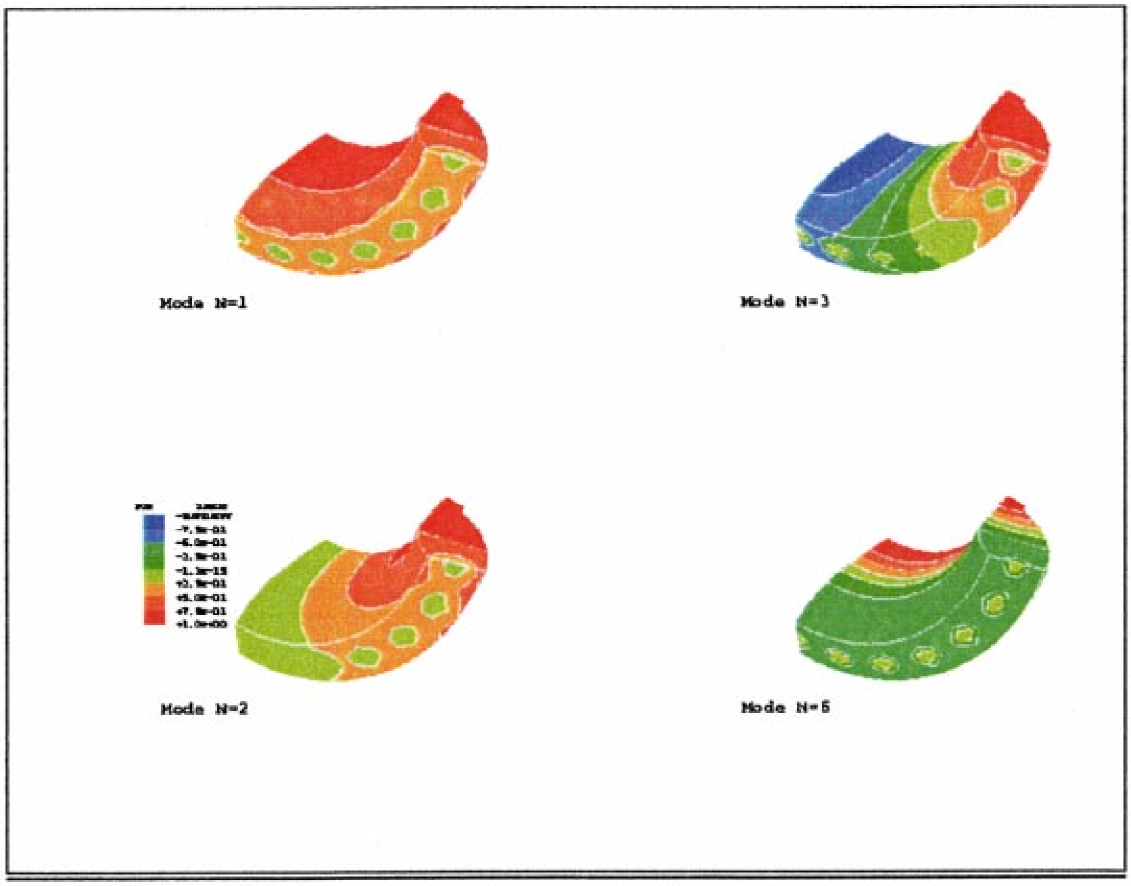

Fig. 7 Selected eigenmodes of the annular combustor with boundary conditions of Problem III. The normalized pressure distribution is shown.

shift frequency ω_s in the range of frequencies one is interested in. An inhomogeneous velocity of sound has been included.

The 200 lowest eigenmodes of an annular combustion chamber are calculated by finite element analysis within a quarter section model. The analysis also provides a normalized pressure distribution identifying the set of nodes of the respective modes. At the burner side different boundary conditions have been imposed. It is demonstrated that this has a strong influence on the eigenfrequency spectrum. Therefore, it is inevitable to know the burner impedance precisely. Since no mixing air is added to the combustion system, the effect of a space-dependent velocity of sound on the spectrum is only about five percent. As observed in every kind of cavity, the eigenfrequency spectrum shows distinct gaps for the lower modes, whereas the higher modes, which have been given to show the quality of the finite element scheme and the role of the boundary conditions, become blurred.

Nomenclature

c = speed of sound
L = axial length of the cylindrically shaped combustor
N = discrete integer values to characterize the individual eigenmodes
$(nlmk)$ = set of integer values N to characterize the eigenmodes of the cylindrically shaped combustor
p = acoustic pressure
r_a = outer radius of the cylindrically shaped combustor
r_i = inner radius of the cylindrically shaped combustor
t = time
V = acoustic velocity
$x=(r,\phi,z)$ = spatial coordinates
Φ = scalar velocity potential
Φ_N = eigenfunction corresponding to the eigenfrequency ω_N
κ = compressibility of acoustic medium
ρ = density of acoustic medium
ω_0 = eigenfrequency normalizing factor (equals the proportionality factor in the limit $N \rightarrow \propto$ according to Eq. (4))
ω_N = eigenfrequency to be characterized by discrete values of N

References

[1] Becker, B., Schulenberg, T., and Termuehlen, H., 1995, ''The 3A-Series Gas Turbines With HBR™ Combustors,'' ASME Paper 95-GT-458.
[2] Samaniego, J. M., Yip, B., Poinsot, T., and Candel, S., 1993, ''Low Frequency Combustion Instability Mechanism in a Side-Dump Combustor,'' Combust. Flame, **94**, pp. 363–380.
[3] Paschereit, C. O., and Polifke, W., 1998, ''Investigation of the Thermoacoustic Characteristics of a Lean Premixed Gas Turbine Burner,'' ASME Paper 98-GT-582.
[4] Prade, B., Streb, H., Berenbrinck, P., Schetter, B., and Pyka, G., 1996, ''Development of an Improved Hybrid Burner—Initial Operating Experience in a Gas Turbine,'' ASME Paper 96-GT-45.
[5] Morse, P. M., and Ingard, K. U., 1986, *Theoretical Acoustics*, Princeton University Press, Princeton, NJ.
[6] Hibbitt, Karlson & Sorenson, Inc., 1997, *ABAQUS User's Manual Version 5.7*.
[7] Krebs, W., Walz, G., Hoffmann, S., and Judith, H., 1999, ''Detailed Analysis of the Thermal Wall Heat Load in Annular Combustors,'' ASME TURBO EXPO, submitted for presentation.

Compressor Exit Conditions and Their Impact on Flame Tube Injector Flows

A. G. Barker

J. F. Carrotte

Rolls Royce University Technology Centre,
Department of Aeronautical and Automotive
Engineering and Transport Studies,
Loughborough University,
Loughborough, Leicestershire LE11 3TU, UK

Within a gas turbine engine the flow field issuing from the compression system is nonuniform containing, for example, circumferential and radial variations in the flow field due to wakes from the upstream compressor outlet guide vanes (OGVs). In addition, variations can arise due to the presence of radial load bearing struts within the pre-diffuser. This paper is concerned with the characterization of this nonuniform flow field, prior to the combustion system, and the subsequent effect on the flame tube fuel injector flows and hence combustion processes. A mainly experimental investigation has been undertaken using a fully annular test facility which incorporates a single stage axial flow compressor, diffuser, and flame tube. Measurements have been made of the flow field, and its frequency content, within the dump cavity. Furthermore, the stagnation pressure presented to the core, outer and dome swirler passages of a fuel injector has been obtained for different circumferential positions of the upstream OGV/pre-diffuser assembly. These pressure variations, amounting to as much as 20 percent of the pressure drop across the fuel injector, also affect the flow field immediately downstream of the injector. In addition, general variations in pressure around the fuel injector have also been observed due to, for example, the fuel injector position relative to pre-diffuser exit and the flame tube cowl. [DOI: 10.1115/1.1383773]

Introduction

In order to achieve efficient combustion and a satisfactory combustor exit traverse it is important to generate the correct flow field and mixing patterns within a flame tube. With this in mind air issuing from the compressor is initially decelerated, by the combustor diffuser system, prior to being distributed to the flame tube and its various features. The complex flow field, generated within the flame tube, is therefore determined by the combustor diffuser flow and its interaction with the porosity and blockage of the flame tube. Current advanced core engines usually incorporate dump diffusers ([1]) in which a pre-diffuser, located immediately downstream of the compressor outlet guide vane (OGV) row, is then followed by a recirculating ''dump'' region surrounding the flame tube head. This abrupt expansion ensures insensitivity to manufacturing tolerances/thermal expansions and provides flow stability over a wide range of engine operating conditions. A large number of investigations have been conducted on such systems, with a comprehensive review being given by Klein [2]. In general these investigations have attempted to identify the most significant parameters which affect diffuser performance, as usually indicated by the overall stagnation pressure loss and static pressure rise within the diffuser. While some of these investigations have also highlighted how overall performance is affected by inlet conditions, very few investigations have considered the generation and transmission of inlet nonuniformities, through the diffuser system, and their local effect on flame tube features. Although the production of turbulence as flow passes around the flame tube head and into each feed annulus may help reduce such nonuniformities in these regions, this may not be the case for the flow which passes directly through the cowl and into the flame tube fuel injectors.

Within a gas turbine engine the flow field issuing from the compression system is highly nonuniform containing, for example, circumferential variations in the flow field due to well-defined wakes from the upstream compressor outlet guide vanes (OGVs). Work already published by various authors including Stevens and Williams [3]. Stevens et al. [4] Klein [5], and Carrotte et al. [6] have indicated that, although some wake mixing occurs within the pre-diffuser, blade wakes are still evident at pre-diffuser exit. This is likely to continue as the general requirement to reduce weight, and thus axial length, tends to decrease the distance available for mixing prior to the flame tube. A further consideration is that OGV/pre-diffuser assemblies usually provide a structural load path, for the nozzle guide vane and combustor pressure loads, and these loads are becoming more critical due to deeper flame tubes and increased pressure ratio engine cycles. As a consequence OGV blades may be thicker or, alternatively, radial struts may be located within the pre-diffuser. Examples of such strutted systems are given by Madden et al. [7] and Barker et al. [8] and the wakes from these struts introduce further flow nonuniformities into the system. Thus, although the design of flame tube fuel injectors is undertaken by assuming a uniform approach flow, such components may be operating in a highly nonuniform environment. This is not only due to the general distortion caused by the presence of the flame tube cowl or other flame tube features, but also local variations associated with the flow approaching the flame tube.

This paper is concerned with characterization of the nonuniform flow field which enters the combustion system and its potential impact on the flame tube airspray fuel injectors. A mainly experimental investigation has been undertaken using an isothermal test facility which incorporates a single stage axial flow compressor, an OGV row with representative aerodynamic loading, a diffuser, and flame tube. The two geometries tested include that of a structural OGV row and an alternative radially strutted system, with both geometries being typical of current engine design practice. Measurements have been made of the flow field entering the diffuser system, within the dump cavity, and that immediately downstream of the fuel injectors within the flame tube. In addition the stagnation pressure distribution delivered to the various fuel injector passages has been obtained within a representative fuel injector geometry. This information is of particular significance

---

Contributed by the International Gas Turbine Institute (IGTI) of THE AMERICAN SOCIETY OF MECHANICAL ENGINEERS for publication in the ASME JOURNAL OF ENGINEERING FOR GAS TURBINES AND POWER. Paper presented at the International Gas Turbine and Aeroengine Congress and Exhibition, Indianapolis, IN, June 7–10, 1999; ASME Paper 99-GT-238. Manuscript received by IGTI, Oct. 1998; final revision received by the ASME Headquarters, March 1999. Associate Editor: D. Wisler.

due to the ever more stringent emissions legislation that necessitates tighter control of fuel air ratios and flame tube mixing patterns.

Experimental Facility

Overall Test Facility. A comprehensive description of the overall experimental facility is given by Wray et al. [9] with the working section approximating a large-scale version of a current engine geometry. Air is drawn from atmosphere into a large plenum, above the vertically mounted facility, prior to passing through the entry flare which also contains a honeycomb flow straightener. Particular emphasis has been placed on obtaining reasonably engine representative inlet conditions to the systems being investigated, and so a single-stage axial compressor rotor is located immediately upstream of the working section. This provides a reasonable compromise between capturing the main compressor outlet/diffuser inlet flow features, present within an engine, while avoiding the high costs associated with running a multistage compressor facility. The compressor consists of an 80-blade inlet guide vane (IGV) row and a rotor, this having a tip clearance of approximately 0.7 percent of blade height, and is driven by a 45 kW DC motor sited in the exhaust plenum below the test rig.

At inlet to the OGV row the mean radius and passage height are 375 mm and 36.6 mm respectively (Fig. 1), and consistent with these dimensions various OGV/pre-diffuser geometries can be accommodated. At pre-diffuser exit the flow then enters the dump cavity and divides to pass either into the outer and inner feed annuli, or directly into the flame tube. In addition, to simulate turbine cooling flow a limited amount of air is removed through a series of plunged holes (Ø43.5 mm) within the inner dump casing, located approximately 160 mm axially downstream of the OGV inlet plane. At an axial location corresponding to traverse planes XO1 and XI1 (Fig. 1), the radial depth of the annular flame tube is 5.5 times the passage height at OGV inlet (h_2) with this ratio increasing to 6.3 downstream of the second cooling ring (XO3, XI3). Flow can enter the flame tube through primary cooling rings, primary ports and secondary cooling rings located within each feed annulus. Porosity through the flame tube head is provided by holes (Ø79.5 mm) in each of the 20 flame tube burner sectors, this flow then entering the combustor primary zone through the fuel injectors and cowl back-plate.

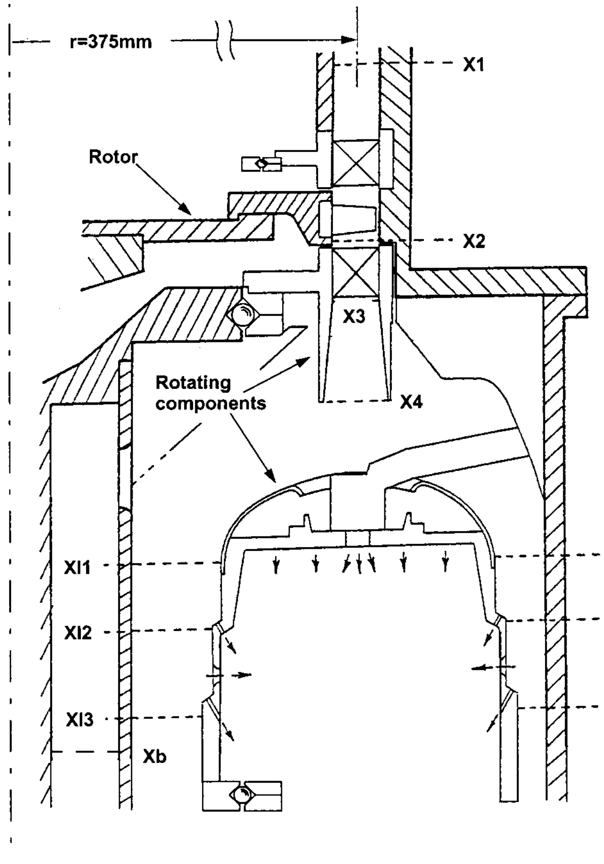

Fig. 1 Test rig

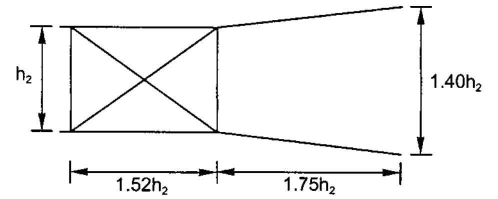

a) Long Chord Structural OGV (108 blades)

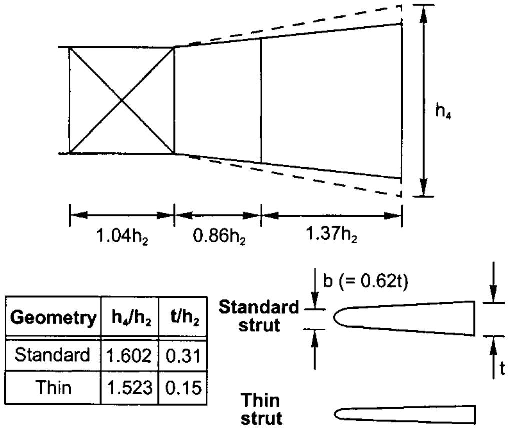

Geometry	h_4/h_2	t/h_2
Standard	1.602	0.31
Thin	1.523	0.15

b) Strutted systems (160 blades)

Fig. 2 Geometric definition of outlet guide vane (OGV) diffuser assemblies

Downstream of the test section a complex series of throttles control the facility and maintain the compressor on its desired operating point. This corresponded to a rotor flow coefficient (ϕ) of 0.4 and a nondimensional speed ($N/\sqrt{T}$) of 169. For a typical ambient temperature of 291 K this resulted in a rotor speed of 2880 rpm and approximately 46 deg of inlet swirl to the compressor outlet guide vanes (OGVs). The throttle system allowed the required mass flow distributions to be set at 24.3 percent (outer feed), 20.4 percent (inner feed), 48.7 percent (flame tube), and 6.4 percent (turbine bleed). Note that the feed annuli and flame tube mass flows were measured downstream of the second cooling rings (planes XI3, XO3), and these distributions could be maintained within ± 0.5 percent (feed annuli) and ± 0.1 percent (turbine bleed) of their respective nominal values.

OGV/Pre-diffuser Geometries. The distance between the OGV leading edge and the downstream combustor was maintained constant in all tests. Within this space OGV/pre-diffuser geometries could be fitted (Fig. 2), the distance between OGV inlet and pre-diffuser exit also being the same for each geometry ($3.27\,h_2$).

The long chord (structural) OGV/pre-diffuser system contains 108 blades through which a limited structural load can be transferred across the gas passage. The chord of each blade is approximately 57 mm with a thickness/chord ratio of 7 percent. This blade row is attached to a pre-diffuser, of area ratio 1.40 and nondimensional length 1.75, and is typical of a modern engine geometry (Fig. 2(*a*)). It should be noted that the ratio of OGVs (108) to fuel injectors (20) is not an integer number. Hence, relative to the injectors the position of the upstream OGVs, and their associated blade wakes, will vary from one sector to another. Within the strutted system (Fig. 2(*b*)) the OGV blades have a 6 percent thickness/chord ratio, but it should also be noted that the blade chord has been reduced from 57 mm to approximately 39 mm. Hence, to maintain a comparable aerodynamic blade loading the number of blades is increased to 160. The shorter blade chord means that for the same overall length, between OGV inlet and pre-diffuser exit, the area ratio of the longer pre-diffuser can be increased to 1.45 whilst maintaining a similar diffuser aerodynamic loading ([10]). In this case the structural load is sustained by radial struts within the pre-diffuser, one per flame tube burner sector, with the struts being circumferentially positioned midway between the trailing edges of the upstream OGV blades. Note that because of the positive pressure gradient in the diffuser the strut thickness increases along the entire length of each strut, in order to ensure that separation is fixed at the blunt trailing edge located at pre-diffuser exit. At this location the blockage, produced by the struts, was approximately 10.6 percent of the datum geometric passage area. At pre-diffuser exit the casing dimensions were therefore adjusted to account for the strut blockage, so maintaining a constant exit passage area. It should also be noted that some tests are reported in which, using a similar design methodology, a thin strut of similar profile was located within the prediffuser. However, the thickness of this strut was half that of the standard strut (Fig. 2(*b*)).

Instrumentation

The majority of measurements were obtained with miniature 5 hole pressure probes of overall diameter 1.7 mm, hole bore 0.25 mm, which were used in a nonnulled mode as outlined by Wray et al. [9]. These provided local mean values of stagnation pressure, static pressure and velocity magnitude and direction. Area traverses could be performed at compressor inlet (X1), rotor exit/OGV inlet (X2), OGV exit (X3), pre-diffuser exit (X4), and at 6 planes within the outer and inner feed annuli (Fig. 1). To enable the collection of additional data the design of the test facility was modified so that the flame tube, OGV, and IGV blade rows were mounted on bearings. Hence the OGV/prediffuser assembly could be rotated to any circumferential position relative to the flame tube fuel injectors. Furthermore, two types of fuel injector could be incorporated within the flame tube.

Simulated Fuel Injectors. For part of the test program simulated fuel injectors were located in the center of each cowl hole (Fig. 3*a*). These have the same external geometry as that of the engine airspray fuel injectors with a comparable effective area. However, they contain no internal geometric features, such as turning vanes, and the annular passages surrounding the main barrel have been approximated by a series of discrete holes (Fig. 3*a*).

The simulated fuel injectors permitted instrumentation access to the dump cavity region, with hot wire anemometry measurements being made at up to four axial planes between pre-diffuser exit and the flame tube cowl. These were obtained by inserting single hot wires, mounted within the flame tube, through the center passage of a simulated fuel injector. Furthermore, within one of these injectors a pitot probe has been located in the center passage (CS), with four pitots also being located in the surrounding holes (Fig. 3(*a*)). These probes are located flush with the top of their respective holes and are used to indicate the stagnation pressure field being presented to the upstream face of the fuel injector. With the flame tube in a fixed position data could be obtained, using this instrumentation, as the upstream OGV/pre-diffuser assembly was rotated to 160 different circumferential positions relative to the flame tube fuel injectors.

Engine Representative Airspray Fuel Injectors. For measurements within the fuel injectors and in the downstream flame tube, fuel injectors were manufactured to include co-rotating swirler passages (Fig. 3(*b*)). The presence of swirl vanes restricted instrumentation access but stagnation pressures were obtained within the core, outer and dome passages using pitot probes located at the exit plane of the turning vanes (Fig. 3(*b*)). At these locations pitot probes were placed midway between vane trailing edges at the swirl vane stagger angle. It is thought that this provided good alignment of the local flow direction with each pitot probe. As with the simulated fuel injectors measurements could be made, using these pitot probes, with the upstream OGV/pre-diffuser assembly located at a variety of circumferential positions.

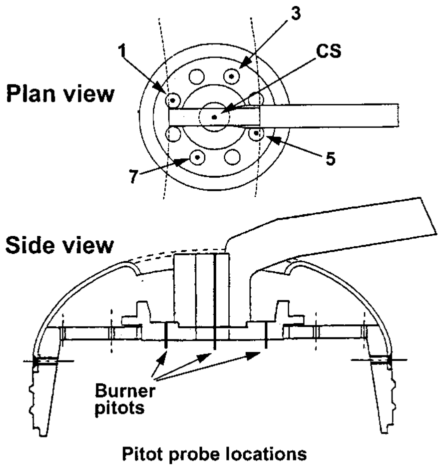

a) Simulated fuel injectors

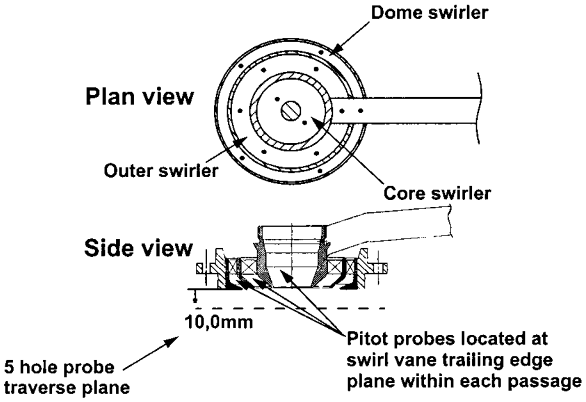

b) Representative fuel injectors

Fig. 3 Flame tube fuel injectors and instrumentation

Within the flame tube measurements were made at a plane located 10 mm downstream of an engine representative fuel injector (Fig. 3(*b*)) which corresponded to approximately 0.5 core passage exit diameters. Traverses could be performed about the fuel injector centreline in either the radial or circumferential directions. Measurements were made with five hole probes in which, relative to the conventional probe geometry, the head was modified so that measurements could be made with flow angles in pitch/yaw as high as 50 deg. In order to obtain frequency information additional measurements were also undertaken with single hot wire probes.

Data Reduction and Analysis

At each traverse point, five hole probes provided information on stagnation and static pressure in addition to velocity magnitude and direction. Using this information the overall mean velocity and mass flow through a traverse plane was calculated as

$$\dot{m}=\int \rho u dA=\rho \overline{U} A \tag{1}$$

where A is the flow passage area at the plane concerned. Spatially averaged values of stagnation ($\overline{P}$) and static ($\overline{p}$) pressure were mainly defined by mass weighting the appropriate individual values, i.e.,

$$\overline{P}=\frac{1}{m}\int_A P\rho u dA \quad \text{and} \quad \overline{p}=\frac{1}{m}\int_A p\rho u dA. \tag{2}$$

Where quoted, the mean pressures at a traverse plane are derived using this mass weighting technique.

It is conventional that static and stagnation pressure are nondimensionalized by a relevant aerodynamic quantity. For various reasons ([10]) the pressure data is nondimensionalised by the total dynamic head ($\overline{P}-\overline{p}$) upstream of the rotor (plane X1) and the mass weighted stagnation pressure at OGV inlet (plane X2). A stagnation pressure coefficient is therefore expressed as $(P-\overline{P}_{X2})/(\overline{P}_{X1}-\overline{p}_{X1})$. All velocity contours $(u/\overline{U})$ are presented relative to the mean velocity at the OGV exit plane $(\overline{U}_3)$.

In addition to the experimental data a convenient theoretical method, as described by Hill et al. [11], has been adopted to indicate the development of turbulent wakes within pressure gradients. The method is based on momentum integral equations and an "eddy viscosity" which is assumed uniform across the wake and proportional to the product of local freestream velocity and momentum thickness. A relative wake depth β is defined as $((U-u_c)/U)$ where U is the freestream velocity and u_c is the velocity at the wake centerline. Using various assumptions Hill et al. [11] outlined the following equation for the wake depth:

$$\frac{\beta}{\beta_o}=\left(\frac{U_o}{U}\right)^2\left(1+\frac{8\pi^2}{\pi^2-4}\times\left(\frac{\varepsilon}{U\theta}\right)\int\frac{U_o}{U}\,d\left(\frac{\beta_o^2 x}{\theta_o}\right)\right)^{-1/2} \tag{3}$$

where the initial freestream velocity, wake momentum thickness, and wake depth are U_o, θ_o and β_o, respectively. The eddy viscosity is evaluated by assuming that $(\varepsilon/U\theta)$ is constant and equal to 0.044. This equation has been successfully applied by Hill et al. [11] for single wakes in both diffusing and accelerating pressure gradients. Here it is used to predict the mixing of a blade wake as it passes down the center of the pre-diffuser passage and is subjected to the pressure gradients present in such regions.

Estimate of Experimental Errors

At a given data point the experimental accuracy, in regions of high flow field gradients, will be influenced by the spatial error associated with the finite distance between the five holes on the probe tip. This was eliminated by radial and circumferential interpolation of the side pressures onto the central measurement hole as described by Wray et al. [9] However, experimental accuracy is also influenced by the proximity of casing surfaces, recording, and digitizing of signals, etc. Due to these various factors the stagnation pressure coefficient measurements, external to the flame tube, were repeatable to within 0.005 and flow angles were in error by up to 1 deg. However, larger errors will occur within the flame tube due to high turbulence levels, highly sheared flow, large angle variations, etc. Such errors are difficult to estimate but at various locations several tests were conducted which revealed the pressure coefficient was repeatable to within 0.015. All hot wire measurements were made with single wire probes which are sensitive, by varying degrees, to all three components of velocity. These measurements were therefore used to give a general indication of the flow velocity and turbulence levels rather than defining an absolute value associated with a specific component. This was sufficient for the results reported here since what was often required was to identify a relative change in the flow field characteristics, produced by differences in the relative positions of the various geometries.

Results and Discussion

The conditions provided by the upstream rotor stage, which have been described in detail elsewhere ([6]), capture the main features that are typically observed downstream of a rotating blade row. This flow field then enters the compressor outlet guide vane (OGV) row and axial velocity contours are presented, at exit from this row, for both the long chord (structural) and short chord OGV blade rows (Fig. 4). Note that inlet guide vane wakes are partially transmitted through the rotor leading both to slight differences of the flow field, between each blade passage, and the requirement to traverse a different number of blade passages in each configuration. The measurements indicate relatively well-behaved blade rows with no significant regions of flow separation but, as to be expected, well-defined blade wakes and casing boundary layers are evident. What must now be assessed is the development of these nonuniform distributions and how they affect both the flow being delivered to the flame tube fuel injectors, and the flow field generated by the fuel injectors within the flame tube.

Flow Within the Pre-diffuser. For the long chord (structural) OGV row the axial velocity contours at pre-diffuser exit (Fig. 5), across a flame tube burner sector, show that within the pre-diffuser some mixing out of each blade wake occurs. Thus although pressure forces can increase the velocity gradients in such regions this wake decay means that, in general, the shear forces generated within the flow are of greater significance. Along each casing some boundary layer growth, due to the positive pressure gradient, is evident although the flow has remained attached to the casings at all circumferential locations. For the short chord OGV blade, which only has a minimal load carrying capability, radial struts are also located within the pre-diffuser. Thus, in addition to the circumferential variations of the flow field, associated with the blade wakes, it can be seen that each strut introduces a well defined wake at pre-diffuser exit which also enters the dump cavity.

Estimates of Wake Mixing. Although the flow field within the diffuser system is complex, some insight into the flow behavior may be gained by using the relatively simple wake decay analysis described by Hill et al. [11] The analysis has been restricted to the central portion of the pre-diffuser (i.e., 50 percent passage height), which contains that flow most likely to be captured by the flame tube fuel injectors. The analysis requires the momentum wake thickness at the OGV trailing edge, and annular cascade tests on compressor blading ([12]) appear to indicate values of approximately 1 percent of the blade chord (i.e., $\theta_o/C\sim 0.01$). However, it is widely acknowledged that in a compressor the values are much greater and based on detailed measurements of the velocity profile and the blade pressure loss, at mid passage height, a value of 2 percent of the blade chord has been used (i.e., $\theta_o/C\sim 0.02$). It has also been assumed that the freestream veloc-

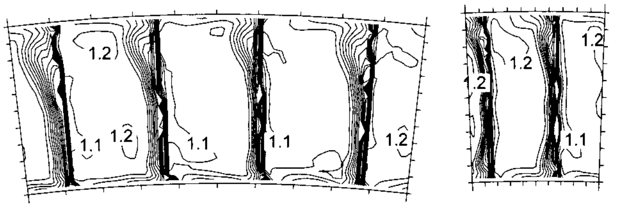

a) Long Chord Structural OGV

b) Standard Strut (short chord OGV)

Fig. 4 Outlet guide vane (OGV) exit axial velocity contours (plane X_3)

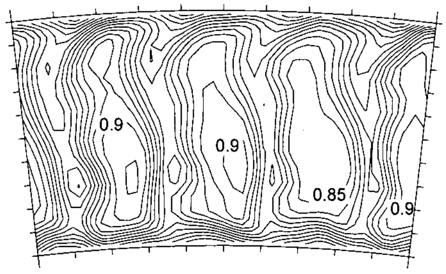

a) Long Chord Structural OGV

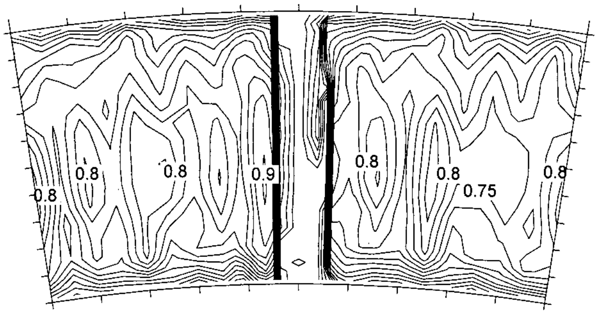

b) Standard Strut (short chord OGV)

contours of $u/\bar{u}_{X3}$, increments of 0.05

Fig. 5 Pre-diffuser exit axial velocity contours (plane X_4)

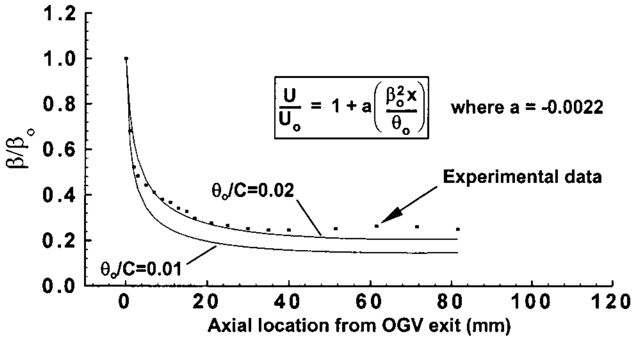

a) Short chord OGV (predicted and experimental) - No struts, Mid height

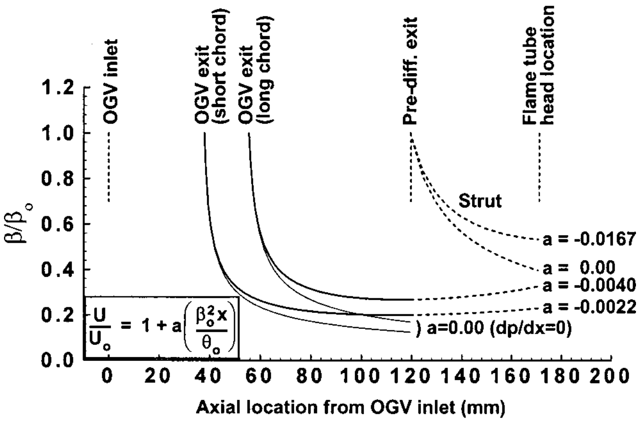

b) Strut, short and long chord OGV predictions

Fig. 6 Experimental and predicted relative wake depths

ity measured at OGV exit and pre-diffuser exit varies in a linear fashion along the pre-diffuser, and using these assumptions the wake depths (β) derived from detailed measurements, downstream of the short chord OGV, can be compared with the predicted values (Fig. 6(*a*)). Allowing for effects such as wakes merging towards pre-diffuser exit, flow redistribution across the pre-diffuser passage by secondary flows, enhanced turbulent levels provided by the upstream rotor, etc., the agreement is thought to be relatively good and captures the most significant features associated with the wake mixing.

Having validated this method the long chord (structural) and short chord (strutted) OGV/pre-diffuser systems have been analyzed. Initial predictions were obtained for mixing of the wake produced by each OGV blade within a zero pressure gradient flow field (i.e., $U/U_o = 1.0$). However, further calculations have included the diffusing pressure gradient where, for simplicity, the freestream velocity distribution assumes a linear change between OGV exit and pre-diffuser exit. The predictions (Fig. 6(*b*)) indicate that, immediately downstream of an OGV blade, rapid wake mixing occurs due to the shear stresses associated with the high velocity gradients and, in the absence of a pressure gradient, these stresses would continue to reduce the wake depth. As to be expected when a pressure gradient is applied the initial rapid mixing of the wake still occurs. However, as the velocity gradients, and hence shear stresses, reduce the pressure forces start to have an increasing effect. Hence, towards the rear of the pre-diffuser the wake depth is approximately constant as the pressure forces become of greater significance, although the pressure gradients are not of sufficient magnitude to cause the wake depths to grow within the pre-diffuser. These predictions are in reasonable agreement with the experimental data where, at pre-diffuser exit, wakes depths (β) in the range of 0.22 to 0.30 (short chord) and 0.28 to 0.42 (long chord) were obtained. Note that this range of values indicated differences in wake mixing, between blades, due to the relative position of the upstream IGVs (i.e., wakes produced by the IGVs influence the OGV wake development). Furthermore it is also interesting to note that a similar comparison was undertaken by Stevens et al. [17] but for OGV wakes decaying downstream of a multistage compressor. Again good agreement was obtained with the predictions based on the analysis of Hill et al. [11] for an isolated wake, indicating the importance of the shear stresses generated by the initial velocity gradients in the wake region. It also follows that, although there is a difference in Reynolds number between the current and engine operating conditions, this difference will have a relatively small effect on the wake generated by the blade and hence the observed mixing characteristics.

At pre-diffuser exit comparison of the predictions (Fig. 6(*b*)) and experimental data (Fig. 5) indicate the same trends; namely the short chord OGV blade wakes are better mixed out, and less well defined, compared with the structural OGV geometry. It can be seen that this is partially due to the longer length of the short chord OGV pre-diffuser ($2.23\,h_2$), relative to the structural blade pre-diffuser ($1.75\,h_2$), so that a greater length is available for mixing out of the blade wakes. Furthermore, the smaller wakes that are produced by the short chord OGV generate larger shear stresses so also leading to a more rapid mixing of the wake (Fig. 5). However, it should be remembered that the radial struts present within the short chord OGV/pre-diffuser system introduce relatively large wakes at pre-diffuser exit. What is difficult to assess is the subsequent development of the various wakes, within the dump cavity, prior to the fuel injectors. Nevertheless since the blade wakes are well developed and the shear stresses small, the blade wakes are likely to persist for some distance downstream of the pre-diffuser exit plane. As an example, an extrapolation of the OGV blade wake development, within the dump cavity, has been considered by assuming the freestream velocity variations prior to the pre-diffuser exit plane continue within the dump cavity (Fig. 6(*b*)). It is also interesting to consider the strut wake, with the predictions being based on an estimated initial momentum thickness (θ_o) of half the trailing edge thickness. The size of this wake means the initial shear stresses are not as large, compared with the wakes from the compressor blading, and so the initial rate of mixing is not as great. Hence, if a pressure gradient is applied then this can have a significant effect on the depth of the strut wake. The problem is that in reality the flow in this region is complex and the pressure distributions difficult to estimate.

Dump Cavity Flow (Simulated Fuel Injectors). So as to obtain an approximate indication of the mean and turbulent flow field a single hot wire was mounted, within the flame tube, and inserted through the center fuel injector passage into the dump region. Traverses were performed by rotation of the upstream short chord OGV and strutted pre-diffuser assembly relative to the stationary flame tube and instrumentation. Note that measurements were also obtained with thin struts whose thickness was half that of the standard struts.

Measurements of the mean velocity are presented at three axial locations for the standard strutted system, with the majority of measurements being concentrated in the vicinity of each strut wake (Fig. 7). The velocity data is presented relative to the circumferential location around a flame tube burner sector. Reductions in the overall velocity levels, with axial location, reflect the upstream blockage effect of the flame tube, while local velocity variations are due to strut and OGV wakes. As a general comment the strut wakes appear to be mixing out, as the flow progresses downstream, but little change is apparent in the OGV wake size. In addition to mean velocities the frequency content of this flow is of further interest. In particular, if the turbulent energy is concentrated at specific frequencies then problems could arise if the subsequent energy release, due to combustion, also becomes concentrated at these frequencies. The frequency spectra obtained midway between struts, such as that presented 20 mm ($x/L=0.377$) downstream of prediffuser exit (Fig. 8), indicate no evidence of a rotor wake passing frequency (~4.8 kHz) or specific frequencies associated with the OGV blade wakes. However, in the vicinity of both the thin and standard struts there is strong evidence of vortex shedding. Furthermore both the frequency and mean velocity data indicate how the rate of wake mixing is dependent on the strut trailing edge thickness. For example, downstream of the thin strut the peak in the frequency spectra is greatest at 38 percent of the dump cavity, with the vortices starting to decay by the 75 percent location. In contrast for the thicker (standard) strut the peak in the frequency spectra is, if anything, greatest at this 75 percent location.

The frequency at which vortices are shed is described by the Strouhal number ($\mathrm{Str}=fl/U$) which incorporates a characteristic velocity (U) and length (l) in addition to the frequency (f) at which shedding occurs. In a complex geometry and flow field such as that being investigated such quantities are difficult to define. However, a crude estimate based on the pre-diffuser exit mean velocity, and the trailing edge strut thickness, suggests Strouhal numbers of approximately 0.24 (thin) and 0.21 (standard). These compare well with the value given by Yang et al. [13] of 0.24 in their tests on V-shaped bluff bodies. Many authors such as Roshko [14], and Bearman [15] have tried to obtain, for bluff bodies, a universal Strouhal number and suggest that the characteristic length is the displacement of the shear layers after

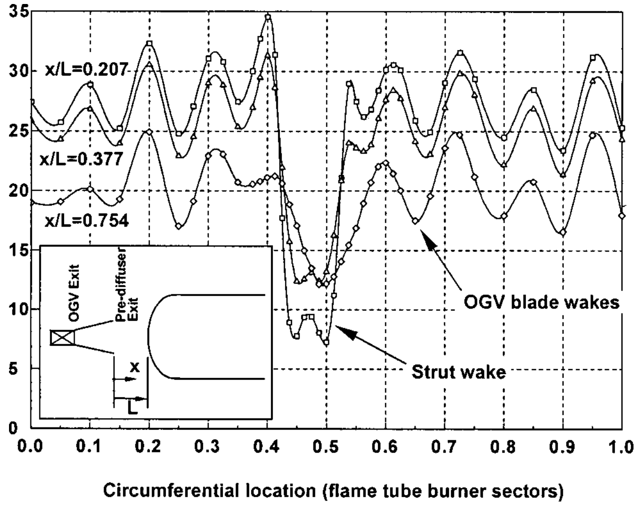

Fig. 7 Hotwire mean velocity profiles within the dump cavity

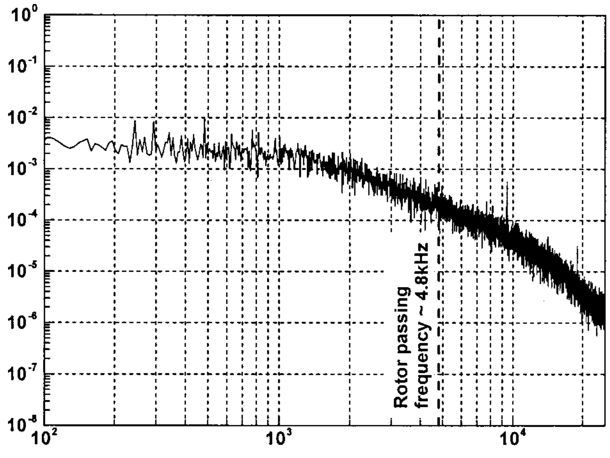

a) Midway between struts, x/L=0.377

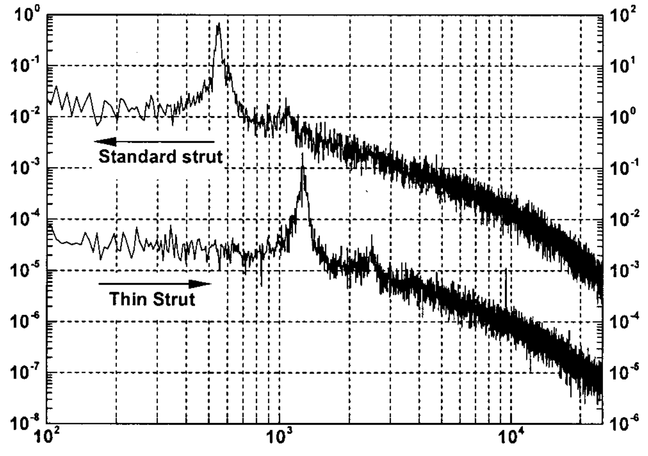

b) Adjacent to struts, x=/L=0.377

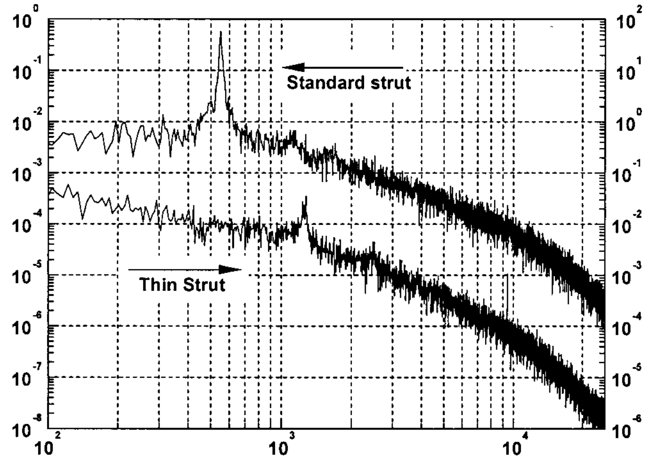

c) Adjacent to struts, x/L=0.754

Fig. 8 Frequency spectrum measured in dump cavity

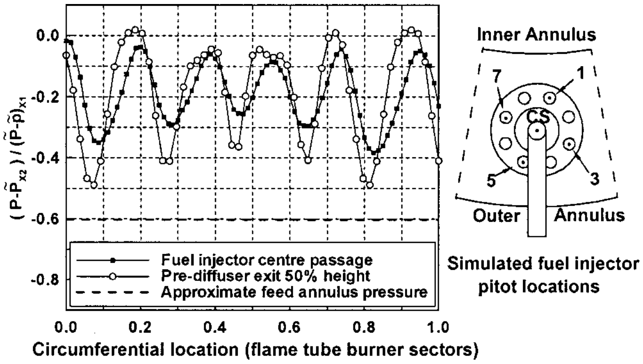

a) Long Chord Structural OGV

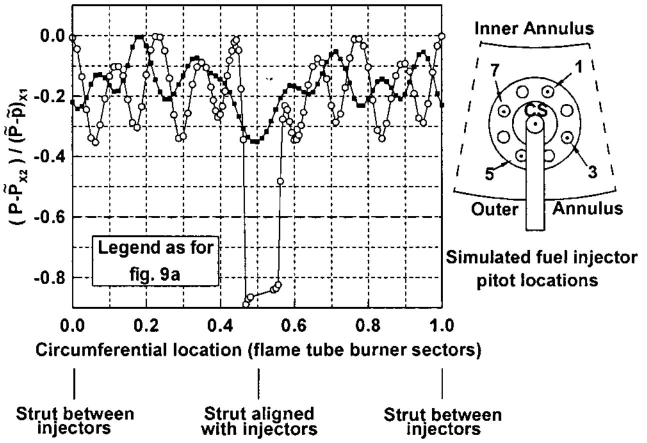

b) Standard strut (with short chord OGV)

Fig. 9 Simulated fuel injector stagnation pressure distributions

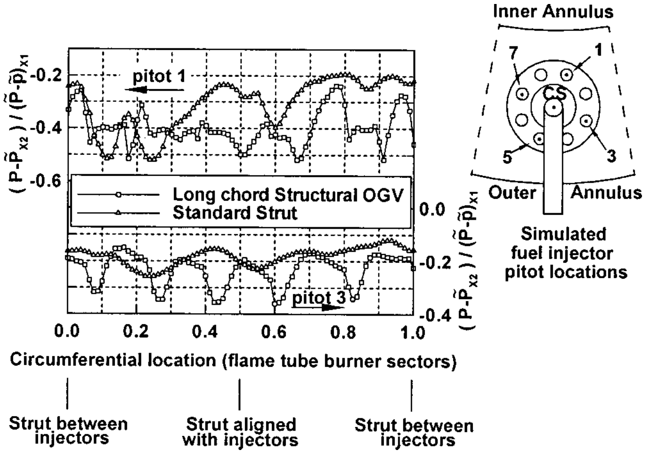

Fig. 10 Simulated fuel injector stagnation pressure distributions

they become parallel downstream of the bluff body. This probably accounts for slight differences in Strouhal number between the thin and standard struts. Since the Strouhal number contains a characteristic length and velocity it should also be noted that the shedding frequencies measured within the test rig will be different and, in this case, lower to those which would occur for the engine on which this facility is approximately based. Furthermore the value of Strouhal number and, indeed, whether strut shedding is present at all, is a function of Reynolds number. Hence, the Reynolds number at which any tests are conducted should be assessed and, as was done in this case, be related to specific engine operating conditions ([16]).

Stagnation Pressures at Fuel Injector Inlet (Simulated Flame Tube Fuel Injectors). Tests were performed in which each OGV/pre-diffuser assembly was rotated, through a complete flame burner sector, relative to the flame tube and fuel injectors which remained fixed. For the long chord (structural) OGV the observed central pitot (CS) pressure variations, with OGV/pre-diffuser circumferential location (Fig. 9(*a*)), are at the same pitch as that of the upstream OGV blades. These variations therefore indicate the sensitivity of this fuel injector passage to the OGV wakes issuing from the pre-diffuser. Comparison with the circumferential pressure distribution at pre-diffuser exit, as measured at 50 percent passage height, indicates a small amount of wake mixing within the dump cavity. However, it has already been noted that at this stage of blade wake development the shear forces are relatively small, so that significant variations are still evident in the vicinity of the fuel injector. For the strutted system (Fig. 9(*b*)) circumferential locations of 0.0 and 1.0 correspond to the struts being located between fuel injectors, while at 0.50 each strut was aligned with an injector centerline. Relative to the structural OGV the smaller blades reduce the associated pressure fluctuations but, not surprisingly, a greater reduction in pressure occurs when the strut wake impinges on the central fuel injector passage. However, comparison with the pre-diffuser exit flow field indicates a rapid mixing out of the strut wake in the dump cavity so it is the shear forces, rather than the pressure forces, which are the dominating influence on strut wake development within the dump cavity. These observations, for the center passage of the fuel injector, support the previously described hot wire measurements made within the dump cavity. Some results are also presented for locations which surround the main barrel of the fuel injector (pitot locations 1, 3 (Fig. 3(*a*))), for which the observed pressure fluctuations are more complex (Fig. 10). These results are repeatable and do indicate sensitivity to the upstream OGV/pre-diffuser geometry. It appears though the whole flow pattern, within the cowl region, is modified rather than just a simple case of impinging wake flows. However, there is some concern that the upstream influence of swirl vanes, which are absent in this configuration, could influence the flow behavior around the fuel injector and the measured stagnation pressures may be affected by misalignment of the Pitot probes with the local flow field.

These measurements indicate the sensitivity of the fuel injector flow to the wakes and other nonuniformities issuing from the prediffuser. It is also interesting to note that in nonstrutted systems the number of compressor OGVs is not an integer number of flame tube burner sectors. Hence, potential sector to sector variations could arise as the position of upstream blades vary, within each sector, relative to the fuel injector. What is difficult to asses though is the relative importance of these effects. For example, relative to the pressure loss of the flow passing to each feed annulus, as indicated on each diagram (Figs. 9 and 10), the pressure variations are relatively large. Of more significance though is the magnitude of these variations relative to the fuel injector pressure drop.

Stagnation Pressure Measurements at Fuel Injector Exit (Engine Representative Flame Tube Fuel Injectors). For the long chord (structural) OGV the stagnation pressure variations, with upstream blade row location, are presented for each passage (Fig. 11).

(a) Core Flow. The magnitude of these variations are comparable with that measured at inlet to the center passage of the simulated fuel injector. Furthermore these variations in the pressure coefficient value, between 0.0 and −0.30, can be compared with the value of −1.4 based on the stagnation pressure at X2 and the static pressure measured within the combustor

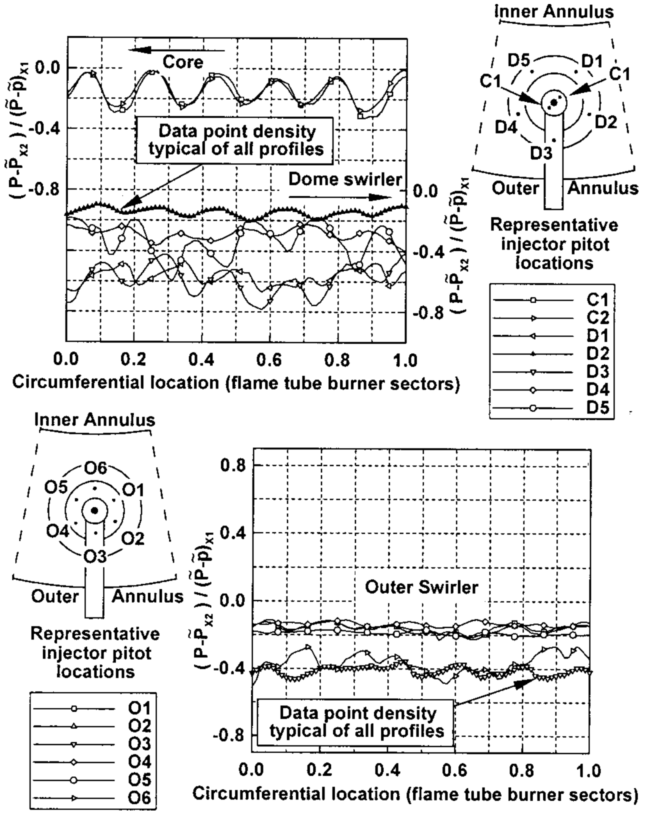

Fig. 11 Engine representative fuel injector stagnation pressure distributions—long chord outlet guide vane (OGV)

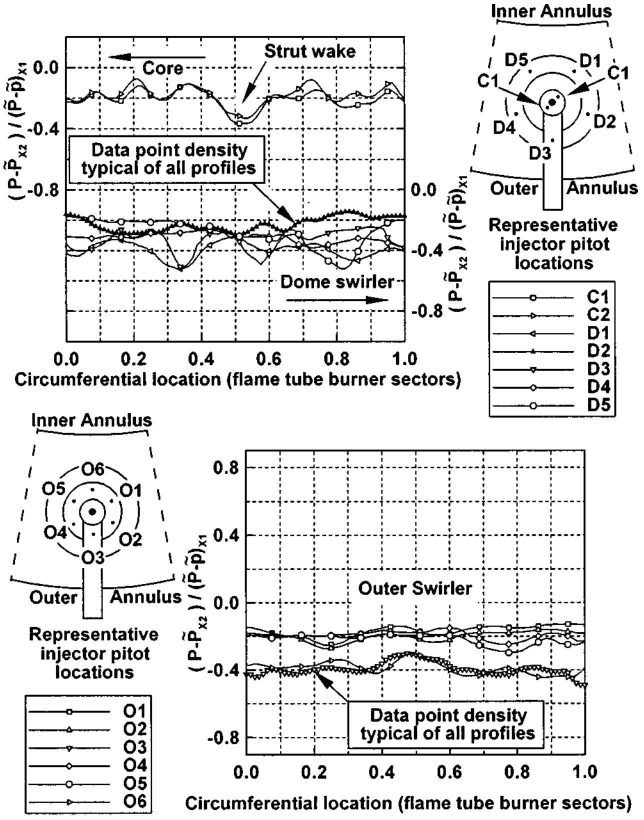

Fig. 12 Engine representative fuel injector stagnation pressure distributions—standard strut, short chord outlet guide vane (OGV)

(b) Outer Swirler Flow. This appears relatively insensitive to the presence of wakes and other circumferential variations of the flow field issuing from the pre-diffuser. However, differences in the overall pressure levels are observed due, it is thought, to the general way in which flow is supplied to the fuel injector. For example the stagnation pressure is relatively low behind the fuel injector feed arm (O3) and in the diametrically opposite location (O6). This supports previous work where it was thought flow of high pressure is supplied to each side of the fuel injector (O1, O2, O4, O5) because these positions are aligned with pre-diffuser exit, whereas O3 and O6 are, respectively, in line with a fuel injector arm and outside the exit diameter of the pre-diffuser. These regions are therefore supplied with low pressure flow due to either (i) this fluid originating from the pre-diffuser boundary layer or (ii) this fluid entering the cowl either side of the fuel injector and then migrating around the injector. These changes to the general pressure levels are of comparable magnitude to the circumferential variations due to blade wakes for the core flow.

(c) Dome Swirler Flow. Flow within the dome passage exhibits some sensitivity to the upstream OGV blade row position. However, relative to the core the pressure variations are more erratic. In addition, general differences in the overall pressure level due to the combustor geometry are apparent. For example, low pressure is recorded in that region of the passage downstream of the fuel injector feed arm (D3).

Results for the strutted pre-diffuser system are similar to those for the long chord (structural) OGV (Fig. 12) although a general reduction of the pressure variations, with OGV/pre-diffuser rotation, is observed. This is thought to be due to both the less well-defined blade wakes and the more axial flow issuing from the pre-diffuser when struts are present ([8]). Not surprisingly for the core flow the stagnation pressure is at a minimum when the struts and fuel injectors are aligned. For the outer swirler passage the same changes in overall level are observed while for the dome passage both the general levels and the circumferential variations appear to be reduced relative to the long chord structural system. This passage is thought to be particularly sensitive to the axial alignment of flow issuing from the pre-diffuser and the presence of any residual swirl.

Pneumatic Measurements Within the Flame Tube (Engine Representative Flame Tube Fuel Injectors). Pressure measurements were made to establish what effect the observed stagnation pressure distributions, within the swirler passages, had on the isothermal flow field produced by the fuel injectors within the flame tube. Although this represents a complex measurement environment with varying pressure gradients, raising some reservations concerning the indicated magnitudes, the instrumentation is thought adequate for detecting a relative change in the flow field. Furthermore, measurements were actually undertaken at three planes within the flame tube ([10]), but results are only presented for the plane 0.5 core diameters (10 mm) downstream of the fuel injector exit.

To establish if the pressure variations associated with the long chord (structural) OGV blade wakes have a significant effect, on the fuel injector flow field, measurements were obtained with the OGV/pre-diffuser assembly located at six different circumferential positions. This range of positions corresponded to an OGV blade space and, at each position, circumferential and radial traverses were performed within the flame tube. Circumferential distributions of stagnation pressure, total, and axial velocity are presented (Fig. 13) for the two profiles exhibiting the largest differences. At this location portions of the core, outer and dome passage flows can be identified but differences between the profiles are also apparent, i.e., the profile changes with upstream location of the OGV blades. The velocity distributions 10 mm downstream of the

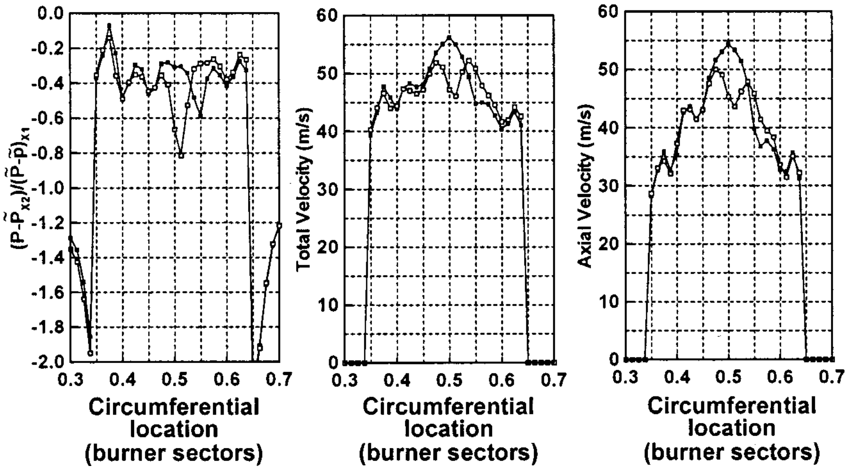

Fig. 13 Circumferential profiles 10 mm downstream of engine representative fuel injector—long chord structural outlet guide vane (OGV)

fuel injector indicate the large variations that arise, particularly for the core passage flow, as the OGV position varies relative to the fuel injector. The stagnation pressure variations are consistent with those measured within, and upstream of, the fuel injector. Furthermore these pressure variations, which were approximately 20 percent of the total pressure drop across the fuel injector, are consistent with the 10 to 15 percent velocity variations observed within the flame tube. Such variations imply possible variations in air flow mixing patterns and hence fuel/air ratio.

For the strutted system similar profiles were obtained as the OGV/pre-diffuser was positioned at five different locations and with the strut approximately midway between fuel injectors. Relative to the long chord (structural) OGV the profile variations are reduced due to the smaller blade wakes. However, a further set of data was obtained with the struts and fuel injectors aligned and, as to be expected, the pressure loss associated with the strut wake has a greater effect on the flow field. Similar circumferential profiles are presented as for the structural OGV case to indicate the differences observed downstream of the fuel injectors (Fig. 14). However, these differences are comparable with the variations observed for the long chord (structural) OGV. This again reinforces the view that within the dump cavity shear forces dominate the strut wake development rather than pressure forces. However, one area of concern is the shedding of vortices from the struts, as indicated by the well-defined frequency measured within the dump cavity. Although the remnants of this process are not evident at many locations, there are regions within the flame tube where these vortices could still be observed (Fig. 15).

Conclusions

Tests have been performed on a fully annular facility and an assessment has been made of the development of nonuniformities, within the diffuser system, and their impact on the flame tube fuel injector flows. The following conclusions have been drawn:

- Downstream of the OGV blade row the steep velocity gradients, and hence high shear stresses, lead to an initial rapid mixing of each blade wake. However, as the wakes thicken and the shear stresses reduce the rate of mixing decreases and, furthermore, the applied pressure gradients have greater significance. The wakes observed at pre-diffuser exit therefore pass through the dump cavity so that pressure variations, associated with the blade wakes, are observed in the vicinity of the flame tube fuel injectors.
- Mixing of the wakes generated by radial struts, located within the prediffuser, occurs within the dump cavity but the associated flow field variations presented to the fuel injectors are greater than those associated with the OGV wakes. Furthermore vortex shedding from these struts was detected within the dump cavity, with

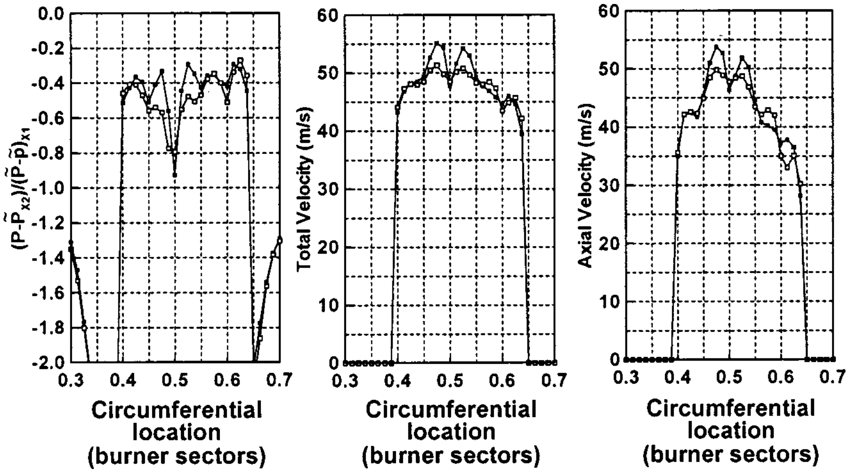

Fig. 14 Circumferential profiles 10 mm downstream of engine representative fuel injector—standard strut (short chord outlet guide vane (OGV))

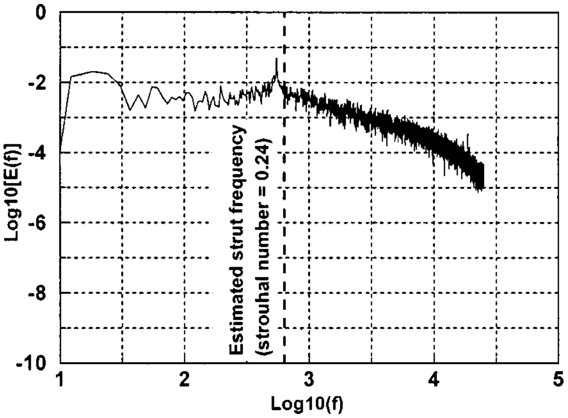

Fig. 15 Frequency spectra upstream and downstream of engine representative fuel injector—standard strut (short chord outlet guide vane (OGV))

Strouhal numbers of between 0.24 and 0.21, and remnants of this vortex shedding were observed, in certain cases, downstream of the fuel injectors within the flame tube.

- The local variation in stagnation pressure delivered to the fuel injector, due to OGV blade wakes, was of order 20 percent of the pressure drop across the fuel injector. The fuel injector core flow was most sensitive to the OGV wakes although the dome swirler passage was also sensitive to the presence of these wakes. Furthermore, within the outer and dome swirler passages variations in overall pressure around each passage were observed due to the way flow is supplied to the fuel injector. For example pressures were relatively high each side of the fuel injector and low behind the fuel injector feed arm and towards the inner annulus.
- Immediately downstream of each fuel injector there is evidence that the flow field is influenced by the upstream blade and strut wakes. Velocity variations of order 15 percent were observed which are broadly consistent with the observed pressure variations presented to the fuel injectors by these components

Although these measurements cannot quantify the impact on fuel/air mixing and energy release within the flame tube, they do indicate that nonuniformities in the approach flow can affect the mixing pattern generated within the flame tube. However, in addition to the potential impact on overall performance it should be remembered that such variations may contribute to observed sector to sector variations. This is because usually the number of OGVs is not an integer number of flame tube burner sectors.

Acknowledgments

This work has been carried out with the support of Rolls-Royce PLC, Bristol and the Defense Research Agency, Pyestock. The authors would also like to acknowledge Messrs. D. Glover, L. Monk and W. Nivin for their assistance in the manufacture of this test rig and to Mr. A. P. Wray for his help in the mechanical design of this facility. In addition, the help of Dr. Paul Denman, in obtaining the hot wire measurements, and the comments of Prof. S. J. Stevens are also greatly appreciated.

Nomenclature

A = area
C = OGV or strut chord
f = frequency
h = annulus passage height
l = characteristic length
L = diffuser axial length
m = mass flow
OGV = compressor outlet guide vane
P, p = local stagnation, static pressure
r = radius relative to rig centerline
r_i, r_o = inner casing, outer casing radius relative to rig centreline
t = strut thickness
Str = Strouhal number (fl/U)
T = ambient temperature K
u = local axial velocity
u_c = wake centerline velocity
U = axial velocity, freestream velocity
Va = flow axial velocity through rotor
x, y = coordinates along diffuser axis and perpendicular to it
β = wake relative wake depth $(U-u_c)/U$
ε = eddy viscosity
θ = wake momentum thickness $\int(u/U)/((1-u/U)dy)$

Superscripts

$-$ = mass weighted spatial mean value

Subscripts

Xn = stations prior to dump cavity (Fig. 1)
CS, n = Pitot position within simulated fuel injector
Cn, Dn = Pitot positions within core and dome passages of engine representative fuel injectors
On = Pitot positions within outer passages of engine representative fuel injectors

References

[1] Carrotte, J. F., McGuirk, J. J., and Stevens, S. J., 1995,"Diffuser Aerodynamic Design—The Impact of Developments in Combustor Technology," Proceedings of the XII ISABE (International Symposium on Air Breathing Engines) Conference, F. S. Billig, ed, Melbourne, Australia, Sept. pp 1033–1044.
[2] Klein, A., 1995, "Characteristics of Combustor Diffusers," Prog. Aerosp. Sci., **31**, pp. 171–271.
[3] Stevens, S. J., and Williams, G. J., 1980, "The Influence of Inlet Conditions on the Performance of Annular Diffusers," ASME J. Fluids Eng., **102**, Sept.
[4] Stevens, S. J., Harasgama, S. P., and Wray, A. P., "The Influence of Blade Wakes on Combustor Shortened Pre-diffusers," J. Aircr., **21**, No. 9.
[5] Klein, A., 1988, "The Relation Between Losses and Entry Flow Conditions in Short Dump Diffusers for Combustors," Z. Flugwiss. Weltraumforsch.
[6] Carrotte, J. F., Bailey, D. W., and Frodsham, C. W., 1995 "Detailed Measurements on a Modern Combustor Dump Diffuser System," ASME J. Eng. Gas Turbines Power, **117**, pp. 678–685.
[7] Madden, T. J., Schlein, B. C., and Wagner, B., "Cascade Pre-diffuser Performance Evaluation," Paper no. AIAA-88-3275.
[8] Barker, A. G., Carrotte, J. F., and Frodsham, C. W., 1997, "The Effect on Combustor Diffuser Performance of Structural OGV/Pre-diffuser systems," ASME 97-GT-304.
[9] Wray, A. P., and Carrotte, J. F., "The Development of a Large Annular Facility for Testing Gas Turbine Combustor Diffuser Systems," Paper no. AIAA 93-2546.
[10] Barker, A. G., and Carrotte, J. F., 1998, "Strutted Pre-diffuser Studies Summary," Dept. of AAETS, Report No. TT98r04.
[11] Hill, P. G., Schaub, U. W., and Senoo, Y., 1963, "Turbulent Wakes in Pressure Gradients," ASME J. Fluids Mech., pp. 518–524.
[12] Lieblein, S., 1965, "Experimental Flow in 2D Cascades," *The Aerodynamic Design of Axial Flow Compressor*, NASA SP36, Chapter 5.
[13] Yang, J. T., Tsai, G. L., and Wang, W. B., 1994, "Near-Wake Characteristics of Various V-Shaped Bluff Bodies," J. Propul. Power, **10**, No. 1.
[14] Roshko, A., 1955, "On the Wake and Drag of Bluff Bodies," J. Aeronaut. Sci., **Feb**.
[15] Bearman, P. W., 1967, "On Vortex Street Wakes," J. Fluid Mech., **28**, Part 4, pp. 625–641.
[16] Sherwood, D., Rolls-Royce, private communication.
[17] Stevens, S. J., Nayak, U. S. L., Preston, J. F., Robinson, P. J., and Scrivener, C. T. J., 1978, "Influence of Compressor Exit Conditions on Diffuser Performance," J. Aircr., **15**, No. 8.

Forced Oscillations in Combustors With Spray Atomizers

M. Zhu

A. P. Dowling

K. N. C. Bray

Department of Engineering,
University of Cambridge,
Trumpington Street,
Cambridge CB2 1PZ, UK

Most types of combustion-driven devices experience combustion instabilities. For aeroengine combustors, the frequency of this oscillation is typically in the range 60–120 Hz and is commonly called "rumble." The rumble oscillations involve coupling between the air and fuel supplies and unsteady flow in the combustor. Essentially pressure fluctuations alter the inlet fuel and air, thereby changing the rate of combustion, which at certain frequencies further enhances the pressure perturbation and so leads to self-excited oscillations. The large residence time of the liquid fuel droplets, at idle and subidle conditions, means that liquid and gaseous phases must both be considered. In the present work, we use a numerical model to investigate the forced unsteady combustion due to specified time-dependent variations in the fuel and air supplies. Harmonic variations in inlet air and fuel flows have been considered and the resulting unsteady combustion calculated. The influence of droplet size distribution has also been investigated. The calculations provide insight into the interaction between atomization, unsteady combustion, and flow oscillations. [DOI: 10.1115/1.1396841]

1 Introduction

Most types of combustion-driven devices experience combustion instabilities. These instabilities can cause serious problems, such as mechanical vibration, noise, enhanced corrosion, and unpredictable performance. Combustors with fuel-spray atomizers are particularly susceptible to a low-frequency oscillation at idle and subidle conditions. For aeroengine combustors, the frequency of this oscillation is typically in the range 60–120 Hz and is commonly called "rumble." In the past, this has caused an audible, and sometimes disturbing noise in the aircraft cabin. However, combustors are required to have ever wider operating ranges and reduced emissions, and this is leading to design changes which can greatly increase the susceptibility to rumble. Radiated sound levels due to rumble have become excessive, and in some cases the pressure fluctuations have been so intense that they stall the engine. Industry has a pressing need for a better understanding of this instability, if it is to be able to predict the effect of design changes. This should enable aeroengine manufacturers to design combustors which run quietly with low emissions, resulting in obvious benefits for both aircraft passengers and people living near airports.

The rumble oscillations involve coupling between the air and fuel supplies and unsteady flow in the combustor. Essentially pressure fluctuations alter the inlet fuel and air flow rates, thereby changing the rate of combustion, which at certain frequencies further enhances the pressure perturbation and so leads to self-excited oscillations. The large residence time of the liquid fuel droplets, at idle and subidle conditions ([1]), means that liquid and gaseous phases must both be considered. The full problem of self-excited oscillation in burners with fuel-spray atomizers is therefore highly complex: It involves a coupled analysis of unsteady two-phase flow, turbulent combustion, and acoustics. In the present work, we have concentrated on the most speculative part, using a numerical model to investigate forced unsteady combustion due to specified time-dependent variations in the fuel and air supplies.

The chosen combustion model involves a Monte Carlo simulation of the Williams' spray equation, together with the equations of turbulent reactive flow, in the form of transport equations for the gas-phase flow field. The spray combustion model has been extended to predict the modulation in the distribution of heat release rate due to specified variations in the fuel mass flow rate and droplet size distribution produced by the fuel injector. These combustion models have been applied to the aeroengine geometry.

In next section, the mathematical models used in the calculations are briefly described. We have investigated the effect of forced fluctuations in the fuel and air supplies to the atomizer. Several test cases were devised and calculated to examine the possible causes of the rumble phenomenon. The results of numerical calculations are described in Section 3. The response of heat release rate due to inlet forcing and the transfer function are analyzed in Section 4. Finally, general conclusions and further work are discussed.

2 Mathematical Models

The gaseous flow field is modeled though the equations of motion in Favre ensemble-averaged form. Source terms appear in the continuity and momentum equations due to evaporation and the force exerted by the liquid phase. The frequency of the rumble oscillation is far below typical turbulent eddy frequencies so quasi-steady flow conditions will prevail. The turbulence time scales, as well as the local turbulence intensity, are therefore obtained by the well-known $k-\epsilon$ turbulence model, which is known to give satisfactory predictions of a gas turbine combustor flow field under steady flow conditions.

In the simulation, the coupling between the turbulence and the chemical reaction is considered by the laminar flamelet presumed pdf method. The fuel used in the calculations is kerosene. The thermo-chemistry is described in terms of the mixture fraction and its variance, which are obtained by solving their transport equations together with momentum and $k-\epsilon$ equations. The mixture fraction distribution is represented by a beta function, which has been shown to be a good approximation for turbulent jets. The laminar flamelets have been computed and stored in a library, from which values are "drawn" by interpolation during the computation.

The description of the spray is based on Williams' spray equation ([2]). This equation can be written as

$$\frac{\partial f_s}{\partial t}+\frac{\partial}{\partial x_i}[U_i f_s]=-\frac{\partial}{\partial U_i}[F_i f_s]-\frac{\partial}{\partial R}[\dot{R} f_s]-\frac{\partial}{\partial e}[\dot{Q} f_s], \quad (1)$$

Contributed by the International Gas Turbine Institute (IGTI) of THE AMERICAN SOCIETY OF MECHANICAL ENGINEERS for publication in the ASME JOURNAL OF ENGINEERING FOR GAS TURBINES AND POWER. Paper presented at the International Gas Turbine and Aeroengine Congress and Exhibition, Indianapolis, IN, June 7–10, 1999; ASME Paper 99-GT-302. Manuscript received by IGTI, Oct. 1998; final revision received by the ASME Headquarters, Mar. 1999. Associate Editor: D. Wisler.

where f_s is the droplet number density function in the joint space spanned by x, U, R, and e. Here U is the droplet velocity; F is the total external force on the droplet per unit mass; R denotes the instantaneous droplet radius, and $\dot{R}$ is its rate of change. $\dot{Q}$ is the rate of change of a droplet's internal energy e. The solution to this spray equation is obtained by means of a Monte Carlo method. The Lagrangian equations for trajectory, velocity, size, and temperature are solved. The droplet dispersion in a turbulent flow is calculated according to the Gaussian distribution ([3]).

The characteristics of the spray to be described in the inlet boundary condition include mean droplet size, droplet size distribution, droplet number density, and cone angle. The atomizer and fuel spray cone are small and the rumble frequency is much lower than the spray cone breakup frequency. We therefore assume that the fuel spray responds in a quasi-steady way to the flow through the atomizer. From results obtained over a wide test range, Lefebvre drew the general conclusion that liquid viscosity has an effect that is quite separate and independent from that of surface tension ([4]). He suggested the following equation to describe the steady-state airblast atomization droplet diameter

$$\overline{D}_{32}=10^{-3}\left(1+\frac{m_f}{m_a}\right)^{0.5}\left[\frac{(\sigma\rho_f)^{0.5}}{\rho_a U_a}+0.06\left(\frac{\mu_f^2}{\sigma\rho_a}\right)^{0.425}\right], \qquad (2)$$

where $\dot{m}$ is the mass flux rate, ρ the density, μ the dynamic viscosity, and σ the surface tension. The suffices a and f denote the air and liquid in the atomizer, respectively. Once the Sauter mean diameter (SMD) $\overline{D}_{32}$ is obtained, the droplet size distribution can be calculated from the nondimensional expression

$$\frac{dV}{V}=13.5\left(\frac{D}{D_{32}}\right)^3 \exp\left(-3\left(\frac{D}{D_{32}}\right)\right) d\left(\frac{D}{D_{32}}\right), \qquad (3)$$

where dV/V is the volume fraction occupied by droplets within the size range D to $D+dD$. We use Eqs. (2) and (3) to relate the fuel droplet size to the instantaneous air and fuel flow for low frequency fluctuations. The fuel spray cone angle is described by random numbers which are generated according to a gamma distribution. Reference [5] may be consulted for a detailed description of how the calculation was implemented.

3 Numerical Results

The study has been conducted in the idealized two-dimensional section of an axisymmetric annular combustor shown in Fig. 1, and summarized in Table 1. The boundary conditions used in the numerical computation were specified to be representative of an aeroengine at idle. The inlet air stagnation temperature is 366 K, and the stagnation pressure is 225 kPa. The exit static pressure is 195 kPa. This leads to an overall air mass flow rate of 5.7 kg/s. Fuel is equally divided between inlets 1 and 2 and injected at a mass flow rate of 0.06 kg/s, speed 70 m/s. The temperature of this liquid fuel is 288 K. The calculation started from a cold flow, and reached the steady-state solution with artificial relaxation. The time-step was selected to ensure that the acoustic waves travel less than one cell per time-step. A contour plot of the steady-state mean temperature distribution is shown in Fig. 2.

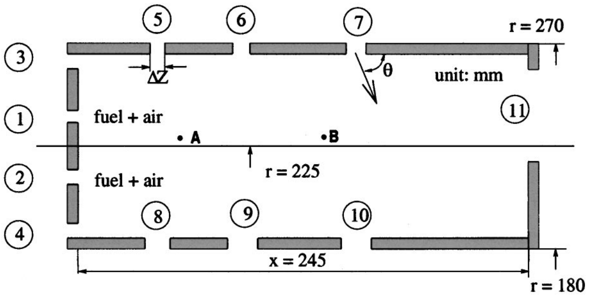

Fig. 1 Schematic diagram of the geometry

The "rumble" unsteadiness is at low frequency and is thought to involve coupling between the combustor and its air and fuel supplies. We have investigated the response to these inlet perturbations through a series of forced calculations. The transfer function between the unsteady flow in the combustor and inlet fluctuations, sinusoidally forced at a single frequency, was also calculated. An advantage of a numerical solution is that we are able to vary parameters in the inlet air and fuel independently and so investigate their relative importance. Although all the variables are coupled to each other in a real situation, it is valuable to decouple them artificially, so that the effects of different factors can be identified separately. In this study, forced sinusoidal oscillations in the gaseous total pressure and in the fuel mass flow rate at the inlets are implemented. In this paper we present sample results in which the frequency of forced oscillation is 65 Hz, and the fluctuation amplitude is equivalent to 20 percent of the mean value of the mass flow rate. The influences of the SMD variation and inlet droplet size distribution are also investigated.

Case 1 Forced Oscillation in Supplied Fuel. First, results for forced oscillations in the injected fuel mass flow rate will be discussed. To separate the influence of changes in the droplet size from the direct effects of fuel flow rate, in the results presented as Case 1, the inlet droplet size distribution is artificially kept fixed as the mean value of SMD. The effects of coupled changes in inlet SMD and distribution due to fuel flow rate as described by Eqs. (2)–(3) are considered in Cases 3 and 4, respectively. The inlet fuel mass flow rate is described by the relationship

$$\frac{m_f(t)}{\overline{m}_f}=1+0.2\sin 400t. \qquad (4)$$

It is essential to understand the interaction between the two phases during the combustion oscillations. For instance, the location of droplet evaporation has the important effects on the mixing and combustion processes. Figure 3 shows the recirculation vortex together with the mass source term due to spray evaporation. It is seen that the majority of droplets evaporate within the recirculation zone. Shown in Fig. 4 is the mixture fraction distribution at the same time. It can be seen that the fuel vapor is distributed and mixed with air by the fluid recirculation. In this region, known as the primary zone, a low-velocity recirculating flow of hot combustion products provides a continuous source of ignition for incoming fuel-air mixture. The mean residence time, estimated from the recirculation time of a fluid particle is roughly 0.003 s in the current calculation.

Figure 5 gives time traces of mixture fraction and heat release rate at two sample points. As shown in Fig. 1, the point A is within the combustion zone, and the point B near the tip of the flame. An increase in the rate of fuel injection leads to an increase in vapor

Table 1 The inlet geometry used in the numerical simulations

Inlet No.	1	2	3	4	5	6	7	8	9	10
x mm	0.0	0.0	0.0	0.0	38.0	77.0	135.0	38.0	77.0	135.0
θ deg	90.0	90.0	90.0	90.0	58.12	51.92	77.859	62.745	57.76	71.91
r mm	238.0	216.0	270.0	180.0	270.0	270.0	270.0	180.0	180.0	180.0
Δz	1.832	2.019	3.572	3.929	3.408	3.030	4.780	5.112	9.415	7.624

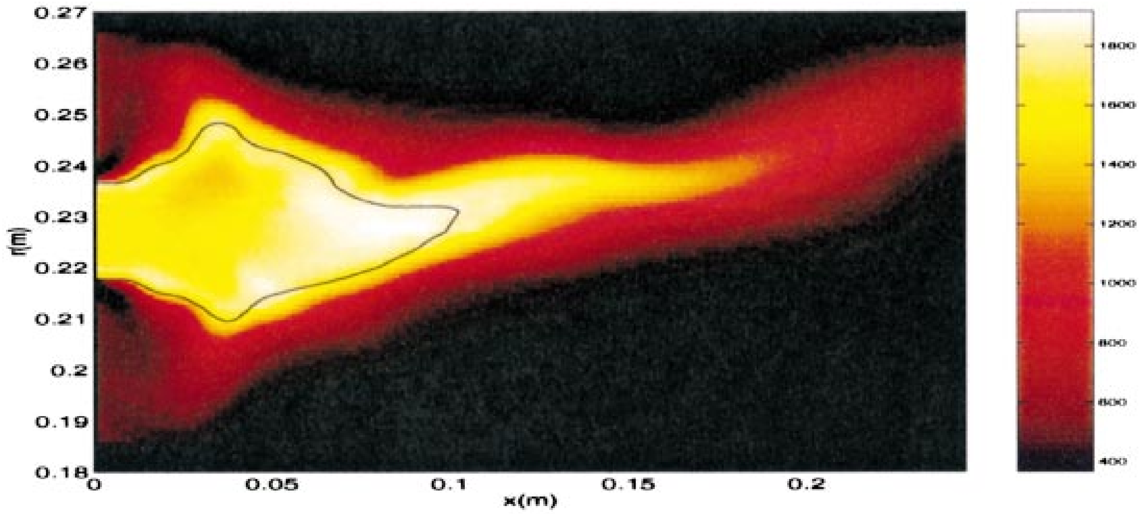

Fig. 2 Contour plot of the mean temperature distribution at idle conditions. The black line indicates the mean position of the stoichiometric curve.

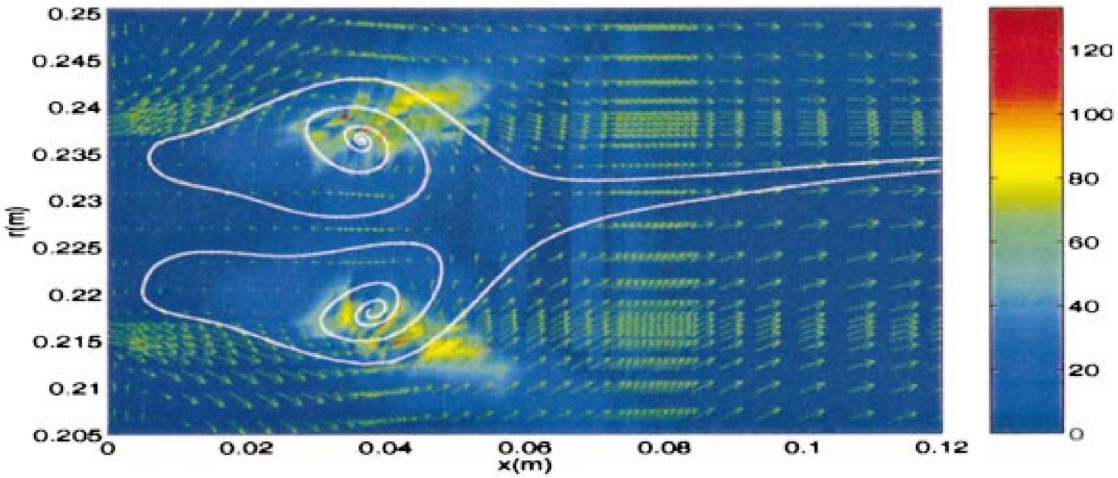

Fig. 3 Contour plot a typical fuel vapor evaporation rate distribution at idle conditions. The white line indicates an instantaneous stream line originating in the recirculation zone. The arrows denote velocity vectors.

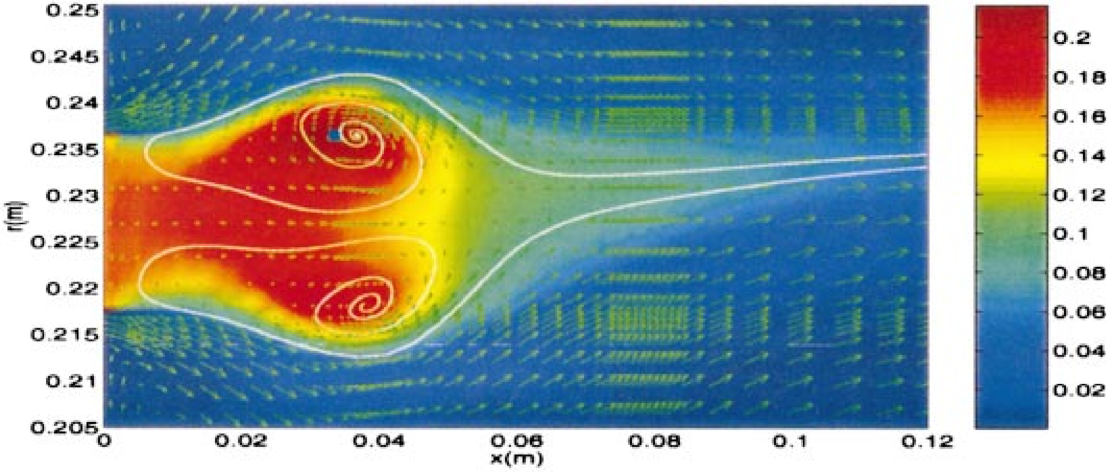

Fig. 4 Contour plot of a typical Favre-averaged mixture fraction at idle conditions. The white line indicates an instantaneous stream line originating in the recirculation zone. The arrows denote velocity vectors.

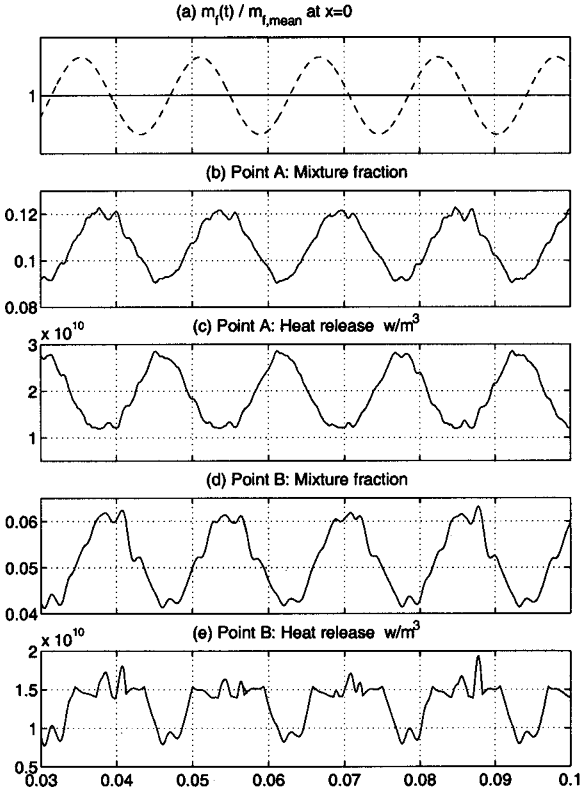

Fig. 5 Case 1: Sinusoidal changes of the fuel mass flow rate in the atomizer lead to the oscillations in the mixture fraction and heat release rate at points A and B

mixture fraction with a convective time delay. For medium size droplets, the convection times from the atomizer to points A and B are larger than the droplet lifetimes. Therefore the droplet evaporation time does not significantly affect the time delays. The time delay to point A is consistent with the recirculation time, while the additional time delay between points A and B is caused by the convection. The fractional amplitude of the perturbation in mixture fraction at points A and B is about 20 percent just as in the inlet disturbance in Eq. (4). The influence of mixture fraction on the rate of heat release depends on whether the mixture is weaker or stronger than stoichiometric value. For a given variance in mixture fraction, which is mainly affected by turbulence, the laminar flamelet library gives a maximum rate of heat release when the mixture fraction is equal to its stoichiometric value of 0.0682 for kerosene (an equivalence ratio of unity). When well below the stoichiometric value, an increase in mixture fraction increases the rate of heat release, whereas above it the rate of heat release is reduced as the mixture becomes richer. This observation explains the phase relationship between the rate of heat release and unsteady fuel addition in Fig. 5. As shown in Fig. 5(*b*), the mixture fraction is larger than the stoichiometric value at point A. An increase in the fuel flow rate further increases the mixture fraction and the rate of heat release/unit volume decreases accordingly (see Fig. 5(*c*)). On the other hand, for the case in Fig. 5(*d*) at the point B, the average mixture fraction is smaller than the stoichiometric value, so that the rate of heat release increases in phase with an increase in mixture fraction.

Case 2 Forced Oscillation in Supplied Air. In this part, the results of the forced oscillations in the total pressure of the air inlets 1 and 2 will be discussed. As in Case 1, in order to separate the effects of droplet size distribution from the forced oscillation, the inlet droplet size was artificially fixed at its mean value. Figures 6(*b*) and 7(*b*) show the distribution of fuel evaporation rate at two times in the cycle, corresponding to a maximum and minimum in inlet air stagnation pressure. Since the distributions of fuel evaporation rate are almost the same, the oscillation of the mixture fraction and heat release rate will be dominated by the air flow rate changes.

Figure 8 shows typical time traces of mixture fraction and heat release rate at sample points A and B. An increase in the total pressure of the air supply leads to more air entering the combustion chamber. The amplitude of the perturbation in the inlet mass flow rate is 20 percentage, just as in Case 1. Comparing with Fig. 5, we can see that the variation of mixture fraction in both cases is of the same order. An increase in supplied inlet air leads to a decrease in the mixture fraction at A with a recirculation time delay (compare the phase of Figs. 5(*b*) and 8(*b*)). In the combustion zone, an increase in the total pressure of air supply has a more complicated effect. It not only has a direct effect of diluting the local vapor/air mixture. It also alters the transport properties, moving the combustion zone further downstream when the air velocity is high. This increases slightly the time delay to point B (see Fig. 8(*d*)). Again as already noted, the mixture fraction is above the stoichiometric value at point A and so the rate of heat release is 180 deg out of phase with mixture fraction, leading to the heat release shown in Fig. 8(*c*). While at the point B, the average value of mixture fraction is smaller than the stoichiometric value, and so the heat release rate is be in phase with the mixture fraction (Fig. 8(*e*)).

Case 3 Effects of Mean Droplet Size. In reality, forced perturbations in the fuel mass flow rate and the total pressure of the gas supplies not only alter the air/fuel mass flow rate, but also the droplet size distribution. In the above calculations, in order to separate the effects of the flow rate and droplet size distribution, inlet droplet size was artificially kept fixed. In the following, coupling between inlet droplet size and the forced oscillation at the inlet boundary is implemented according to Eq. (2). In order to separate the effects of droplet size distribution from the SMD variation, in this part, the sizes of droplets at inlet boundary vary as the instantaneous SMD, but the variance of the droplet size distribution is set as zero.

The variations of the SMD due to fuel and air mass flow rate forcing oscillations are shown as solid lines in Figs. 9(*a*) and 10(*a*), respectively. It is evident that, for same percentage change, the variation of inlet SMD due to fuel mass flow rate oscillation is smaller than due to air mass flow rate oscillation. From Eq. (2), it is seen that an increase of the air mass flow rate and gas velocity lead to a decrease of droplet size due to the larger momentum difference between the two phases.

The effects of the oscillation of the fuel mass flow rate on the time traces of the mixture fraction and heat release rate at the sample points A and B are shown in Fig. 9. Since the influence of the inlet droplet size variation is insignificant, there is no apparent difference from those in Fig. 5.

The effects of unsteadiness oscillation in the total pressure of air supply on the SMD has also been investigated. In this calculation, the variation of inlet droplet size is larger than for the fuel forcing case. It can be seen that this variation is asymmetrical. For the same percentage change of total pressure (air mass flow rate), a decrease in total supplied pressure leads to larger change in droplet size. In this situation, because of the so-called d^2-law, the evaporation time of the larger droplets is much longer than that for droplets with the mean size. The droplet size is minimum when the inlet air total pressure is at its peak. It can be seem from Fig. 6(*c*) that then the fuel evaporates closer to the atomizer. (The heavy red color in Figs. 6 and 7 indicate high rates of fuel evaporation.) The situation a half-cycle later is shown in Fig. 7(*c*). Then the droplets have their maximum size. The location of evaporation is moved downstream due to the longer time required to heat up the droplets. It can also be seen that the amount of fuel vapor is

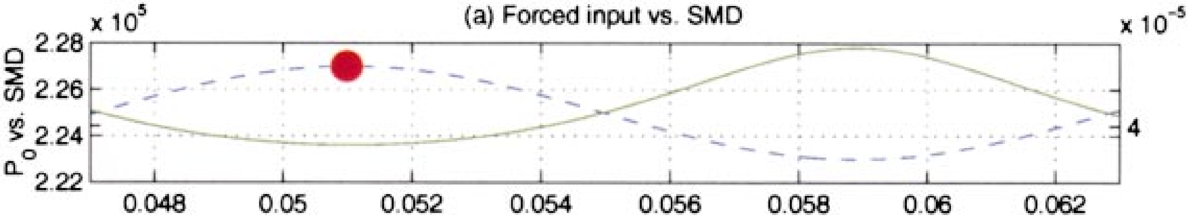
(a) Forced input vs. SMD

(b) Droplet size fixed as mean SMD

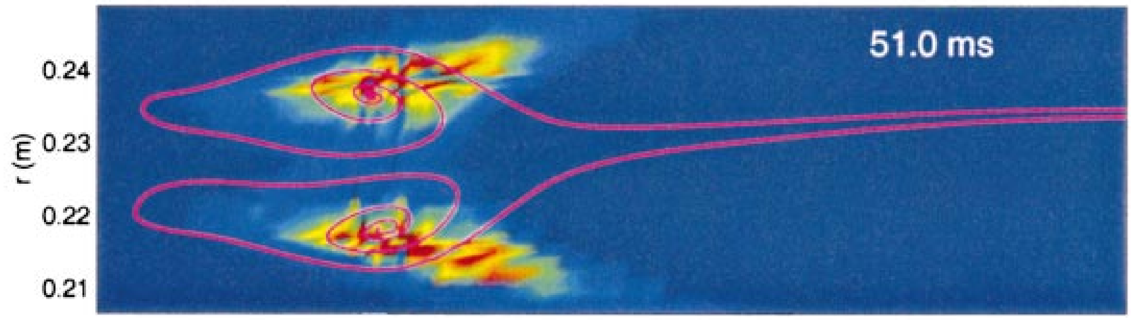

(c) Droplet size varies as SMD with zero variance

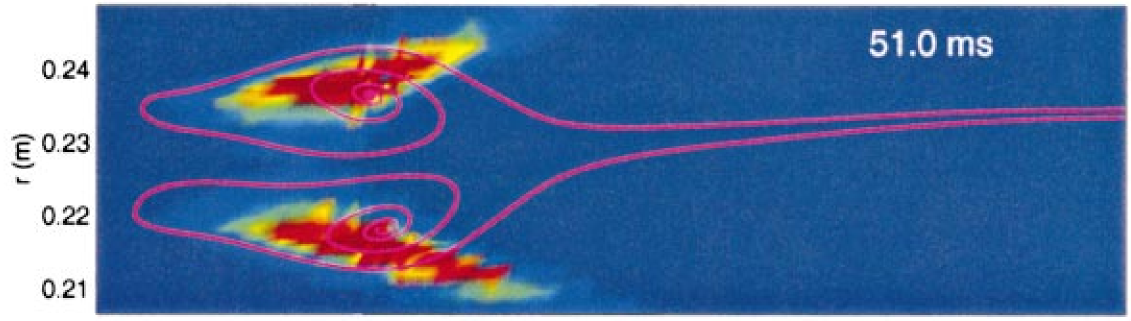

(d) Droplet size varies as SMD with distribution

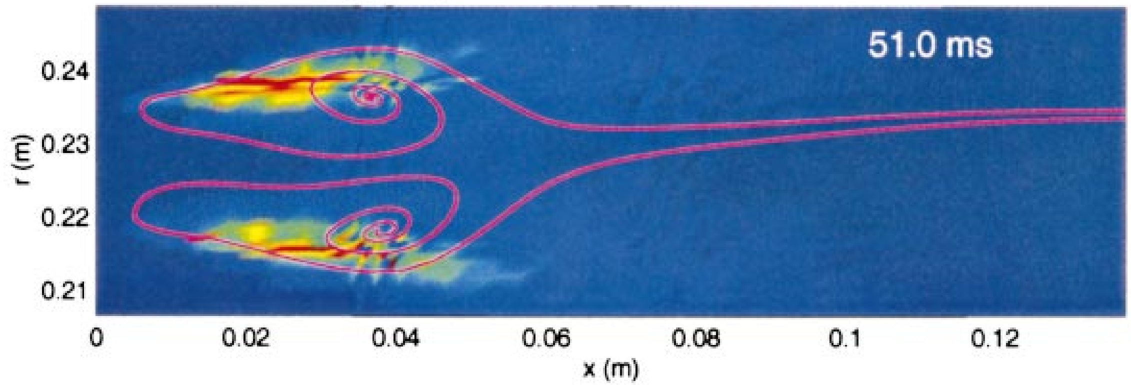

Fig. 6 Instantaneous contour plots of fuel vapor evaporation rate distribution in the air forcing calculations, at the time of maximum inlet air stagnation pressure. The streamline from Figs. 3 and 4 is overlaid in red to indicate the recirculation zone.

less than in Fig. 6(*c*). Actually, at this phase of the oscillation, some droplets are too big to evaporate before they move out the primary zone.

Comparing the time traces of the mixture fraction in Figs. 8 and 10 at points A and B, it can be seen that the mean value of mixture fraction is slightly decreased. This is because some big droplets do not contribute fuel vapor to the primary zone. As a result, the heat release rate will increase in the recirculation zone and decrease downstream. It can also be seen that the variation of droplet size changes the phase relationship between mixture fraction and inlet air, because some droplets are too large to evaporate in the primary zone. Therefore, the change in droplet size due to oscillations in the air velocity through the atomizer plays an important role in the fuel vapor distribution, and has a strong influence on the unsteady combustion that can drive the flow to instability.

Case 4 Effects of Droplet Size Distribution. In this case, the inlet droplet size is described by the variable SMD and size

(a) Forced input vs. SMD

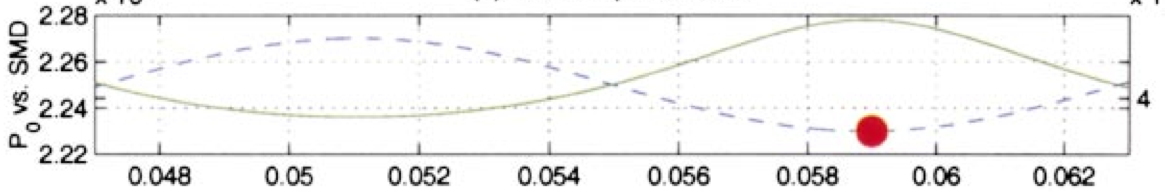

(b) Droplet size fixed as mean SMD

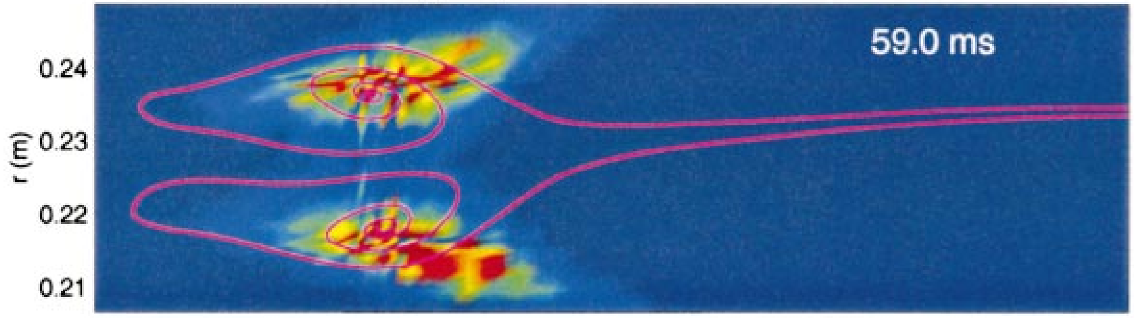

(c) Droplet size varies as SMD with zero variance

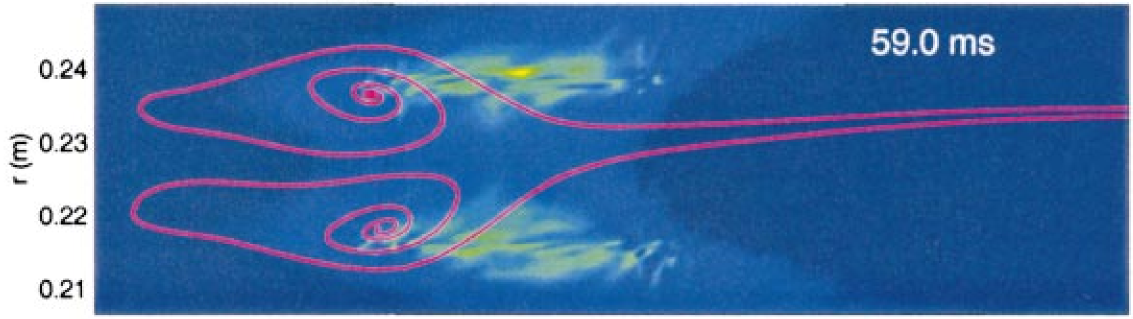

(d) Droplet size varies as SMD with distribution

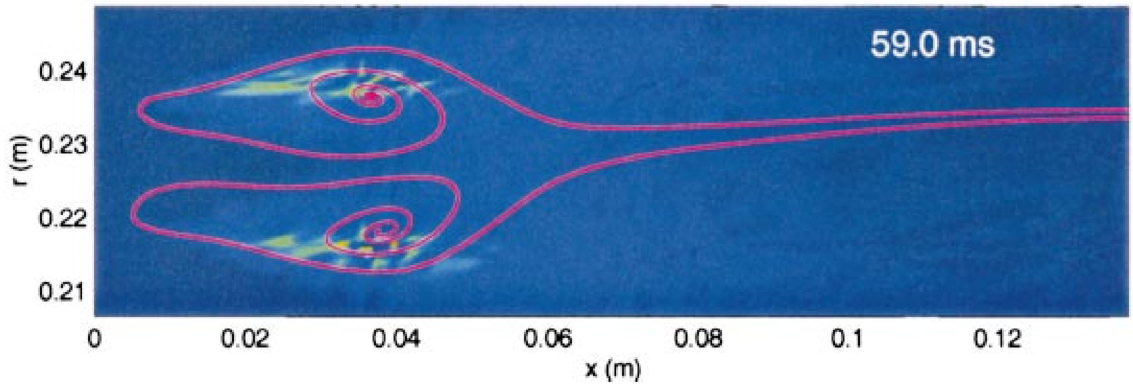

Fig. 7 Instantaneous contour plots of fuel vapor evaporation rate distribution in the air forcing calculations, at the time of minimum inlet air stagnation pressure. The streamline from Figs. 3 and 4 is overlaid in red to indicate the recirculation zone.

distribution according to Eqs. (2) and (3). At each time-step, the inlet droplet size is calculated by the random generation from the instantaneous SMD and distribution. As a result, droplet sizes are distributed in a wide band around the instantaneous SMD. Compared with the previous case, more big droplets in the combustor means that the distribution of fuel vapor will change significantly.

Shown in Figs. 11 and 12 are the local history of mixture fraction and heat release rate in fuel and air forcing cases, respectively. In comparison with Cases 1 and 2, the values of mixture fraction at A are decreased by about 20 percent in the primary zone. This brings the minimum mixture fraction at A to a value close to stoichiometric, leading to a double peak in each cycle in the local rate of heat release (see Figs. 11(*c*) and 12(*c*)). We will see later that since the primary region is weaker, the combustion zone moves forward close to the atomizer exit. This reduces the time delays as is apparent from a comparison of the mixture fraction time histories in Figs. 5 and 11 or Figs. 8 and 12.

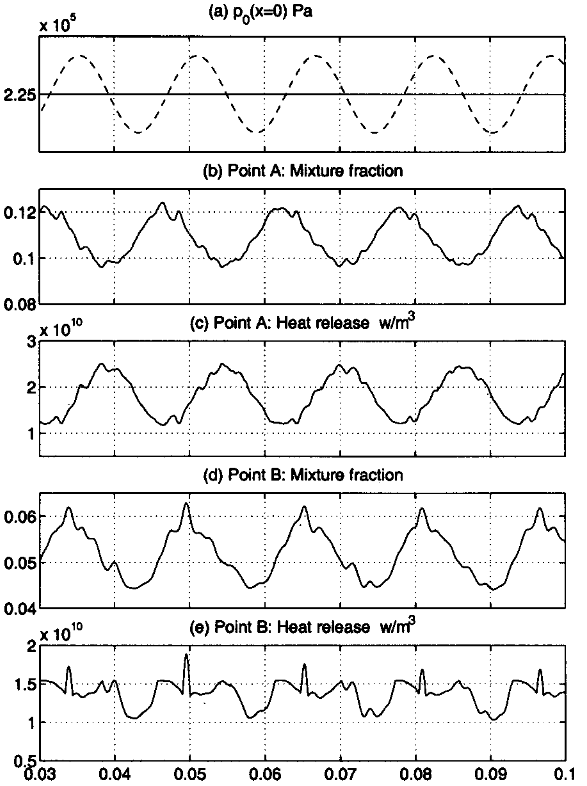

Fig. 8 Case 2: Sinusoidal changes of the total pressure in the air inlets lead to the oscillations in the mixture fraction and heat release rate at points A and B

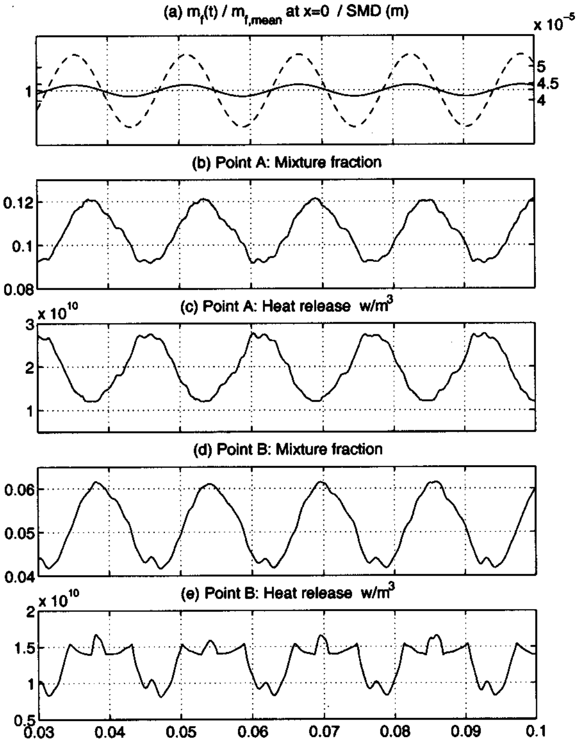

Fig. 9 Case 3: Sinusoidal changes of the fuel mass flow rate in the atomizer lead to the oscillations in the mixture fraction and heat release rate at points A and B

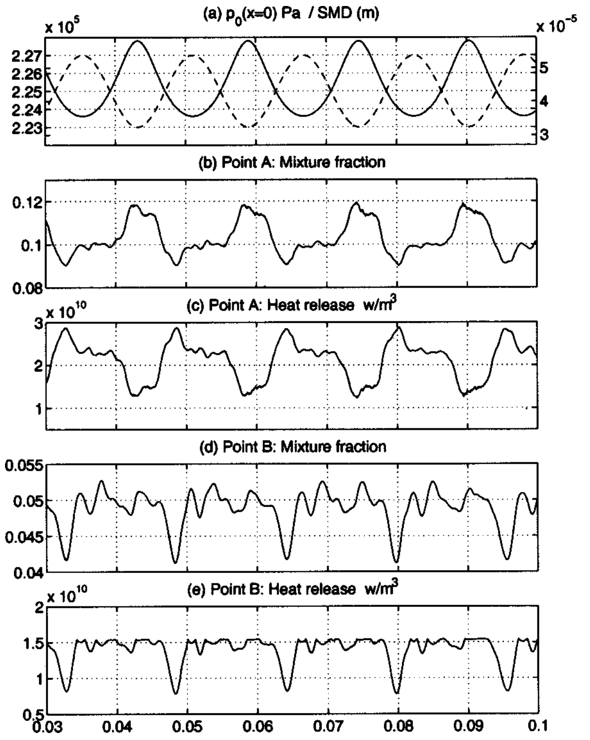

Fig. 10 Case 3: Sinusoidal changes of the total pressure in the air inlets lead to the oscillations in the mixture fraction and heat release rate at points A and B

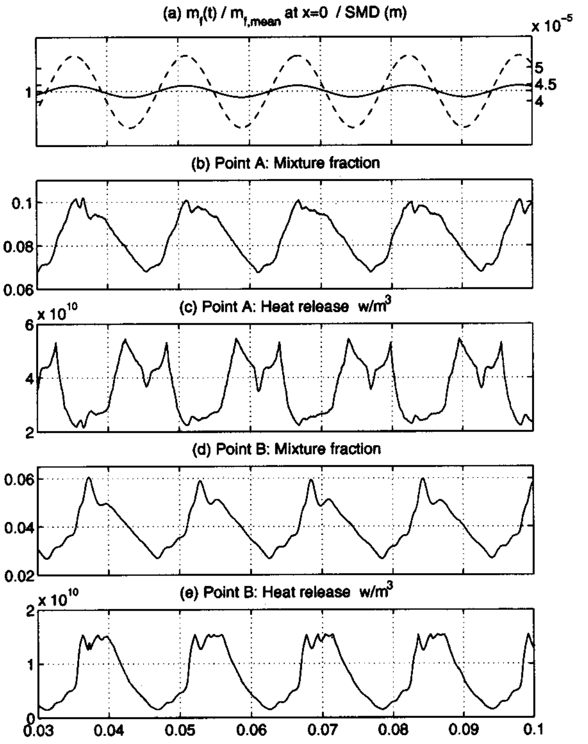

Fig. 11 Case 4: Sinusoidal changes of the fuel mass flow rate in the atomizer lead to the oscillations in the mixture fraction and heat release rate at points A and B

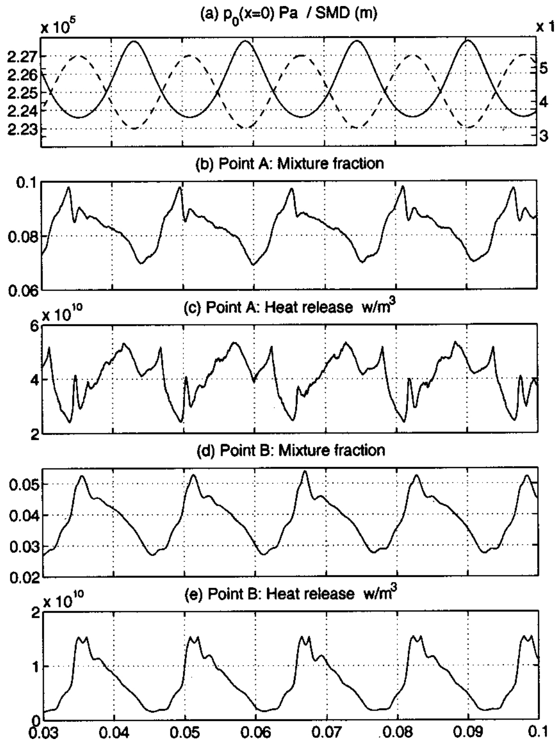

Fig. 12 Case 4: Sinusoidal changes of the total pressure in the air inlets lead to the oscillations in the mixture fraction and heat release rate at points A and B

4 Analysis of Results

Heat Release Rate $q(x,t)$. The unsteady calculations lead to a large amount of flow data. These data can be managed by integration over the combustor cross section to investigate the rela tionship between $q(x,t)$, the rate of heat release/unit length of combustor and the inlet fuel and air flows. The phase relationship between this integrated rate of heat release and the pressure perturbation is crucial to understanding the driving mechanism to instability ([6]). Figure 13 illustrates the change in heat release rate due to the oscillation in inlet fuel. In these plots, we show the heat release rate/unit length, $q(x,t)$, as a function of x and t. The rates of heat release at different x are displaced vertically as indicated by x-values on the ordinate. It is seen that the primary zone, combustion zone, and dilution zone are clearly demonstrated. The length and strength of each zone varies harmonically with the same frequency of forcing oscillation, but with different phase relationships.

Figure 13(b) shows the variation of heat release rate due to the oscillation of fuel mass flow rate, where the droplet sizes are fixed as the mean SMD. Compared with Fig. 5, the trends we saw locally at points A and B are also evident in the area-integrated rate of heat release. The mixture is rich upstream of $x \approx 0.08$ m. In the primary zone, increasing the fuel mass flow rate at inlet leads to a richer mixture fraction, and decreasing heat release rate. An increase in supplied fuel also leads more fuel vapor convected downstream, and consequently, to a modest increase in the length of combustion zone. Downstream of $x \approx 0.08$ m, which correspond to the dilution zone, the mixture fraction is weaker than the stoichiometric value. After a convective time delay, a low-frequency increase in fuel flow rate therefore increases the rate of heat release in this downstream region.

Figure 14(b) illustrates the change in heat release rate due to the oscillation of total air pressure in the inlets 1 and 2. Not surprisingly, through comparison with Fig. 6(b), we can see that the different phase is clearly demonstrated. It is because, as we discussed, the forced oscillation of gas and liquid fuel supplies causes different effects on the variations of mixture fraction and heat release rate.

Figure 13(c) shows a distribution of the rate of heat release little different from that in Fig. 13(b), indicating that the change in inlet droplet size due to the change in fuel flow rate has little effect. In contrast, for air forcing, a comparison of Figs. 14(b) and (c) clearly demonstrated the shift in the combustion zone which moves very close to the exit of the atomizer a short time delay after the droplets reach their maximum size. This can be explained by the long time taken to evaporate these larger droplets. They are convected out of the primary zone before they evaporate. The primary zone is then relatively weak and periodically the combustion zone moves forward to the atomizer.

Figures 13(d) and 14(d) show the area-averaged rate of heat release for fuel and air forcing when the droplet size varies about the instantaneous as SMD in Eq. (3). It is not surprising to see that the length of the primary zone is significantly decreased. In limiting situations, when the fuel mass flow rate is minimum for the fuel forcing case or the SMD maximum for the air forcing case, the mixture fraction is so lean that the primary zone almost vanishes. For the reference signal which is chosen here for the input forcing for the responses of heat release rate are at similar phases.

Transfer Function. The frequency response can be highlighted by evaluating the temporal Fourier transforms of $q(x,t)$ and the input forcing signals. For Case 4, in which the droplet sizes vary around the instantaneous SMD at inlet, the magnitude and phase of the transfer function $\hat{q}(x)/\hat{m}_f$ at the forcing frequency are plotted in Fig. 15. Two regions with distinct and different forms of flame response are now evident. The gradual decrease in phase throughout the region $x > 0.08$ m indicates a convective time delay. Extending this part of the phase curve back to $x = 0$, we find that it passes through the origin, confirmation that throughout the downstream region, where the mixture ratio is weaker than stoichiometric, the rate of heat release is in phase with the mixture fraction, which lags the inlet fuel variation by a convection time delay. The increase in phase between $x = 0$ and 0.06 m indicates a forward convection in the recirculation zone: the supplied fuel droplet evaporation in the center of the recirculation (see Fig. 3) and then the mixture is transported forwards by the recirculating vortex. Near the tip of flame, the rate of heat release is insensitive to fluctuations in mixture fraction and this accounts for the minimum in $|\hat{q}|$ near $x \approx 0.08$ m. Two local maxima in $|\hat{q}|$ near 0.035 m and 0.1 m can be interpreted in terms of the rich and weak locations where the rate of heat release is most sensitive to changes in mixture fraction. As already noted, in the predominately rich combustion zone $x < 0.08$ m the unsteady rate of heat release is approximately out of phase with the rate of fuel supplied.

The transfer function between heat release and forced oscillation in the total pressure of air supply for Case 4 is shown in Fig. 16. It is found that the variation in the amplitude with axial position is similar in form to that due to fuel forcing in Fig. 15. Again there are two local maxima where the rate of heat release is most sensitive to changes in mixture fraction. Near the tip of the flame, the rate of heat release is insensitive to fluctuations in mixture fraction. In the downstream region, the phase of the heat release slowly decreases in the axial direction, indicating an increasing time delay. The rapid change in phase near $x \approx 0.08$ m is because of the different phase relationship between rate of heat release and mixture fraction on the two sides of the stoichiometric curve. The opposite signs of the slopes in the primary zone and the dilution zone mean that the fuel-rich spots move forward in the primary zone due to the recirculation. Whereas, in the dilution zone, the mixture fraction propagates to downstream by convection. Similar conclusions have also been drawn from Fig. 15.

(a) Forced input vs. SMD

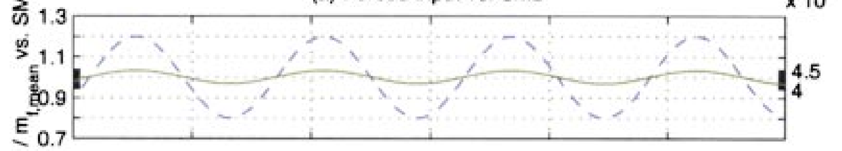

(b) Case 1: Droplet size fixed as mean SMD

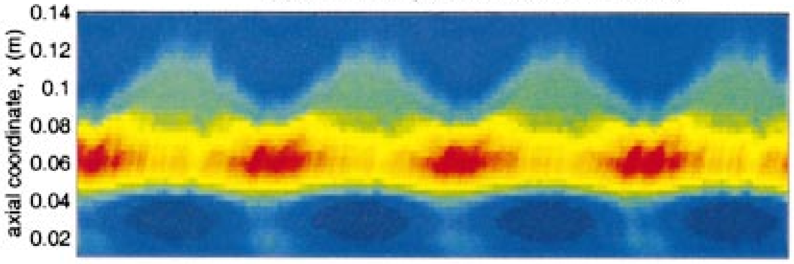

(c) Case 3: Droplet size varies as SMD with zero variance

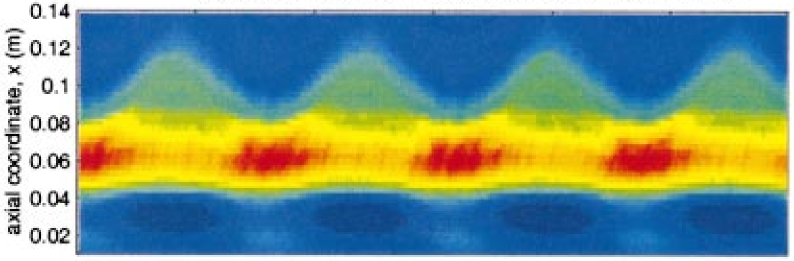

(d) Case 4: Droplet size varies as SMD with distribution

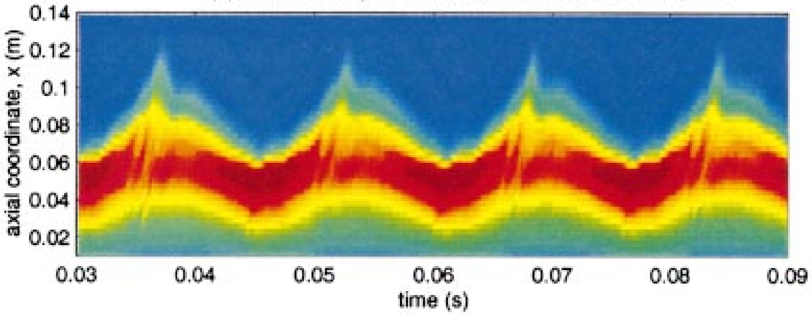

Fig. 13 The variation of the area-averaged rate of heat release/unit length due to the sinusoidal changes of the fuel mass flow rate in the atomizer, which are shown as dash line in (*a*). The solid line indicates the variation of Sauter mean diameter (SMD) according to Eq. (2).

5 Conclusions

The oscillating behavior of spray combustion has been investigated through time-dependent calculations of the combustion process. The coupling between forced oscillations in inlet fuel and air, atomization and chemical kinetic processes greatly influences the dynamical flame behavior. Due to the complexity of this interaction and to identify the main influences on engine rumble, several test cases were calculated. Harmonic oscillation of the inlet fuel and air flows have been considered and the resulting unsteady combustion calculated. The effects of the SMD and droplet size distribution due to these perturbations have also been investigated.

Some conclusions can be drawn from the current study. The change of local heat release rate is influenced by the local variation of the mixture fraction, which is caused by the forced oscillation at the atomizer inlets. The maximum rate of heat release occurs when the mixture fraction is closest to stoichiometric. The phase of the heat release therefore changes across the stoichiometric line. For the same percentage change based on the mass flow rate, perturbations in either air or fuel flow rate through the atomizer produces the same order of fluctuations in the heat release rate. However, since the mean pressure drop across the inlet air is much less than across the fuel supply, pressure fluctuations have a bigger effect on the air flow rate. The main mechanism is that the modulations in the air flow alter the inlet fuel droplet size distribution and hence the local ratio of fuel vapor to oxidizer throughout the combustor, thereby changing the location and time delay to combustion.

Although encouraging results are obtained in the present study, it represents only the first step in the full investigation. Further work will concentrate on (a) development of simple models of the air and fuel supply system so that changes in inlet fuel and air can be coupled to changes in the combustion for simulation of self-excited oscillations, (b) predication of the transfer function between $q(x,t)$, and injected air and fuel flow as functions of frequency, obtained by Fourier transformation of data like that in Fig. 16. This will incorporated into a one-dimensional linear stability analysis ([7]) to interpret the numerical results, to give a

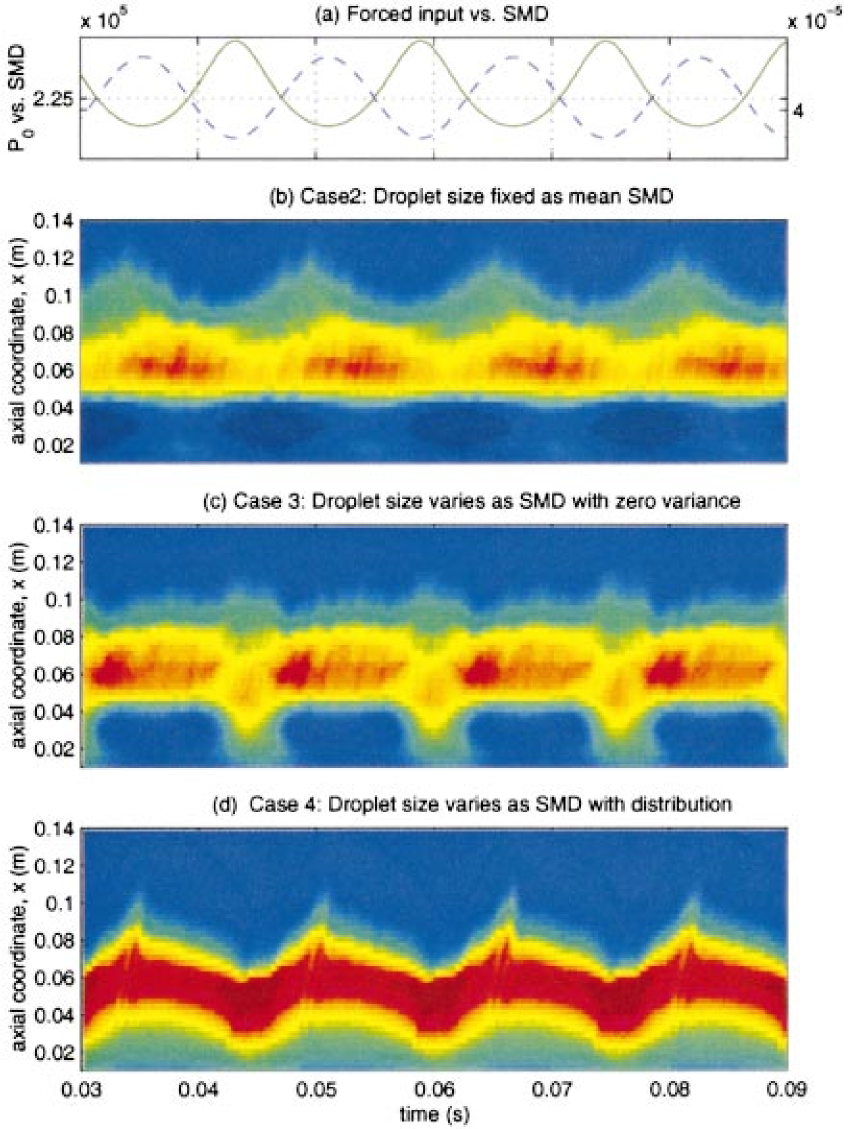

Fig. 14 **The variation of the area-averaged rate of heat release/unit length due to the sinusoidal changes of the total pressure in the air inlets, which are shown as dash line in (*a*). The solid line indicate the variation of Sauter mean diameter (SMD) according to Eq. (2).**

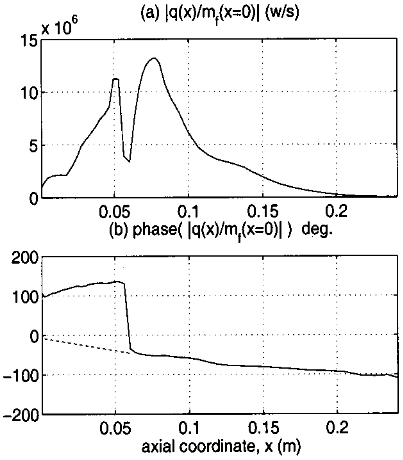

Fig. 15 **The transfer function between the heat release rate per unit length and the sinusoidal changes of the fuel mass flow rate**

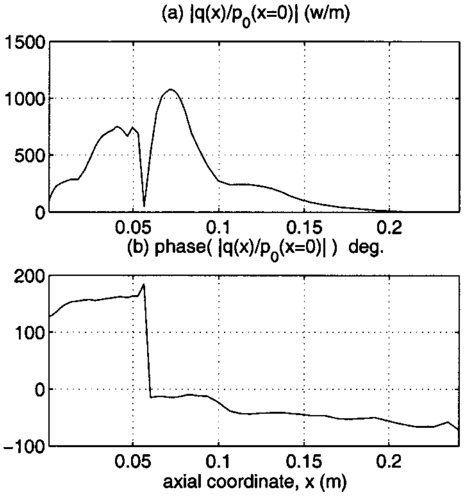

Fig. 16 **The transfer function between the heat release rate per unit length and the sinusoidal changes of the total pressure in the air inlets**

better understanding of the feedback mechanism and to enable extrapolation from the axisymmetric geometry to three dimensions.

Acknowledgment

This work was funded by the Engineering and Physical Sciences Research Council and Rolls-Royce whose support is gratefully acknowledged.

References

[1] Tolpadi, A., 1995, ‘‘Calculation of Two-Phase Flow in Gas Turbine Combustors,’’ ASME J. Eng. Gas Turbines Power, **117**, pp. 695–703.

[2] Williams, F., 1985, *Combustion Theory*, 2 Ed., Benjamin/Cummings, Menlo Park, CA.

[3] Gosman, A., and Ioannides, E., 1983, ‘‘Aspects of Computer Simulation of Liquid-Fueled Combustors,’’ J. Energy, **7**, No. 6, pp. 482–490.

[4] Lefebvre, A., 1989, *Atomization and Sprays*, Hemisphere, New York.

[5] Zhu, M., 1996, ‘‘Modelling and Simulation of Spray Combustion With PDF Methods,’’ Ph.D. thesis, University of Cambridge, Cambridge, UK.

[6] Rayleigh, L., 1896, *The Theory of Sound*, Macmillan, London.

[7] Dowling, A. P., 1995, ‘‘The Calculation of Thermoacoustic Oscillations,’’ J. Sound Vib., **180**, No. 4, pp. 557–581.

Predictions of NO_x Formation Under Combined Droplet and Partially Premixed Reaction of Diffusion Flame Combustors

N. K. Rizk

J. S. Chin

A. W. Marshall

M. K. Razdan

Rolls-Royce Allison,
Indianapolis, IN 46206

A methodology is presented in this paper on the modeling of NO_x formation in diffusion flame combustors where both droplet burning and partially premixed reaction proceed simultaneously. The model simulates various combustion zones with an arrangement of reactors that are coupled with a detailed chemical reaction scheme. In this model, the primary zone of the combustor comprises a reactor representing contribution from droplet burning under stoichiometric conditions and a mixing reactor that provides additional air or fuel to the primary zone. The additional flow allows forming a fuel vapor/air mixture distribution that reflects the unmixedness nature of the fuel injection process. Expressions to estimate the extent of deviation in fuel/air ratios from the mean value, and the duration of droplet burning under stoichiometric conditions were derived. The derivation of the expressions utilized a data base obtained in a parametric study performed using a conventional gas turbine combustor where the primary zone equivalence ratio varied over a wide range of operation. The application of the developed model to a production combustor indicated that most of the NO_x produced under the engine takeoff mode occurred in the primary as well as the intermediate regions. The delay in NO_x formation is attributed to the operation of the primary zone under fuel rich conditions resulting in a less favorable condition for NO_x formation. The residence time for droplet burning increased with a decrease in engine power. The lower primary zone gas temperature that limits the spray evaporation process coupled with the leaner primary zone mixtures under idle and low power modes increases the NO_x contribution from liquid droplet combustion in diffusion flames. Good agreement was achieved between the measured and calculated NO_x emissions for the production combustor. This indicates that the simulation of the diffusion flame by a combined droplet burning and fuel vapor/air mixture distribution offers a promising approach for estimating NO_x emissions in combustors, in particular for those with significant deviation from traditional stoichiometry in the primary combustion zone. [DOI: 10.1115/1.1391280]

1 Introduction

The exhaust concentration of the pollutants produced by gas turbine combustors are governed by mean residence time in the combustion zone, reaction rates, and mixing rates. Oxides of nitrogen (NO_x) are produced in the central hot region of the combustor by the oxidation of the atmospheric nitrogen, and most of the NO_x emitted in the exhaust is nitric oxide (NO). Conventional gas turbine combustors operating on typical diffusion flame concepts emit significant levels of NO_x due to the high temperatures associated with fuel droplet burning. In order to limit the formation of NO_x in this widely used combustor type, significant modifications to the fuel/air stoichiometry is needed in the combustor. These modifications may require a fuel staging strategy in the combustor design in order to operate satisfactorily over the gas turbine engine operating envelope.

To meet the often conflicting requirements of enhanced performance and minimized pollutant formation, improved design tools are needed to guide the combustor design. Lefebvre [1] utilized a large data base obtained for several production engines to reach a quantitative relationship for NO_x emission. In his calculation method, the combustion process is simulated by global expressions. NO_x present in the exhaust is assumed to vary with the system pressure raised to a power of 0.25, residence time in the primary zone, and an exponential term that includes the stoichiometric temperature. Plee and Mellor [2] defined a mean characteristic time in the combustion recirculation zone to provide such important parameter as ignition, blowout, carbon monoxide (CO), and NO_x.

The obvious advantages offered by these global expressions for conventional combustors are the simplicity and capability of providing overall performance parameters of conventional combustors. The success of such approaches relies on the accurate estimation of important parameters including length or volume of the combustion zone, recirculation zone characteristics, fraction of total air utilized in primary zone combustion, and fuel spray characteristics. The application of the global methods to low emissions combustors concepts is, however, limited due to the deviation from the conventional primary zone stoichiometry adopted in these combustors. For example, the need to use a fuel lean primary zone to minimize the formation of NO_x will require the development of a design tool that reflects the different stoichiometry used in this approach. This is needed to enable predicting the impact of changes in the combustor configuration and air distribution on performance.

One approach applied to gas turbine combustors divides the combustor into a number of reactors in series or in parallel to simulate various combustion regions. Fletcher and Heywood [3]

Contributed by the International Gas Turbine Institute (IGTI) of THE AMERICAN SOCIETY OF MECHANICAL ENGINEERS for publication in the ASME JOURNAL OF ENGINEERING FOR GAS TURBINES AND POWER. Paper presented at the International Gas Turbine and Aeroengine Congress and Exhibition, Indianapolis, IN, June 7–10, 1999; ASME Paper 99-GT-357. Manuscript received by IGTI, Oct. 1998; final revision received by the ASME Headquarters, Mar. 1999. Associate Editor: D. Wisler.

modeled the combustor primary zone as (1) a partially stirred reactor burning fuel over a distribution about the mean equivalence ratio, (2) a lateral reactor, and (3) a plug flow reactor. The discrepancy observed between calculations and measurements in this investigation was attributed to ignoring the evaporation time in the calculations. Rizk and Mongia [4] followed a similar approach to model the emissions produced by various types of combustor concept. In their model, the primary zone of the combustor consisted of two central reactors in series. The first contained the initial mixing and reaction of the fuel spray, and the reaction continued through the second reactor. Two other reactors occupied the near-wall region in the primary zone, and were parallel to the central reactors. The fuel/air ratio was corrected to account for the spray evaporation delay time through the estimation of spray mean drop size and evaporation constant. The calculations utilized a detailed chemical kinetic mechanism to provide the trends of variation of pollutant formation with operating parameters. The developed calculation method was employed by Rizk and Smith [5] to propose an effective means of establishing the engine emissions characteristics over the entire flight envelope using a limited number of tests. The approach utilized only the four power points defined by the International Civil Aviation Organization (ICAO) to provide the total aircraft mission emissions.

In conventional combustors, liquid fuel is injected into the combustor flow field forming a spray that contains a wide variation of drop sizes. Typically, the radial fuel concentration in the spray is not uniform, but rather follows highly peaked profiles. In such a spray, the fine droplets rapidly evaporate in the high temperature environment of the primary zone, while larger liquid drops continue traveling through the primary zone forming surrounding flammable envelopes. The combustion process proceeds with a combination of droplet burning under a stoichiometric fuel/air ratio, and a partially premixed flame with a mixture strength corresponding to the local fuel vapor concentration. Because the NO_x formation is directly connected to the reaction temperature, the formation process could be visualized as two simultaneous mechanisms. One mechanism proceeds under stoichiometric conditions over a certain duration that corresponds to the droplet life. The second mechanism is governed by the variation in gas temperatures due to fuel vapor/air ratio profile in the combustion zone.

Kelkar et al. [6] used a laser-induced fluorescence technique to provide insight into the radial profiles of velocity, temperature, and NO_x concentration in turbulent premixed flames. Their measurements demonstrated that the location of the peak values of NO_x concentration corresponded to the maximum temperature regimes in the flame. They also noted that the radial profile of NO_x flattens out further downstream due to the combined action of diffusion and convection. Yule and Bolado [7], described their experimental finding of fine-droplet spray as a fast evaporation of small droplets making the gas-phase combustion much more significant than the droplet combustion. As spray droplets become larger, the individual droplet burning becomes more possible, and a mixed combustion mode of gas-phase flame and droplet combustion is present. They observed in the experiments a massive droplet burning with envelope or wake flames as the spray drop size is further increased.

According to Law and Chung [8], in the spray combustion process, droplets may undergo various subprocesses as the heating up, vaporization, ignition, burning, and possible extinction based on their atomization conditions and the local environment. In general, droplets may be ignited and sustain flames if the local conditions are in favor of droplet ignition and burning. Cooper [9] demonstrated in his experiments the roles played by droplet burning and vapor phase burning on total NO_x emissions for partially vaporized mixtures. He observed that for overall equivalence ratios of 0.6 or less, increasing the fuel vapor fraction results in a continuous decline in NO_x concentration. This is mainly attributed to the diminishing presence of droplet burning in the combustion zone. He also observed that a minimum exists in total NO_x for overall equivalence ratios above 0.7. He attributed that to the tradeoff between reduction in vapor phase NO_x contribution due to the decrease in the vapor phase equivalence ratio, and a corresponding increase in liquid fraction that increases the NO_x contribution from liquid droplet burning.

Several other investigations have demonstrated the strong link between the fuel/air unmixedness in the primary zone and NO_x emissions. In an earlier study, Pompei and Heywood [10] investigated the influence of initial conditions and subsequent mixing in a kerosine-fueled combustor. Atomizing pressure was varied to affect mixing and subsequently NO_x emissions. Fric [11] used an unmixed parameter that was employed in earlier investigation by Dimotakis and Miller [12] to quantify temporal fluctuations in fuel concentration of methane-air flames. The amount of mixing of the methane-air mixture was varied by changing the distance from injection point to the flameholder and/or by diverting some air from co-flowing air to the fuel jet. Two cases with similar mean fuel concentrations but with different levels of mixedness parameter demonstrated experimentally significant increase in NO_x as unmixedness parameter increased.

The observations reported in the aforementioned investigations have been utilized in the present development of the NO_x model for diffusion flame combustion. The model accounts for both spray burning and premixed flame that follows fuel concentration profile in the primary combustion zone. The model utilizes an arrangement of several reactors representing various combustion zones, and is coupled with detailed chemical reaction scheme. A description of the NO_x model is presented in the next section.

2 Model Formulation

In this section, the two main elements needed to develop the NO_x model are presented. These are (1) the formulation of the combustor multiple-reactor flow model, and (2) the derivation of both the partially premixed NO_x model considering fuel concentration profile and NO_x formation under stoichiometric droplet burning.

2.1 Combustor Flow Model. Because the emissions from gas turbine combustors are significantly affected by the details of the front end and the subsequent admittance of air into various zones, the combustor needs to be divided into a number of regions for modeling purposes. Each combustor region is, thus, treated as a single chemical reactor. Nicol et al. [13] demonstrated the importance of selecting the appropriate reactor arrangement in simulating the actual interaction between various zones of the combustor. They observed that the effects of system pressure and inlet air temperature on exit NO_x concentration were better defined when a combination of well stirred and plug flow reactors was used. Rizk and Mongia [14] selected different arrangements of reactors to simulate a diffusion flame combustor as well as low emissions concepts such as rich/lean and lean premixed combustors. Their findings confirmed the need to closely represent the combustion processes in the primary combustion zone in order to obtain good agreement with the data.

The configuration of reactors selected for modeling the diffusion flame combustor in the present study is illustrated in Fig. 1. The arrangement simulates both elements of the diffusion flame concept, namely droplet burning and partially premixed flame

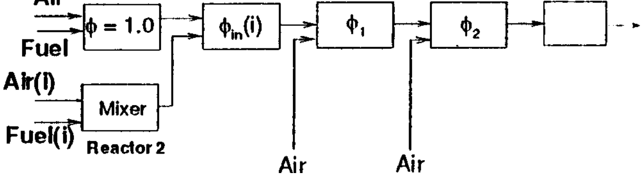

Fig. 1 Reactor model for diffusion flame simulation

considering primary zone fuel concentration profiles. Two parallel reactors are used to simulate the initial reaction and mixing in the combustor primary zone. Reactor 1 is a well-stirred reactor that represents the droplet burning by allowing the reaction to proceed under stoichiometric fuel/air ratio. Reactor 2 is used as a mixer to bring the overall fuel/air ratio admitted through the combustor front end to the actual stoichiometry in the primary combustion zone (Reactor 3). No reaction is allowed in Reactor 2. In order to account for the fuel concentration profile in the primary zone caused by the nonuniformity of the fuel injection process, the inlet flow to Reactor 2 follows a predefined distribution. In the next subsection, the derivation of the parameters describing this distribution is presented.

A series of plug flow reactors are used in the combustor flow model to represent other downstream combustion zones. Radial air jets and cooling air are admitted into the relevant reactors according to the combustor configuration details, and using engineering estimates of the air distribution. Based on the flow conditions through each reactor, the residence time and local fuel/air ratio are estimated and used as an input to the detailed chemical reaction calculations. The comprehensive reaction mechanism utilized in the present calculation approach incorporates 163 elementary reactions and accounts for 41 species. Westbrook and Pitz [15] proposed this model and demonstrated the capability to reproduce measurements over a wide range of operation. The reaction mechanism also combines the detailed kinetic scheme with the extended Zeldovich mechanism for NO_x formation ([16,17]).

2.2 NO_x Model Formulation and Validation. Traditionally, conventional combustors operating on the diffusion flame principle are tested under conditions dictated by the aircraft engine cycles. In other words, the combustor performance is evaluated at conditions representing the landing/takeoff cycle, in addition to those related to the aircraft mission and altitude flight requirements. The test parameters, including air inlet pressure, temperature, and overall fuel/air ratio, all vary from one test point to another. As a result, such database cannot provide insight into the separate effect of each governing parameter on the combustor NO_x emissions. Moreover, information on the important role of the fuel/air mixture strength in the combustor primary zone is not easily determined. It should, however, be emphasized that such data are useful in later stages of model development when used as a tool for model validation.

To successfully develop a NO_x model for diffusion flames encountered in gas turbine combustors, it is essential to utilize emissions data that demonstrate the effect of the primary zone fuel/air ratio (FAR) on overall NO_x. The database should also provide sufficient details on the effects on inlet pressure (P_3) and temperature (T_3) of combustor air on NO_x formation.

In the present investigation, the results obtained in a parametric study performed on an experimental combustor have been used. The combustor utilized an airblast atomizer/dome swirler combination employed in a conventional gas turbine combustor. Examples of the NO_x measurements acquired in this study are plotted in Fig. 2. The results represent both low power/idle conditions, as well as intermediate and takeoff engine operating modes, obtained over a wide range of equivalence ratio. The variation of the NO_x formation with the overall fuel/air ratio demonstrates a strong dependency that reflects the net effect of the reaction temperature on NO_x. The NO_x data points shown in the figure represent the combined contributions from spray droplet burning and fuel vapor/air reaction.

The diffusion flame combustor data base described above was used to derive the two main elements of the NO_x model. They are essentially related to the combustion of single fuel droplets and to that of partially premixed flame. The combined effects of these two combustion mechanisms are responsible for the overall NO_x emissions produced by the combustor.

The approach utilized in the development of the spray burning NO_x model is based on the assumption that the reaction proceeds under stoichiometric conditions for a certain residence time. This residence time should vary in a real combustor environment according to droplet sizes in the spray, droplet life time, surrounding temperature, and fuel/air ratio in the primary combustion zone. The modeling of the partially premixed flame considers the fuel vapor concentration in the primary zone to follow a certain profile. A normal probability distribution of the fuel/air ratio is employed in the calculation with a standard deviation related to the unmixedness nature of the fuel injection process. A profile with a zero deviation from the mean value indicates a fully premixed flame. The evaluation of the degree of spread in the fuel/air distribution focuses on correlating the distribution of the deviation parameter with the degree of mixing allowed in the combustor design.

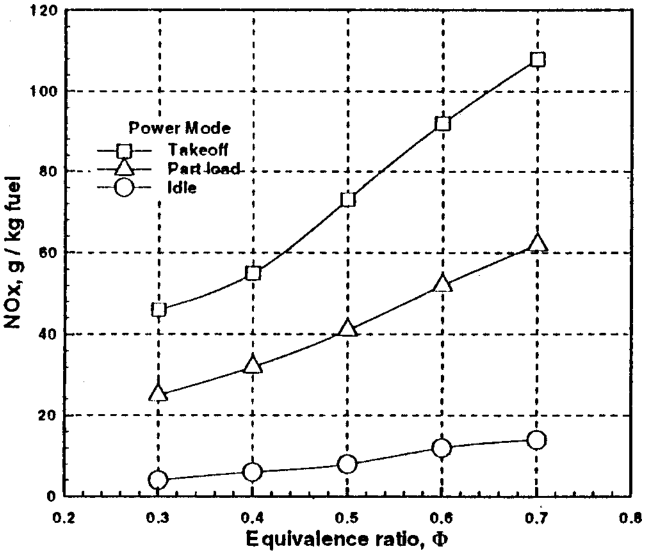

Fig. 2 NO_x emissions of experimental combustor

Equally spaced bands are used to simulate the entire distribution and to define the distribution of fuel/air ratios in the primary zone, as illustrated in Fig. 3. The width of the selected hands should be fine enough to closely represent the distribution, and yet should not require very lengthy computations. In the present cal-

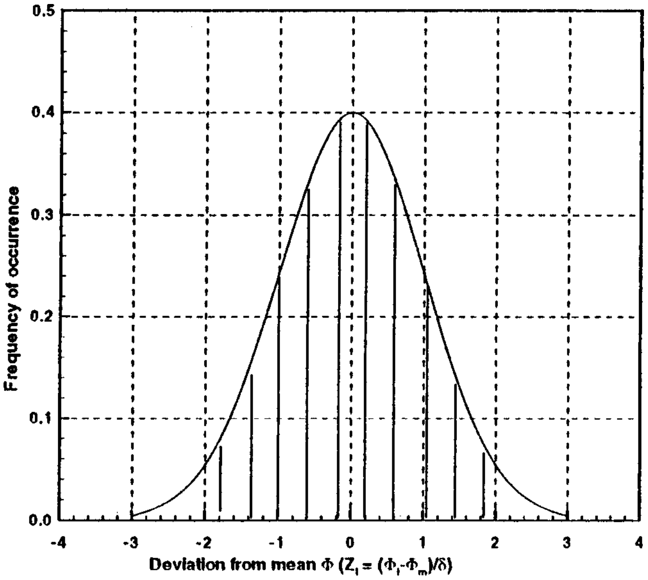

Fig. 3 Simulation of Φ distribution in primary zone

culations, the fuel/air ratio profile was divided into eleven bands, resulting in 15.86 percent of primary zone flow having a flame proceeding at the mean equivalence ratio (Φ_m). The probability on either side of the mean value drops rapidly as the deviation from the mean equivalence ratio increases. For example, following the normal distribution concept indicates that combustion would occur under Φ at ± 2 standard deviation level with 3.20 percent probability on each side of the Φ_m.

The approach employed to develop the necessary formulations in the present effort comprised a multistep iterative procedure. The first step involves defining the appropriate chemical reactor arrangement for the combustor flow field, as described in the previous section and given in Fig. 1. The next step is to calculate the equivalence ratios that correspond to the various bands in the distribution and based on an assumed value of the distribution standard deviation (δ). The value of Φ_i for the i band is calculated in terms of Φ_m, δ, and the normalized deviation from mean Z_i, using the following expression:

$$\Phi_i = \Phi_m (1.0 + Z_i \cdot \delta). \tag{1}$$

The inlet fuel and air fractions to the reactor flow model are then determined based on the calculated primary zone Φ distribution and the subsequent admission of air into other downstream reactors. The next step is to estimate the residence time in each reactor using air flow rate, fuel/air ratio, reaction temperature, and combustor liner geometry. An estimate of the residence time in the stoichiometric reactor is also made at this stage. This information is used as an input to the detailed chemical kinetic scheme to provide an estimate of NO_x formation in the combustor. This calculation is repeated for each Φ_i band described by the normal probability distribution. The calculation of the overall NO_x is then performed using the composite of NO_x contributions from various bands and considering the weighted average of each band. The final step of the calculation procedure involves comparing the estimated overall NO_x concentration with the measured value under the same operating conditions. The process is repeated until calculated and measured NO_x are matched, yielding optimum values of standard deviation of Φ distribution (δ) and the residence time in the stoichiometric reactor (τ_{st}).

The expression for δ that has been found to best fit the data is given in terms of inlet equivalence ratio to the combustor primary zone Φ_{in} as

$$\delta = 11.47 \cdot \Phi_{in}^{-5.45} \exp(-3.74 \cdot \Phi_{in}^{-0.85}). \tag{2}$$

The values of δ and τ_{st} for a wide range of operating conditions were accumulated in the present effort to form a basis for deriving the appropriate correlations of the NO_x model. Examining the trends of the variation in τ_{st} with key parameters indicated a strong dependency on air inlet pressure (P_3) and temperature (T_3), in addition to the inlet fuel/air equivalence ratio (Φ_{in}). Best correlations of the analytical results revealed the following expression:

$$\tau_{st} = B \cdot \Phi_{in}^{-0.3} \cdot \exp(A \cdot \Phi_{in}^{7.2}) \tag{3}$$

where

$$A = 0.244 - 0.000277 \cdot P_3 \tag{4}$$

$$B = 0.245 \cdot (T_3/1000)^8 \cdot \exp(0.135 \times 10^8 \cdot T_3^{-2.35}). \tag{5}$$

For T_3 greater than 811 K, the expression for the parameter B is given by

$$B = 0.00089 \cdot T_3 - 0.394. \tag{6}$$

The units of P_3 and T_3 used in these equations are kPa and K, respectively.

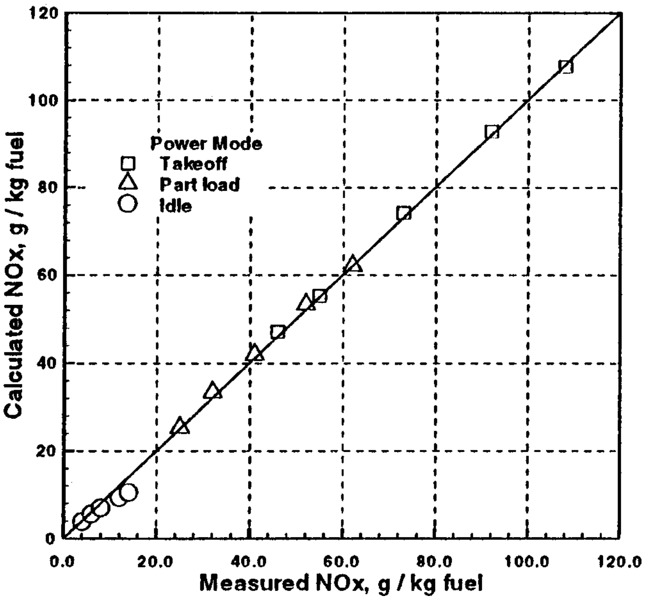

Fig. 4 Comparison between model calculations and measurements of NO_x

The agreement between the calculated NO_x emissions using the developed NO_x model and the actual measurements is demonstrated in Fig. 4. The results shown cover wide ranges of inlet pressure of 400 to 2000 kPa. inlet temperature from 480 to 850 K, and inlet primary zone equivalence ratio from 0.15 to 0.7.

An example of the calculated equivalence ratio in various reactors of the combustor flow model is given in Fig. 5. The figure illustrates the estimated values of Φ for the selected 11 bands of the normal distribution of fuel concentration. The figure also reports the weighted average bands of reaction under various equivalence ratios. The inlet air and fuel flow through the combustor dome, and the subsequent admittance of air through the liner govern the equivalence ratio in each chemical reactor, as shown in the figure. The spread in Φ at each axial location in the combustor becomes smaller as the downstream distance increases. This reflects the flow field characteristics of the combustor, where the highly nonuniform distribution of fuel delivered by the injector continuously moves towards a more uniform one as the flow proceeds downstream. Typical values of gas turbine combustor exit gas pattern factor are within a range of 0.15 to 0.25. The pattern factor represents the maximum deviation from the mean

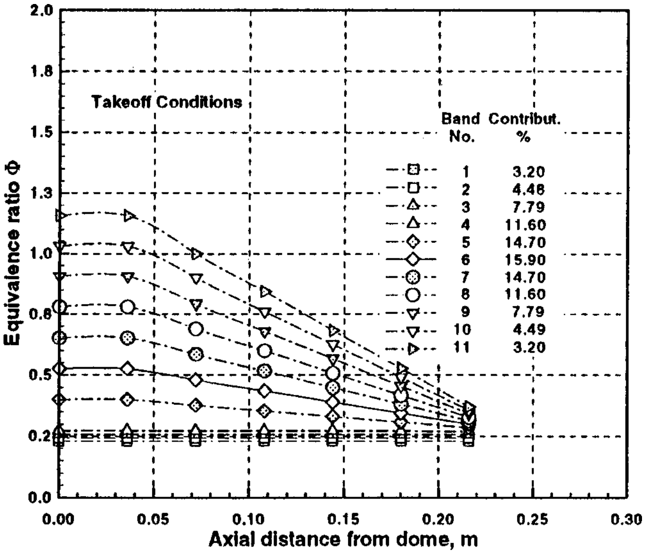

Fig. 5 Estimation Φ distribution in experimental combustor

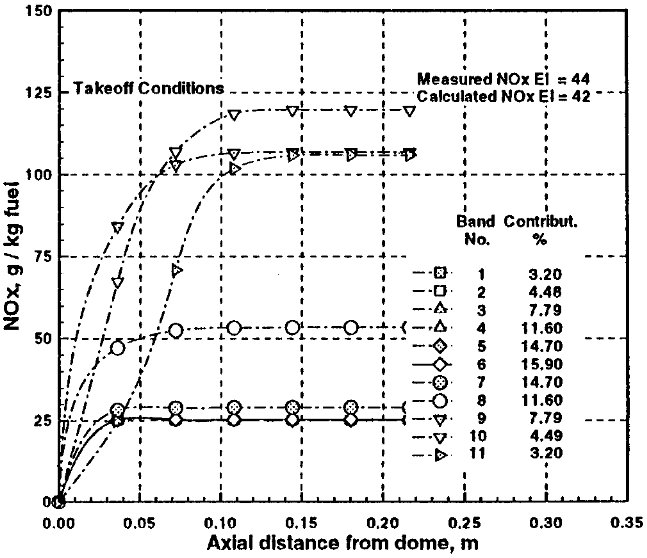

Fig. 6 Estimation of NO_x formation profiles in experimental combustor

exit temperature normalized with respect to combustor temperature rise. This range corresponds to a standard deviation of the equivalence ratio distribution at the combustor exit of about 0.10 to 0.12 around the mean value.

The corresponding levels of NO_x formation within the experimental combustor that reflect the consideration of the Φ distribution in the primary zone are plotted in Fig. 6. The total NO_x formation is the summation of the contributions from the 11 bands of the Φ distribution. Two important conclusions can be drawn from this figure. First, if the modeling of the diffusion flame was based only on the mean equivalence ratio in the primary zone (band no. 6 in the figure), the estimated overall NO_x emissions under these conditions would be about 25 g/kg fuel. This estimated value is far below the measured NO_x emission of 44 g/kg fuel. Second, the importance of considering the presence of the fuel vapor/air ratio profile in the primary zone is demonstrated in the good agreement between the model calculations and measurements. Due to this Φ distribution, the probability of having mixtures closer to the stoichiometric level in the primary zone would create favorable conditions for excessive NO_x formation there.

3 Model Application to Production Combustor

An effective means of evaluating the capability of the developed NO_x model as a design tool is to apply the model to a practical gas turbine combustor. The combustor employs a conventional piloted airblast atomizer/shrouded swirler dome configuration, and radial air injection into various combustion and dilution zones. The reactor network used to simulate the combustor flow field is illustrated in Fig. 7. The network is a modified version of the one described earlier in Fig. 1 that reflects the nature of air admission into the combustor. The stoichiometric reactor receives the proper air and fuel flow rates needed to achieve an equivalence ratio of 1.0. The balance of the flows required to bring the initial primary zone equivalence ratio to the design value is admitted into the parallel mixer reactor. The range of the fuel vapor/air ratio distribution caused by the nonuniform profile of fuel concentration is evaluated using Eq. (2) given in the previous section. The distribution is then used to estimate the input flows to the mixer reactor for each band of the primary zone equivalence ratio $\Phi_{in}(i)$, described in Fig. 3. For each data point utilized in the model validation effort, the residence time in the stoichiometric reactor was calculated using Eq. (3). The residence times in all other reactors were estimated based on flow and combustion characteristics in each reactor, in addition to the combustion liner dimensions.

An example of the fuel/air stoichiometry in various primary, intermediate, and dilution zones of the combustor at engine takeoff conditions, is illustrated in Fig. 8. The dividing lines between the three main combustion regions were arbitrary located at mid points between adjacent axial planes that contained the air injection holes. For this operating point, the equivalence ratio immediately downstream of the combustor dome is almost 50 percent higher than the stoichiometric value, as shown in the figure. The estimated equivalence ratio at mid point between the primary and intermediate jets drops to about 0.66 due to admitting cooling air in this region and primary air jets.

The calculated equivalence ratio in various reactors of the production combustor flow model are given in Fig. 9 for the takeoff operating mode. The model estimates that fairly fuel rich mix-

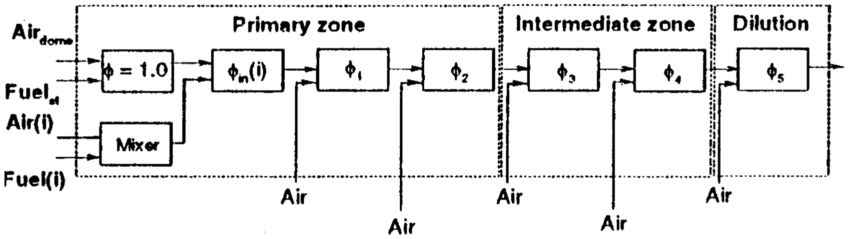

Fig. 7 Reactor network for production combustor

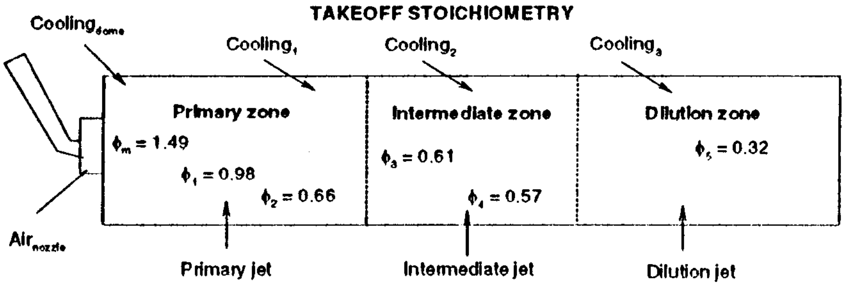

Fig. 8 Fuel/air stoichiometry in main combustor zone

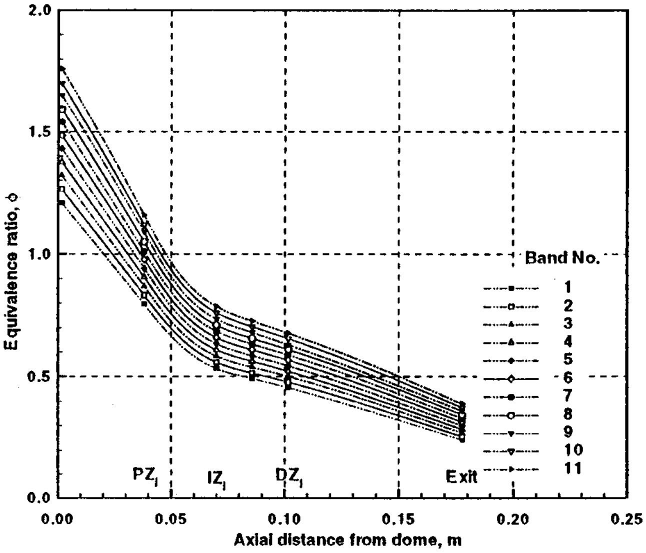

Fig. 9 Equivalence ratio profiles at takeoff mode in a production combustor

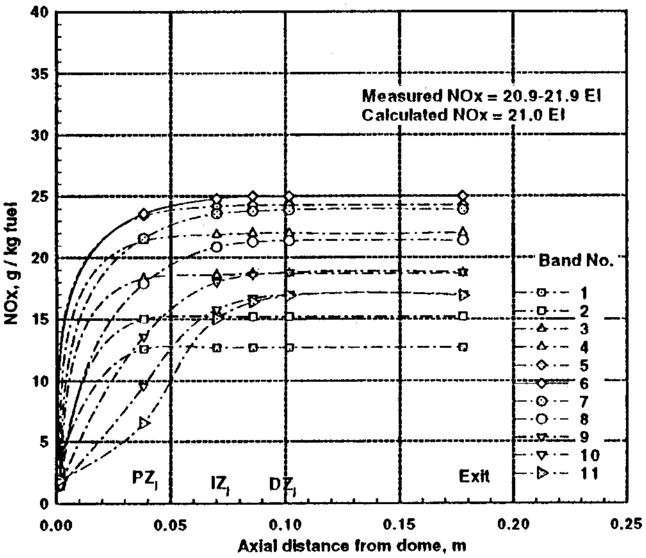

Fig. 11 NO_x formation under takeoff conditions in production combustor

tures, with equivalence ratios as high as 1.8, may exist locally in the combustor primary zone due to the highly peaked fuel injection process. Figure 10 illustrates the change in the calculated gas temperature with axial combustor location for various hands of initial fuel concentration profile in the primary zone. The results demonstrate the impact of the primary jets in bringing the fuel/air ratio closer to the stoichiometric value causing the gas temperature to peak in this region. High rates of NO_x formation are, thus, expected to occur in the vicinity of the radial air injection location in the primary zone. On the other hand, the calculated exit gas temperature distribution indicates that the pattern factor under this power mode is about 0.21, which is in a good agreement with the actual measurement for the production combustor.

Figure 11 shows the NO_x formation in each combustor region as given by the developed NO_x model. The calculations indicate that most of the NO_x formation in the combustor occurs in the primary and intermediate regions, with formation ending almost at the dilution jet plane. This finding agrees with the detailed calculation of NO_x emissions from a similar annular combustor, as reported by Rizk [18]. Because this combustor operates on a fuel rich primary zone. each band of the Φ distribution will have to go through a stoichiometric mixture at some stage before becoming leaner towards the exit of the combustor. The overall NO_x emissions for this operating point is calculated based on the summation of contributions from all bands of the Φ distribution and considering the weighted average presence of each Φ at the inlet to the combustor primary zone. The predicted overall NO_x emission index at the takeoff conditions is 21.34 g/kg fuel versus a measured range between 20.9 and 21.9 g/kg fuel.

The developed model was also applied to evaluate the capability to estimate the NO_x formation under off-design conditions of the production combustor. A 50 percent part load and idle power mode data were utilized in this effort. For the part load point, the average equivalence ratio at the combustor front end is almost stoichiometric. The calculated distribution of equivalence ratios at the combustor dome and the subsequent changes in their values at various locations in the combustor are illustrated in Fig. 12. Fig-

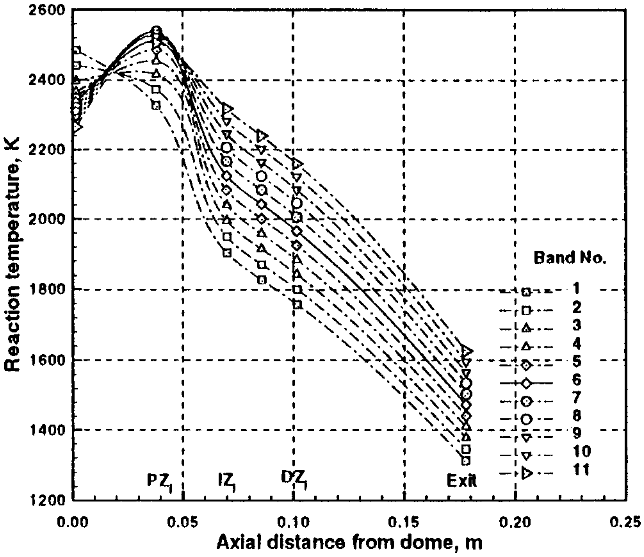

Fig. 10 Calculated gas temperatures in production combustor flow field at takeoff conditions

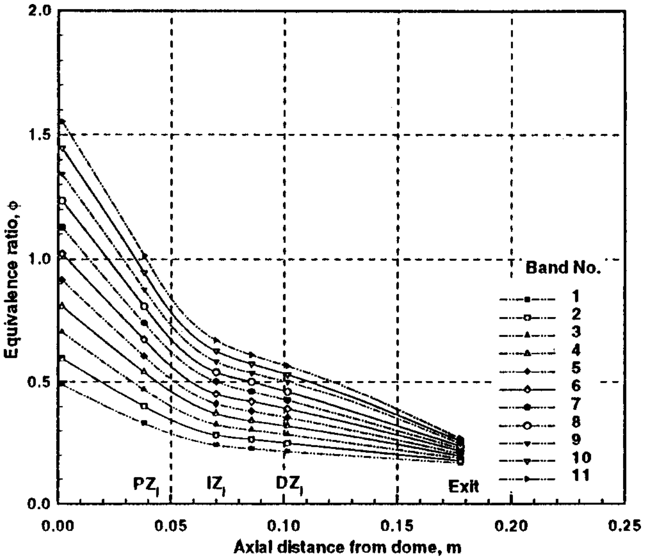

Fig. 12 Equivalence ratio distribution under engine part load conditions

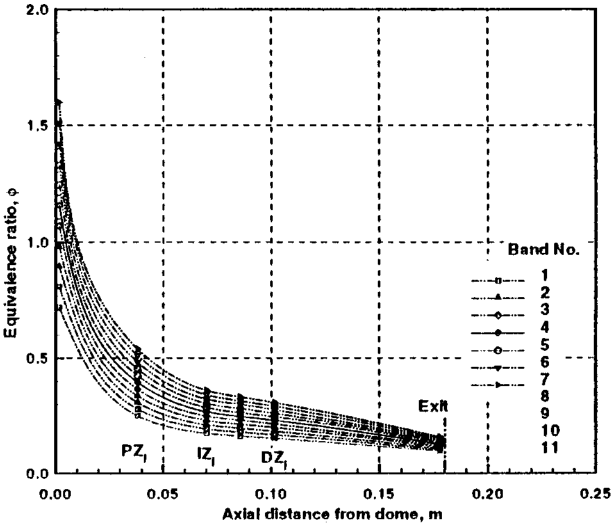

Fig. 13 Idle equivalence ratio profiles

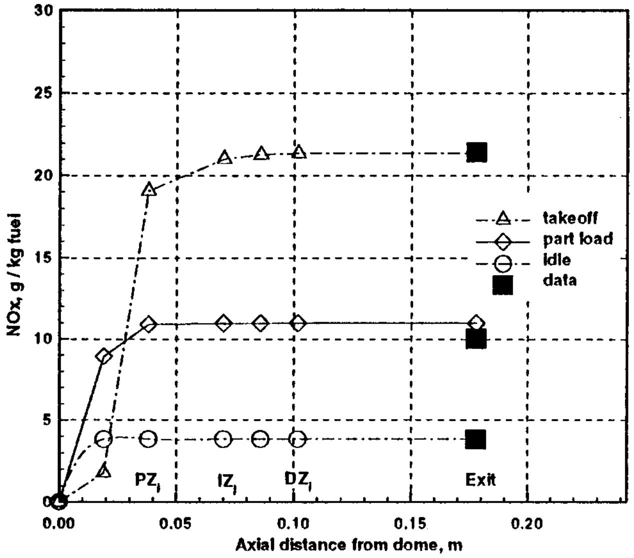

Fig. 15 Cumulative NO_x formation in production combustor

ure 13 shows the model predictions of the fuel/air stoichiometry under the engine idle mode. Based on the total fuel flow rate injected into the combustor and the amount of air admitted through the combustor dome, the estimated equivalence ratio at the front end is about 0.6. Because, at idle power mode, the fuel is injected only through the pilot pressure atomizer, the local fuel/air mixture in the vicinity of the pilot exit is higher and slightly on the rich side. The mixing of the fuel spray with the additional dome air rapidly reduces the primary zone stoichiometry to a fairly lean mixture.

Figure 14 illustrates the NO_x formation profiles in the production combustor under a number of engine operating modes. It is noted that the highest NO_x formation occurs, as expected, under takeoff conditions. The figure also demonstrates that the peak of the NO_x formation profile moves further downstream as the power level goes up. This reflects the change in the stoichiometry within the combustor as the combustor operating conditions vary. The cumulative NO_x emissions in the combustor at the same engine power settings were calculated and plotted in Fig. 15. The measured NO_x data at the exit of the combustor are also plotted in the figure. The level of agreement between the model predictions and the measured data demonstrated in the figure indicates the successful simulation of both elements of diffusion flame; namely the droplet burning and the nonuniformity of the fuel vapor/air mixture in the combustor primary zone. The estimated times for the droplet burning under a stoichiometric fuel/air ratio for the takeoff, 50 percent part load, and idle modes, as given by Eq. (3), are 0.05, 0.26, and 0.8 ms, respectively. The increase in the stoichiometric time at low power and idle is in good agreement with the findings of Cooper [9]. The low primary zone temperature at these conditions that limits the evaporation rates, coupled with the lean mixture in primary zone, increases the contribution of liquid droplet burning to overall NO_x formation in the combustor.

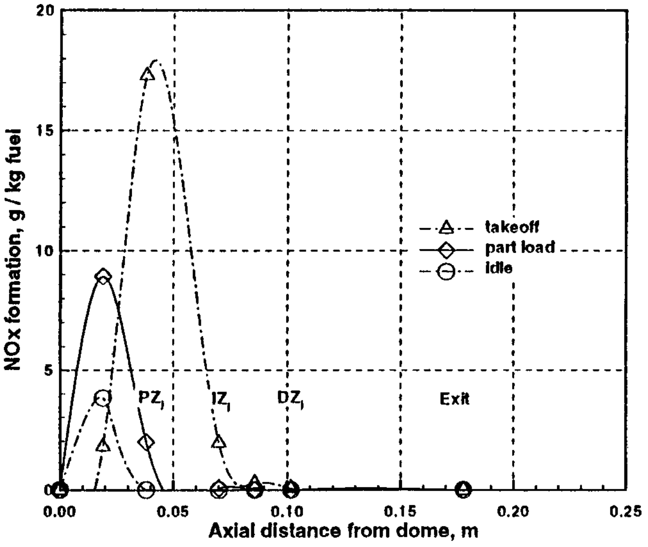

Fig. 14 Variation of NO_x formation with axial distance of production combustor

Although the results presented in this section are for diffusion flame combustion, the model can be applied equally well to unconventional premixed or partially premixed combustion concepts. In addition, in premixed type of combustor, a significant NO_x formation occurs under idle and low power operation where pilot diffusion flame is usually employed in the design. In these designs, spray pattern and drop sizes follow those encountered with airblast and pressure atomizer applications.

4 Summary and Conclusions

A model has been developed that addresses the formation of NO_x in a diffusion flame, where both droplet burning and partially premixed combustion take place simultaneously. A method has been presented to estimate the unmixedness nature of fuel injection in a practical combustor expressed as a normal probability distribution of fuel/air ratio in primary zone, and the residence time under stoichiometric conditions reflecting the droplet burning. The model development utilized a data base obtained in a parametric study performed on a conventional gas turbine combustor, where the primary zone equivalence ratio varied over a wide range of conditions. A reactor network used to simulate both elements of the diffusion flame concept involved a stoichiometric reactor representing the droplet burning, and a mixing reactor to account for the nonuniformity of the fuel/air mixtures in the primary zone. A comprehensive chemical reaction mechanism was utilized to calculate the NO_x emission contribution from every reactor used in the combustor simulation.

The application of the developed model to estimate the NO_x formation in a production combustor indicated that most of the NO_x produced under engine takeoff condition occurred late in the primary and intermediate regions, with formation ending almost at the dilution jet location. The delay in NO_x formation in the combustor is attributed to the fact that the combustor operates on a fuel rich primary zone concept resulting in a less favorable conditions for NO_x formation there.

The calculated residence time representing the droplet burning under stoichiometric conditions increased as the engine power decreased. The lower primary zone gas temperatures associated with idle and low power modes limit the evaporation process. Lower fuel vapor fraction coupled with the leaner mixtures in the combustor primary zone give rise to the NO_x contribution from liquid droplet burning. These observations are supported by the results reported in the literature for diffusion flame investigations.

The measured NO_x emissions for the combustor used in a production gas turbine engine and the model predictions are in good agreement. The change in the combustor flow field stoichiometry due to subsequent admission of air through dilution holes and cooling devices, and due to changing engine power conditions was found to be critical to the prediction of NO_x formation. The good agreement indicates that the simulation of the diffusion flame by droplet burning under stoichiometric condition and a distribution of air/fuel ratios representing the combustion of partially premixed fuel vapor and air can form an effective tool for designing unconventional combustor concepts.

Nomenclature

FAR = fuel/air ratio
NO_x = NO_x emissions, g/kg fuel
P_3 = system pressure, kPa
T_3 = inlet air temperature, K
Z_i = normalized deviation of ϕ from mean value
δ = standard deviation of ϕ distribution
Φ = fuel/air equivalence ratio
Φ_i = equivalence ratio for i band in distribution
Φ_{in} = inlet equivalence ratio to primary zone
Φ_m = mean equivalence ratio
τ_{st} = residence time in stoichiometric reactor, ms

References

[1] Lefebvre, A. H., 1984, ‘‘Fuel Effects on Gas Turbine Combustion-Liner Temperature, Pattern Factor, and Pollutant Emissions,’’ AIAA J. Aircraft **21**, No. 11, pp. 887–898.
[2] Plee, S. L., and Mellor, A. M., 1979, ‘‘Characteristic Time Correlation for Lean Blowoff of Bluff-Body-Stabilized Flames,’’ Combust. Flame, **35**, pp. 61–80.
[3] Fletcher, R. S., and Heywood, J. B., 1971, ‘‘A Model for Nitric Oxide Emissions From Aircraft Gas Turbine Engines,’’ AIAA Paper No. 71–123.
[4] Rizk, N. K., and Mongia, H. C., 1993, ‘‘Semianalytical Correlations for NOx, CO, and UHC Emissions.’’ ASME J. Eng. Gas Turbines Power, **115**, pp. 612–619.
[5] Rizk, N. K., and Smith, D. A., 1994, ‘‘Regional and Business Aircraft Mission Emissions,’’ ASME Paper No. 94-GT-300.
[6] Kelkar, A. S., Ramakrishna, Ch., Sivathanu, Y. R., and Gore, J. P., 1996, ‘‘Temperature and Velocity Statistics of Lean Premixed Jet Flames for NOx Calculations,’’ AIAA Paper No. 96-0818.
[7] Yule, A. J., and Bolado, R., 1984, ‘‘Fuel Spray Burning Region and Initial Conditions,’’ Combust. Flame, **55**, pp. 1–12.
[8] Law, C. K., and Chung, S. H., 1980, ‘‘An Ignition Criterion for Droplet in Sprays,’’ Combust. Sci. Technol., **22**, pp. 17–26.
[9] Cooper, L. P., 1980, ‘‘Effect of Degree of Fuel Vaporization Upon Emissions for a Premixed Partially Vaporized Combustion System,’’ NASA Technical Paper No. 1582.
[10] Pompei, F., and Heywood, J. B., 1972, ‘‘The Role of Mixing in Burner-Generated Carbon Monoxide and Nitric Oxide,’’ Combust. Flame, **19**, pp. 407–418.
[11] Fric, T. F., 1992, ‘‘Effects of Fuel-Air Unmixedness on NOx Emissions,’’ AIAA 92-3345.
[12] Dimotakis, P. E., and Miller, P. L., 1990, ‘‘Some Consequences of the Boundedness of Scalar Fluctuations,’’ Phys. Fluids, **2**, No. 11, pp. 1919–1920.
[13] Nicol, D. G., Malte, P. C., and Steele, R. C., 1994, ‘‘Simplified Models For NOx Production Rates in Lean-Premixed Combustion,’’ ASME Paper No. 94-GT-432.
[14] Rizk, N. K., and Mongia, H. C., 1994, ‘‘Emissions Predictions of Different Gas Turbine Combustors,’’ AIAA Paper No. 94-0118.
[15] Westbrook, C. K., and Pitz, W. J., 1984, ‘‘A Comprehensive Chemical Kinetic Reaction Mechanism for Oxidation and Pyrolysis of Propane and Propene,’’ Combust. Sci. Technol., **37**, pp. 117–152.
[16] Glassman, I., 1977, *Combustion*, Academic Press, San Diego, CA.
[17] Toof, J. L., 1986, ‘‘A Model for the Prediction of Thermal, Prompt, and Fuel NOx Emissions from Combustion Turbines,’’ ASME J. Eng. Gas Turbines Power, **108**, pp. 340–347.
[18] Rizk, N. K., 1995, ‘‘Calculation Method For NOx Production in Gas Turbine Combustors,’’ AIAA Paper No. 95-0282.

Quantifying Fuel/Air Unmixedness in Premixing Nozzles Using an Acetone Fluorescence Technique

J. H. Stufflebeam

D. W. Kendrick

W. A. Sowa

United Technologies Research Center,
Aeromechanical, Chemical and Fluid Systems,
411 Silver Lane,
East Hartford, CT 06108

T. S. Snyder
Pratt & Whitney,
400 Main Street,
East Hartford, CT 06108

The ability of a lean-premixed combustion system to minimize emissions while maintaining combustion stability over the operating curve relies upon how well the fuel nozzle premixes the fuel and air. As the level of premixing increases, NO_x emissions at a given flame temperature decrease until a perfectly premixed condition is achieved. The objective of this paper is to quantify the level of premixing achieved by a premixing nozzle using an acetone fluorescence technique and determine its relationship to NO_x emissions and combustion stability. The technique of using acetone fluorescence has been used as a fast and quantitative diagnostic to map the fuel-air distribution. This technique has been applied to the development of a lean premixing nozzle to measure the fuel air distribution at the fuel nozzle exit plane. In this study, the fuel air distribution is presented as two-dimensional images. The average fuel/air ratio and the standard deviation are calculated at various annular regions to determine the distribution as a function of radius. A single unmixedness parameter (σ/μ) over the entire annulus is also calculated to allow relative ranking of the various fuel nozzle configurations. The fluorescence data is acquired for various nozzle hardware configurations in an atmospheric test facility. Fuel and air flow conditions are determined by scaling engine conditions to cold flow conditions and matching the fuel to air momentum ratio at the fuel injection site. Measured fuel/air distributions, six mm downstream of the nozzle exit plane, from the acetone fluorescence technique are correlated to emissions and acoustic measurements made at full pressure and temperature conditions in a single-nozzle test rig. The paper includes a description of the acetone fluorescence technique, the method for optimizing the fuel/air distribution through changes to the main gas fuel injection array, and correlations made between the fuel/air distribution, nozzle geometry, power setting, emissions, and combustor acoustics. [DOI: 10.1115/1.1396840]

Introduction

Snyder et al. [1] documented the emission characteristics (NO_x and CO) of tangential entry fuel nozzles used to premix fuel and air in industrial gas turbines. They correlated the penetration of fuel across the inlet air slot width for various fuel injector arrays with the emissions measurements in a single nozzle rig (SNR) test facility. The results indicated their high penetration fuel distribution yielded the lowest NO_x levels over the operating range of flame temperature. Because a large sensitivity to NO_x was observed, they recommended quantifying the level of premixing and refining the injector orifice array to further reduce the NO_x levels. Rutar et al. [2] reported on theoretical studies incorporating probability density function methods with chemical reactor modeling. Their conclusion was that NO_x emissions from practical, lean-premixed combustors is sensitive to premixing quality. Barnes and Mellor [3,4] estimated the unmixedness of fuel and air at combustion conditions through correlations of measured NO_x and CO with a characteristic time model that incorporates fluid dynamics and chemical kinetics. In these cases, the fuel air distribution could be correlated to combustor performance.

Several investigators have designed experiments to quantify the level of fuel-air premixing. Effects of fuel-air unmixedness were reported by Fric [5]. Laser induced fluorescence of fuel seeded with NO_2 provided spatial and temporal mixing data from cold-flow experiments. The unmixedness was correlated with NO_x emissions measured during separate combustion experiments in the same apparatus. Studies of fuel premixing were undertaken by Mongia et al. [6]. The local equivalence ratio of the fuel-air mixture from a laboratory burner was measured with Rayleigh scattering of a laser sheet under nonreacting conditions. They also developed an optical probe to experimentally measure the CH_4 concentration at a point in the flow of a reacting fuel mixture with laser absorption of the 3.39 micron transition. The work included a modeling effort that showed the dramatic effect of incomplete mixing on NO_x emissions. Lee and Santavicca [7] investigated fuel premixing in nonreacting flows through a seeding technique. Acetone was mixed with air and injected as a jet into an annular coflow of air. Their fiber optic probe excited the acetone and collected the fluorescence at a point in the flow, the fluorescence signal level was a measure of the fuel to air ratio. By traversing the probe, the fuel to air ratio was mapped over the radial dimension at several axial planes downstream of the jet exit. Acetone fluorescence was used by Frazier et al. [8] in cold flow experiments to investigate the axial distribution of fuel, downstream of a dual annular, counter-rotating, swirler premixer. Temporal measurements provided data on large scale turbulent structures that aided the understanding of flow dynamics.

Kendrick et al. [9] continued to study the combustion characteristics of a tangential entry, premixing fuel nozzle in a high-pressure single-nozzle rig. Combustor acoustic measurements were found to be a strong function of the centerbody design. This study demonstrated that a bluff-body centerbody in a tangential entry nozzle was superior to an aerodynamically stabilized design for minimizing combustion-induced pressure oscillations. An additional study was made in conjunction with acetone fluorescence measurements to quantify the emissions and acoustic sensitivity of the bluff-body centerbody to changes in the main gas fuel orifice

---

Contributed by the International Gas Turbine Institute (IGTI) of THE AMERICAN SOCIETY OF MECHANICAL ENGINEERS for publication in the ASME JOURNAL OF ENGINEERING FOR GAS TURBINES AND POWER. Paper presented at the International Gas Turbine and Aeroengine Congress and Exhibition, Indianapolis, IN, June 7–10, 1999; ASME Paper 99-GT-399. Manuscript received by IGTI, Oct. 1998; final revision received by the ASME Headquarters, Mar. 1999. Associate Editor: D. Wisler.

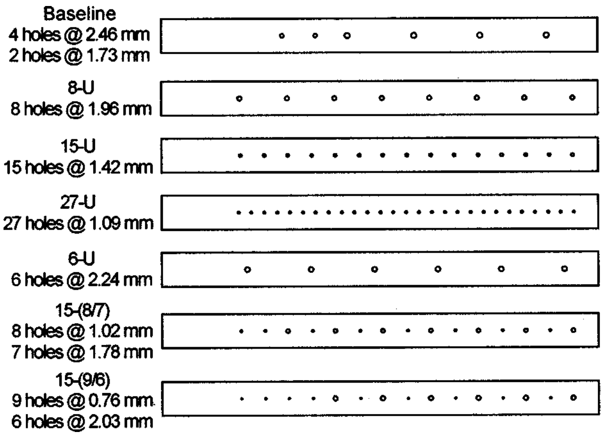

Fig. 1 Main fuel distribution orifice arrays evaluated in mixing studies. When inserted in the nozzle, the downstream end of the fuel tube is to the right.

array. The comparison of fuel/air distribution measurements to the corresponding emissions and acoustic measurements in a single-nozzle rig form the basis of this paper.

Experimental Approach

The objective of this study was to optimize and quantify the level of premixing achieved by a tangential entry fuel nozzle having a bluff-body centerbody based upon how the fuel/air distribution affected the nozzle's emissions and acoustic performance. The approach was to obtain a quantitative, two-dimensional measurement of the fuel to air ratio exiting the premixing fuel injector using actual engine hardware. The premixing level was changed by altering the distribution and penetration of the main fuel along the air inlet slot. This was accomplished by modifying a standard tangential entry nozzle, described in detail by Snyder et al. [1] to accept removable fuel tubes which served as fuel distribution plenums. Figure 1 describes each of the seven fuel tubes evaluated. The fuel was simulated using a technique developed by Lozano et al. [10], whereby a mixture of air is seeded by acetone (2 percent by weight). This mixture was metered separately for the main gas fuel and the pilot fuel injected at the nozzle's centerbody tip. The fuel/air momentum ratio at the injection site was set to match the momentum ratios experienced in the engine.

The acetone fluorescence experiments were performed in a cold flow facility at one atmosphere pressure to allow rapid configuration changes. Engine flow conditions were simulated through pressure/temperature scaling. Two different centerbodies were also studied, they differed in the diameter of the bluff-body end cap. The experiments with the centerbodies are distinguished in this paper by the ratio of the radius of the bluff body to the radius of the nozzle exit plane, $r_{\mathrm{CB}}/r_{\mathrm{exit}}$. The effective nozzle and fuel injector areas were kept constant for all configurations studied.

The fuel-air measuring apparatus is shown in Fig. 2. The nozzle is contained in a large plenum whose volume supplies the main air, the air flow rate is metered by a venturi from a 400 psi supply. The nozzle flow is confined in a 20.3-cm-diameter pipe and exhausted up a stack to avoid acetone accumulation in the laboratory. Acetone is heated to 70°C and pressurized to 200 psi (maintaining the liquid phase) to augment its vaporization. The acetone supply is divided into two streams (i.e., main and pilot) and the flow rate is measured with rotameters that were calibrated for the liquid phase flow. These two acetone flows are combined with a corresponding main air and pilot air streams which are measured separately with venturis. These main fuel and pilot fuel lines are subsequently heated (to 32°C) to insure the acetone remains vaporized. The acetone seeded air main flow supplies fuel to the two main fuel tubes and the acetone seeded air pilot flow supplies fuel to the pilot located in the nozzle centerbody. These fuel flows are mixed with the main air by the fuel nozzle.

The optical details are shown in Fig. 3. A laser sheet (10.2 cm wide×0.25 cm thick, $\lambda=266$ nm) (the fourth harmonic of Nd:YAG) is projected across the flow, 6 mm downstream of the fuel nozzle exit plane, exciting the acetone and generating fluorescence over a bandwidth from 350–550 nm in the visible region of the spectrum. The laser is Q-switched at 20 Hz and has a 10-nsec pulsewidth. A planar laser–induced fluorescence (PLIF) image is acquired in a 90-second exposure with a CCD camera and is quantified by comparison to a similar image taken with a uniform acetone/air mixture at known concentration. The 12-bit dynamic range and low noise of the camera afforded the long exposures. Typical dynamic range of the fluorescence images, after subtracting the background, was 500. This technique provides a map of the fuel-air distribution in a plane at the exit of the fuel nozzle. The two-dimensional map contains approximately 160,000 separate fuel-air measurements (pixels) per image, providing spatial resolution of 0.3 mm. Spatial resolution is improved by over an order of magnitude when compared with conventional sampling probes and data is acquired at a far superior rate.

Data Analysis. The fuel-air ratio at the nozzle exit plane is constructed from three separate experimental images acquired from the CCD camera: a background, response, and data image. The background image is simply a picture of the laser sheet and

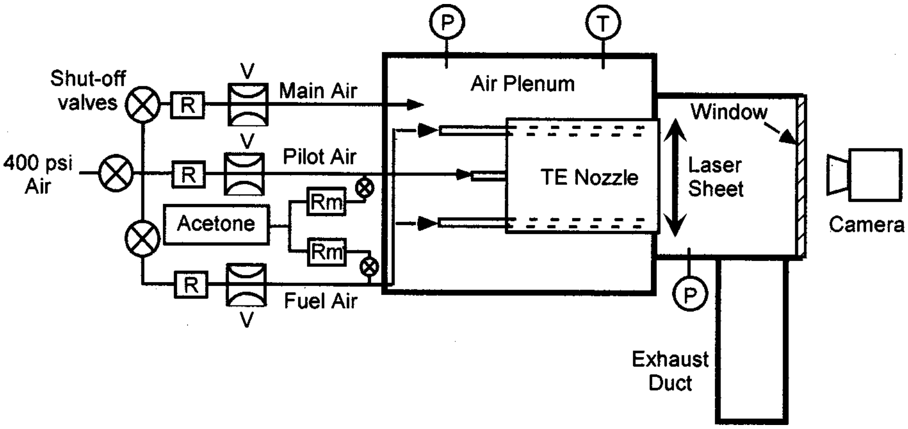

Fig. 2 Air flow facility for acetone PLIF measurements. Laser sheet is 6 mm from nozzle exit plane. R, regulator; V, venturi; Rm, rotameter; P, pressure transducer; T, thermocouple.

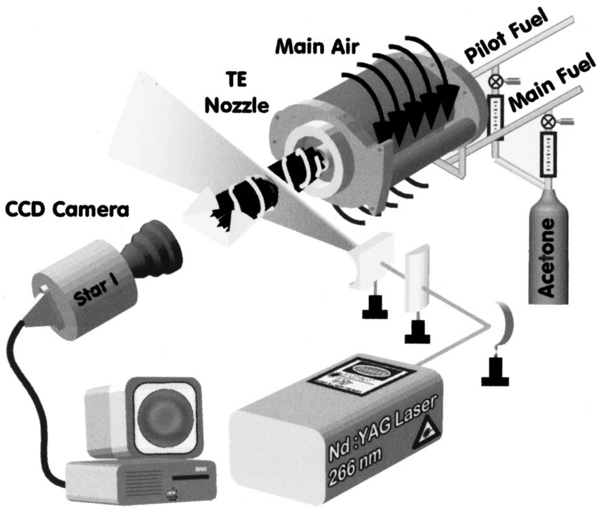

Fig. 3 Acetone PLIF experimental apparatus

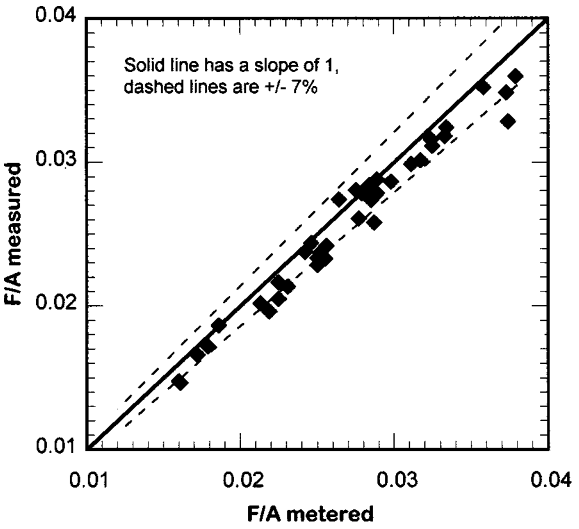

Fig. 4 PLIF accuracy

the fuel nozzle. It contains information on laser scatter and noise, no main air or fuel simulant is flowing during the acquisition of the background image. The response image is a picture of the laser sheet and the fuel simulant (fuel-air plus acetone only). The purpose of the response image is to optically correct for the laser intensity variation and quantify the image to known seeding levels. In this case, the image defines 100 percent fuel, or perfectly unmixed. The data image is obtained with both the main air and fuel simulant flowing and contains quantitative information on how well the fuel nozzle mixes the two flows. A larger (metered) level of acetone is used to increase the signal strength of the fuel simulant because there is a much larger volume of air (main air) to dilute the acetone signal. All images are acquired over the same time interval (90 sec) to have equal noise contributions from thermal electrons and readout noise. Each image is modeled as an array of i separate detectors (pixels) which are sensitive to the number of acetone molecules passing through the laser sheet, i.e., linear fluorescence. The first step of the analysis is to subtract the background image (B_i) from the response image (R_i) and data image (D_i).

$$r_i = R_i - B_i$$

$$d_i = D_i - B_i$$

Now the images contain only fluorescence information. The response image calibrates the signal for laser variation and the known acetone concentration.

$$r_i = k \cdot I_i \cdot \dot{n}_{\text{ace}} = k \cdot I_i \cdot \left[\frac{\dot{m}_{\text{ace}}}{\dot{m}_{\text{fair}} + \dot{m}_{\text{ace}}} \right] = k \cdot I_i \cdot \left[\frac{c_0}{1 + c_0} \right]$$

Similarly, the data image, taken with main air flowing and the same flow of fuel air is analyzed:

$$d_i = k \cdot I_i \cdot \left[\frac{\dot{m}'_{\text{ace}}}{\dot{m}_{\text{air}} + \dot{m}_{\text{fair}} + \dot{m}'_{\text{ace}}} \right]$$

$$\frac{\dot{m}'_{\text{ace}}}{\dot{m}_{\text{fair}}} = c_1,$$

a known higher seeding level

$$d_i = k \cdot I_i \cdot \left[\frac{c_1}{\left(\frac{\dot{m}_{\text{air}}}{\dot{m}_{\text{fair}}} \right)_i + 1 + c_1} \right].$$

The data image is now normalized by the response to account for laser intensity spatial variations and the geometrical factor, k. This produces the signal image, S_i, which is converted to a two-dimensional map of fuel-air ratio.

$$S_i = \frac{d_i}{r_i} = \frac{\left[\dfrac{c_1}{\left(\frac{\dot{m}_{\text{air}}}{\dot{m}_{\text{fair}}} \right)_i + 1 + c_1} \right]}{\left[\dfrac{c_0}{1 + c_0} \right]}$$

using $c_0 \sim 0.001, \ll 1$ and $c_1 \sim 0.01, < 1$ to simplify

$$S_i = \left(\frac{c_1}{c_0} \right) \cdot \left[\frac{(f/a)_i}{1 + (f/a)_i} \right].$$

Each image, S, is presented as a two-dimensional, color-coded map of the fuel/air ratio in the annular region of the bluff-body nozzle. The data is normalized to the average fuel/air ratio of each image to facilitate comparisons between different configurations. Statistics are computed to yield an average f/a ratio over the entire image as well as the standard deviation of the multiple measurements contained within. The overall mixing efficiency is characterized by the σ/μ parameter, the standard deviation of the pixel data from the mean fuel/air ratio of the image. The data is also presented in forms useful for engineering analysis. The radial distribution of f/a, averaged for adjacent annular rings (0.25-cm width), is plotted versus the annular opening at the nozzle exit, i.e., as percent of the span between the radius of the centerbody and the outer radius of the nozzle. These views of the data quickly show ID-peaked, OD-peaked, or flat fuel distributions. Relevance to the engine operating envelope is gained from plots of the mixing efficiency, σ/μ, versus the fuel to main air momentum ratio, J.

The accuracy of the acetone fluorescence experiments can be quantified by comparing the acetone-measured average f/a at the exit of the nozzle with the known, metered flows of air supplied to the experiment. The data are shown in Fig. 4 for the fuel tube and centerbody configurations tested in this study. The measured values underestimate the metered flows, reflecting uncertainties in precision of the meters used for these tests. A linear least-squares regression of the data indicate a correlation coefficient of 4.5 percent. Over 80 percent of the data points are within the ±7 percent limits shown in the figure.

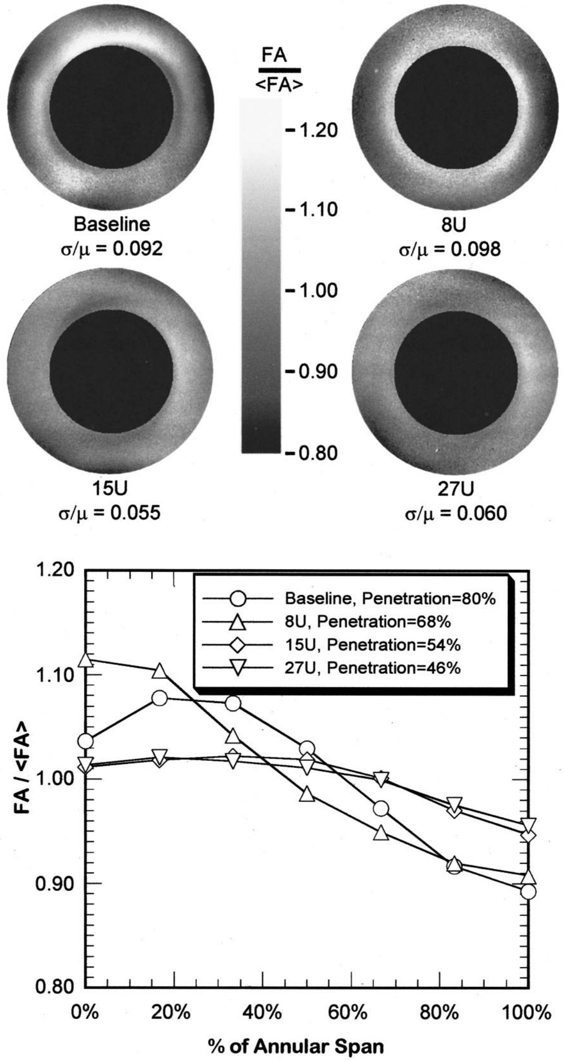

Fig. 5 Normalized F/A distribution 6 mm from exit plane for different levels of fuel penetration, $r_{CB}/r_{exit}=0.60$

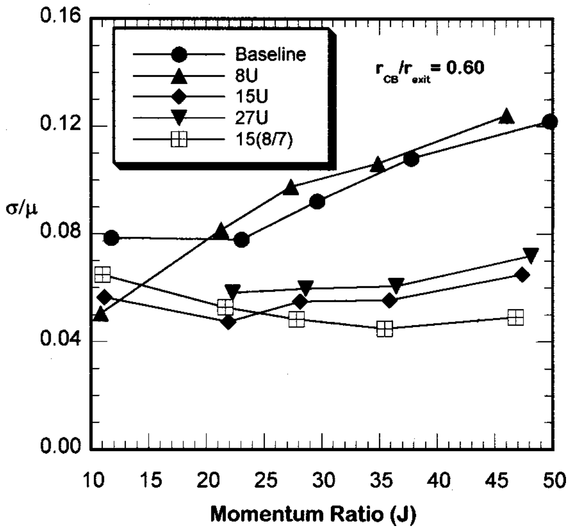

Fig. 6 Mixing efficiency over range of fuel momentum ratios

Experimental Results and Discussion

Fuel Air Ratio Measurements. The acetone PLIF apparatus was used to measure the fuel distribution at the exit plane of the nozzle for each of seven fuel tube configurations. Figure 5 shows the fuel air distribution measured for the $r_{CB}/r_{exit}=0.60$ centerbody for the baseline, 8-U, 15-U, and 27-U fuel tubes. This series of tests was designed to determine the f/a distribution as a function of penetration. The penetration was calculated using a correlation developed by Hautman et al. [11] for gas jets injected normal to a crossflow. The correlations were developed under varying air flow conditions to provide scaling for environments typical of subsonic propulsion devices. In these cases the number of holes are increased causing the penetration to decrease from 80 percent to 46 percent while the axial spacing between holes decreases. All data shown in Fig. 5 were acquired at an overall momentum ratio of 28. The baseline case, a high penetration orifice array, was developed in the earlier tests by Snyder et al. [1] using a different centerbody. The earlier tests indicated 80 percent penetration was best for that centerbody design. The results of Fig. 5 show that the 15-U pattern with penetration of 54 percent is best for this bluff body design. The images show the f/a sensitivity to centerbody design and the importance of fuel penetration and axial spacing. The lower plot in Fig. 5 shows the radial distribution of fuel/air across the nozzle annulus. A perfectly premixed condition is approached when $FA/FA_{avg}=1.0$ over the entire span. Examination of the curves reveals that the 15-hole and 27-hole pattern provided the best distribution of fuel and air, however, the 15-hole has the best σ/μ.

It is desired to have NO_x emissions minimized over a wide range of engine operating conditions, thus it is important to determine how the f/a distribution changes as a function of power setting. Tests were performed over a wide range of momentum ratios corresponding to the desired engine cycle. The mixing efficiency for five fuel tube configurations, with the $r_{CB}/r_{exit}=0.60$ centerbody, are plotted in Fig. 6. Two of the five configurations have large premixing sensitivity to changes in momentum ratio. This data shows that an orifice array that is the most uniform at low momentum ratios (i.e., 8U is best at $J=10$) may not be the best over the operation envelope. The optimum configuration should have the lowest σ/μ and the flattest distribution of mixing efficiency over the momentum ratio required. The optimum orifice array for this centerbody is the 15(8/7) configuration.

The optimum penetration for a bluff-body centerbody was shown to be different than the original centerbody evaluated by Snyder et al. [1]. In order to determine the sensitivity of the nozzle's premixing level to the bluff body centerbody, the size of the centerbody (i.e., r_{CB}/r_{exit}) was changed and additional fuel tube configurations were evaluated for their influence on the f/a distribution near the exit plane. The results are displayed in Fig. 7. These data show that the exit fuel/air distribution profile can be tailored by shifting fuel upstream or downstream in the inlet slot. Shifting fuel downstream (Baseline, 15(8/7), 15(9/6)) can shift the f/a distribution at the exit plane from ID-peaked, to centered, to OD-peaked. The 15(8/7) configuration demonstrated the highest level of premixing for both the $r_{CB}/r_{exit}=0.47$ and 0.60 centerbodies.

The mixing efficiency versus momentum ratio is plotted in Fig. 8 for both centerbodies with identical fuel tube configurations. These data show that the 15(8/7) hole pattern is also the best over the momentum ratio range of interest. Examination of the data for the 15(8/7) fuel tube indicate the best premixing occurs at different momentum ratio for $r_{CB}/r_{exit}=0.47$ than for $r_{CB}/r_{exit}=0.60$. The 8-U data set shows the highest sensitivity to changes in centerbody geometry. The data for the baseline case shows significantly different trends for the two centerbodies; for $r_{CB}/r_{exit}=0.47$, σ/μ increases as momentum ratio decreases, whereas σ/μ increases with momentum ratio for $r_{CB}/r_{exit}=0.60$.

At some conditions, a pilot may be used at the tip of the bluff-body centerbody to enhance combustion stability. Fuel/air distri-

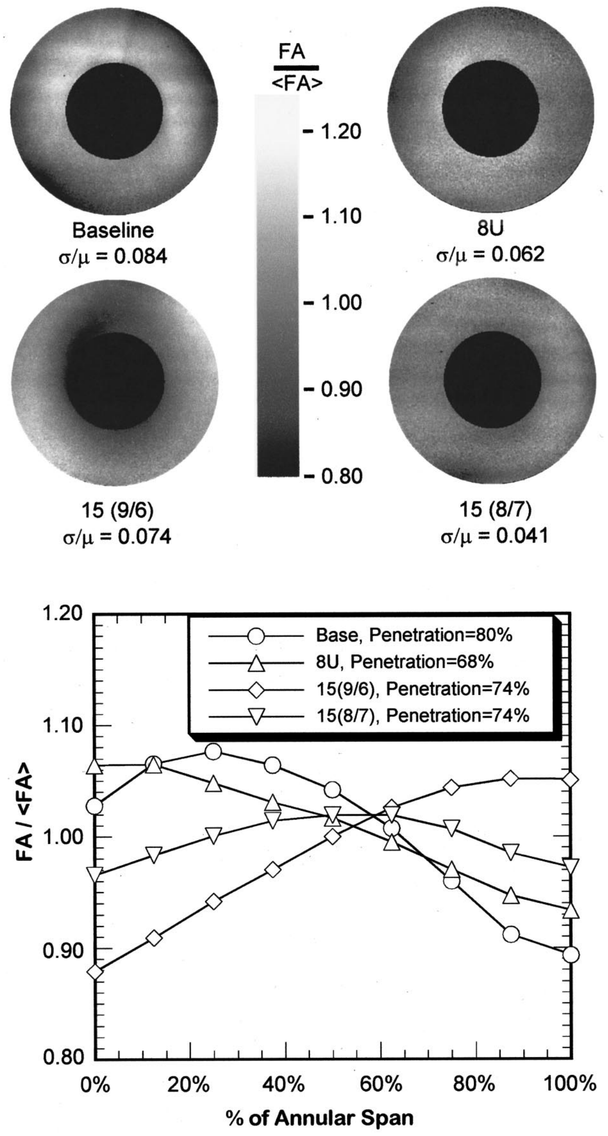

Fig. 7 Normalized F/A distribution 6 mm from exit plane for different fuel distributions along the inlet slot length, $r_{CB}/r_{exit}=0.47$

bution measurements were made with various levels of pilot to determine how the f/a distribution varies as piloting levels increase. The preferred centerbody, $r_{CB}/r_{exit}=0.47$, and main gas fuel orifice array, 15(8/7), were used for this piloting study. Fuel/air distribution measurements are presented in Fig. 9 for zero, two, five, and seven percent pilot. This investigation required measurements of the f/a distribution across the entire exit plane, not just the annulus as presented in earlier figures. The zero percent pilot condition of Fig. 9 is the f/a data from the 15(8/7) case of Fig. 7, analyzed over the full exit plane diameter. Notice that the σ/μ increases from 0.041 to 0.065 when the entire diameter is used versus the annulus. The zero percent pilot actually has fuel depression behind the centerbody, contributing to its higher σ/μ relative to the two percent case. Studies by Kendrick et al. [9] indicated that combustor acoustics could be significantly reduced by adding two percent pilot. What is interesting in Fig. 9 is that the σ/μ for the two percent case is actually lower than without pilot. The addition of five percent and seven percent pilot significantly increase the σ/μ and discrete fuel jets are visible for these conditions.

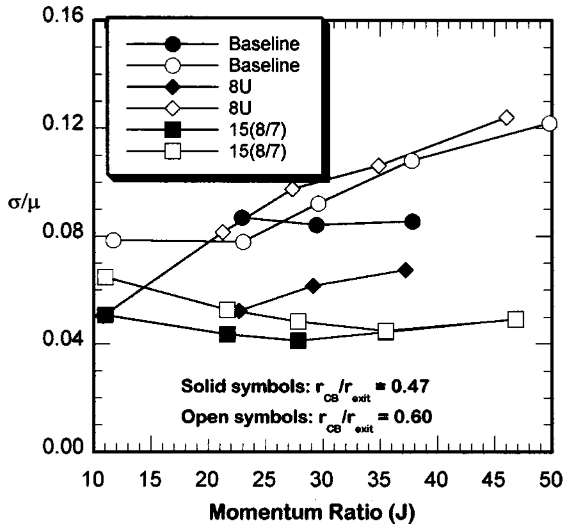

Fig. 8 Mixing efficiency over range of fuel momentum ratio for two different r_{CB}/r_{exit}

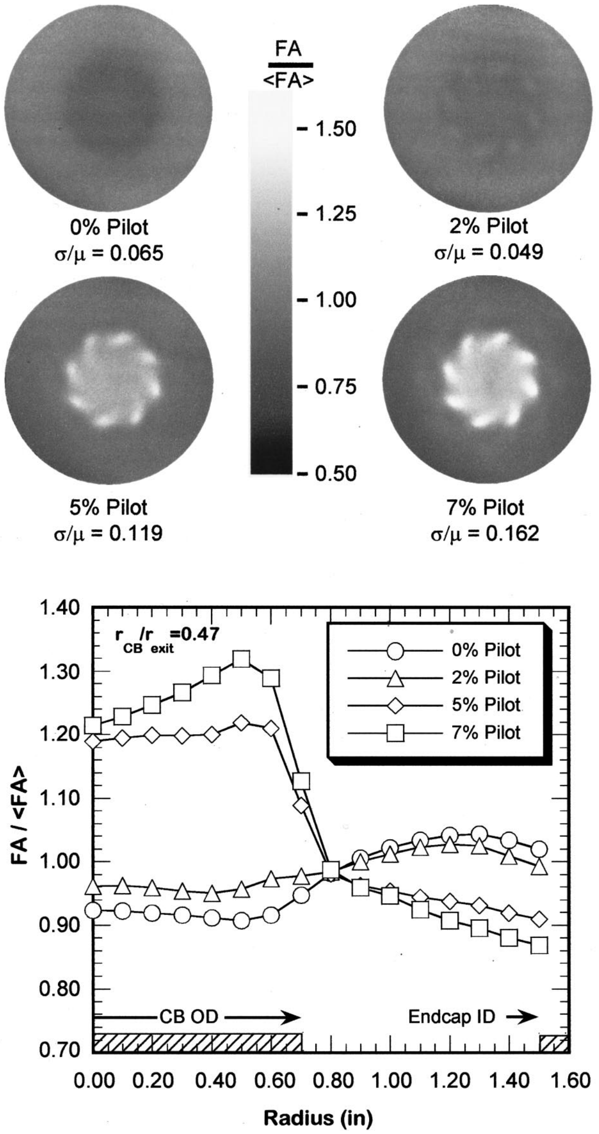

Fig. 9 F/A distribution 6 mm from exit plane of premixing nozzle with 15(8/7) main fuel orifice array for several levels of centerline pilot

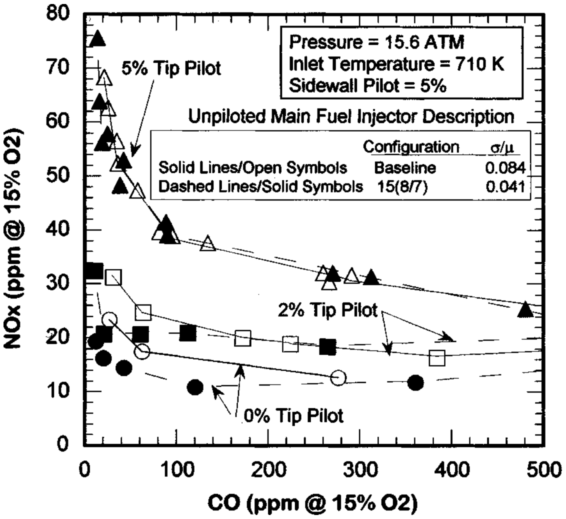

Fig. 10 Emission results from SNR for $r_{CB}/r_{exit}=0.47$ and 15(8/7) fuel tubes

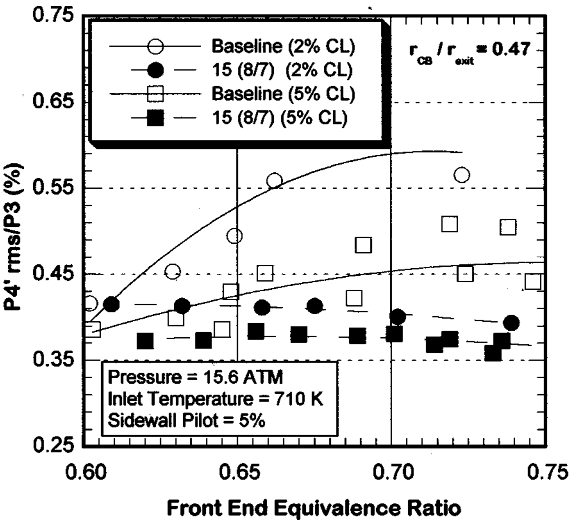

Fig. 11 Acoustic data from combustion tests of baseline and 15(8/7) orifice arrays with $r_{CB}/r_{exit}=0.47$ in the SNR

Comparisons With Combustion Test Data. A bluff-body TE nozzle with the baseline and 15(8/7) hole pattern was installed into a single nozzle rig (SNR) for actual combustion tests as described in detail by Kendrick et al. [9]. The SNR provides an ideal test bed for investigation of prospective nozzle configurations since it closely models the actual engine's geometry, pressures and temperatures. Dynamic pressure measurements were made inside the plenum chamber and combustion chamber (liner) using infinite tube transducers (ITPs) which had to be corrected in both amplitude and phase due to the length of the tube connecting the liner and the transducer. Uncertainty in the rms measurement was typically less than 2 percent. Emissions measurements were made through the use of an array of water-cooled probes inserted into a flange immediately downstream of the combustor liner. Uncertainties in these measurements were less than 3 ppm for NO_x and 10 ppm for CO. A T-Section downstream of this plate diverted the hot flow to allow optical access for PMT measurements and flame visualization.

Emission Measurements. Emissions measurements were made in the SNR to determine the impact that f/a distribution has on NO_x and CO emissions. Tests were conducted at 15.6 atm with an inlet temperature of 710 K over a range of fuel air ratios (0.60–0.75). These fuel/air ratios were set higher than normal gas turbine engine conditions to accommodate rig operation constraints. Figure 10 shows NO_x and CO emissions for the baseline and 15(8/7) main fuel orifice arrays with various levels of tip pilot. Five percent sidewall pilot was kept constant for all test conditions thus, the lowest NO_x levels possible are not shown here. With 0 percent and 2 percent tip pilot, the difference between baseline and 15(8/7) is clearly observed. For the unpiloted case, reducing the σ/μ from 0.084 to 0.041, shifts the NO_x versus CO curve to the lower left. This shift indicates improved premixing levels and the ability to reduce both NO_x and CO by increasing the premixing level. At the operating point where CO levels are low, NO_x levels are reduced by 25 percent. As the tip pilot level increases beyond 2 percent, NO_x production is dominated by the pilot. Thus, changes to the main gas fuel array do not affect the NO_x/CO curve.

Analysis of the σ/μ over the entire exit diameter for the 15(8/7) case indicated that the premixing level actually decreased when 2 percent pilot is added yet NO_x/CO emissions were higher. This result suggests that fuel is mixing rapidly behind the centerbody in the nonreacting measurements whereas in the combustion tests it is burning like a diffusion flame before mixing.

Acoustic Measurements. Inherent in the design of any fuel-air premixer is its ability to yield minimal acoustic levels (combustor pressure fluctuations) over the engine's power curve. Acoustic measurements made in the SNR were compared to acetone fluorescence measurements to determine how the premixing level and main gas orifice array affect combustion dynamics. Figure 11 compares the combustor acoustic levels for the baseline and 15(8/7) orifice arrays at two levels of centerline piloting (2 percent and 5 percent). The transducer was located 2.54 cm downstream of the nozzle's exit plane. In both cases, side-wall diffusion piloting was kept constant at 5 percent. Apparent for both configurations is the acoustic attenuation with increasing centerline piloting due to the increased stability of the central recirculation zone and less favorable acoustic-heat release coupling as described in detail by Kendrick et al. [9]. More importantly, however, is the observation that the 15(8/7) scheme yields reduced combustor acoustic levels compared with its baseline counterpart for identical piloting levels. Hence in addition to promoting a more homogenous f/a distribution and consequently reduced emission levels (Fig. 7), the 15(8/7) injection scheme has also provided superior acoustic levels.

A thorough investigation of combustion systems cannot be achieved without addressing the chemical-acoustic interactions that inevitably occur. As shown by others [12,13] it is this interaction between the pressure and the heat release which typically sustains the instabilities. Thus, changing the main gas fuel array changes the convective time between the injection site and the reaction zone. Quantification of this coupling is achieved through the use of the Rayleigh index which can be represented mathematically as

$$R=\frac{\gamma-1}{\gamma\bar{p}}\int_V dV\int_t^{t+\tau}p'(\mathbf{x},t)q'(\mathbf{x},t)dt$$

where p' and q' are the fluctuating components of pressure and heat release, respectively, and γ, $\bar{p}$, and V are the ratio of specific heats, mean pressure, and volume. Integration over both spatial and temporal variables, therefore, yields a global Rayleigh index which characterizes the level of overall acoustic coupling or driving. This global index is presented for both main fuel injection schemes in Fig. 12 for 5 percent centerline piloting. Unfortunately, the lack of accurate PMT data for other centerline percentages did not permit a more thorough comparison. It is seen that the 15(8/7) injection scheme's improved acoustic levels (Fig. 11) are a result of a shifting in the temporal location of the heat

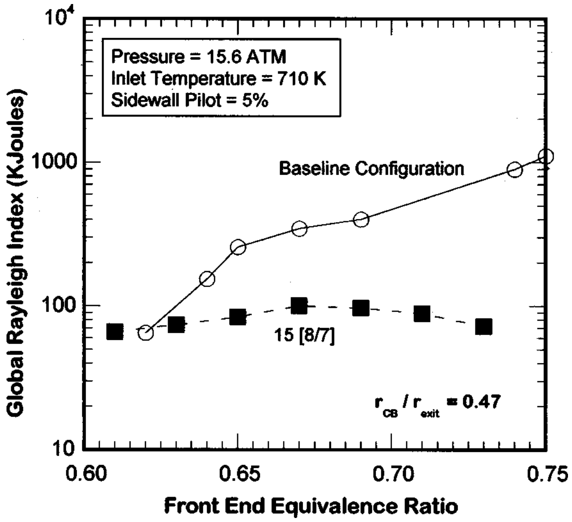

Fig. 12 Global Rayleigh indexes for both injection schemes at 15.6 atm, and five percent CL piloting

release profile relative to the acoustic cycle as evidence by the reduced global Rayleigh indices. These results indicate that changing the main gas fuel array from the baseline to the 15(8/7) reduced combustor acoustics in addition to reducing the emissions levels and improving the fuel/air distribution near the nozzle exit plane.

Conclusions

- An acetone fluorescence technique has been applied to measure the fuel air distribution at the exit plane of various premixing nozzle configurations. The ratio of the measured to metered f/a value was found to be 1.0 ± 0.07 (80 percent confidence interval).
- The f/a distribution is a strong function of centerbody geometry, fuel orifice size and distribution and, momentum ratio. Thus, the main gas fuel array should be evaluated over the entire momentum range of interest and reevaluated for nozzle geometry changes.
- The f/a distribution at the exit of a tangential entry nozzle can be tailored by shifting fuel along the inlet slot length. Increasing fuel to the upstream end of the slot changes the exit plane f/a distribution from an OD-peaked to an ID-peaked profile.
- The f/a distribution across the entire premixer exit diameter and the premixer annulus should be evaluated to optimize fuel nozzle design for both emissions and acoustics when piloting is used. For unpiloted cases, only the main fuel annulus should be used.
- Improving the level of premixing for the main fuel injector orifice array from $\sigma/\mu=0.084$ to 0.041, for the unpiloted case, shifts the NO_x, versus CO curve to lower left. NO_x levels can be improved by nearly 25 percent.
- Changing the main fuel orifice array can improve both the premixing level and reduce the Global Rayleigh Index leading to reduced combustor acoustic levels.

Acknowledgments

The authors wish to thank Mr. Joseph Poplawski for operation of the acetone fluorescence facility and Mr. Mark Anderson for programming the data analysis software to produce the images, statistics and plots.

Nomenclature

$\dot{m}_{\rm fair}$ = mass flow of fuel simulant
$\dot{m}_{\rm air}$ = mass flow of main air
$\dot{m}_{\rm ace}$ = mass flow of acetone
$(f/a)_i$ = $(\dot{m}_{\rm fair}/\dot{m}_{\rm air})_i$, local fuel to air ratio at the *i*th pixel
$c_0=\dot{m}_{\rm ace}/\dot{m}_{\rm fair}$, = ($\sim$0.1 percent acetone seeding)
$n_{\rm ace}\sim\dot{m}_{\rm ace}$, = number of acetone molecules within the spatial location mapped by the *i*th pixel
k = geometric factor including window attenuation, magnification and pixel gain
I_i = laser intensity at the *i*th pixel, same for background, response, and data images
B_i = *i*th pixel of the background image
R_i = *i*th pixel of the response image
D_i = *i*th pixel of the data image
S_i = *i*th pixel of the signal image
σ = standard deviation
μ = mean F/A
$r_{\rm CB}$ = radius of nozzle centerbody
$r_{\rm exit}$ = radius of nozzle exit

References

[1] Snyder, T. S., Rosfjord, T. J., McVey, J. B., Hu, A. S., and Schlein, B. C., 1996, "Emission and Performance of a Lean-Premixed Gas Fuel Injection System for Aeroderivative Gas Turbine Engines," ASME J. Eng. Gas Turbines Power, **118**, pp. 38–45.
[2] Rutar, T., Martin, S. M., Nicol, D. G., Malte, P. C., and Pratt, D. T., 1997, "Effect of Incomplete Premixing on NO_x Formation at Temperature and Pressure Conditions of LP Combustion Turbines," ASME Paper 97-GT-335, presented at the International Gas Turbine & Aeroengine Congress & Exhibition, Orlando, FL, June 2–5.
[3] Barnes, J. C., and Mellor, A. M., 1998, "Effects of Unmixedness in Piloted-Lean Premixed Gas-Turbine Combustors," J. Prop. Power, **14**, pp. 967–973.
[4] Barnes, J. C., and Mellor, A. M., 1998, "Quantifying Unmixedness in Lean Premixed Combustors Operating at High-Pressure, Fired Conditions," J. Prop. Power, **14**, pp. 974–980.
[5] Fric, T. F., 1992, "Effects of Fuel-Air Unmixedness on NO_x Emissions," AIAA Paper 92-3345, presented at the 28th AIAA/SAE/ASME/ASEE Joint Propulsion Conference & Exhibit, Nashville, TN, July 6–8.
[6] Mongia, R. K., Tomita, E., Hsu, F. K., Talbot, L., and Dibble, R. W., 1996, "Use of an Optical Probe for Time-Resolved in situ Measurement of Local Air-to-Fuel Ratio and Extent of Fuel Mixing with Applications to Low NO_x Emissions in Premixed Gas Turbines," presented at the 26th Symposium (International) on Combustion, Napoli, Italy, pp. 2749–2755.
[7] Lee, J. G., and Santavicca, D. A., 1997, "Fiber-Optic Probe for Laser-Induced Fluorescence Measurements of the Fuel-Air Distribution in Gas-Turbine Combustors," J. Prop. Power **13**, pp. 384–387.
[8] Frazier, T. R., Foglesong, R. E., Coverdill, R. E., Peters, J. E., and Lucht, R. P., 1998, "An Experimental Investigation of Fuel/Air Mixing in an Optically Accessible Axial Premixer," AIAA Paper 98-3543, presented at the 34th AIAA/ASME/SAE/ASEE Joint Propulsion Conference & Exhibit, Cleveland, OH, July 13–15.
[9] Kendrick, D. W., Anderson, T. J., Sowa, W. A., and Snyder, T. S., 1998, "Acoustic Sensitivities of Lean-Premixed Fuel Injectors in a Single Nozzle Rig," ASME Paper 98-GT-382, Presented at the International Gas Turbine & Aeroengine Congress & Exhibition, Stockholm, Sweden, June 2–5.
[10] Lozano, A., Yip, B., and Hanson, R. K., 1992, "Acetone: A Tracer for Concentration Measurements in Gaseous Flows by Planar Laser-Induced Fluorescence," Exp. Fluids, **13**, pp. 369–376.
[11] Hautman, D. J., Haas, R. J., and Chiappetta, L., 1991, "Transverse Gaseous Injection into Subsonic Air Flows," AIAA Paper 91-0576, Presented at the 29th Aerospace Sciences Meeting, Reno, NV, Jan. 7–10.
[12] Keller, J. O., and Barr, P. K., 1996, "Premixed Combustion in a Periodic Flow Field," *Unsteady Combustion*, F. Culick, M. N. Heitor, and J. H. Whitelaw, eds., Kluwer Academic, Dordrecht.
[13] Raun, R. L., Beckstead, M. W., Finlinson, J. C., and Brooks, K. P., 1993, "A Review of Rijke Burners and Related Devices," Prog. Energy Combust. Sci., **19**, pp. 313–364.

Determination of Thermoacoustic Response in a Demonstrator Gas Turbine Engine

C. A. Arana

B. Sekar

Propulsion Directorate,
Air Force Research Laboratory,
Wright Patterson AFB, OH 45433-7251

M. A. Mawid

Engineering Research & Analysis Company,
Dayton, OH 45440-4429

C. B. Graves

Pratt and Whitney,
East Hartford, CT

This paper describes an analytical and experimental investigation to obtain the thermoacoustic response of a demonstrator gas turbine engine combustor. The combustor acoustic response for two different fuel injector design configurations was measured. It was found that the combustor maximum peak to peak pressure fluctuations were 0.6 psi to 2 psi for configuration A and B, respectively. Based on the measured acoustic response, another experimental investigation was conducted to identify the design features in configuration B that caused the increase in the acoustic response. The data showed that by changing the fuel injector swirler's vane to inner passage discharge area ratio, the engine acoustic response could be lowered to an acceptable level. A simplified analytical model based on the lumped-parameter approach was then developed to investigate the effect of geometrical changes upon the engine response. The analytical model predicted the fuel injector/swirlers acoustic response as a function of the swirlers inner passage discharge area ratio and frequency. The predictions were consistent with the experimental observations, in particular, it was predicted that as the area ratio was increased, the system reactance was decreased and as a result the system changed from a damping to an amplifying system. [DOI: 10.1115/1.1374200]

1 Introduction

The Air Force Integrated High Performance Turbine Engine Technology (IHPTET) combustors must operate free of combustion-driven dynamic instabilities that could compromise the structural integrity of high performance engines. To double the thrust-to-weight ratio, as required for future high-performance military engines, the combustion system, which includes the diffuser, combustion chamber, and fuel injectors/swirlers, will be required to operate at much higher overall design equivalence ratios, inlet pressures, and temperatures than the existing military aircraft engines combustors.

A key element in the combustion system is the fuel injector/airswirler module which dictates ground ignition, altitude relight, lean blowout (stability), pattern factor and smoke emission characteristics of the engine's combustor. Improved understanding of the fuel injector/swirler performance and its influence on the overall combustor performance for both the low and high-power conditions is currently obtained through high-quality databases. These high-quality databases combined with modeling efforts can then provide information on design features and characteristics that will lead to either optimum or deteriorated performance of the combustion system. Fuel injection system performance is mainly measured based upon its stability (lean blowout) characteristics and smoke emissions level. An improved fuel injector/swirler design would broaden the turn-down fuel-air ratio which is defined as the maximum allowable fuel-air ratio at which the flame blows out. The increase in the turn-down fuel-air ratio is dictated by the need for greater range of high to low-power operation for military engines. Each new military combustor, whether it is a new design or simply a derivative version of an existing design has typically required a higher temperature rise than the preceding design. This has been accomplished by increasing the fraction of airflow to the injectors/swirler module and fuel flow. The implication is that a more demanding requirement is placed on the injector design and performance to provide an acceptable level of lean blowout, smoke emissions, and engine dynamic stability. To meet future high-performance military engines combustor design requirements and to allow a return to simpler, more affordable single-annular combustor designs, innovative air-swirler technology has become increasingly important for improving low-power stability while simultaneously increasing high-power temperature rise in a combustor with minimized volume. This presents a challenge to the historical manner in which combustors have been designed.

The understanding of the effect of fuel injector design features on the combustion dynamic stability remains very challenging. This is due to the fact that most existing fuel injector/swirler and combustors design databases lack a provision for predicting combustion-driven instabilities during the pre-design and design phases. Currently, a need exists to predict and quantify combustion instabilities in high-performance military fuel injectors and combustors during the design stage. Axial, tangential, and radial instability modes may all develop in the combustors that could severely impact the engine performance and its structural integrity. Various approaches are presently used to predict combustion instabilities. These approaches range from one-dimensional linear stability based [1–3], to one, two, and three-dimensional nonlinear-CFD-based [4–8]. Mohanraj et al. [5] developed a one-dimensional computer model using a heuristic mixing model along with a semi empirical open loop active controller. Quinn and Paxon [9] used a one-dimensional model to study thermoacoustic instabilities in combustion systems. Mawid and Sekar [10] used a one-dimensional model to actively control combustion oscillations. Other analytical models [11–18] based upon the unsteady-pressure equation in one and three dimensions were also developed and calibrated/anchored to experiments under controlled conditions such that extrapolation to other conditions could be performed.

In order to optimize fuel injector/swirler performance improvements, development efforts that include the design, analysis, and testing of advanced fuel injector/swirler have been carried out. To enhance the performance of military combustors, a new fuel injector concept was designed. The fuel injector was tested and its performance was demonstrated in a military engine demonstrator

---

Contributed by the International Gas Turbine Institute (IGTI) of THE AMERICAN SOCIETY OF MECHANICAL ENGINEERS for publication in the ASME JOURNAL OF ENGINEERING FOR GAS TURBINES AND POWER. Paper presented at the International Gas Turbine and Aeroengine Congress and Exhibition, Munich, Germany, May 8–11, 2000; Paper 00-GT-091. Manuscript received by IGTI Oct. 1999; final revision received by ASME Headquarters Oct. 2000. Associate Editor: D. R. Ballal.

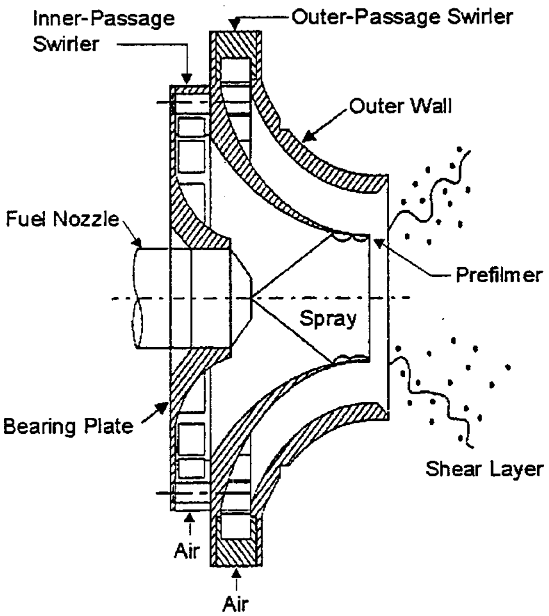

Fig. 1 Schematic of the baseline fuel injector design configuration A

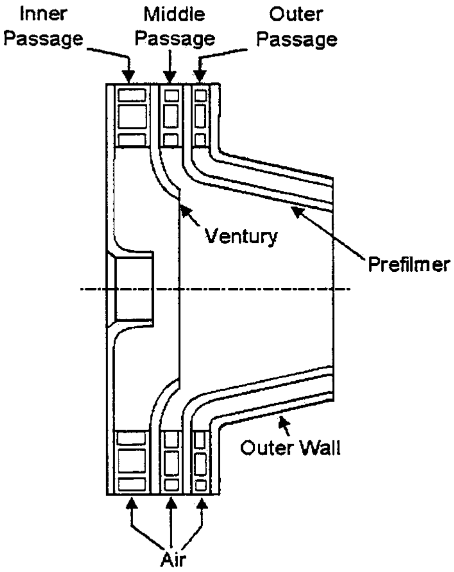

Fig. 2 Schematic of new fuel injector, design configuration B

for improved injector lean blow out, lower smoke production level and dynamic stability. The primary vision was to provide a database of a high quality with sufficient information that could be used by combustor designers to design fuel injectors/swirlers with higher turn-down fuel-air ratios. To demonstrate the benefits of an improved database a goal of 20 percent increase in the turn-down fuel-air ratio was established. An existing hybrid airblast injector with inner and outer airflow passages was selected as a baseline design—concept A, Fig. 1. After extensive analysis and testing of this concept, the observations were that fuel injectors with low smoke numbers were likely to have higher swirl flows in the proximity of the spray point and that good ignition and stability (lean blowout) characteristics were achieved for fuel injectors/swirlers with lower swirl flows in the proximity of the spray point. These conclusions therefore led to the development of new injector design concepts, which in turn would simultaneously satisfy the apparent conflicting requirements for high and low swirl flows in the proximity of the spray point.

A design concept B, Fig. 2, with 16 design variances, was extensively evaluated and characterized using a design of experiments approach for lean blowout performance.

Co-rotating and counter-rotating swirlers variances were characterized for the different passages. The injectors were tested in an atmospheric ignition rig for improved stability performance. Eight of these new injectors were selected for further smoke emissions testing at high-pressure conditions. The test matrix injectors were then compared against high stability and low smoke baseline designs as design concept A. It was shown that various versions of the new design concept improved stability relative to the low smoke baseline design and reduced smoke level relative to the high stability baseline injector design. When these two results were combined in the best overall performance of design concept B, the 20 percent goal in increasing the turn-down fuel-air ratio was accomplished. Diagnostic testing for fuel spray patternation, penetration using Laser Doppler Velocimetry (LDV) and Particle Doppler Phase Analyzer (PDPA) was performed to obtain the flow field characteristics and to derive a homogeneity factor for smoke performance.

The best performing injector design derived from concept B was then implemented into an advanced military engine demonstrator. The fuel injector was tested for altitude relight characteristics, and high-pressure pattern factor and smoke emissions in a full annular rig. Under these tests, the injector design concept B was proven to perform as tested in the rig. However, under static sea level testing, an acoustic resonance was measured at greater amplitude than for the baseline injector design concept A. This result was considered significant enough to remove the new injector design from the engine. Moreover, this result also led to additional efforts to identify the root causes of measured acoustic resonance and identify an appropriate diagnostic test and model to help in the early detection and prevention of future occurrences. A simplified model based on the lumped-parameter approach was developed and applied to the design. The model predicted the trends that were measured experimentally. In particular, the fuel injector response factor was predicted and found to vary substantially as the fuel injector geometrical areas changed as will be shown later.

The engine demonstrator acoustic response due the implementation of the fuel injector design concept B will be first presented in the next section, which will be followed by a section on the acoustic response tests for the baseline fuel injector, Fig. 1, and the new fuel injector design swirlers, Fig. 2, with and without combustion. The final two sections will be on an attempt to develop a simple acoustic model to investigate the acoustic response of the engine combustor followed by a section on conclusion.

2 Engine Acoustic Response Test

As mentioned above, the improved fuel injector design configuration B was tested in annular combustor rigs for pattern factor, smoke, and altitude relight capability. The tests were successful, where no increase in smoke output was measured and the altitude relight capability was further extended another 5 K ft compared to the baseline design configuration A. The combustor was then assembled into a development military engine demonstrator and during testing, the combustor demonstrated an acoustic instability. The oscillations were severe enough with the new injector design that removal of the injector from the demonstrator engine was necessary, in spite of its improved performance.

The acoustic data were obtained from high-frequency response pressure probes that were placed at various locations in the engine during sea level operation. The base combustor configuration is shown in Fig. 3. The baseline combustor design employed 24 fuel injectors around the circumference of the bulkhead. The air is fed to the combustor through a stepped diffuser, which is a combination of a normal prediffuser and two fairings, which continue the diffusion process after a small dump loss occurs.

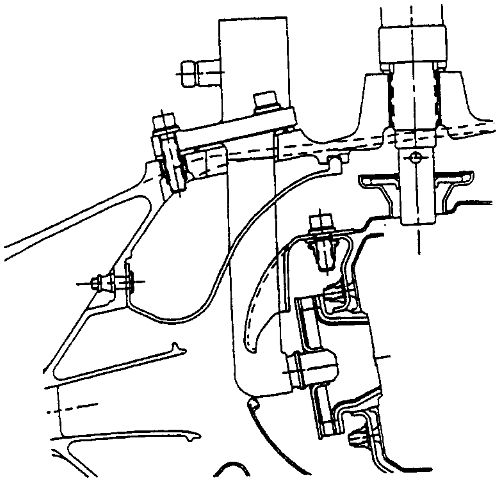

Fig. 3 Front-end cross section of the base combustor configuration

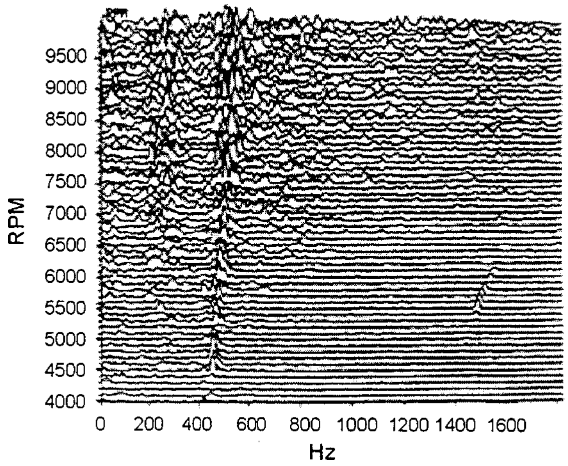

Fig. 5 Waterfall graphs for pressure fluctuations for fuel injector configuration B

The baseline fuel injectors based on configuration A were first tested in the demonstrator engine. Measurements of peak to peak pressure fluctuations as a function of the frequency were obtained and are shown in Fig. 4, which shows the fast Fourier transform of the pressure oscillations in the combustor cavity as a function of the power setting. The *x*-axis is the frequency domain for which responses are measured and the *y*-axis is a normalized peak to peak measure as a function of engine speed. The line at the bottom of the graph shows the peak to peak fluctuations at the lowest engine speed and the line at the top of the graph shows the peak to peak fluctuations at the highest engine speed recorded. The data clearly show that for the baseline fuel injector configuration (design concept A), a maximum peak to peak pressure fluctuation of 0.6 psi in 400 to 500 Hz frequency range was obtained. The combustion mean pressure was 15 psi. This peak to peak pressure fluctuation was deemed acceptable to the turbine. The 400 to 500 Hz region appears to always display the greatest peak pressure fluctuation. The first tangential mode of the baseline combustor corresponds to a frequency of about 250 Hz and the 400 to 500 Hz range corresponds to a quarter wave frequency.

When the new fuel injectors, based on design configuration B, were tested in the engine combustor, the peak to peak pressure fluctuations increased to 1.5 psi as shown in Fig. 5. The peak to peak value is seen to be more confined to 400 to 500 Hz region. The pressure fluctuation data was further backed up with turbine stress data from instrumented blades in both the HP and LP turbines. The higher turbine stress was caused by the buffeting action due to pressure fluctuations. These effects combined pushed the turbine stress levels over the limit. The new fuel injectors were considered to be the root cause of the problem and were removed from the engine.

In another attempt to test the new fuel injectors, the airflow swirlers were made with greater precision for geometrical dimensions and flow by machining them as compared to the first test where the injector set was cast in a rapid prototype process. The measurements, however, yielded worse peak to peak pressure fluctuations in the 400 to 500 Hz range than any previous test. The maximum peak to peak, as shown in Fig. 6, was approximately 2 psi and was completely unacceptable. Figure 6 clearly shows a very pronounced response in the 400 to 500 Hz ranges which is a clear evidence that the combustor section has a preferred resonance in the 400 to 500 Hz range. This resonance is amplified when the new injector designs were employed with the consequences of unacceptable turbine buffet stresses.

On the basis of this test, the development efforts addressed two new objectives. The first was to make measurements that would potentially indicate that an injector design would lead to acoustic instability. The second was to determine a way to address the acoustic issues and identify the design features that would lead to an acoustic response while maintaining an improved performance as will be discussed in the next section.

3 Fuel Injector Acoustic Response Tests

The acoustic response that was measured in the demonstrator engine led to two important challenges. The first challenge was to

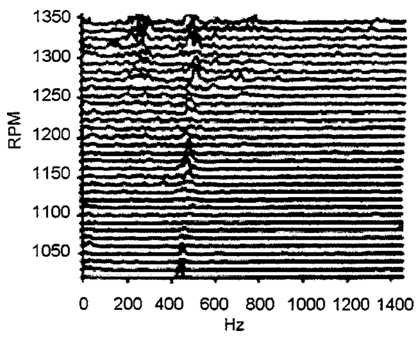

Fig. 4 Waterfall graphs for pressure fluctuations for fuel injector configuration A

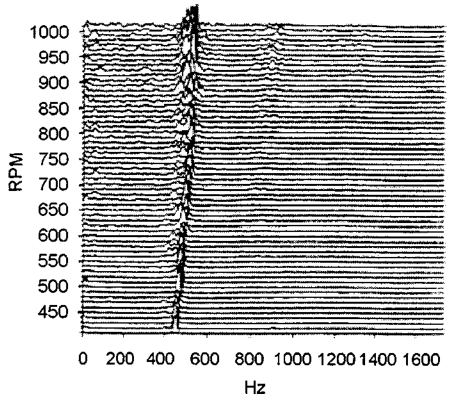

Fig. 6 Waterfall for pressure fluctuations for fuel injector configuration B

understand what led to the acoustic combustion instability in the annular combustor and devise an appropriate diagnostic test and an analytical model to screen future injector designs. The second challenge was to identify the design features which led to the instability in the new injector design and eliminate them without compromising the lean blowout and smoke performance achieved.

Three different tests were devised in increasing complexity to determine the characteristics acoustic pressure fluctuations of a fuel injector with swirlers. The three tests differ as follows:

- Swirler Free Aero Acoustic: The individual swirlers were flowed and their acoustic characteristics were documented. This test assumes that the swirler acoustics drive the response.
- Swirler Forced Aero Acoustics: The acoustic response of the swirler to a fluctuating pressure inputs was measured. This test assumes the swirler to be an acoustic filter.
- Combustion Heat Release Rate Acoustic Response: A combusting fuel air mixture from the swirler/injector was subjected to fluctuating pressure input and the pressure response was documented.

The key approach was to identify which design feature(s) of the new injector concept was potentially responsible for the measured combustion instability in the full annular combustor. The new injector design swirler differed from the baseline design in three clear ways, which were contained in the inner airflow passage. First, the inner passage was a mixture of air streams from two swirlers and the mixing layer starts at the end of inner passage venturi. This venturi end was believed to be a potential source of vortex shedding. Second, the mixing process occurs between counter-rotating flow fields which leads to a shearing action internal to the swirler which again would potentially lead to vortex shedding. The third feature was the ratio of vane area to discharge area in the new injector design swirler was much greater than that of the baseline design. The objective of the injector tests was to determine which of the key design feature differences between the baseline and the new design was most responsible for the occurred combustion instability. The venturi end, counter-rotation and the area ratio of vane to discharge features were therefore varied in the tests, one at a time. The metric of a successful test was that the test showed a clear discriminator between the baseline and the new injector design.

3.1 Swirl Free Aero Acoustic Test. A set of cold flow free acoustic tests was performed to test whether or not the new injector swirler was acting as an exciter. These tests were based upon the premise that any radial inflow swirler is a type of vortex whistle, which was studied and characterized by Vonnegut [19]. A specially damped plenum was configured to provide a minimum level of upstream disturbances. The acoustic characteristics of the discharge stream were analyzed using a microphone and a Fast Fourier Transform signal analyzer. The peak frequency was recorded as a function of the pressure drop for the baseline and new injector swirlers as shown in Fig. 7.

As can be seen in Fig. 7 that the new injector swirler design has a frequency characteristic which is about twice the natural frequency of the annular combustor observed previously. This is indicative of the beating type frequency.

3.2 Swirl Forced Response Aero Acoustics Test. The radial swirlers represent the primary conduits of air between the external combustor shrouds and the internal combustion chamber. This means that if coupling and amplification between the chambers is the root cause of the instability observed, then it is important to test the swirlers response to a forcing function by measuring the impedance of the conduit. The impedance is defined as the total opposition (both resistance and reactance) exerted by the swirlers to the forced (or pulsed) airflow of a given frequency. The impedance of the swirlers was determined by measuring the transfer function of the swirlers. In these tests, the measured upstream parameter was the pressure. The measured downstream parameter was velocity over a range of frequencies.

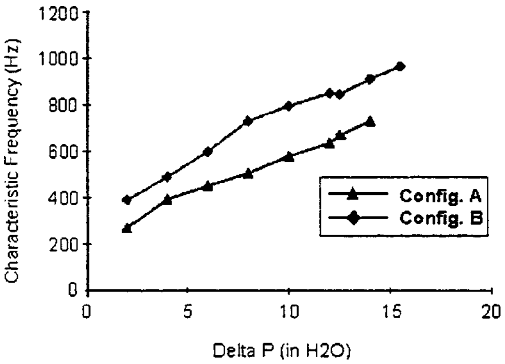

Fig. 7 Frequency versus pressure drop

As mentioned earlier, the new injector design (configuration B) differed from the baseline design configuration A in three ways, namely the venturi, counter-rotating airflow swirlers of the venturi and middle passage, and in the ratio of the vane area to the discharge area. The major difference between the two designs was in the vane area of the new design, which was about 40–60 percent greater than the vane to discharge area ratio for the baseline design. The implication is that the new injector design swirler would exhibit less resistance to dynamic changes in the pressure, particularly at higher frequency. For this reason, the transfer functions measured were the ratio of the upstream pressure to the downstream velocity, which would be expected to maintain a higher level at higher frequencies.

Figures 8 and 9 show respectively the measured transfer functions as the ratio of the upstream pressure to the downstream velocity oscillations and the corresponding phase angle relationship of the transfer functions for two baseline designs, named here A_1 and A_2 and the new design configuration B. Note here that the difference between the A_1 and A_2 baseline swirlers designs is in the effective areas Acd. It can be seen that the new design swirlers exhibit a higher value of the transfer function in the 400 to 500 Hz region, which was the natural frequency of the annular combustor. This is indicative of a dynamic response as opposed to a static response. This is also demonstrated in the phase angle relationship between pressure and velocity oscillations in Fig. 9.

The effect of the venturi elimination and counter rotation of new design swirlers was then considered. Figure 10 shows the response characteristics of the venturi elimination injector referred to as B_1 and the change from counter-rotation to corotation of the middle passage referred to as B_2 which are both compared to the new baseline design configuration B. The transfer function between the upstream pressure and downstream velocity show that there is little or no change in the dynamic response characteristics. These measurements clearly indicated that the counter rotation and the addition of the third passage for the new design were not responsible for the acoustic response measured in the demonstrator engine.

The third difference between the baseline design configuration A and new design configuration B was in the vane to discharge area ratio, which was considered. Figure 11 shows the transfer functions for the baseline design swirlers baseline design A) and new design swirlers with two modifications, namely the area ratio for B_3 and vane angle (or vane offset) B_4. The modified designs response characteristics were compared to the original baseline design A as shown in Fig. 11. It can be clearly seen that the new design with a modified area ratio exhibits a reduced response in the 400 to 500 Hz range which is similar to the baseline one. Figure 11 also shows the changing the area ratio of the new design swirlers is far more productive in reproducing the baseline response characteristics relative to vane offset.

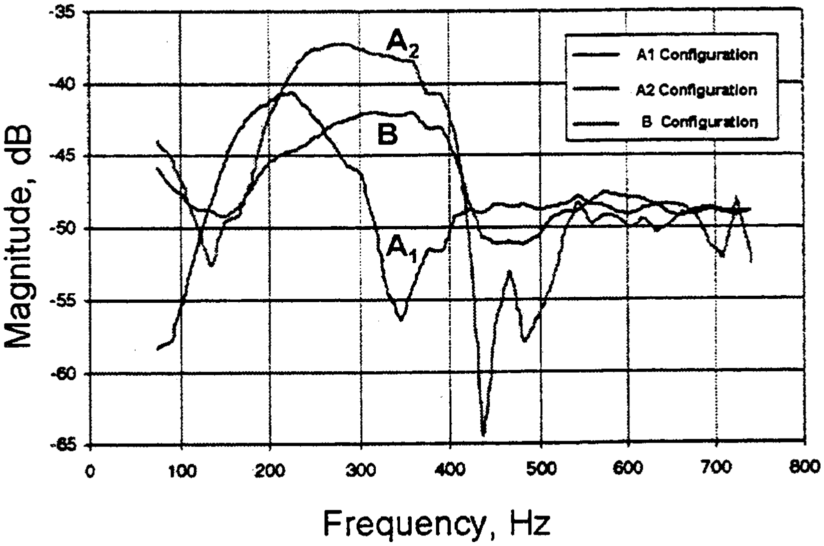

Fig. 8 Ratio of the fluctuating upstream pressure for downstream velocity (transfer function)

These tests point out that vortex shedding from the venturi and the mixing of the counter-rotating passages seemed to have little effect on the forced response of the swirlers. The strongest effect observed was the vane to discharge area ratio. It was shown that if the new design configuration B was modified to have a vane to discharge area ratio similar to that of the baseline design A, a similar response characteristic could be obtained.

3.3 Combustion Heat Release Rate Acoustic Response. A schematic view of the combustion rig is shown in Fig. 12. The rig consists of a planar sector with combustion and cooling holes and a LING acoustic driver that would be used to apply a forcing function in the event the injectors fail to be self-exciting. High-speed pressure transducer probes were installed in upstream plenum and combustion chamber for determination of the upstream and downstream power spectral density (PSD), the transfer function and the phase angle relationship between pressure measurements. The rig can be run in four different modes. The combustion chamber could be run with or without back pressure and thus providing very different acoustic boundary conditions. The rig could also be run where the inlet pressure can be modulated using a controlled pressure driver that is referred to as the LING driver. The rig could therefore be run with or without pressure feedback and with and without pressure input. Further, the rig was constructed such that it can be run with or without dilution holes which would tend to attenuate the acoustic response characteristics.

The primary objective of the tests here was to identify a quantifiable discriminator between the baseline and new injector designs in the frequency range of interest, which was 400 to 500 Hz.

The rig was first operated in a back-pressure mode as a result

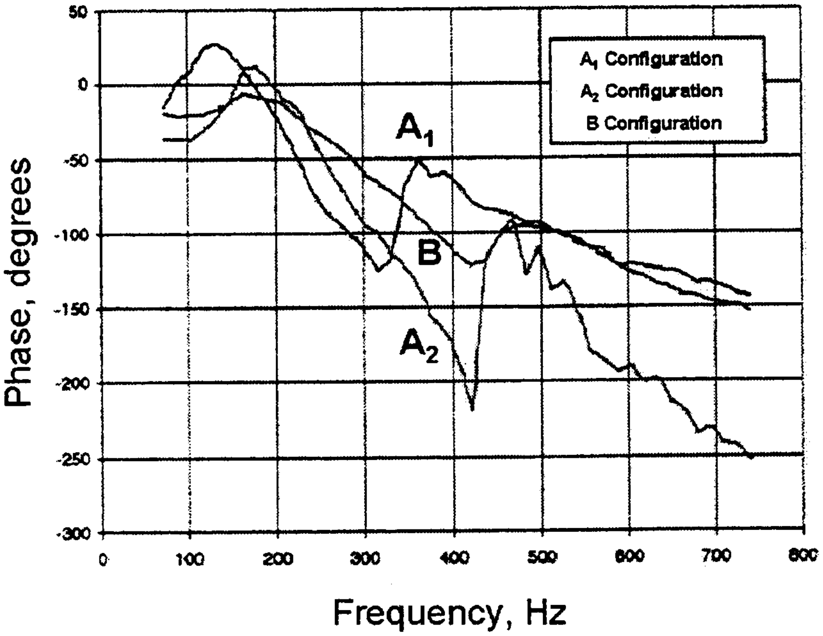

Fig. 9 Phase relationship for ratio of upstream pressure to downstream velocity

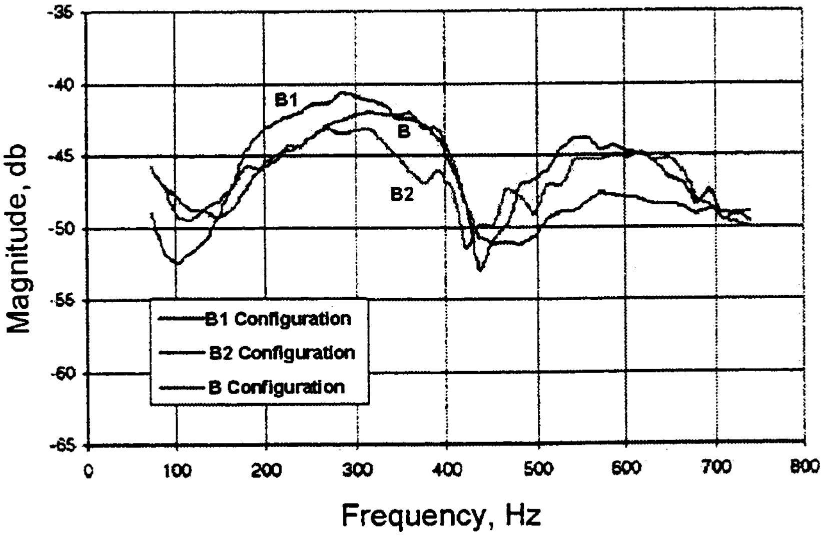

Fig. 10 Ratio of the fluctuating upstream pressure to downstream velocity for design configuration B

the combustion process quickly reached a limit cycle within the combustion chamber. The sound was clearly audible and significant pressure oscillations were in the combustion chamber. The downstream power spectral densities for the baseline and the new injector designs are shown in Fig. 13. Examination of these PSD data shows a strong coupled response in the range of 175 to 200 Hz. This response appears to correspond to the half-wave frequency of the upstream plenum chamber. The plenum was long enough to justify such a low frequency. The combustion chamber itself could only have resonated in that frequency range due to a Helmholtz mode. The PSD measurement in Fig. 13, however, show peaks at the second, third, and fourth harmonic of the base frequency, which is clearly indicative that this resonance was due to a characteristic length of the plenum chamber. It would not be possible for Helmholtz resonator to produce harmonics.

In the second test, the rig was operated with choke plates opened. In this test, the rig lacked the restriction required to significantly change the pressure feedback in the combustion chamber. Figure 14 displays a comparison of the transfer function between the pressure transducer upstream of the combustion chamber and the downstream transducer without LING excitation. It is seen that the combustion chamber provided a source of broadband noise. This is why the frequency function is greater than one throughout the frequency band measured. These results also appear to provide very little discrimination between the injector designs.

In the third test, the rig was then set with the LING transducer, to operate as a driver. The LING transducer was actuated to sweep across fairly wide frequency range several times while the transducer gathered data. A comparison of the transfer functions of the baseline swirler and new swirler is shown in Fig. 15. When the LING was activated, the pressures in the combustion chamber more or less attenuated to the input pressures in the frequency range of interest. The data appear to show consistently that in the range of 300 Hz, the combustor cavity does appear to amplify the input pressure. The 300 Hz amplification may correspond to a characteristic length starting at the bulkhead of the chamber to next point of reflectance which is the forward facing panel in the exhaust duct. The data show another peak at 700 Hz which well corresponds to the quarter-wave frequency of the combustion chamber. The signal is generally attenuated outside these two peaks of 300 and 700 Hz. The data does not clearly show a discriminator between the baseline and new improved design. The

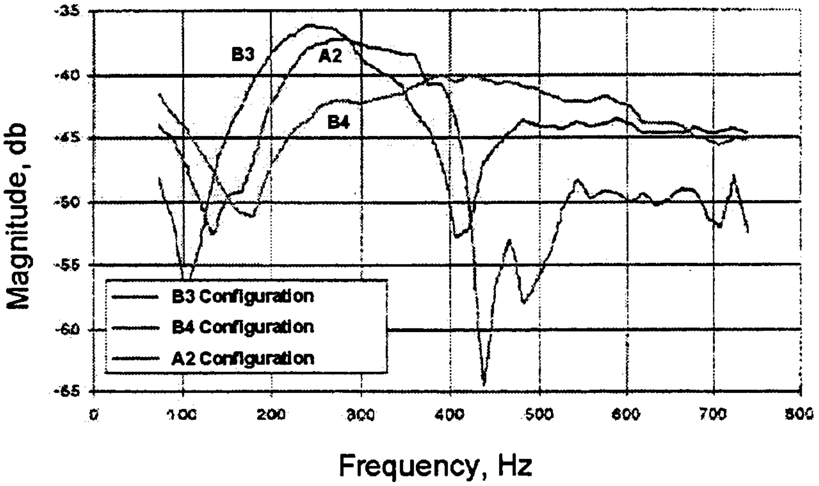

Fig. 11 Ratio of the fluctuating upstream pressure to downstream velocity for design configurations A and B

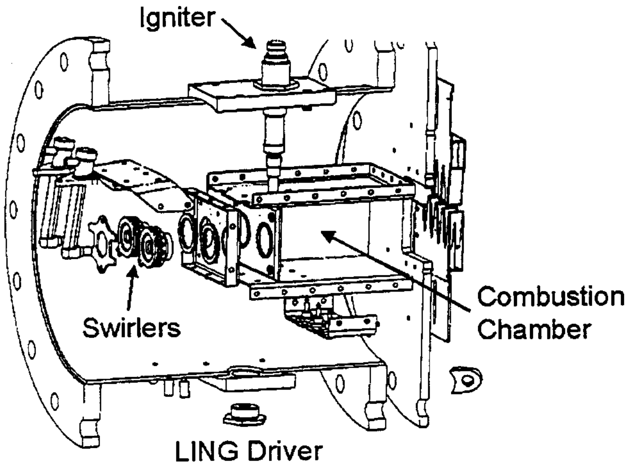

Fig. 12 Schematic of the combustion rig

small difference in the acoustic characteristics was due to the slight difference in the overall fuel-air ratio. Note that the injectors could not be run at precisely the same overall fuel-air ratio. This could cause the resonance of the chamber to be slightly altered due to the temperature difference within the chamber.

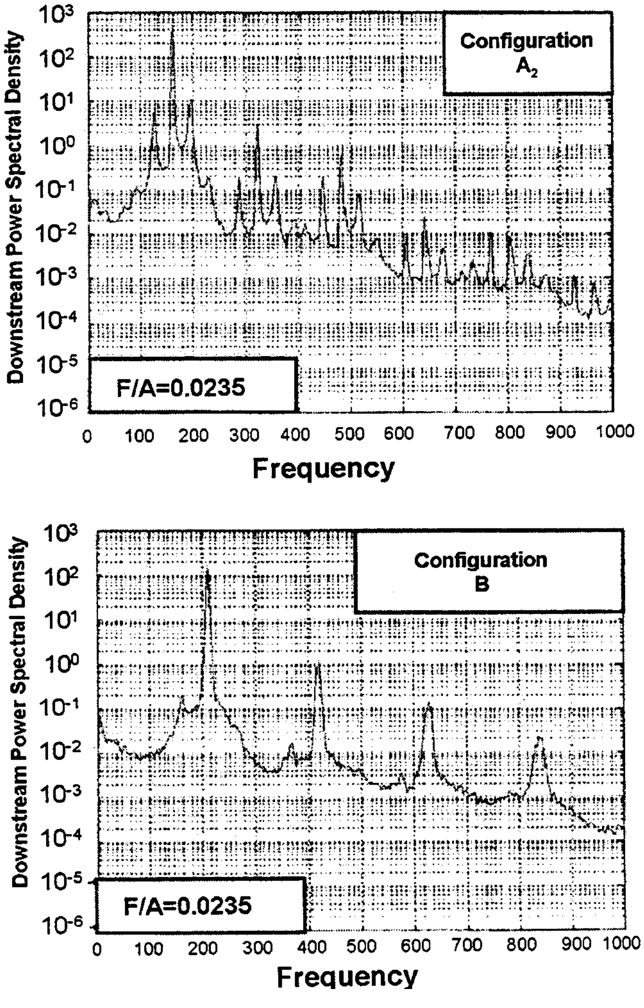

Fig. 13 (*a*) and (*b*) Measured spectral density (PSD) versus frequency

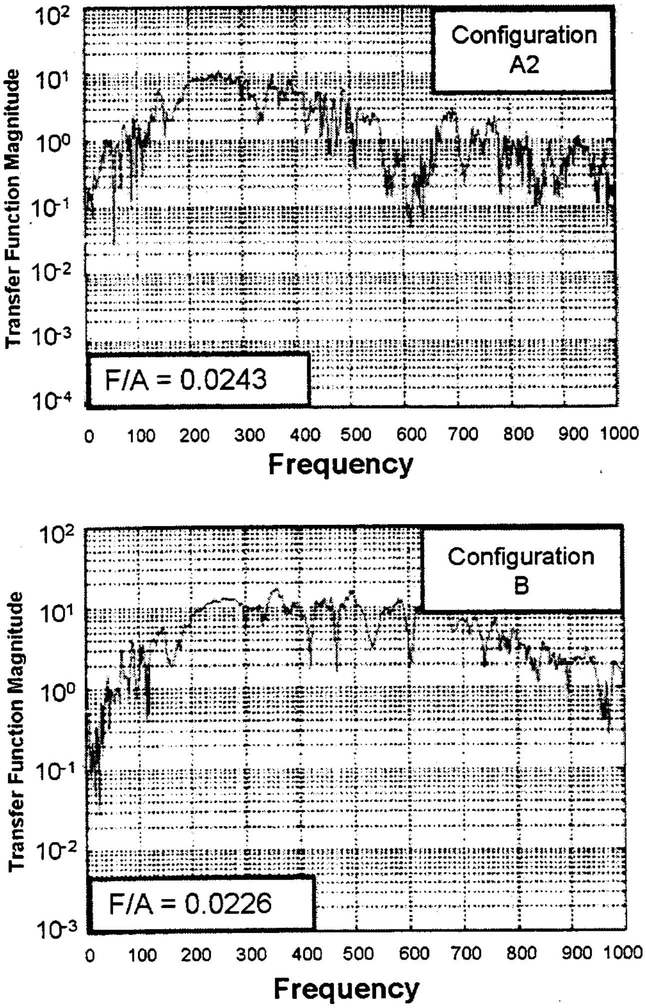

Fig. 14 (*a*) and (*b*) Measured transfer function

4 Acoustic Model Development

The experimental results clearly showed that the acoustic response measured in the new fuel injector design configuration B was mainly due to the change in the vane to discharge area ratio. As was shown in Fig. 11, when the new design swirler's vane to discharge area was considered, the acoustic response of the swirler was changed. This was reflected in the decrease in the swirler's impedance as determined by the transfer function. In this case, the swirler represents the primary conduit of air between the external combustor shrouds and the internal combustion chamber. The swirler can be considered as an orifice through which a significant amount of the air flows.

Pressure fluctuations in the combustor, if occurred, will feedback to the combustor outer shroud or diffuser through the swirler. The swirler in this case represents a connector between the two cavities. The implication is that the swirler acts as an acoustic filter whose impedance characteristics would either facilitate or potentially eliminate the feedback between the two cavities.

The elements that make up the impedance of a flowing system (as in electrical circuits) are the inductance (inertia), capacitance (volume), and resistance (pressure drop). The capacitance, inductance, and resistance all contribute to the impedance of a swirler. The swirler's resistance represents the static component of the impedance, while the capacitance and inductance represent the dynamic components of the impedance. The fuel injector swirler's vane and inner passage discharge areas represent the inductance,

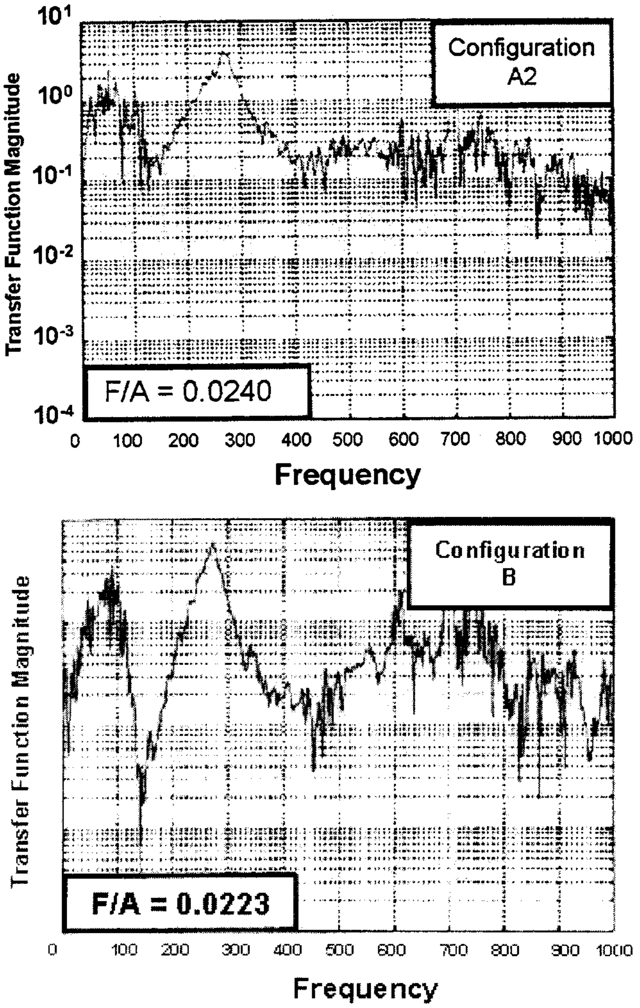

Fig. 15 (*a*) and (*b*) Measured transfer function versus frequency with LING excitation

the volume represents capacitance and the pressure drop across the vanes or the effective flow area Acd is the resistance. In the new and baseline designs, the effective areas or pressure losses were more or less identical and thus the resistance is about the same. The capacitance of the system is related to the volume of the swirler passages and the degree of compressibility of the fluid. The capacitance for the new and baseline designs were also about equal. A close examination of the measured transfer functions for the baseline injector's swirler passage and the new injector's swirler passage, however, revealed that the design feature responsible for the measured acoustic response was the new injector's vane to inner passage discharge area ratio. This area ratio of the new injector was about 40–60 percent greater than that of the baseline design. Therefore, it is to be expected that a significant decrease in the inductance of the new injector swirler would occur. As a result, the new injector's swirler passage would provide less resistance to dynamic changes in pressure for the 400–500 Hz range. The transfer function between the pressure upstream and the velocity downstream therefore maintained a higher level for the new injector design than for baseline design as shown in Fig. 8.

In an attempt to understand the engine acoustic response and the associated flow process, a simplified model based on the lumped-parameter approach was considered. The fluid system is modeled by an equivalent network consisting of resistance, capacitance, and inductance. As a first step, only the swirlers and the inner passage will be considered and be modeled as a lumped-element system. Although the swirlers and the inner passage probably cannot be precisely described by a lumped element system, the results should serve to illustrate the importance of the flow system coupling through the swirler vane and inner passage discharge area ratio.

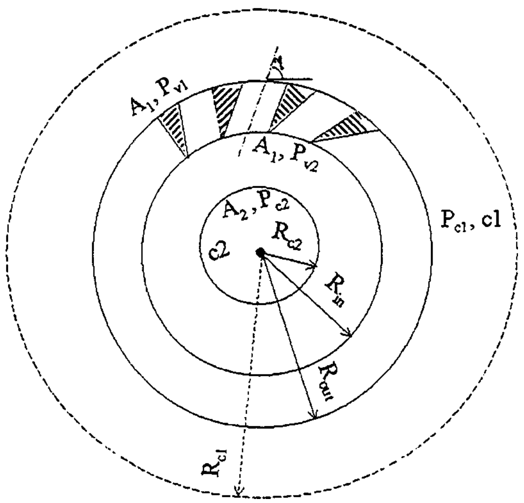

Fig. 16 Schematic swirler and inner passage of fuel injector as a lumped sum

In Fig. 16, a single swirler and the inner passage element of the air flow system is shown. It consists of a swirler's vane passage of a given slot width, slot height and swirl angle that is connected to the outer combustor shroud or cavity one of volume V and to the inner passage of the injector or cavity two. The radius of cavity two is defined by the discharge radius of the inner passage swirler. It is also assumed that cavity one is supplied at a constant flow rate $\dot{W}_{\rm in}$. The dimensions of the injectors are given in Table 1. A transfer function for these elements will be first derived (see the Appendix), which would then be used to model the effect of the vane area.

The system transfer function was derived in the Appendix and is given as

$$G(s)=\frac{\dot{W}'(s)}{p'_{c2}(s)}=\frac{\alpha_1 s}{\alpha_2+\alpha_3 s+\alpha_4 s^2}. \tag{1}$$

Setting $s=j\omega$ gives

$$G(j\omega)=\frac{j\alpha_1\omega}{(\alpha_2-\alpha_4\omega^2)+j\alpha_3\omega}. \tag{2}$$

Table 1

Slot width	3.73×10^{-3} m
Slot height	5.08×10^{-3} m
Discharge radius	0.028174 m
Total Acd	0.7
f_1	1
f_2	1
F/A	0.025 to 0.046
P_3	689,754.93 Pa
T_3	699.81 K
(L)c1	0.0508 m
$(R_{\rm in})_{c1}$	0.0418465 m
$(R_{\rm out})_{c1}$	0.028194 m
$W_{\rm air}$	0.19373 kg/s
$\dot{W}_f$	0.024702 kg/s

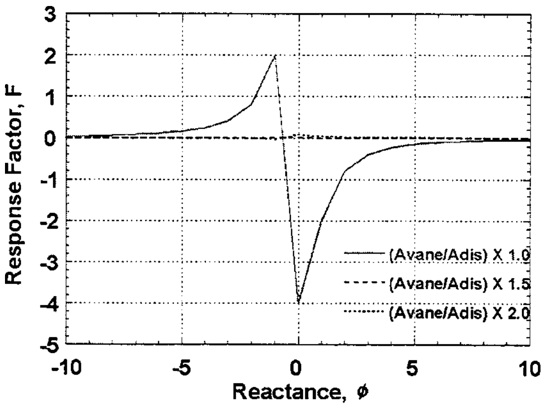

Fig. 17 Predicted fuel injector lumped-system response factor

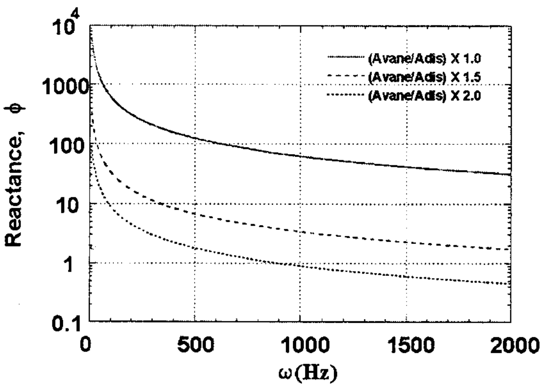

Fig. 18 Predicted fuel injector reactance as a function of frequency

The imaginary part of amplitude of the transfer function is given as

$$|\mathrm{Im}G(\omega)|=\frac{\alpha_1\omega}{[(\alpha_2-\alpha_4\omega^2)^2+(\alpha_3\omega)^2]^{1/2}} \tag{3}$$

and phase relationship is given as

$$\theta=\frac{\pi}{2}-\tan^{-1}\left(\frac{\alpha_3\omega}{\alpha_2-\alpha_4\omega^2}\right). \tag{4}$$

The system response factor for sinusoidal oscillation is given as

$$F=\frac{W'_{\max}}{p'_{\max}}\cos\,\theta \tag{5}$$

where $W'=W'_{\max}\sin(\omega t+\theta)$

$$p'=p'_{\max}\sin\,\omega t$$

Using Eqs. (3–5), the response factor is derived as

$$F=\frac{\alpha_1\omega}{[(\alpha_2-\alpha_4\omega^2)^2+(\alpha_3\omega)^2]^{1/2}}\cos\,\theta. \tag{6}$$

A system reactance ϕ can be defined as

$$\phi=\frac{\alpha_5-\alpha_6\omega^2}{\alpha_7\omega}. \tag{7}$$

Thus, the system response factor can be written as

$$F=\frac{-\frac{1}{\sqrt{\phi^2+1}}\cos\left(\frac{\pi}{2}-\tan^{-1}\frac{1}{\phi}\right)}{\alpha_8} \tag{8}$$

where the coefficients α_1 through α_8 are given in the Appendix.

4.1 Results. As mentioned earlier that the objective of deriving the lumped-element model was to predict the fuel injector/swirler system response to changes in the swirler's vane to inner passage discharge area. The operating conditions used in the analysis are given in Table 1. These operating conditions correspond to a high-power operation.

The fuel injector/swirlers lumped system dynamic response is represented analytically by Eq. (8). By plotting Eq. (8) as a function of the system reactance, Eq. (7), the response of the fuel injector to the flow is obtained. Figure 17 shows the fuel injector dynamic response as a function of the reactance with the swirler's vane to inner passage discharge area ratio as a parameter. An area ratio equal one is the baseline design configuration A. Whereas area ratios of 1.5 and 2 represent an increase in the area ratio from the baseline case. Both positive and negative values of the reactance were used. It can be seen that for the baseline case, as the fuel injector reactance increases in the positive direction, the injector response factor remains negative. This indicates that the fuel injector tends to damp the oscillations and the mass flow rate oscillations are out of phase with cavity two (or combustion chamber) flow oscillations. At large reactance values either positive or negative, the response factor approaches zero, which indicates that the flow no longer responds to pressure oscillations and the phase angle approaches 90 deg. The fuel injector can be considered tuned and the flow oscillations are 180 deg out of phase with the pressure oscillations. The value of the response factor then depends only on the resistive pressure drop terms in Eqs. (5)–(8).

The fuel injector response factor becomes positive as the system reactance becomes more negative. This is indicative of a phase displacement between the system flow and pressure oscillations. The system attains its peak response value for a reactance of approximately one. At this point, the flow and pressure oscillations are in phase and the fuel injector becomes an amplifying device. The effect of varying the swirler's vane to inner passage discharge area ratio is also shown in Fig. 17. It is clearly seen that for the operating conditions and geometrical dimensions considered here, an increase in the area ratio by a factor of 1.5 and 2 results in a fuel injector system through which the flow no longer responds to pressure oscillations. The implication is that the fuel injector switches from a responsive to a nonresponsive device and as a result no resistance is exerted to prevent the pressure oscillations from propagating upstream.

Figure 18 shows the predicted fuel injector reactance plotted against frequency with the vane to discharge area ratio as a parameter. It can be seen that as the frequency of pressure oscillations is increased, the system reactance rapidly decreases. This behavior is indicative of the inability of the fuel injector to filter the high-frequency oscillations. In the 400–500 Hz range, however, the fuel injector/swirler system still shows a measurable degree of reactance to the pressure oscillations. As the swirler's vane to discharge area ratio is increased, less system reactance is predicted for a given frequency. It is interesting to notice here that the fuel injector designs, both configurations A and B, show more impedance to the lower frequencies of the pressure oscillations. This demonstrates that by reducing the combustion chamber natural frequency, the fuel injectors swirlers will act more to filter the combustion chamber pressure oscillations and thus less feedback would occur.

Figure 19 shows the fuel injector response factor versus frequency with the area ratio being a parameter. It is observed that the system response factor is negative for frequencies less than about 300 Hz. As predicted above, a negative value of the response factor is indicative of a damping behavior of the system

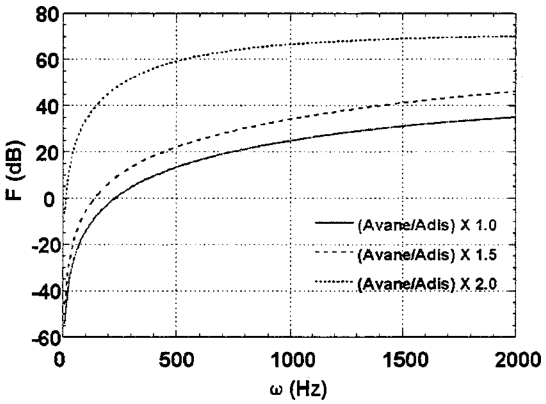

Fig. 19 Predicted fuel injector response factor versus frequency

and no feedback between upstream and downstream oscillations takes place. Moreover, as the area ratio is increased, lesser (smaller than 300 Hz) frequencies are required to attenuate the fuel injector response. In fact, for an area ratio of twice that of the baseline fuel injector, frequencies of less than 100 Hz would be required to attenuate the fuel injector. It is of importance to notice here that the 400–500 frequency range, in which the combustion chamber natural frequency lies, still shows a positive response factor, though of a smaller magnitude compared to the ones with a larger area ratio. The implication is that a frequency of less than 400 Hz of the combustion chamber would still provide better attenuation and less acoustic response.

Figure 20 displays the imaginary part of the fuel injector transfer function, Eq. (3), plotted against frequency and for different vane to discharge area ratios. The *y*-axis is the excess of the absolute value of $|G(\omega)|$ from 1. It is seen that the response function is increased as the frequency is increased. This again demonstrates that the system provides less resistance to dynamic changes in pressure at higher frequencies and thus stronger coupling between the upstream and downstream oscillations. The effect of varying the vane to discharge area is also shown in Fig. 20. The transfer functions appear to produce larger values as the area ratio is increased. The increase in the response function with the area ratio is a clear indication of amplification of the oscillations and thus higher instability.

It should be mentioned here that the trends predicted here are consistent with the experimental data presented earlier for the fuel injector transfer functions. However, the absolute value of the predicted transfer functions could not be compared directly to the experimental data because a linear analysis was used here to derive and predict the system response to self-excited and externally excited pressure oscillations.

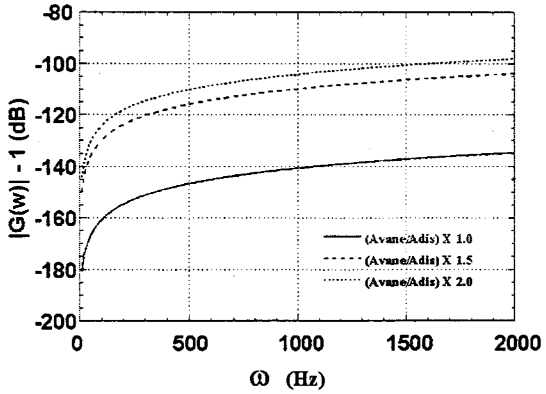

Fig. 20 Predicted magnitude of the imaginary part of the fuel injector transfer function versus frequency

5 Conclusion

The thermoacoustic response of a demonstrator gas turbine combustor engine was investigated experimentally and analytically. The experimental data revealed that as geometrical dimensions in the combustor fuel injectors were made, the engine acoustic response, in terms of peak to peak pressure oscillations, was significantly altered. In particular, it was shown that increasing the fuel injector swirler's vane and discharge areas resulted in an amplification of the peak to peak pressure oscillations. It was also shown that by modifying the fuel injector swirlers and discharge areas, the combustor response can be reduced to an acceptable level. A simplified model based on the lumped parameter concept was then developed to investigate the effects of varying the fuel injector geometrical dimensions on the system acoustic response. The simplified model predicted the system behavior as changes in the fuel injector dimensions were altered. The predicted system trends were consistent with the experimental data. However, direct comparisons between the data and predictions were not possible because a linear stability analysis was used in the model.

Acknowledgment

Partial funding for this work was provided by the United States Air Force, Contract No. F33615-90-C-2042.

Nomenclature

A_1 = swirler's entrance passage area
A_2 = swirler's exit passage area
A_W = swirler's passage weighted area
f = weighting factor
g = gravitational force
$G(s)$ = system transfer function
k = orifice discharge coefficient
L = effective length of vane passage
M = mass
p = pressure
p_{c1} = pressure at the cavity 1
p_{c2} = pressure at the cavity 2
p_{v1} = pressure at the entrance of the inner passage
p_{v2} = pressure at the end of the inner passage
$\bar{p}_{c1}$ = time-averaged pressure at the cavity 1
$\bar{p}_{c2}$ = time-averaged pressure at the cavity 2
$\bar{p}_{v1}$ = time-averaged pressure at the entrance of the inner passage
$\bar{p}_{v2}$ = time-averaged pressure at the end of the inner passage
p'_{c1} = unsteady pressure fluctuation at the cavity 1
p'_{c2} = unsteady pressure fluctuation at the cavity 2
p'_{v1} = unsteady pressure fluctuation at the entrance of the inner passage
p'_{v2} = unsteady pressure fluctuation at the end of the inner passage
s = Laplace operator
t = time
V = volume of cavity 1
$\dot{W}_{\text{in}}$ = mass flow rate into cavity
$\dot{W}$ = averaged mass flow rate

Subscripts

$c1$ = cavity 1
$c2$ = cavity 2
$v1$ = vane passage inlet
$v2$ = vane/passage discharge

Greek Letters

γ = specific heat ratio, c_p/c_v
θ = phase angle
ρ = density
ω = frequency

Appendix A

Using Fig. 16 notations, the following equations for the swirler system elements may be derived. The equations in perturbation form will be linearized.

Cavity 1 (Capacitance). A mass balance gives

$$\frac{dM}{dt}=\dot{W}_{\mathrm{in}}-\dot{W} \tag{A1}$$

where $M=\rho V$ and $\dot{W}_{\mathrm{in}}$, is mass flow rate into cavity 1 and it is assumed constant. In perturbation form, Eq. ($A1$) becomes

$$\frac{\overline{\rho}_{C1}V}{\overline{\dot{W}}}s\rho'_{c1}=-\dot{W}' \tag{A2}$$

where subscript *c1* stands for cavity 1. The equation of state in perturbation form is given as

$$p'=\gamma\rho' \tag{A3}$$

where $p=\rho^{\gamma}$.

Using Eq. ($A3$), Eq. ($A2$) then becomes

$$\frac{\overline{\rho}_{c1}V}{\gamma\overline{\dot{W}}}sp'_{c1}=-\dot{W}' \tag{A4}$$

where s is the Laplace operator which is a complex variable.

Entrance Loss Resistance from Cavity 1. Flow from cavity 1 into swirler vane passage (opening area) is represented by a resisting entrance loss, for which the orifice flow relation is assumed and is given as

$$\dot{W}=kA_1\sqrt{(p_{c1}-p_{v1})\rho g} \tag{A5}$$

where p_{v1} is the pressure at the entrance of the swirler's passage. Equation ($A5$) is written in perturbation form as

$$\dot{W}'=\frac{1}{2}\left[\frac{\overline{p}_{c1}}{\Delta p_{c1}}p'_{c1}+\left(\frac{1}{\gamma}-\frac{\overline{p}_{v1}}{\Delta p_{c1}}\right)p'_{v1}\right] \tag{A6}$$

where $\Delta p_{c1}=\overline{p}_{c1}-\overline{p}_{v1}$.

Vane Flow Loss (Inductance).

$$p_{v1}-p_{v2}=\frac{L}{A_Wg}\frac{d\dot{W}}{dt} \tag{A7}$$

where p_{v2} is the pressure at the end of the inner passage. Equation ($A7$) in perturbation form is given as

$$\overline{p}_{v1}p'_{v1}-\overline{p}_{v2}p'_{v2}=\frac{\overline{\dot{W}}L}{gA_W}s\dot{W}'. \tag{A8}$$

Assuming that $\overline{p}_{v1}=\overline{p}_{v2}$, Eq. ($A8$) becomes

$$p'_{v1}-p'_{v2}=\frac{\overline{\dot{W}}}{g\overline{p}_2A_W}s\dot{W}' \tag{A9}$$

where A_W is the swirler's passage weighted area which is defined as

$$\frac{f_1A_1+f_2A_2}{f_1+f_2} \tag{A10}$$

and f_1 and f_2 are weighting factors. If $f_1=f_2=1$, then, a mean passage area is obtained.

Entrance Loss Resistance from Inner Passage into Cavity 2. Flow from the inner passage vane into cavity 2 is represented by

$$\dot{W}=kA_2\sqrt{(p_{v2}-p_{c2})\rho g} \tag{A11}$$

or in perturbation form

$$\dot{W}'=\frac{1}{2}\left[\frac{\overline{p}_{v2}}{\Delta p_{v2}}p'_{v2}+\left(\frac{1}{\gamma}-\frac{\overline{p}_{c2}}{\Delta p_{v2}}\right)p'_{c2}\right] \tag{A12}$$

where

$$\Delta p_{v2}=\overline{p}_{v2}-\overline{p}_{c2}.$$

By combining Eqs. ($A1$) through (A12), the system transfer function can be obtained and given as

$$G(s)=\frac{\dot{W}'(s)}{p'_{c2}(s)}=\frac{\alpha_1 s}{\alpha_2+\alpha_3 s+\alpha_4 s^2} \tag{A13}$$

where the coefficients α_1 through α_4 as follows:

$$\alpha_1=\frac{1}{4}\left(\frac{\overline{\rho}\overline{V}}{\gamma\overline{\dot{W}}}\right)\left(\frac{1}{\gamma}-\frac{\overline{p}_{c2}}{\Delta p_{v2}}\right)\left(\frac{1}{\gamma}-\frac{\overline{p}_{v1}}{\Delta p_{c1}}\right)$$

$$\alpha_2=\frac{1}{4}\frac{\overline{p}_{v2}}{\Delta p_{v2}}\frac{\overline{p}_{c1}}{\Delta p_{c1}}$$

$$\alpha_3=\frac{1}{2}\left(\frac{\overline{\rho}\overline{V}}{\gamma\overline{\dot{W}}}\right)\left(\frac{1}{\gamma}-\frac{\overline{p}_{v1}}{\Delta p_{c1}}-\frac{\overline{p}_{v2}}{\Delta p_{v2}}\right)$$

$$\alpha_4=\frac{1}{4}\left(\frac{\overline{\dot{W}L}}{g\overline{p}_2A_1}\right)\left(\frac{\overline{\rho}\overline{V}}{\gamma\overline{\dot{W}}}\right)\left(\frac{\overline{p}_{v2}}{\Delta p_{v2}}\right)\left(\frac{1}{\gamma}-\frac{\overline{p}_{v1}}{\Delta p_{c1}}\right).$$

Also, the coefficients α_5 through α_8 in Eqs. (7) and (8) in text as follows:

$$\alpha_5=\left(\frac{\overline{p}_{c1}}{\overline{p}_{v2}-\Delta p_{v1}/\gamma}\right)\bigg/\left(\frac{\overline{\rho}_3V}{\gamma\overline{\dot{W}}}\right)$$

$$\alpha_6=\frac{\overline{\dot{W}L}}{A_{\mathrm{eff}}\overline{p}_{v2}}$$

$$\alpha_7=2\left(\frac{\overline{p}_{c1}\Delta p_{v1}}{\overline{p}_{c1}(\overline{p}_{v2}-\Delta p_{v1}/\gamma)}+\frac{\Delta p_{v2}}{\overline{p}_{v2}}\right)$$

$$\alpha_8=\left(\frac{\overline{p}_{v2}}{\overline{p}_{c2}-\Delta p_{v2}/\gamma}\right)\alpha_7.$$

References

[1] Darling, D., Radhakrishnan, K., Oyediran, A., and Cowan, E., 1995, ‘‘Combustion-Acoustic Stability Analysis for Premixed Gas Turbine Combustors,’’ NASA TM 107024.

[2] Bloxsidge, G. J., Dowling, A. P., and Langhorne, P. J., 1988, ‘‘Reheat Buzz: An Acoustically Coupled Combustion Instability, Part 2: Theory,’’ J. Fluid Mech., **193**, pp. 445–473.

[3] Bloxsidge, G. J., Dowling, A. P., and Langhorne, P. J., 1988, ‘‘Active Control of Reheat Buzz,’’ AIAA J., **26**, No. 7, pp. 783–790.

[4] Shyy, W., and Udaykumar, 1990, ‘‘Numerical Simulation of Thermo-Acoustic Effect on Longitudinal Combustion Instabilities,’’ 26th JPC, AIAA 90-2065.

[5] Mohanraj, R., and Zinn, B. T., 1998, ‘‘Numerical Study of the Performance of Active Control Systems for Combustion Instabilities,’’ 36th JPC, AIAA 98-0356.

[6] Smith, C. E., and Leonard, A. D., 1997, ‘‘CFD Modeling of Combustion Instability in Premixed Axisymmetric Combustors,’’ ASME Paper No. 97-GT-305.

[7] Habiballah, M., and Dubois, I., 1995, ‘‘Numerical Analysis of Engine Instability,’’ 31st JPC, AIAA 95-37213.

[8] Kim, Y. M., Chen, C. P., Ziebarth, J. P., and Chen, Y. S., 1992, ''Prediction of High Frequency Combustion Instability in Liquid Propellent Engines,'' 28th JPC, AIAA 92-3763.

[9] Quinn, D. D., and Paxson, D. E., 1998, ''A Simplified Model for the Investigation of Acoustically Driven Combustion Instability,'' 34th JPC, AIAA-98-3764.

[10] Mawid, M. A., and Sekar, B., 1999, ''A Numerical Study of Active Control of Combustion-Driven Dynamic Instabilities in Gas-Turbine Combustors,'' 35th JPC, AIAA 99-2778.

[11] Hsiao, G., Pandalai, R., Hura, H., and Mongia, H. C., 1998, ''Combustion Dynamic Modeling for Gas Turbine Engines,'' 34th JPC, AIAA-98-3380.

[12] Ohtsuka, M., Yoshida, S., Inage, S., and Kobayashi, N., 1998, ''Combustion Oscillation Analysis of Premixed Flames at Elevated Pressures,'' ASME Paper No. 98-GT-581.

[13] Yang, V., and Anderson, W., 1995, ''Liquid Rocket Engine Combustion Instability,'' Prog. Astronaut. Aeronaut., **169**.

[14] Paxson, D. E., 1992, ''A General Numerical Model for Wave Rotor Analysis,'' NASA TM 105740, July.

[15] Paxson, D. E., 1993, ''An Improved Numerical Model for Wave Rotor Design and Analysis,'' AIAA Paper 93-0482, Jan. (also NASA TM 105915).

[16] Paxson, D. E., 1995, ''A Comparison Between Numerically Modeled and Experimentally Measured Loss Mechanisms in Wave Rotors,'' AIAA J. Propul. Power, **11**, No. 5, pp. 908–914 (also NASA TM 106279).

[17] Nalim, R. M., and Paxson, D. E., 1997, ''A Numerical Investigation of Premixed Combustion in Wave Rotors,'' ASME J. Eng. Gas Turbines Power, **119**, pp. 668–675.

[18] Crocco, L., and Cheng, S. I., 1958, ''Theory of Combustion Instability in Liquid Rocket Engines,'' AGAR Dograph No. 8, Butterworths Scientific Publications, London, 1956.

[19] Vonnegut, B., 1998, ''A Vortex Whistle,'' J. Acoust. Soc. Am., **26**, No. 1, pp. 18–20.

Modeling of Inhomogeneously Premixed Combustion With an Extended TFC Model

W. Polifke[1]
Lehrstuhl für Thermodynamik,
Technische Universität München,
D-85747 Garching, Germany
e-mail: polifke@td.mw.tum.de

P. Flohr
Alstom Power Technology,
CH-5405 Baden, Switzerland
e-mail: peter.flohr@power.alstom.com

M. Brandt
Lehrstuhl für Thermodynamik,
Technische Universität München,
D-85747 Garching, Germany
e-mail: brandt@td.mw.tum.de

In many practical applications, so-called premixed burners do not achieve perfect premixing of fuel and air. Instead, fuel injection pressure is limited, the permissible burner pressure drop is small and mixing lengths are curtailed to reduce the danger of flashback. Furthermore, internal or external piloting is frequently employed to improve combustion stability, while part-load operation often requires burner staging, where neighboring burners operate with unequal fuel/air equivalence ratios. In this report, an extension of the turbulent flame speed closure (TFC) model for highly turbulent premixed combustion is presented, which allows application of the model to the case of inhomogeneously premixed combustion. The extension is quite straightforward, i.e., the dependence of model parameters on mixture fraction is accounted for by providing appropriate lookup tables or functional relationships to the model. The model parameters determined in this way are adiabatic flame temperature, laminar flame speed and critical gradient. The model has been validated against a test case from the open literature and applied to an externally piloted industrial gas turbine burner with good success.
[DOI: 10.1115/1.1394964]

Introduction

New market forces in the power generation business demand low cost, robust power generation technologies capable of operating in a highly flexible manner while meeting ever-increasing environmental standards. For the gas turbine combustor designer, these market forces pose a severe challenge: Lower emissions can in principle be achieved by perfecting the lean-premixed combustion technology, striving for nearly perfectly homogeneous fuel/air mixtures at low adiabatic flame temperature. However, doing so brings the combustion process at part load operation very soon dangerously close to lean extinction or thermoacoustic combustion instability. This ultimately limits part load operational flexibility, unless complex staging or piloting schemes are adopted, which in turn usually increase costs and NO_x emissions while threatening reliability, availability, and maintainability.

With these seemingly incompatible demands and design constraints, the need for higher accuracy in the prediction of flame stability and part load behavior is evident.

Concerning flame stability, we note that frequently *interactions* between premixed burners, possibly operating at different fuel equivalence ratios, determine the lean blow out limit. Alternatively, interactions between premixed and diffusion type ''pilot'' burners are involved. Furthermore, flame extinction as well as combustion instabilities are inherently instationary processes requiring also instationary tools for their prediction. Given the geometrical and fluid-dynamic complexities of typical gas turbine burners and combustors, any tool for instationary phenomena must be very efficient and exhibit robust convergence behavior if it is to be used to address design questions.

In this work, we present an extension of the turbulent flame speed closure (TFC) model (see [1,2] or [3]) which meets a few of the challenges listed in the previous paragraph. The TFC model describes highly turbulent, premixed combustion by solving only one additional (compared to the nonreacting case) transport equation for a mean progress variable c. Closure for this transport equation is achieved through a source term involving a *turbulent flame speed* S_T and the modulus of the gradient of the progress variable c,

$$\overline{\dot{w}_c} = \rho_u S_T |\nabla \tilde{c}|. \tag{1}$$

It was already noted by Zimont et al. [3] that the TFC model is very robust and fast—both in terms of CPU time per iteration as well as number of iterations required until convergence. Indeed, Polifke et al. [4] have observed that the TFC formulation is significantly more efficient than multistep reaction mechanisms with turbulent and global-kinetic rate coefficients (see, e.g., [5]), let alone models that require integration over multidimensional probability distribution functions (although remarkable speed-ups can be achieved for the latter case when integration results are tabulated).

However, the original formulation of the model is limited to perfectly premixed, adiabatic combustion, and the technological challenges mentioned above cannot be addressed with this restriction. Cokljat et al. [6] introduced a straightforward extension of the TFC model, involving an additional transport equation for sensible enthalpy with a source term proportional to the source term $\dot{w}_c$ in Eq. (1) minus a correction for radiative or convective heat losses downstream of the heat release zone.

The next step is the extension to the case of an inhomogeneous fuel/air mixture and is explored in the present work. We note that some of the physico-chemical parameters controlling the turbulent flame speed S_T depend on the equivalence ratio of the fuel/air mixture upstream of the flame front. By introducing a transport equation for fuel mixture[2] fraction f, we can solve for the progress variable c with

$$S_T = S_T(f). \tag{2}$$

Of course, in the definition of the progress variable c and in the computation of density ρ from c, one must take into account that

---

[1] To whom correspondence should be addressed.

Contributed by the International Gas Turbine Institute (IGTI) of THE AMERICAN SOCIETY OF MECHANICAL ENGINEERS for publication in the ASME JOURNAL OF ENGINEERING FOR GAS TURBINES AND POWER. Paper presented at the International Gas Turbine and Aeroengine Congress and Exhibition, Munich, Germany, May 8–11, 2000; Paper 00-GT-135. Manuscript received by IGTI Nov. 1999; final revision received by ASME Headquarters Feb. 2000. Associate Editor: D. R. Ballal.

[2] Throughout this paper, we use the mixture fraction f to describe the mixing of fuel and oxidizer stream. It is helpful to remind oneself that one may think of the mixture fraction as an *unburnt* fuel mass fraction Y_u, i.e., the mixture fraction equals the mass fraction of fuel that would be found if chemical reaction was absent.

adiabatic flame temperature and correspondingly hot gas density change with mixture fraction *f*.

Before discussing model details, we comment briefly on the envisaged range of applications of the extended TFC model. The combustion submodel is formulated in terms of first moments only, i.e., we assume that $\overline{S_T(f)} \approx S_T(\overline{f})$. Higher order effects resulting from small-scale temporal fluctuations of fuel concentration on the combustion process can therefore not be addressed with this model. Such small-scale fluctuations are most likely present in every industrial burner, and their effect might be important near the extinction limit, where the fluctuations in fuel concentration can lead to local and momentary extinction of the flame (presumably a very nonlinear phenomenon) and influencing thereby also the ''mean'' flame stability. However, description of such effects requires the introduction of the variance (or even higher moments) of fuel mass fraction and more advanced modeling concepts, and shall not be attempted here.

In this respect, the model presented here differs from other models for imperfectly premixed combustion, see, e.g., [7,8]. The interested reader is also referred to a model developed for combustion in SI engines by Kech et al. [9], which exhibits some interesting parallels as well as dissimilarities to our approach.

Typical applications of the extended TFC model could be

- layout of premixed burners with fuel enriched—but not necessarily fuel-rich, i.e., $\phi > 1$—regions.
- study of burner-burner interactions, where burners are fired at different equivalence ratios.
- investigation of combustion instabilities, where velocity and pressure fluctuations introduce low-frequency and long-range (compared to turbulent time and length scales) fuel inhomogeneities, which in turn control fluctuations in momentary heat release rate.

In particular in regard to the last class of applications, the efficiency and robustness of the TFC model are important. Note that the model, although developed for combustion in the premixed regime, also produces in our experience reasonable results for highly turbulent, lifted diffusion flames, as demonstrated below.

Model Formulation

In the original formulation of the TFC model for turbulent reacting flows, the state of the combustible mixture of fuel and air is described by a progress variable *c*, defined as a normalized mass fraction of products such that $c = 0$ in the unburnt mixture of reactants while $c = 1$ in the burnt gas. Using a standard modeling approach for turbulent flows based on Reynolds and Favre averages, a transport equation for *c* is obtained:

$$\frac{\partial}{\partial t}(\overline{\rho}\widetilde{c}) + \frac{\partial}{\partial x_k}(\overline{\rho}\widetilde{u}_k\widetilde{c}) = \frac{\partial}{\partial x_k}\left(\overline{\rho}\frac{\nu_t}{Sc_c}\frac{\partial \widetilde{c}}{\partial x_k}\right) + \overline{\dot{w}_c}. \tag{3}$$

which is closed by introducing the following expression for the source term $\overline{\dot{w}_c}$ of the progress variable:

$$\overline{\dot{w}_c} = \rho_u S_T |\nabla \widetilde{c}|. \tag{4}$$

The turbulent flame speed S_T is the velocity with which the turbulent flame brush moves in the flame surface normal direction towards the reactants. Zimont and Lipatnikov [1] have proposed the following expression for the turbulent flame speed:

$$S_T = AGu'^{3/4} S_L^{1/2} \chi_u^{-1/4} l_T^{1/4}. \tag{5}$$

This expression is argued to be valid in the regime of thickened turbulent flames where $\mathrm{Re}_t^{3/4} \gg \mathrm{Da}^{3/2} \gg 1$. For the model constant *A*, the value $A = 0.52$ is suggested in the case of hydrocarbon fuels ([1,2]). The so-called *stretch factor G* is introduced to model the reduction in turbulent flame velocity at high turbulent intensities $u'/\overline{u}$, which is believed to be due to the quenching of the flame by small-scale fluid dynamic strain or stretching. *G* is modeled to depend on a *critical stretch rate* g_{cr} in the following way:

$$G = \frac{1}{2}\operatorname{erfc}\left\{-\sqrt{\frac{1}{2\sigma}}\left(\ln\frac{15\nu g_{cr}^2}{\widetilde{\varepsilon}} + \frac{\sigma}{2}\right)\right\}. \tag{6}$$

In this formulation, the local value of turbulent dissipation $\widetilde{\varepsilon}$ is set in relation to the critical stretch rate by using dimensional arguments: If $\widetilde{\varepsilon} \ll 15\nu g_{cr}^2$, the value of *G* is very close to unity and flame stretch does not influence the flame speed. However, if $\widetilde{\varepsilon}$ rises to values above $15\nu g_{cr}^2$, then $G \to 0$, the source term of the *c*-transport equation vanishes and the flame extinguishes. The TFC model is made complete by introducing a coupling between reaction progress and fluid dynamics via density:

$$\rho = \frac{\rho_u T_u}{(1-\widetilde{c})T_u + \widetilde{c}T_b}, \tag{7}$$

where the ideal gas law has been used, assuming constant pressure and constant mean molecular weight.

The above equations summarize the original TFC model, appropriate for perfectly premixed, adiabatic combustion at high turbulent Reynolds numbers. Cokljat et al. [6] proposed an alternative formulation to allow for nonadiabatic effects by adding a transport equation for sensible enthalpy *h* to the model. Heat generation due to combustion and radiative or convective heat losses are now represented as sources $\overline{\dot{w}_h}$ of the transport equation of sensible enthalpy. For the combustion term, we recall that the progress variable *c* is defined as the normalized product mass fraction. Therefore multiplying the source term for *c* with the heat of combustion ΔH and the fuel mixture fraction *f* gives the required source for sensible enthalpy:

$$\overline{\dot{w}_h} = \rho_u S_T |\nabla c| \Delta H f. \tag{8}$$

Note that this formulation is only valid for lean combustion $\phi < 1$. For fuel rich conditions, oxygen is scarce and not all the fuel can be converted into products and heat. This requires that a corresponding correction be inserted into the above equation.

Of course, the temperature rise is in this case no longer proportional to *c*, but is obtained from the thermodynamic relation

$$h(T) = h_{\text{ref}} + \int_{T_{\text{ref}}}^{T} c_p(T')\,dT'. \tag{9}$$

Similarly, the density ρ is no longer explicitly coupled to the progress variable *c* (see Eq. (7)) but instead must be obtained from the equation of state. In a multicomponent system, the mixture specific heat capacity c_p is the mass fraction weighted sum over species heat capacities. Ignoring intermediate species, the mixture composition can in principle be determined from the reactants and products composition and the progress variable. However, often an overall fit for c_p as a polynomial in temperature *T* with fit data taken from, say, a laminar flame computation, is sufficiently precise.

Note that the nonadiabatic TFC model as proposed by Cokljat et al. [6] is not applicable to situations where significant heat losses occur upstream of or within the heat release zone, for example when a flame touches a cold wall. In this case, heat losses would reduce temperature and significantly influence the chemical kinetics, i.e., reduce the rate of reaction progress, and such an effect could not be reproduced with the nonadiabatic formulation by Cokljat et al. [6]. In this sense, only weakly nonadiabatic flames can be modeled.

Consider now the case of inhomogeneously premixed combustion, where the mixture fraction $f = f(\mathbf{x})$ is no longer constant, but varies with position $\mathbf{x}$. Examining the TFC model, we note that among the physico-chemical parameters which control the turbulent flame speed S_T, only two depend significantly on the mixture fraction *f*, i.e., the laminar flame speed S_L and the critical velocity gradient g_{cr}. The density ρ_u and the thermal diffusivity χ_u of the reactant mixture also depend on mixture fraction. However, at

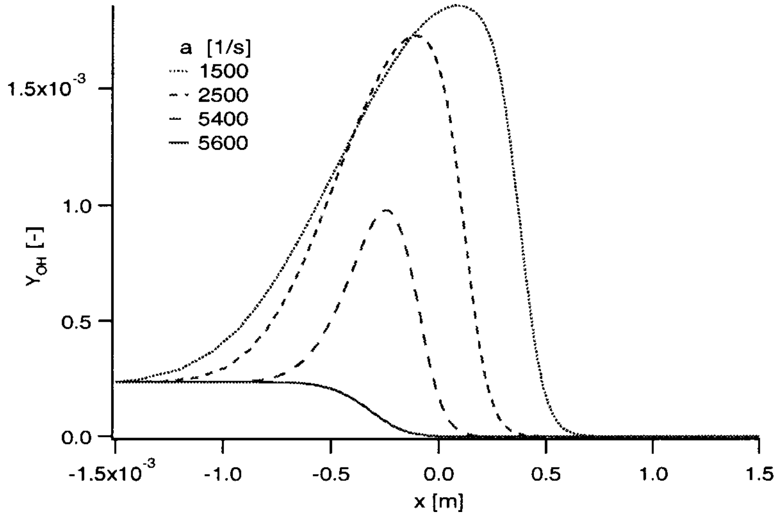

Fig. 1 Influence of strain rate on OH mass fraction in a strained f2b flame

least for flammable mixtures of hydrocarbon fuels and air, the influence is small and neglected in this work. Besides the turbulent flame front velocity S_T, the coupling between reaction progress c and temperature T or specific enthalpy h also changes with equivalence ratio.

In the following, we discuss the various possibilities to describe the dependence of the model parameters on mixture fraction.

Laminar Flame Speed. The computation of the laminar flame speed S_L with detailed chemical mechanisms for hydrocarbon fuels up to C_3H_8 is nowadays a standard exercise for which a number of tools are available, e.g., Rogg [10].

For given operating pressure p and preheat temperature T_u, the flame speed S_L can easily be determined for a range of equivalence ratios ϕ_i, $i=1,\ldots N$. For an equivalence ratio ϕ, $\phi_i<\phi<\phi_{i+1}$, simple linear interpolation between $S_L(\phi_i)$ and $S_L(\phi_{i+1})$ may be considered sufficiently precise for the present needs.

Alternatively, computational results may be fitted to a function $S_L(\phi,p,T_u,\ldots)$. This has been done by Göttgens et al. [11] and Müller et al. [12], using a functional form

$$S_L=Ff_u^m\frac{T_u}{T^0}\left(\frac{T_b-T^0}{T_b-T_u}\right)^n e^{-G/T_0}, \tag{10}$$

obtained from asymptotic analysis of methane-air flames. The inner layer temperature T^0 and the adiabatic flame temperature T_b are obtained from relations

$$T^0=\frac{E}{\ln_p^B} \tag{11}$$

and

$$T_b=aT_u+b+c\phi+d\phi^2+e\phi^3, \quad 0.2\leqslant\phi\leqslant 1. \tag{12}$$

Values for the fit parameters B, E, F, G, n, a, b, c, d, and e for various fuels are given by Müller et al. [12].

Critical Velocity Gradient. Zimont et al. [3] have already commented that the critical velocity gradient g_{cr} cannot be determined directly from laminar flame computations or asymptotic analysis. Instead, it was recommended to look upon g_{cr} as a tuning parameter, chosen for a given configuration to assure optimum agreement between experiment and computation for a relevant set of validation cases. However, for the present purpose, a more systematic way to express the dependence of the critical velocity gradient on the local equivalence ratio is required.

Using the code by Rogg [10] to compute stretched laminar flames, the following strategy has been explored: For given pressure p and preheat temperature T_u, a series of computations with increasing strain is carried out until extinction occurs. If required, additional runs can be carried out to determine the extinction strain rate a_x more accurately with a root-finding algorithm, e.g., the bisection method.

However, the event of "extinction" is not for all relevant flame configurations as easily defined or identified as one may think. In the case of the symmetrical *back-to-back* configuration ("b2b"), where opposing streams of fresh reactants flow towards a central reaction zone, extinction can clearly be identified by tracing the temperature maximum $T_{\max}$ in the computational domain as strain increases: As the extinction strain rate a_x is approached, $T_{\max}$ decreases very rapidly towards the preheat temperature T_u. However, from fluid dynamic considerations we argue that the asymmetrical *fresh-to-burnt* configuration ("f2b"), where opposing streams of fresh reactants and hot products face each other, should be more frequently encountered in a turbulent flow where turbulent eddies distort and strain a flame front. Now, in the f2b configuration, the maximum of temperature $T_{\max}$ cannot be used to indicate extinction events, as it is always located at the "burnt" boundary of the computational domain, and it is always equal to the adiabatic flame temperature. Instead, we have selected the OH radical as an indicator for extinction or quenching by strain. In a freely propagating or mildly strained hydrocarbon flame, the intermediate species OH occurs as a by-product of fuel-breakdown reactions and is eventually converted to stable products in the downstream part of the reaction zone. At intermediate temperatures OH concentration profiles display a prominent peak several orders of magnitude above chemical equilibrium. This peak disappears rather suddenly with increasing strain (see, e.g., Fig. 1), indicating that chemical reactions cease, as the extinction strain rate a_x is approached. Note that the OH radical is also frequently used in experimental work to identify reaction zones in hydrocarbon flames. See, e.g., the work of Dinkelacker et al. [13] where the structure of highly turbulent, strongly strained turbulent premix flames was studied.

Working through this procedure for an f2b flame at pressure $p=1$ bar and preheat temperature $T_u=630$ K, we find that for the equivalence ratio $\phi=0.55$ the extinction strain rate a_x matches nicely the critical gradient $g_{cr}=8000\,\mathrm{s}^{-1}$, which was found to produce good agreement with validation experiments at the same equivalence ratio ([3]). We propose therefore that strained laminar flame computations in the f2b configuration provide directly an

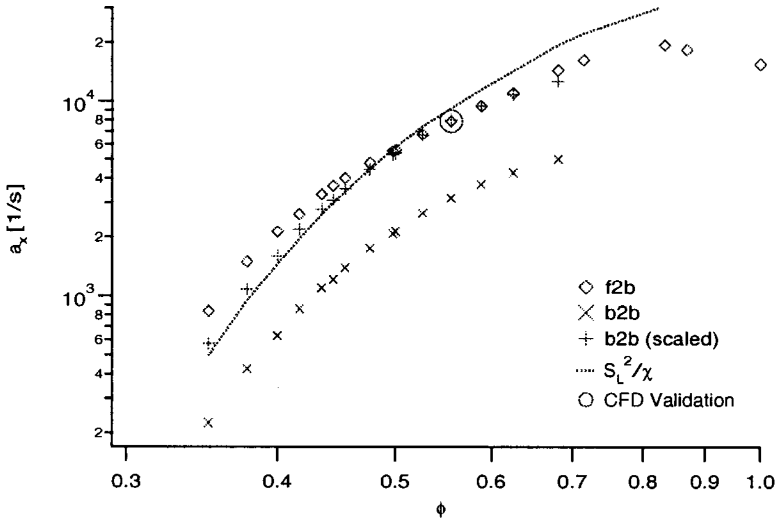

Fig. 2 Critical gradients and extinction strain rates for lean premixed combustion at $p=1$ bar, $T_u=630$ K; value of g_{cr} recommended by CFD validation study (○). Extinction strain rate α_x of f2b flame (◇), and b2b flame (× unscaled, + unscaled); Eq. (13) (···).

estimate for the critical velocity gradient. When using the b2b model, the extinction strain rate a_x has to be scaled by a factor of approximately 2.5 to match the results of the validation study. Once the extinction strain rates from the b2b computations are scaled by this factor, they almost match the results from the asymmetrical f2b configuration. These findings are summarized in Fig. 2.

Using dimensional arguments, Zimont [14] has proposed the following expression for the critical velocity gradient:

$$g_{cr} \sim \frac{S_L^2}{\chi}. \tag{13}$$

Accurate estimates for the laminar flame speed S_L can be obtained with the methods discussed in the previous section. For the thermal diffusivity $\chi = \lambda / \rho c_p$, we argue that diffusive heat losses near the adiabatic flame temperature are relevant for extinction processes and therefore use $\chi(T_{ad})$ in the above relation. The estimates for g_{cr} obtained from this relation are also shown in Fig. 2, where the proportionality factor in (13) was set to the value 8.4.

More validation studies of turbulent flames at various operating conditions (some of them possibly close to extinction) are needed before definite judgement can be passed on the various methods of estimating the critical velocity gradient presented here.

Density and Temperature Versus Reaction Progress. For constant pressure combustion and neglecting changes in the mean molecular weight W_M of the reacting gas mixture due to changes in chemical composition, density ρ and temperature T are inversely proportional to each other even in the case of variable fuel concentration:

$$\rho T = \frac{p W_M}{R}, \tag{14}$$

where R is the universal gas constant. However, the relation between reaction progress c and density and temperature is more complicated when fuel inhomogeneities are present. The essential difficulty lies with the concept of a progress variable c defined as a *normalized* product mass fraction. For the case of variable fuel concentration, the question is how to properly choose the normalization constant. If the global maximum of product mass fraction was chosen as normalization factor, then reaction should cease at values of c less than unity—clearly at odds with the concept of a progress variable, and difficult to implement with a gradient-based source term as in (4). We therefore define c as the local products mass fraction normalized with the products mass fraction that would result if all the fuel and oxidizer at the present location would be converted to products as completely as stoichiometry allows. This is almost[3] equivalent to a definition based on local adiabatic flame temperature:

$$c = \frac{T - T_u}{T_b(f) - T_u}, \tag{15}$$

and this formulation has been used in the present work.

If this convention is adopted, mixture fraction gradients cannot result in spurious changes in the value of c, and pure mixing processes (i.e., mixing without reaction far upstream or downstream of the flame brush) are represented thermodynamically consistent. More than this, even the diffusive burning mode along the stoichiometric line of a so-called *triple flame* (see [8]) can be represented with this formulation without the need for an extra source term for *diffusion mode burning*. Combustion along the stoichiometric line is (rate) controlled by the diffusion of oxygen from the lean side and fuel from the rich side towards each other. This mixing process is represented by the transport equation for the mixture fraction. As soon as fuel and oxidizer come into contact, the heat of reaction is released. The corresponding increase in temperature is reproduced by the model provided that the adiabatic flame temperature T_b is linked directly to the local mixture fraction (see below). The result of a simple example computation, which illustrates this effect, is shown in Fig. 3. Here co-flowing streams of combustion products ($c=1$) enter the computational domain on the left side. The upper and lower streams are fuel-rich and fuel-lean, respectively. As expected, the model reproduces a zone of high temperatures near the centerline, which broadens in the downstream direction, matching the mixing of fuel and oxidizer across the stoichiometric line (not shown).

The adiabatic flame temperature $T_b(f)$ or equivalently $T_b(\phi)$ can be determined from chemical equilibrium computations ([15]). Alternatively, the approximate expression (12) may be used, which is applicable for the range $T_u = 300-750$ K, $p = 1-30$ bar and $0.2 < \phi < 1$. For sufficiently lean conditions ($T_b < 2000$ K) effects of dissociation can be neglected with reasonable accuracy. Then the simple relation

---

[3] There is no exact equivalence because the mixture specific heat c_p depends slightly on temperature.

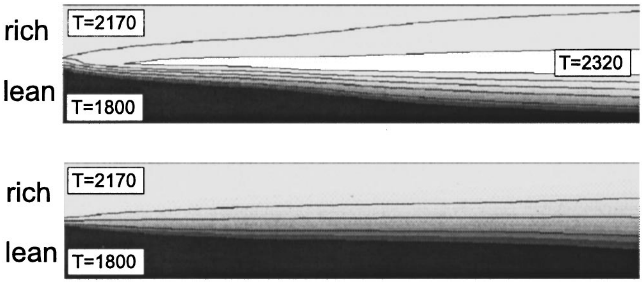

Fig. 3 Temperature distribution of diffusive burning along the stoichiometric line. Two coflowing streams of combustion products ($c=1$) enter the domain from the left in fuel-rich and fuel-lean conditions, while the adiabatic formulation of the extended TFC model correctly predicts additional heat release along the stoichiometric line (*a*) no such behavior is captured by the nonadiabatic formulation (*b*).

$$T_b = T_u + \Delta T \phi \tag{16}$$

holds, where $\Delta T = \Delta H / c_p$, neglecting changes in specific heat c_p with temperature.

For the nonadiabatic case, the source term (8) for the enthalpy equation can be used in the same form as the adiabatic case. Note, however, that the diffusive branch of a triple flame cannot be computed with the extension of the TFC model for the nonadiabatic case presented above, Eqs. (8) and (9), because with this formulation, production of sensible enthalpy $\overline{w_h}$ will not occur when fuel and oxygen-containing products (both with $c=1$!) mix across the stoichiometric line.

Model Validation

The implementation of the extended TFC model in a standard CFD code is fairly straightforward, as the equations for the reaction progress c and the fuel mass fraction or mixture fraction f are both in standard form. Look-up tables or simple correlations are used to obtain the model parameters (that depend on the fuel mass fraction only) to compute the reaction source (1). The standard finite volume CFD solver is based on the SIMPLE pressure-correction scheme; the QUICK discretization has been used for the convective fluxes of all flow and scalar (turbulent quantities, progress variable, sensible enthalpy) variables; the discretization of the pressure in the pressure correction step is second-order accurate.

To test and validate the implementation we selected a 300 kW industrial burner that has been studied experimentally at the Burner Engineering Research Laboratory (BERL), see Sayre et al. [16]. This configuration has also been investigated numerically using a Magnussen finite-rate reaction model (Fluent Validation Manual [17]) so that we can compare both with experimental data and a conceptually different combustion model. The flow considered is an unstaged natural gas flame in a swirl-stabilized burner. The burner consists of 24 radial methane nozzles around a bluff center body; a swirl generator imparts swirl onto the co-flowing air that enters the combustor through an annular inlet tube into which the methane is injected before the air enters the furnace. A sketch of the combustor geometry is given in Fig. 4. The furnace is of octagonal cross section with refractory-lined walls and has a conical furnace hood and a cylindrical exhaust duct.

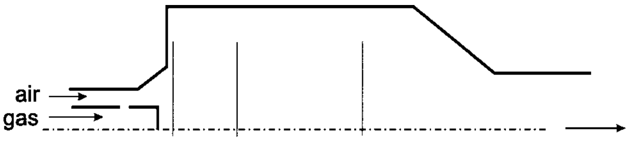

Fig. 4 Sketch of the BERL 300 kW combustor

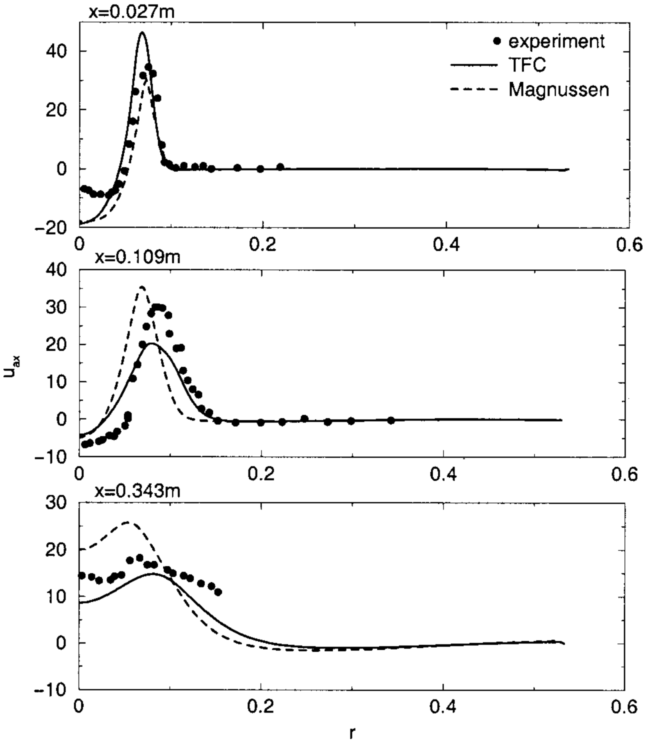

Fig. 5 Axial velocity profiles of the BERL combustor at three downstream positions

The numerical setup of the combustor has been adopted from the Magnussen finite rate simulation (Fluent Validation Manual [17]). Here, the configuration is modeled by assuming two-dimensional axisymmetry (where appropriate area rescalings are made); the cooled combustor walls are described by a given temperature distribution and the swirling air inflow is specified by velocity inlet profiles. The computational grid is a hexagonal body-fitted nonorthogonal grid with 100×183 nodes in the radial and axial directions with grid refinement near the axis and in the vicinity of the gas injection. Turbulence is modeled with the standard $k-\varepsilon$ model. Additionally, the effect of radiation is taken into account via the P1 radiation model. Both air and methane enter the combustor at a preheat temperature of 312 K and atmospheric pressure, and the burner operates at a nominal air excess ratio of $\lambda = 1/\phi = 1.1$ with a mean air flow rate of 0.119 kg s^{-1}.

The TFC model parameters for this case were obtained as follows. The adiabatic flame temperature for a range of air excess ratios ($0.8 < \lambda < 1.5$) was found from a simple energy balance where a correction due to dissociation at high temperatures has been included. Because this validation case includes nonadiabatic walls as well as radiation, the coupling of reaction progress and fluid density is done via the enthalpy equation (see discussion above). Accordingly, a 6th-order polynomial of the specific heat coefficient $c_p(T)$ was used where the coefficients were fitted based on the appropriate adiabatic flame temperatures. The laminar flame speed was computed from one-dimensional detailed chemistry for λ in the range $\lambda = 0.8$ to 1.5 in intervals of $\Delta\lambda = 0.1$; from these, discrete values of the critical strain rate g_{cr} were obtained from Zimont's dimensional argument $g_{cr} = C S_L^2 / \chi$ where $C = 8.4$. Linear interpolation between these tabulated values was used to obtain laminar flame speeds and critical strain rates for intermediate values of λ.

In Figs. 5 and 6 we present the axial velocity and static temperature profiles in the radial direction for three different downstream positions. In general, the agreement for the axial velocity profiles is satisfactory for both the extended TFC model and the

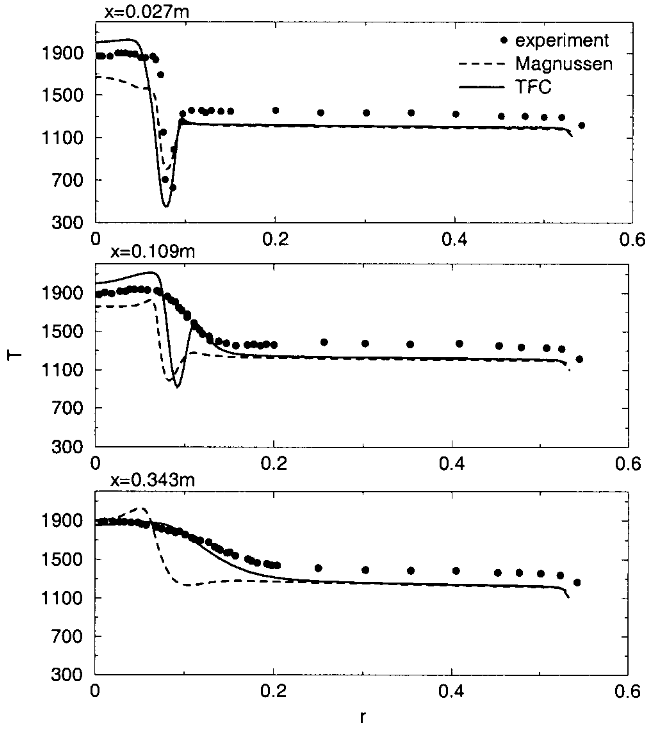

Fig. 6 Static temperature profiles of the BERL combustor at three downstream positions

Magnussen finite-rate model. In the vicinity of the burner exit ($x = 0.027$ m) both models have the tendency to overpredict the recirculation velocity near the axis whereas very good agreement with the experiment is found for the TFC model for larger values of r. Further downstream, both models scatter around the experimental data with some degree of inaccuracy and where the TFC model first is somewhat more diffusive than Magnussen and underpredicts axial velocity peaks ($x = 0.109$ m), it then again follows more closely the experimental trends ($x = 0.343$ m). Temperature profiles are shown in Fig. 6 for the same axial positions. At $x = 0.027$ m the temperature from experiment peaks at approximately 1900 K within the inner recirculation zone around which the methane-rich flame ($\lambda < 1$) is stabilized; outside this zone the temperature drops sharply to around 550 K before it raises again to approximately 1350 K in the outer recirculation zone where a lean flame ($\lambda > 1$) is observed. This trend is found from both combustion models with the TFC model performing slightly better in the inner recirculation zone. At $x = 0.109$ m the simulations wrongly predict a temperature drop outside the inner recirculation whereas the experiment already shows a smooth and monotonic transition between the outer and inner regions. At $x = 0.343$ m the TFC model follows this trend of a smooth transition while the Magnussen computation still displays very large deviations from the experiment and a significant temperature drop at $r = 0.1$ m. Both models underestimate the temperatures in the outer region ($r > 0.2$ m) by about 200 K. We have no explanation for this discrepancy other than the errors introduced by the choice of our boundary conditions and additional deficiencies in the radiation model. To summarize: in this preliminary two-dimensional validation study, the extended TFC model produced significantly better agreement with experimental data than the popular Magnussen formulation. It is remarkable that such improved accuracy was achieved with significantly reduced computational cost and without any "tuning" of model parameters.

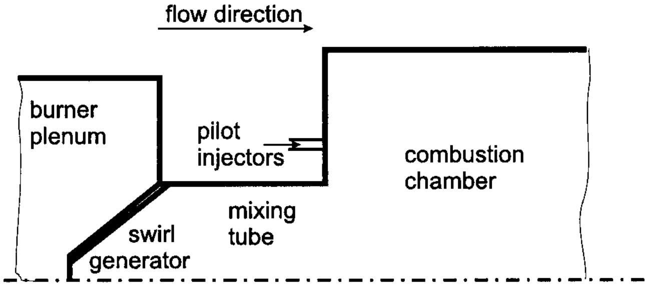

Fig. 7 Sketch of the ABB gas turbine burner

Application to Gas Turbine Burners

Applications of the original TFC model to gas turbine combustion that have been reported previously have focused on ABB's double cone burner at atmospheric pressure and assuming perfectly premixed conditions, and results have been successfully validated against detailed experimental data ([4]). In the present paper, we investigate a similar (but further developed) premix burner configuration at two different operating conditions (see Fig. 7). The first operating point is also fully premixed, however, at typical base load conditions of a gas turbine. As it turns out, the critical strain rate can be notoriously difficult to estimate if detailed chemistry results are not at hand. In fact, Zimont's simple dimensional argument (13) appears to be not appropriate for the high pressures at base load conditions, as we demonstrate in this test case. The second case selected includes local unmixedness of the fuel before the flame front. The chosen operating point is close to lean extinction where small streams of gas enter the combustor unmixed in order to stabilize the premixed flame, and we explore whether the extended TFC model is able to reproduce this stabilizing effect.

The burner that is modeled here comprises a swirl generator which is based on four sections of a cone that are shifted with respect to each other in the radial direction such that inlet slits of constant width are formed. A strong swirling component is imparted to the air entering the burner through the slits where also the gaseous fuel is injected through small holes along the slits. The swirler is followed by a tube of constant cross-section where fuel and air become well mixed. The degree of swirl is chosen such that a vortex-breakdown forms at the end of this tube where the flow enters the combustor. Additional pilot fuel injectors are distributed around the circular burner exit and may be used to stabilize the flame. The preheated ($T = 760$ K) and compressed ($p = 20$ bar) air enters the burner plenum with a nominal mass flow of 3 kg s^{-1} in both cases and natural gas is injected at an air excess ratio of $\lambda = 2.14$ and $\lambda = 2.5$, respectively.

The geometry of the burner, the combustor and the upstream burner plenum have been modeled by an unstructured hybrid mesh of approximately 550,000 cells; tetrahedral cells have been used in regions of complex geometry, i.e., the swirl-generator with the upstream plenum and the near region of the pilot injectors at the burner front panel; hexahedral cells could be used in the mixing section and the circular combustor; and pyramids were used at the conformal interfaces between the two other cell types. This modeling allowed both, an efficient grid generation where even minute details such as pilot fuel holes could be resolved, as well as the use of a higher-order discretization scheme (QUICK) for the finite volume solver, in combination with a Reynolds stress turbulence model that is known to be superior to the standard $k-\varepsilon$ model for highly swirling flows.

The TFC model parameters for the simulations are given as follows. The adiabatic flame temperature was found, as in the validation case above, from a simple energy balance for various air excess ratios in the range $\lambda = 1$ to 3. It was observed that these values could be very well approximated by a simple functional of the form $T_{ad} = 2519.7\lambda^{-0.4716}$. For example, we find $T_{ad} = 1760$ K for $\lambda = 2.14$ and $T_{ad} = 1630$ K for $\lambda = 2.5$. Laminar flame speeds based on detailed chemistry were computed for excess air ratios in the range $\lambda = 1.6$ to 2.2. These values are very well ap-

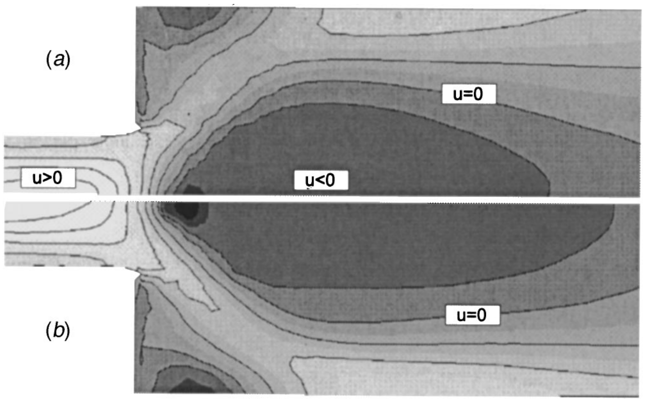

Fig. 8 Axial velocity contours for $\lambda=2.14$; (*a*) TFC model; (*b*) Magnussen finite rate model

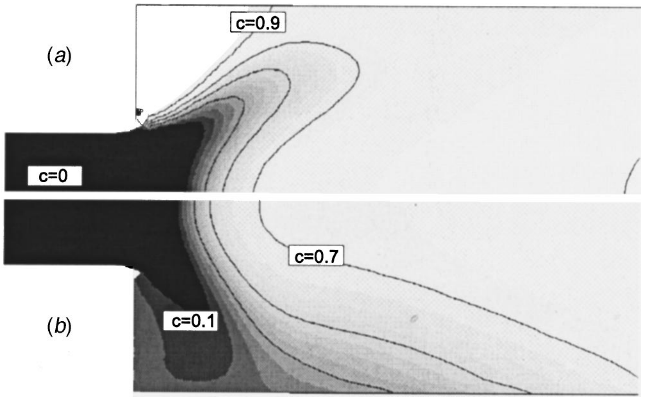

Fig. 10 Reaction progress for $\lambda=2.5$; (*a*) with pilot fuel injection; (*b*) without pilot fuel injection

proximated by a functional of the form $S_L=5.3294$ $\exp(-1.5721\lambda)$, which results in reasonable values for S_L for $\lambda>1$; in particular, $S_L=0.2\,\mathrm{m\,s^{-1}}$ for $\lambda=2.14$ and, by extrapolation, $S_L=0.1\,\mathrm{m\,s^{-1}}$ for $\lambda=2.5$. It should be stressed that there is no deeper reason behind our choice of the functionals for T_{ad} and S_L and they are used for convenience only. Detailed chemistry was used to determine the critical strain rate g_{cr} based on the OH criterium (see discussion above). However, in this way only values in the range $\lambda=0.8$ to 1.8 could be found because for higher values of λ no clear peak in OH emerged. Comparing the critical strain rates in this range of λ for $p=1$ bar and $p=20$ bar, it was observed that critical straining at 20 bar is approximately 10–12 times higher than at 1 bar, which implies by extrapolation $g_{cr}\approx 44000-53000\,\mathrm{s^{-1}}$ for $\lambda=2.14$. By contrast, the dimensional argument of Zimont (13) results for $\lambda=2.14$ in $g_{cr}=13000\,\mathrm{s^{-1}}$ only (using the proportionality factor 8.4 that was found from atmospheric data!). As a consequence, we had to resort to our simulations to decide upon the most realistic estimate for g_{cr}. The simulations supported the higher values of g_{cr} and we used therefore $g_{cr}=44000\,\mathrm{s^{-1}}$ to fit a functional of the form $g_{cr}=2.0133\times 10^6\exp(-1.7809\lambda)$ which is valid for $\lambda>1.2$ and which we used to extrapolate the critical strain for $\lambda>2.14$.

Results for base load conditions are presented in Figs. 8 and 9. Figure 8 shows axial velocity contours for base load conditions, and we compare our results from the TFC model with the standard Magnussen finite rate model where a two-step reaction mechanism with optimized rate coefficients ([5]) has been used. The plot displays a strong axial jetting in the mixing tube and the vortex breakdown occurring shortly after the expansion into the combustor; no significant differences in the velocity field were observed between the two combustion models. By contrast, noticeable differences in the flame front position are evident from Fig. 9 and, as a consequence of the further downstream located flame front, the temperature in the outer recirculation zone is approximately 600 K lower for the TFC model. The position of the flame front is directly linked to the choice of the model constant g_{cr}, and a lower value of g_{cr} leads to a positioning of the flame front at a location further downstream. In fact, $g_{cr}=13000\,\mathrm{s^{-1}}$ (as obtained from (13)) leads to a complete loss of the reaction zone. Even $g_{cr}=45000\,\mathrm{s^{-1}}$ appears to be rather at the lower limit of appropriate values and with some fine tuning one may easily reach very good agreement with the reference computation, which is, however, not the purpose of this study.

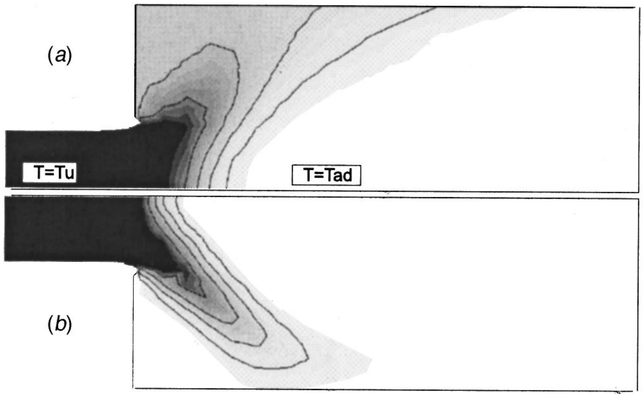

Fig. 9 Temperature contours for $\lambda=2.14$; (*a*) TFC model; (*b*) Magnussen finite rate model

In Fig. 10, we present results from simulations at $\lambda=2.5$. It is known from experiments that under these conditions the flame is close to lean extinction and a small fraction of the fuel is therefore injected through pilot nozzles at the burner exit in order to stabilize the flame. The lower half of the figure shows the fully premixed simulation with no pilot injection. The flame front appears at the expected location; however, the reaction progress is not completed within the combustor. In fact, no significant reaction at all is observed in the outer recirculation $(c=0.1)$, and a maximum of $c=0.7$ is reached at the combustor exit. By contrast, in a simulation where 10 percent of the fuel is injected through the pilot nozzles (upper half of Fig. 10) the flame is well stabilized at the outer recirculation $(c=1)$ and also the reaction progress in the inner recirculation is increased to $c=0.9$. Given the present uncertainties in the model parameter g_{cr}, it is remarkable how well the simulations reflect qualitatively the experimental findings near lean blow-off.

It may be added that the model is computationally robust and very efficient, especially when compared with other combustion models. For example, when comparing the extended TFC model with Magnussen we found that the simulations of the gas turbine combustor are more than four times faster using the extended TFC model: each time step[4] takes about half the time it takes for Magnussen, and additionally only 1500 iterations instead of 3500 are needed until full convergence is reached.

Summary and Outlook

A model for premixed turbulent combustion, based on a turbulent flame speed closure (TFC), has been extended to inhomogeneously premixed case. It has been validated against experimental data, the agreement with the reference data was satisfactory and, in particular, the model performed better than the standard Mag-

---

[4] On a SGI octane workstation (single processor R10000, 250MHz) one time step of a TFC computation with 550,000 cells takes about two minutes.

nussen finite rate model. An example from a gas turbine combustor demonstrated its ability to reproduce qualitative features of the reactive flow, even near the lean extinction limit.

The various possibilities for obtaining the model parameters—adiabatic flame temperature, laminar flame speed, and critical strain rate—have been discussed. We stress that the expressions for the model parameters are semi-empirical and not generally applicable. Damköhler was perhaps the first to suggest that depending on the ratio of turbulent to chemical time scales, fundamentally different combustion regimes and turbulent flame speeds should be expected. These ideas have been refined in recent years, and it has become clear that ‘‘one-for-all’’ combustion models can achieve only very limited agreement—in fact, often qualitative disagreement—with experiment, because ‘‘universal’’ models do not take into account the existence of the different regimes of combustion. Therefore, a trade-off has to be expected between accuracy and generality, and the TFC model clearly is an attempt to achieve better agreement with experiment even if it means that model parameters must be adjusted to operating conditions. It is important, however, that the model parameters are not simply ‘‘tuned’’ to give best agreement with validation experiments. Instead, prescriptions based on physico-chemical reasoning are provided to derive model parameters from first principles or at least from chemical-kinetic model systems with detailed chemical mechanisms.

Of these model parameters, reliable estimates of the critical strain can be difficult to obtain if no reference data or results from detailed chemistry calculations are at hand. In particular, it was shown that Zimont's dimensional argument (13) does not take into account the effect of pressure appropriately. Further investigations of the critical strain, perhaps also experimentally, are needed to gain confidence in numerical values of this parameter for a broad range of operating conditions.

Acknowledgments

We are indebted to Bernhard Rogg and Weigang Wang for making the RUN-1DL computer code available.

References

[1] Zimont, V. L., and Lipatnikov, A. N., 1995, ‘‘A Model of Premixed Turbulent Combustion and Its Validation,’’ Chem. Phys. Reports, **14**, No. 7, pp. 993–1025.

[2] Karpov, V. P., Lipatnikov, A. N., and Zimont, V. L., 1994, ‘‘A Model of Premixed Turbulent Combustion and Its Validation,’’ Archivum Combustionis, **14**, No. 3–4, pp. 125–141.

[3] Zimont, V. L., Polifke, W., Bettelini, M., and Weisenstein, W., 1998, ‘‘An Efficient Computational Model for Premixed Turbulent Combustion at High Reynolds Numbers Based on a Turbulent Flame Speed Closure,’’ ASME J. Eng. Gas Turbines Power, **120**, pp. 526–532.

[4] Polifke, W., Bettelini, W., Geng, W., Müller, U. C., Weisenstein, W., and Jansohn, P., 1998, ‘‘Comparison of Combustion Models for Industrial Applications,’’ *ECCOMAS'98*, John Wiley and Sons, London.

[5] Polifke, W., Geng, W., and Döbbeling, K., 1998, ‘‘Optimization of Rate Coefficients for Simplified Reaction Mechanisms With Genetic Algorithms,’’ Combust. Flame, **113**, pp. 119–134.

[6] Cokljat, D., Polifke, W., and Wild, P., 1998, ‘‘A Non-Adiabatic Method for Calculation of Premixed Flames Using a Turbulent Flame Speed Closure,’’ *7th Int. Conference on Numerical Combustion*, March 30–April 1, York, UK, SIAM (United Kingdom and Republic of Ireland).

[7] Phillip, M., 1991, ‘‘Experimentelle und theoretische Untersuchungen zum Stabilitätsverhalten von Drallflammen mit zentraler Rückströmzone.’’ Dissertation Universität Karlsruhe, Germany.

[8] Peters, N., 1997, ‘‘Four Lectures on Turbulent Combustion,’’ ER-COFTAC Summer School, Sept. 15–19, Aachen.

[9] Kech, J. M., Reissing, J., Gindele, J., and Spicher, U., 1998, ‘‘Analysis of the Combustion Process in a Direct Injection Gasoline Engine,’’ *COMODIA 98, 4th Int. Symp. on Diagnostics and Modeling of Combustion in Internal Combustion Engines*, published by The Japan Society of Mechanical Engineers, Tokyo, Japan.

[10] Rogg, B., 1992, ‘‘RUN-1DL: The Cambridge Universal Laminar Flamelet Computer Code,’’ *Reduced Mechanisms for Applications in Combustion Systems*, N. Peters and B. Rogg, eds., Springer, Berlin.

[11] Göttgens, J., Mauss, F., and Peters, N., 1992, *Twenty Fourth Symposium (Int.) on Combustion*, The Combustion Institute, Pittsburgh, PA, pp. 125–129.

[12] Müller, U. C., Bollig, M., and Peters, N., 1997, ‘‘Approximations for Burning Velocities and Markstein Numbers for Lean Hydrocarbon and Methanol Flames,’’ Combust. Flame, **108**, pp. 349–356.

[13] Dinkelacker, F., Soika, A., Most, D., Hofmann, D., Leipertz, A., Polifke, W., and Döbbeling, K., 1998, ‘‘Structure of Locally Quenched Highly Turbulent Lean Premixed Flames,’’ *27th. Int. Symposium on Combustion*, Boulder, CO, pp. 857–865.

[14] Zimont, V. L., 1997, private communication.

[15] Lutz, A. E., Rupley, F. M., and Kee, R. J., 1996, ‘‘EQUIL: A CHEMKIN Implementation of STANJAN, for Computing Chemical Equilibria,’’ SAND96-xxxx, Sandia National Laboratories, Livermore, CA.

[16] Sayre, A., Lallemant, N., Dugue, J., and Weber, R., 1985, ‘‘Scaling Characteristics of Aerodynamics and Low-NO_x Properties of Industrial Natural Gas Burners, The Scaling 400 Study, Part IV: The 300kW BERL test results,’’ *IFRF Doc F40/y/11*, International Flame Research Foundation.

[17] Fluent Inc., 1996, *Fluent Validation Manual* (TM-235), Fluent Inc., NH.

Implementation and Validation of a New Soot Model and Application to Aeroengine Combustors

M. Balthasar
e-mail: Michael.Balthasar@forbrf.lth.se

F. Mauss
e-mail: Fabian.Mauss@forbrf.lth.se

Division of Combustion Physics,
Lund Institute of Technology,
22100 Lund, Sweden

M. Pfitzner[1]
e-mail: Michael.Pfitzner@UniBW-Muenchen.de

A. Mack
e-mail: Andre.Mack@brr.de

BMW Rolls-Royce AeroEngines,
Eschenweg 11,
D-15827 Dahlewitz, Germany

The modeling of soot formation and oxidation under industrially relevant conditions has made significant progress in recent years. Simplified models introducing a small number of transport equations into a CFD code have been used with some success in research configurations simulating a reciprocating diesel engine. Soot formation and oxidation in the turbulent flow is calculated on the basis of a laminar flamelet library model. The gas phase reactions are modeled with a detailed mechanism for the combustion of heptane containing 89 species and 855 reactions developed by Frenklach and Warnatz and revised by Mauss. The soot model is divided into gas phase reactions, the growth of polycyclic aromatic hydrocarbons (PAH) and the processes of particle inception, heterogeneous surface growth, oxidation, and condensation. The first two are modeled within the laminar flamelet chemistry, while the soot model deals with the soot particle processes. The time scales of soot formation are assumed to be much larger than the turbulent time scales. Therefore rates of soot formation are tabulated in the flamelet libraries rather than the soot volume fraction itself. The different rates of soot formation, e.g., particle inception, surface growth, fragmentation, and oxidation, computed on the basis of a detailed soot model, are calculated in the mixture fraction/scalar dissipation rate space and further simplified by fitting them to simple analytical functions. A transport equation for the mean soot mass fraction is solved in the CFD code. The mean rate in this transport equation is closed with the help of presumed probability density functions for the mixture fraction and the scalar dissipation rate. Heat loss due to radiation can be taken into account by including a heat loss parameter in the flamelet calculations describing the change of enthalpy due to radiation, but was not used for the results reported here. The soot model was integrated into an existing commercial CFD code as a post-processing module to existing combustion CFD flow fields and is very robust with high convergence rates. The model is validated with laboratory flame data and using a realistic three-dimensional BMW Rolls-Royce combustor configuration, where test data at high pressure are available. Good agreement between experiment and simulation is achieved for laboratory flames, whereas soot is overpredicted for the aeroengine combustor configuration by 1–2 orders of magnitude. [DOI: 10.1115/1.1377596]

1 Introduction

Modern aeroengines have to satisfy very low emissions requirements. The optimization of the combustors of these engines is therefore an integral and difficult part of the development of the engines.

Due to ever increasing demands for reduction of development time and cost, there is growing focus on the prediction of the performance characteristics of engine components by analytical tools. Combustion CFD increasingly is used in the combustor development and optimization process to predict the temperature field, the exit traverse, and gaseous emissions. In particular, the emissions of NO_x at high power, which are dominated by the Zeldovich process, can be predicted well if the temperature field is reproduced correctly.

The prediction of soot emissions has been notoriously difficult since up to 99.9 percent of the soot that is formed in the combustion chamber is oxidized before it is finally emitted. Hence a ten percent error in soot formation may cause a large error in the exhaust concentration. In addition, the growth rate of soot depends on the soot volume fraction itself. Since the whole system is highly nonlinear, small errors made by calculating the early phase of soot formation may result in huge errors in later phases of soot particle growth and oxidation. The accuracy of the soot model has thus to be much higher than the accuracy of any other chemistry model. In the past, well-validated models for soot generation and consumption were not available, so that soot reduction mainly had to rely on correlations, experience, and a trial-and-error approach.

In recent years new soot models based on an improved understanding of the details of soot chemistry have been developed. These models have been successfully validated with several different laboratory flames at a variety of pressures and have also been successfully applied to soot prediction in reciprocating engines. Therefore there is now hope that these models can also be applied to predict the soot inside an aeroengine combustor locally, thus providing a means of focussing the effort to reduce soot emissions and thus save time and money.

This paper describes the application of a recently developed soot model to an aeroengine combustor configuration. The first section of the paper gives an overview of the soot modeling technique, and shows the validation using a laboratory jet flame using

---

[1] Now at the University of the German Armed Forces, Thermodynamics Institute, Werner-Heisenberg-Weg 39, D-85577 Neubiberg, Germany.

Contributed by the International Gas Turbine Institute (IGTI) of THE AMERICAN SOCIETY OF MECHANICAL ENGINEERS for publication in the ASME JOURNAL OF ENGINEERING FOR GAS TURBINES AND POWER. Paper presented at the International Gas Turbine and Aeroengine Congress and Exhibition, Munich, Germany, May 8–11, 2000; Paper 00-GT-142. Manuscript received by IGTI Oct. 1999; final revision received by ASME Headquarters Oct. 2000. Associate Editor: D. R. Ballal.

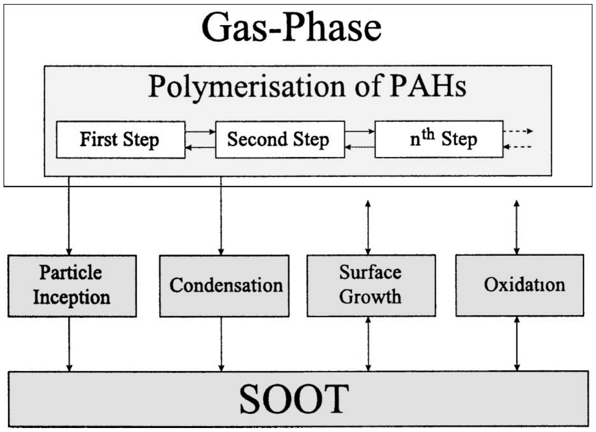

Fig. 1 Schematic representation of the soot model

ethylene as fuel. The next section describes the fitting procedure of the various quantities contained in the soot source term and the implementation into a commercial CFD code (CFD-ACE). The last section shows results from the application to a three-dimensional staged combustor configuration and draws some conclusions.

2 Soot and Chemistry Modeling

The description of the different processes occurring in the gas phase and on the surface of the soot particles is based on detailed chemical and physical models.

The soot model can be subdivided into three different parts (see Fig. 1). Chemical reactions in the gas phase leading to the first small polycyclic aromatic hydrocarbons (PAH), the growth of the PAHs, and the different processes involving soot particles like particle inception, surface growth, fragmentation, and oxidation. The different modeling approaches that are applied will be described briefly in the following. A more detailed description can be found in [1,2].

2.1 Modeling of the Gas-Phase Chemistry and PAH Growth. The chemical reactions in the gas phase are described by a detailed reaction mechanism for the combustion of n-heptane containing 89 species and 855 reactions. The mechanism was originally developed by Chevalier et al. [3] and has been modified with recent kinetic data ([4]). Its performance has extensively been tested in fuel rich premixed and counterflow flames ([1]).

The mechanism contains two pathways to benzene and describes the formation of the first small PAH, a species containing 18 carbon atoms. This species defines the interface between the gas phase mechanism and the further growth of the PAHs.

This molecule grows in a repeating cycle of H-radical abstraction and addition of acetylene. After the addition of two acetylene molecules a ring closure takes place and a new six-membered aromatic ring is added. This process is repeated forming large PAHs that can coagulate and form the first soot particles (see Fig. 1).

The growth of the PAHs is modeled as a fast polymerization process with the assumption that the PAH reactions are fast or in other words that the formation of soot from the PAH is fast. The different PAH molecules can thus be assumed to be in steady state resulting in a system of algebraic equations for the concentrations of the PAHs.

2.2 Soot Modeling. The soot model is based on a detailed description of the different physical and chemical processes involved in the formation, growth, and oxidation of soot. Coagulation of two PAHs leads to the formation of the first soot particles. These particles can grow further by heterogeneous reactions of gas phase species with radical sites on the surface of the soot particles. This growth process takes place in a similar manner as the growth of the PAHs.

First, a hydrogen radical is abstracted from the soot surface followed by an addition of C_2H_2 (HACA-mechanism, hydrogen-abstraction-acetylene-addition ([20])). This process is assumed to be reversible and can lead to a fragmentation of acetylene from the soot surface at high temperatures ([1,15]). The soot particles can also grow due to condensation of PAH molecules onto the soot surface. The particles are oxidized by heterogeneous surface reactions of molecular oxygen and hydroxyl radicals.

Detailed chemical reaction schemes are used for all heterogeneous surface reactions. The coagulation processes are described by the Smoluchowski equation ([5]) in the formulation for the free molecular regime.

The aim in modeling soot formation is generally to obtain the size distribution function of the soot particles (PSDF). Since solving the PSDF would be too time-consuming the method of moments introduced by Frenklach ([6,7]) is applied.

The method is based on the fact that solving an infinite number of moments is equivalent to solving the PSDF itself and the assumption that the consideration of just some moments is sufficient to obtain good results in most applications. The moments of the PDSF are given by

$$^{s}M_r=\sum_{i=1}^{\infty} i^r N_i; \quad r=0,1,\ldots,\infty. \tag{1}$$

Important features like the number density and the soot volume fraction can be extracted from these moments.

3 Coupling to the Flow Field

The soot model described above can be applied to simple one-dimensional laminar flame calculations. For the use in turbulent multidimensional reactive flows a modeling approach is needed to couple the soot model to the turbulent flow field. The laminar flamelet approach developed by Peters [8] is applied in this study and described briefly in the following.

3.1 The Flamelet Model. The basic idea of the flamelet approach is to decouple the chemical reactions from the turbulent flow field based on an analysis of the corresponding time scales. A coupling function, the mixture fraction, is introduced and it can be shown that under the assumption that the chemical reactions are fast compared to the turbulent time scales and occur in a thin reaction zone all species mass fraction are solely a function of this coupling function and the scalar dissipation rate χ.

The turbulent flame can thus be regarded as an ensemble of laminar flamelets. The strain that the flow field introduces to the laminar flamelets is described by the scalar dissipation rate χ. A one-dimensional transport equation for the temperature and the species mass fraction is solved a priori to the flow field calculations. The stationary flamelet equations for temperature and species mass fractions by assuming equal diffusivities and $\mathrm{Le}=\lambda/\rho D c_p=1$ can be written as

$$\rho\frac{\chi}{2}\frac{\partial}{\partial Z}\left(c_p\frac{\partial T}{\partial Z}\right)+\rho\frac{\chi}{2}\sum_{i=1}^{n}c_{p,i}\frac{\partial Y_i}{\partial Z}\frac{\partial T}{\partial Z}=\sum_{i=1}^{n}h_i\dot{w}_i+\dot{q}_R \tag{2}$$

$$\rho\frac{\chi}{2}\frac{\partial^2 Y_i}{\partial Z^2}=-\dot{w}_i \tag{3}$$

$$\tilde{\chi}=c_\chi\frac{\tilde{\varepsilon}}{\tilde{k}}\widetilde{Z''^2}. \tag{4}$$

The resulting mass fractions and temperature can be stored in the mixture fraction/scalar dissipation rate space into so-called flamelet libraries. Transport equations for the mean and the variance of the mixture fraction Z are solved in the flow field and used to obtain the shape of presumed pdfs of mixture fraction and

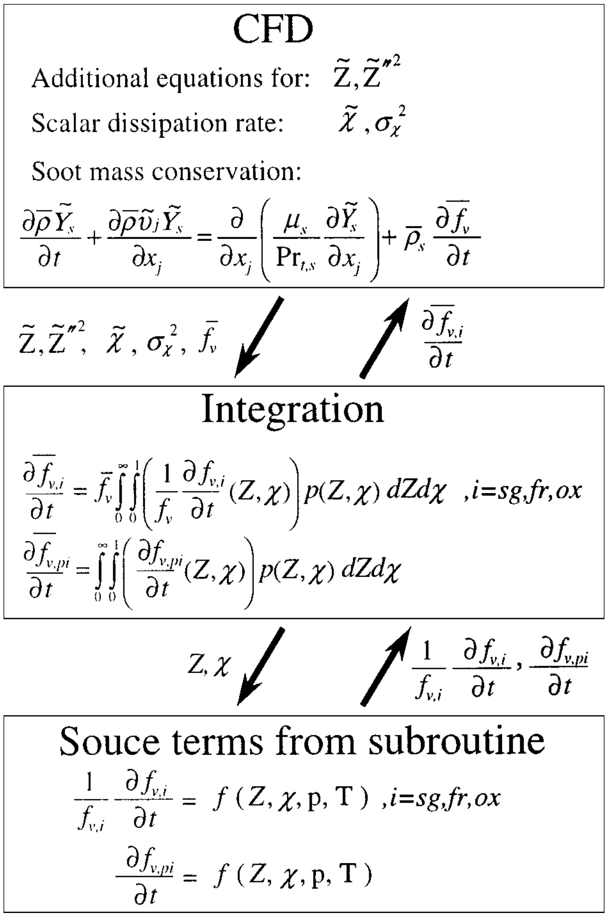

Fig. 2 Interface between the CFD code and the subroutine containing the rates of soot formation

scalar dissipation rate. The mean mass fractions and temperature can then be obtained with the help of the pdfs and the flamelet libraries. No transport equations for the species mass fractions have to be solved in the CFD code. This approach is called flamelet library approach.

Since soot formation is assumed to occur at time scales that are much larger than the turbulent time scales of the flow field the classical flamelet library approach as described above is not valid for the calculation of soot formation. Therefore a transport equation for soot mass fraction Y_s has to be solved in the flow field (see Fig. 2) and the rates of soot formation are precalculated in the flamelet calculations and stored in the flamelet libraries. The rate of soot formation is divided into the rates of particle inception, surface growth, fragmentation, and oxidation. The rates of surface growth, fragmentation, and oxidation are normalized with the soot volume fraction to account approximately for their surface dependence.

As in the classical flamelet model a transport equation for the mean and the variance of the mixture fraction is solved in the flow field and the mean source terms are obtained from averaging the instantaneous source terms from the flamelet library with the help of presumed pdfs for mixture fraction and scalar dissipation rate. The beta-function was used to model the pdf of mixture fraction and a clipped Gaussian ([8]) for the scalar dissipation rate. A delta-function pdf is assumed for the soot volume fraction in the averaging procedure.

Pitsch et al. [9] could also show that one flamelet that is solved in interaction with the CFD code could be sufficient to predict soot formation in a diesel engine. In this approach the mean conditional scalar dissipation rate calculated from the flow field is used. Since some transient effects like ignition and extinction cannot be described with this approach, Mauss et al. [10] proposed a Lagrangian transport of the flamelet in the turbulent flow. This interactive flamelet approach was recently applied to simulate combustion and pollutant formation in the same staged combustor as studied here ([11]).

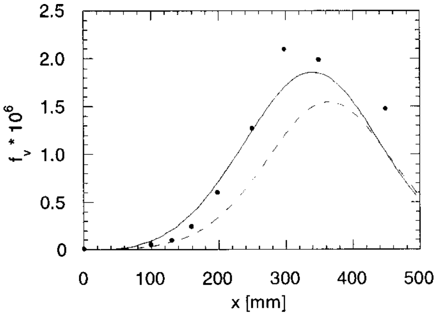

Fig. 3 Comparison between measured (symbols) and calculated (lines) soot volume fraction on the center line of a turbulent jet diffusion flame. Calculations have been done with surface reactions proportional to soot surface (line) and proportional to soot volume fraction (broken line).

However, the flamelet library approach appears to be much less CPU time-consuming and much simpler to implement into a comercial CFD code. We therefore concentrate in the following on the this approach.

3.2 Validation in Laminar and Turbulent Jet Diffusion Flames. The flamelet library approach for soot formation has successfully been validated first in laminar jet diffusion flames ([2]) and consecutively in a turbulent C_2H_4/air jet diffusion flame ([12]) burning at a pressure of $p = 1$ bar. A comparison between the mean calculated and measured soot volume fraction as a function of height above the burner is shown in Fig. 3. Good agreement was achieved between computations and measurements ([13]) for soot volume fraction and mixture fraction.

In contrast to the present study both soot formation and combustion chemistry were modeled via the flamelet approach. The full flamelet libraries were used in this study including the effect of radiation on the flamelet calculations. Therefore a third parameter, in addition to mixture fraction and scalar dissipation rate, had to be introduced in the flamelet library describing the intensity of radiation heat losses from the flamelet. The enthalpy is then included in the flamelet library and the appropriate flamelet is selected during the CFD calculations by comparing the local enthalpy in the flow field with the enthalpies in the flamelet library. A similar approach could be used for the calculation of soot formation in gas turbine combustors if radiation is supposed to be of importance.

Results of a recent study ([14]) show good agreement between the stationary flamelet library and the interactive model, but more work is required in the application to aeroengine combustor soot predictions. In Fig. 3 calculations are shown assuming the surface reactions to be proportional to the surface of the soot particles $(\sim S, \sim d_p^2)$ and to be proportional to the soot volume $(\sim f_v, \sim d_p^3)$. For the latter the rates of the surface reactions have been decreased by a factor of 8 ([15]). Results achieved with surface reactions proportional to f_v show a slightly later onset of surface growth. The maximum of the soot volume fraction appears more downstream. The agreement with the experiment is slightly worse. It can also be seen that the oxidation of soot is slower if calculated proportional to fv and if the same conversion factor (8) is used for both surface growth and oxidation reactions. This finding is important for the discussion of the comparison of calculated and measured soot emissions from the gas turbine.

Table 1 Range of the flamelet calculations

Composition fuel	100%N-C_7H_{16}
Composition oxidizer	79% N_2, 21% O_2
Temperature fuel side	335 (K)
Temperature oxidizer side	$T=400-1000$ (K)
Pressure	$p=1-100$ (bar)
Scalar dissipation rate	χ=0.01–extinction limit (s^{-1})

3.3 The Flamelet Library Calculations and Simplification. Flamelet libraries of the rates of soot formation have been calculated varying in a wide range of scalar dissipation rate, temperature on the oxidizer side, and pressure (see Table 1). This wide range of boundary conditions was chosen to make the library applicable to simulation of soot formation in gas turbine combustors as well as diesel engines.

An in-house code was used for the calculation of the flamelet libraries using an adaptive grid method in mixture fraction space to increase accuracy and a pseudo-arclength method automating the variation over scalar dissipation rate. As an example for the shape of these rates the rate of particle inception as a function of mixture fraction and scalar dissipation rate at $p=1$ bar and $T(ox)=850$ K is shown in Fig. 4.

The first soot particles are formed in the fuel rich region ($Z_{st}=0.056$) and the particle inception rate peaks at an equivalence ratio of about ϕ=4.1 at a corresponding temperature of $T=1650$ (K). The rate increases first with increasing scalar dissipation rate due to a change in temperature and quenches at a certain scalar dissipation rate depending on pressure and temperature. The quenching of particle inception occurs at lower scalar dissipation rates than the quenching of the flamelet itself. With the calculated libraries mean source terms for the transport equation of soot mass fraction for CFD calculations could be obtained.

A further simplification is required for practical use of the method in three-dimensional CFD simulations due to some restrictions:

(a) the library of soot formation and oxidation rates requires about 80 MB of memory space,
(b) an interpolation of the soot source terms from the library in four dimensions at every grid point is very time-consuming, and
(c) a numerical integration of the laminar source terms over the mixture fraction and the scalar dissipation rate for turbulent averaging is also very time-consuming.

The flamelet libraries are therefore fitted and expressed in simple analytical functional form. The beta-function was found to be the best choice to fit the source terms to the mixture fraction (see Fig. 5(*a*)). The source terms as a function of mixture fraction Z are first normalized to have an area of unity. The source terms are then modeled as follows:

$$S(Z,\chi)=B(Z,\alpha,\beta)F(\chi) \tag{5}$$

where $B(Z,\alpha,\beta)$ represents a standard beta function and $F(\chi)$ is a factor to scale the dependence of the source terms on the scalar dissipation rate. The beta function has the form

$$B(Z,\alpha,\beta)=\frac{\Gamma(\alpha+\beta)}{\Gamma(\alpha)\Gamma(\beta)}Z^{(\alpha-1)}(1-Z)^{(\beta-1)}. \tag{6}$$

The parameters α and β are themselves functions of the mixture fraction Z and the scalar dissipation rate χ.

Choosing the beta-function includes another CPU time-saving aspect beside the advantage of having just two parameters. Since the beta function is also selected to be the presumed pdf for the mixture fraction the integration of the source terms over mixture fraction results in the integration of two beta functions which can be solved analytically. Thus both time-consuming numerical methods, the interpolation of the library values and the integration of the pdf of the source terms of soot formation, are avoided.

In the next step of the fitting procedure the variables obtained from the fit as function of mixture fraction (Fig. 5(*a*)) are fitted as function of the scalar dissipation rate (Fig. 5(*b*)). The rates are finally fitted to pressure and temperature.

The accuracy of this approach is of course limited. The fitted functions were therefore tested in the range of boundary conditions needed for the present study. Future studies will include more advanced compression techniques to be applied to the flamelet library. More details about the flamelet library and the fitting procedure can be found in Karlsson et al. [16].

The fitting procedure results in a small subroutine containing the rates of soot formation in analytical form as function of mixture fraction, scalar dissipation rate, pressure, and temperature. This subroutine is easily implemented into any CFD code which allows the definition of additional transported scalars with user

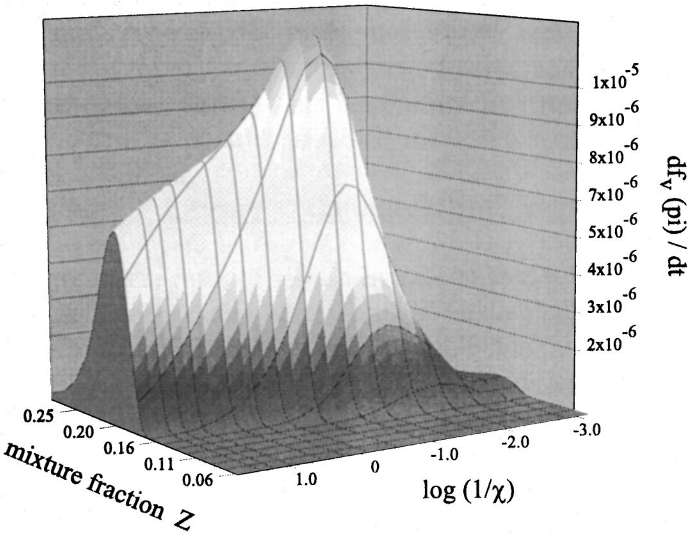

Fig. 4 Particle inception rate in the mixture fraction scalar dissipation rate space as calculated from the flamelet model

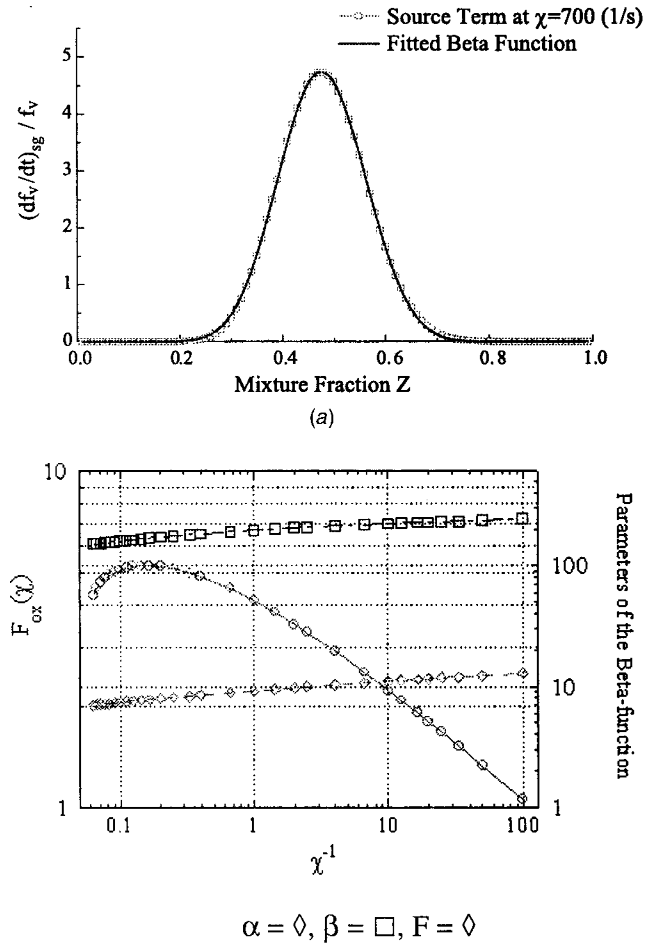

(*a*)

(*b*)

Fig. 5 (***a***) **The beta function fitted to the source term of particle inception** (***p*** $=$ **1 bar,** T_{ox} $=$ **850 K,** χ $=$ **700 s**$^{-1}$); (***b***) **parameters of oxidation soot source term—symbols: flamelet calculations, lines: fits**

defined source terms. Within these subroutines the turbulent averaging using the pdf as function of mixture fraction and scalar dissipation rate is also performed.

The soot simulation can be run as a post-processing step using a precalculated combusting flow field. The soot source terms are quite smooth and well behaved and the iteration of the soot mass fraction transport equation converges usually very quickly.

4 CFD Calculations

4.1 Implementation of Soot Transport Equation into Commercial CFD Code. In the current work, the subroutines calculating the soot source term of the transport equation of the soot mass fraction Y_s have been implemented into the commercial CFD package CFD-ACE from CFD Research, Huntsville, USA. This code solves a low Mach number formulation of the pressure correction type (SIMPLE) with a standard $k-\varepsilon$ turbulence model. A RNG $k-\varepsilon$ can also be chosen. An upwind space discretization was used for the turbulence quantities, second-order discretization for all other quantities. The combustion model uses an assumed beta function pdf of the mixture fraction with equilibrium chemistry. The soot model has been demonstrated with gaseous and liquid fuel, but only gaseous fuel has been used for the results presented here.

For calculation of the local soot mass und volume fractions the post-processing approach was used. This is feasible since the soot mass fraction in a well-designed gas turbine combustor represents only a small fraction of the total fuel present. A CFD solution of the combusting flow field was generated for the configurations neglecting the influence of soot onto the flow field. The soot volume fraction field is calculated using the local mixture fraction and scalar dissipation rates from the fully converged flow field.

In CFD-ACE, currently the user defined source terms for a scalar transport equations can only be a linear function of the transported variable. This is the case for the source terms as described in Fig. 2. The particle inception term is independent of soot volume fraction, while the surface growth, fragmentation, and oxidation terms depend linearly on the soot mass and volume fractions.

The surface growth and oxidation terms should scale with the effective surface area of all soot particles. This is taken into account by introducing a conversion factor of 1/8 ([15]). An alternative is to model the dependence on surface more directly using a source term which is proportional to $(f_v)^{2/3}$.

This is the case with soot models from other authors [17,18]. The present soot model is being generalized so that formulations based on a linear and fractional dependence on soot volume fraction can be compared.

The effect of turbulent mixing onto the soot field was incorporated by multiplication of the (laminar) source terms with the pdf of mixture fraction and scalar dissipation rate and integration these variables as shown in Fig. 2. The pdf distribution of the scalar dissipation rate χ was assumed to be a log normal distribution with a width σ_χ derived from the turbulent viscosity ratio ([12]).

The integration with respect to the mixture fraction was carried out analytically assuming that the distribution function in Z behaves like a beta function. The integration was performed here using a ten-point Gauss-Hermite quadrature.

The effect of radiation has been neglected in the coupling to the commercial solver. In a typical aeroengine combustor configuration at high power, previous work has shown that the coupling of the soot model to radiation has only a small effect ([18]). The reason is that here radiation cannot leave the combustor can and at high power and relatively high soot concentration the gas/soot mixture approaches the optically thick limit. Most of the radiation to the walls is reflected back into the can. Any heat absorbed by the walls is fed back into the combustor by the wall cooling air. Thus the specific heat loss in a combustor configuration is much smaller than from an open flame, where the optically thin limit applies.

4.2 Verification and Validation of the Implementation into CFD-ACE. The implementation of the transport equation was verified directly by comparing the soot generated by the CFD code in a frictionless tube flow at constant velocity and stoichiometry with results from stirred reactor calculations.

The implementation is being validated with experimental results from the jet flame ([13]), which has been used to validate the full flamelet calculations presented in Fig. 3.

Results using the fits in the CFD-ACE code deviate from the measurements considerably more than with the full model. The reason is that for this configuration the radiation effects cannot be ignored since the flame is optically thin and can radiate freely to the surroundings. This is reflected in the measurements of gas temperature, which are overpredicted by almost 200 K if radiation effects are neglected.

5 Application to Three-Dimensional Configurations

Typically, modern aeroengine combustors are annular combustors with injection of liquid hydrocarbon fuel (kerosene) through airspray injectors. The fuel is burning as a turbulent diffusion flame or a partially premixed flame. Most of the NO_x and soot emissions are generated at high power (typically at combustor

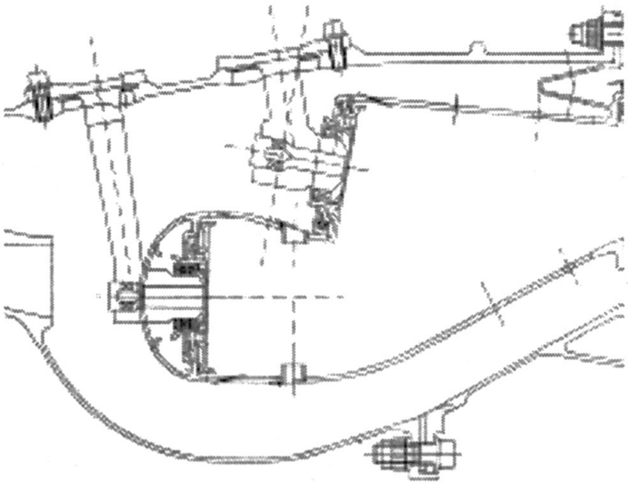

Fig. 6 BRR staged combustor configuration

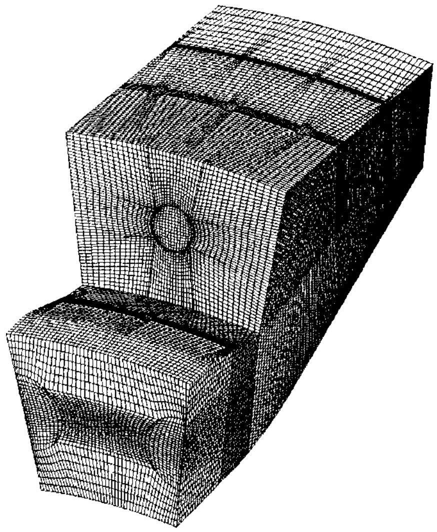

Fig. 7 BRR staged combustor computational grid

inlet temperatures of 850 K and pressures of 35 bar), whereas CO and UHC emissions come mainly from low power performance points.

Since more stringent aeroengine emissions certification requirements are expected for coming years, an axially staged combustor ([19]) has been developed at BRR in the framework of the German Aeronautics Engine 3E 2010 ‘‘Efficient, Environmentally friendly Economic Engine’’ research program.

The injection of fuel is split between a pilot zone and a main zone. The main zone injects most of the fuel at high power but is switched off at low power. The pilot zone is designed to achieve good altitude relight, weak extinction, idle emissions and efficiency at low power whereas the main zone is designed to yield low NO_x at high power. The configuration is shown in Fig. 6.

The research combustor has been investigated experimentally in a 90-deg sector high pressure rig, a full annular intermediate pressure rig and in a BR700 core engine. In the core engine a reduction of NO_x emissions by 25 percent could be demonstrated using the staged combustor compared to the BR700 single annular combustor, which represents latest low NO_x technology.

A three-sector rectangular rig with optical access capable of pressures up to 20 bar has also been investigated in depth at the DLR at Cologne. First results of simultaneous distributions of fuel and OH fluorescence up to pressures of 20 bar have been demonstrated using kerosene and n-heptane fuel. Investigations of local soot concentrations using LII are planned in the future.

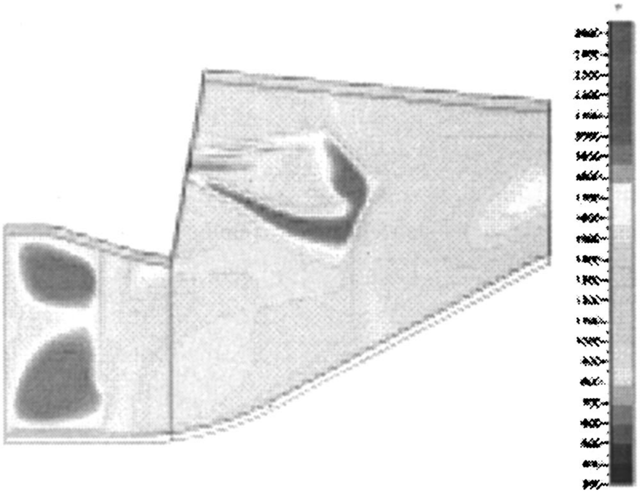

Fig. 8 BRR staged combustor temperature contours (main zone plane)

An assumed (top hat) pdf CFD solution has been generated using a grid composed of two blocks and a total of 355,000 cells. In the computation gaseous n-heptane (C_7H_{16}) fuel was used.

Figures 7,8 show the computational grid and temperature contours in an axial plane cutting through the main fuel injector. The conditions are BR715 take-off conditions scaled down to a pressure of 20 bar. Maximum temperatures of around 2500 K are reached in this simulation near the fuel injector, which are near the peak equilibrium temperature at the chosen inlet temperatures (850 K).

6 Results

6.1 Numerical Performance of CFD-ACE Implementation. The numerical solution of the additional scalar transport equation for the soot mass fraction proved to be very well behaved and usually converged within 100–300 iterations. As initial conditions and at inflow boundaries the soot mass fraction is set to zero.

The effect of the turbulent mixing mainly smoothes the soot source terms in space. Since the (laminar) source terms at low values of the scalar dissipation rate are low, the integration of the pdf with respect to scalar dissipation rate increases the source terms in regions of low mean scalar dissipation rate. Changes to the soot concentration field of up to a factor of 2 are observed comparing solutions using mean values of mixture fraction and scalar dissipation rate in the soot source terms with solutions incorporating the effect of turbulent mixing by integration over the two-dimensional pdf.

The CPU expenses for performing the integration with regard to the mixture fraction are negligible. The additional effort for the integration over the scalar dissipation rate pdf is considerable (factor 10) as the integration is done numerically. A study is currently under way to investigate whether the pdf integration with respect to the scalar dissipation rate can be performed prior to the CFD simulation in the generation of the flamelet library generation and the fit functions.

6.2 Application to Staged Combustor Configuration. The soot model was run in post-processing mode using the precomputed fully converged CFD solution of the staged combustor described in Section 5. Fits of the source terms were generated using a flamelet library for n-heptane fuel. The fits are valid for pressures between 1 and 100 Bar and air inlet temperatures up to 600°C.

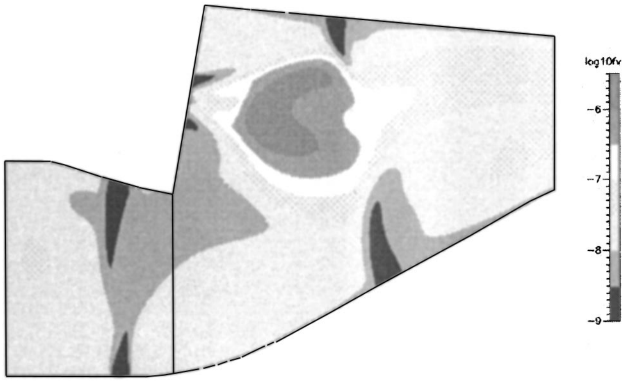

Fig. 9 BRR staged combustor (main zone plane: contours of soot volume fraction (log10)

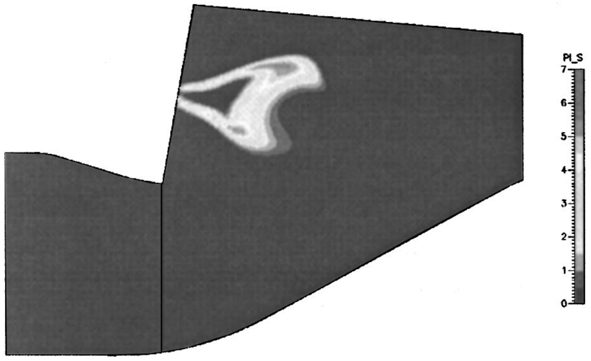

Fig. 11 BRR staged combustor (main zone plane): contours of particle inception source term

The solution of the soot mass fraction transport equation took 200 iteration steps to converge and the CPU time for solving the soot transport equation represents a few percent of the time required to converge the flow solution.

The logarithm of the soot volume fraction in an axial plane cutting through the main fuel injector is shown in Fig. 9. Figure 10 shows contours of the logarithm of the mixture fraction in the same plane. It can be seen that a considerable amount of soot is produced near the main fuel injector. Most of the soot is oxidized towards the rear of the combustor.

Contours of the different source terms of the transport equation of the soot mass fraction Y_s are shown in Figs. 11–13. Figure 11 shows the particle inception term, Fig. 12 the surface growth and Fig. 13 the oxidation term.

The particle inception source term is concentrated near the fuel injector in the rich region. The surface growth occurs further downstream, while oxidation occurs mainly in even leaner areas mainly at $\phi<1$.

It should be noted that the peak soot concentration depends roughly linearly on a constant prefactor of the particle inception term, whereas changes in a similar prefactor of the surface growth and oxidation terms lead to an exponential change. A reduction of the oxidation term by only 30 percent can lead to a tenfold increase of soot volume fraction in the jet flame validation configuration.

The soot emissions at the exit of the combustor was measured using a standard emissions rake. The measurements were done using kerosene fuel on high pressure 90-deg sector rig at a pressure of 20 bar and realistic combustor inlet temperatures of approximately 850 K. The kerosene fuel, which contains aromatic components is expected to produce more soot than the n-heptane fuel which was used in the predictions of the soot model. The soot emissions measurements indicate a soot volume fraction of the order of $10^{-9}\,(\mathrm{m}^3\,\mathrm{soot/m}^3\,\mathrm{gas})$.

Figure 14 shows an isosurface of soot mass fraction of $Y_s=5*10^{-4}$ colored by contours of temperature. This picture shows that most of the soot is oxidized at a temperature around $T=2000\,\mathrm{K}$. A streak of high soot concentrations in the exit plane at the lower left corner can also be seen.

The mean soot volume fraction at combustor exit from the soot model is of the order of $5*10^{-8}\,(\mathrm{m}^3\,\mathrm{soot/m}^3\,\mathrm{gas})$, so the exhaust soot concentration is overpredicted by approximately one-two orders of magnitude. It is expected that a stronger oxidation of soot

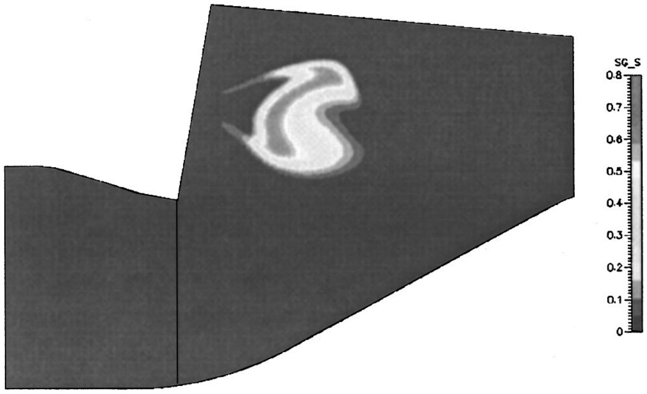

Fig. 12 BRR staged combustor (main zone plane): contours of surface growth source term

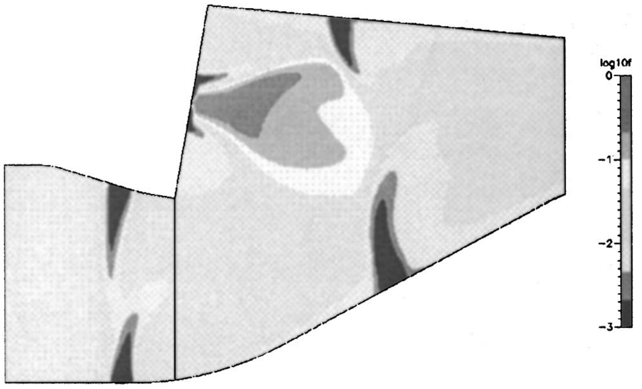

Fig. 10 BRR staged combustor (main zone plane): contours of mean mixture fraction (log10)

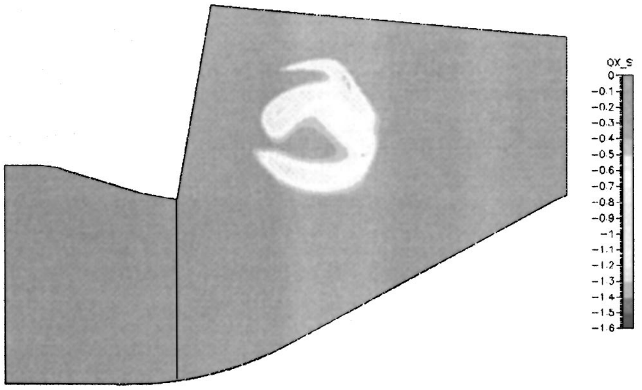

Fig. 13 BRR staged combustor (main zone plane): contours of oxidation source term

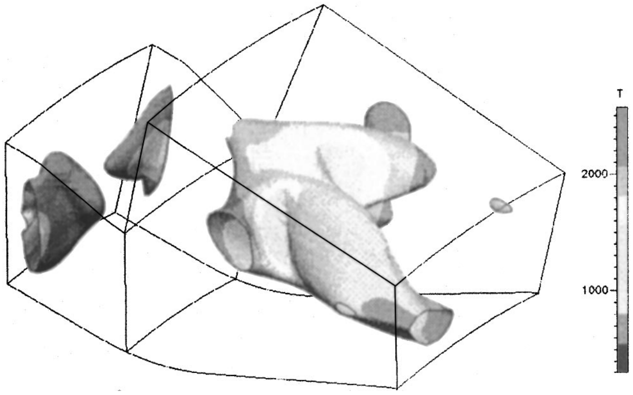

Fig. 14 BRR staged combustor: isosurface of soot mass fraction $Y_s = 5*10^{-4}$ colored by temperature contours

will be achieved, if the surface reactions are assumed to be proportional to the soot surface instead of the soot volume. This will be done in future calculations.

The calculate exhaust gas emissions with the model applied here are consistent with results obtained by Brocklehurst [18], where a Moss soot model and full coupling to radiation was used. Looking at the soot measurements reported there, the soot concentration in the primary zone is predicted with reasonable accuracy. However, the soot concentration drops by four orders of magnitude towards the exit of the combustor in the measurements while the simulations predict only a drop by two-three orders of magnitude.

Nevertheless, the predictions of the location of the soot production and consumption are already now improving the understanding of the origins of soot emissions and help to find design solutions to reduce soot emissions. Furthermore, the soot concentrations field can be coupled to the temperature field and a radiation model and can yield an estimate of the radiation flux towards the combustor walls. This is expected to be more accurate than the soot exit emissions predictions since the level of soot concentrations in the primary zone appears to be predicted more accurately.

7 Conclusions

A soot model, which has been developed in recent years and validated with laboratory flames, has been implemented into a commercial CFD code using user-defined subroutines.

The soot model is based on solving a single transport equation for the soot mass fraction with a source term using fits to a comprehensive flamelet library. The soot model operating with the full flamelet library compares well with soot measurements from a laboratory jet flame. The model has also been applied successfully to combustion in a reciprocating engine application. The soot source terms in the current formulation are linear functions of the soot volume fraction (surface growth, fragmentation, and oxidation). A formulation using surface area for the growth and oxidation terms is currently tested.

The effect of turbulence is implemented via a probability density function of mixture fraction and scalar dissipation rate. Radiation effects are not yet included, but work is in progress to incorporate these by solving an additional equation for enthalpy.

The soot model is operated in post processing mode using converged combusting flow fields. It converges quickly and the numerical effort is negligible compared to the generation of the flow field CFD solution.

The application of the soot model to the three-dimensional staged combustor configuration indicates that the soot volume fraction at the exit of the combustor is overpredicted by one to two orders of magnitude, which is consistent with results reported elsewhere in the literature. The soot model is extremely sensitive to the soot source terms and more work is needed to optimize these terms. It is expected that the agreement between model and experiment will become better if the surface reactions are calculated to be dependent on the soot surface instead of the soot volume.

There is experimental evidence from combustor development tests that soot emissions can be very sensitive to details of the fuel injector configuration. The extreme sensitivity of the combustor exit field to small changes in hardware configuration can also be seen in full annular tests, where there is often a quite large variation in temperature and soot emission exit traverses even for nominally identical upstream geometry.

This indicates that the CFD solution has to be very accurate to capture such effects. In particular, the fuel injector has to be modeled very accurately and the effect liquid fuel two-phase flow has to be taken into account. The number of grid points in a typical combustor CFD calculation (300,000–500,000 nodes) is still far from sufficient to achieve even a grid-independent solution of the combusting flow field. Thus a quantitative prediction of soot emissions in aeroengine combustors awaits the development of computers which are at least one order of magnitude faster and have a tenfold increased memory.

Nevertheless, the knowledge of the location of regions of high soot concentration and high production and consumption rates enables the combustor designer to optimize the soot emissions and predict the correct trends even with such an imperfect tool.

Further research is required to improve the soot model and to remove the critical sources of inaccuracy in the flow field simulation.

Acknowledgments

The work presented in this paper has been partially supported by the Swedish Center of Strategic Research in Combustion Science and Technology CECOST.

The staged combustor application of the CFD code has been financially supported by the German Ministry of Research and Technology BMBF in the framework of the German Aeronautics Research Program (Engine 3E 2010).

Nomenclature

B = beta-function
c_p = heat capacity
$c_{p,i}$ = heat capacity of ith chemical species
D = diffusion coefficient
ε = turbulent dissipation rate
k = turbulent kinetic energy
F = area
f_v = soot volume fraction
h_i = Enthalpy of ith chemical species
LII = laser induced incandescence
p = pressure
p, pdf = probability density function
PAH = polycyclic aromatic hydrocarbon
Pr_l = turbulent Prandtl number
PSDF = Particle size distribution function
μ = viscosity coefficient
ϕ = fuel/air equivalence ratio
Pr_t = Prandtl number
$\dot{q}_R$ = radiative heat loss
ρ = density
σ = width of scalar dissipation rate, Gaussian distr.
t = time
T = temperature
v_j = velocity components
$\dot{w}_i$ = source term of ith chemical species
x_α = spatial coordinate
Y_i = mass fraction of ith chemical species
Y_s = soot mass fraction

χ = scalar dissipation rate
Z = mixture fraction
Z''^2 = variance of mixture fraction

References

[1] Mauss, F., 1997, ''Entwicklung eines kinetischen Modells der Russbildung mit schneller Polymerization,'' Ph.D. thesis, RWTH, Aachen.

[2] Balthasar, M., Heyl, A., Mauss, F., Schmitt, F., and Bockhorn, H., 1996, ''Flamelet Modelling of Soot Formation in Laminar Ethyne/Air Diffusion Flames,'' Proc. Combust. Inst., **26**, p. 2369.

[3] Chevalier, C., Louessard, P., Mueller, U. C., and Warnatz, J., 1990, ''A Detailed Low-Temperature Reaction Mechanism of n-Heptane Auto-Ignition,'' *Int. Symp. on Diagnostics and Modelling of Combustion in Internal Engines COMODIA 90*, Kyoto.

[4] Baulch, D. L., Cobos, C. J., Cox, R. A., Frank, P., Hayman, G., Just, T., Kerr, J. A., Murrells, T., Pilling, M. J., Troe, J., Walker, R. W., and Warnatz, J., 1992, ''Evaluated Kinetic Data for Combustion Modelling,'' J. Phys. Chem. Ref. Data, **21**, p. 411.

[5] Smoluchowski, M. V., 1917, Z. Phys. Chem., **92**, p. 129.

[6] Frenklach, M., and Warnatz, J., 1987, ''Detailed Modeling of PAH-Profiles in a Sooting Low Pressure Acetylene Flame,'' Combust. Sci. Technol., **51**, p. 265.

[7] Frenklach, M., and Harris, S. J., 1987, ''Aerosol Dynamics Modeling Using the Method of Moments,'' J. Colloid Interface Sci., **118**, No. 1, p. 252.

[8] Peters, N., 1984, ''Laminar Diffusion Flamelet Models in Non-premixed Turbulent Combustion,'' Prog. Energy Combust. Sci., **10**, p. 319.

[9] Pitsch, H., Barths, H., and Peters, N., 1996, ''Three-Dimensional Modeling of NO_x and Soot Formation in DI-Diesel Engines Using Detailed Chemistry Based on the Interactive Flamelet Approach,'' SAE-paper 962057.

[10] Mauss, F., Keller, D., and Peters, N., 1990, ''A Lagrangian Simulation of Flamelet Extinction and Re-Ignition in Turbulent Jet Diffusion Flames,'' Proc. Combust. Inst., **23**, p. 693.

[11] Barths, H., Peters, N., Brehm, N., Mack, A., Pfitzner, M., and Smiljanovski, V., 1998, ''Simulation of Pollutant Formation in a Gas-Turbine Combustor Using Unsteady Flamelets,'' Proc. Combust. Inst., **27**, p. 1841.

[12] Bai, X. S., Balthasar, M., Mauss, F., and Fuchs, L., 1998, ''Detailed Soot Modelling in Turbulent Jet Diffusion Flames,'' Proc. Combust. Inst., **27**, p. 1623.

[13] Young, K. J., and Moss, J. B., 1995, ''Modelling Sooting Turbulent Jet Flames Using an Extended Flamelet Technique,'' Combust. Sci. Technol., **105**, p. 33.

[14] Dederichs, A., Balthasar, M., and Mauss, F., 1999, ''Pollutant Formation in Turbulent Non-Premixed Combustion Using Different Flamelet Models,'' 17th International Colloquium on the Dynamics of Explosions and Reactive Systems, ICDERS, Heidelberg, Germany.

[15] Mauss, F., Schäfer, T., and Bockhorn, H., 1994, ''Inception and Growth of Soot Particles in Dependence of the Surrounding Gas Phase,'' Combust. Flame, **99**, p. 697.

[16] Karlsson, A., Magnusson, I., Balthasar, M., and Mauss, F., 1998, ''Simulation of Soot Formation Under Diesel Engine Conditions Using a Detailed Kinetic Soot Model,'' SAE-paper 981022.

[17] Leung, K. M., Lindstedt, R. P., and Jones, W. P., 1991, ''A Simplified Reaction Mechanism for Soot Formation in Nonpremixed Flamesl,'' Combust. Flame, **87**, p. 289.

[18] Brocklehurst, H. T., Priddin, C. H., and Moss, J. B., 1997, ''Soot Predictions Within an Aero Gas Turbine Combustion Chamber,'' ASME paper 97-GT-148.

[19] Brehm, N., Schilling, T., Mack, A., and Kappler, G., 1998, ''NO_x Reduction in a Fuel-Staged Combustor by Optimization of the Mixing Process and the Residence Time,'' *AVT (AGARD) Symposium on Gas Turbine Engine Combustion, Emissions and Alternative Fuels*, Lisbon, Portugal.

[20] Frenklach, M., and Wang, H., 1990, ''Detailed Modelling of Soot Particle Nucleation and Growth,'' Proc. Combust. Inst., **23**, p. 1559.

U. T. J. Grönstedt
Department of Thermo and Fluid Dynamics,
Chalmers University of Technology,
SE-412 96 Gothenburg, Sweden
e-mail: thgr@tfd.chalmers.se

P. Pilidis
School of Mechanical Engineering,
Cranfield University,
Cranfield, Bedford MK43 0AL, UK
e-mail: p.pilidis@cranfield.ac.uk

Control Optimization of the Transient Performance of the Selective Bleed Variable Cycle Engine During Mode Transition

The transient performance of the selective bleed variable cycle engine (VCE) has been optimized during the transition from subsonic to supersonic mode. The selective bleed VCE concept has been developed with a short take-off vertical landing (STOVL) aircraft in mind and the engine is characterized by its twin mode VCE feature. The transition optimization is constrained by the requirement of maintaining thrust and compressor surge margins. The engine variable geometry component schedules and the fuel flow are used as optimization variables. A differential algebraic formulation of an inter-component volume model is used to model the transient behavior of the engine. Sequential quadratic programming (SQP) is applied to the nonlinear transient engine model directly, in order to solve the multivariable control problem. It is predicted that the mode switch can be carried out safely without violating the constraints and that the time required is limited by the actuator time of the hydraulic system. [DOI: 10.1115/1.1394965]

Introduction

Selecting optimal cycle parameters for a mixed aircraft mission with substantial amounts of fuel consumption required during both supersonic and subsonic flight, normally implies great compromises in engine performance. When integrated in short take-off vertical landing (STOVL) aircraft, the selective bleed variable cycle engine shows great potential for achieving superior mixed mission performance, in comparison with conventional turbofan engines ([1]). The design target is to obtain a powerplant that enables the aircraft to take off from a very short runway, cruise economically at Mach 1.6 (dry operation), loiter at Mach 0.6, and land vertically.

The selective bleed VCE operates in two different modes depending on flight conditions; the subsonic and the supersonic mode. During subsonic operation air is bled at the back of the low pressure compressor powering a continuously vectorable convergent nozzle. The nozzle is vertically positioned for take-off and horizontally positioned for subsonic cruise. The intermediate compressor operates with closed stator vanes. During supersonic operation the front nozzle is closed and the air is discharged through a convergent-divergent nozzle. The intermediate compressor is high flowed by opening its stator vanes. This gives the rear nozzle the specific thrust suitable for dry supersonic cruise at Mach 1.6.

A number of studies assessing the performance of the selective bleed engine have been carried out at Cranfield University ([1–4]). These studies have focused on selecting a suitable engine design point for the specified aircraft mission and optimizing the steady-state control system of the engine. This work addresses the key issue of the safe and efficient handling of the transient engine performance during the switch from subsonic to supersonic mode.

All numerical tests have been conducted with a new general transient and steady-state code, GESTPAN (general stationary and transient propulsion analysis), developed at Chalmers University of Technology, The Royal Institute of Technology and at Volvo Aero Corporation ([5]). The tool has been developed using Fortran 90. For this work a dynamic connection feature was programmed, to make the use of one engine model representing all three simulation modes possible (the third mode, operation with both nozzles partially opened, is used during the mode transition transient).

The Selective Bleed Engine

The two operating modes of the selective bleed variable cycle engine are illustrated in Fig. 1.

Selection of Design Point. A detailed study on the design point optimization and cycle selection of the selective bleed VCE has been performed by Nascimento and Pilidis [1]. In that study, two separate engine models representing the subsonic and the supersonic modes were used, in combination with a matching procedure that ensured that the two cycles corresponded to the same engine design.

Since the transient operation of the mode switch must use both nozzles actively the separate engine approach was not suitable for this work. Instead the engine design was carried out in the inter-

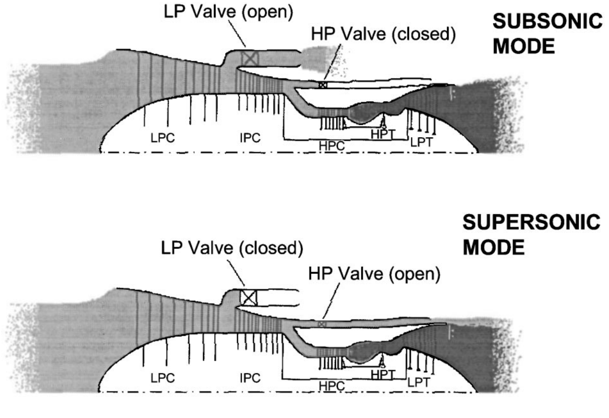

Fig. 1 The operating modes of the selective bleed engine ([4])

Contributed by the International Gas Turbine Institute (IGTI) of THE AMERICAN SOCIETY OF MECHANICAL ENGINEERS for publication in the ASME JOURNAL OF ENGINEERING FOR GAS TURBINES AND POWER. Paper presented at the International Gas Turbine and Aeroengine Congress and Exhibition, Munich, Germany, May 8–11, 2000; Paper 00-GT-148. Manuscript received by IGTI Nov. 1999; final revision received by ASME Headquarters Feb. 2000. Associate Editor: D. R. Ballal.

Table 1 Engine design point at SLS (sea level static)

Design Parameter	Value	Design Parameter	Value
h	0.0m	π_{HPC}	3.60
M	0.0	η_{HPC}	0.88
π_{LPC}	3.0	$\dot{m}_{\mathrm{core}}$	170 kg/s
η_{LPC}	0.88	TIT	1500.0 K
BPR_1	0.62	η_{HPT}	0.90
π_{IPC}	2.40	η_{LPT}	0.90
η_{IPC}	0.88	π_{nozzles}	0.98
BPR_2	0.24		

mediate mode and a feature for dynamic connections to switch between the intermediate mode and two single nozzle modes was developed. The design point, see Table 1, was selected in such a way that it would match the mission optimized design obtained by Nascimento and Pilidis [1] as closely as possible.

Engine Variable Geometry and Controls. The engine model has six variable geometry control signals; variable geometry in all three compressors as well as in the three nozzles. Additionally, the fuel flow has to be controlled in a suitable manner, giving a total of seven degrees-of-freedom for the control optimization. The variable geometry compressor model is identically the same as the one used by Oggero and Pilidis [4] to optimize the steady-state control of the selective bleed VCE.

Selection of the Transition Point

The selection of the transition point could be made in a straight forward way. The specific fuel consumption (SFC) of the engine was minimized for a number of flight cases in both the subsonic and the supersonic mode. Subsequently, a suitable point for transition could be selected among these optimal cruise points, defining both the initial and the end point of the trajectory as well as the flight case at which the transition will occur.

To ensure safe and stable operation in the optimal cruise points a number of constraints had to be imposed on the control optimization. The constraints are given in Table 2. The same definition of surge margin as the one used for optimizing the steady-state controls of the selective bleed VCE ([4]), was used here:

Table 2 Constraints

Ψ_{LPC}	$\leqslant$	0.8
Ψ_{IPC}	$\leqslant$	0.8
Ψ_{HPC}	$\leqslant$	0.8
TIT	$\leqslant$	1650.0 K
Net thrust	$\geqslant$	134.0kN
Mass flow	$\leqslant$	Design mass flow

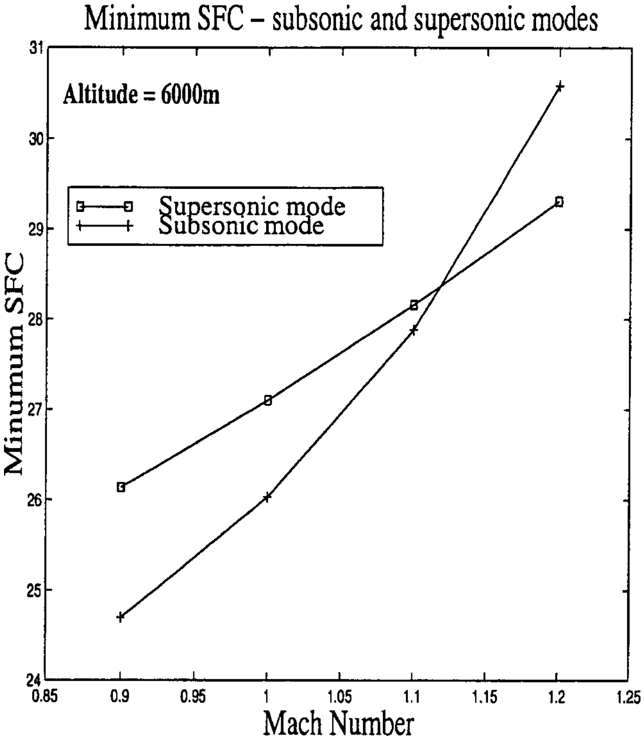

Fig. 2 Minimum specific fuel consumption (SFC) for the two modes

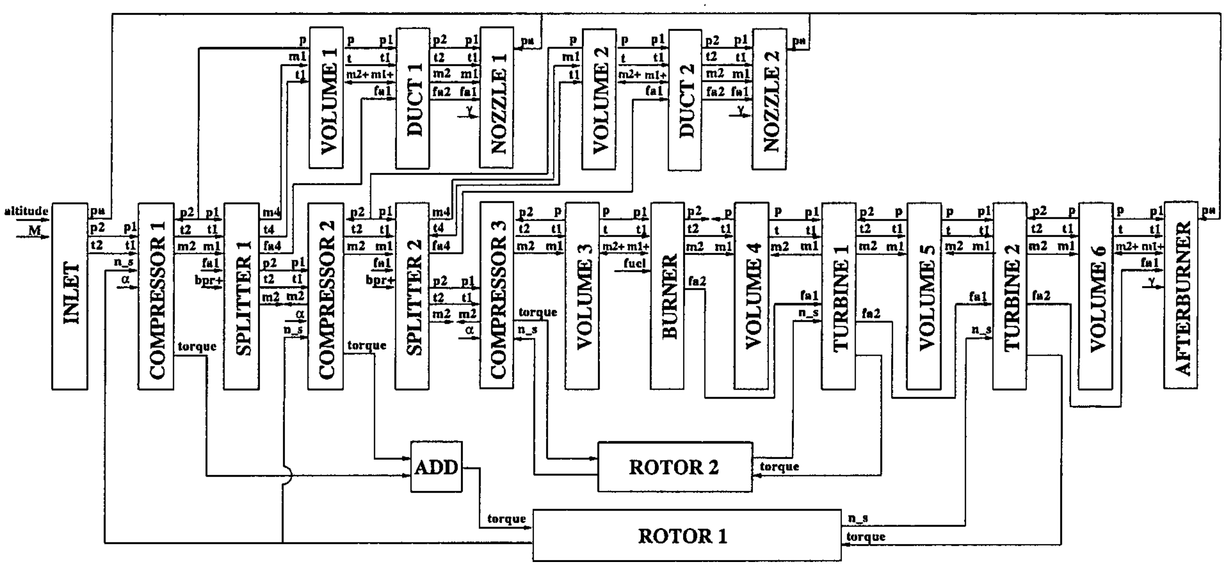

Fig. 3 Wiring diagram of the transient selective bleed variable cycle engine (VCE) model

$$\Psi = \frac{\pi - \pi_{\text{choke}}}{\pi_{\text{surge}} - \pi_{\text{choke}}}. \tag{1}$$

By this definition surge would occur for $\Psi = 1.0$. Thrust requirements for the entire flight mission of the STOVL aircraft have been given in Nascimento and Pilidis [1].

The selection of the transition point is of crucial importance for the successful control of the transient. For instance, if the rotational speeds of the subsonic mode cruise point and the supersonic mode cruise point differ considerably, inertia of the rotors will make it very difficult to perform the transient within a reasonable time. Also, if the steady-state cruise points are selected too close to the limits of safe and stable operation, the margin is likely to be insufficient for carrying out a successful mode transition. For this reason a more conservative selection of constraints was made for the steady-state cruise optimization.

The original design point optimization of the supersonic mode of the selective bleed variable cycle engine was carried out for a flight Mach number of 1.2 and an altitude of 6000 m ([1]). For comparative reasons this altitude was selected for the mode transition. A number of optimizations of the control settings were carried out to determine a suitable Mach number for transition. The optimal cruise SFC curves for the two modes are shown in Fig. 2. Although Fig. 2 indicates that the most optimal point for transition is around $M = 1.12$, the ($h = 6000$ m, $M = 1.2$) flight case was the final selection of transition point, since this flight case was the supersonic mode design optimization point and also part of the STOVL aircraft mission specification.

Table 3 Cruise optimized control settings for the transition point ($M = 1.2$, $h = 6000$ m)

	Subsonic Mode	Supersonic Mode
LPC restagger	−2.03696 deg	4.44104 deg
IPC restagger	12.2441 deg	−9.66672 deg
HPC restagger	−0.772156 deg	−0.531882 deg
Front nozzle	0.331422 (m^2)	0.000000 (m^2)
Mid nozzle	0.000000 (m^2)	0.116615 (m^2)
Exhaust nozzle	0.456220 (m^2)	0.741889 (m^2)
Fuel flow	4.105108 (kg/s)	3.927331 (kg/s)

The fact that the thrust requirement of the engine can be achieved also in the subsonic mode, indicates that the engine has been somewhat oversized. This observation is further strengthened by the fact that the highest turbine inlet temperature required for any of the STOVL aircraft mission thrust requirements was 1577 K.

The optimization problem was solved using sequential quadratic programming. The NAG implementation of the algorithm, based on the work of Gill et al. [6] was found to work very efficiently.

The new dynamic connection feature of GESTPAN made it very simple to specify the subsonic and supersonic modes with the engine design specified in Table 1 as the starting point. The subsonic mode was obtained by deleting all connections to the DUCT 1 and NOZZLE 1 modules, see Fig. 3 (note that the steady-state model used for finding optimal cruise points has no rotor or volume components). The supersonic mode was obtained in the same way.

The variable geometry and fuel flow schedules for the two

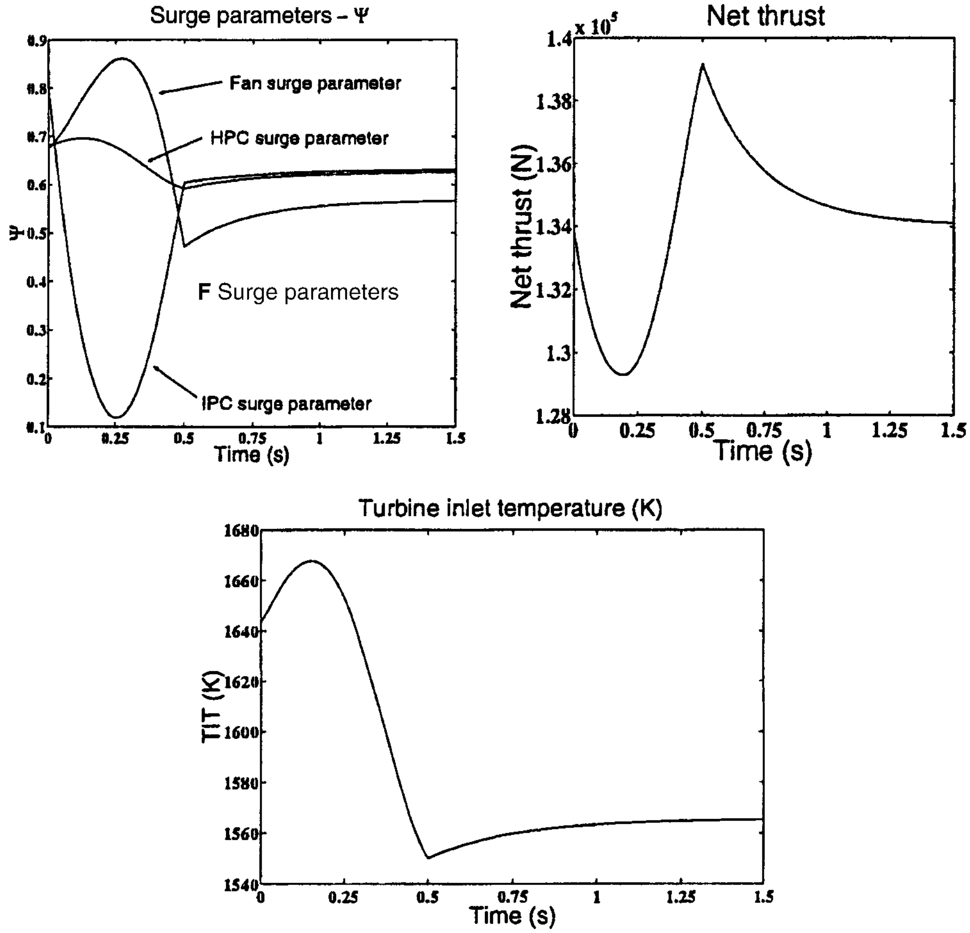

Fig. 4 Constraint variables—linear scheduling of controls

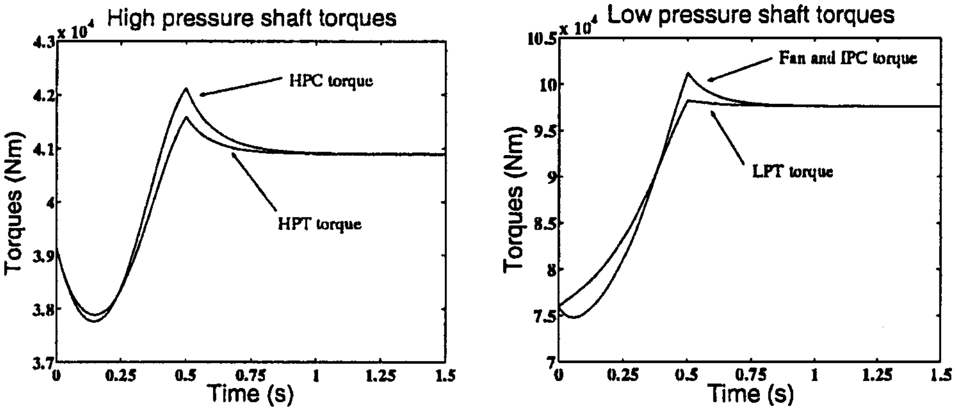

(*a*) I_{LP}=15 kgm^2, I_{HP}=10 kgm^2 (*b*) I_{LP}=15 kgm^2, I_{HP}=10 kgm^2

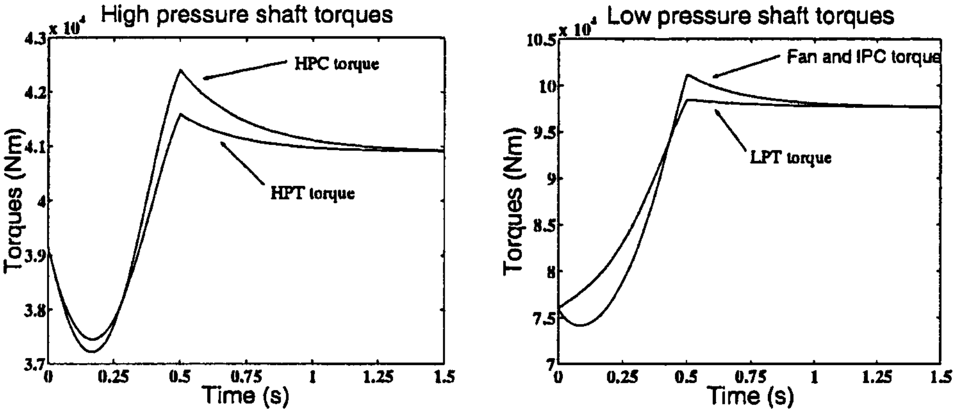

(*c*) I_{LP}=30 kgm^2, I_{HP}=20 kgm^2 (*d*) I_{LP}=30 kgm^2, I_{HP}=20 kgm^2

Fig. 5 Effect of doubling shaft inertias

modes were selected by optimizing the cruise SFC for this flight condition. The optimal control settings are given in Table 3.

Another approach to model the two engine modes would have been to use the intermediate mode model directly, by using very small areas to model the closed nozzles. However, this would add additional numerical difficulties due to the small mass flow operating range of the nozzles. Attempts to use the intermediate mode directly for optimization were made, but they were not successful.

Optimization of the Mode Transition

To model the transition trajectory an inter-component volume model was assembled. The wiring diagram of the engine model is illustrated in Fig. 3.

Numerically the engine was represented by a differential algebraic equation system with 14 states and 6 equations. The numerical procedure used to solve the equations has been outlined in detail in the work by Grönstedt [7] which is based on the public domain code DASSL developed and implemented by Petzold [8]. The DASSL code is a variable order, variable step length, backward differentiation method (implicit method) used to solve the differential and the algebraic equations simultaneously. Further description of the use and the underlying theory of the DASSL solver can be found in Brenan et al. [9].

The start and end points of the trajectory were approximated as intermediate points with nozzle areas 0.0001 times the areas given in Table 3. The optimal control schedules obtained for the subsonic and supersonic mode cruise points were not corrected for this very small deviation in initial and end points.

Optimality Criteria During Mode Transition. To ensure safe operation of the engine during the mode transition all three compressors must operate well away from the surge line. Furthermore, the engine thrust should not drop below the aircraft thrust requirement. A small increase in thrust during the transient is probably in agreement with most aircraft system requirements. The surge margin requirement was relaxed for the transient mode switch and was limited to 0.95. Also, the turbine inlet temperature was allowed to reach 1700 K during the transient. Shaft inertias were set to $I_{\mathrm{LP}}=30\,\mathrm{kgm}^2$ and $I_{\mathrm{HP}}=20\,\mathrm{kgm}^2$, and volume sizes were all set to 0.0001 m^3. The selection of the rotor inertias and volume sizes are motivated below.

Linear Interpolation of the Schedules. The first attempt to control the engine during transition was made by a simple linear interpolation of the optimal schedules determined for the subsonic and supersonic mode cruise points. The engine was scheduled to switch within 0.5 seconds. The resulting surge margins, thrust and turbine inlet temperature trajectories are shown in Fig. 4. It is observed that there is a drop in thrust during the first fraction of the transient, but the compressors operate well away from surge.

Component Modeling Assumptions. The component off-design behavior has been predicted using a number of empirical correlations described in Grönstedt [10]. These correlations do not

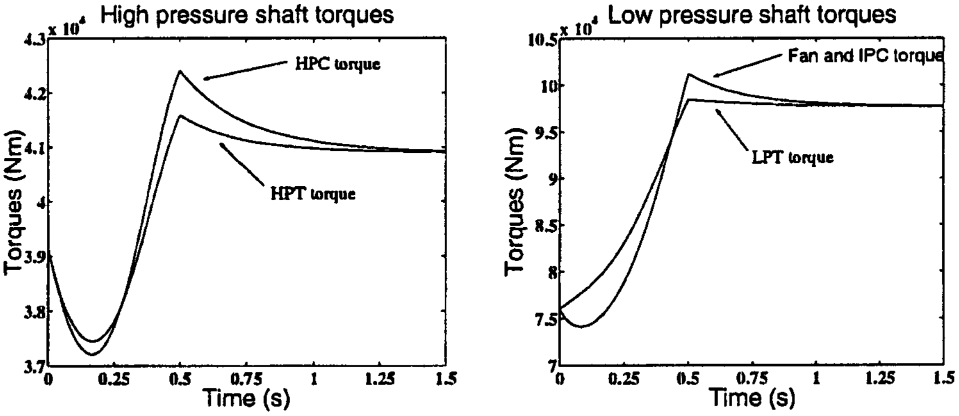

(a) $V_i = 0.0001m^3$ (b) $V_i = 0.0001m^3$

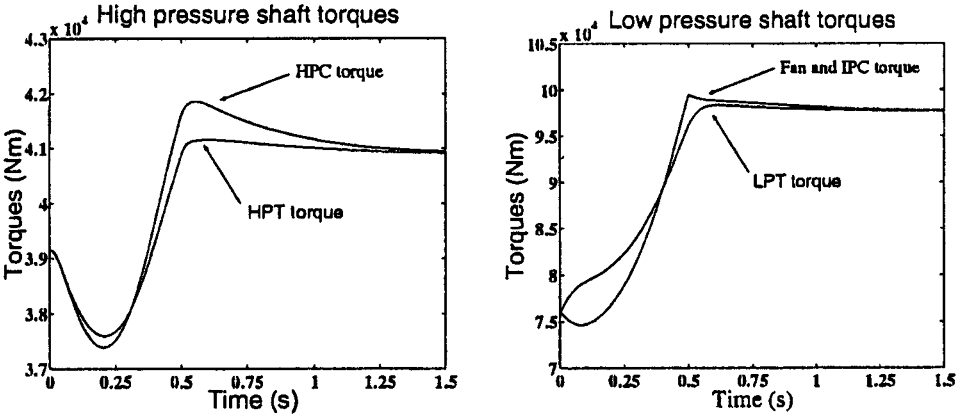

(c) $V_i = 0.5m^3$ (d) $V_i = 0.5m^3$

Fig. 6 Effect of change in intercomponent volume sizes

include any methods for estimating the moment of inertia of the shafts or the inter-component volume sizes. However, the dependency of the trajectory on the values selected for the shaft inertias and the volume sizes was observed to be very limited.

Dependency on Shaft Inertia. Since the high pressure shaft only changed its rotational speed from 153.7 rps to 158.1 rps and the low pressure shaft from 207.4 rps to 205.0 rps the effect of uncertainty in estimating shaft inertias on the trajectory was very limited. The shaft torques for two simulations with different values on shaft inertia are shown if Fig. 5. The proximity of the turbine and compressor torques also demonstrate that the intermediate points are relatively close to equilibrium points.

Dependency on Inter-Component Volume Sizes. Since the dynamics of the volumes is much faster than the time required for the mode switch the effect of uncertainties estimating volume sizes is also limited. Two simulations with volume sizes of 0.0001 m^3 and 0.5 m^3 are shown if Fig. 6. Note that the implicit solver technique makes the use of very small volume sizes possible, without any notable change in computational time. Very small volumes give rise to eigenvalues with large negative real parts, which makes the ordinary differential algebraic system stiff. The efficiency of the implicit solvers for solving stiff problems are related to their large stability regions which, in contrast to the explicit methods, causes the accuracy and not stability to be the limiting factor for increasing the time steps. Several authors have reported the successful use of low-order (first/second) implicit solvers ([11–14]) and recently also high-order implicit solvers ([7]), for the efficient solution of stiff gas turbine transients.

Optimization of the Trajectory. Since the linear interpolation of the control schedules produced an initial drop and a fairly large variation in thrust, some further development of the control methodology was undertaken. The initial 0.5 s during which the control scheduling occurs was discretized into three time intervals; (0,0.167), (0.167.0.333) and (0.333,0.5). At $t = (0.167, 0.333)$ the values of the nozzle area schedules, the burner fuel flow and the IPC variable geometry parameter were allowed to vary with 20 percent around the schedules produced by the linear interpolation. The control settings at all the intermediate points could then be obtained with interpolating cubic splines ([15]).

The resulting control optimization problem thus had eight degrees-of-freedom. The constraints on the compressor surge margins, the turbine inlet temperature and the thrust trajectories form five nonlinear constraints. The goal function was formed by minimizing the maximum thrust during the mode switch. This selection of goal function would minimize the total thrust variation.

Final Control Settings. The surge margins, turbine inlet temperature, and thrust trajectories resulting from the optimization are shown in Fig. 7, and the corresponding control parameters are shown in Fig. 8. Both the fan surge constraint and the turbine inlet

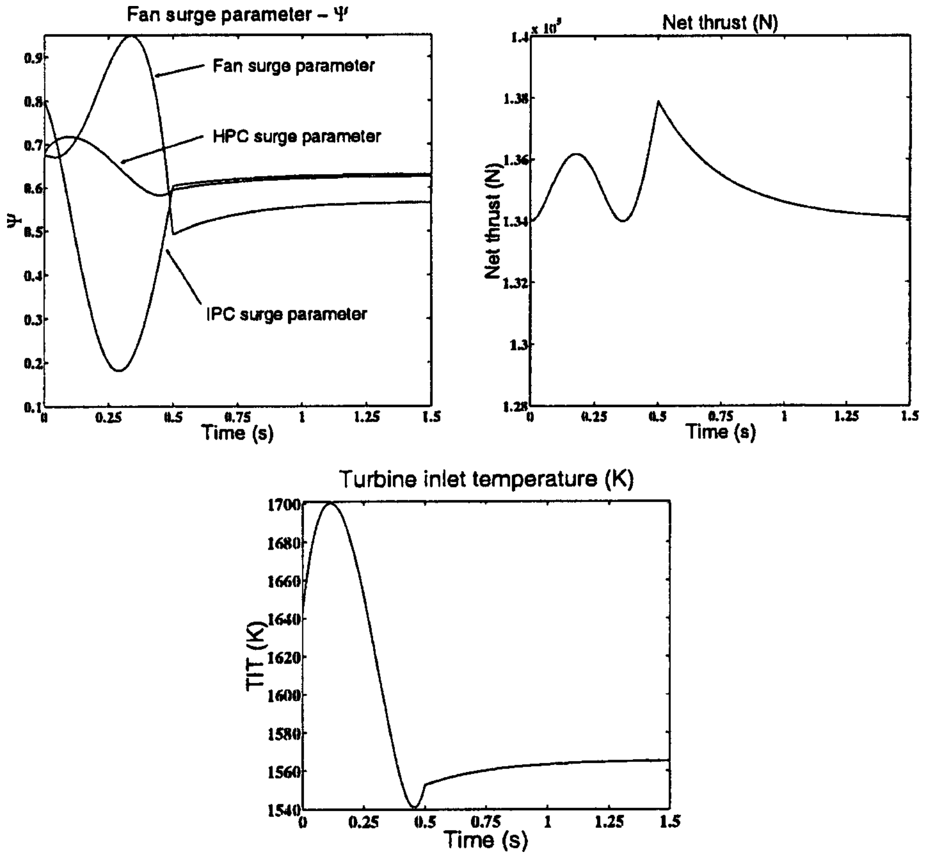

Fig. 7 Constraint variables—optimized scheduling of controls

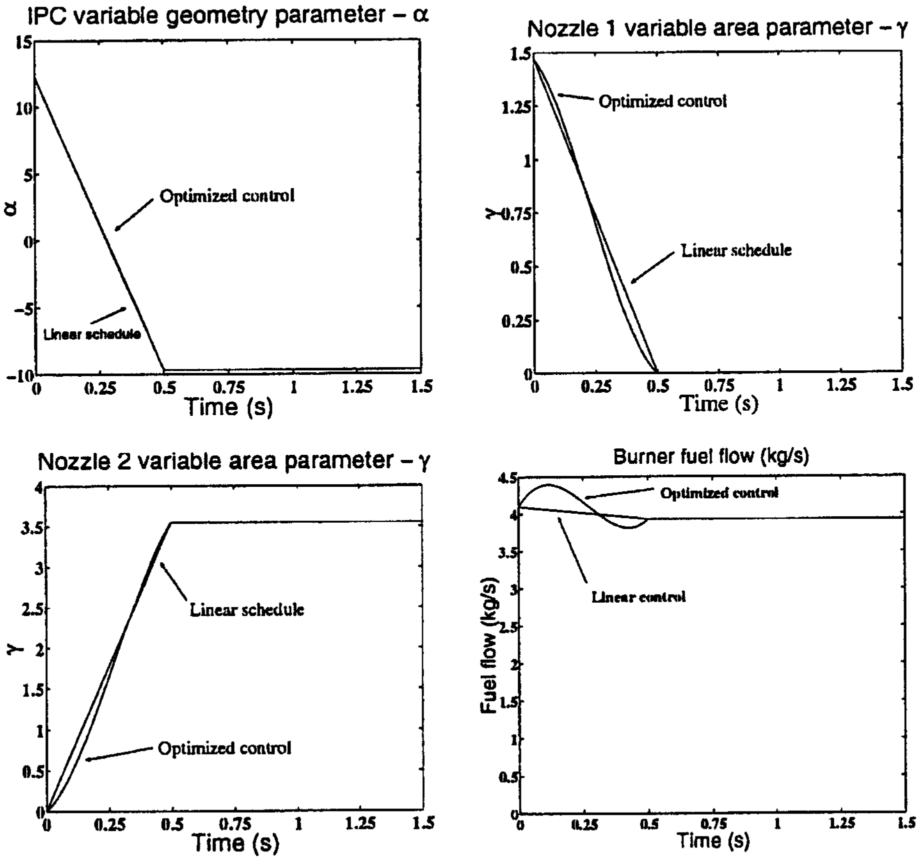

Fig. 8 Control schedules

constraint are active, i.e., the maximum allowed value is obtained at some point along the trajectory. The optimization has eliminated the initial drop in thrust and total variation in thrust has been reduced from 7.4 percent to 2.9 percent.

This methodology can be further refined by introducing more discretization points of the control variables as well as using also the fan, the HPC and the afterburner area variable geometry parameters as optimization variables. Too many discretization points might result in control schedules requiring variations in control signals to occur faster than the response times of the control system. Furthermore, such refined controls might be misleading if the accuracy of transient model is not sufficient. Also, large variations in the schedules can cause convergence problems for the differential algebraic solver, e.g., some combination of control variables evaluated during optimization could cause some of the nonlinear component models to operate outside their region of definition. However, the present results are sufficient for demonstrating the usefulness of the method and also to demonstrate that the transient can be controlled both safely and efficiently.

Conclusions

It has been shown that the mode switch of the selective bleed VCE can be carried out safely without violating surge and thrust constraints, and that the time for the mode switch is of the same order as the actuator times of a typical hydraulic system. Also, the modeling uncertainties introduced due to the estimation of the inter-component volume sizes and the shaft inertias were very limited on the trajectory selected for the mode switch. Furthermore, it has been observed that the thrust requirements set by the aircraft mission can be fulfilled at a considerably lower turbine inlet temperature than has been reported by previous authors. This indicates that by an optimal use of the control system the present design can be downsized.

Nomenclature

BPR = bypass ratio
h = altitude (m)
M = Mach number
HPC = high pressure compressor
HPT = high pressure turbine
IPC = intermediate pressure compressor
LPC = low pressure compressor
LPT = low pressure turbine
SBVCE = selective bleed variable cycle engine
SFC = specific fuel consumption (mg/Ns)
SQP = sequential quadratic programming
STOVL = short take-off vertical landing
TIT = turbine inlet temperature (K)
VCE = variable cycle engine
Ψ = surge margin
π = pressure ratio
η = isentropic efficiency

References

[1] Nascimento, M. A. R., and Pilidis, P., 1991, ‘‘The Selective Bleed Variable Cycle Engine,’’ ASME Paper 91-GT-388.
[2] Nascimento, M. A. R., 1992, ‘‘The Selective Bleed Variable Cycle Engine,’’ Ph.D. thesis, Cranfield Institute of Technology.
[3] Ulizar, I., and Pilidis, P., 1995, ‘‘Transition Control and Performance of the Selective Bleed Variable Cycle Turbofan,’’ ASME Paper 95-GT-286.
[4] Oggero, L., and Pilidis, P., 1998, ‘‘A Novel Optimization Method for Variable Cycle Engines,’’ ASME Paper 98-GT-142.
[5] Grönstedt, U. T. J., 2000, ‘‘Development of Methods for Analysis and Optimization of Complex Jet Engine Systems,’’ Ph.D. thesis, Chalmers University of Technology.
[6] Gill, P. E., Murray, W., Saunders, M. A., Hammarling, S. J., and Wright, M. H., 1986, ‘‘Users guide for LSSOL,’’ Department of Operations Research, Stanford University, Report, SOL 86-1.
[7] Grönstedt, U. T. J., 1999, ‘‘Advanced Solvers for General High Performance Transient Gas Turbine Simulation Tools,’’ 14th International Symposium on Air Breathing Engines, Florence, Italy.
[8] Petzold, L. R., 1983, ‘‘A Description of DASSL: A Differential/Algebraic System Solver,’’ *Scientific Computing*, R. S. Stepleman et al., eds. North-Holland, Amsterdam, pp. 65–68.
[9] Brenan, K. E., Campbell, S. L., and Petzold, L. R., 1989, *Numerical Solution of Initial-Value Problems in Differential-Algebraic Equations*, Elsevier, New York.
[10] Grönstedt, U. T. J., 1997, ‘‘Mission Dependent Optimization of Advanced Fighter Engines,’’ 13th International Symposium on Air Breathing Engines, Chattanooga, TN.
[11] Daniele, C. J., Krosel, M. S., John, R. S., and Westerkamp, E. J., 1983, ‘‘Digital Computer Program for Generating Dynamic Turbofan Engine Models (DIGTEM),’’ NASA-TM-83446.
[12] Chappel, M. A., and McLaughlin, P. W., 1993, ‘‘Approach to Modeling Continuous Turbine Engine Operation from Startup to Shutdown,’’ J. Propul. Power, **9**, pp. 466–471.
[13] Schobeiri, M. T., Attia, M., and Lippke, C., 1994, ‘‘GE-TRAN: A Generic, Modularly Structured Computer Code for Simulation of Dynamic Behavior of Aero- and Power Generation Gas Turbine Engines,’’ ASME J. Eng. Gas Turbines Power, **116**, pp. 483–494.
[14] Garrard, D., Davis, M., Jr., Hale, A., Chalk, J., and Savelle, S., 1997, ‘‘Analysis of Gas Turbine Engine Operability With the Aerodynamic Turbine Engine Code,’’ ISABE97-7034, Chattanooga, TN, pp. 223–232.
[15] Dierckx, P., 1993, *Curve and Surface Fitting With Splines*, Oxford University Press, New York.

Natural Gas Decarbonization to Reduce CO_2 Emission From Combined Cycles—Part I: Partial Oxidation

G. Lozza

P. Chiesa

Dipartimento di Energetica,
Politecnico di Milano,
Piazza Leonardo da Vinci, 32
Milan 20133, Italy

This paper discusses novel schemes of combined cycle, where natural gas is chemically treated to remove carbon, rather than being directly used as fuel. Carbon conversion to CO_2 is achieved before gas turbine combustion. Therefore CO_2 can be removed from fuel (rather than from exhausts, thus utilizing less demanding equipment) and made available for long-term storage, to avoid dispersion toward the atmosphere and the consequent contribution to the greenhouse effect. The strategy here proposed to achieve this goal is natural gas partial oxidation. The second part of the paper will address steam/methane reforming. Partial oxidation is an exothermic oxygen-poor combustion devoted to CO and H_2 production. The reaction products are introduced in a multiple stage shift reactor converting CO to CO_2. Carbon dioxide is removed by means of physical or chemical absorption processes and made available for storage, after compression and liquefaction. The resulting fuel mainly consists of hydrogen and nitrogen, thus gas turbine exhausts are virtually devoid of CO_2. The paper discusses the selection of some important parameters necessary to obtain a sufficient level of conversion in the various reactors (temperature and pressure levels, methane-to-air or methane-to-steam ratios) and their impact on the plant integration and on the thermodynamic efficiency. Overall performance (efficiency, power output, and carbon removal rate) is predicted by means of a computational tool developed by the authors. The results show that a net efficiency of 48.5 percent, with a 90 percent CO_2 removal, can be obtained by combined cycles based on large heavy duty machines of the present technological status, either by using chemical or physical absorption. [DOI: 10.1115/1.1395581]

1 Introduction

Greenhouse gases emissions are subject to limitations imposed by international agreements (Kyoto Protocol). For the power industry, those restrictions mainly apply to carbon dioxide emissions. Now, two main strategies have been individuated to achieve the Kyoto Protocol requirements: (i) switching from coal or oil to natural gas (improving, at the same time, the conversion efficiency by substituting old steam plants with state-of-the-art combined cycles) and (ii) resorting to a limited amount of renewable energy sources. However, an extensive recourse to these methods cannot be considered practical and feasible (both for economic and technological reasons), if a substantial reduction of CO_2 emissions below 1990 levels should be accomplished in the future. Carbon dioxide sequestration is therefore increasingly regarded as an effective strategy to limit greenhouse gases emissions in a power market dominated by fossil fuels.

On the subject of CO_2 sequestration, the authors of the present paper have considered some plant configuration based on the use of coal as the fuel ([1–4]). The reasons for referring to coal (and, in particular, to coal gasification and IGCC technology) are quite straightforward: (i) coal combustion produces more CO_2 per kWh, (ii) coal is the most utilized and abundant fossil fuel resource. However, the complexity and cost of CO_2 removal added to the ones of IGCCs makes such configurations poor candidates for the realization of pilot or demonstration plants for the near future. As a matter of fact, natural gas combined cycles are now a sound and effective technology and the application of novel sequestration technologies can be proposed with limited risks.

Generally speaking, three removal strategies can be proposed: (i) CO_2 separation from flue gases, (ii) using CO_2 as the main working fluid in a power cycle, and (iii) fuel conditioning to remove carbon prior to combustion. The first strategy was considered by many authors (see, for instance, [5,6]). According to our analyses (for IGCC, [2,4], for natural gas combined cycles, [7]), the best results are obtained by chemical absorption with semi-closed gas turbine cycles, in which exhausts are partially recirculated to the compressor inlet, in order to increase CO_2 concentration in flue gas ([8]). Power cycles based on CO_2 as the main working fluid require pure oxygen as the oxidizer and bring about large modifications to existing machines. They were addressed by Chiesa and Lozza [1], Mathieu and De Ruyck [9], Ulizar and Pilidis [10], using gas turbine cycles, and by Mathieu and Nihart [11] using liquid phase compression cycles. For natural gas combined cycles, this strategy is less attractive than for IGCCs, since the high hydrogen content of methane claims for a large oxygen requirement per kg of produced CO_2. The latter strategy (fuel decarbonization) is of particular interest, because separation treatments are concentrated on the fuel, rather than on exhausts or oxidizer ([12,13]). Therefore, much lower gas quantities must be conditioned with reduced equipment size and cost and lower energy requirements. Chiesa and Consonni [3] studied IGCC systems with shift reactors to convert CO to CO_2 and with subsequent CO_2 separation from synthetic gas. Chiesa et al. [4] and Doctor et al. [14] recognized a certain superiority of this system, compared to ones based on the previous strategies.

The aim of the present paper is to apply the fuel decarbonization concept to natural gas, to efficiently remove CO_2 from com-

---

Contributed by the International Gas Turbine Institute (IGTI) of THE AMERICAN SOCIETY OF MECHANICAL ENGINEERS for publication in the ASME JOURNAL OF ENGINEERING FOR GAS TURBINES AND POWER. Paper presented at the International Gas Turbine and Aeroengine Congress and Exhibition, Munich, Germany, May 8–11, 2000; Paper 00-GT-163. Manuscript received by IGTI November 1999; final revision received by ASME Headquarters February 2000. Associate Editor: D. R. Ballal.

bined cycles with limited addition of new equiment. Two basic chemical reactions can be addressed to obtain hydrogen and carbon monoxide from methane:

- partial oxidation: $CH_4+\frac{1}{2}O_2 \rightarrow CO+2H_2+35.67$ kJ/mol
- reforming: $CH_4+H_2O \rightarrow CO+3H_2-206.158$ kJ/mol

and a third one is required to convert CO to CO_2:

- shift: $CO+H_2O \rightarrow CO_2+H_2+41.154$ kJ/mol.

Therefore methane can be converted to carbon dioxide (to be separated, compressed, and liquefied for long-term storage or deep sea disposal) and hydrogen, to be used as the fuel in the combined cycle. These concepts are here studied and applied to integrated plant configurations: the first part of the paper will consider partial oxidation schemes, while reforming will be addressed in the second part, together with cost estimation.

2 Partial Oxidation: Basic Plant Concept and Chemistry

Figure 1 shows the rate of conversion of the carbon present in the natural gas[1] in an adiabatic reactor as a function of the air/natural gas mass ratio, for three operating pressures. The influence of steam addition is also considered. The resulting gas composition is calculated by chemical equilibrium. The figure shows that the air flow is the main parameter governing the methane conversion, necessary to obtain the fuel decarbonization. Pressure is relevant especially at low air/natural gas ratios. To obtain an elevated conversion rate of natural gas (ng) into CO or CO_2 (higher than 99 percent), lower air quantities would be required for an atmospheric reactor (4.25 to $4.5\ kg_{air}/kg_{ng}$), but the use of a pressurized process is fully compatible with an elevated CO_2 removal, provided that higher air quantities are used (5.25 to $5.5\ kg_{air}/kg_{ng}$). The addition of steam contributes to reduce the air requirement and moderates the operating temperature, due to the endothermic steam reforming reaction. The advantages of a pressurized solution are mainly related to the reduced size and cost of: (i) reactors and catalysts, (ii) equipments necessary to gas expansion and fuel compression, and (iii) heat exchangers for reactants pre-heating and syngas cooling. An atmospheric solution was considered by Bordiga and Campagna [15] not showing efficiency improvements with respect to pressurized solutions, due to the losses in those components. Therefore, we will only address pressurized partial oxidation schemes.

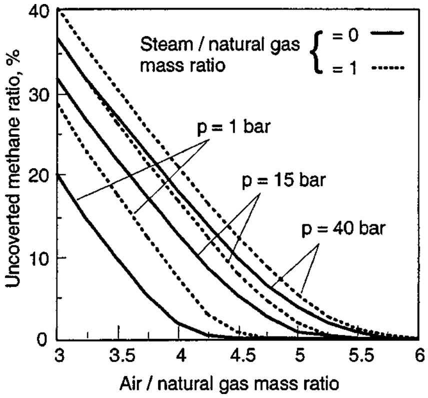

Fig. 1 Rate of methane conversion in an adiabatic partial oxidation reactor, at three operating pressures. The input flows are natural gas and steam at 565°C and air at 400°C.

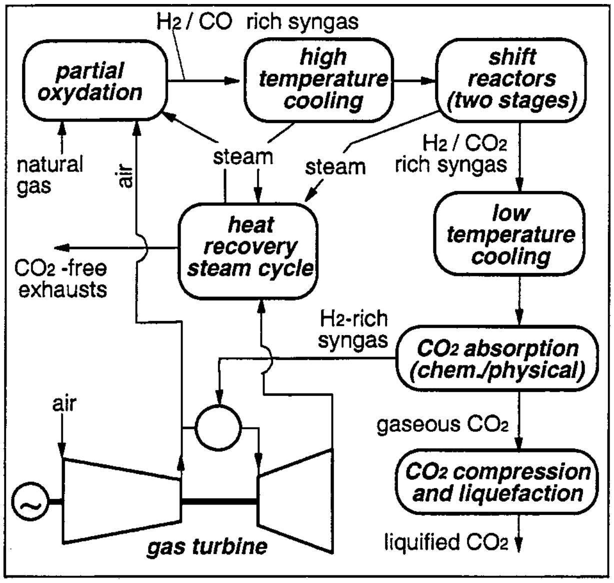

Fig. 2 Conceptual plant scheme of a combined cycle with partial oxidation

A combined cycle power plant including the fuel partial oxidation and CO_2 removal is conceptually represented by Fig. 2. The synthetic gas produced from natural gas, air, and steam is cooled down and enters the shift reactors, whereby CO_2 and H_2 are formed by consuming steam, previously added to syngas. Shift reaction is exothermic and heat is removed by steam production. To enhance CO conversion to CO_2 a second shift reactor is used at lower temperatures, favoring shift advancement. The syngas is cooled down to near-ambient temperature, suitable for CO_2 separation. Both chemical or physical absorption will be addressed: the former can be carried out at any gas pressure, the latter requires a rather high pressure (about 40 bar) to achieve a sufficient removal (as we will discuss later). Decarbonized synthetic fuel can now be used by a conventional combined cycle (differences are limited to the combustion system and to the steam flows required by integration with the fuel treatment section). Separated CO_2 is eventually liquefied by compression and made available for long-term storage.

3 Method of Calculation and Power Section Characteristics

Before addressing with more detail the plant configuration, let us recall briefly the main features of the method of calculation used for predicting the on-design overall performance and the energy balance of the plant. It was described in previous papers, with reference to the gas turbine model ([16,17]), the steam plant model ([18]). The main features are: (i) capability of reproducing very complex plant schemes by assembling basic modules, such as turbine, compressor, combustor, steam section, chemical reactor, heat exchanger, etc., (ii) built-in correlations for efficiency prediction of turbomachines, as a function of their operating conditions, (iii) built-in correlations for predicting cooling flows of the gas turbine, (iv) calculation of gas composition at chemical equilibrium at reactors exit temperature: If necessary, approach temperature difference can be imposed to better reproduce gas composition. Ideal gas behavior is assumed for all gaseous species, with the exceptions of water/steam in the steam cycle module and of carbon dioxide during its final compression and liquefaction (a particular calculation module was used to perform this task: Details are given by Chiesa and Lozza, [1]). The method enables the possibility of studying heavily integrated processes and of performing a complete second-law analysis of the entire

---

[1] Natural gas molar composition is here assumed as: 91.18 percent CH_4, 4.41 percent C_2H_6, 0.1 percent C_3H_8, 4.31 percent N_2. Molecular mass is 17.2, lower and higher heating values are 46.3 and 51.3 MJ/kg. One kg of natural gas produces 2.5656 kg of CO_2. Different natural gas compositions cannot alter significantly the results here presented.

Table 1 Performance and characteristics of the reference combined cycle.

Gas Turbine Cycle	Steam Cycle
Air flow: 625 kg/s	Three pressure—reheat
Pressure ratio: 15.1	HP steam pressure: 140 bar
Turbine inlet temp.$^{(*)}$:1315°C	RH/IP steam pressure: 30 bar
Turbine outlet temp.: 611°C	LP steam pressure: 4 bar
Natural gas @40 bar, 15°C	Condensing pressure: 0.05 bar
Ambient temperature: 15°C	HP/RH steam temp: 565°C
Pressure loss in/out: 1/3 kPa	ΔT at pinch-point: 10°C
Power output: 237.6 MW_e	Turbine output: 139.8 MW_e
Efficiency: 35.72 percent	Auxiliaries: 4.2 MW_e
Combined cycle net power output: 373.2 MW_e	
Combined cycle net efficiency: 56.11 percent	
Specific CO_2 emission: 0.3555 kg/kWh	

(*) first rotor total inlet temperature.

Table 2 Main assumptions used for calculation of the syngas treatment components and of the separation processes

Chemical reactors and heat exchangers:
  Thermal losses: 0.7 percent of exchanged power
  Pressure losses: 15 percent in the entire syngas circuit
  Minimum ΔT in heat transfer: 10°C
Chemical absorption:
  CO_2 concentration at absorber inlet: 0.15 mols/mol_{DEA}
  Minimum ΔT at solution regenerator: 10°C
  Stripping pressure: 16 bar
  Steam supply @8 bar (ΔT in reboiler$=$5°C)
  Max. gas Δp in absorber/stripper: 4/10 kPa
  Number of intercoolers for CO_2 compressor: 2
Physical absorption:
  CO_2 concentration at absorber inlet: 0.1 $\text{mols/mol}_{SELEXOL}$
  Number of flash chambers: 4
  Last chamber pressure: to obtain 95 percent CO_2 removal
  Number of intercoolers for CO_2 compressor: 3

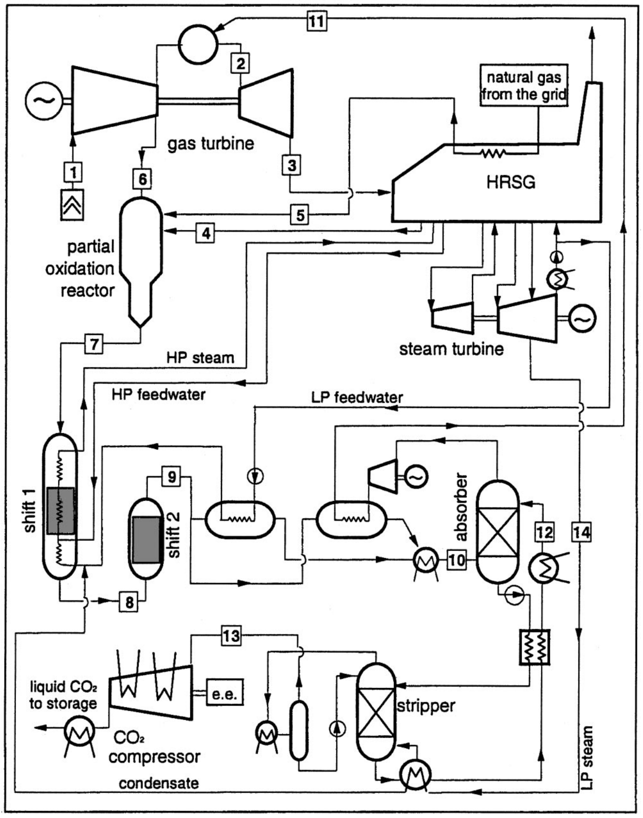

Fig. 3 Plant configuration of the partial oxidation combined cycle with chemical absorption

plant. Chemical absorption processes are studied by means of commercial software Aspen™ ([19]): Given the composition of the inlet gas, power and steam requirements are calculated, as well as the composition of the separated gases. Those data are given back to our model for the final plant balance. The same procedure is adopted for physical absorption, but based on a model developed by the authors for systems using Selexol™ absorption medium. The configuration of both systems will be addressed later.

Coming back to the power section, the assumptions used for calculating the performance of the various components are reported in a previous work ([20]). In this paper, the power section is based on an heavy-duty gas turbine of the present technology, usually referred as "FA." The main characteristics and performance of the "reference" combined cycle (without CO_2 removal techniques) are reported in Table 1, as calculated by our computer model. The assumptions for calculating components performance will be kept unmodified for the cycles here proposed. If necessary, IP and LP steam pressure will be optimized for each plant, while HP pressure will be set at 140 bar. The configurations here analyzed will be based on the same gas turbine engine of the reference combined cycle: In particular the compressor air flow of 625 kg/s will impose the actual size of the considered plants.

The main assumptions used for calculating the plant components not included in the power section are reported in Table 2. For all cycles considered, auxiliaries power consumption accounts for feedwater pumps and for cooling water circulation pumps: for the latter, an electricity consumption of one percent of the discharged heat was assumed (a realistic figure for sea or river water availability) for all types of heat exchangers releasing heat to the ambient (condensers, intercoolers, etc.).

4 System Based on Chemical Absorption

4.1 Detailed Plant Configuration. Figure 3 provides a full overview of a plant layout based on chemical absorption. The partial oxidation reactor is fed by natural gas (previously preheated in the HRSG—heat recovery steam generator—point 5), pressurized air from the gas turbine compressor (thus setting the reactor pressure at about 15 bar—point 6) and superheated steam from the HRSG (point 4). The synthetic gas (point 7) is introduced into a heat exchanger including three sections: the high temperature convective cooler, the high temperature shift reactor (with a cooled catalyst bed), and an intermediate temperature cooler. The first two sections rise superheated high pressure steam, to be ducted to the steam turbine, the last section warms up high pressure feedwater to be evaporated in the previous sections together with feedwater coming from the HRSG high pressure economizer. The syngas at moderate temperature (point 8) is treated by the second low-temperature adiabatic shift reactor. The reason for dividing into two stages the shift reaction is to produce the highest possible quantity of high pressure steam in the high temperature reactor. The second reactor enables an elevated CO conversion efficiency (favored by low temperature), limiting the amount of intermediate (rather than high) pressure steam generated by the shift reactions. A final heat recovery is performed by splitting the gas into two streams, one to warm up cold feedwater for the high temperature heat recovery, one for preheating fuel gas after separation. The syngas is cooled down to near-ambient temperature and treated by the absorber, whereby most of the CO_2 is removed. The remainder (mostly hydrogen and nitrogen) is compressed to the pressure necessary to gas turbine combustor, preheated and eventually utilized as the fuel.

The separation plant scheme is quite conventional for chemical absorption. CO_2 is absorbed by a diethanolamine (DEA) aqueous solution at 40 percent weight (selected to minimize corrosion problems, according to [21]). The rich solution from the absorber is preheated by the lean solution and regenerated in a stripping column by means of steam generated at the column bottom, making use of heat provided by a steam flow extracted from the steam

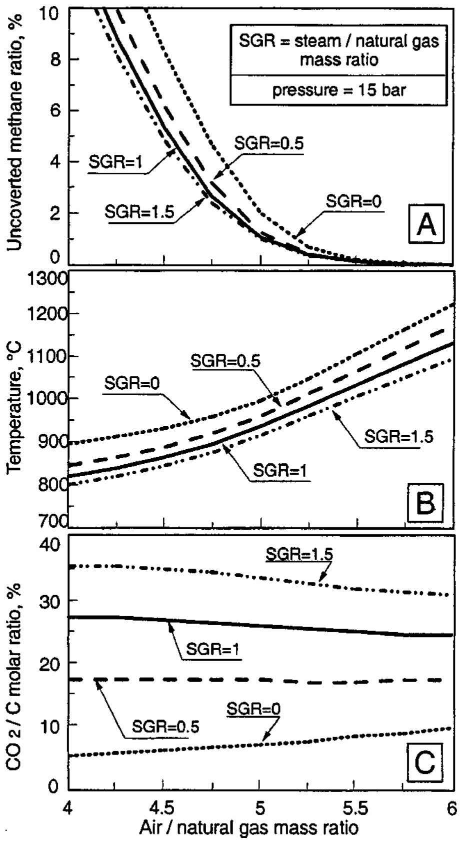

Fig. 4 Influence of the air and steam additions on the operating characteristics of an adiabatic partial oxidation reactor at a pressure of 15 bar. Inlet temperatures at 400°C for air, 565°C for steam and natural gas.

turbine (warm condensate is re-used as feedwater for the high temperature syngas cooler). The CO_2 steam mixture from the top of the stripper is condensed, leaving almost pure CO_2 in the gaseous phase: it is compressed to the final pressure of 80 bar by an intercooled compressor and liquefied in a final cooler, making CO_2 available for storage or disposal.

In the stripping process, pressure can be freely selected: with a low stripping pressure, low pressure steam can be supplied, reducing the power loss from the steam turbine, but higher CO_2 compression power is required. Performed calculations (not reported here for brevity) demonstrate that, for stripper pressures from 2 to 16 bar, the two effects compensate reciprocally with limited influence on the plant efficiency (less than 0.1 percentage point). Therefore an elevated stripping pressure (16 bar) was selected, due to the reduced size of the stripper and the lower cost of the pumping system (if a low pressure is selected, a solution expander is recommended to balance the power needs of the solution pump).

4.2 Optimization and Discussion of Results. A preliminary analysis of the partial oxidation–shift system was carried out to properly select the mass flow rate of air and steam necessary for achieving an elevated natural gas conversion rate to carbon dioxide, sufficient to allow for a 90 percent carbon dioxide removal. The first step is the conversion of carbon from natural gas into oxidated species, carried out in the partial oxidation reactor. With a stipulated pressure of 15 bar (selected to use the compressed air at about 400°C available at the heavy-duty gas turbine compressor discharge), Fig. 4(*a*) (giving a better detail than those of Fig. 1) shows that an air/natural gas higher than 5.25 is required to convert more than 99 percent of carbon. Considering that an excessive air consumption is detrimental to the cycle efficiency and reduces the gas heating value, the air/natural gas mass ratio of 5.25 was stipulated. The selection of the water consumption is more questionable, because it also involves the following shift reaction. Even if Fig. 4(*a*) shows that it is not strictly necessary to partial oxidation, Fig. 4(*b*) suggests that it moderates the reactor operating temperature (endothermic steam reforming takes place, removing sensible heat) and Fig. 4(*c*) demonstrates that larger amount of CO_2 is produced (due again to steam reforming). In addition to these two positive effects, it must be considered that steam addition is mandatory to complete the carbon conversion to CO_2 in the shift reactors. Figure 5 shows the rate of carbon conversion to CO_2 after shift reactors, at 15 bar, 230°C and $5.25\,kg_{air}/kg_{ng}$. It is clearly shown that a mass ratio of about 1 must be selected if a carbon conversion higher than 94 percent should be achieved (this value is necessary to obtain a final CO_2 removal of 90 percent). Higher values of steam addition are not suggested, because of the power loss of the steam turbine. Given the generality of the discussed curves and the hypothesis of chemical equilibrium, the results of Fig. 5 are practically independent of the position for steam addition, i.e., it can be introduced in the partial oxidation reactor or before the shift reactor. The first solution was therefore preferred, for the reasons outlined by Figs. 4(*a*) and 4(*b*). It can be summarized that the best compromise between efficiency and elevated CO_2 removal is achieved by imposing:

- an air/natural gas mass ratio of 5.25;
- a steam/natural gas mass ratio of 1;
- the full steam addition into the partial oxidation reactor rather than into the shift reactor.

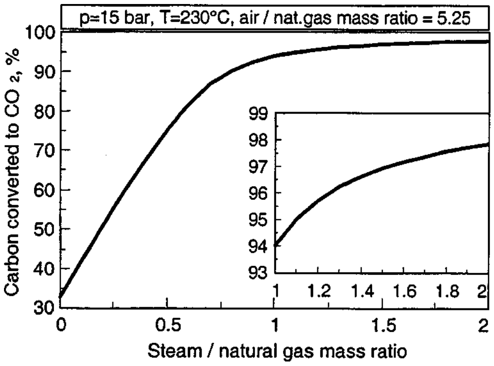

Fig. 5 Carbon conversion efficiency of a shift reactor, following a partial oxidation reactor, as a function of the steam addition

Table 3 Results obtained for the partial oxidation configuration with chemical absorption of Fig. 3. The plant size is determined by the gas turbine compressor air flow of 625 kg/s.

Plant Configuration With Chemical Absorption	
Electric power balance, MW_{el}	
Gas turbine output	233.4
Steam turbine gross output	177.1
Syngas compressor	5.6
CO_2 compressor	4.4
Solution pump	0.3
Auxiliaries	6.2
Net power output	394.0
Heat released to cooling water, MW_{th}	
Steam cycle condenser	234.4
Absorption condenser and coolers	69.3
CO_2 compressor coolers	14.2
Heat to stripper reboiler, MW_{th}	68.5
Solution regenerator load, MW_{th}	190.0
CO_2 removal rate, percent	90.1
Specific CO_2 emission, kg/kWh	0.0409
Natural gas input (LHV), MW	812.8
Overall net efficiency, percent	48.47

Table 4 Mass flow, pressure, temperature, and chemical composition of the most important points of the particle oxidation scheme with chemical absorption. Points are reported in Fig. 3.

Point	*G*	*p*	*T*	Ar	CH_4	CO	CO_2	H_2	H_2O	O_2	N_2	LHV	MHV
Fig. 3	kg/s	bar	°C	percent molar composition								MJ/kg	
1	625	1.00	15	.92	-	-	.03	-	1.03	20.7	77.3	-	-
2	506	14.7	1368	.88	-	-	.58	-	15.2	9.06	74.3	-	-
3	614	1.04	604	.89	-	-	.49	-	12.9	11.0	74.8	-	-
4	17.6	24.0	565	-	-	-	-	-	100	-	-	-	-
5	17.6	40.0	568	-	91.2	-	-	-	-	-	4.31	46.3	51.3
6	92.2	15.2	397	.92	-	-	.03	-	1.03	20.7	77.3	-	-
7	127	14.8	980	.45	.06	11.6	3.95	29.6	16.1	-	38.3	5.41	6.45
8	127	14.5	180	.45	0.6	4.08	11.5	37.1	8.55	-	38.3	5.25	6.29
9	127	14.0	222	.45	.06	.76	14.8	40.5	5.23	-	38.3	5.18	6.22
10	122	13.7	35	.47	.07	.80	15.5	42.5	.42	-	40.2	5.42	6.40
11	81.1	17.4	197	.55	.08	.94	.94	49.8	.51	-	47.2	8.14	9.60
12	517	14.5	35	Diethanolamine-water 40 percent solution								-	-
13	40.6	14.9	35	-	-	-	100	-	-	-	-	-	-
14	26.7	8.00	411	-	-	-	-	-	100	-	-	-	-

Based on those statements and on the assumptions of Section 2, the cycle calculation does not require further discussion. The power balance and the overall efficiency of the plant configuration of Fig. 3 are reported in Table 3. Pressure, temperature, mass flow, and composition of the main points are reported in Table 4. We can comment that a loss of efficiency of about eight percentage points was found, with respect to the reference combined cycle of Table 1 (a detailed discussion will be given later). On the contrary, the net power output at the same air flow increases (395 versus 373 MW), due to an higher steam turbine output (177 versus 140 MW), able to override the power consumption of the syngas and CO_2 compressors and the power loss of the gas turbine (−4.2 MW, due the lower gas flow in the expansion, deprivated of the CO_2). Even if a large steam extraction is necessary for the stripper (26.7 kg/s), a relevant high-pressure steam flow comes from the high temperature heat recovery from syngas (81 kg/s): the steam flow at turbine admission is therefore as large as 127 kg/s versus 74.1 of the reference combined cycle. Such a large steam production is made possible by the larger natural gas input (809 versus 665 MW) caused by the lower efficiency.

5 System Based on Physical Absorption

5.1 Detailed Plant Configuration. The system based on the physical absorption is shown in Fig. 6. Apart from the absorption system itself, differences from the previous scheme rise from a selected pressure of 40 bar (rather than 15) for the oxidation-shift-absorption processes. Being the physical absorption based on the variation of the solubility of CO_2 within a solvent at different pressures, an elevated absorption pressure results into a limited void fraction within the last flash chamber. The pressure level of 40 bar is achieved by introducing a booster compressor between the gas turbine compressor and the oxidation reactor. To limit the operating temperature of this machine at 550°C and to reduce power requirement, air is cooled before entering the booster, by generating high pressure steam. Natural gas is preheated in the HRSG. The gas history (partial oxidation, shifts, heat recovery, absorption) is very similar to the previous case. However, the larger pressure claims for a slightly higher air/natural gas mass ratio to obtain the same methane conversion of the previous case (5.35 versus 5.25), as shown in Fig. 1. The final syngas, deprivated of CO_2, is expanded (rather than compressed) and heated before and after the expansion by recovering heat from the raw

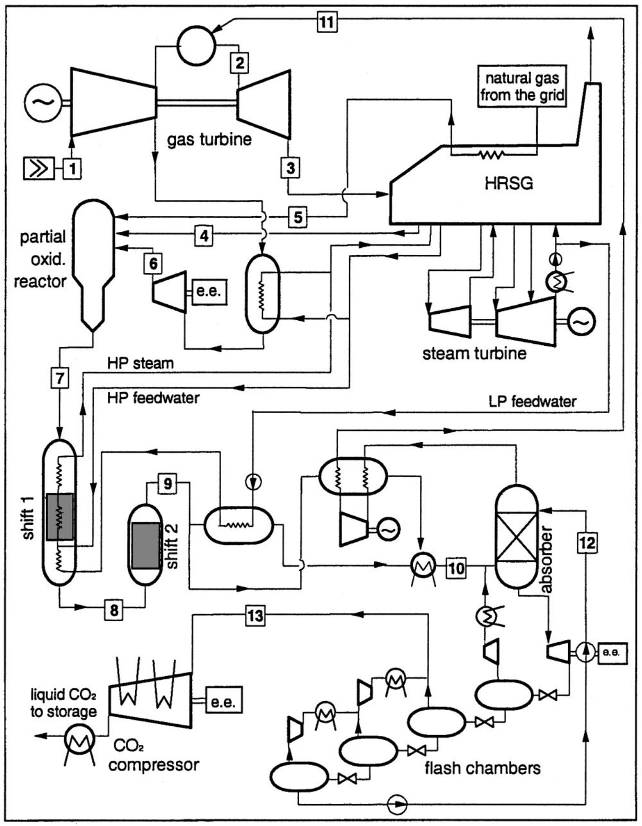

Fig. 6 Plant configuration of the partial oxidation combined cycle with physical absorption

Table 5 Results obtained for the partial oxidation configuration with physical absorption of Fig. 6. The plant size is determined by the gas turbine compressor air flow of 625 kg/s.

Plant Configuration With Physical Absorption	
Electric power balance, MW_{el}	
Gas turbine output	232.3
Steam turbine gross output	216.0
Syngas expander	11.4
Air booster compressor	24.0
CO_2 compressor	19.1
Solution pump	4.3
Auxiliaries	6.4
Net power output	405.9
Heat released to cooling water, MW_{th}	
Steam cycle condenser	312.0
Final syngas cooler	6.3
CO_2 compressor coolers	28.9
CO_2 removal rate, percent	90.1
Specific CO_2 emission, kg/kWh	0.0404
Natural gas input (LHV), MW	834.7
Overall net efficiency, percent	48.63

Table 6 Mass flow, pressure, temperature, and chemical composition of the most important points of the partial oxidation scheme with physical absorption. Points are reported in Fig. 6.

Point	G	p	T	Ar	CH_4	CO	CO_2	H_2	H_20	O_2	N_2	LHV	MHV
Fig. 6	kg/s	bar	°C	percent molar composition								MJ/kg	
1	625	1.00	15	.92	-	-	.03	-	1.03	20.7	77.3	-	-
2	504	14.7	1368	.88	-	-	.58	-	15.4	8.76	74.4	-	-
3	613	1.04	604	.89	-	-	.49	-	13.0	10.8	74.9	-	-
4	18.0	40	387	-	-	-	-	-	100	-	-	-	-
5	18.0	40	568	-	91.2	-	-	-	-	-	4.31	46.3	51.3
6	96.5	40	557	.92	-	-	.03	-	1.03	20.7	77.3	-	-
7	133	38	1042	.45	.14	11.7	3.70	28.6	16.7	-	38.8	5.29	6.31
8	133	37	182	.45	.14	3.88	11.5	36.4	8.86	-	38.8	5.12	6.15
9	133	36	222	.45	.14	.68	14.7	39.6	5.67	-	38.8	5.06	6.08
10	126	35	35	.47	.15	.72	15.5	41.9	.16	-	41.0	5.33	6.28
11	84.1	17.4	125	.56	.17	.85	.89	49.2	.19	-	48.1	7.97	9.39
12	1611	35	25				Selexol					-	-
13	41.7	3	25	-	-	-	100	-	-	-	-	-	-

syngas. The bottom part of Fig. 6 shows the absorption system, which consists of a number of flash chambers in which CO_2 is simply released by lowering the solution pressure. Gas released by the first chamber includes a substantial amount of CO and hydrogen and is recycled to the absorber. Multiple flash allows a reduced compression power: large part of the CO_2 is released at intermediate pressures. From the last chamber, the lean solution is pumped back to the absorber. The pump is partially driven by a solution expander. The last flash chamber pressure is determined by the imposed removal rate. A near-atmospheric chamber allows for a 79.6 percent CO_2 separation. To obtain a removal rate of 95 percent a pressure as low as 0.25 bar is necessary, according to our calculation.

5.2 Results. The calculation results are shown in Tables 5 and 6. Compared to the previous case with chemical absorption, Table 5 shows approximately the same gas turbine power and a larger steam turbine output (+39 MW), because of the absence of the steam extraction for the stripper. The syngas is expanded (11.4 MW) rather than compressed, but the air booster compressor requires as much as 24 MW. The CO_2 compressor power consumption is larger (19.1 versus 4.4 MW), due to the higher pressure ratio. The net power output is 404 MW (versus 392 of the previous case). The natural gas input is slightly higher. This is due to the larger air flow used by the partial oxidation reactor, at higher temperature, thus increasing the heat available for steam generation from syngas cooling. This heat amount must be provided by a larger fuel consumption, being the heat input to the gas turbine imposed by the assumed air flow.

As a result, the net efficiency does not change significantly, as well as the syngas characteristics shown by Table 6. As a matter of fact, the two plants are very similar, apart from the separation system. A more detailed discussion about efficiency will be given in Part II, Section 5, by means of the second law analysis applied to both partial oxidation and reforming techniques.

5.3 Sensitivity to Air and Steam Addition. The results are influenced by the air and steam mass flow added into the partial oxidation reactor, as anticipated in Section 4.2. A sensitivity analysis is shown in Table 7, substantiating the trends qualitatively exposed in that chapter:

- With respect to the base case of Table 5, a 15 percent increase of the air/n.g. ratio (case 2) primarily yields to an higher water, rather than hydrogen, production in the oxidation reactor. This reduces the syngas heating value: therefore, larger thermal input is required to drive the same gas turbine. The steam flow produced by syngas heat recovery increases, due to the higher syngas temperature and mass flow, leading to increased steam turbine output. The larger water fraction within syngas increases the efficiency of the shift conversion, resulting in a better CO_2 removal (92.5 versus 90 percent). The loss of thermodynamic efficiency is relevant (one percentage point) due to the larger heat flow handled by the steam section rather than by the combined cycle.
- A 15 percent increase of the steam flow to oxidation reactor is useful to improve the shift conversion and the CO_2 removal efficiency (91.4 versus 90 percent), at the expenses of a power loss from the steam turbine. To obtain the same removal efficiency of case 2, a steam addition as large as 1.62 is required, in which case efficiency drops to 47.5 percent.
- Case 4 considers the 15 percent steam flow augmentation applied to case 2: it results into a comparable power loss (2 MW), but the increase of the removal efficiency is much lower (0.4 versus 1.2 points): for case 2 steam is already abundant for an efficient shift reaction.

Table 7 Performance of configurations with physical absorption, characterized by different air and steam/natural gas mass ratios (case 1: base, case 2: +15 percent air, case 3; +15 percent steam, case 4: +15 percent air and steam)

	Case 1	Case 2	Case 3	Case 4
Air/natural gas mass ratio	5.350	6.153	5.350	6.153
Steam/natural gas mass ratio	1.000	1.000	1.150	1.150
Natural gas input, MW_{LHV}	834.7	901.8	835.2	902.1
Sequestrated CO_2, kg/s	41.71	46.24	42.31	46.46
CO_2 removal efficiency, percent	90.17	92.53	91.41	92.94
Gas turbine output MW	232.3	228.8	232.3	228.8
Steam turbine output, MW	216.0	251.9	214.3	249.8
CO_2 sep./compression, MW	23.4	26.1	23.6	26.2
Net power output, MW	406.0	430.3	404.0	428.1
Net plant efficiency, percent	48.64	47.71	48.37	47.46

6 Conclusions

Natural gas partial oxidation may represent an effective strategy for CO_2 sequestration from fossil fuel power plants. The conversion efficiency decay is about 7.5 percentage points, when compared to a conventional combined cycle of the same technology level. When evaluating this loss, it must be kept into account that the CO_2 cannot be produced separately without a loss of mechanical power, even with reversible processes, and this accounts for about three points of efficiency (see Part II). The use of chemical absorption at moderate syngas pressure (15 bar) or of physical absorption at elevated pressure (40 bar) does not alter significantly the plant efficiency, provided that the operating parameters are carefully optimized. More details about thermodynamic aspects will be given in Part II, by means of the second-law analysis, together with an assessment of the plant economic aspects and of the additional cost of electricity.

Acknowledgments

The present work was performed within the ''Low CO_2 Emission Fossil Fuel Power Plants'' research program, co-funded by the Italian Ministry of University, Science and Technology (MURST–Cofin '99).

References

[1] Chiesa, P., and Lozza, G., 1998, ''CO_2 Emission Abatement in IGCC Power Plants by Semiclosed Cycles. Part A: With Oxygen-Blown Combustion,'' ASME J. Eng. Gas Turbines Power, **121**, pp. 635–641.
[2] Chiesa, P., and Lozza, G., 1998, ''CO_2 Emission Abatement in IGCC Power Plants by Semiclosed Cycles. Part B: With Air-Blown Combustion and CO_2 Physical Absorption,'' ASME J. Eng. Gas Turbines Power, **121**, pp. 642–648.
[3] Chiesa, P., and Consonni, S., 1999, ''Shift Reactors and Physical Absorption for Low CO_2 Emission IGCCs,'' ASME J. Eng. Gas Turbines Power, **121**, pp. 295–305.
[4] Chiesa, P., Consonni, S., and Lozza, G., 1998, ''A Comparative Analysis of IGCCs With CO_2 Sequestration,'' *Proc. of 4th International Conference on Greenhouse Gas Control Technologies*, Interlaken, CH, pp. 107–112, Pergamon, Amsterdam, NL, Aug., Interlaken, Switzerland, Pergamon, Amsterdam, pp. 107–112.
[5] Smelser, S. C., Stock, R. M., and McCleary, G. J., 1991, ''Engineering and Economic Evaluation of CO_2 Removal From Fossil-Fuel-Fired Power Plants—Vol. 1, Pulverized-Coal-Fired Power Plants,'' EPRI Report IE-7365.
[6] Eliasson, B., Riemer, P., and Wokaun, A., eds., 1999, *Greenhouse Gas Control Technologies*, Pergamon, Amsterdam.
[7] Chiesa, P., and Consonni, S., 1999, ''Natural Gas Fired Combined Cycles With Low CO_2 Emissions,'' ASME paper 99-GT-370.
[8] Corti, A., Lombardi, L., and Manfrida, G. P., 1998, ''Absorption of CO_2 With Amines in Semiclosed GT Cycle: Plant Performance and Operating Costs,'' ASME paper 98-GT-395.
[9] Mathieu P., and De Ruick J., 1993, ''CO_2 Capture in CC and IGCC Power Plants Using a CO_2 Gas Turbine,'' *ASME Cogen-Turbo*, Vol. 8, New York.
[10] Ulizar, I., and Pilidis, P., 1997 ''Design of a Semiclosed Cycle Gas Turbine With Carbon Dioxide—Argon as Working Fluid,'' ASME Paper 97-GT-125.
[11] Mathieu, Ph., and Nihart, R., 1998, ''Zero Emission Matiant Cycle,'' ASME Paper 98-GT-383.
[12] Schütz, M., Daun, M., Weinspach, P. M., Krumbeck, M., and Hein, K. R. G., 1992, ''Study on the CO_2-Recovery From an IGCC Plant,'' ''Proceedings of the 1st Int'l Conference on Carbon Dioxide Removal,'' Amsterdam, pp. 357–364.
[13] Audus H., Kaarstad O., and Skinne, G., 1998, ''CO_2 Capture by Precombustion Decarbonization of Natural Gas,'' *Proc. of 4th International Conference on Greenhouse Gas Control Technologies*, Aug., Interlaken, Switzerland, Pergamon, Amsterdam, pp. 107–112.
[14] Doctor, R. D. et al., 1994, ''Gasification Combined Cycle: Carbon Dioxide Recovery, Transport and Disposal,'' U.S. Department of Energy, Contract No. W-31-109-Eng-38.
[15] Bordiga, G., and Campagna, M., 1999, ''Natural Gas Fired Combined Cycles With Abatement of CO_2 Emissions,'' graduation thesis, Politecnico di Milano, Italy, in Italian.
[16] Consonni, S., Lozza, G., Macchi, E., Chiesa, P., and Bombarda, P., 1991, ''Gas Turbine-Based Cycles for Power Generation. Part A: Calculation Model,'' *Proc. of International Gas Turbine Congress 1991*, Oct., Yokohama, Japan, pp. III 201–210.
[17] Consonni, S., 1992, ''Performance Prediction of Gas/Steam Cycles for Power Generation,'' Ph.D. thesis No. 1893-T, Mechanical and Aerospace Engineering Department, Princeton University, Princeton, NJ.
[18] Lozza, G., 1990, ''Bottoming Steam Cycles for Combined Gas-Steam Power Plants: A Theoretical Estimation of Steam Turbine Performance and Cycle Analysis,'' *Proc. 1990 ASME Cogen-Turbo*, New Orleans, LA, ASME, New York, pp. 83–92.
[19] Anon., 1999, *ASPEN PLUS*, Release 10.1, Reference Manual.
[20] Chiesa, P., and Lozza, G., 1997, ''Intercooled Advanced Gas Turbines in Coal Gasification Plants, With Combined or 'HAT' Power Cycle,'' ASME paper 97-GT-039.
[21] Kohl, A., and Riesenfeld, F., 1985, *Gas Purification*, 4th Ed., Gulf Publishing Company, Houston, TX.

Natural Gas Decarbonization to Reduce CO_2 Emission From Combined Cycles—Part II: Steam-Methane Reforming

G. Lozza

P. Chiesa

Dipartimento di Energetica,
Politecnico di Milano,
Piazza Leonardo da Vinci, 32
Milan 20133, Italy

This paper discusses novel schemes of combined cycle, where natural gas is chemically treated to remove carbon, rather than being directly used as fuel. Carbon conversion to CO_2 is achieved before gas turbine combustion. The first part of the paper discussed plant configurations based on natural gas partial oxidation to produce carbon monoxide, converted to carbon dioxide by shift reaction and therefore separated from the fuel gas. The second part will address methane reforming as a starting reaction to achieve the same goal. Plant configuration and performance differs from the previous case because reforming is endothermic and requires high temperature heat and low operating pressure to obtain an elevated carbon conversion. The performance estimation shows that the reformer configuration has a lower efficiency and power output than the systems addressed in Part I. To improve the results, a reheat gas turbine can be used, with different characteristics from commercial machines. The thermodynamic efficiency of the systems of the two papers is compared by an exergetic analysis. The economic performance of natural gas fired power plants including CO_2 sequestration is therefore addressed, finding a superiority of the partial oxidation system with chemical absorption. The additional cost of the kWh, due to the ability of CO_2 capturing, can be estimated at about 13–14 mill\$/kWh. [DOI: 10.1115/1.1395582]

1 Introduction and Basic Plant Concept

Steam reforming was considered by several authors as a possibility to improve the efficiency of gas turbine cycles (see, for instance, [1,2,3]). The basic concept of those cycles (often addressed as CRGT: chemically recuperated gas turbine) is the utilization of heat available at the turbine discharge to improve the heating value of the input fuel by producing hydrogen. The goal pursued by CRGTs is the achievement of an elevated conversion efficiency without resorting to a closed steam cycle (thus eliminating steam turbine, condenser, etc.). In those cycles, it is not essential to obtain an elevated conversion of methane into reforming reaction products (CO and H_2) because the unconverted methane is utilized as fuel. The situation is very different for the plant configurations here considered: unconverted methane generates CO_2-rich exhausts, contrarily to the scope of the analysis. This claims for methane conversion higher than 95 percent.

In general terms, the methane conversion rate by means of steam reforming is a function of pressure, temperature, and steam/methane ratio, as shown by Fig. 1 under the hypothesis of chemical equilibrium and for the assumed natural gas composition (see Part I). We can comment that

- the effect of pressure is very important: since the moles of products are larger than those of reactants, a low pressure is essential to obtain high conversion. For a pressure of 15 bar (the minimum necessary for fuel of an industrial gas turbine), temperatures exceeding 900°C and large steam additions would be necessary.
- a steam addition much larger than stoichiometric greatly helps in reducing the operating temperature.
- even with low pressure and high steam consumption, an operating temperature of 550–600°C, typical of gas turbine exhausts, is not sufficient for elevated conversion.

Therefore, if the reformer operating temperature is to be kept below 700–750°C for evident technological problems (material costs and stress, availability, operating life, etc.) and if conversion rates exceeding 95 percent are necessary, Fig. 1 shows that it is mandatory to adopt a near-atmospheric reactor and a steam/natural gas ratio higher than 3. As far as steam is concerned, it must be considered that a large fraction of the unconverted steam will be used in the following shift reactor; anyway any steam consumption, in addition to what is strictly necessary to the chemistry, is detrimental to the cycle efficiency.

Another very important point is that the gas turbine exhausts cannot provide the heat consumed by the reforming reaction at a sufficient temperature level: supplementary firing will be therefore required.

Since for CRGTs full methane conversion is not compulsory, very different operating conditions can be assumed for the reformer, addressing to different cycle arrangements (pressurized operations, absence of supplementary firing).

The conceptual plant configuration selected for our analysis (Fig. 2) directly derives from the above considerations. The reformer reactor converts the entering mixture of natural gas and steam (derived from the steam cycle) into a H_2/CO-rich fuel, at near-atmospheric pressure. Heat necessary to reforming is provided by the gas turbine exhausts, whose temperature is elevated by supplementary firing: final decarbonized fuel must be used, not to produce CO_2. The fuel is therefore treated by shift reactors to convert CO to CO_2. CO_2 is removed by a chemical absorption system (physical absorption cannot be used because of the low gas

---

Contributed by the International Gas Turbine Institute (IGTI) of THE AMERICAN SOCIETY OF MECHANICAL ENGINEERS for publication in the ASME JOURNAL OF ENGINEERING FOR GAS TURBINES AND POWER. Paper presented at the International Gas Turbine and Aeroengine Congress and Exhibition, Munich, Germany, May 8–11, 2000; Paper 00-GT-164. Manuscript received by IGTI November 1999; final revision received by ASME Headquarters February 2000. Associate Editor: D. R. Ballal.

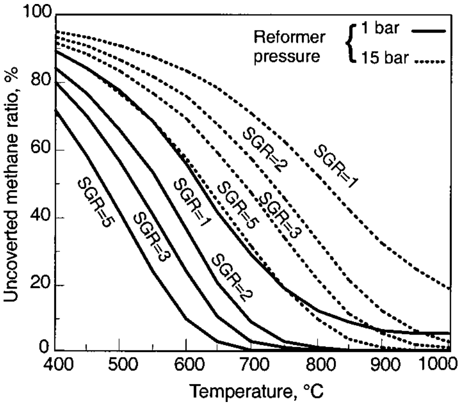

Fig. 1 Rate of methane conversion in a reformer reactor as a function of the temperature, as predicted by chemical equilibrium for two pressures (1 and 15 bar) and for different steam/natural gas mass ratios (SGR)

pressure) and subsequently compressed and liquefied for storage. The decarbonized fuel is eventually used for the gas turbine (after compression) and for the supplementary firing.

2 Detailed Plant Configuration

An overview of the selected plant configuration for the basic reforming cycle is shown in Fig. 3. The reformer operates at near-atmospheric pressure (1.15 bar on fuel side) and treats a mixture of steam and natural gas (3.1:1 mass ratio-point 5′). Before mixing, natural gas is expanded from the feed pressure (40 bar) with a two-stage expander and reheated by exhausts heat recovery, while steam (point 4) is extracted from the steam turbine and from an LP drum. The mixture is preheated up to 565°C by exhausts heat recovery and enters the first adiabatic section of the reformer. The second section retrieves heat from the gas turbine exhausts and (mainly) from the fuel (point 6) introduced into various burners in the catalyst bed. This configuration was selected to obtain a temperature profile inside the reformer as shown qualitatively by Fig. 4, i.e., (i) to maximize the exhaust heat recovery: a temperature drop of about 120°C (with a limited rate of conversion) on the gas/steam side in the adiabatic section makes possible to cool the exhausts at the selected value of 480°C (point 3′); (ii) to keep the operating temperature of the catalyst bed at acceptable values (a temperature exceeding 1000°C would have been obtained with a single supplementary firing operation); and (iii) to obtain a final reformed gas temperature of 700°C (point 7), sufficient to achieve a very high methane conversion.

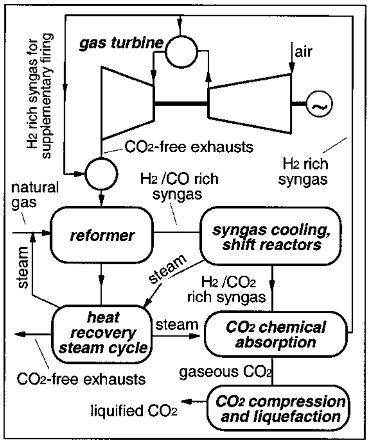

Fig. 2 Conceptual plant scheme of a combined cycle with steam/methane reforming

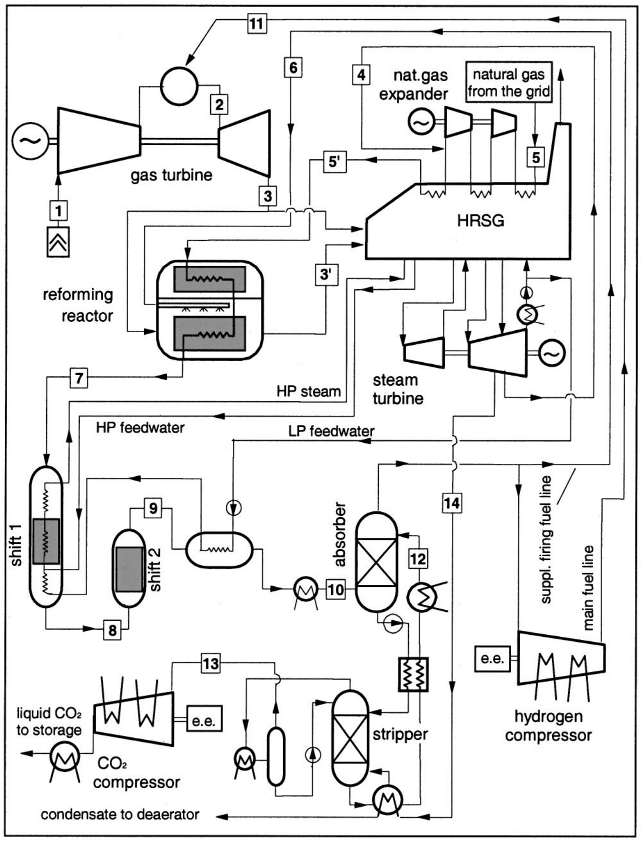

Fig. 3 Plant configuration of a combined cycle with steam reforming and CO_2 sequestration by chemical absorption

The treatments of the reformed gas are similar to those shown in Part I: The high temperature shift reactor is cooled by raising HP steam, while the conversion of CO to CO_2 (favored by low temperature) is completed in a low temperature shift reactor and heat is recovered by feedwater preheating. An absorption system retrieves CO_2 from the reformed fuel (point 10): A chemical system based on diethanolamine-water solution is here adopted (due to the low gas pressure) fully similar to the one described in Part I, Section 4.1. Its operating conditions are different, because the gas pressure here is lower (1.08 versus 14 bar) but the CO_2 fraction is much higher due to the absence of nitrogen into the mix-

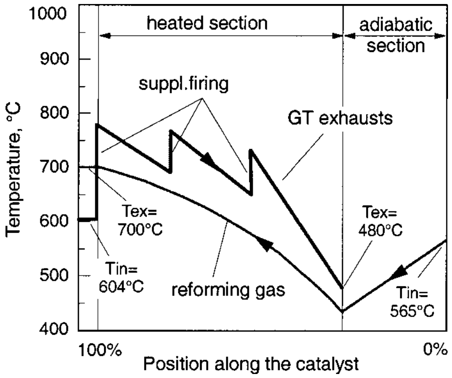

Fig. 4 Qualitative temperature profile inside the reformer, as stipulated for the plant configuration of Fig. 3

Table 1 Results obtained for the methane/steam reforming configurations with chemical absorption of Fig. 3. The results in the last column are relative to a reheat gas turbine. The plant size is determined by the compressor air flow of 625 kgs/s.

Plant Configurations With Reforming	Simple Cycle	Reheat Cycle
Electric power balance, MW_{el}		
Gas turbine output	247.3	292.0
Steam turbine gross output	102.8	107.9
Natural gas expander	8.2	8.9
Hydrogen compressor	29.5	35.0
CO_2 compressor	9.8	10.7
Auxiliaries (incl. solution pump)	3.6	3.8
Net power output	315.4	359.3
Heat released to cooling water, MW_{th}		
Steam cycle condenser	57.2	55.8
Absorption condenser and coolers	94.5	103.4
CO_2 compressor coolers	19.0	20.8
Heat to stripper reboiler, MW_{th}	93.9	102.7
Solution regenerator load, MW_{th}	140.5	153.8
CO_2 removal rate, percent	90.0	90.0
Specific CO_2 emmission, kg/kWh	0.0434	0.0415
Natural gas input (LHV), MW	684.1	748.7
Overall net efficiency, percent	46.10	47.99

ture. The final fuel (mainly hydrogen-point 11) is compressed before being used by the gas turbine: The compressor includes two intercoolers at pressures optimized to limit the compression work while keeping an assumed maximum final temperature of 225°C.

On the power plant point of view, a particular feature is that only a part (about 45 percent) of the exhausts is ducted to the reformer (and therefore reintroduced in the HRSG at 480°C), reducing its size. Superheated and reheated steam together with preheated natural gas/steam mixture at 565°C are raised from the remainder fraction of gas turbine exhausts at 604°C.

3 Discussion of the Results

Calculations were performed by using the same set of assumptions described in Part I (Section 3). The results are reported by Table 1 (''simple cycle'' column) and Table 2.

Compared to the cases analyzed in Part I, the power balance shows a larger gas turbine output (+14 MW, due to the absence of air extraction, not fully compensated by the lower fuel flow), but a severe reduction of the steam turbine output: More than 73 MW are lost with respect to the chemical absorption system of Part I. This is due to four factors: (i) HP steam produced by syngas heat recovery is much less, because of the lower syngas mass flow and temperature; (ii) temperature of gases coming from the reformer to the HRSG is lower than for gas turbine exhausts; (iii) a 2.6 times larger steam flow is extracted for the reformer rather than for partial oxidation, even if at a lower pressure; and (iv) the steam requirement for the stripper is larger (data for comparison from Table 2 and Table 4 of Part I). This is confirmed by the much lower thermal power discharged by the condenser. The increased requirements of the separation plant can be attributed to the near-atmospheric operations: The reduced CO_2 partial pressure claims

Table 2 Mass flow, pressure, temperature, and chemical composition of the most important points of the reforming scheme with chemical absorption. Points are reported in Fig. 3.

Point	*G*	*p*	*T*	Ar	CH_4	CO	CO_2	H_2	H_2O	O_2	N_2	LHV	HHV
Fig. 3	kg/s	bar	°C				% molar composition					MJ/kg	
1	625	1.00	15	.92	-	-	.03	-	1.03	20.7	77.3	-	-
2	522	14.7	1368	.85	-	-	.39	-	15.1	12.0	71.6	-	-
3	634	1.05	604	.86	-	-	.33	-	12.7	13.5	72.6	-	-
3′	283	1.04	480	.83	-	-	.48	-	18.8	9.89	70.0	-	-
4	45.8	1.15	156	-	-	-	-	-	100	-	-	-	-
5	14.8	50.0	15	-	91.2	-	-	-	-	-	4.31	46.3	51.3
5′	60.6	1.15	565	-	23.0	-	-	-	74.7	-	1.1	11.3	14.4
6	2.77	1.10	35	-	.89	.54	.98	90.3	6.31	-	1.02	57.2	68.1
7	60.6	1.15	700	-	.63	9.24	7.15	55.5	26.7	-	.73	13.8	16.9
8	60.6	1.12	187	-	.63	3.19	13.3	61.5	20.6	-	.73	13.6	16.7
9	60.6	1.11	222	-	.63	.38	16.0	64.4	17.8	-	.73	13.5	16.6
10	60.6	1.10	35	-	.73	.44	18.5	74.5	5.20	-	.84	16.9	20.1
11	8.95	17.4	224	-	.93	.57	1.03	95.0	1.42	-	1.08	73.8	87.2
12	769	2.0	35				Diethanolamine-water 40% solution						
13	34.1	2.0	35	-	-	-	100	-	-	-	-	-	-
14	38.2	1.90	234	-	-	-	-	-	100	-	-	-	-

Table 3 Exergetic analysis of the reference combined cycle (without CO_2 separation) and of the plant configurations with partial oxidation, described by Part I, and with steam-methane reforming. "Reactants and fuel treatments" include (according to the plant layout) air, steam, and natural gas preheating, syngas compression, natural gas expansion, air cooling, and compression.

	Reference Combined Cycle		Configuration With Chemical Absorption		Configuration With Physical Absorption		Configuration With Steam Reforming	
	MW	%	MW	%	MW	%	MW	%
Exergy input (natural gas)	699.2	100	855.6	100	878.6	100	722.6	100
Exergy output								
Net electricity production	373.2	53.38	394.0	46.05	405.9	46.20	315.4	43.65
Separated CO_2	-	-	26.3	3.08	27.1	3.09	22.2	3.07
Exergy destruction								
Gas turbine compressor	16.9	2.41	16.9	1.97	16.9	1.92	16.9	2.33
Gas turbine combustor	196.5	28.11	158.4	18.51	165.7	18.86	162.0	22.41
Gas turbine expansion	32.2	4.61	32.7	3.82	32.8	3.74	33.6	4.65
Heat recovery steam cycle	48.3	6.90	47.7	5.58	55.3	6.29	26.6	3.68
Exhaust discharge	19.6	2.80	17.3	2.03	17.3	1.97	24.5	3.40
El./mech. losses and auxiliaries	12.5	1.79	13.8	1.62	14.2	1.62	12.8	1.77
Reactants and fuel treatments	-	-	1.12	0.13	3.9	0.44	8.9	1.23
Partial oxid. reactor/reformer	-	-	95.3	11.14	90.8	10.34	59.8	8.27
Syngas heat recovery and shift	-	-	30.1	3.52	31.9	3.63	15.9	2.19
CO_2 separation and compression	-	-	21.9	2.56	16.8	1.91	24.2	3.34

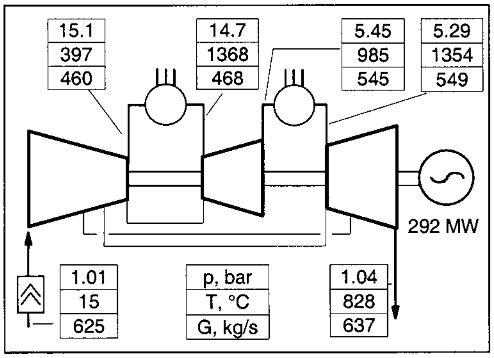

Fig. 5 Operating conditions of the reheat gas turbine optimized for application within a combined cycle with steam reforming

a larger solution flow to remove the same gas flow, thus resulting in a more demanding energy balance. From Table 3, a large power consumption (not compensated by the sophisticated natural gas expansion system) is caused by the hydrogen compressor (29.5 MW), due to its huge volumetric flow. The net power output is substantially lower than for previous cases, even if the plant is based on the same gas turbine. The natural gas consumption is lower, due to the reduced contribution to the steam cycle, but the net efficiency is about 2.5 percentage points lower than for plants using partial oxidation.

4 Reheat Gas Turbine

To increase the efficiency and the power output, a better utilization of the fuel ducted to supplementary firing within the reformer can be pursued by means of a reheat gas turbine. In the basic cycle of Fig. 3, a 23 percent of the hydrogen produced is used to provide heat to the endothermic reforming reaction. If this fuel would be used by a second gas turbine combustor, the turbine work would improve and higher temperature exhausts would be available for reformer operations.

This concept requires a gas turbine engine different from those available on the market: for instance, the only commercial reheat machine (the ABB GT24/26, [4]) does not comply with the cycle requirements, because its exhausts are too cold for the purpose (640°C, due to its high pressure ratio) and cannot provide a sufficient natural gas conversion into the reformer. Therefore we will refer to the same gas turbine of the previous cases, ad hoc modified to include reheat at an intermediate pressure selected to provide sufficiently hot exhausts. Unfortunately, the hypothesis of resorting to commercial engines drops, even if the resulting machine does not require any particular technology advancement (but a substantial development effort!). Our calculation are therefore devoted to substantiate the potential of new cycle configurations.

The cycle improvements by means of a reheat machine are shown in the last column of Table 1, with the operating gas turbine conditions reported by Fig. 5. In particular, a turbine exhausts temperature of 830°C is sufficient to provide the required thermal power to the reformer without supplementary firing. All turbine blades require cooling. A 14 percent power output and two percentage point of efficiency can be gained, but the performance remains poorer than for partial oxidation cycles (making use of the standard engine).

5 Exergetic Analysis

The ability of producing carbon dioxide as a separated flow yields to a loss of electric efficiency of 7.5 percentage points for the two plants described in Part I, and of ten points for the basic plant with steam reforming, when compared to the reference combined cycle using the same power plant technology. To better understand the reasons for this loss, an exergetic analysis was performed for the four configurations. From the results reported in Table 3, we can comment that

- the separated, pressurized CO_2 is a thermodynamic asset produced by the plant (on the exergy point of view, it corresponds to the reversible work produced by isothermal expansion of the liquefied, pressurized CO_2 to the partial pressure of CO_2 in the environment). It accounts for 3.08 percent of the exergy input by natural gas, according to the stipulated removal rate (90 percent, with very little variations among the three configurations). For instance, it can be said that the exergetic efficiency of the physical absorption partial oxidation plant (under a strictly thermodynamic approach) would be 49.29 rather than 46.20, as coming from the electricity produced. This reduces the gap from the combined cycle to 4.09 percentage points, a relatively small figure.
- the losses in the separation systems (pressure loss for physical process, steam consumption and heat transfer for chemical systems, nonreversible compressions, etc.) are lower for the physical process (1.91 percentage points), while the chemical absorption systems performance depends on the required solvent mass flow, much higher for the reformer configuration.
- a relevant exergy destruction takes place in the partial oxidation reactor, but it is very closely compensated by a much lower gas turbine combustor loss. This is not surprising, because the combustion products are the same, independently on ''where'' oxidation takes place.
- the situation is different for the reformer. Losses of the reformer include natural gas/steam mixing, heat transfer and hydrogen combustion (the latter accounts for about five of the eight percentage point loss). Their amount is lower than for partial oxidation: fuel is ''conditioned,'' rather than ''burnt,'' apart from the one used to supply heat.
- the syngas cooling processes provide a 3.5–3.6 percent loss of efficiency for the partial oxidation plants, mainly due to the high temperature of syngas used for steam production. Another contribution comes from the treating of the reactants (air and natural gas, to be heated, expanded or compressed). For the reformer case, with lower temperatures, losses related to heat transfer and steam production are reduced, but the irreversibilities of the hydrogen compressor are to be taken into account.
- for the partial oxidation schemes, the percentage losses in the power cycle components (gas turbine compressor and expander, steam cycle) are generally lower than for the combined cycle, due to the higher natural gas input. However, in terms of MW lost due to irreversibilities, the gas turbine machine shows little variations, while the steam cycle shows higher losses caused by the larger steam flow. The exhaust discharge loss is higher for the combined cycle, because it also accounts for the CO_2 dissipated.
- for the reformer scheme, the losses of the power section are not different, in terms of MW, from the other cases (they are even lower for the steam cycle, due to the reduced power output), but they are higher when referred to the smaller natural gas input. Looking at the second law analysis, one reason of the poorer performance of this cycle is its reduced ability to treat the input fuel with the same hardware (providing the same losses in absolute terms).

6 Technology Considerations

The plant configurations here proposed are conceived for prompt utilization in the power industry, especially as far as the power section is concerned. Excluding the reheat turbine of Section 4, the most important point is that very limited modifications are required for the gas turbine engine, only regarding the combustion system. For partial oxidation schemes the fuel heating value is comparable to that of IGCC applications: However, in most IGCC systems (the ones not including integrated air separation processes) a larger turbine flow is to be handled, sometimes calling for nozzle modifications or for partial-load compressor operations. This is not required here, because air is retrieved ahead

Table 4 Parameters adopted to scale investment costs. The cost C of a piece of hardware with size S is given by: $C = C_0(S/S_0)^f$.

Component	Scale Parameter	Base Specific Cost, C_0	Base Size, S_0	Scale Factor, f
Gas turbine	Electric power	220 \$/kW	240 MW	-
Steam turbine	Electric power	370 \$/kW	200 MW	2/3
Electric machines and power section balance of plant	Electric power	100 \$/kW	450 MW	2/3
Partial oxidation and syngas cooling	Fuel thermal input	25 \$/kW	800 MW	2/3
Shift reactors and cooling	Fuel thermal input	12.5 \$/kW	1377 MW	2/3
High pressure absorbers	Gas mass flow rate	$30000\ \$/(\mathrm{kg}\cdot \mathrm{s}^{-1})$	120 kg/s	2/3
Low pressure absorbers	Gas volumetric flow rate	$52000\ \$/(\mathrm{m}^3\cdot \mathrm{s}^{-1})$	60 m^3/s	1
Components of chemical absorption other than absorbers	Solvent mass flow rate	$23000\ \$/(\mathrm{kg}\cdot \mathrm{s}^{-1})$	160 kg/s	1
Components of physical absorption other than absorbers	Solvent mass flow rate	$20000\ \$/(\mathrm{kg}\cdot \mathrm{s}^{-1})$	200 kg/s	1
CO_2 compression system	Power consumption	400 \$/kW	30 MW	2/3

of the compressor and the turbine flow is slightly lower than for the original machine. In addition, fuel is largely diluted by nitrogen, keeping the stoichiometric flame temperature about 300 K below the one of natural gas: This is a good indication about limited NO formation. For the reformer plant, the mass flow balance of the gas turbine is closely similar to the original situation, due to the absence of air extraction and to very high heating value of the fuel (95 percent hydrogen: see Table 2). The flame temperature is very high (200 K higher than for natural gas) and the NO_x control may become a problem: Premixed combustor technology is more difficult to be applied with a very reactive fuel as hydrogen, while a massive steam dilution will lead to a further loss of efficiency. For both systems, CO emission will be negligible, due to the virtual absence of carbon.

On the fuel treatment section point of view, the partial oxidation process, including the shift reactors, should not represent a technological challenge: Temperature levels are not extreme and clean reactants are used. Therefore, problems affecting IGCC syngas treatments should not be encountered here. The same holds for the CO_2 separation system.

On the contrary, the reformer reactor represents a challenging device, mainly due to the elevated operating temperatures for the heat exchanger-catalyst tube bank. In addition, it handles near-atmospheric gaseous streams, thus claiming for large volumes, heat transfer areas and costs. The same holds for the heat recovery exchangers and for the shift reactors.

7 Economic Analysis

The scope of this chapter is the evaluation of the cost of ‘‘CO_2-free’’ electricity, produced by the here considered power plants. An increase of the cost of electricity, compared to conventional combined cycle, can be easily anticipated, due to additional hardware and lower efficiency. To assess its amount, the investment cost of the various component must be estimated. Table 4 reports the stipulated values used for this task, retrieved from a critical analysis of the public literature (for instance, [5–9]). It must be specified that the cost estimation is very rough and valid only for a preliminary analysis, especially for new hardware not encountered in the usual power plant practice, as reactors and catalysts. The cost estimation was performed for five plant arrangements:

- NGCC: the natural gas fired combined cycle used for reference in this paper (see Part I).
- PO-CA: the partial oxidation plant with chemical absorption, described section 4 of Part I.
- PO-FA: the partial oxidation plant with physical absorption, described section 5 of Part I.
- CC-CA: a conventional combined cycle with a chemical absorption system removing carbon dioxide from the exhausts, at the end of the HRSG; steam for stripping is extracted from the steam turbine; it was described by [10], based on the same assumptions of the present paper: Its net efficiency is 50.61 percent, with a power output of 336.6 MW.
- SCC-CA: a semi-closed combined cycle with chemical absorption from the exhausts; it differs from the previous case because of exhausts recirculation at the compressor inlet, to improve the CO_2 concentration in the exhausts with the aim of reducing the absorber size and steam consumption: Its efficiency is 51.09 percent with a power output of 331.6 MW ([10]).

The reformer configuration was not considered, mainly due to the large uncertainties about the cost of the additional equipment, in particular for the specific reformer configuration here addressed. However, considering the lower performance, the technological issues outlined in the previous chapter and some literature indications [11,12], it cannot be regarded at present as a winning competitor.

The two systems based on CO_2 removal from the exhaust gases show a larger efficiency than the here presented plants and a simpler plant configuration. Their drawbacks are: (i) a loss of power output based on the same gas turbine unit (about 335 MW versus 400 MW of the present schemes), due to the large steam extraction, (ii) the huge size of the absorption system, and (iii) the possibility of amine contamination by oxygen present in the exhausts (an issue requiring further investigation and posing some doubts about the system feasibility). In addition, for the SCC-CA the combustion system requires large development work because of the low oxygen content of the oxidizer, thus claiming for a combustor design different from the usual gas turbine practice. These problems are eliminated by the present proposals, at the cost of a more complicated fuel process.

The investment costs of the five systems are reported by Table 5; the resulting cost of electricity is shown by Table 6. We can comment that

- the ability of removing CO_2 yields to an increase of the electricity cost from 13 to 15 mills/kWh, i.e., about 40 percent compared to a conventional combined cycle.
- the lower cost improvements are provided by the PO-CA and the SCC-CA systems, with very little difference between them. It must be outlined that additional costs for the above quoted combustor development were not considered for the gas turbine unit.
- the PO-FA system has higher investment costs of the physical (rather than chemical) absorption plant, according to our evaluations (Table 5). The CC-CA requires a huge and expensive absorber. In general, the differences are mostly given by the investment costs.
- the fuel costs differs because of the efficiency. The O&M costs of the SCC-CA and CC-CA are higher due to the amount stipulated for DEA substitution and integration.

Eventually, Fig. 6 shows the rise of the cost of electricity due to

Table 5 Breakdown of estimated investment costs, according to Table 4

Plant Configuration	NGCC	PO-CA	PO-FA	CC-CA	SCC-CA
Gas turbine, M$	52.3	52.3	52.3	52.3	52.3
Steam cycle, M$	58.3	68.2	77.9	51.6	56.0
Power section balance of plant, M$	40.0	42.3	44.9	38.3	38.6
Partial oxidation and syngas cooling, M$	-	20.2	20.6	-	-
Shift reactors and cooling, M$	-	12.1	12.3	-	-
Absorbers, M$	-	3.6	4.2	28.8	13.0
Other components of absorption process, M$	-	11.9	32.2	23.6	18.8
CO_2 compression, M$	-	3.3	5.9	5.6	5.5
Cost of process facilities, M$	151	214	250	200	184
Balance of plant			12 % of process facilities		
Cost of engineering			7 % of process facilities		
Contingencies (percent of process facilities)	5 %		10%		
Total cost, M$	187	276	323	258	238
Specific cost, $/kW	500	701	795	767	717

Table 6 Cost of electricity for the five considered plant configurations. Assumptions: amortization carried out in current U.S. dollars, based on a discount rate of 10 percent, an inflation rate of 2 percent, a plant life of 25 years; income tax rate of 40 percent, tax recovery based on straight-line depreciation over 20 years; period of construction of two years for NGCC, three years for other plants; plant operation at equivalent full load of 7000 hours/year; natural gas cost of 3.3 $/GJ. O&M costs (fixed and variables) conform to the indications of TAG (1993), including costs of consumables (DEA integration and substitution) as quoted by Hendriks [7]. The evaluation includes the cost of CO_2 storage, assumed as 10 $/ton as quoted for storage in deep oceanic waters for power plants placed by the sea shore Fujioka et al., 1997 ([15]).

Plant Configuration		NGCC	PO-CA	PO-FA	CC-CA	SCC-CA
Net plant efficiency, percent	Design	56.11	48.47	48.63	50.61	51.09
	Yearly average	54.99	47.50	47.66	49.60	50.07
Net power output, MW		373.2	394.0	405.9	336.6	331.6
Yearly average CO_2 emissions, kg/kWh		0.363	0.0417	0.0411	0.0363	0.0363
Specific cost, $/kW		500	701	795	767	717
Interest during construction, percent		3.92	8.05	8.05	8.05	8.05
COE due to plant amortization, mill$/kWh		11.07	16.12	18.30	17.65	16.49
COE due to O&M, mill$/kWh		2.04	2.45	2.64	3.45	3.35
COE due to fuel, mill$kWh		21.60	25.01	24.93	23.95	23.73
COE due to CO_2 storage, mill$/kWh		-	3.78	3.78	3.66	3.62
Total COE, mill$/kWh		34.72	47.37	49.65	48.71	47.19
Recovery cost, $/tonn of avoided CO_2		-	39.39	46.42	42.86	38.20

the introduction of a "carbon tax," i.e., a penalty to be paid for each tonn of CO_2 dispersed toward the atmosphere. The break even with a conventional combined cycle can be found for a carbon tax of about 40 $/tonn, yielding to a 2.2 $/GJ improvement of the natural gas cost.

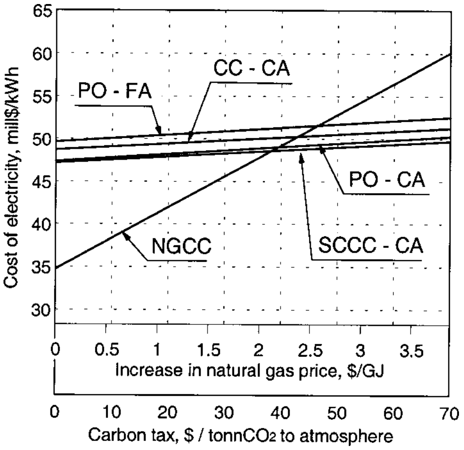

Fig. 6 Cost of electricity of the configurations described by Table 5, as a function of a "carbon tax" applied to the carbon dioxide released to the ambient

8 Conclusions

The two papers presented three power plant configurations able to produce electricity from natural gas at an elevated efficiency, with very limited CO_2 gaseous emission: 90 percent of the carbon dioxide produced is made available as a pressurized liquid at 80 bar. The most promising option is based on natural gas partial oxidation, especially if coupled with a chemical absorption system. This configuration has a net efficiency of 48.5 percent. It is 7.6 points lower than that of a combined cycle of the same technology, but, generally speaking, it represents an acceptable figure on the economic point of view (for instance, it is higher than the one of steam power station and comparable to that of a combined cycle of the first 90's). The components development does not require particular technological efforts and the utilization of commercial gas turbines is granted. Very similar performance and characteristics are obtained by a system using a physical absorption method, but the investment costs are somewhat higher.

The economic analysis shows that a "CO_2-free" kWh can be produced at an additional cost of about 13 mill$/kWh.

The plant configuration based on steam/methane reforming presents poorer performance (2.5 percentage point lower efficiency and 22 percent loss of power output, based on the same gas turbine unit). The atmospheric operations anticipate higher dimensions and costs of the heat transfer equipment, of the catalyst beds and of the absorption system. However, a very important point is that the reforming system produces pure (95 percent) hydrogen, while partial oxidation provides a fuel with large nitrogen dilution. This is not an advantage for electricity production by means of combined cycles (on the contrary it may cause larger NO_x

formation), but it can be a winning point if a direct use of the hydrogen is made (for instance, petroleum industry, chemical plants) together with electricity generation and/or if different (and futuristic) types of cycles are considered: semi-closed steam cycles with hydrogen-oxygen combustion, operating at extremely high temperatures and pressure ([13,14]). This can be the subject of future works.

Acknowledgments

The present work was performed within the ''Low CO_2 Emission Fossil Fuel Power Plants'' research program, co-funded by the Italian Ministry of University, Science and Technology (MURST–Cofin '99).

References

[1] Newby, R. A., Yang, W. C., and Bannister, R. L., 1997, ''Use of Thermochemical Recuperation in Combustion Turbine Power Systems,'' ASME paper No. 97-GT-36.

[2] Carcasci, C., Facchini, B., and Harvey, S., 1998, ''Design & Off-Design Analysis of a CRGT Cycle Based on a LM2500-STIG Gas Turbine,'' ASME Paper No. 98-GT-36.

[3] Bram, S., Minsart, O., and De Ruyck, J., 1999, ''The Potential of Fuel Reforming and Water Evaporation in Gas Turbine Cycles,'' ASME Paper No. 99-GT-368.

[4] Mayer, A., and van der Linden, S., 1999 ''GT24/26 Advanced Cycle System Power Plant Progress for the New Millenium,'' ASME Paper No. 99-GT-404.

[5] Audus, H., Kaarstad, O., and Skinne, G., 1998, ''CO_2 Capture by Precombustion Decarbonization of Natural Gas,'' *Proc. of 4th Int'l Conference on Greenhouse Gas Control Technologies*, Aug., Interlaken, Switzerland, Pergamon, Amsterdam, pp. 107–112.

[6] ''TAG—Technical Assessment Guide (Electric Supply),'' 1993, EPRI Report TR-102275 Vol. 1, Rev. 7, Palo Alto, CA.

[7] Hendriks, C., 1994, ''Carbon Dioxide Removal From Coal-Fired Power Plants,'' Ph.D. thesis, University of Utrecht, The Netherlands.

[8] McMullan, J. T., 1995, ''Techno-Economic Assessment Studies of Fossil Fuels and Fuel Woods Power Generation Technologies,'' Joule II Program *R&D in Clean Coal Technology*, Report to the European Commission, Brussels, Belgium.

[9] Corti, A., Lombardi, L., and Manfrida, G. P., 1998, ''Absorption of CO_2 With Amines in Semiclosed GT Cycle: Plant Performance and Operating Costs,'' ASME Paper No. 98-GT-395.

[10] Chiesa, P., and Consonni, S., 1999, ''Natural Gas Fired Combined Cycles With Low CO_2 Emissions,'' ASME Paper No. 99-GT-370.

[11] Gaudernack, B., and Lynum, S., 1996, ''Natural Gas Utilization Without CO_2 Emissions,'' Energy Convers. Manage., **38**, Suppl., pp. S165–S172.

[12] Göttlicher, G., and Pruscheck, R., 1996, ''Comparison of CO_2 Removal Systems for Fossil-Fueled Power Plant Processes,'' Energy Convers. Manage., **38**, Suppl., pp, S173–S178.

[13] Bannister, R. L., Newby, R. A., and Yang, W., 1998, ''Final Report on the Development of Hydrogen-Fueled Combustion Turbine Cycle for Power Generation,'' ASME Paper No. 98-GT-21.

[14] Funatsu, T., Fukuda, M., and Dohzono, Y., 1997, ''Start-Up Analysis of a H_2-O_2 Fired Gas Turbine Cycle,'' ASME Paper No. 97-GT-491.

[15] Fujioka, Y., Ozaki, M., Takeuchi, K., Shindo, Y., and Herzog, H. J., 1997, ''Cost Comparison of Various CO_2 Ocean Disposal Options,'' Energy Convers. Manage., **38**, Suppl., pp. S273–S277.

First Experiments on an Evaporative Gas Turbine Pilot Power Plant: Water Circuit Chemistry and Humidification Evaluation

N. D. Ågren
Comsol AB, Tegnérgatan 23,
SE-111 40 Stockholm, Sweden
e-mail: niklas@comsol.se

M. O. Westermark

M. A. Bartlett

Department of Chemical Engineering
and Technology/Energy Processes,
Royal Institute of Technology,
SE-100 44 Stockholm, Sweden

T. Lindquist
Department of Heat and Power Engineering,
Lund Institute of Technology,
P. O. Box 118,
SE-221 00 Lund, Sweden

The evaporative gas turbine (EvGT), also known as the humid air turbine (HAT) cycle, is a novel advanced gas turbine cycle that has attracted considerable interest for the last decade. This high-efficiency cycle shows the potential to be competitive with Diesel engines or combined cycles in small and intermediate scale plants for power production and/or cogeneration. A 0.6 MW natural gas-fired EvGT pilot plant has been constructed by a Swedish national research group in cooperation between universities and industry. The plant is located at the Lund Institute of Technology, Lund, Sweden. The pilot plant uses a humidification tower with metallic packing in which heated water from the flue gas economizer is brought into direct counter current contact with the pressurized air from the compressor. This gives an efficient heat recovery and thereby a thermodynamically sound cycle. As the hot sections in high-temperature gas turbines are sensitive to particles and alkali compounds, water quality issues need to be carefully considered. As such, apart from evaluating the thermodynamic and part-load performance characteristics of the plant, and verifying the operation of the high-pressure humidifier, much attention is focused on the water chemistry issues associated with the recovery and reuse of condensate water from the flue gas. A water treatment system has been designed and integrated into the pilot plant. This paper presents the first water quality results from the plant. The experimental results show that the condensate contains low levels of alkali and calcium, around 2 mg/l $\Sigma(K,Na,Ca)$, probably originating from the unfiltered compressor intake. About 14 mg/l $NO_2^- + NO_3^-$ comes from condensate absorption of flue gas NO_x. Some Cu is noted, 16 mg/l, which originates from copper corrosion of the condenser tubes. After CO_2 stripping, condensate filtration and a mixed bed ion exchanger, the condensate is of suitable quality for reuse as humidification water. The need for large quantities of demineralized water has by many authors been identified as a drawback for the evaporative cycle. However, by cooling the humid flue gas, the recovery of condensed water cuts the need of water feed. A self-supporting water circuit can be achieved, with no need for any net addition of water to the system. In the pilot plant, this was achieved by cooling the flue gas to around 35°C. [DOI: 10.1115/1.1397778]

Introduction

Since the early 1980s the utilization of gas turbines for power generation has increased rapidly. Gas turbines in simple cycles or combined cycles are rather dominating on the international market, while investments in new steam turbine power plants are currently sparse ([1]). The clear advantages of gas turbines compared with steam turbines include high efficiencies, low capital costs, quick startup times, low manpower operating needs, ready availability, and small size. The most important development trends for gas turbines are increased temperatures, increased pressure ratio, and the introduction of intercoolers and recuperators. By refining the thermodynamic cycle even further, several advanced cycles of different complexity have been proposed in the literature, amongst others steam injected gas turbines (STIG) and the evaporative gas turbine (EvGT). The steam injected gas turbine (STIG) involves a variation on the simple cycle gas turbine theme, wherein steam, generated in a turbine exhaust heat recovery steam generator (HRSG), is injected before or into the combustor to augment power output and the efficiency of power generation. The history and status of steam injection technology has been reviewed by Larson and Williams [2] and Tuzson [3].

The evaporative gas turbine cycle (EvGT) uses water vapor in the form of humidified air to increase the thermal efficiency and the power output of the gas turbine. This replaces the steam turbine in a combined cycle. In the EvGT cycle, the HRSG in the STIG concept is replaced with a multistage counter-current humidification tower. In the humidification tower, which is placed after the compressor, the compressed air is brought into counter current contact with heated water, causing the water to evaporate. The temperature of the water decreases through the column, in the flow direction of the water, and the humidity of the air increases in the flow direction of the air. This is called evaporation: Water is evaporated into an inert air phase as opposed to vaporization of pure water in a boiler. The evaporation process allows water to evaporate at temperature levels below the boiling point at the total pressure, because of the lower partial pressure in the air-water mixture. Therefore the EvGT cycle is able to recover humidification heat from the flue gases down to a lower temperature than

---

Contributed by the International Gas Turbine Institute (IGTI) of THE AMERICAN SOCIETY OF MECHANICAL ENGINEERS for publication in the ASME JOURNAL OF ENGINEERING FOR GAS TURBINES AND POWER. Paper presented at the International Gas Turbine and Aeroengine Congress and Exhibition, Munich, Germany, May 8–11, 2000; Paper 00-GT-168. Manuscript received by IGTI, Nov. 1999; final revision received by ASME Headquarters, Feb. 2000. Associate Editor: D. R. Ballal.

steam injection cycles. This results in increased heat recovery, more humidification and improved efficiencies first pointed out by Ågren et al. [4].

Most of the recent studies on the evaporative gas turbine cycle have concentrated on the directly fired gas turbine which operates only on premium fuels, while less attention has been focused on gasified coal or gasified biomass. The evaporative gas turbine with water injection by spraying of fine droplets was proposed by Gasparovic and Stapersma [5] and was further studied by Mori et al. [6]. Frutschi and Plancherel [7] presented a cycle called Intercooler/Recuperated Evaporation Cycle which is one type of the evaporative gas turbine cycles. Different advanced gas turbine systems including the evaporative gas turbine have been compared by Annerwall and Svedberg [8]. The heat recovery system coupled with the evaporative gas turbine cycle has been investigated by Barthelemy and Lynn [9]. Different configurations of the evaporative gas turbine cycles have been evaluated by amongst others Yan et al. [10], Stecco et al. [11], and Rosén [12].

Fluor Daniel Inc. has studied ([13,14]) and patented ([15]) some variations of the HAT cycle. They have compared the HAT cycle with combined-cycle power plants in integration with the coal gasification process, and in natural gas-fired plants. The potential to integrate the HAT cycle with other new approaches to power generation has been discussed by Cohn [16]. These new approaches are CASH (Compressed-Air Storage with Humidification) cycle, IGCASH (Integrated Gasification CASH), and CASHING (compressed-air Storage with humidification, integrated with natural gas). Chiesa et al. [17] have compared intercooled recuperated STIG (called RWI by Chiesa) and HAT cycles.

In Sweden, evaporative gas turbine system studies were initiated at Lund Institute of Technology and the Royal Institute of Technology in 1989. The EvGT technology has now been demonstrated for the first time in Sweden. A theoretical pilot study was performed in 1993–1994 in cooperation between NUTEK (Swedish National Board for Industrial and Technical Development), universities and industry, which resulted in a technical report ([18]). Presently, the ongoing phase of this project involves a demonstration program in which a small scale (600 kW) pilot EvGT plant has been constructed, including the development of the water circuit and flue gas condensation. Experimental studies of the dynamics of the plant in dry mode have been published by Gustafsson et al. [19]. Economic and technical simulation studies of mid-size plants (70–80 MW) are also included in the project [20]. A new refined humidification strategy, based on humidification of only about 30 percent of the compressed air, has also been presented within the project ([4,21]).

General Description of the Pilot Plant

Figure 1 shows a simplified flowsheet of the EvGT plant as constructed at LTH. Compressed air is led through a pressurized humidification tower, where heated water is evaporated in direct counter current contact with the air, a process involving coupled heat and mass transfer. The heat of vaporization is mostly supplied by the water circuit that in turn recovers heat from the flue gas in the economizer. The cooling of the compressed air when passing through the humidifier also contributes to the humidification. In a fully developed cycle, humidifying the compressed air would provide an increased mass flow through the turbine and hence increased power output. However, in order to utilize the existing turbo package, air is bled off before the humidifier to maintain the mass flow balance between the compressor and expander. Also

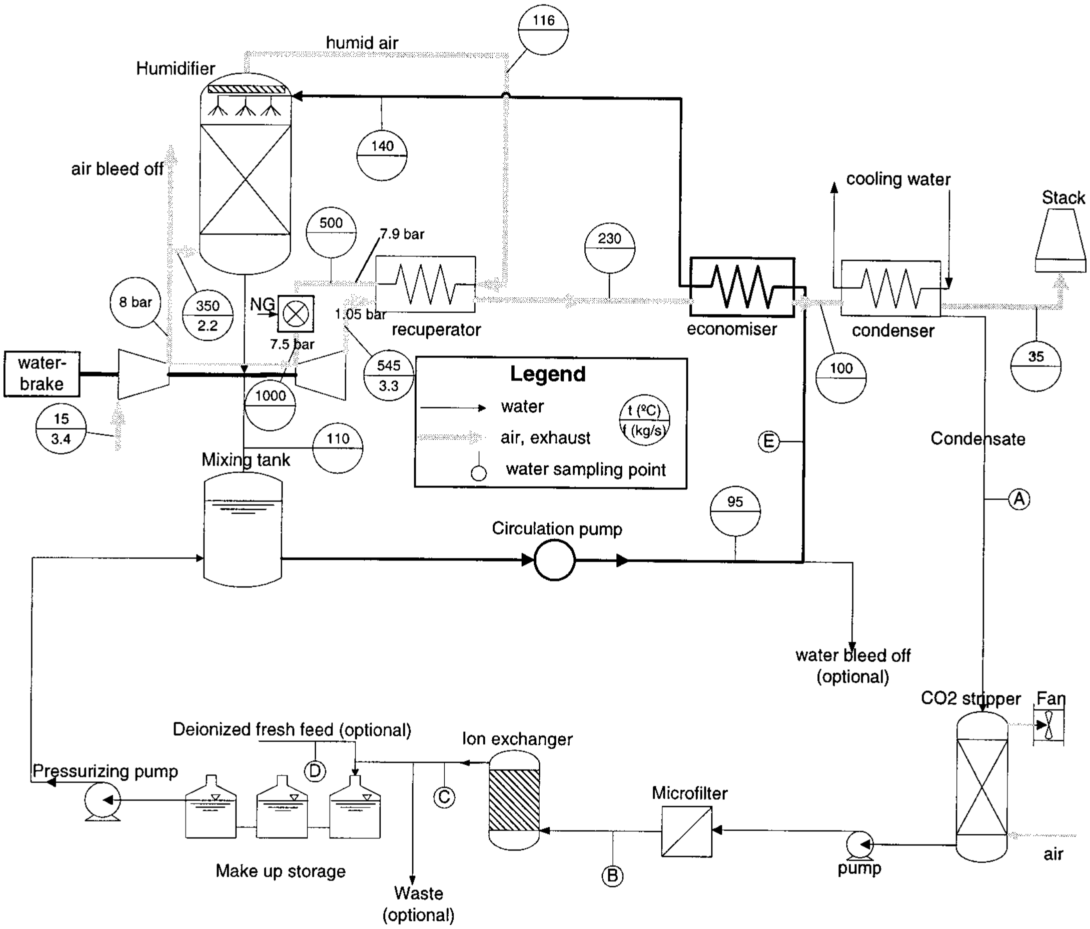

Fig. 1 Simplified pilot plant flowsheet with typical approximate flow data a 480 kW load

depicted in Fig. 1 is the humidification tower water circuit. Feed water for make up of the humidification circuit is pumped from the water reservoir into a pressurized tank. The water in the humidification circuit is then heated in the economizer and conveyed to the humidification tower where a fraction is evaporated. The bulk is then returned to the pressurized mixing tank. A possibility for water bleed off is offered at this point, in order to control the buildup of salts.

The humidification tower is equipped with structured packing, 900 mm high, to accomplish good mass and heat transfer. A number of spray nozzles are also installed to ensure even water distribution. To minimize the droplet entrainment, an inertia mist eliminator is mounted at the top of the column, capturing entrained water droplets.

After being combusted with natural gas and expanded through the turbine, the flue gas is cooled by the humidified air and the humidifying water in the recuperator (REC) and economizer (ECO), respectively. An important aspect of the EvGT system is the water cycle, both with regards to the water quality and cost of the water supply. It has been shown previously ([4,22]) that an EvGT cycle can be self sufficient regarding water consumption. This is done through lowering the temperature of the exiting flue gas sufficiently in the flue gas condenser (FGC) and recycling the resulting condensate to the humidification circuit.

The evaporative process enables the humidified air to be cooled to reasonably low temperatures, allowing a large amount of high quality heat to be transferred in the recuperator. The chilled humidifying water provides a low temperature internal heat sink. The plant presented in this paper is not optimized, but is instead one of the simplest configurations of the EvGT concept. Improvements to the cycle can include an intercooled compressor, an aftercooler between the compressor and humidification tower or a divided humidification tower with different water flows as described by Ågren et al. ([4]). Preliminary measured electric efficiencies of the pilot at 80 percent load are 20 percent (dry non recuperated), 24 percent (dry recuperated), and 33 percent (evaporative).

Water Balance

It is in the nature of an evaporative gas turbine plant that the exhaust holds a fair amount of humidity, since the humidification process is the key to waste-heat recovery and high-cycle efficiency. In cycle simulation studies, humidification up to around 0.15 kg water per kg dry intake air have been presented ([19,23,24]). In order to avoid high water consumption, it is sensible to recover the water in the humid exhaust gases for reuse. From a mass balance point of view, it is important to analyze how far the exhaust gas should be cooled in a flue gas condenser to produce a sufficient amount of condensate. For that purpose, a system boundary can be drawn around the power process to illustrate the water flows through the plant.

In Fig. 2, the water flows are indicated with W (kg/s). A water mass balance over the dash-dotted system boundary will then be $W_I + W_F + W_C = W_E + W_B$. An interesting question is if the plant can be self-sufficient with water. In such a case W_F is set to 0. The bleed-off may also for a moment be set to 0. The mass balance is then reduced to

$$W_I + W_C = W_E. \quad (1)$$

This can be called a water-balanced plant. W_I can be calculated from the humidity of the ambient air and the compressor mass flow, $W_I = \omega_a F_c$, where ω_a (kg water/kg dry air) is the ambient absolute humidity and F_c is the dry air flow (kg/s) through the compressor. W_C depends, for a certain fuel, only on the turbine inlet temperature and is calculated with the reaction chemistry (1 kg methane produces 2.25 kg H_2O).

W_E depends only on the temperature to which the exhaust is cooled in the condenser, $W_E = \omega_{\text{sat}}(t) F_E$, where ω_{sat} is the temperature-dependent saturation absolute humidity and F_E is the dry flue gas flow. This temperature is calculated to satisfy Eq. (1). For a typical case with the studied turbine, calculations show that a condensation to 35°C generates a sufficient condensate flow for the need for external water feed to be nullified, except for the initial system fill-up before start. One other important conclusion is that W_I is inferior compared with W_C, which means that the ambient humidity at ISO conditions does not notably affect the cooling temperature requirement in the condenser. Together, this leads to the conclusion that the condensation temperature required for a water-balanced plant is mainly a function of natural gas consumption per kg air, which varies with the turbine inlet temperature, for any EvGT configuration. A certain amount of water needs to be bled off to avoid impurity buildup with time, and a corresponding amount of extra feed water needs to be added. This extra feed can in turn be avoided by condensing some degrees below 35°C. In Fig. 3 the required condensation temperature for full satisfaction of humidification is plotted against methane consumption. If a water bleed-off is employed, more water has to be condensed. For example, if 5 percent of the humidification rate is bled off, the plant is said to have a blowdown ratio of 5 percent. This case is included in Fig. 3. A more general use of this diagram is achieved if the abscissa is converted to hydrogen equivalents. Methane contains 1/4 hydrogen by molecular weight, and hence the values on the abscissa should be multiplied by 0.25. With this new abscissa, the diagram can also be used for other fuels such as mixtures of light hydrocarbons or oil.

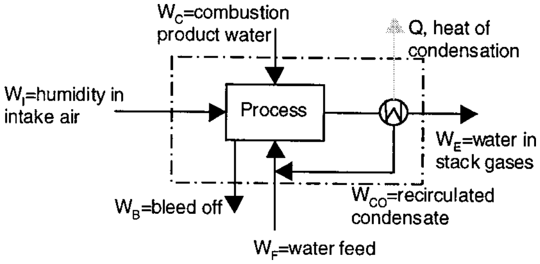

Fig. 2 Net water flows in an EvGT plant

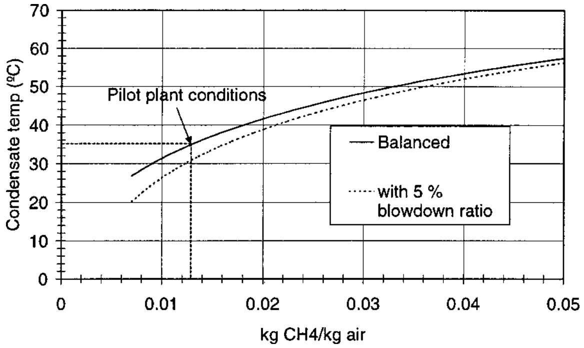

Fig. 3 Condensate temperature versus fuel consumption for water balanced mode

Impurity Build-Up

Through the course of the EvGT cycle, impurities such as salt and particles are introduced to the airflow and thereafter captured in the condensate. In order to satisfy the corrosion and erosion requirements of the cycle, especially for the gas turbine hot-gas path, the condensate needs to be carefully processed before reuse in the cycle. Within the water cycle, two points can be found where the water and air streams are in direct contact, first in the humidification tower and secondly in the flue gas condenser. At these two points of contact it is possible for contaminants to be transferred between the two media.

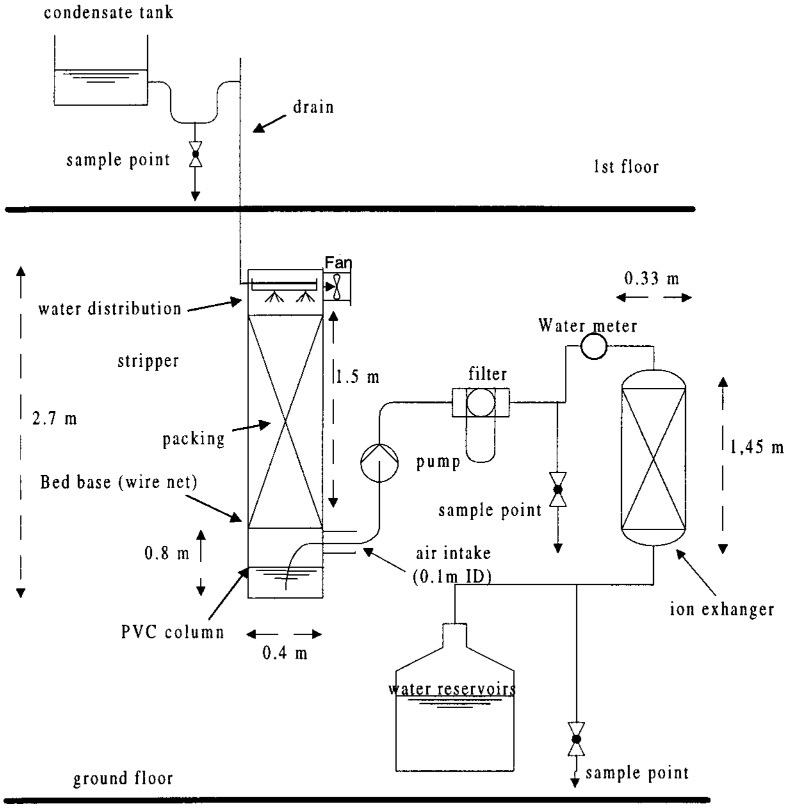

Fig. 4 Water treatment flowsheet

The most critical contaminant requirement in the EvGT cycle concerns the air quality through the gas turbine. At this point metal ions in the air stream, particularly alkaline metals, can cause severe corrosion of the turbine blades at elevated temperatures (above 800°C). This is because of salt-smelt that can deposit on the rotor blades. In the smelt, highly mobile ions are present, which in turn gives a corrosive environment. Also, salt sublimation can occur on the rotor blades, forming an incrustation that can severely damage the turbine. The ions can be introduced to the system through the fresh air intake, as corrosion products from the equipment, and, importantly, from the feed water to the humidification tower. Here, the ions can enter the air stream as salt dissolved in droplets that are entrained with the air. These droplets evaporate before the turbine, leaving a salt dust. This can not only damage the turbine, but the salts can also deposit on heat exchanger walls in the high temperature sections of the cycle. An example of alkali tolerance for a gas turbine is 4 μg Na/kg flue gas ([25]). As water is continuously being evaporated from the humidifying water, the salt concentration in the circuit will build up with time, leading to a higher risk of ions entering the air stream. This concentration can be regulated through bleeding off water and adding deionized water to the circuit.

Apart from absorbed metal ions, the condensate contains dissolved gases such as carbon dioxide, oxygen, nitrogen, nitrate, and nitrite. Additionally a high carbon dioxide level results in a lower pH of the water. Another source of contamination is the combustion byproducts. Soot can coat the piping and lead to corrosion, while partially oxidized products such as formic acid can lower the water pH.

Water Cleaning Process

To ensure a clean recycled condensate in the pilot plant, a water treatment process has been installed, which is depicted in Fig. 4. The ion exchange resin captures metal and other ions and releases OH^- and H^+ in exchange. The bed in this installation is of mixed an/cat type, which can achieve higher purity than a series of anion and cation beds. The condensate is treated in a CO_2 stripper to remove dissolved carbon dioxide. The carbonate will saturate the ion exchanger resin if carbon dioxide is not removed in the stripper. A particle filter is also installed before the ion exchanger to remove any dust that might clog the ion exchanger.

Equipment

Gas Turbine. A natural gas fired gas turbine of type Volvo VT600 is used. This turbo package is designed primarily for small-scale power production or combined power and heat production. The designed full load electric power for the standalone gas turbine is 600 kW. The combustion chamber has been modified for combustion with humidified air and has a diffusion burner. Natural gas is used as fuel. The combustion mixing temperature is around 1000°C. Maximum absolute humidity for the combustion air is approximately 0.2 kg water/kg dry air. To make up for the mass flow imbalance between the compressor and the expander caused by the added water vapor, a bleed-off duct has been installed for the removal of a portion of the compressed air. Design compressor air flow is 3.44 kg/s. The pressure ratio is around 8 bar.

Humidifier. Total height of the shell including fittings is 3000 mm. The shell inner diameter is 700 mm, and the material is SIS 2343-28. The effective packing height: 900 mm, achieved by three modules of 300 mm each. The packing type is a structured packing of stainless steel, and has a specific surface of 240 m^2/m^3. The mist eliminator is of inertia type and has a lamella spacing of 25 mm.

Economizer Condenser. The economizer and condenser are integrated in the same shell. The tubes are made of copper, with copper fins. The heat load for the economizer and condenser are around 0.4 and 1.2 MW, respectively.

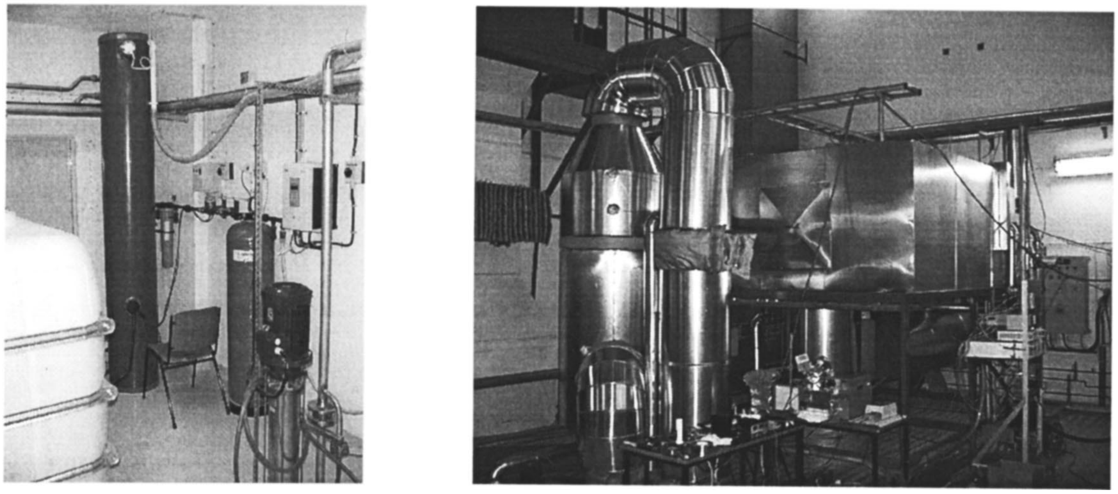

Fig. 5 Water treatment (left). Humidifier and heat recovery (right).

CO_2 Stripper. The CO_2 stripper removes CO_2 from the condensate upstream of the ion exchanger in order to reduce the number of regenerations. The condensate passes through the carbon dioxide stripper where it is contacted with ambient air. For full condensation (35°C), the maximum condensate flowrate is 1.1 m^3/h to 1.6 m^3/h. In order to obtain an increased contact area, approximately 400 l of packing (1.5 meters of 1 inch polypropene Pall-rings from Norton Chemical Process Products Corporation) was used. Around 0.005 m^3/s air is drawn through the PVC column by a fan situated at the air outlet. The dimensions of all the equipment are given in Fig. 4.

Filter. A particle filter with a polypropene cartridge of of 35 μm pore size was used.

Ion Exchanger. A mixed-bed ion exchanger was used (type: DX90-T, supplier: Vattenteknik AB, P.O. Box 50345, S-202 13 Malmö, Sweden). Its capacity between regenerations is 26 mole-equivalents. Height: 1450 mm, diameter: 330 mm. Maximum flow: 2.1 m^3/h. An automatic alarm for resin regeneration is activated when the conductivity of the outlet water is >5 mS/m.

Pump. A small pump (800 W, max 3.3 m^3/h) removes the water from the base of the PVC column, controlled by two level switches, and pumps it through the filter to remove any particles present. The flow of water is then measured cumulatively before it enters the ion exchanger.

Make-Up Water. Deionized make-up water was bought in tanks from Barsebäck nuclear power station. Seven polypropene reservoir tanks of 2000 l each (Fig. 5) were installed for this purpose.

Analytical Methods

Laboratory Analysis. The water analyses were performed by an accredited laboratory. For metal ions, ICP (inductively coupled plasma) spectroscopy is used. For organic compounds TOC-NPOC+IR (total organic carbon—non-purgible organic carbon coupled with IR spectroscopy) method is used. This method combusts the sample at high temperature and evaluates the CO_2 formed using IR spectroscopy. For nitrite and nitrate, photometry is used, and for chloride ion chromatography is used.

At the low concentrations that are presented in this study, there are significant risks of measurement errors. One source of error can be pollutants in the test bottles. This risk is dealt with by rinsing the bottles with the sampling water a few times before taking the test amount. The uncertainty of the analytical methods used vary between ±2 and ±4 percent depending on species and method.

At-Line Analysis. To get a direct approximate measurement of some critical components, the following direct methods were used:

In order to gain an immediate at-line indication of the sodium levels in the water circuits, both from the condenser and within the humidification tower, a Metrohm sodium ion (Na^+) specific, glass membrane electrode was used. The voltage is measured against a silver/silver chloride (Ag/AgCl) reference electrode by a Metrohm pH/Ion meter and the concentration thereby gained from a calibration curve. Additionally, the concentration of copper ions in the condensate was measured by using a Merck microquant copper test kit in order to monitor the level of corrosion in the condenser and within the economizer.

Experimental Procedure

The plant is run at differing loads on the turbine (50–480 kW shaft power after gearbox) with the liquid to gas mass flow ratio in the humidifier varied from 0.5 to 1 kg/kg for each load. Water samples were taken from the sample points labeled in Fig. 1. The first sample point (A) is for untreated condensate (before the stripper), the second (B) after the stripper, the third (C) after the ion exchanger, before the treated water enters the water reservoir and the fourth (D) after the water reservoir. One additional sample point (E) is located before the economizer for the feed water to the humidification tower. These samples were then analyzed with both indicative, "on the spot" tests and later more precisely by an accredited laboratory. The properties of interest are the level of dissolved carbon dioxide and NO_x before and after the stripper, the pH of the water at all sample points, and the level of sodium, copper, and chloride ions at all sample points. To avoid risk of contamination, the sample bottles were thoroughly rinsed with the sampling water before a sample was secured. Samples were taken after at least ten minutes of continuous operation to ensure steady-state conditions.

Results and Discussion

Table 1 shows a compilation of test results from a run at 80 percent load, corresponding to 480 kW shaft power after gearbox. To make the plant self supporting with water, the exhaust is cooled to 35°C (Fig. 2). The leading letters in the headings in Table 1 refer to the notation in Fig. 1.

Table 1 Measurement results

Sampling Point Analysis	A, Cond ppm	B, After Filter ppm	C, After IEx ppm	D, Make Up ppm	E, Circ. Water ppm
Total organic carbon	*<1*	*<1*	*<1*	*<1*	2.2
Al	*<0.05*	*<0.05*	*<0.05*	*<0.05*	*<0.05*
As	*<0.1*	*<0.1*	*<0.1*	*<0.1*	*<0.1*
Pb	*<0.05*	*<0.05*	*<0.05*	*<0.05*	*<0.05*
B	*<0.05*	*<0.05*	*<0.05*	*<0.05*	*<0.05*
Fe	*<0.05*	*<0.05*	*<0.05*	*<0.05*	*<0.05*
Cd	*<0.01*	*<0.01*	*<0.01*	*<0.01*	*<0.01*
Ca	0.18	*<0.01*	*<0.01*	0.26	8.7
K	0.44	*<0.1*	*<0.1*	*<0.1*	0.47
Si	0.44	*<0.3*	*<0.3*	*<0.3*	1.5
Co	*<0.01*	*<0.01*	*<0.01*	*<0.01*	*<0.01*
Cu	16	15	*<0.01*	*0.01*	0.05
Cr	*<0.01*	*<0.01*	*<0.01*	*<0.01*	0.11
Li	*<0.01*	*<0.01*	*<0.01*	*<0.01*	*<0.01*
Mg	*<0.1*	*<0.1*	*<0.1*	*<0.1*	1.1
Mn	*<0.01*	*<0.01*	*<0.01*	*<0.01*	*<0.01*
Mo	*<0.01*	*<0.01*	*<0.01*	*<0.01*	*<0.01*
Na	1.1	0.52	*<0.2*	*<0.2*	4.7
Ni	*<0.01*	*<0.01*	*<0.01*	*<0.01*	*<0.01*
St	*<0.01*	*<0.01*	*<0.01*	*<0.01*	0.12
S	0.9	1.5	*<0.3*	*<0.3*	2.3
V	*<0.01*	*<0.01*	*<0.01*	*<0.01*	*<0.01*
Zn	0.1	0.1	*<0.01*	0.02	0.1
NO_2^-	12.8		*<0.002*		
NO_3^-	1.2		*<0.1*		
Cl	*<1.0*		*<1.0*		

In the condensate (A). The sum of concentrations of Na, K, and Ca is about 2 mg/l. The condensing film is very efficient in capturing particles, as well as absorbing gases, depending on the solubility of the gas. These metal ions originate from condensate film absorption from the flue gases. The main source is the intake compressor air. The intake air is not filtered in the pilot plant and always contains small amounts of dust from natural and industrial sources (flue ash particles, soil particles, pollutants from traffic, salt particles from the sea, etc). In comparison, this condensate can be considered as very low in mineral content and cheap to deionize. Scandinavian drinking water typically contains 20–100 mg/l alkali.

After the particle filter (B), the Ca, K, and Si concentrations have dropped considerably. This indicates that these species are partly present as undissolved particles (suspended solids) in the condensate, which are removed by the filter. Note that the ICP metal analysis of the condensate involves acidification of the sample, and represents the total metal content, both dissolved and solid. The most likely explanation is that the undissolved particles originate from the dust particles in the intake air.

In the condensate (A), the highest metal ion concentration is that of Cu^{2+} (16 mg/l). The copper originates from corrosion of the condenser equipment, where the heat exchanger tubes are made of copper. On the condensing side of the tubes there is an acidic environment, caused by HNO_2 and HNO_3 from absorption of NO_x from the flue gas. In commercial equipment the condenser should be made from a more suitable material to avoid corrosion. The copper content is virtually unaffected through the filter, which indicates that copper corrosion product is mostly present as dissolved ions.

The TOC (total organic carbon) is a measurement of all intermediate combustion products that are absorbed in the condenser. These organic species are formed when the natural gas is not fully combusted. In this 480 kW load case, the TOC was below detection level (<1 mg/l) in the condensate. This indicates an efficient combustion process in the run. However, a condensate from the lowes: load indicated 3–11 mg/l TOC. At low loads, the combustion temperature is lower, resulting in less complete reactions and therefore higher amounts of partly combusted hydrocarbons. If TOC is detected, a more detailed GC analysis can be made to identify the actual species. Formic acid (HCOOH) was identified at low loads. Other probable TOC constituents are methanol, methanal and acetic acid ([26]).

The sample after the ion exchanger (C) shows concentrations below the detection limit on all species, indicating a good performance of the mixed-bed ion exchanger. The treated condensate is even cleaner than the deionized water used for fresh make up. The make up sample (D) serves as a reference. This does not contain any notable impurities.

The circulation water sample (E) contains 8.7 ppm Ca, a factor 30 higher than the make up deionized water. This is partly because of the salt buildup in the water circuit (the water is evaporated in the humidifier, but most of the salts are contained within the humidification circuit). In the pilot plant runs, no bleed-off of water was employed during the runs and the salt content then gradually increases. In a commercial plant, bleed-off should be adopted to reach an acceptable steady-state concentration in the humidifier. The same buildup of concentration is valid for other components. Dust particles in unfiltered intake air probably also contributes to salt buildup. Some particles are probably captured already in the humidifier, which then acts as a scrubber. Other particles may be captured in the condenser as discussed above.

Cr, Ni, Fe, and Mo appear with rather low concentrations which indicates a low corrosion rate for the stainless steel used. The copper concentration is low in the circulation water, indicating much lower copper corrosion rate on the inside of the copper tubes than on the outside, the latter being exposed to acidic compounds.

Conclusions

- Recycling of condensate can be realized both when it comes to water quality and quantity: An EvGT-cycle with self-supporting water circuit has been achieved by flue gas cooling to 35°C, with no fresh water feed needed. The water cleaning equipment installed stands well up to the quality demands for recycling. No water bleed-off was used in the runs.
- Very low concentrations of organic compounds (TOC) were measured in the condensate. Slightly higher concentrations were noted at low loads, because of incomplete combustion.

- All condensate concentrations except for Cu (16 mg/l) proved to be very low because of limited corrosion in the equipment. The high copper concentrations can be traced to the copper tubes in the condenser. Copper equipment is not recommended for commercial plants but was used in the lab rig because of lower cost. A buildup of metal ion concentrations was noted in the EvGT water system. The ions originate partly from the intake air, partly from equipment corrosion, and, to a smaller extent, from the fuel, and can be controlled with a water bleed-off.
- The condensate contains, e.g., dissolved CO_2, approximately 14 mg/l $NO_2^- + NO_3^-$ from NO_x absorption, approximately 2 mg/l Na+K+Ca, probably from the unfiltered intake air. After CO_2 stripping, condensate filtration and a mixed bed ion exchanger, the condensate is suitable for reuse as humidification water. Filtering of the intake air probably would reduce the salt content considerably.

Acknowledgments

The financial support from the Swedish National Energy Administration (Statens Energimyndighet), ABB STAL, Sydkraft, Volvo Aero Corporation, Vattenfall and Elforsk is gratefully acknowledged.

References

[1] IGTI, 1996, *Global Gas Turbine News*, **36**, No. 3.
[2] Larson, E. D., and Williams, R. H., 1987, ''Steam-Injected Gas Turbines,'' ASME J. Eng. Gas Turbines Power, **109**, pp. 55–63.
[3] Tuzson, J., 1992, ''Status of Steam-Injected Gas Turbines,'' ASME J. Eng. Gas Turbines Power, **114**, pp. 682–686.
[4] Ågren, N., Cavani, A., and Westermark, M., 1997, ''New Humidification Concept for Evaporative Gas Turbine Cycles Applied to a Modern Aeroderivative Gas Turbine,'' *Proceedings, ASME Advanced Energy Systems Division*, M. L. Ramalingam et al., eds., ASME, New York, Vol. 37, pp. 223–230.
[5] Gasparovic, N., and Stapersma, D., 1973, ''Gas Turbine With Heat Exchanger and Water Injection in the Compressed Air,'' Combustion, Dec., **45**, pp. 6–16.
[6] Mori, T. R., Nakamura, H., Takahashi, T., and Yamamoto, K., 1983, ''A Highly Efficient Regenerative Gas Turbine System by New Method of Heat Recovery With Water Injection,'' *Proceedings, 1983 Tokyo International Gas Turbine Congress*, Vol. 1, GTSJ, Japan, pp. 297–303.
[7] Frutschi, H. U., and Plancherel, A., 1988, ''Comparison of Combined Cycle With Steam Injection and Evaporation Cycles,'' *ASME COGEN-TURBO, 2nd Sym. on Turbomachinery, Combined-Cycle Technologies and Cogeneration, IGTI* ASME, New York, Vol. 3, pp. 137–145.
[8] Annerwall, K., and Svedberg, G., 1991, ''A Study on Modified Gas Turbine Systems With Steam Injection or Evaporative Regeneration,'' *Proceedings 1991 ASME COGEN TURBO POWER, IGTI*. ASME, New York, Vol. 6.
[9] Barthelemy, N. M., and Lynn, S., 1991, ''Improved Heat Recovery and High-Temperature Clean-Up for Coal-Gas Fired Combustion Turbines,'' Report No. LBL-31079, Lawrence Berkeley Laboratory, Berkeley, CA.
[10] Yan, J., Eidensten, L., and Svedberg, G., 1995, ''Investigation of the Heat Recovery System in Externally Fired Evaporative Gas Turbines,'' ASME Paper No. 95-GT-72.
[11] Stecco, S. S., Desideri, U., Frachini, B., and Bettagli, N., 1993, ''The Humid Air Cycle: Some Thermodynamic Consideration,'' ASME Paper No. 93-GT-77.
[12] Rosén, P., 1993, ''Evaporative Gas Turbine Cycles—A Thermodynamic Evaluation of Their Potential,'' licentiate thesis, Department of Heat and Power Technology, Lund Institute of Technology, Lund, Sweden, ISRN LUTMDN/TMVK-7010-SE.
[13] Rao, A. D., and Joiner, J. R., 1990, ''A Technical and Economic Evaluation of the Humid Air Turbine Cycle,'' *7th Annual International Pittsburgh Coal Conference*, Sep. 10–14.
[14] Day, W. H., and Rao, A. D., 1992, ''FT4000 HAT With Natural Gas Fuel,'' *ASME COGEN-TURBO* I.G.T.I., ASME, New York, Vol. 7, pp. 239–245.
[15] Rao, A. D., 1989, ''Process for Producing Power,'' U.S. Patent No. 4829763, May 16.
[16] Cohn, A., 1993, ''Power Plant Cycles Featuring Air Humidification,'' EPRI, Oct./Nov.
[17] Chiesa, P., Lozza, G., Macchi, E., and Consonni, S., 1995, ''An Assessment of the Thermodynamic Performance of Mixed Gas-Steam Cycles: Part B—Water-Injected and HAT Cycles,'' ASME J. Eng. Gas Turbines Power, **117**, pp. 499–508.
[18] Eidensten, L., Svedberg, G., Yan, J., and Ågren, N., 1994, ''New Heat and Power Production Processes,'' (Nya el- och värme-produktionsprocesser)'' Technical Report (in Swedish), Royal Institute of Technology, ISSN 1104-3466/TRITA-KET R19.
[19] Gustafsson, J-O., von Heiroth, P., and Lindquist, T., 1998, ''Transient Analysis of a Small Gas Turbine to be Used in an Evaporative Cycle,'' ASME Paper No. 98-GT-353
[20] Nilsson, P. A., ed., 1996, ''EvGT—Evaporative Gas Turbine—Block 3,'' Technical Report, Lund Institute of Technology, Department of Heat and Power Technology, Lund, Sweden.
[21] Westermark, M., 1996, ''Method and Device for Generation of Mechanical Work and, if Desired, Heat in an Evaporative Gas Turbine Process,'' International Patent Application No. PCT/SE96/00936.
[22] Annerwall, K., 1990, ''Gas Turbines With Steam Injection or Evaporative Regeneration,'' licentiate treatise, Royal Institute of Technology, Department of Chemical Engineering/Energy Processes, Stockholm, Sweden.
[23] Gallo, W., Bidini, G., Bettagli, N., and Facchini, B., 1995, ''The Evaporator Process Simulation and the HAT Cycle (Humid Air Turbine) Performance,'' ASME Paper No. 95-CTP-59.
[24] Xiao, Y., Rui, X., and Lin, R., 1996, ''Modeling HAT Cycle and Thermodynamic Evaluation,'' *Proceedings, ECOS'96, Efficiency, Costs, Optimization, Simulation and Environmental Aspects of Energy Systems*, P. Alvfors, et al., ed., Stockholm, Sweden, ISBN 91-7170-664-X.
[25] Bretz, E. A., 1989, ''Examine Full Impact of Injecting Steam Into Gas-Turbine Systems,'' Power Journal, June, pp. 53–61.
[26] Lewis, B., and von Elbe, G., 1961, *Combustion, Flames and Explosions of Gases*, Academic Press, San Diego CA, ISBN 99-0840474-1.

Assessment of Molten Carbonate Fuel Cell Models and Integration With Gas and Steam Cycles

A. F. Massardo
Dipartimento di Macchine,
Sistemi Energetici e Trasporti,
Universita di Genova,
Genova, Italy
e-mail: massardo@unige.it
Mem. ASME

B. Bosio
Dipartimento di Ingegneria Ambientale,
Universita di Genova,
Genova, Italy
e-mail: bosio@diam.unige.it

The aim of this work is to investigate the performance of molten carbonate fuel cells (MCFCs), with external sensible heat reformer and gas turbine/steam turbine (GT/ST) combined cycles. The analysis of these MCFC-GT/ST combined cycles has been carried out using the thermo economic modular program (TEMP) modified to allow MCFC, external sensible heat reformer, and catalytic burner performance to be carefully taken into account. The code has been verified through the use of a detailed MCFC model and of the data available for an existing MCFC unit. The thermodynamic and exergy analysis of a number of MCFC combined cycles is presented and discussed, taking into account the influence of technological constraints, also evaluated with the sophisticated model, and the influence of the post-combustion of the fuel directly in the external catalytic burner. The results are presented and discussed in depth. [DOI: 10.1115/1.1398551]

Introduction

Among the different kinds of fuel cells under development today, molten carbonate fuel cells (MCFCs) are of particular interest because of their operating temperature (≈923 K). The latter, in fact, is not too high to involve material or corrosion problems, but is sufficiently high to allow the use of non-noble catalysts. Such catalysts are less expensive and insensitive to certain fuel contaminants, so that, in principle, MCFCs may use a range of gaseous fuels, such as natural gas, biogas or coal gas. However, the more significant advantage, discussed in this paper and related to the relatively high operating temperature, is the possibility of cogeneration, which increases revenue and overall efficiency exploiting the exergy of the exhaust gases. Moreover, MCFC technology is now at the stage of scaling-up to commercialization and many developers, worldwide, have shown significant progress.

In this scenario, we have chosen to base our study on the plant scheme developed and tested by Ansaldo Ricerche ([1]) with a 100 kW module called compact unit (CU). This pilot plant represents an intermediate step for the project of a modular 250/500 kW plant within the MOLCARE program ([2]).

MCFC Compact Unit

The studied CU configuration, whose simplified scheme is shown in Fig. 1, is based on the sensible heat reforming (SHR) concept, which marks out this plant, allowing its autothermal running. In the SHR, in fact, the reforming endothermic reaction ($CH_4+H_2O \rightarrow CO+3H_2$) occurs without help of additional heaters or burners, but thanks to the excess heat of the recycled anode gas. In this way the fresh fuel methane is converted into H_2 richer mixture then consumed in the cells to dispatch electrical power.

The MCFC electrochemical core of the CU, simplified in Fig. 1 as an anode and a cathode separated and coupled, consists of 150 planar square cells of 0.75 m^2 connected in series and superimposed to form two MCFC stacks.

Each cell is formed by a matrix in $\gamma LiAlO_2$ filled with Li and K carbonates and coupled with two electrodes: an anode in Ni/Cr and a cathode in $Li_xNi_{1-x}O$ ([3]).

The fuel and the oxidant gas are fed separately, and the tile prevents gas crossover and guarantees an adequate ionic conduction and electronic insulation.

In the MCFCs the following reactions occur:

$$\text{at the anode } H_2+CO_3^{--} \rightarrow H_2O+CO_2+2e^- \qquad (1)$$

$$\text{at the cathode } CO_2+1/2O_2+2e^- \rightarrow CO_3^{--}. \qquad (2)$$

Taking into account that the amount of CO_2 produced at the anode is required at the cathode, the stream coming from the anode is split to the cathode, so the overall reaction is

$$H_2+1/2O_2 \rightarrow H_2O+\text{heat}+\text{electrical power}.$$

However, due to the presence of unreacted H_2, CO, and CH_4 in the anode exhaust stream, a cathode catalytic burner (CCB) is used to oxidise all these species before they enter the cathode side.

The two high-temperature blowers are used to balance pressure drops on the anode and cathode recycles. Finally, CU exhausts are completely burnt in the exhaust catalytic burner (ECB) and then come out at a temperature suitable for use in a heat recovery system, as it is discussed in this paper.

Models

Two different mathematical models of MCFCs for steady-state operation have been considered and compared to experimental data.

The first one is a three-dimensional theoretical model, developed by the authors and presented elsewhere ([4]). This model takes into account mass, energy, and momentum balances at cell and stack level.

In the model, as well as electrochemical reactions, water gas shift reaction ($CO+H_2O \rightarrow CO_2+H_2$) is evaluated in the anodic side and is assumed to be at the thermodynamic equilibrium on the basis of experimental data.

The kinetics of the electrochemical reactions are summarized in the following equation of total electrical resistance:

$$R_{\text{tot}}=\frac{A\cdot e^{E/T}}{\Pi p_i^{\beta_1}}+c_{iR}+D\cdot e^{F/T} \qquad (3)$$

where A, β, c_{iR}, D, E, and F are phenomenological coefficients evaluated by experimental data ([4]).

The simulation results show the distribution of gas and solid temperatures, compositions, and flow rates of the gaseous streams, electrical current density, Nernst voltage, polarization, internal re-

---

Contributed by the International Gas Turbine Institute (IGTI) of THE AMERICAN SOCIETY OF MECHANICAL ENGINEERS for publication in the ASME JOURNAL OF ENGINEERING FOR GAS TURBINES AND POWER. Paper presented at the International Gas Turbine and Aeroengine Congress and Exhibition, Munich, Germany, May 8–11, 2000; Paper 00-GT-174. Manuscript received by IGTI, Nov. 1999; final revision received by ASME Headquarters, Feb. 2001. Associate Editor: D. R. Ballal.

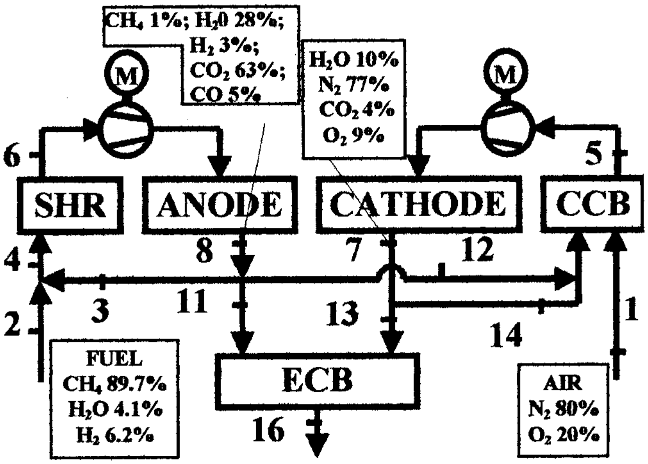

	1	2	3	4	5	6
m[kg/s]	0.139	.00416	0.4325	0.4367	0.5168	0.4367
T[K]	465	505	958	946	893	855
p[kPa]	350	350	348.7	348.7	348.7	345.2

7	8	11	12	13	14	16
0.467	0.4864	0.0024	0.051	0.141	0.326	0.1433
947	960	958	958	945	945	964
348.7	348.7	348.7	348.7	348.7	348.7	348.7

Fig. 1 Simplified scheme of the MCFC-CU with simulation results related to nominal operating conditions (compositions are reported as volumetric fractions)

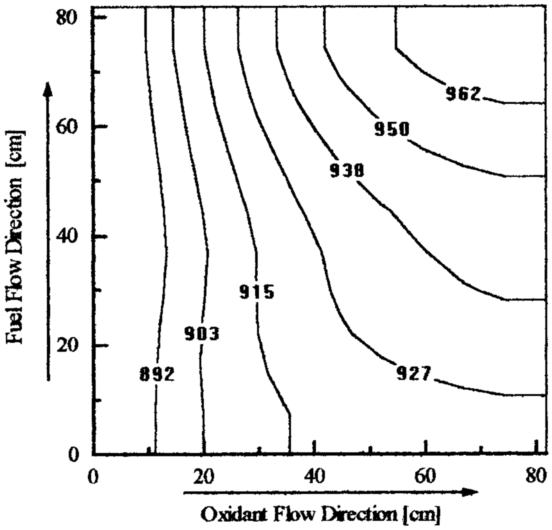

Fig. 2 Solid temperature (K) distribution on the plane of a stack cell calculated at operating conditions of Case 1 in Table 1 by means of the detailed MCFC model

sistance, and pressure drops on the plane of each cell of the stack. An example of calculated solid temperature distribution on cell plane is shown in Fig. 2.

The second model ([5]) is based on a simplified approach which does not allow a detailed knowledge of the flows inside the stack, but is particularly well suited for analysis and optimization of complex energy systems, including MCFCs. In this model, in fact, cell stack integration in a power plant is studied calculating all the operating parameters only at cell stack inlet and outlet.

In particular, also this model takes account of shift and electrochemical reactions, but only total reaction rates are calculated, assuming, respectively, the thermodynamic equilibrium at stack outlet temperature and the above resistance formulation for an average temperature between stack inlet and outlet.

With regard to energy balance in this case, a heat split factor has been introduced to evaluate the heat reaction fraction that, produced at the electrodes, comes out in the anode or in the cathode stream, disregarding the calculation of local heat exchange between solid and gases. On the base of experimental data it has been assumed that 0.61 percent of reaction heat is kept at the anode. In this way the simplified MCFC model has been integrated in the plant scheme of Fig. 1, and the analysis has been carried out by means of the Thermo Economic Modular Program TEMP version 5.1. This is a modular simulator tool for the thermoeconomic analysis of advanced thermal energy systems developed by the authors ([6]). The targets of the tool are: thermodynamic and exergy analysis, and thermoeconomic analysis including environomic and optimization. The capability of the original modular simulator tool has been demonstrated for gas, steam, and complex combined plants ([7]). Besides the MCFC module, it has been necessary to develop other new modules, which were not foreseen by TEMP: catalytic burners and sensible heat reformer. The particularities of these units are that the first ones (CBs) work at lower temperature than traditional burners, while the second one (SHR) converts methane without the common auxiliary burner closely integrated with the reforming catalyst bed.

The main hypotheses assumed to simulate these components are the same as used in a previous simulation activity performed to carry out CU process analysis ([8]). The reactions considered at the SHR are

$$CO+H_2O \leftrightarrow CO_2+H_2 \tag{4}$$

$$CH_4+H_2O \rightarrow 3H_2+CO_2 \tag{5}$$

and at the CBs are

$$H_2+1/2O_2 \rightarrow H_2O \tag{6}$$

$$CO+1/2O_2 \rightarrow CO_2 \tag{7}$$

$$CH_4+O_2 \rightarrow CO_2+2H_2O. \tag{8}$$

The conversion degree of reactions in the SHR is estimated to be at the thermodynamic equilibrium condition (at the outlet temperature). For the conversion in the CCB and the ECB it is supposed that H_2 and CO are burnt conforming to the expected catalytic performance. At full power the anode to anode (AAR), anode to cathode (ACR) and cathode to cathode (CCR) recycles have been fixed. The following values have been considered to guarantee a gas temperature sufficiently high for reaction in the SHR as well as useful values of cathode and anode inlet temperature and flow rates: AAR 89 percent, ACR 10.5 percent, CCR 69.8 percent.

Model Assessment

The detailed model of the MCFC has been validated on experimental data which show good agreement between calculated and measured values in terms of performance as well as temperature distribution ([4]).

These results have been compared to the results obtained with the simplified model. The comparison has been performed assuming the conditions shown in Table 1. The results are shown in Fig. 3 where the overall stack voltage and outlet temperature differences are compared: The difference is always negligible (<2 percent).

Moreover, the results obtained by means of the TEMP code and reported in Fig. 1 have been compared with the ones previously calculated studying the system behavior and then experimentally confirmed ([8]).

Table 1 Reference operating conditions for the comparison of the two MCFC models

	Case 1	Case 2	Case 3
Anode total flow rate [kg/s]	0.028	0.028	0.027
Anode CO2	6.4	6.4	6.9
Anode H2	20.3	20.3	22.0
Anode H2O	15.0	15.0	9.2
Anode N2	58.3	58.3	61.9
Cathode total flow rate [kg/s]	0.114	0.114	0.105
Cathode O2	16.7	16.7	16.7
Cathode N2	69.8	69.8	70.2
Cathode CO2	13.5	13.5	13.1
Temperature anode inlet [K]	858	858	855
Temperature cathode inlet [K]	867.5	867.5	853.5
Operating pressure [bar]	3.5	3.5	3.2
Current density [A/m^2]	1316	876	876

The comparison has been carried out at the following nominal operating conditions: current density 1580 A/m^2; pressure 350 kPa, air as oxidant and a mixture of 4 percent H_2O, 6 percent H_2, and 90 percent CH_4 as fuel. In Fig. 4 the temperatures are compared at different CU points identified in accordance with Fig. 1, while with regard to gas composition an error lower than 0.01 percent has been observed.

Simulation activity discussed in the following paragraphs has been carried out by means of the above computational device obtained by integration of the simplified MCFC model in TEMP. Moreover, in order to guarantee safe running of the MCFC stack, local operating conditions can be verified with the detailed model. In fact, some parameters have to be controlled in the cells (maximum and minimum temperature, maximum gas pressure drops, maximum pressure difference between anode and cathode, etc.) and the results available from the simplified model concerning MCFC stack inlet and outlet could hide inadmissible local values ([9]).

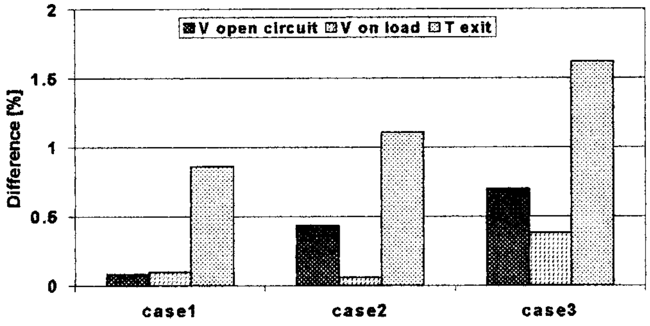

Fig. 3 Comparison of detailed and simplified MCFC model results

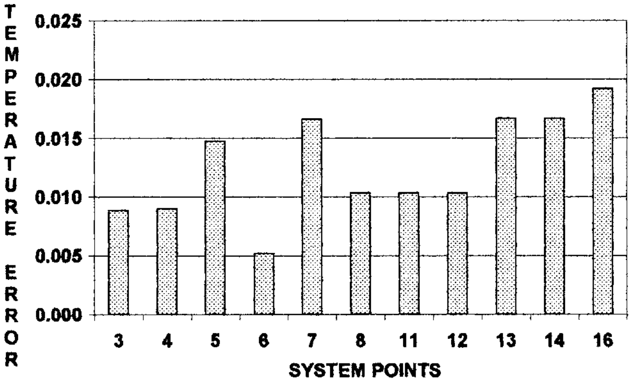

Fig. 4 Comparison of referenced and calculated temperatures using code TEMP ([12])

MCFC Combined Cycles

Several high-efficiency proposals have been presented in literature for MCFC and gas turbine (GT) or steam turbine (ST) integration. Two main different solutions can be used: (i) the MCFC is used as a bottoming cycle of an existing GT; (ii) the MCFC is used as a topping cycle of a GT/ST system.

In this work the first option was not taken into account for the following reasons: (a) when MCFC-CU is used as a bottoming cycle some modifications to such a complex and advanced system would be required; (b) more fuel must be burnt in the combustion chamber of the topping GT system, and in this way the advantage of the MCFC direct electrochemical conversion is partially lost, in addition NO_x emissions are not negligible as in the MCFC-CU case.

Taking into account the data shown in Fig. 1, it is possible to note that the MCFC's exhaust gas has a high temperature (~973 K) and an interesting pressure level (350 kPa).

In this way the first option to recover energy from the cell exhaust gas consists of a bottoming GT system. The layout of the plant is shown in Fig. 5, where the results of the simulation carried out with the code TEMP are also reported. It is possible to note that in the layout the MCFC-CU is exactly the same as that reported in Fig. 1. The layout named MCFC-GT has the following overall performance: efficiency 60.4 percent, specific work 871 kJ/kg, P_{MCFC} 10940 kW, P_{GT} 1188 kW, P_{plant} 12128 kW.

The results have been obtained assuming the following flow rate values: fuel 0.417 kg/s; air 13.93 kg/s. Taking into account the size of the GT system the compressor and expander efficiencies have been carefully evaluated ([10,11]). The increase in efficiency is about 8 percent while the GT power contribution is about 13 percent.

An important difference between the present analysis and a previous one carried out by the authors for IRSOFC-GT combined cycles ([12]) is due to the pressurization level of the cell. In the cited work the cell pressure was used as a variable (in the range from atmospheric pressure to 3000 kPa) for the definition of the optimum bottoming cycle layout. In this case, as a particular MCFC-CU reference configuration has been assumed, the cell pressure is fixed and this degree-of-freedom cannot be used to improve the combined cycle performance. However, the computational codes allow the evaluation of pressure influence on the plant performance ([5]).

To increase the heat recovery efficiency at the MCFC-CU outlet it is possible to generate steam in a heat recovery steam generator (HRSG), taking into account that the stack temperature for the MCFC-GT layout is about 747 K. The steam can be used in two different ways: injected upstream from the GT expander inlet section (steam injection−SI) or expanded in a steam turbine (based on the HRSG's pressure levels two different plants have been considered in the following—1PL one pressure Level, and 2PL two pressure Level).

The first option, named MCFC-SI, is shown in Fig. 6: The steam is injected upstream from the GT inlet, and it increases the enthalpy drop inside the GT expander, and obviously also the GT power. The efficiency of this plant is 62.6 percent and the specific work is 908 kJ/kg. The GT power is about 1.7 MW (17 percent of the total plant power). It is interesting to note that the water to gas weight ratio at the GT expander inlet is about 13 percent, a value frequently used in the STIG and Cheng systems. The stack temperature is 413 K, while in the MCFC-GT case this value is 747 K.

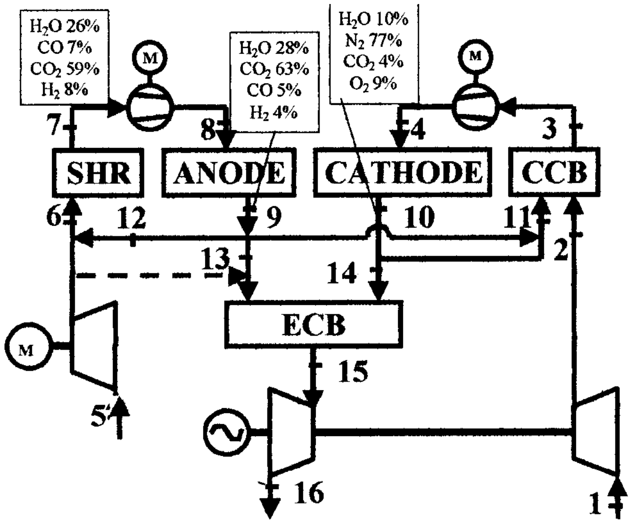

	1	2	3	4	5	6	7	8
m[kg/s]	13.93	13.93	51.77	51.77	0.417	43.67	43.67	43.67
T[K]	298	455	902	904	298	969	333	878
p[kPa]	101	350.5	348.8	348.8	101	348.9	345.4	350.6
	9	10	11	12	13	14	15	16
m[kg/s]	48.72	46.72	37.84	43.25	24	14.11	14.35	14.35
T[K]	981	964	967	982	981	964	964	747
p[kPa]	348.8	348.8	348.8	348.8	348.8	348.8	348.8	101

Fig. 5 MCFC-GT layout (GT=gas turbine)

The efficiency increase is about 10 percent compared to MCFC-CU data, and also the specific work increase is evident. Nevertheless, this layout suffers from two main negative aspects: (i) the maximum pressure of the steam in the HRSG is lower than its optimum value since it is constrained by the MCFC-CU operative pressure; (ii) the steam expands only to atmospheric pressure (this aspect is always present when GT with steam injection is used).

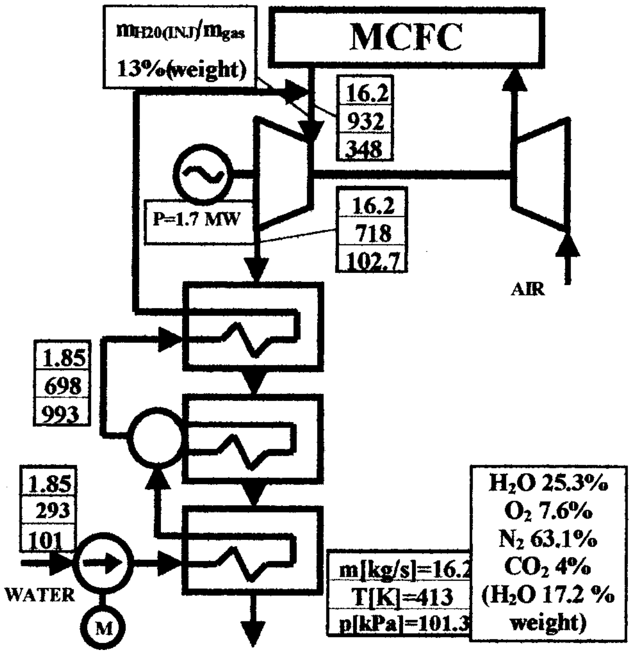

Fig. 6 MCFC-SI layout (SI=steam injection)

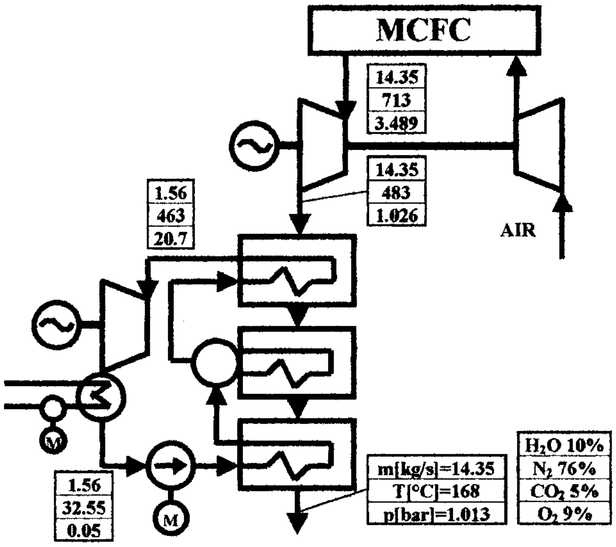

Fig. 7 MCFC-1PL layout (1PL=one pressure level)

To avoid the previous negative aspect the solution shown in Fig. 7 can be considered: In this case a combined cycle is used. The steam generated in the HRSG (single pressure or two pressure levels) is expanded in a steam turbine (ST). Taking into account the GT outlet temperature (756 K) it is possible generate steam at 736 K at 2070 kPa.

The choice of the steam pressure (in this case this parameter is not constrained by the cell operative pressure) has been carried out through the use of the optimization section of the code TEMP. Figure 8 shows the behavior of plant efficiency and power versus steam pressure. It is possible to observe that the optimum point is in the region near 2500 kPa for both power and efficiency. This value is lower than that used for a heavy-duty single-pressure combined cycle since, in the present analysis, the gas temperature is low.

The plant named MCFC-1PL has the following performance: efficiency 67.4 percent, specific work 977 kJ/kg, stack temperature 441 K, GT power 12 percent, ST power 11 percent P_{plant} 13608 kW (P_{GT} 1168 kW, P_{ST} 1500 kW).

An obvious extension of the MCFC-1PL layout is the MCFC-2PL system, where the HRSG operates with two different pressure levels. In this case the degrees-of-freedom are the two steam pressures. Also in this case their values have been obtained with the code TEMP, and in Fig. 9 the plant efficiency is shown versus the steam low pressure (SLP) and the steam high pressure (SHP). Based on this analysis the data used for the calculation are: SLP 500 kPa and SHP 10000 kPa. Using these data the plant efficiency

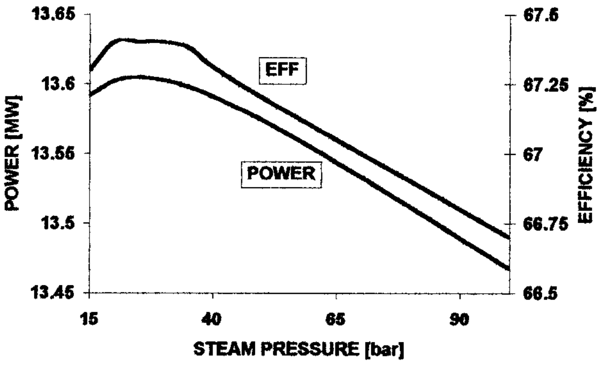

Fig. 8 MCFC-1PL power and efficiency versus steam pressure

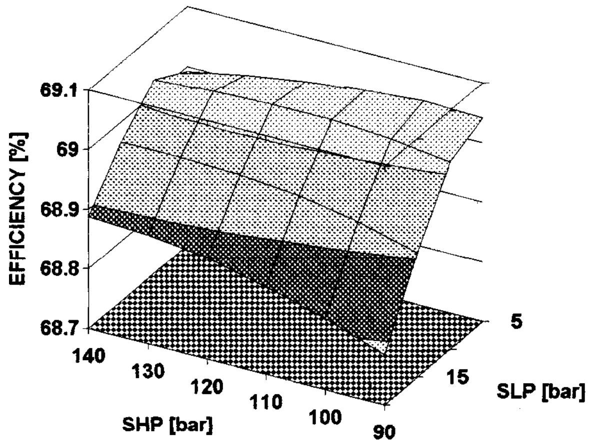

Fig. 9 MCFC-2PL efficiency versus SHP (steam high pressure) and SLP (steam low pressure)

is 69.1 percent, the specific work is 1000 kJ/kg, the stack temperature is 381 K, the total power is 13947 kW (76 percent CU, 11 percent GT, 13 percent ST). The increase of both efficiency and specific work is noteworthy mainly if they are compared to MCFC-CU data.

Exergy Analysis

A very useful way to compare the performance of the CU and the combined solutions presented here is the use of the exergy analysis, using the apt section of the TEMP code. Figure 10 shows the irreversibility rate of the plant components.

The second law efficiency of the CU is about 40 percent while a noteworthy increase is evident for the combined systems. The low efficiency value for the CU is mainly due to the irreversibility rate of the exhaust gases (stack): the data for the cell is very low (about 6 percent), while the burner contributions are more evident (about 9.5 percent). The CU irreversibility rate without the stack contribution is about 24 percent. Using bottoming cycles the stack irreversibility rate is greatly reduced: from 34.7 for the CU solution to 15 percent for the GT plant, and five, three, and two percent for SI, 1PL, and 2PL systems. In this way the second law efficiency increases from 40 to more than 65 percent. The irreversibility rates of the bottoming cycle components are always very small.

Fired Bottoming Cycles

When the MCFC-CU is used for the development of high-efficiency combined cycles two important aspects must be considered: (a) the CU exhaust gas has a low pressure level; (ii) the CU exhaust gas does not have a very high temperature to be used in a GT expander.

Unfortunately, as already stated, increasing the pressure to obtain more work from the GT section is very difficult since it is strictly correlated to the CU operative pressure. However, the gas temperature can be increased if part of the fuel is directly burnt in the ECB (fired bottoming cycles), as shown in Fig. 5 where the gas bypass is shown with a dotted line.

To analyze the performance of such a system the post-combustion ratio (PCR) is defined as: fuel mass flow rate by-passed into ECB to fuel mass flow rate used in the cell. The range of such a parameter has been considered between 0 and 25 percent. It allows the GT inlet temperature to always be under the value where blade cooling is necessary (1173 K).

The results obtained for the last three bottoming cycles are shown in Fig. 11 and Fig. 12, where the specific power and efficiency are plotted versus PCR. When the post-combustion solution is used the efficiency reduces, while the specific work increases. The efficiency reduction is quite evident for the MCFC-SI system (5 percent), while for the MCFC-1PL and 2PL systems the reduction is very small (less than 2 percent).

This different behavior can be explained taking into account that when part of the fuel is burnt in the ECB the exhaust gas temperature at the GT inlet increases and also the turbine outlet temperature. Due to these modifications the steam maximum temperature can also be increased. Nevertheless the HRSG performance can be optimised only if the steam pressure can be chosen without the MCFC-CU operative pressure constraint. In fact in the MCFC-SI case the change in the steam temperature cannot be compensated for the pressure modification (for 1PL and 2PL such a choice is possible).

Another important aspect correlated to the use of post-combustion layout is the modification of the power ratio between cell and bottoming system. In fact the specific work increase is only due to the increase of the bottoming system power (see Fig.

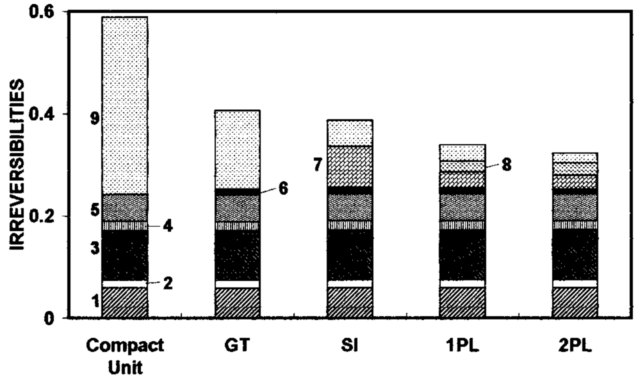

Fig. 10 Irreversibility rate distributions: 1=fuel cells; 2=SHR; 3=ECB and CCB; 4=blowers; 5=gas mixing; 6=gas turbine; 7=HRSG; 8=steam turbine; 9=stack

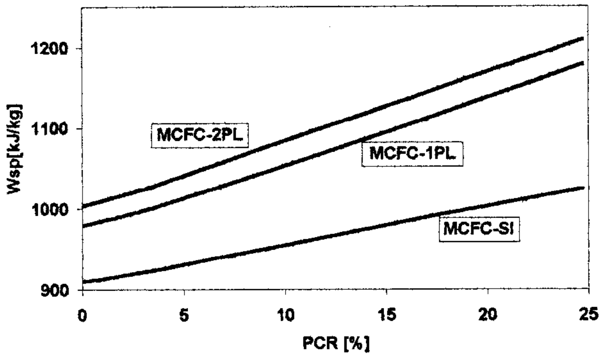

Fig. 11 MCFC combined cycle specific work versus PCR

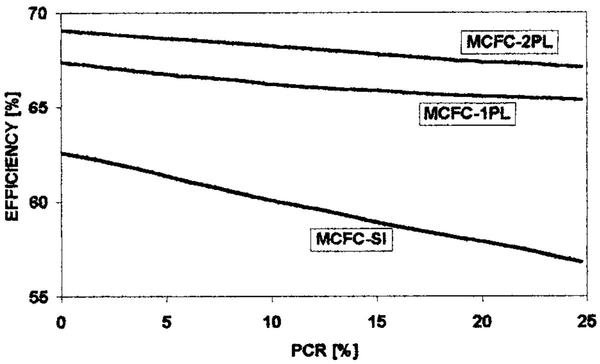

Fig. 12 MCFC combined cycle efficiency versus PCR

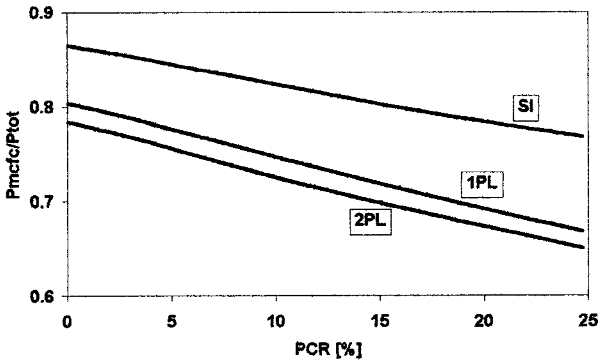

Fig. 13 MCFC power to plant power ratio versus PCR

13). This parameter is particularly important from the economic point of view as already shown by the authors for SOFC-GT plants ([8]). Taking into account that the MCFC cost is, at the moment, higher than the cost of bottoming systems, a capital cost reduction can be obtained through the use of post-combustion increasing of the power generated in the low cost section and reducing the cell power, size, and cost. Nevertheless, for the evaluation of the COE (cost of electricity, c$/kWh) it is necessary to also take into account the operating costs (fuel, maintenance, etc.), mainly dependent on plant efficiency. Thus the effect on the PCR is the opposite: reduction of capital cost, increase of fuel consumption (efficiency reduction): the problem can be completely solved using the thermoeconomic approach, as already carried out for the IRSOFC-GT systems by the authors ([13]). However, this aspect is beyond the scope of this work.

Finally, Fig. 14 shows a comparison between the performance of two classical energy conversion systems (gas turbines and combined cycles) and the systems here proposed. In the cited figure the plant efficiency is plotted versus the plant specific work. In the field of gas turbine based cycles specific work (kW/kg/s) is one of the more used parameter as discussed by Wilson and Korakianitis [9] and by Massardo [10]. The data shown for gas turbine and combined cycle are representative of the state of the art. For the power range here investigated (10–15 MW) the data shown are probably overestimated. The data for the MCFC-CU is reported to fix the starting data of the combined cycles here investigated. The increase of the specific work and efficiency when the bottoming cycles are used are both evident. Also the influence of the PCR is reported in the figure, as already discussed.

In conclusion, from the figure it is evident that there is the possibility to use energy conversion systems operating with efficiency higher than 65 percent and specific work higher than 1000 kJ/kg in the power range already discussed (10–15 MW) using MCFC-CU and mature technology for the bottoming system.

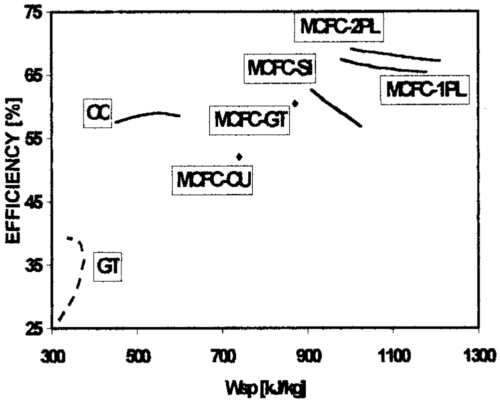

Fig. 14 Comparison between GT, combined cycle, and MCFC combined cycles

Conclusions

In this paper the assessment of the performance of a molten carbonate fuel cell (MCFC) system with external sensible heat reformer has been described on the basis of two mathematical models developed by the authors.

Also the assessment of the thermodynamic performance of a number of MCFC combined cycles using gas turbine, steam injection, or steam turbines has been presented.

The main conclusions of this work are as follows:

(i) The MCFC models are reliable and their results agree well with the available experimental data.

(ii) The complex model can be very useful for cell development, and for the definition of apt constraints when the simplified model is utilized.

(iii) The MCFC-CU system concept has been considered for coupling with several bottoming cycles. In this way the exhaust gas temperature and pressure are always fixed.

(iv) The analysis carried out with the 5.1 version of the TEMP code, including modules for MCFC, SHR, ECB, CCB, has been restricted to configurations where the MCFC-CU is the topping system.

(v) This assumption allows the MCFC-CU operating conditions to be maintained fixed. In this way all the technical aspects addressed for the CU development are unchanged.

(vi) The size of the plants here investigated is in the range 10–15 MW. The cell size is about 10 MW, and this power can be obtained through the use of several CU (20 CU each of 500 kW).

(vii) The efficiency of the MCFC combined cycles is considerably higher (60–69 percent) than simple cycle gas turbine and combined gas and steam cycles.

(viii) Also the MCFC combined cycle specific work is higher than the data of gas and combine cycles.

(ix) The power is mainly generated by the MCFC section (about 80–85 percent). However, when a post combustion solution is used the bottoming cycle power can be increased and the cell power can be reduced to 70–75 percent.

(x) CO_2 and NO_x emissions are particularly reduced because of the very high efficiency level (CO_2) and the low operating temperature of MCFC electrochemical device and catalytic burners (NO_x).

In this work it has been demonstrated that MCFC combined cycles could be very attractive, although reliability and durability comparable with conventional power, and low cost, essential to market entry, have still to be proved. From this point of view the thermoeconomic investigation of such systems, also taking into account the environmental impact (environmental cost internalisation), should be the next step of this activity.

Acknowledgments

Thanks are expressed to A. Torazza of Ansaldo Ricerche for the permission to publish the data of the MCFC Compact Unit. The authors also thank P. Bedont and M. Pistoni for their useful help during this work.

The work has been carried out with the economic support of the MURST of Italy (Cofinanziamento 1999).

Nomenclature

1PL = one pressure Level
2PL = two pressure Level
AAR = anode to anode recycle
ACR = anode to cathode recycle
CCB = cathode catalytic burner
CCR = cathode to cathode recycle
CU = compact unit

ECB = exhaust catalytic burner
EFF = efficiency
GT = gas turbine
HRSG = heat recovery steam generator
IRSOFC = internal reforming solid oxide fuel cell
m = mass flow rate
MCFC = molten carbonate fuel cell
P = electrical power
PCR = post-combustion ratio
p_i = partial pressure of component i
R_{tot} = total electrical resistance
SHP = steam high pressure
SHR = sensible heat reformer
SI = steam injection
SLP = steam low pressure
ST = steam turbine
T = temperature
V = voltage
W_{sp} = specific work

References

[1] Parodi, F., Alvarez, T., Bosio, B., Passalacqua, B., Simon, J., and Zappaterra, M., 1999, ''Recent Achievements of MOLCARE Programme: Conditioning and Preliminary Testing of the 100 kW MCFC Stack,'' 3rd IFCC, Nagoya Congress Center, Japan.

[2] Torazza, A., Rocchini, G., and Scagliotti, M., 1998, ''Present Status of Some Technological Activities Supporting MOLCARE Project,'' *Proc. of Fuel Cell Seminar*, Palm Spring, Orlando, FL, p. 390.

[3] Bosio, B., Costamagna, P., Parodi, F., and Passalacqua, B., 1998, ''Industrial Experience on the Development of the Molten Carbonate Fuel Cell Technology,'' J. Power Sources, **74**, No. 2, pp. 175–187.

[4] Bosio, B., Costamagna, P., and Parodi, F., 1999, ''Modeling and Experimentation of Molten Carbonate Fuel Cell Reactors in a Scale-Up Process,'' Chem. Eng. Sci. **54/13**, pp. 2913–2922.

[5] Bedont, P., 1999, ''Modellizzazione di celle a combustibile a carbonati fusi ed integrazione con impianti per la conversione di energia,'' degree thesis, University of Genoa, Genoa, Italy.

[6] Agazzani, A., and Massardo, A. F., 1997, ''A Tool for Thermoeconomic Analysis and Optimization of Gas, Steam and Combined Plants,'' ASME Trans. J. Eng. Gas Turbines Power, **119**, pp. 885–892.

[7] Massardo, A. F., and Scialo, M., 2000, ''Thermoeconomic Analysis of Gas Turbine Based Cycles,'' ASME J. Eng. Gas Turbines Power, **122**, pp. 27–35.

[8] Bosio, B., Parodi, F., Arato, E., and Costamagna, P., 1999, ''Process Analysis of a Molten Carbonate Fuel Cell Pilot Plan,'' *Proc. of ICheaP4 Conference*, Firenze (Italy), pp. 651–654.

[9] Arato, E., Bosio, B., Massa, R., and Parodi, F., 1999, ''From Square to Rectangular Cells in a MCFC Scale-Up Process: Experimental and Simulation Results Optimizing Operating Conditions,'' Sixth Grove Fuel Cell Symposium, London.

[10] Wilson, D. G., and Korakianitis, T., 1997, *The Design of High Efficiency Turbomachinery and Gas Turbines*, Prentice-Hall, Englewood Cliffs, NJ.

[11] Massardo, A. F., 1999, ''Gas Turbine Power Stations,'' *John Wiley Encyclopedia of Electronic and Electrical Engineering*, J. Webster, Ed., Vol. 8, John Wiley and Sons, New York, pp. 258–270.

[12] Massardo, A. F., and Lubelli, F., 2000, ''Internal Reforming Solid Oxide Fuel Cell—Gas Turbine Combined Cycles (IRSOFC-GT). Part A: Cell Model and Cycle Thermodynamic Analysis,'' ASME J. Eng. Gas Turbines Power, **122**, pp. 664–671.

[13] Massardo, A. F., and Magistri, L., 2001, ''Internal Reforming Solid Oxide Fuel Cell—Gas Turbine Combined Cycles (IRSOFC-GT). Part B: Exergy and Thermoeconomic Analysis,'' ASME Paper No. 01-GT-0380.

Microturbine/Fuel-Cell Coupling for High-Efficiency Electrical-Power Generation

A. F. Massardo
DISMET
Universita di Genova,
Via Montallegro 1,
16145 Genova, Italy
e-mail: massardo@unige.it

C. F. McDonald
McDonald Thermal Engineering,
1730 Castellana Road,
La Jolla, CA 92037-3838
e-mail: kmcdonal@san.rr.com

T. Korakianitis
Washington University,
Cambus Box 1185,
St. Louis, MO 63130
e-mail: tk@me.wustl.edu

Microturbines and fuel cells are currently attracting a lot of attention to meet future users needs in the distributed generation market. This paper addresses a preliminary analysis of a representative state-of-the-art 50-kW microturbine coupled with a high-temperature solid-oxide fuel cell (SOFC). The technologies of the two elements of such a hybrid-power plant are in a different state of readiness. The microturbine is in an early stage of pre-production and the SOFC is still in the development phase. It is premature to propose an optimum solution. Based on today's technology the hybrid plant, using natural gas fuel, would have a power output of about 389 kW, and an efficiency of 60 percent. If the waste heat is used the overall fuel utilization efficiency would be about 80 percent. Major features, parameters, and performance of the microturbine and the SOFC are discussed. The compatibility of the two systems is addressed, and the areas of technical concern, and mismatching issues are identified and discussed. Fully understanding these, and identifying solutions, is the key to the future establishing of an optimum overall system. This approach is viewed as being in concert with evolving technological changes. In the case of the microturbine changes will be fairly minor as they enter production on a large scale within the next year or so, but are likely to be significant for the SOFC in the next few years, as extensive efforts are expended to reduce unit cost. It is reasonable to project that a high performance and cost-effective hybrid plant, with high reliability, will be ready for commercial service in the middle of the first decade of the 21st century. While several microturbines can be packaged to give an increased level of power, this can perhaps be more effectively accomplished by coupling just a single gas turbine module with a SOFC. The resultant larger power output unit opens up new market possibilities in both the industrial nations and developing countries. [DOI: 10.1115/1.1398552]

Introduction

The first generation of microturbines (25–75 kW), currently being introduced into the distributed electrical power generation market have thermal efficiency levels of about 28 to 30 percent based on state-of-the-art component technology. To advance significantly beyond this level will require an increase in turbine inlet temperature, this necessitating the use of ceramics in the hot-end components. However, ceramics technology is still in its infancy, and these components, including the combustor, turbine, and recuperator, currently lack the reliability mandatory for the power generation market.

Another power source, also viewed as being well suited to meeting the needs of small energy users, is the fuel cell. Based on today's technology, and due to their current high cost, it is likely to be several years before they are commercialized and available on a large scale. The impetuous for their cost reduction comes from the automobile industry.

The coupling of a microturbine with a high-temperature fuel cell has the potential for an efficiency of over 60 percent, and it is perhaps fortuitous that two of the basic parameters in both of these power generating systems are compatible. The clean effluent from a SOFC at about 900°C matches well the turbine inlet temperature of first generation microturbines. Also the value of the compressor discharge pressure of about 4 atmospheres facilitates increased power output and higher efficiency from a given SOFC frame size.

Existing microturbines, rated at approximately 50 kW and with a thermal efficiency of about 30 percent, are well suited to meeting the energy needs of small users such as schools, apartment buildings, restaurants, offices, and small businesses. New markets will open up when such a microturbine is coupled with a SOFC, to give an output of about 300–400 kW, at an efficiency of 60 percent. These include supermarkets, factories, malls, military bases, hospitals, villages, and small towns in the developing nations. High fuel utilization efficiency (about 80 percent) can be achieved if the high-grade waste heat is utilized. Applications include heating, drying, cooling, desalination, and several others.

This paper addresses the coupling of a state-of-the-art 50-kW microturbine with an SOFC in its present state of evolution. At this stage it does not necessarily represent an optimum approach from the features, systems, and parameter selection standpoints. It is a first step towards exploring the performance potential, and the identification of areas of technical concern, and mismatching problems that must be resolved before the hybrid cycle is developed, commercialized, and deployed for the electrical power generation and combined power and heat markets. A near emission-free advanced small microturbine/fuel cell plane, operating on natural gas, will offer users attractive possibilities in the first decade of the 21st century.

Microturbine Technology

Major Features. About a dozen companies are currently involved in the development of microturbines, and several of these ahave been discussed previously ([1]). To meet low-cost goals the engine configurations are kept as simple as possible, with many of the machines embodying the following features: (1) single-stage radial compressor, (2) single-stage radial inflow turbine, (3) direct-drive high-speed air-cooled generator, (4) multifuel com-

---

Contributed by the International Gas Turbine Institute (IGTI) of THE AMERICAN SOCIETY OF MECHANICAL ENGINEERS for publication in the ASME JOURNAL OF ENGINEERING FOR GAS TURBINES AND POWER. Paper presented at the International Gas Turbine and Aeroengine Congress and Exhibition, Munich, Germany, May 8–11, 2000; Paper 00-GT-175. Manuscript received by IGTI, Nov. 1999; final revision received by ASME Headquarters, Feb. 2000. Associate Editor: D. R. Ballal.

Table 1 Salient features of representative microturbine

Component	Feature
Thermodynamic cycle	Recuperated Brayton cycle
Normal rating, kW	50 (at 50/60 Hz)
Turbomachine type	Variable speed single shaft rotor
Rotational speed, rpm	Approx. 100,000
Compressor	Single stage radial flow
Compr. Pressure ratio	4.0
Turbine	Single stage radial inflow
Turbine inlet temp., °C	900
Combustor	Low emission annular or can type
Recuperator	Compact primary-surface type
Bearing type	Air bearings (journal and thrust)
Generator	Air-cooled two pole brushless permanent magnet type
Frequency control	Power electronics converter
Control system	Digital system
Natural gas supply	Electric motor-driven compressor
Machine start	Generator run as motor from battery
Technology status	State-of-the-art
Commercialization	1999-2000

bustor (conventional or catalytic), (5) compact high-effectiveness recuperator, and (6) a simple control system. An additional attractive feature is the use of air bearings to support the single high-speed rotor. A 30-kW microturbine with air bearings is currently in service ([2]). A lubricant-free bearing system is desirable for an application involving the coupling of a microturbine with a SOFC, since it obviates any oil or oil vapor contaminating the fuel cell during any severe system transients, or in the case of a bearing failure.

There is considerable flexibility in the packaging of the turbogenerator, particularly regarding the position and the installation of the recuperator ([3]). A separately mounted recuperator, say behind and inline with the rotating machinery, with external ducts and manifolds, facilitates simple gas flow path coupling with the fuel cell vessel, as discussed in a later section. The salient features of a representative microturbine are given in Table 1.

State-of-the-Art Microturbine Performance. Large gas turbines have the advantage of both economies of performance and scale. The reverse is true for very small gas turbines. Compared with axial flow machines, microturbines with radial compressors and turbines have significantly larger aerodynamic efficiencies. This is a result of smaller blade heights, Reynolds number effects, tip clearance effects, manufacturing tolerances, and surface finish, all of which adversely impact efficiency. In addition, the geometries associated with small radial turbines make blade cooling very difficult, and thus advances in turbine inlet temperature are solely dependent on materials technology.

It is difficult for simple-cycle microturbines to achieve thermal efficiencies much above 20 percent ([4]). A recuperator is mandatory for microturbine efficiencies of 30 percent and higher ([5,6]). The recuperator in the coupled plant mode allows air at a higher temperature to be transported to the SOFC.

A convenient and simple way of portraying the effect of turbine inlet temperature and recuperator effectiveness on thermal efficiency for low-pressure-ratio microturbines, based on radial flow turbomachinery, is shown in Fig. 1. Regime Number 1 is representative of first generation state-of-the-art operating recuperated microturbines, that are well suited for coupling with a SOFC. With a compressor pressure ratio of 4, a turbine inlet temperature of 900°C, and a recuperator effectiveness of 0.87, the estimated thermal efficiency is 29.5 percent. Factoring in other aspects, including the generator and power conditioning efficiencies, and the power required for the fuel compressor, the overall efficiency of the stand-alone microturbine is 27 percent. A summary of the various microturbine parameters is given in Table 2. These parameters do not reflect a particular engine, but are viewed as being representative of a first generation 50 kW microturbine based on proven technology.

Microturbine Performance Evolution. The technology advancement projected trend line shown on Fig. 1 illustrates the microturbine potential for performance growth, and this is further illustrated in Fig. 2, which shows an evolutionary increase in both specific power and thermal efficiency.

In November 1997, the President's Committee of Advisors on Science and Technology, suggested that R&D be undertaken to achieve a microturbine efficiency goal of 50 percent by the year 2010 ([7]). Data in Figs. 1 and 2 indicate this goal is very ambi-

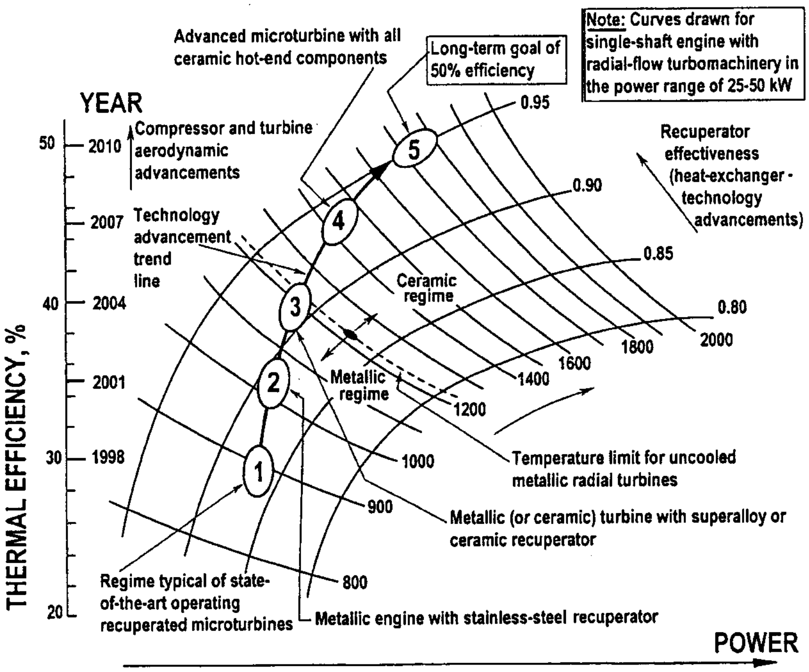

Fig. 1 Projected recuperated microturbine performance

Table 2 Microturbine operating conditions

Operating Mode	Gas Turbine Alone Combustion Mode	Coupled Gas Turbine and Fuel Cell
Technology status	State-of-the-art	Adv. applicn.
Thermodynamic cycle	Recuperated	Combined
Generator inlet temp., °C	15	15
Compr. temp. inlet/outlet, °C	18/194	18/194
Compr. flow, kg/sec	0.49	0.49
Compr. pressure ratio	4	4
Compr. efficiency, %	79.0	79.0
Turbine operating gas	Comb. products	SOFC effluent
Turbine inlet temp., °C	900 (from Comb.)	907 (from SOFC)
Turbine outlet temp., °C	637	651
Turbine flow, kg/sec	0.494	0.503
Turbine efficiency, %	84.0	84.0
Recuperator effectiveness	0.87	0.87
Recup. air temp. inlet/outlet, °C	194/577	194/591
Recup. gas temp. inlet/outlet, °C	637/254	651/254
Combustor efficiency, %	98.0	-
Mechanical efficiency, %	95.0	95.0
System pressure loss, %	10.0	15.0
Thermal efficiency, %	29.5	-
Generator efficiency, %	96.0	96.0
Power conditioning efficiency, %	95.0	95.0
Natural gas flow, kg/sec	0.0047	0.013
Gas compressor efficiency, %	30.0 (PR4.5)	50.0(PR4.5)
Gas compressor flow, kW	3.5	7.5
Compressed gas temp., °C	413	255
Gas turbine gross power, kW	53.5	62.5
Gas turbine power output, kW	50.0	55.0
SOFC power output, kW	-	334
Plant power output, kW	50.0	389
Plant overall efficiency, %	27.0	60.0
Heat recovery system in/out °C	254/175	254/50
Potential thermal kW in exhaust	40.0	112.0
Fuel utilization efficiency, %	50	80

tious and would require a significant increase in turbine inlet temperature, necessitating the extensive use of ceramics. The challenge in this regard is the recuperator, since ceramic technology for this under-developed component is still very much in its infancy ([8]).

While microturbine performance will surely increase in the next decade or so, it is the authors' view that the realization of even higher efficiencies, say in the low 60s, can best be achieved by coupling a microturbine with a high-temperature fuel cell.

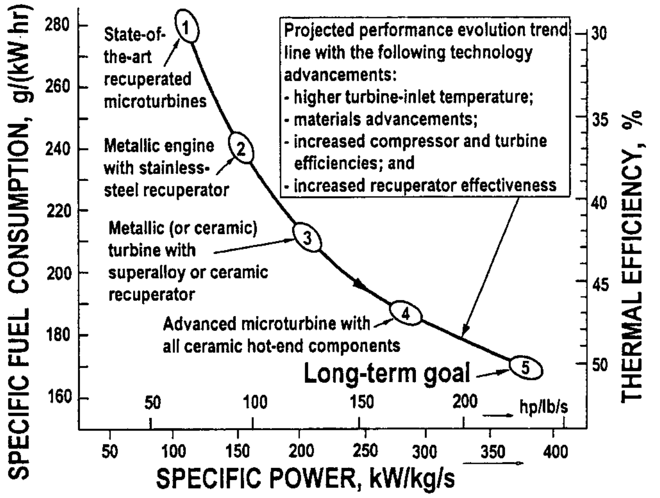

Fig. 2 Microturbine performance evolution

Fuel Cell Technology

There are several types of fuel cells being developed for a variety of applications ([9,10]) and these have been extensively discussed in the open literature.

The type best suited for coupling with a gas turbine is the SOFC. Unlike other variants, this fuel cell is entirely solid state with no liquid components. Operation at elevated temperature is needed to achieve the necessary level of conductivity in the cell's solid electrolyte for it to operate efficiently. With an outlet temperature in the range of 900–1000°C, the efficiency of the cell alone is about 50 percent. A 100 kW solid oxide fuel cell operating at atmospheric pressure has been in service since 1997 ([11]).

Typically the fuel cell system consists of SOFC generator modules in a parallel flow arrangement, with the number of standard modules being determined by the plant power requirement. The SOFC generator module embodies a number of tubular cells, which are combined to form cell bundle rows, several of which are arranged side by side to make up the complete assembly.

The tubular ceramic fuel cell has the oxygen electrode inside the tube and the hydrogen electrode outside the tube. These are separated by a solid electrolyte, which when heated to about 1000°C conducts oxygen ions from one electrode to the other. The fuel cell requires two gaseous fuel streams, oxygen, and hydrogen. Oxygen is supplied from the compressor discharge air. For the SOFC coupling with a microturbine the fuel is natural gas. The SOFC operates at sufficiently high temperature to incorporate an internal reformer within the pressure vessel. The exhaust anode gases are sufficiently rich in high temperature steam to provide all needed water to reform the natural gas. A recirculation loop within the vessel transports the water for the fuel reforming reaction. Radiated heat from adjacent bundles provides the exothermic reaction. Utilizing this heat along with the recycled steam and a catalyst, the natural gas is converted into a hydrogen-rich gas.

Fuel cell electrodes are adversely affected by the presence of sulfur, so for operation on natural gas a desulfurization unit is necessary. The sulfur emissions from this plant are virtually zero, and as will be mentioned in a later section, this has a positive aspect in terms of waste heat recovery, namely the low level of temperature to which the final exhaust gas can be discharged to the environment.

The high efficiency of the system means that less carbon dioxide is generated than in contemporary power plants. In addition, the fuel is oxidized electrochemically without any interaction with atmospheric nitrogen so negligible amounts of nitrogen oxide are discharged to the environment.

The SOFC has flexibility in terms of coupling with a gas turbine, since the number of modules can be selected to match the gas turbine power in the range of a few kilowatts to multimegawatt plants. In this paper, such a coupling is limited to a representative, and available 50 kW recuperated microturbine.

Microturbine/Fuel Cell Coupling

Background. The coupling of high temperature fuel cells with gas turbines is by no means new, and has been discussed for several years. Recent technical papers have covered a wide range of topics, these including the following: (1) systems involving midsized and large gas turbines ([12–14]); (2) dynamic modeling, performance, technical issues, and integration considerations ([15–19]); (3) microturbine specific studies ([20–21]); and (4) details of experimental programs to demonstrate the coupling of a microturbine with a SOFC ([22,23]).

These papers cover the topic in a comprehensive manner for a wide range of power applications, and include a variety of thermodynamic cycles including intercooling, recuperation, reheat, bottoming cycles, and cogeneration.

Hybrid System/Performance. The modeling and performance of the suggested hybrid approach is based on the utilization

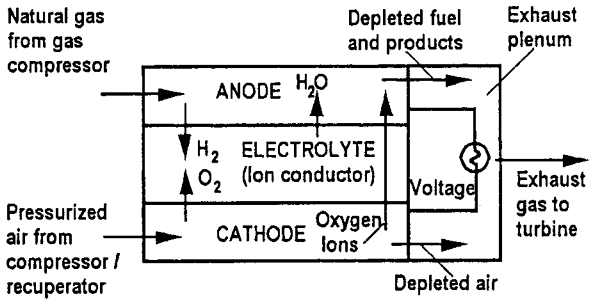

Fig. 3 Solid-oxide fuel cell (SOFC) principle/model

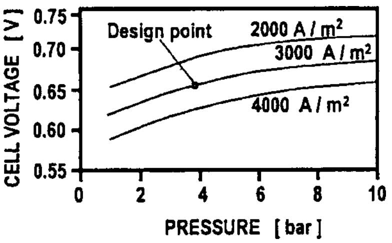

Fig. 5 Estimated solid-oxide fuel cell performance

of a systems computer code that has been discussed previously ([19]). A rather simplistic sketch illustrating the pressurized SOFC system is given in Fig. 3.

A simple flow schematic of the proposed hybrid system is shown in Fig. 4. Microturbines are being developed in the power range of 25–75 kW, and for the purpose of this study a representative 50 kW turbogenerator based on proven technology was assumed. The complete microturbine package is regarded as a stand-alone unit that can be operated independent of the fuel cell. However, plumbing and control modifications must be incorporated for the overall plant to operate in a hybrid mode.

At this stage, the basic parameters were not necessarily optimized, but rather selected to be in concert with available hardware. For example, operation at elevated pressure yields a higher voltage, at a given current, and this permits higher cell efficiency and greater output, with the optimum pressure perhaps being in the 5 to 10 atmosphere range. However, in microturbines with radial flow turbomachinery, the compressor pressure ratio is modest, with a representative valve being 4. The relationship between cell voltage, current density and system pressure is shown in Fig. 5. The thermal efficiency for a state-of-the-art microturbine with a turbine inlet temperature of 900°C, and a 0.87 effectiveness recuperator is 29.5% (Table 2).

The flow schematic shown in Fig. 4 represents the system in its simplest form, and it is recognized that more detailed analysis may necessitate changes that will make it more complex. A startup air heater is shown at the cell inlet. In its simplest form this could be an electric unit. For steady-state operation it is assumed that the heated air from the recuperator with a temperature of 591°C enters the cell directly.

Additions to the system for hybrid operation include the fuel heater, a natural gas desulfurizer, and a purge gas unit. New sections of ducting, together with various valves require alterations to the microturbine external plumbing, and replacement of the natural gas compressor as will be covered in a later section. The plant control system must also be updated.

A topic not discussed in detail in other papers is compressing the natural gas prior to its injection into the combustor or fuel cell. In the combustion mode the gas flow is low, and utilizing existing hardware the efficiency of the very small gas compressor is modest, this resulting in a discharge temperature of about 413°C for an assumed pressure ratio of 4.5. In the hybrid mode, the gas flow to the SOFC is higher, and an improved efficiency for the large compressor was assumed, this resulting in a discharge temperature of 255°C.

It is necessary to heat the natural gas to a higher temperature than this prior to its entering the cell anode. Utilizing a gas bleed from the turbine exit, the natural gas could be heated to about 600°C in a small heat exchanger. This could be further increased if necessary using an electric heater, the actual value being determined by what percentage of the heat addition is done within the cell. Using a bleed from the turbine inlet, the fuel could be heated to about 875°C, but this would require a very high temperature heat exchanger, and would penalize the turbine power. As will be mentioned in a later section a better and safer solution might be to use an electric heater.

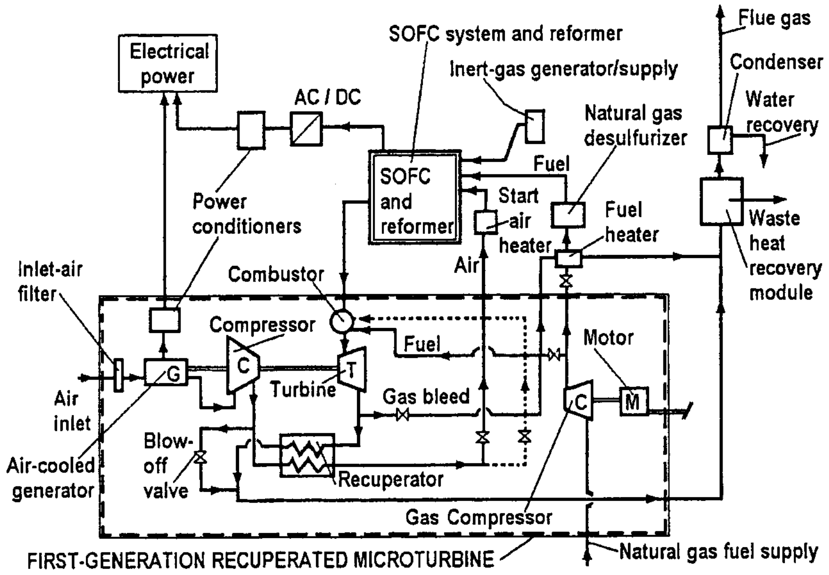

Fig. 4 Flow schematic of hybrid microturbine/fuel-cell power plant

Table 3 Fuel cell features/operating conditions

High Temperature Fuel Cell	Feature Parameter
Fuel cell type	Pressurized SOFC (PSOFC)
Technology/status	Advanced technology
Fuel	De-sulfurized natural gas
Reformer type	Radiant heated internally integrated
Operating pressure, atm	Approx. 4
SOFC current density, Å/m^2	3000
SOFC voltage, volts	0.66
SOFC pressure loss	5
SOFC heat loss, %	2
Airflow, kg/sec	0.49
Air inlet temperature, °C	591 (from recup.)
Fuel flow, kg/sec	0.013
SOFC effluent temp., °C	907
SOFC effluent (by volume)	H_2O 8% CO_2 4%, N_2 74%, O_2 12%, CO 1%, H_2 1%
SOFC power, kW	352
Power conditioning eff., %	95
SOFC AC output, kW	334*

*Power for fuel gas compressor (7.5 kW) debited from microturbine output.

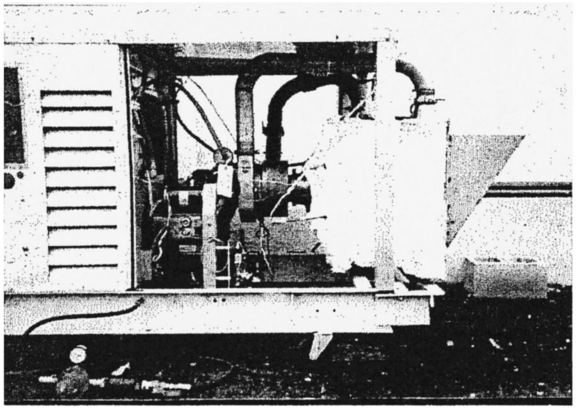

Fig. 6 Microturbine with compact rear-mounted recuperator installation (courtesy Elliott Energy Systems)

Utilizing the aforementioned code, a series of analyses were undertaken to select the fuel cell parameters for compatibility with a representative microturbine. The major features and operating conditions of the fuel cell are given in Table 3. When operating on the effluent from the SOFC the power from the microturbine would increase. This is a result of the higher mass flow rate, and the different fluid properties giving an increased enthalpy drop across the turbine. In this mode of operation the microturbine power would be 62.5 kW, and in subtracting the power required by the small gas compressor, the power output would be 55 kW. The power from the fuel cell is 334 kW, giving a total plant output of 389 kW, with an overall efficiency of 60 percent. This is not regarded as the optimum value, but rather is what was calculated from the systems model, and the assumption of utilizing state-of-the-art technologies. The gas outlet temperature from the recuperator to the heat recovery module is 254°C.

Hybrid System Operation. Detailed analyses of the various operating modes, including startup, steady-state, transients, load shedding, and shutdown are beyond the scope of this paper, but have been addressed previously ([22]).

The control system would be engineered to permit the microturbine to operate independent of the fuel cell. In the startup mode the microturbine would be brought up to full speed. Because of the recuperator thermal capacitance, it would likely take at least three minutes for the microturbine system to reach thermal equilibrium.

The first step towards initiating the hybrid mode of operation will be to purge the cell. In its simplest form the purge gas unit could be cylinders of an inert gas. In order to maintain acceptable temperature gradients and associated thermal stresses to prolong cell life, the temperature of the equipment within the pressure vessel will be brought up gradually in a controlled manner. The valve installed in the recuperator air outlet duct would then be modulated, and hot air bled to the cathode to bring the fuel cell, ducting, and vessel internals up to temperature.

The next operation involves supplying the cell cathode with the natural gas fuel. The efficiency of the small natural gas compressor is modest, and for a pressure ratio of 4.5 the discharge temperature would be about 255°C. Before entering the anode, the gas would be further heated using either a heat exchanger or an electric heater. The valve at the gas compressor exit would be modulated to gradually decrease the fuel flow to the microturbine combustor, and increase the flow to the fuel heater and SOFC. During the combustion mode, a small gas flow bled from the turbine exit would flow through the heat exchanger to heat the fuel before it enters the cell vessel. With SOFC light off the electrochemical process would start, and the fuel cell gradually brought up to full power. During this transition period there will likely be a drop in turbine speed and power output as the SOFC temperature increases. To avoid compressor surge during this transient (and others) a blow-off valve is incorporated in the compressor discharge. Once the SOFC reaches thermochemical equilibrium, the microturbine would return to full power, now operating on the cell effluent.

The above process would be reversed for the system shutdown. Following cessation of flow to the microturbine combustor, the temperature of the complete system would be brought down to a low level in a controlled manner to avoid thermal stresses. If an external electric power source is available, or by using the battery, the microturbine could be motored (by means of the generator) to gradually cool down the system.

Installation. The merits of using an annular recuperator ‘‘wrapped-around’’ the rotating machinery have been discussed previously ([24]). These include good gas flow paths with minimum pressure losses, elimination of external ducts and bellows, and the realization of a very compact turbogenerator.

Because of the ‘‘buried’’ nature of the package it would be difficult to couple it with the fuel cell pressure vessel.

For the hybrid plant, it is better to utilize a microturbine configuration in which the recuperator is installed behind the turbomachinery. An example of this type of installation is shown in Fig. 6. The external ducts are accessible, and could be simply replumbed to incorporate the transition sections (incorporating the necessary valves) to couple the turbogenerator with the fuel cell vessel.

Waste Heat Utilization. In the hybrid mode the temperature of the gas leaving the recuperator is about 254°C. A waste heat module can be included to utilize this thermal energy after the power cycle. Depending on the end user, this could include the generation of low-grade steam, hot-water supply, chiller, hot-air supply for drying, and desalination.

Since the natural gas has been desulfurized before entering the fuel cell, there is no concern about sulfuric acid formation and corrosion in the exhaust system (as for combustion turbines), and the final discharge temperature can be reduced to a low value. If the discharge temperature to the atmosphere was 50°C, the available thermal energy in the exhaust would be about 112 kW. The overall fuel utilization efficiency of the hybrid plant would be about 80 percent.

Downstream of the heat recovery module a flue gas condenser would be utilized. This would facilitate water recovery from the exhaust gas prior to discharge to the environment. In some applications, this recovered water could have economic worth, particularly in arid regions.

Hybrid Plant Cost. There is a paucity of definitive cost data in the open literature for both microturbines and fuel cells. The ranges of the former is \$300–400/kW, and \$1000–4000/kW for the latter. In light of this, establishing realistic capital and power generating costs for the hybrid plant was considered beyond the scope of this paper. Further, really meaningful costs for commercial units must come from industry, and even these are premature today since development programs are still in progress for both microturbines and SOFCs.

Systems Mismatching/Areas of Concern

In this paper it has been assumed that an essentially off-the-shelf microturbine will be used and a custom built SOFC generator will be coupled with it. Understanding the operation of the overall plant is complex. Issues such as system control, startup and shutdown, load following, turndown capability, load shed, systems dynamics, transients, and upset conditions, and safety have been addressed recently ([13]). A better understanding of these will be realized with the imminent test of a coupled system ([22]), and this will facilitate more accurate system modeling in the future.

The following areas of concern relate to system hardware, mainly associated with the microturbine. In the hybrid mode the mass flow rate through the turbine will be slightly higher. The increased losses in the system, including the cell and ducts, will lower the turbine inlet pressure. The nondimensional turbine flow function $[W(T)^{(1/2)}/P]$ will thus be higher, and the turbine nozzle area may need to be changed. Also, will the vapor-laden SOFC effluent affect turbine performance, and are possible erosion and corrosion in the turbine of concern?

The SOFC natural gas fuel flow is greater than for the gas turbine combustion mode. The actual value is determined by the selection of the appropriate air/fuel ratio at the cell inlet. Accordingly, the small natural gas fuel compressor must either have the necessary extra capacity and power, or be replaced with a larger unit, with the latter being the most likely. Operating on SOFC effluent the turbine enthalpy drop is larger, and slightly more power will be generated, and a check if the generator and the power conditioning system can accommodate this is required.

The performance of the recuperator will be impacted, likely improved, when operating with the water vapor laden SOFC effluent on the hot side, and with a different thermal capacity rate ratio. Data from the aforementioned test will allow this to be realistically factored into an updated model.

It has been assumed that the temperature of the natural gas fuel will be increased in a heat exchanger utilizing a small hot gas bleed from the turbine exit (Fig. 4). Providing a heat exchanger to operate at elevated temperature is a challenge. To ensure safe operation it may be necessary to utilize a double-barrier leak-proof type of construction ([25]) to prevent a hazardous situation if the hot gas and the fuel came into contact as a result of a leak in the heat exchanger. An alternate approach may be to use an electric heater. The practicality and cost of this should be studied.

It can also be seen from the flow schematic (Fig. 4) that several valves are required in the coupled system. Several of these are modulated, and operate in a high temperature environment. The reliability of these valves is a concern.

From a black start it will likely take several minutes for the hybrid system to reach full-power equilibrium conditions. Perhaps technology transfer from automobile fuel and programs, although they are based on different systems, will contribute to the startup time being reduced. With a piston engine, automobile users expect full engine power available essentially at the turn of the ignition key. Efforts to match this with future vehicular fuel cell power plants are in progress in the automobile industry.

Many more areas of concern, and issues resulting from system and parameter mismatching, will become apparent during the initial testing of a hybrid system.

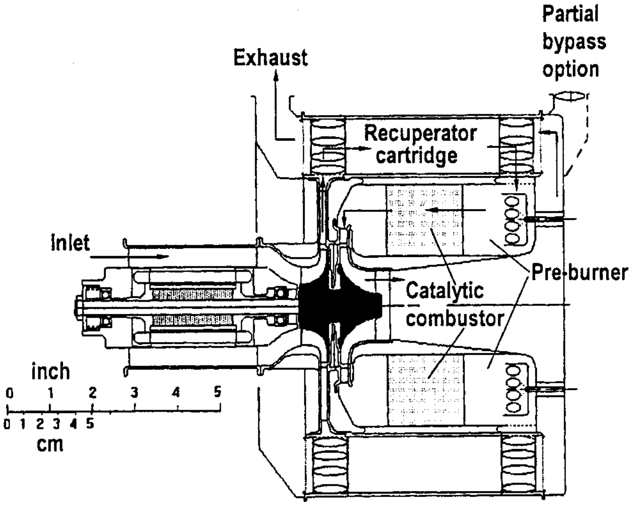

Fig. 7 Microturbine concept, power output 5 kW (courtesy C. Rodgers, ITC, 1999)

Future Developments

This paper has addressed the coupling of a representative first generation 50 kW microturbine with a SOFC to give a plant power output of 389 kW, which, while too great for an individual domestic dwelling, could be used in a wide range of facilities.

This paper has focused on a hybrid topping system based on a first generation microturbine and a SOFC. It is recognized that there are other variants that could have been considered, but were viewed as being beyond the scope of this paper, and could include the following, 1) a bottoming system in which the gas turbine exhaust is used as the working fluid of a fuel cell such as the molten carbonate fuel cell, 2) various cogeneration systems, and 3) more complex higher pressure ratio cycles utilizing multiple turbomachinery spools with the fuel cell split into high and low pressure generators.

With some vision, a projection has been made that by the end of the next decade, individual homes will have a personal turbine (PT) in their cellar ([26]). To meet this postulated market, studies are in an early stage of design definition ([27]) for a 5 kW recuperated personal turbine that could meet the total energy needs of an individual home, including electrical power, hot water supply, and air conditioning. It may also be possible by that time to couple such a small power plant with a superconducting-magnet electrical-energy-storage system.

Based on the use of proven technology, this small PT (shown in Fig. 7) has an estimated thermal efficiency of about 23%. The overall assembly is very compact, with a turbogenerator diameter of 230 mm, and length of 300 mm.

When coupled with a SOFC, such a hybrid power plant, with an output of about 30 kW, would have an overall efficiency on the order of 60%. Such a postulated small-scale coupling warrants a detailed engineering and economic assessment.

Summary

Current recuperated microturbines have a thermal efficiency of about 30 percent. This could be increased to about 40 percent with an all-metallic engine as shown in Fig. 1. To approach 45 percent or higher requires the use of ceramics in all of the hot end components. Currently, there is no evidence of an intensive development program in the U.S. to achieve this goal. A more realistic approach to establishing very high efficiency in small plants is the coupling of a microturbine with a high temperature fuel cell.

A representative first generation 50 kW microturbine based on proven technology has a thermal efficiency of 29.5 percent. Coupling this with a customized pressurized SOFC would give a hybrid plant with an output of about 389 kW, with an overall efficiency of about 60%. If the waste heat is effectively utilized the overall fuel utilization efficiency would be about 80%. It is germane to mention that other researchers have quoted efficiencies higher than these values. Indeed, this may well be the case for their specific modeling of an optimum system.

Both microturbines and fuel cells will shortly penetrate the distributed generation market to meet the needs of a variety of end users. In this paper it was felt to be premature, based on the current state of technology readiness, to identify an optimum hybrid plant in terms of parameter selection, efficiency, major feature selection, and cost. The system discussed is based on the best technology available today. This will evolve rapidly as experience is gained with microturbines that will enter commercial service within the next year or so, and from pressurized SOFCs that are still in an early stage of development.

An early assumption was made that an essentially off-the-shelf microturbine could be directly coupled with a SOFC. However, some areas of concern and possible mismatching were identified that would require changes to some of the components to facilitate the coupling. Many of these will become more apparent with the forthcoming test of a small hybrid plant.

It was convenient to select a power rating of 50 kW, since this is in the midrange of microturbines being developed; but the results presented are not unique to a specific power rating. Much smaller natural gas-fired microturbines, say as low as 5 kW, may become a reality within the next decade to meet the total energy needs of an individual home. The coupling of such a small personal turbine (PT) with a SOFC has incredible potential and would seem to be a topic that will surely be studied within the next year or so.

Acknowledgments

The first author thanks the University of Genoa and the MURST of Italy (Cofinanziamento 1999) for their financial support of this work. Thanks are expressed to Colin Rodgers (ITC) for discussions and guidance on the performance of very small gas turbines, and for his innovativeness in establishing a compact 5 kW personal turbine. The authors also thank Dr. Paola Costamagna (Princeton University) for her guidance on fuel cells. This paper has been enhanced by the inclusion of hardware photographs, and the authors express their thanks to those concerned, with credits being duly noted.

References

[1] de Biasi, V., 1998, ''Low Cost and High Efficiency Make 30 to 80 kW Microturbines Attractive,'' Gas Turbine World, Jan.–Feb., 1999, pp. 26–31.
[2] Craig, P., 1997, ''The Capstone Turbogenerator as an Alternative Power Source,'' SAE Paper No. 970202.
[3] McDonald, C. F., 2000, ''Low Cost Recuperator Concept for Microturbine Applications,'' to be published.
[4] Rodgers, C., 1997, ''Turbochargers to Small Gas Turbines,'' ASME Paper No. 97-GT-200.
[5] McDonald, C. F., 1996, ''Heat Exchangers for Very Small Gas Turbines,'' Intl. J. Turbo Jet Eng., **13**, No. 4, pp. 239–261.
[6] McDonald, C. F., 1999, ''Emergence of Recuperated Gas Turbines for Power Generation,'' ASME Paper No. 99-GT-67.
[7] R&D Magazine, 1998, ''Energy Spending Proposals Being Weighted by Congress,'' Apr., pp. 22–26.
[8] McDonald, C. F., 1997, ''Ceramic Heat Exchangers—The Key to High Efficiency in Very Small Gas Turbines,'' ASME Paper No. 97-GT-463.
[9] Moore, T., 1997, ''Market Potential High for Fuel Cells,'' EPRI J., **22**, No. 3, pp. 6–17.
[10] Scientific American, 1999, ''The Future of Fuel Cells,'' July, 72–83.
[11] Modern Power Systems, 1998, ''Westervoort SOFC: The Road to Commercialization,'' May, pp. 29–32.
[12] Bevc, F. P., et al., 1996, ''Solid Oxide Fuel Cell Combined Cycles,'' ASME Paper No. 97-GT-447.
[13] Stephenson, D., and Ritchey, I., 1997, ''Parametric Study of Fuel Cell and Gas Turbine Combined Cycle Performance,'' ASME Paper No. 97-GT-340.
[14] Veyo, S. O., and Lundberg, W. L., 1999, ''Solid Oxide Fuel Cell Power System Cycles,'' ASME Paper No. 99-GT-419.
[15] Liese, E. A., et al., 1999, ''Technical Development Issues and Dynamic Modeling of Gas Turbine and Fuel Cell Hybrid Systems,'' ASME Paper No. 99-GT-360.
[16] White, D. J., 1999, ''Hybrid Gas Turbine and Fuel Cell Systems in Perspective Review,'' ASME Paper No. 99-GT-410.
[17] Ali, S. A., and Moritz, R. R., 1999, ''The Hybrid Cycle: Integration of Turbomachinery With a Fuel Cell,'' ASME Paper No. 99-GT-361.
[18] Campanari, S., and Macchi, E., 1998, ''Thermodynamic Analysis of Advanced Power Cycles Based Upon Solid Oxide Fuel Cells and Gas Turbines and Ranking Bottoming Cycles,'' ASME Paper No. 98-GT-585.
[19] Massardo, A. F., and Lubelli, F., 1998, ''Internal Reforming Solid Oxide Fuel Cell—Gas Turbine Combined Cycles (IRSOFC-GT), Part A: Cell Model and Cycle Thermodynamic Analysis,'' ASME Paper No. 98-GT-577.
[20] Campanari, S., 1999, ''Full Load and Part Load Performance Prediction for Integrated SOFC and Microturbine Systems,'' ASME Paper No. 99-GT-65.
[21] Campanari, S., and Macchi, E., 1999, ''The Combination of SOFC and Microturbine for Civil and Industrial Cogeneration,'' ASME Paper No. 99-GT-84.
[22] Leeper, J. D., 1999, ''The Hybrid Cycle: Integration of a Fuel Cell With a Gas Turbine,'' ASME Paper No. 99-GT-430.
[23] de Biasi, V., 1999, ''250 kW Fuel Cell-Gas Turbine Hybrid to Start Operational Testing,'' Gas Turbine World, July–Aug., pp. 12–16.
[24] Rodgers, C., 1993, ''Small (10–200 kW) Turbogenerator Design Considerations,'' *ASME COGEN-TURBO, IGTI* Vol. 8, ASME, New York.
[25] McDonald, C. F., 1997, ''A Leak-Proof Plate-Fin Heat Exchanger Concept for Process Industries,'' *Proceedings of 32nd IECEC Conference*, Vol. 2, American Institute of Chemical Engineers, New York, pp. 1497–1502.
[26] Armstrong, L., 1999, ''Energy Ideas for the 21st Century,'' Bus. Week, **23**, p. 84.
[27] Rodgers, C., 2000, ''25-5 kW Microturbine Design Considerations,'' to be published.

A. Glahn
United Technologies Research Center,
411 Silver Lane, M/S 129-19,
East Hartford, CT 06108

S. Busam
Institut für Thermische Strömungsmaschinen,
Universität Karlsruhe,
Kaiserstr. 12,
Baden-Württemberg
76128 Karlsruhe, Germany

M. F. Blair
United Technologies Research Center,
411 Silver Lane, M/S 129-19
East Hartford, CT 06108

K. L. Allard
Pratt & Whitney,
400 Main Street, M/S 163–09,
East Hartford, CT 06108

S. Wittig
Institut für Thermische Strömungsmaschinen,
Universität Karlsruhe,
Kaiserstr. 12,
Baden-Württemberg,
76128 Karlsruhe, Germany

Droplet Generation by Disintegration of Oil Films at the Rim of a Rotating Disk

A fundamental study has been performed to examine oil film disintegration mechanisms at the rim of a rotating disk. The configuration investigated is an abstraction of one of the droplet generation sources in an aeroengine bearing compartment. The paper aims to contribute to both the determination of directly applicable droplet characteristics and the establishment of a database that can be used for the development of droplet generation models. The near-term objectives of the study are (i) to identify disintegration modes relevant with respect to aeroengine bearing compartment operating conditions, (ii) to determine droplet sizes under those operating conditions, and (iii) to measure individual droplet diameter/velocity relationships. The long-term objective is to incorporate this information into advanced CFD-based design tools. The disintegration modes identified here were similar to previously reported flow regimes generated by rotary atomizers. However, slightly different transition characteristics are documented for the turbine oil considered here, indicating a transition occurring at either higher speeds or higher flow rates. Droplet diameters and velocities are presented for relevant bearing compartment conditions. In this mode, droplet diameters appear to be insensitive to the volume flow rate, but show a finer atomization for increasing rotational speeds. Eventually a speed is reached beyond which no further droplet diameter reduction is obtained. For the first time, size class resolved droplet velocities are presented. A variation of operating parameters at a constant radial location does not have a significant impact on either the normalized droplet velocity or the flow angle. Radial traverses show a decrease of the droplet velocity with increasing distance from the rim of the disk and a transition from a more tangentially oriented droplet trajectory to a more radial motion.
[DOI: 10.1115/1.1400753]

Introduction

In addition to striving for higher reliability and better maintainability, the major development goal for new engines is still the desire to increase the gas turbine's efficiency. This goal is accomplished by increases of both the overall pressure ratio and the turbine inlet temperature. In combination with the high rotational speeds of the turbine rotor, these conditions result in specific problems within the heat management of the engine's lubrication system ([1]). More heat is generated due to enhanced churning and windage inside bearing compartments and gearboxes as well as due to heat conduction from the hot turbine disks. Furthermore, lubrication loop/fuel heat exchange offers less potential due to the efficiency increases and the resulting reductions of the specific fuel consumption. In order to avoid an overheating of the lubricant, which would have a variety of negative consequences and could lead to a catastrophic failure of the engine, additional air coolers have to be integrated into the oil system. However, this technique comes with the penalty of higher parasitic losses and limitations due to the additional weight and volume of coolers, pumps, and filters. As a consequence, the design margin for the lubrication system becomes smaller and design tool improvements are a stringent requirement to meet the challenges of current and future engine developments.

In recent years, progress has been made on the identification of bearing compartment flow patterns ([2]) the characterization of oil film flows ([3,4]), and the heat transfer along the internal bearing chamber housing walls ([5–7]). Droplet flows in a rotating, annular two-phase flow environment were studied for air/water mixtures at low speeds by Zaidi et al. [8] Although encouraging and an important step towards a physics-based bearing compartment design process, as opposed to purely empirical approaches, the results obtained so far were taken for simplified geometries and do not reflect the extremely complicated designs found in actual engines. A viable approach towards an improved bearing compartment design would be to use CFD methods to predict the two-phase air/oil flow in lubrication system components. A study presented by Glahn et al. [9] suggested the feasibility of such an approach. However, a prerequisite for a successful implementation of these tools into a standard design environment is the availability of boundary conditions and the development of submodels which describe the complex phase interaction mechanism and atomization effects prevailing in these parts.

As the first phase of a multiyear, fundamental investigation into generic oil system atomization processes, the current study examined the disintegration of oil films at the rim of a rotating disk. The objectives were as follows: (i) to identify disintegration modes relevant with respect to aeroengine bearing compartment operating conditions, (ii) to determine droplet sizes under those operating conditions, and (iii) to measure individual droplet diameter/velocity relationships.

The current experimental paper aims to contribute to both the definition of directly usable droplet characteristics and the establishment of a database that can be used for analytical model development. Prior to the discussion of experimental findings, which will address all of the above-mentioned issues, basic atomization processes at rotating surfaces are described. The experimental setup developed and built for this task is introduced and experimental techniques for flow visualization and individual droplet diameter/velocity measurements are described briefly.

Contributed by the International Gas Turbine Institute (IGTI) of THE AMERICAN SOCIETY OF MECHANICAL ENGINEERS for publication in the ASME JOURNAL OF ENGINEERING FOR GAS TURBINES AND POWER. Paper presented at the International Gas Turbine and Aeroengine Congress and Exhibition, Munich, Germany, May 8–11, 2000; Paper 00-GT-279. Manuscript received by IGTI, Nov. 1999; final revision received by ASME Headquarters, Feb. 2000. Associate Editor: D. R. Ballal.

Experimental results are presented in terms of samples from the visualization work, a disintegration map, characteristic spray diameters as a function of rotational speed and flow rate, and comparisons with an empirical droplet size correlation available from rotary atomizer studies. Droplet-size-dependent velocities, which are available for the first time for these applications, will be presented and discussed for independently varied operating parameters.

Rotary Atomization

Phenomenological Description. Remarkable similarities can be found between some of the basic flow features expected to exist in bearing compartments and the flow in rotary atomizers, which are used in chemical engineering and process technology. Lefebvre [10] gives an overview on the working principle and summarizes performance correlations for this kind of atomizer.

In rotary atomizers, liquid is fed onto a rotating surface, e.g., a flat disk, where it spreads out under the action of the centrifugal force. Several mechanisms of atomization are observed, depending on the flow rate of the liquid and the rotational speed of the disk. At low values for both parameters, the liquid spreads out across the surface and is centrifuged off as discrete drops of uniform size. This phenomenon is named direct drop formation. Droplets generated by this type of disintegration are shown in Fig. 1(*a*) which was obtained within this study for the atomization of lubrication oil (Mobil Jet 2) at a temperature of $T_{\mathrm{oil}}=295\,\mathrm{K}$, i.e., for a highly viscous fluid.

If either the flow rate or the rotational speed is increased, ligaments are formed which are converted into a series of fine drops of fairly uniform size. The process is a discontinuous one and occurs from place to place at the periphery of the rotating cup or disk. The number of ligaments increases with increasing flow rate up to a maximum value, beyond which it remains constant. The increase in flow rate does not change the atomization process in principle, except the ligaments, which are formed along the entire periphery, are larger in diameter. This process is termed atomization by ligament formation and is shown in Fig. 1(*b*).

With further increases in flow rate or speed, the condition is eventually reached where the ligaments can no longer accommodate the flow of liquid. A thin continuous sheet is formed that extends radially outward from the rim of the disk until an equilibrium is reached, at which the surface tension force at the free edge is equal to the kinetic energy of the advancing liquid sheet. A thick film is produced, which again disintegrates into ligaments and drops. However, the ligaments are formed in an irregular manner that results in a larger variation in drop sizes. This process is referred to as atomization by film formation and is shown in Fig. 1(*c*).

Critical Flow Rates. For practical applications, it is important to identify the disintegration mode prevailing at a given set of operating conditions and, even more important, to characterize the spray generated. Several empirical and semi-empirical correlations have been proposed to calculate the critical flow rates corresponding to the transition from one mode of atomization to another ([10]). The usage of the available database and correlations derived from it is problematic due to strong differences in geometry and fluid properties. More importantly, none of the studies known to the authors considers a sufficient range of rotational speeds which makes an extrapolation difficult. Therefore, own investigation were required to examine the quality of available correlations with respect to typical bearing compartment conditions. However, a correlation proposed by Matsumoto et al. [11] for the transition from direct drop to ligament formation,

$$V^{+}=0.0333\cdot \mathrm{On}^{-0.9}\cdot \mathrm{We}^{*\,-0.85} \tag{1}$$

and a proposal made by Hinze and Milborn [12] for the transition from ligament formation to film formation,

$$V^{+}=0.5083\cdot \mathrm{On}^{-0.333}\cdot \mathrm{We}^{*\,-0.60}, \tag{2}$$

were included in the analysis and considered as a reference to our own investigations.

Note that both Eq. (1) and Eq. (2) were rearranged slightly from the form given in the original papers to obtain nondimensional parameter groups, which are commonly used in atomization, namely the modified Weber number,

$$\mathrm{We}^{*}=\frac{1}{8}\,\frac{\rho_L\omega^2D^3}{\sigma}.$$

and the Ohnesorge number.

$$\mathrm{On}=\frac{\mu_L}{\sqrt{\rho_L\cdot D\cdot\sigma}}.$$

The asterisked Weber number, which is the ratio of destabilizing aerodynamic forces to stabilizing surface tension forces, refers to the fact that it was defined with the liquid density, ρ_L, rather than the density of the gaseous phase. The Ohnesorge number summarizes fluid properties, which have an impact on the atomization process. In addition, both equations use a nondimensional flow rate defined as follows:

$$V^{+}=\frac{\rho_L q^2}{\sigma\cdot D^3}.$$

Using Eqs. (1) and (2), a disintegration map can be obtained to identify breakup mechanism as a function of operating conditions. An example is shown in Fig. 2.

The exponential relationships shown in Fig. 2 delineate the boundaries of the three disintegration modes in terms of flow rate (x-axis: $V^{+\,1/2}\propto q$) and rotational speed (y-axis: $\mathrm{We}^{*\,1/2}\propto\omega$). Note that Eqs. (1) and (2) have different exponential relationships between flow rate and property group ($V^{+}\propto \mathrm{On}^{m}$) and, therefore, the actual representation of Eq. (1) and the comparison shown in Fig. 2 holds only for the specified temperature.

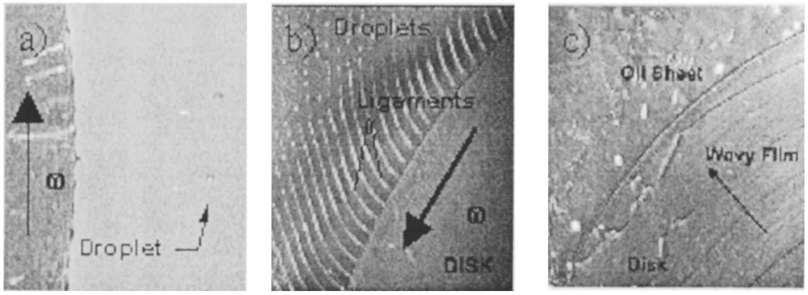

Fig. 1 Droplet disintegration modes; (*a*) direct drop formation, (*b*) ligament formation, (*c*) film formation

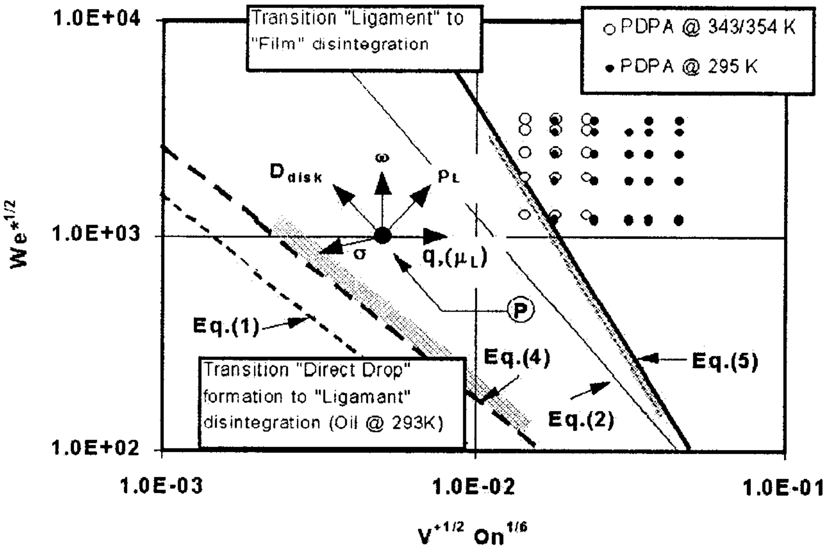

Fig. 2 Droplet disintegration map

Considering a given operating point P, it might be interesting to know if the disintegration mode changes with any variation of fluid properties or geometrical and experimental boundary conditions. The impact of flow rate and speed has already been discussed with the phenomenological description of the atomization processes. Figure 2 illustrates again that increases for both parameters tend to shift the breakup mechanism towards film formation.

Furthermore, effects of fluid properties have been illustrated: Higher density will make film formation more likely, whereas a higher surface tension, as expected, will be able to maintain ligament (or direct droplet) formation at higher flow rates and speeds. Viscosity tends to shift the disintegration mechanism towards film formation, but the effect is much smaller than the impact of a flow rate increase ($\propto \mu^{1/6}$). It is interesting to note that variations of the driving geometrical parameter, namely the disk diameter, move the operating point towards higher Weber numbers, but also towards lower nondimensional flow rates. Thus, the operating point moves parallel to the transition curves and the disintegration mode is not expected to change due to this variation.

Based on these observations, a simple test rig was designed with the goal to simulate relevant engine conditions in terms of Weber numbers and nondimensional flow rates. The rig and the measuring techniques applied are described in the next section.

Experimental Setup and Techniques

Test Rig. The first goal within this experimental study was to identify oil film breakup mechanisms at rotating surfaces for relevant bearing compartment conditions. Though Fig. 2 defines transition curves between individual modes, it had to be validated for lubrication oil and high rotational speeds. Furthermore, it had to be checked whether or not all disintegration modes occurring for turbine oil were identified. In order to cover a large portion of the disintegration map for these validations, the flow rate-property group, $V^{+1/2}\mathrm{On}^{1/6}$, can be easily varied by adjusting the volumetric oil flow rate. However, the physical dimensions and the rotational speed of the rig set the maximum Weber number. Both parameters had to be chosen such that two goals were met: (i) to achieve modified Weber numbers relevant for bearing compartments and (ii) to aim for a simple rig design that allows full optical access for droplet sizing and velocimetry.

Using actual engine lubrication oil for the current fundamental tests and considering that density and surface tension are only weakly dependent on temperature, engine Weber numbers are obtained for

$$\frac{\mathrm{We}^*_T}{\mathrm{We}^*_E}=1\approx\left(\frac{\omega_T}{\omega_E}\right)^2\left(\frac{D_T}{D_E}\right)^3. \tag{3}$$

Equation (3) suggests that it would be favorable to simulate the modified Weber number by aiming for a higher disk diameter. Increasing the disk diameter allows the rotational speed to be held at moderate levels, allowing a much simpler design. A disk diameter of 0.2 m (7.874 in.) and a maximum speed of almost 6000 rpm set the maximum Weber number for this investigation to about $1.5\cdot 10^7$. The actual test rig is shown in Fig. 3. The disk is supported in a cantilever arrangement in order to have a flush, fully accessible disk face. The shaft, positioned by spindle bearings, is driven by an electro-motor in combination with a flexible coupling and a flat belt. The disk is located in a stationary housing with an inner diameter of 0.301 m (11.85 in.). It consists of an aluminum frame supporting a transparent thermoplastic that allows optical access throughout the whole circumference.

Oil is pumped out of a reservoir through an electrical oil heater ($T_{\mathrm{max}}=473\,\mathrm{K}$ for $=0.1$ kg/s) into the rig. It is fed along the centerline onto the spinning disk using a tube with an inner diameter of $6\cdot 10^{-3}$ mm. Atomized oil is collected at the stationary, trans-

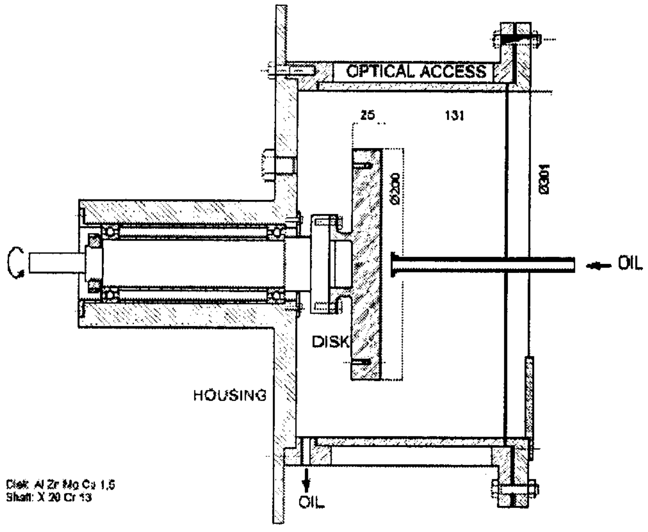

Fig. 3 Test rig

parent housing walls. Gravitation forces the oil to flow downward into the oil sump from where it is drained via holes back into the reservoir. The oil flow rate is bypass controlled.

Measuring Techniques. The experimental objectives of this study, namely the identification of disintegration modes and the quantitative characterization of the various modes, required applying techniques for flow visualization as well as laser-Doppler techniques for the droplet sizing and velocimetry.

For the first task, stroboscopic illumination along with a simple video camera was used to obtain a detailed documentation of oil flow patterns. All flow phenomena were monitored on a screen, recorded on videotape, and examined in detail using digital picture processing.

A single particle counter, Aerometrics' PDPA, was used for the measurement of droplet sizes and velocities. In recent years, the PDPA has become a standard technique for atomization studies. Thus, a lengthy description of the measuring principle is not included here and the interested reader is referred to the specific literature (e.g., [13]). However, the adaptation of this measuring technique to the current test is special because it uses a backscatter arrangement at an off-axis angle of 130 deg. Measurements in the reflection mode were possible due to the fact that refractive indices for oil are greater than 1.4. As a consequence the region between the first and second rainbow, the so-called Alexander's darkband, opens and measurement configurations with negligible Gaussian beam and slit effects are feasible. A comprehensive analysis of this configuration is given by Willmann et al. [14].

Experimental Results

Flow Visualization. Flow visualization studies were performed following two test procedures: (i) a given flow rate was adjusted and droplet generation mechanism were identified and recorded for various speed settings; (ii) the rotational speed was prescribed and the flow regimes were characterized as a function of flow rates. A total of 62 different operating conditions were examined. The rotational speed was varied in the range of $250\,\mathrm{rpm} \leqslant n \leqslant 5000\,\mathrm{rpm}$, whereas flow rates were varied within $1\,\mathrm{l}/h \leqslant q \leqslant 120\,\mathrm{l}/h$ $(2.78\cdot 10^{-7}\,\mathrm{m}^3/\mathrm{s} \leqslant q \leqslant 3.33\cdot 10^{-5}\,\mathrm{m}^3/\mathrm{s})$. Fluid property variations were achieved by setting two different temperature levels, namely $T_{\mathrm{oil}} = 295\,\mathrm{K}$ and $T_{\mathrm{oil}} = 364\,\mathrm{K}$. Typical samples from the flow visualization work have already been presented in Fig. 1. The major result of this part of the investigation was the revision of the disintegration map.

For the sake of clarity, instead of individual marks pointing at certain disintegration modes as a function of operating conditions, only the transition lines and bands illustrating the experimental scatter were included in the disintegration map given in Fig. 2. In comparison with Eqs. (1) and (2), this study suggests slightly modified characteristics, which shift the transition lines towards higher flow rates or speeds. The following equations, derived from modifications of the empirical correlation coefficients, were found to give a better description of the transition for the current application:

Direct drop to ligament formation,

$$V^+ = 0.0854\cdot \mathrm{On}^{-0.9}\cdot \mathrm{We}^{*-0.85}, \tag{4}$$

and ligament formation to film formation,

$$V^+ = 0.1378\cdot \mathrm{On}^{-0.33}\cdot \mathrm{We}^{*-0.435}. \tag{5}$$

As another important result, it was confirmed that no other than the three modes described above occurred. Based on these observations, it is now possible to make a judgement as to which mode is relevant for bearing compartment-type oil atomization processes at spinning surfaces. Assuming a rotating shaft or a disk surface in a bearing compartment with a diameter of 0.1 m, spinning at a minimum rotational speed of 6000 rpm, the Weber number is at least in the order of 10^7. Therefore, considering a low local flow rate (i.e., close to the disk) of about $25\,\mathrm{l}/h (6.94\cdot 10^{-6}\,\mathrm{m}^3/\mathrm{s})$ and turbine oil properties, it can be concluded from Fig. 2 that film formation is the relevant disintegration mode. As discussed before, higher flow rates and higher rotational speeds will move the operating point even farther into the film formation region.

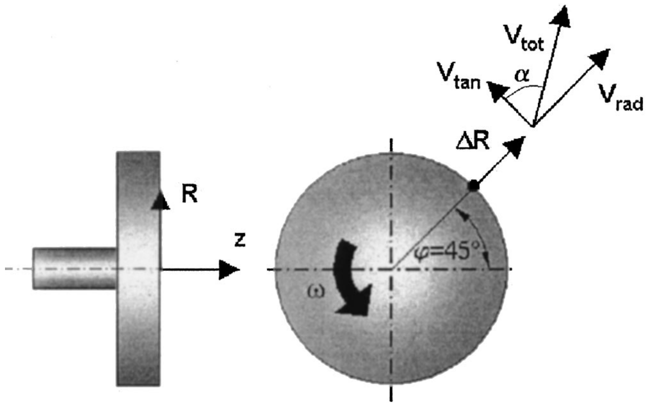

Fig. 4 Test nomenclature

Test Matrix for Droplet Sizing and Velocimetry. Measurements for the characterization of sprays generated by film formation were carried out for 39 different operating conditions that cover a range of rotational speeds, oil flow rates, and temperatures. All conditions are highlighted in the disintegration map of Fig. 2. The nominal measurement location was defined to be in the plane of the disk face at a distance of $25\cdot 10^{-3}\,\mathrm{m}$ (1 in.) from the rim ($z=0$, $\Delta R = 25\cdot 10^{-3}\,\mathrm{m}$, Fig. 4).

The angular position for all measurements was $\varphi = 45\,\mathrm{deg}$. In addition to operating parameter variations at a given location, measurements were obtained in order to study the spatial distributions of spray characteristics. Traverses in z and R were measured for two temperature levels at constant speed and flow rate condition of $\mathrm{We}^* = 1.15\cdot 10^7$ and $V^+ = 7.16\cdot 10^{-2}$, respectively.

In the following paragraphs, some typical results will be presented. First, results will be discussed in terms of actual dimensional quantities, which are often more intuitive than nondimensional parameters. However, the major part of the experimental results will be discussed as a function of nondimensional operating conditions in order to allow a scaling to other applications.

Typical Droplet Sizes and Velocities. Figure 5 shows results in terms of average droplet diameter (D_{10}), area-averaged droplet diameter (D_{20}), and volume-averaged droplet diameter (D_{30}), obtained from a radial traverse extending from the rim of the disk $(\Delta R = 0\,\mathrm{mm})$ to the stationary housing $(\Delta R = 50\,\mathrm{mm})$. A significant reduction of droplet diameters is observed at a radial distance of $\Delta R = 20\,\mathrm{mm}$. Keeping in mind that the droplet formation mode considered here is initiated by a film layer which separates from the face of the disk and disintegrates somewhat radially outward from the rim, Fig. 5 visualizes the transition from the film separation to the actual spray. Apparently, the atomization process is completed at a distance of about $\Delta R = 20\text{--}25\,\mathrm{mm}$. At larger radii the characteristic droplet diameter remains constant. Note that all parameter variations and the investigation of their impact on the spray diameter and individual droplet velocities, which will be shown subsequently, were measured at the location $\Delta R = 25\,\mathrm{mm}$ $(\Delta R/D = 0.125)$. Thus, it can be concluded that transitional modes due to an incomplete atomization did not have an impact on the results discussed here.

Figure 6(*a*) presents characteristic spray diameters for a variation of rotational speeds at a constant oil flow rate of $103\,\mathrm{l}/h (q = 2.78\cdot 10^{-5}\,\mathrm{m}^3/\mathrm{s})$. Spray diameters $D_{V,x}$ represent the fraction x of the droplet volume bounded in droplets with diameters smaller than the given value. A tracking of these values allows determi-

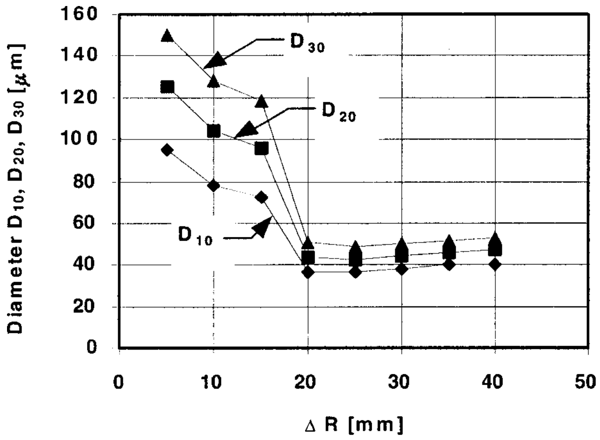

Fig. 5 Radial droplet diameter distribution ($q = 2.87.10^{-5}$ m^3/s, $z = 0$ m, $\omega = 523.6$ s^{-1}, $T = 295$ K)

nation of whether the spray becomes coarser or finer under certain operating conditions. Thus, a conclusion to be drawn from Fig. 6(*a*) is that the spray quality is sensitive to variations of the rotational speed. Up to about 3000–4000 rpm, higher rotational speeds tended to produce finer sprays— with a stronger effect at lower speeds. Figure 6(*a*) suggests that no further decrease of spray diameters can be obtained beyond a certain condition.

Figure 6(*b*) presents ensemble averaged velocities for the same conditions, i.e., an averaged velocity representation of all size classes that are smaller than or equal to the given characteristic diameter, and allows a comparison with the rim speed of the rotating disk. All characteristic droplets show the same trend towards higher velocities with increasing disk speed, though the velocity deficit compared to the rim increases as well. The smaller droplets apparently have a lower velocity, which indicates the expected stronger impact of the surrounding quiescent air on a small particle ($\text{drag}\,\tilde{\propto}\,D^2$ while $\text{momentum}\,\tilde{\propto}\,D^3$). However, as it was shown before, the characteristic diameters vary also with speed. Therefore, it is difficult to draw any other than qualitative conclusions from ensemble-averaged velocities.

A much better way of analyzing the velocity data is shown in Fig. 6(*c*). Velocities for two droplet sizes of 50 μm and 100 μm were extracted from the raw data and plotted as a function of rotational speed. Using this method, it is possible to separate the impact of operating conditions on droplet sizes and velocities and cause/effect relationships can be studied. An example is given in the next section with results analyzed in terms of nondimensional, size class resolved droplet velocity distributions.

Figure 7 presents characteristic spray diameters for a variation of oil flow rates at a fixed speed of 5000 rpm ($\text{We}^* = 1.15 \cdot 10^7$). The chart leads to the conclusion that the spray quality—within the disintegration mode considered here—is relatively insensitive to variations of the oil flow rate, showing only a weak increase of the diameters with the flow rate.

Mean Droplet Diameters as a Function of Nondimensional Operating Conditions. One of the objectives of this investigation was to define droplet characteristics for bearing compartment fluids and operating conditions. For scaling purposes, it is instructive to discuss the results obtained for this application in terms of nondimensional parameters. Assuming that the atomization product is a function of the same quantities as the atomization process, Sauter mean diameters (SMD), which have been normalized with the disk diameter, are plotted in Fig. 8 as a function of nondimensional speeds ($\text{We}^{*1/2}$) and flow rates ($V^{+1/2}\text{On}^{1/6}$). A comparison is made with an empirical correlation developed for the characterization of rotary atomizers ([15]):

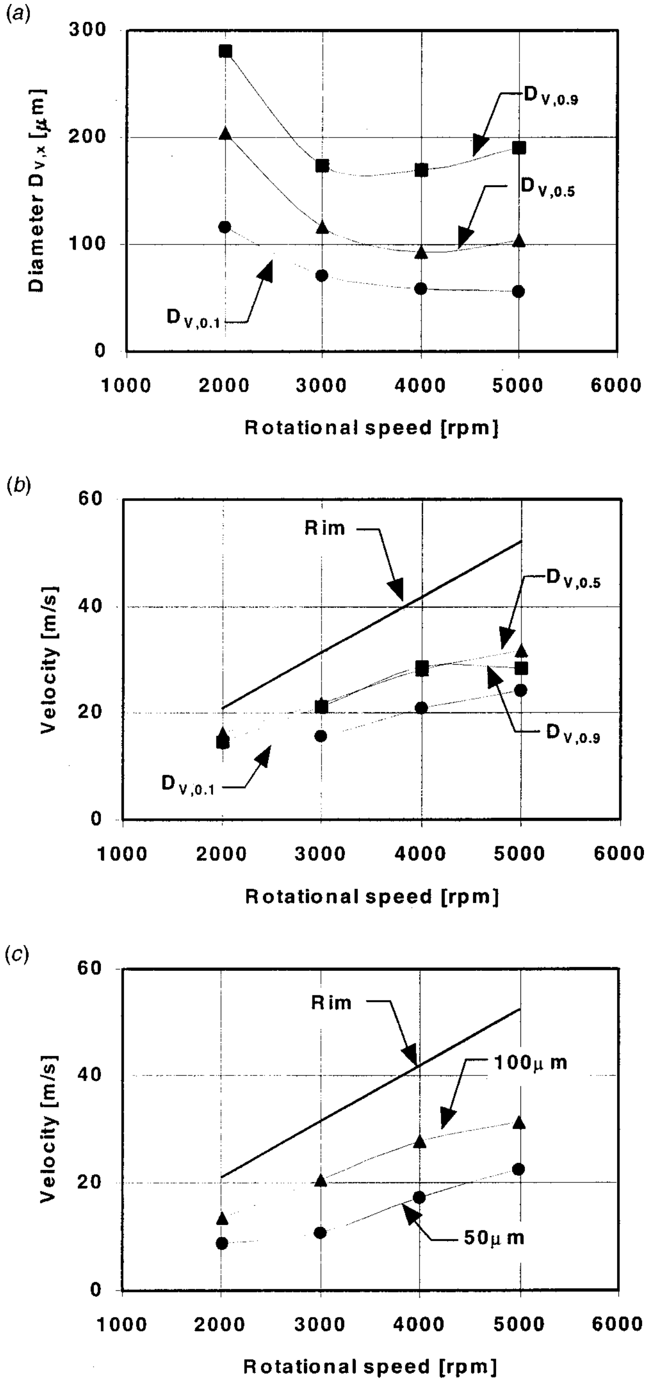

Fig. 6 Characteristic diameters and velocities versus rotational speed ($\Delta R = 25.10^{-3}$ m, $z = 0$ m, $q = 2.872.10^{-5}$ m^3/s, $T = 295$ K)

$$\text{SMD} = \frac{15.6}{n}\left(\frac{\sigma}{D^2 \cdot \rho_L}\right)^{0.4} q^{0.5}. \tag{6}$$

According to Lefebvre [10] Eq. (6) will result in a SMD given in [m], as long as all other parameters are used in SI units. However, a dimensional analysis does not confirm this statement. Furthermore, it may already be concluded from Fig. 7 that the relation $\text{SMD} \propto q^{0.5}$, as suggested by Eq. (6), would not reflect the experimental findings discussed here. However, it is the only correlation known for the SMD produced by this atomization mode and, therefore, it is worthwhile to use for a comparison.

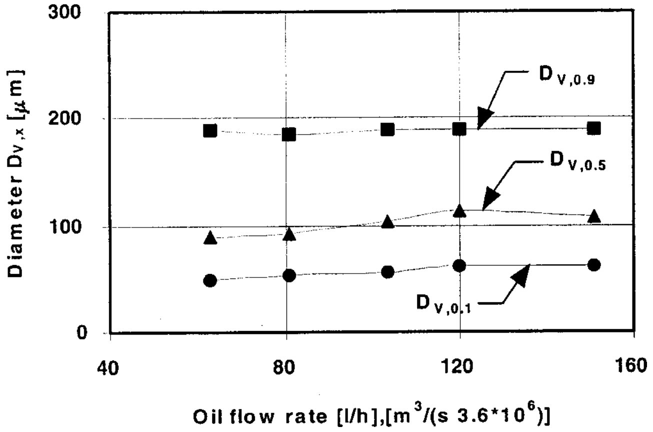

Fig. 7 Characteristic diameters versus oil flow rate ($\Delta R=25\cdot10^{-3}$ m, $z=0$ m, $\omega=523.6$ s^{-1}, $T=295$ K)

A comparison of Fig. 8(*a*) and 8(*b*) shows that the mean spray diameter is underpredicted for a high flow rate and over predicted for low flow rate—another indication for a mismatch of the flow rate impact on the SMD by Eq. (6).

A remarkable result can be seen in the relationship between the nondimensional speed and the droplet size. At low and moderate speeds, droplets follow the proposed relationship SMD$\propto\omega^{-1}$ $\propto V_{\text{rim}}^{-1}$, indicating that increasing aerodynamic forces are leading to finer sprays. However, the data shown in Fig. 8 suggest that eventually a condition could be reached beyond which a further decrease appears to be impossible. The possibility that the Sauter mean diameter remains constant—within some experimental scatter—or actually increases, as shown in Fig. 8, needs to be analyzed in further studies.

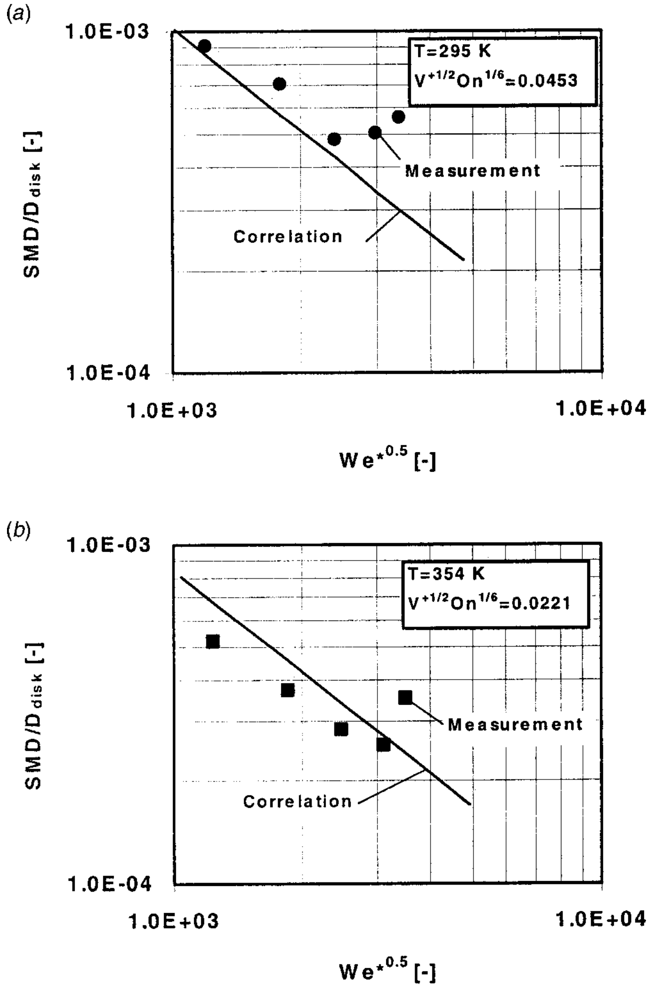

Fig. 8 Sauter mean diameter (SMD) versus nondimensional rim speed at different oil flow rates

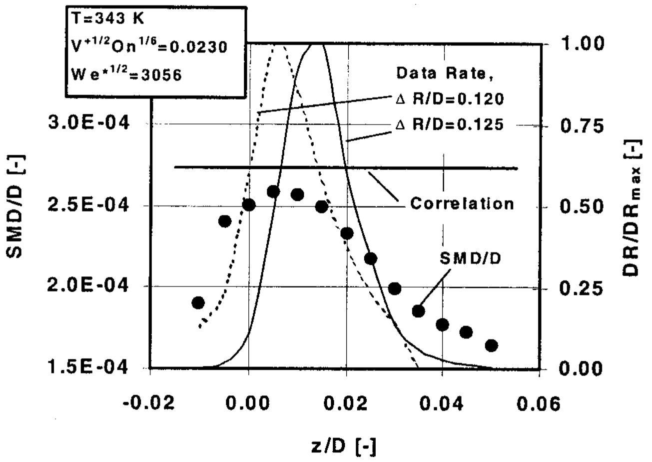

Fig. 9 Axial droplet diameter distribution ($\Delta R=25\cdot10^{-3}$ m, $\omega=523.6$ s^{-1}, $q=2.897\cdot10^{-5}$ m^3/s, $T=343$ K)

Axial and Radial Diameter Distributions. Axial and radial traverses were measured to study the droplet propagation in the vicinity of the rotating disk rim. Figure 9 shows the SMD as a function of the axial distance from the disk as it was defined in Fig. 4. Close to the plane of the disk face, the mean diameter is represented fairly well by the empirical correlation given in Eq. (6). As the measurement location moves either farther away (positive *z*-direction) or behind the atomization plane (negative *z*-direction), only small droplets are observed and the SMD drops accordingly. This is due to the higher inertia of larger droplets, which tends to keep their trajectories in the atomization plane, i.e., larger droplets have a narrow spray angle in the *R*-*z*-plane. An illustration for the overall spray angle can be seen in data rate distributions, which are also shown in Fig. 9 for two radial locations. At both radii, good data rates, *DR*, are observed in a narrow range of $\Delta z/D=0.02$. Closer to the rim ($\Delta R/D=0.12$) the peak data rate is closer to the face of the disk. However, even at the larger distance ($\Delta R/D=0.125$) the data rate distribution indicates that any axial transport phenomena may be neglected in this analysis. Weighing the measured SMD with the data rate enables some judgement on the volumetric flow rate. Thus, another conclusion from Fig. 9 is that the empirical correlation given in Eq. (6) represents the SMD for the major portion of the oil flow rate fairly well. Droplet data at larger distances from the disk face represent a second order effect with respect to the atomization quality, however, this kind of information is useful for a validation of computational prediction methods for the turbulent droplet motion.

Figure 10 shows a radial SMD distribution for the same operating condition and traverse as presented in Fig. 5. The qualitative trend has already been discussed before. At this point, it should be highlighted that the empirical correlation defined by Eq. (6) is well suited to characterize the SMD for the completed atomization process.

Size Class Resolved Droplet Velocity Distributions. In order to calculate the oil distribution inside a bearing compartment or to assess the impact of local flow phenomena like droplet impingement it is necessary to determine both the droplet size and velocity distributions for a given operating condition. As it was

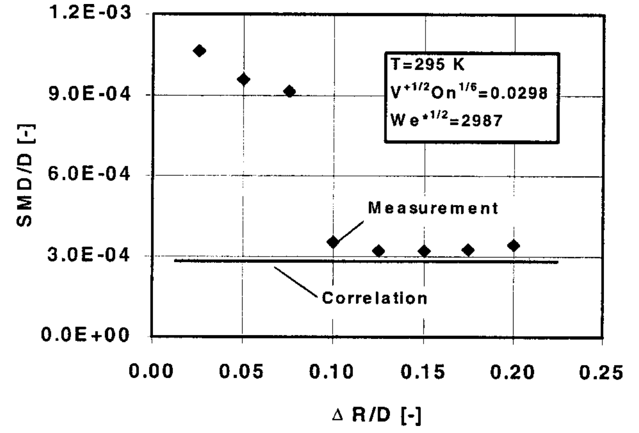

Fig. 10 Radial droplet diameter distribution ($q=2.87\cdot10^{-5}$ m^3/s, $z=0$ m, $\omega=523.6$ s^{-1}, $T=295$ K)

demonstrated in Fig. 6, this information has to be provided in terms of size class resolved velocities as opposed to ensemble-averaged velocity for certain characteristic diameters.

Figure 11 provides this information in a nondimensional form by referring total velocities of 50 μm and 100 μm droplets to the rim speed (Fig. 11(*a*)) and by identifying the flow angle, α, relative to the rotating disk (Fig. 11(*b*)). Operating conditions are characterized by the nondimensional rotational speed, (We$^{*1/2}$), and three different flow rates. However, as can be seen from an examination of both Figs. 11(*a*) and 11(*b*), the flow rate does not have any significant impact on the individual droplet velocities. Furthermore, it is interesting to note that 50 μm droplet velocities remain constant at $V_{\mathrm{tot}}(50\,\mu\mathrm{m})/V_{\mathrm{Rim}}=0.4$, whereas the larger droplet size class shows a weak dependency from the rotational speed and varies within $0.6<V_{\mathrm{tot}}(50\,\mu\mathrm{m})/V_{\mathrm{Rim}}<0.7$. The droplet flow angle (Fig. 11(*b*)) does not show any dependency on either the rotational speed or the flow rate and, in addition, is about the same for both size classes ($\alpha\approx37$ deg).

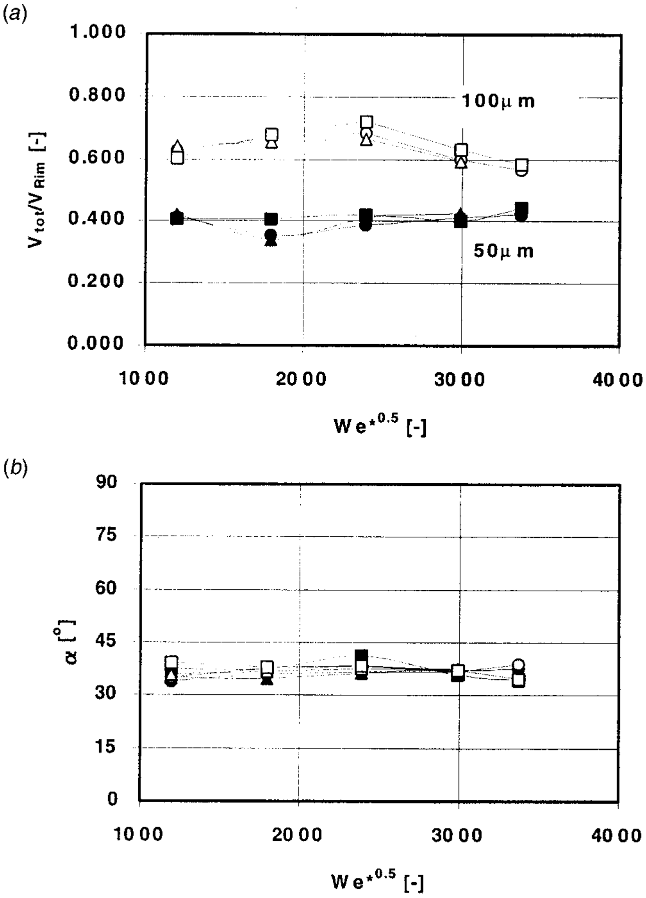

Fig. 11 Droplet flow vector versus operating conditions ($q=2.24\cdot10^{-5}$ to $3.33\cdot10^{-5}$ m^3/s, $\Delta R=25\cdot10^{-3}$ m, $z=0$ m, $T=295$ K)

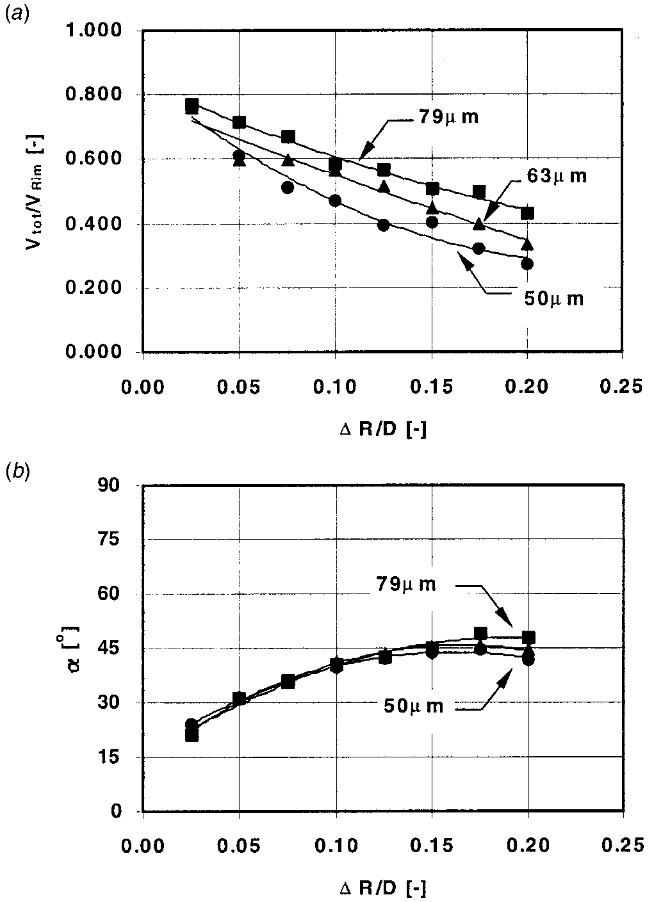

Fig. 12 Droplet trajectories ($q=2.87\cdot10^{-5}$ m^3/s, $z=0$ m, $\omega=523.6$ s^{-1}, $T=295$ K)

Radial distribution of size class resolved velocities are plotted in Fig. 12 for 50 μm, 63 μm, and 79 μm droplets. As shown in Fig. 12(*a*), the velocity for all size classes decreases with increasing distance from the disk rim. As expected, the largest droplet is able to maintain the highest velocity. At the largest radius, the velocity ratio $V_{\mathrm{tot}}(50\,\mu\mathrm{m})$: $V_{\mathrm{tot}}(63\,\mu\mathrm{m})$: $V_{\mathrm{tot}}(79\,\mu\mathrm{m})$ is about the same as the droplet diameter ratio, namely 1:1.24:1.59. This is a plausible result, because once the atomization process is completed, the forces determining the droplet motion are the droplet's inertia and the friction against the gaseous environment. Thus, the droplet Reynolds number $\mathrm{Re}_D\propto D_d$ is expected to characterize the behavior of different size classes.

Flow angles for all three diameters are shown in Fig. 12(*b*). As it was observed before (Fig. 11(*b*)), all size classes have basically the same flow angle characteristic with smaller angles, i.e., a more tangentially orientated trajectory, closer to the rim and increasing angles approaching a value of $\alpha=45$ deg as the droplets move radially outward.

Conclusions

Several conclusions with an impact on the modeling of droplet flows in bearing compartments can be drawn from the fundamental studies described in the present paper:

A disintegration map has been established which indicates that all droplet generation mechanisms reported for rotary atomizers also occur for viscous oil on rotating disks. However, the transition between the modes shifts towards higher rotational speeds and flow rates, respectively. Correlations for critical flow rates have been modified to account for this effect.

Droplet generation by film formation is the relevant disintegration mode for bearing compartment flows and has to be considered for the droplet flow analysis.

The impact of the liquid flow rate on the spray characteristic is negligible. In contrast, the rotational speed strongly affects the droplet size distribution. Up to a certain condition, high speed tends to produce a finer spray. Beyond a maximum speed, which has to be defined in further studies from a broader database, no further decrease appears to be possible.

Conditions have been identified for which an empirical correlation is able to predict fairly well the spray quality in terms of the Sauter mean diameter.

Size class resolved velocities are available for the first time for this application. Total droplet velocities normalized with the rim speed as well as the droplet flow angles are insensitive to the flow rate and the rotational speed.

Based on the measurements and results of the present paper, a database describing a fundamental droplet generation mechanism is available in a nondimensional form and can be scaled to similar applications. Furthermore, the results presented here can be used as benchmark data for numerical predictions.

Acknowledgments

The authors are grateful to Dipl.-Ing. O. Schäfer, Institut für Thermische Strömungsmaschinen, University of Karlsruhe, for his passionate and helpful assistance in arranging the optical equipment used in this investigation for the droplet sizing and velocimetry. Special thanks are due to Lou Dobek, Pratt & Whitney, East Hartford, CT, for his encouragement and support of the work presented here.

Nomenclature

D = disk diameter [m]
D_D = droplet diameter [m]
$D_{10,20,30}$ = averaged droplet diameters based on number, surface area, and volume [m]
$D_{V,x}$ = characteristic droplet diameter, representing the fraction x of the total droplet volume accumulated at the specified diameter [m]
DR = data rate, number of validated droplet measurements per unit time [1/s]
N = rotational speed [1/s]
On = Ohnesorge number
q = volumetric flow rate [m^3/s]
R, φ, z = cylindrical coordinates [m, deg, m]
ΔR = radial distance measured from the rim [m]
SMD = Sauter mean diameter, $\mathrm{SMD}=D_{30}^3/D_{20}^2$ [m]
T = Temperature [K]
V = Velocity [m/s]
V^+ = Nondimensional volumetric flow rate
We* = modified Weber number
α = flow angle, $\tan\alpha = V_{\mathrm{rad}}/V_{\mathrm{tan}}$ [deg]
ρ = density [$\mathrm{kg/m^3}$]
μ = dynamic viscosity [kg/(m·s)]
σ = surface tension [N/m]
ω = angular velocity [1/s]

Subscripts

E = engine conditions
L = liquid
max = maximum value
rim = rim of the disk
rad = radial
T = test conditions
tan = tangential
tot = total

References

[1] Zimmermann, H., Kammerer, A., Fischer, R., and Rebhahn, D., 1991, ''Two-Phase Flow Correlations in Air/Oil Systems of Aero Engines,'' ASME Paper 91-GT-54.
[2] Wittig, S., Glahn, A., and Himmelsbach, J., 1994, ''Influence of High Rotational Speeds on Heat Transfer and Oil Film Thickness in Aero Engine Bearing Chambers,'' ASME J. Eng. Gas Turbines Power, **116**, pp. 395–401.
[3] Chew, J., 1996, ''Analysis of the Oil Film on the Inside Surface of an Aero-Engine Bearing Chamber Housing,'' ASME Paper 96-GT-300.
[4] Glahn, A., and Wittig, S., 1996, ''Two-Phase Air Oil Flow in Aero Engine Bearing Chambers—Characterization of Oil Film Flows,'' ASME J. Eng. Gas Turbines Power, **118**, pp. 578–583.
[5] Glahn, A., Busam, S., and Wittig, S., 1997, ''Local and Mean Heat Transfer Coefficients along the Internal Housing Walls of Aero Engine Bearing Chambers,'' ASME Paper 97-GT-261.
[6] Busam, S., Glahn, A., and Wittig, S., 2000, ''Internal Bearing Chamber Wall Heat Transfer as a Function of Operating Conditions and Chamber Geometry,'' ASME J. Eng. Gas Turbines Power, **122**, 314–320.
[7] Glahn, A., and Wittig, S., 1999, ''Two-Phase Air Oil Flow in Aero Engine Bearing Chambers—Assessment of an Analytical Prediction Method for the Internal Wall Heat Transfer,'' Int. J. Rotating Mach, **5**, No. 3, pp. 155–165.
[8] Zaidi, S. H., Ishaq G., Aroussi A., and Azzopardi, B. J., 1998, ''Two-Phase Flow Study Around a Rotating Liquid Film Using Laser Techniques,'' *Proceedings of the VSJ-SPIE98*, Dec. 6–9, Yokohama, Japan.
[9] Glahn, A., Kurreck, M., Willmann, M., and Wittig, S., 1996, ''Feasibility Study on Oil Droplet Flow Investigations inside Aero Engine Bearing Chambers—PDPA Techniques in Combination with Numerical Approaches,'' ASME J. Eng. Gas Turbines Power, **118**, pp. 749–755.
[10] Lefebvre, A. H., 1989, *Atomization and Sprays*, Hemisphere, Washington, DC.
[11] Matsumoto, S., Belcher D. W., and Crosby, E. J., 1985, ''Rotary Atomizers: Performance Understanding and Prediction,'' *Proceedings of the 3rd International Conference on Liquid Atomization and Spray Systems (ICLASS-85)*, London.
[12] Hinze, J. O., and Milborn, H., 1950, ''Atomization of Liquids by Means of a Rotating Cup,'' ASME J. Appl. Mech., **17**, Paper 49-SA-2, pp. 145–153.
[13] Bachalo, W. D., and Houser, M. J., 1984, ''Phase Doppler Spray Analyzer for Simultaneous Measurements of Drop Size and Velocity Distributions,'' Opt. Eng., **23**, pp. 583–590.
[14] Willmann, M., Glahn, A., and Wittig, S., 1997, ''Phase-Doppler Particle Sizing with Off-Axis Angles in Alexander's Darkband,'' Part. Part. Syst. Charact., **14**, No. 3, pp. 122–128.
[15] Tanasawa, Y., Miyasaka, Y., and Umehara, M., 1978, ''Effect of Shape of Rotating Disks and Cup on Liquid Atomization,'' *Proceedings of the 1st International Conference on Liquid Atomization and Spray Systems*. Tokyo, pp. 165–172.

Flow and Heat Transfer in an Industrial Rotor-Stator Rim Sealing Cavity

A. V. Mirzamoghadam

Z. Xiao

Advanced Engine Development,
Siemens Westinghouse Power Corporation,
4400 Alafaya Trail, MC-205,
Orlando, FL 32826

Flow and heat transfer in the row-1 upstream rotor-stator disk cavity of a large 3600-rpm industrial gas turbine was investigated using an integrated approach. A two dimensional axisymmetric transient thermal analysis using aeroengine-based correlations was performed to predict the steady-state metal temperatures and hot running seal clearances at ISO rated power condition. The cooling mass flow and the flow pattern assumption for the thermal model were obtained from the steady-state two dimensional axisymmetric CFD study. The CFD model with wall heat transfer was validated using cavity steady-state air temperatures and static pressures measured at inlet to the labyrinth seal and four cavity radial positions in an engine test which included the mean annulus static pressure at hub radius. The predicted wall temperature distribution from the matched thermal model was used in the CFD model by incorporating wall temperature curve-fit polynomial functions. Results indicate that although the high rim seal effectiveness prevents ingestion from entering the cavity, the disk pumping flow draws air from within the cavity to satisfy entrainment leading to an inflow along the stator. The supplied cooling flow exceeds the minimum sealing flow predicted from both the rotational Reynolds-number-based correlation and the annulus Reynolds number correlation. However, the minimum disk pumping flow was found to be based on a modified entrainment expression with a turbulent flow parameter of 0.08. The predicted coefficient of discharge (Cd) of the industrial labyrinth seal from CFD was confirmed by modifying the carryover effect of a correlation reported recently in the literature. Moreover, the relative effects of seal windage and heat transfer were obtained and it was found that contrary to what was expected, the universal windage correlation was more applicable than the aeroengine-based labyrinth seal windage correlation. The CFD predicted disk heat flux profile showed reasonably good agreement with the free disk calculated heat flux. The irregular cavity shape and high rotational Reynolds number (in the order of 7×10^7) leads to entrance effects that produce a thicker turbulent boundary layer profile compared to that predicted by the 1/7 power velocity profile assumption. [DOI: 10.1115/1.1400754]

1 Introduction

Investigation of the flow and heat transfer in heated rotating cavities are of particular interest to the aero-based gas turbine industry because of their relevance to performance, weight, and safety concerns. Proper definition of the thermal and flow environment in rim sealing, interstage, and interdisk cavities of compressors and turbines leads to the prediction of reliable disk/rim temperature distributions and the use of minimum cooling flow rates. In existing gas turbines, the amount of air required to seal one turbine disk rim can be reduced to approximately one percent of the compressor air flow which leads to an improvement in efficiency. In particular, the nature of the flow-field and effectiveness of cooling (or heating) in turbine rotor-stator (or rotor-rotor) cavities depends on the amount and orientation at which the superimposed compressor cooling flow is introduced. The amount is balanced against hot gas ingress due to disk fluid entrainment requirements and nonaxisymmetric static pressures in the mainstream flow, as well as heat conduction from the blade/vane attachment areas to produce acceptable disk/rim temperatures.

In large heavy-duty industrial gas turbines, however, reliable predictions of temperature and cooling mass flow have only recently become more critical to the manufacturers because of the evolving competitive industry and changing market requirements. In these gas turbines, massive turbine disks exist which although running at a maximum angular speed of 3600 rpm, the high rim radius can produce a rotational speed which is higher than the disk rim speed belonging to an aero engine. Therefore, rotational and annulus Reynolds numbers can be an order of magnitude higher. Another feature is the shape of the labyrinth seal which can have many fins and grooves on both rotor and stator surfaces unlike the aero-based labyrinth seal which is finned on only one side. Since most of the data cited in the literature which support rotating cavity theory are in the Reynolds number range of aeroengine gas turbines, the primary motivation for carrying out this investigation was to assess the validity of applying aeroengine-based design correlations of flow and heat transfer to an industrial cavity exceeding this range. The criteria used for selecting the cavity was that it needed to be simple for benchmarking against measured data but yet include the important effects of the labyrinth seal, the rotating cavity irregular geometry, the rim seal, and the effect of annulus ingestion. Based on this criteria, the design correlations under investigation are the minimum cooling flow to seal the rim, the coefficient of discharge (*Cd*), windage heating through a labyrinth seal as well as the rotor-stator cavity, wall heat transfer, and boundary layer thickness. In addition, the flow pattern with respect to cavity geometry and the criterion for annulus ingestion can be investigated.

The design criteria to determine the minimum cooling flow to seal the disk rim against hot gas ingestion is a topic of continuous research. The complexity to estimate such flows accurately arises

---

Contributed by the International Gas Turbine Institute (IGTI) of THE AMERICAN SOCIETY OF MECHANICAL ENGINEERS for publication in the ASME JOURNAL OF ENGINEERING FOR GAS TURBINES AND POWER. Paper presented at the International Gas Turbine and Aeroengine Congress and Exhibition, Munich, Germany, May 8–11, 2000; Paper 00-GT-285. Manuscript received by IGTI November 1999; final revision received by ASME Headquarters February 2000. Associate Editor: D. R. Ballal.

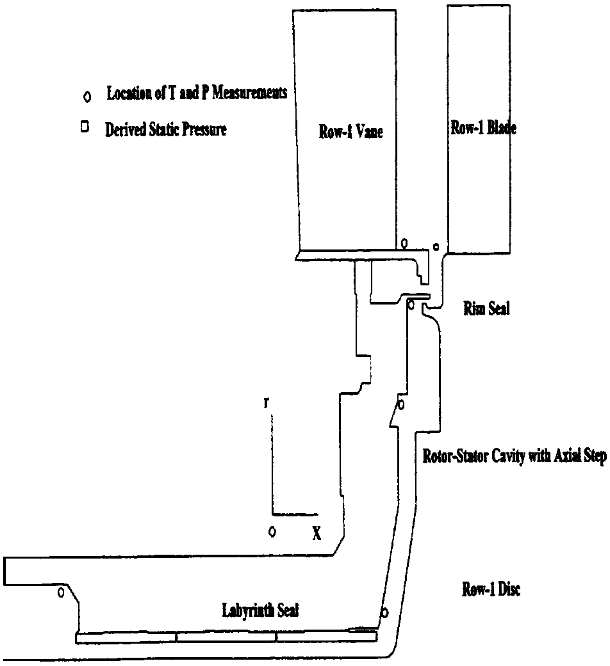

Fig. 1 Rim seal cavity geometry

as a result of higher annulus Reynolds number and a larger min-to-max annulus circumferential static pressure variation across the rim seal. In addition, the effect of the labyrinth seal preswirl and cavity geometry on fluid dynamics is important. In their study of a simple model rotor-stator disk cavity with a rim discourager and the effect of the mainstream air, Roy et al. [1] report the existence of a recirculation region in the source region (i.e., lower cavity) with strong radial outflow along the disk and a rather weak inflow along the stator. They report the source region of the cavity to be dominated by radial flow and the tangential velocity increased with radius. Radial inflow along the stator was observed near the discourager; However, the mean tangential velocity in the core region (i.e., at the upper part of the cavity) was higher. They also measured static pressure distribution and found that the circumferential pressure asymmetry in the mainstream flow had been dissipated across the discouragers. The effect of an external flow field on the sealing of a rotor-stator cavity has previously been investigated by others such as Vaughan [2], and later by Phadke and Owen [3], Ko and Rhode [4], Chew et al. [5], Green and Turner [6], and Bohn et al. [7]. More recently, Bohn et al. [8] and Reichert and Lieser [9] discuss the parameters relevant to rim sealing effectiveness. These studies show that for a given seal clearance, increasing the mass flow parameter (*Cw*) or the ratio of seal axial velocity to mainstream gas velocity leads to an increase in the sealing effectiveness. The heat transfer aspects of rotor-stator cavities have been studied by a number of investigators such as Owen and Rogers [10], Chen et al. [11], and Roy et al. [12].

The geometry under consideration represents the row-1 rim sealing cavity of a large industrial gas turbine shown in Fig. 1. It consists of an industrial labyrinth rim seal with 18 grooves and 18 fins (equally divided between rotor and stator), a rotor-stator cavity with an axial step occurring mid way, a radial rim seal, and the mainstream gas flow plenum between the first stage vanes and blades. At steady-state rated power condition, the rotational Reynolds number at the rim seal location is 7.4×10^7, the annulus axial Reynolds number is 6.4×10^6, the cavity has an irregular geometry in the radial direction with a radius ratio of 0.75, and the axial gap ratio is nonuniform with a minimum of 0.014 and a maximum of 0.04. In Section 2 which follows, the aerothermal analysis method and integrated approach including the validation process using the available steady-state temperatures and static pressures are described. The results are presented in Section 3 which consist of thermal analysis/CFD model validation, and comparison of the results with aero-based correlations. A sensitivity study was performed on the validated CFD model to establish the minimum rim sealing flow which prevents annulus ingestion and/or stator inflow. The conclusions of this investigation are summarized in Section 4.

2 Aerothermal Method

The approach used to realize the objectives of this investigation was the integration of a simultaneous validation process of thermal analysis and CFD using the measurements.

2.1 Thermal Model. The process in developing the thermal model involves data input and applying boundary conditions to a two-dimensional axisymmetric finite element model using the proprietary thermal-mechanical analysis code developed at Rolls-Royce Plc. The specifics on modeling procedure and applying boundary conditions including a theoretical background on the governing equations for tracking the airflow temperature were described in a previous paper Mirzamoghadam [13]. The rotor thermal model includes four turbine stages as well as the stationary surface of the labyrinth and rim seal of row-1 disk (in Fig. 1, only row-1 is shown). The secondary air system and annulus gas flow are modeled as boundary conditions. Since the heat transfer and windage correlations are based on Reynolds numbers which are either rotational speed or throughflow mass-dependent, iterations were performed on the measured effective fluid temperature at the designated radii based on the assumed net mass flow, windage heating, and heat transfer enhancement or reduction factor. The measured pressures and annulus gas running conditions were used directly in the thermal model and the assumed mass flow, wall temperature distribution, and hot-running radial seal clearances were used as iteration parameters between the thermal model and the CFD model until the findings of both models were consistent. The thermal model was then declared validated. The numerical accuracy of the thermal solution was set at 5 K.

2.2 CFD Model. Version 5.0 of Fluent/UNS was used to construct the two dimensional axisymmetric CFD model shown in Fig. 2. For the case where hot gas ingestion may occur, it is not feasible to set realistic conditions at the outlet plane where simultaneous inflow and outflow could occur. The reason being that little is known about the condition of the ingested fluid. Therefore, the outlet conditions were specified well away from the seal outlet by incorporating the annulus plenum in the CFD model. Furthermore, the small semi-closed cavity just above the rim seal was neglected by assuming that its presence does not alter the outflow at the rim seal for the two-dimensional model. The model was set up assuming compressible flow and the standard $k-e$ turbulence model with wall functions was applied. The controlling main inlet boundary conditions of the model were defined as the circumferentially averaged total pressure/temperature at inlet to the labyrinth seal (e.g., the value of the measured quantity), and at inlet to the annulus plenum which was essentially the derived stator outlet temperature. The mean static pressure at outlet of the annulus plenum was established by matching all inner cavity measured pressures as well as the aerodynamically derived value of the circumferentially averaged static pressure at the rim seal/annulus junction (see Fig. 1). The latter was based on the measured pressure probes at the vane trailing edge as shown in Fig. 1. The number of quad elements after refinement became 71000 with a $y+$ value ranging between 30 and 80. About 4000 iterations on the CFD model led to an acceptable accuracy level of 10^{-4} (or better) on the residuals. The final seal running clearances and wall temperature distribution from the thermal model led to a flowfield satisfying all measurements within the rim seal rotor-stator cavity at an acceptable accuracy level of less than two percent for

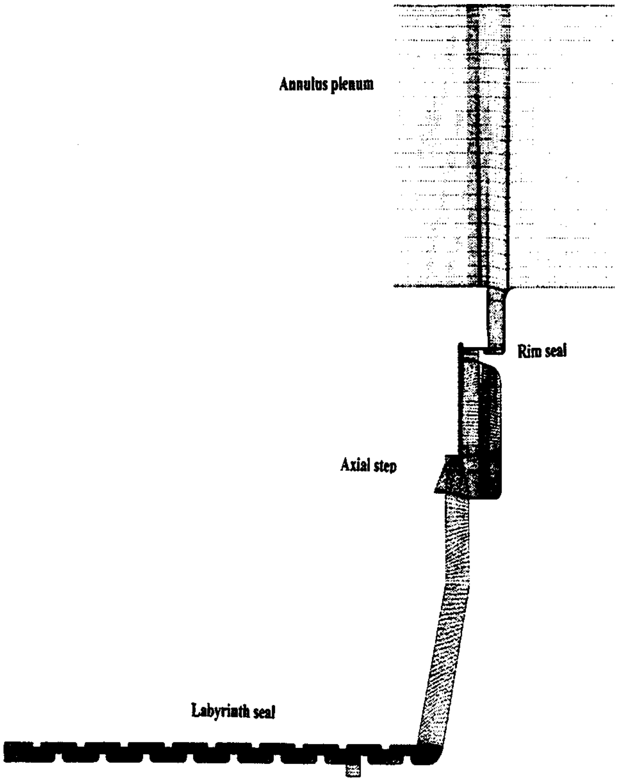

Fig. 2 CFD model geometry and grid

pressure and within 3 K for temperature. The computed rim seal cooling mass flow parameter (C_w) is 1.5×10^5 based on a nondimensional clearance (*Gc* actual clearance over local radius) of 0.002 and 0.0014 for the labyrinth seal and rim seal, respectively.

2.3 Measurements and Operating Cycle. A complete engine run was performed and steady-state measurements of temperature and static pressure at the locations shown in Fig. 1 were obtained. The thermocouples were positioned close to the stator wall such that the total and static temperatures would be nearly the same. The engine was run at ISO rated power condition for several days yielding steady-state data. The rim seal cavity data were assessed against those obtained on a run made at an earlier date with similar power conditions and the reliability was established based on error bounds of one percent or better for pressure. For the temperature measurements, the error is less than 0.8 percent at inlet and outlet of the labyrinth seal, but at the axial step and the rim seal locations, the computed error is 4.5 percent and 3.2 percent, respectively. Although, the transient operating cycle of the test was simulated in the thermal model, the validation process was performed on only the steady-state data.

3 Results

3.1 Model Validation

3.1.1 Wall Temperature. The iteration process between the CFD model and thermal analysis led to the wall temperature distribution. Starting from the labyrinth seal (Fig. 3), the stator surface axial temperature at inlet generally follows the seal throughflow mass temperature whereas the rotor surface temperature is slightly lower. In the rotor-stator cavity (Fig. 4), the disk radial surface temperature distribution has been approximated with a second-degree polynomial. The quadratic approximation is consistent with the assumed turbulent flow free disk heat transfer expression of Eq. (1) ([10]) with n (in $T_w = T_o + T(r/R_o)^n$) equal to 2, and the result is satisfactory. The equation is valid for $\mathrm{Re}_U > 3.0\times10^5$ and is based on the 1/7 power-law velocity profile in the boundary layer. The stator wall temperature drops below the rotor at the upper radii due to the assumption of low hot gas leakage.

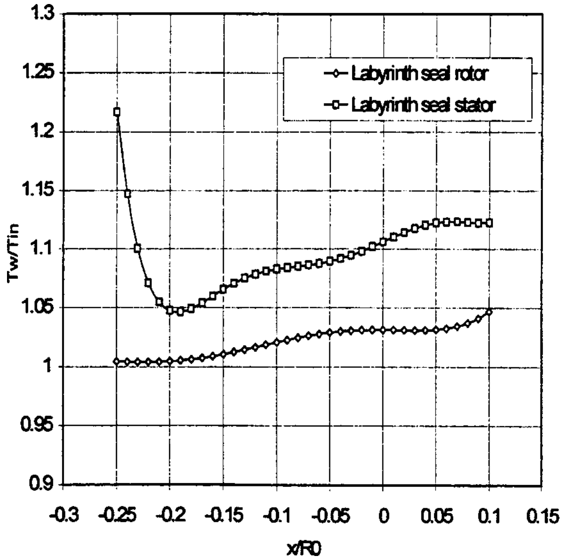

Fig. 3 Lab seal wall temperature distribution

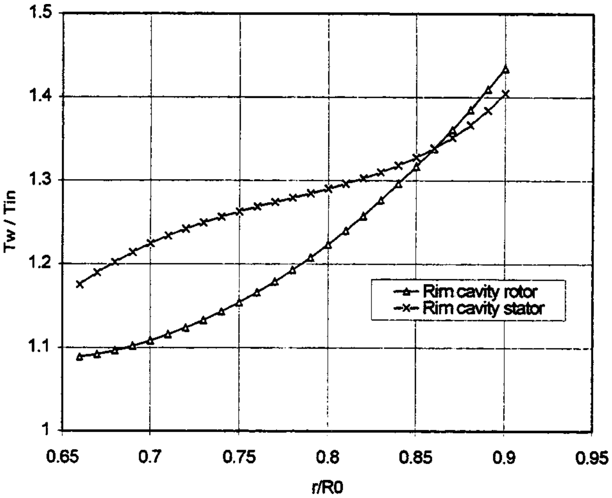

Fig. 4 Rotor-stator wall temperature distribution

$$\mathrm{Nu}_r = 0.0197(n+2.6)^{0.2}\,\mathrm{Re}_U^{0.8}\,\mathrm{Pr}^{0.6} \tag{1}$$

3.1.2 Air Temperature. The air temperature rise through the industrial labyrinth seal and the measured values at the inlet/outlet are shown in Fig. 5. The effects of heat transfer and windage heating are also illustrated. As expected, wall heat transfer tends to smooth out the heating due to windage. The groove/fin profile of the labyrinth seal is reflected in the oscillatory profile of the temperature rise curve.

Referring to Fig. 6, the axially mean temperature rise in the rotor-stator cavity has a break as shown in the curves due to the axial step at a radius ratio of 0.83. The total relative temperature is based on the relative tangential velocity between disk and mean flow at a given radius. It is higher than the total absolute temperature due to a lower than 0.5 mean axial swirl ratio (see Fig. 7). The measurement points follow more closely the static temperature rise, confirming that the thermocouples are picking up the static temperature. Near the rim seal, the static temperature shows

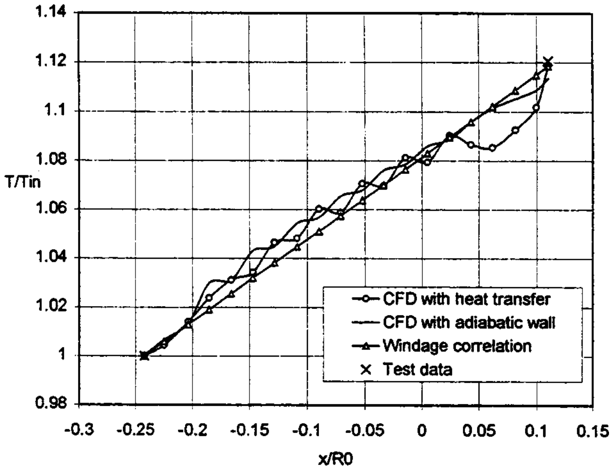

Fig. 5 Temperature rise in the labyrinth seal

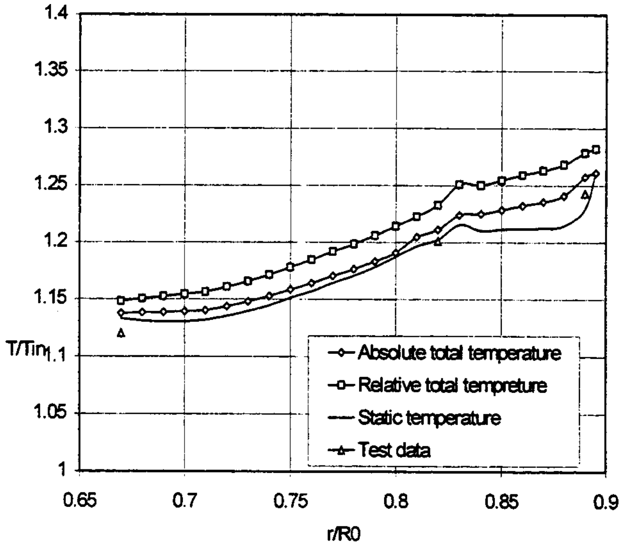

Fig. 6 Temperature rise in the rotor-stator rim-seal cavity

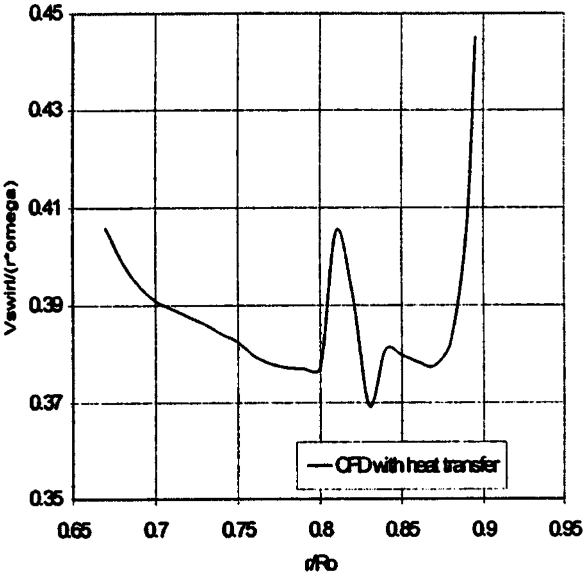

Fig. 7 Mean swirl velocity ratio in the cavity

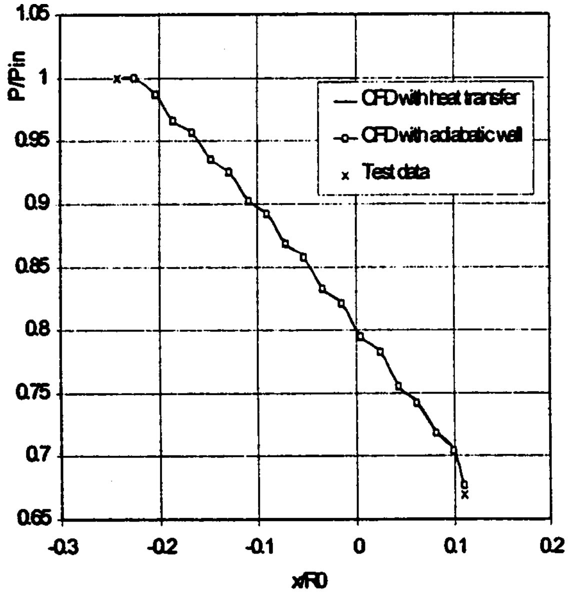

Fig. 8 Pressure drop in the labyrinth seal

a rapid rise. This is due to the curved disk/platform surface which enhances heat transfer and raises the static temperature.

The mean axial swirl ratio profile (Fig. 7) clearly illustrates the axial step effect in the industrial rim seal cavity. The oscillatory behavior dampens out near the platform curvature, and the swirl ratio rises rapidly. It is interesting to note that the flow exiting the labyrinth seal enters the cavity with a preswirl ratio of approximately 0.41 which leads to an increase in total relative temperature. Figure 7 clearly demonstrates the two different flow patterns resulting from the axial step midway the cavity. The lower subcavity shows that the swirl ratio is dropping as the radius increases. This drop in swirl ratio, however, changes from an approximate free-vortex behavior at the beginning of the cavity to an almost constant swirl ratio near the axial step. The axial step disturbs the flow, and the upper rim seal geometry transforms the disturbed flow into a forced vortex flow. The mean swirl ratio in the cavity is approximately 0.39.

3.1.3 Air Pressure. The pressure drop across the labyrinth seal is shown in Fig. 8. The unsmooth profile is due to the 18 grooves and fins throughout the seal. The data verifies that wall heat transfer is insignificant in pressure drop estimation. Figure 9 shows the pressure rise in the cavity due to pumping and its comparison with the measured data at three radii.

3.1.4 Cavity Flow-Field. The resulting cavity flow field is shown in Fig. 10. The streamline contours indicate the step changing flow pattern through the seal, outflow along the disk, and inflow along the stator. The axial step midway the cavity produces a discontinuity in the flow-field leading to a thinning of the boundary layer thickness and oscillatory flow pattern. The curvature along the disk under the rim seal accelerates the entrainment flow leading to a thickening of the boundary layer. The recirculation of the cavity flow to meet the entrainment requirements of the disk begins at the rim seal radius.

3.2 Comparison With Aero-Based Correlations

3.2.1 Coefficient of Discharge (Cd). The predicted *Cd* value of the labyrinth seal using the CFD calculated massflow, effective flow area, and pressure drop yields 0.14. The correlation for straight through labyrinth seals from Zimmermann and Wolff [14] along with the proposed carryover factors were used to check the validity of the predicted *Cd* from CFD. The total number of fins (i.e., 18) in Eq. (2) yields the ideal throughflow mass. The total

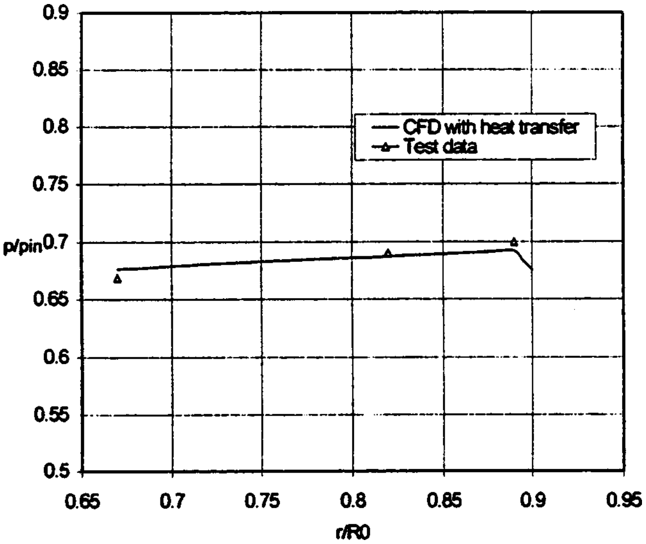

Fig. 9 Mean static pressure distribution in the cavity

carryover effect (i.e., k) for the industrial labyrinth seal was modified by applying the actual number of fins on the rotor and stator surfaces separately (i.e., (9)) and simply adding the two effects. The result is a Cd value of 0.16.

$$m_{id}=(AP_t\sqrt{}T_t)\sqrt{}\{[1-(P_s/P_t)^2]/[R(n^*-\ln(P_s/P_t))]\} \tag{2a}$$

where

$$m_{\mathrm{act}}=(k_r+k_s)Cdm_{id} \tag{2b}$$

$$k=k_1k_2 \tag{2c}$$

$$k_1=\{1-[(n^*-1)/n^*][s/t]/[s/t+0.02]\}^{-0.5} \tag{2d}$$

and

$$k_2=\sqrt{}n^*/(n^*-1). \tag{2e}$$

3.2.2 Windage Heating. The CFD results of air temperature rise through the labyrinth seal due to windage heating with and without heat transfer indicated wall heat transfer to be less significant than was initially assumed in the thermal model. Sensitivity studies were performed on the thermal model using the aero-based straight labyrinth seal windage and heat transfer correlations of Rolls-Royce, Plc. In order to match the temperature measurements and be consistent with the CFD findings, factors of 2.5 and 0.5 were applied to the windage and heat transfer correlations, respectively. The high factor of 2.5 on the windage correlation, in particular, which is limited by the number of fins and rotational speed, became a concern and the same sensitivity study was conducted using the universal windage logarithmic correlation for disks, cones, and cylinders, see Eq. (3). This correlation considers the basic windage formulas for disks [15] and also shafts and cones as originally developed by Rolls-Royce Plc. in 1970 to conclude the universal formula for all geometries. The result was that the measured air temperature rise and heat transfer effect can be obtained without applying any enhancement factor to this correlation. Referring to Fig. 5, the prediction from the universal windage correlation is compared with the CFD predictions. Except close to the exit where there is a drop in air temperature due to the local cooling effect of a separate leakage (simulated as a larger groove on the rotor side), the result is satisfactory. The range of Re for this correlation is from 10^5 to 10^8 which falls within the range of the industrial cavity.

$$\Delta T_{pu}=[1.2275(\log \mathrm{Re}_U)^{-2.58}-0.5502(\log \mathrm{Re}_U)^{-3.58}]b \tag{3a}$$

where

$$b=\rho\omega^3r^4(\sin\theta)^{0.2}s/mC_{\mathrm{p}} \tag{3b}$$

and $\theta=22$ deg is the assumed half-cone angle relative to the axis of rotation.

In the rotor-stator subcavity below the axial step, the universal windage correlation as is produced the desired temperature rise and the effect of heat transfer was again insignificant. On the other

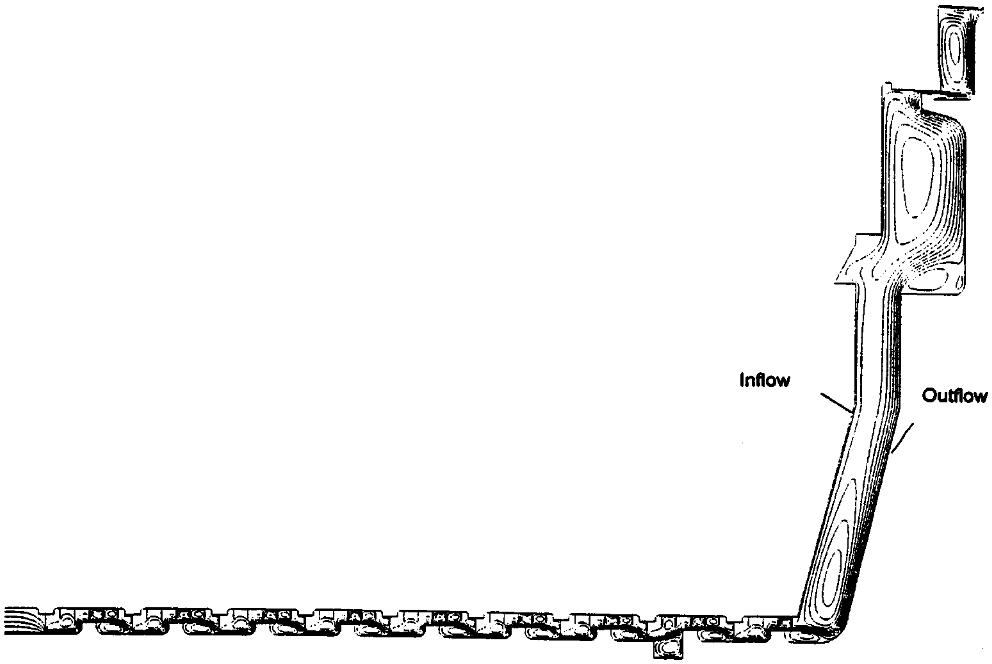

Fig. 10 Cavity/lab seal streamlines (showing outflow along rotor and inflow along stator)

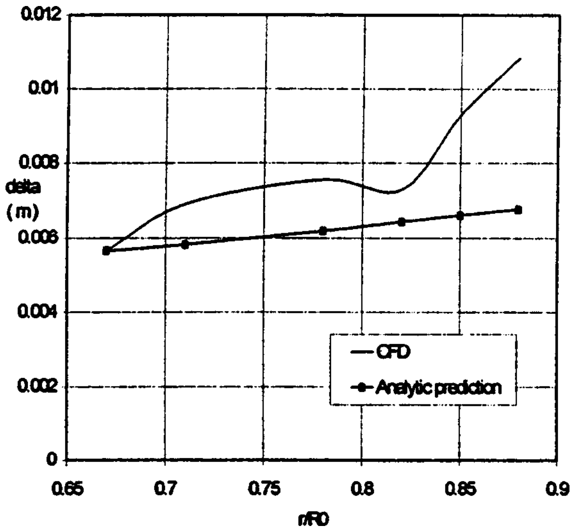

Fig. 11 Rotor boundary layer thickness

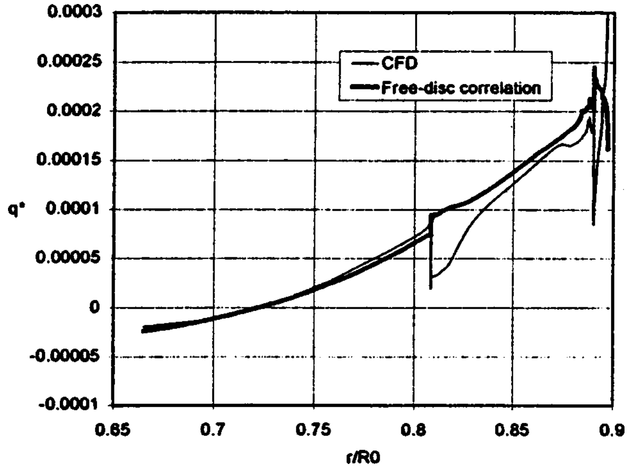

Fig. 12 Nondimensional disk-wall heat flux profile

hand, the static air temperature rise in the upper subcavity is mainly driven by wall heat transfer rather than windage. The relative air temperature as seen by the disk for flow through a vortex (see Fig. 6) is higher than the total temperature which is affected by frictional heating due to windage.

3.2.3 Boundary Layer Thickness. The analytical expression for computing turbulent momentum boundary layer thickness along the rotor from Owens and Rogers [10] is based on the 1/7 velocity profile assumption. As illustrated by Eq. (4) and Fig. 11, the thickness grows as $r^{0.6}$ but in this case, the axial mean relative tangential velocity was used. This selection was based on the CFD predicted boundary layer thickness which considers the local tangential velocity reaching 99 percent of the core value. All along the cavity, the disk boundary layer is thicker than that predicted by the expression especially near the rim seal. A factor of 1.2 applied to Eq. (4) will significantly reduce the gap. The effect of the midway axial step in the cavity is to retard the growth of the boundary layer in the lower subcavity.

$$\delta=0.526r\,\mathrm{Re}_{\varphi,r}^{-0.2} \qquad (4)$$

3.2.4 Wall Heat Transfer. The turbulent free disk heat transfer coefficient (Eq. (1)) and the temperature difference between local wall and cavity inlet air temperature were used to predict the disk wall heat flux profile. The analytical prediction was then compared with the CFD-based wall heat flux profile. The results are shown in Fig. 12 where the wall heat flux is normalized with the cavity entrance advection (similar to a Stanton number which normalizes the heat transfer coefficient) as shown in Eq. (5). The lower subcavity shows excellent agreement. The wall heat flux computed by CFD is able to catch the effect of the axial step midway the cavity which leads to a drop in local heat flux compared to the analytical prediction. Near the rim seal radius, the heat flux in both cases is oscillatory owing to the temperature difference. Typical values of the Nusselt number range from 15,000 to 25,000.

$$q^*=q_w/(\rho r_i \omega C_p T_{in}) \qquad (5)$$

3.2.5 Sealing Mass Flow and Entrainment. In predicting the minimum flow to seal the rim, the following correlation from Owen and Rogers [10] based on pressure measurements and annulus circumferential pressure symmetry was obtained.

$$C_{w,\min}=0.028Gc^{0.291}\,\mathrm{Re}_{Uo}^{0.949} \qquad (6)$$

The value calculated for sealing the rim is 1.2×10^5. The CFD predicted net mass flow parameter is 1.5×10^5. Since the supply cooling flow is more than the minimum sealing flow, no ingestion is to be expected, and from the temperature measurement near the inlet to the rim seal, there is no indication of ingestion. However, the CFD predicted flow field has revealed an inflow along the stator penetrating as low as the labyrinth seal radius. The outflow along the disk, therefore, is more than the supply cooling flow. Figure 13 illustrates the predicted outflow mass parameter. The peak points on the curve can be attributed to cavity entrance and geometry effects which induce secondary airflow recirculation regions. The region between the peaks (i.e., between radii of 0.75 and 0.8) is rather uniform with a mass flow parameter of about 1.95×10^5 which shows that the disk is pumping more flow than the supply flow. The ratio of the seal axial velocity (based on $C_w=1.5\times 10^5$) to the local peripheral speed is roughly 0.2. According to Chew et al. [5], the seal efficiency is about 0.90 indicating that the additional flow to meet disk pumping could not be supplied through the rim seal. Moreover, even in the presence of a five percent max-to-min annulus circumferential static pressure variation (i.e., ΔP), the minimum sealing flow parameter based on annulus controlled ingestion from Owen and Rogers [10] is only

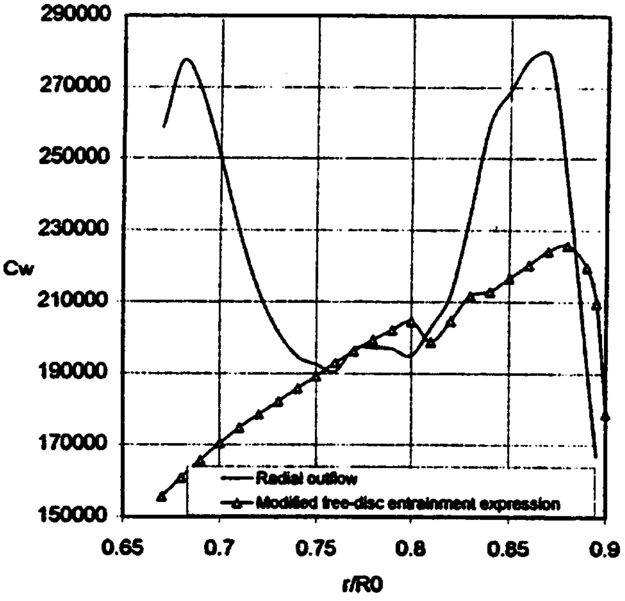

Fig. 13 Mass-flow parameter in the rim-seal cavity

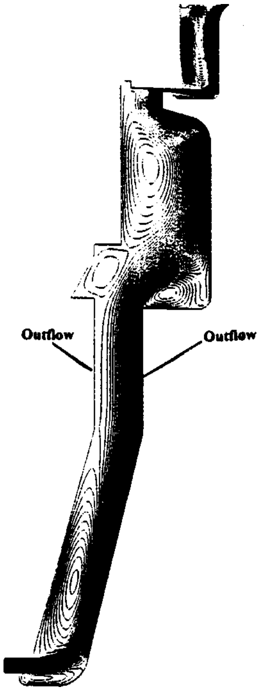

Fig. 14 Increased cooling flow showing total outflow in lower subcavity

7000 (see Eq. (7)) which leads to the conclusion that the rim sealing flow requirement in this case has to be rotational speed-dependent.

$$C_{w,\min}=2\pi Cd(2A)^{0.5}Gc\,\mathrm{Re}_w[\Delta P^{0.5}/(\rho^{0.5}u)] \qquad (7)$$

Figure 13 illustrates the comparison between the geometry corrected free disk entrainment massflow parameter (Eq. (8)) and the CFD predicted values in the radial direction. The free disk values which are based on the axial mean relative tangential velocity, reasonably predict the uniform section of the CFD curve for pumping requirement.

$$C_{w,fd}=0.22\,\mathrm{Re}_{\varphi,r}^{0.8}[1-(ri/ro)^5] \qquad (8)$$

The amount of make-up flow (or stator inflow/ingestion flow) necessary as a result of disk rotation can be defined as the difference between the CFD predicted and the supply mass flow parameters. This amount is the minimum outflow along the disk (excluding the effect of a rim seal) which will be generated even in the absence of the supply flow. It was found that in order to predict the minimum disk flow at the outer radius of the lower subcavity (i.e., 0.8), Eq. (8) took the following form with a reduced λ_T.

$$C_{w,d}=0.08\,\mathrm{Re}_{\varphi,r}^{0.8} \qquad (9)$$

3.3 Cavity Sensitivity Study. Although, the supplied cooling flow was higher than the rim sealing flow and the rim sealing effectiveness was high enough to prevent ingestion from entering the cavity, the CFD computed mass flow parameter along the disk was higher than the supplied cooling flow in all locations. In order to verify the entrainment criterion for stator inflow to satisfy the disk pumping requirement mentioned in Section 3.2.5, a sensitivity study was conducted on the CFD model which consisted of increasing the labyrinth seal flow by a factor of 2. This amount of outflow was selected based on Eq. (8) predicting the maximum massflow (i.e., at the rim seal radius and without the geometry correction factor). Referring to Fig. 14, the streamlines along the referenced radii, in this case, are all in the outflow direction. Moreover, the selected amount was found to be the minimum to sustain outflow along the stator in the lower subcavity between radii of 0.75 and 0.8. Thus, recirculations due to the entrance and geometry effects are maintained but in the core of the lower cavity, the supplied cooling flow is equal to the rotor-stator outflow, and the modified free disk entrainment expression of Eq. (8) is the criterion for total outflow.

4 Conclusions

The iteration process between measured data, CFD input/output, and thermal model input/output led to an assessment of the assumed aero-based empirical correlations, more confidence on the predicted hot-running clearances, and to a better understanding of the physics of flow in industrial rim sealing cavities. It has been demonstrated that the joint validation process between thermal analysis and CFD along with the interactive approach of information exchange leads to an effective mechanism for improving the knowledge database for complex rotating cavity flow systems. The results of this investigation have revealed a low labyrinth seal *Cd* value, the ripple effect of an axial step midway the cavity, the entrance and exit secondary flow recirculation regions, and a highly effective rim seal whose sealing is controlled by disk rotation rather than annulus pressure asummetry. A three dimensional study is anticipated in the future to delineate the effects of rotation and annulus asymmetry on ingestion.

The aeroengine-based correlations of windage heating, free disk heat transfer and entrainment flow, rim sealing flow, and turbulent boundary layer thickness were all assessed. Despite the high Reynolds number, the analytical expressions are valid for the industrial rotor-stator cavity. The CFD computed disk wall heat flux profile was compared against the heat flux calculated using the free-disk correlation and a good agreement was achieved. However, expressions for the free disk entrainment flow and the turbulent boundary layer thickness were modified by using the axial mean relative tangential velocity. Values of the turbulent flow parameter were found to be 0.08 for the minimum disk flow (with stator inflow) and 0.22 for total rotor-stator outflow. Moreover, windage heating for the industrial labyrinth seal was seen to conform more closely with the universal windage correlation rather than that with the aeroengine-based labyrinth seal.

Acknowledgment

The publication of this paper is dedicated to my father, Victor A. Mirzamoghadam (Mechanical Engineer and former ASME member), who died the day before I presented this paper in Munich, Germany on May 10, 2000.

Nomenclature

A = flow area, m^2
Cd = Coefficient of discharge
C_p = specific heat at constant pressure
C_w = nondimensional massflow parameter ($=m/\mu r$)
G_c = gap ratio ($=s/Ro$)
h = local heat transfer coefficient (W/m^2-K)
k = thermal conductivity of fluid; turbulent kinetic energy; carryover effect
m = mass flow rate, kg/s
n = exponent in power-law equation for surface temperature
n^* = number of fins for the labyrinth seal
Nu = local Nusselt number ($=hr/k$)
P = pressure, N/m^2
Pr = fluid Prandtl number ($=\mu Cp/k$)
q = heat flux, W/m^2
r = local disk radius, m
R = gas constant
Ro = cavity outer radius, rim seal radius (m)
Re_U = rotational Reynolds number ($=\rho\omega r^2/\mu$)
Re_w = annulus Reynolds number ($=\rho uRo/\mu$)
$\mathrm{Re}_{\varphi r}$ = $\rho V\varphi r/\mu$

s = axial gap between rotor and stator; radial seal clearance, (m)
T = Temperature
t = pitch of labyrinth seal, m
u = annulus mean axial velocity, m/s
$V\varphi$ = axial mean flow tangential relative velocity, m/s
x = axial coordinate
Δ = difference
δ^* = nondimensional boundary layer thickness (δ/Ro)
ρ = fluid density, kg/m^3
μ = dynamic viscosity, kg/m-s
μ = shaft rotational speed, 1/s
λ_T = turbulent flow parameter $(C_w/\mathrm{Re}_{\varphi,r}^{0.8})$

Subscripts

act = actual
fd = free disk
i = inner
id = ideal
in = inlet
o = outer; reference
pu = (heat) pickup
r = local radius; rotor
s = static; stationary
t = total
U = local disk peripheral speed
w = at the wall surface

References

[1] Roy, R. P., Devasenathipathy, S., Xu, G., and Zhao, Y., 1999, ''A Study of the Flow Field in a Model Rotor-Stator Disk Cavity,'' ASME Paper No. 99-GT-246.

[2] Vaughan, C., 1986, ''A Numerical Investigation into the Effect of an External Flow Field on the Sealing of a Rotor-Stator Cavity,'' Ph.D. thesis, University of Sussex.

[3] Phadke, U. P., and Owen, J. M., 1988, ''Aerodynamic Aspects of the Sealing of Gas Turbine Rotor-Stator Systems, Part 3: The Effect of Nonaxisymmetric External Flow on Seal Performance,'' Int. J. Heat Fluid Flow, **9**, No. 2, pp. 113–117.

[4] Ko, S. H., and Rhode, D. L., 1992, ''Thermal Details in a Rotor-Stator Cavity at Engine Conditions With a Mainstream,'' ASME J. Turbomach., **111**, pp. 333–340.

[5] Chew, J. W., Green, T., and Turner, A. B., 1994, ''Rim Sealing of Rotor-Stator Wheelspaces in the Presence of External Flow,'' ASME Paper No. 94-GT-126.

[6] Green, T., and Turner, A. B., 1994, ''Ingestion into the Upstream Wheelspace of an Axial Turbine Stage,'' ASME J. Turbomach., **116**, pp. 327–332.

[7] Bohn, D., Johann, E., and Krüger, U., 1995, ''Experimental and Numerical Investigations of Hot Gas Ingestion in Rotor-Stator Systems With Superimposed Cooling Mass Flow,'' ASME Paper No. 95-GT-143.

[8] Bohn, D., Rudzinski, B., and Suerken, N., 1999, ''Influence of Rim Seal Geometry on Hot Gas Ingestion into the Upstream Cavity of an Axial Turbine Stage,'' ASME Paper No. 99-GT-248.

[9] Reichert, A. W., and Lieser, D., 1999, ''Efficiency of Air-Purged Rotor-Stator Seals in Combustion Turbine Engines,'' ASME Paper No. 99-GT-250.

[10] Owen, J. M., and Rogers, R. H., 1989, *Flow and Heat Transfer in Rotating Disk Systems. Vol. I: Rotor-Stator Systems*, Research Studies Press, Taunton, UK.

[11] Chen, J. X., Gam, X., and Owen, J. M., 1996, ''Heat Transfer in an Air-Cooled Rotor-Stator System,'' ASME J. Turbomach., **118**, pp. 444–451.

[12] Roy, R. P., Agarwal, V., Devasenathipathy, S., He, J., Kim, Y. W., and Howe, J., 1997, ''A Study of the Flow Field and Convective Heat Transfer in a Model Rotor-Stator Cavity,'' *Experimental Methods in Heat Transfer*, HTD-Vol. 353, ASME, New York, pp. 97–107.

[13] Mirzamoghadam, A. V., 1996, ''Investigation of the Flow and Heat Transfer in a Low Pressure Turbine Interdisc Cavity with Skewed Radial Jet-Flow,'' ASME Paper No. 96-GT-308.

[14] Zimmermann, H., and Wolff, K. H., 1998, ''Air System Correlations, Part 1: Labyrinth Seals,'' ASME Paper No. 98-GT-206.

[15] Dorfman, L. A., 1963, *Hydrodynamic Resistance and Heat Loss of Rotating Solids*, Oliver and Boyd, London.

Influence of a Honeycomb Facing on the Heat Transfer in a Stepped Labyrinth Seal

K. Willenborg
e-mail:klaus.willenborg@its.uni-karlsruhe.de

V. Schramm

S. Kim

S. Wittig

Lehrstuhl und Institut für Thermische
Strömungsmaschinen,
Universität Karlsruhe
Kaiserstr. 12,
D-76128 Karlsruhe, Germany

The influence of a honeycomb facing on the heat transfer of a stepped labyrinth seal with geometry typical for modern jet engines was investigated. Heat transfer measurements were obtained for both a smooth stator and a stator lined with a honeycomb structure. In addition, an LDV system was used with the scaled up geometry to obtain a high local resolution of the velocity distribution in the seal. The experiments covered a wide range of pressure ratios and gap widths, typical for engine operating conditions. Local heat transfer coefficients were calculated from the measured wall and gas temperatures using a finite element code. By averaging the local values, mean heat transfer coefficients were determined and correlations for the global Nusselt numbers were derived for the stator and the rotor. The LDV results showed strong geometrical effects of the honeycomb structure on the development of the flow fields for the honeycomb seal. The distribution of the local heat transfer coefficients are compatible with the flow features identified by the LDV results and reveal a significantly reduced heat transfer with the honeycomb facing compared to the smooth facing. [DOI: 10.1115/1.1403459]

Introduction

Labyrinth seals represent an important element of the internal air system of modern gas turbines. Whereas the leakage losses strongly affect the overall efficiency of the engine, the heat transfer characteristics affect the global heat balance of the engine and determine the thermal loads of the adjacent engine components. In order to reduce losses in the internal air system in many applications, the smooth seal geometry is replaced by a labyrinth configuration with a honeycomb facing mounted on the stator. The honeycomb structure withstands the severe operating conditions in terms of high temperatures and high rotational speeds while allowing limited rubbing of the stator fins at the rotor without the danger of seal failure. Therefore, a significantly tighter seal clearance, which represents a leakage-reducing factor, can be realized. Furthermore, for certain geometrical conditions, an additional roughness further restricting the flow through the seal can arise from the honeycombs.

The flow in smooth labyrinth seals has been the subject of many previous studies (e.g., [1–8]). Despite of the widespread use of the honeycomb structure in seal applications, only little information regarding the aerodynamic behavior is available in the literature. Among other geometries Stocker [9] examined the leakage behavior of straightthrough labyrinth seals and observed that for the honeycomb configuration a significant increase in leakage occurred for small gap widths whereas for larger seal clearances an enhanced seal performance was obtained. Depending on the seal clearance and honeycomb cell size, the effective gap width is increased or the honeycomb structure causes an increased roughness of the stator surface. The data obtained by Stocker [9] is included in the list of correlations given by Zimmermann et al. [10]. The flow visualization performed by Brownell et al. [11] showed a significant change in the density distribution for the straight-through seal with honeycomb facing. The density contours obtained with the optical technique of holographic interferometry indicate a faster diffusion of the flow resulting in a reduced leakage rate. Childs et al. [12] investigated the leakage and the rotordynamic behavior of annular honeycomb seals. Compared to smooth configurations the honeycomb stators showed superior seal performance. In agreement with Stocker [9], a distinct sensitivity of the discharge characteristics to changes in the cell geometry was observed. Friction factors for several honeycomb surfaces have been determined by Ha et al. [13,14]. For all honeycomb geometries, generally higher friction factors were obtained compared to the smooth surface. Again, the absolute level showed a strong dependence on the gap width and cell geometry. Millward et al. [15], who were mainly focused on temperature rise due to windage heating, observed a reduced mass flow for honeycomb configurations of straight through seals compared to smooth geometries in their experiments.

The lack of data regarding the heat transfer behavior of honeycomb lands is even more serious. To the authors' knowledge, no information has been published on the heat transfer of honeycomb seal configurations. There are a few publications available concerning the heat transfer in labyrinth seals with a smooth stator. For a stepped labyrinth seal, Kapinos et al. [16] obtained increasing global Nusselt numbers with increasing seal clearance. Witting et al. [4] conducted both numerical and experimental investigations of the heat transfer of plain labyrinth seals. In their study, the highest local heat transfer coefficients at the stator were observed directly opposite of the fin positions. For the rotor, the highest values of the heat transfer coefficients were found at the top of the fins. A relative maximum in the distribution of the heat transfer coefficients was obtained in the middle of the chamber, underneath the forward facing step of the stator. The Nusselt numbers showed distinct gap size dependence in terms of increasing Nusselt numbers with increasing seal clearance. Following these investigations in nonrotating geometries, the influence of the rotation on the heat transfer has been the subject of further studies by Kapinos et al. [17] and Waschka et al. [18,19].

The main objective of the present study is to determine and to quantify the influence of a honeycomb facing on the heat transfer of a nonrotating stepped labyrinth seal. In this study no rotational effects have been measured. The stationary two-dimensional setup allowed for a simplified test rig and the acquisition of detailed LDV measurements in the complex labyrinth geometry. The correction of data from nonrotating geometries for rotational effects can be obtained by applying the results of Waschka et al. [18,19].

Contributed by the International Gas Turbine Institute (IGTI) of THE AMERICAN SOCIETY OF MECHANICAL ENGINEERS for publication in the ASME JOURNAL OF ENGINEERING FOR GAS TURBINES AND POWER. Paper presented at the International Gas Turbine and Aeroengine Congress and Exhibition, Munich, Germany, May 8–11, 2000; Paper 00-GT-290. Manuscript received by IGTI, Nov. 1999; final revision received by ASME Headquarters, Feb. 2000. Associate Editor: D. R. Ballal.

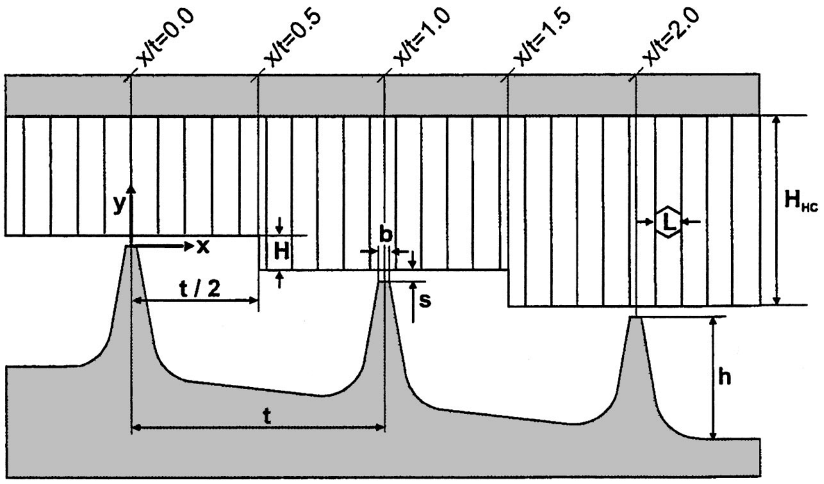

Fig. 1 Labyrinth seal geometry: $h/t=0.46$, $H/t=0.14$, $b/t=0.047$, $H_{HC}/t=0.86$, $L/t=0.23$, $s/t=0.043\ldots0.114=28$ mm

Waschka et al. found that regardless of the seal geometry, rotation has to be considered if the peripheral velocity exceeds the axial velocity of the flow. For higher rotational speeds, an increase of the heat transfer was observed.

The geometry investigated in the present study is shown in Fig 1. In order to allow optical access for the LDV measurements, the labyrinth geometry of the real engine was scaled up by a factor of four. The flow direction was always from the left to the right, i.e., the stator forms a forward-facing step. Note that the geometrical dimensions for the two configurations (with and without honeycombs) are identical. For the smooth configuration, the honeycomb structure as shown in Fig. 1 is replaced by a solid design of the stator. In the experiments, the overall pressure ratio π has been varied from 1.05 to 1.6. Three different gap widths ($s/t=0.043$, 0.071, 0.114; denoted as s1, s2, s3 in the following sections) have been employed. The LDV measurements were performed for two pressure ratios (1.1 and 1.5) for the smallest and largest gap width.

Experimental Approach

Test Facility and Rig Instrumentation. The present experiments were carried out in a test facility, which has been used in previous studies of leakage loss and heat transfer in labyrinth seals ([4,5,18,19]). The test facility, as shown in Fig. 2, allows to discharge air at variable temperatures and pressures through the test section.

A compressor provides the air to the test facility. The bypass valve serves to keep the pressure at the orifice meters at a constant value of three bars. According to the respective flow rate, one of the three orifice meters is chosen for the accurate measurement of the air mass flow. A high-precision differential pressure transducer is used to determine the pressure drop at the respective orifice meter. The pressure in the calming section and hence at the inlet of the test section is adjusted with the valves downstream of the orifice meters. For all experiments, the pressures at the outlet of the test section were ambient. The overall pressure ratios from 1.05 to 1.6 in the present experiments resulted in air flow rates from 15 to 120 g/s.

The intercooler and the heater serve to adjust the temperature of the air flow. A variable-power heater allowed for exit temperatures to 400°C. In order to generate a uniform velocity and temperature distribution, the calming section positioned upstream of the labyrinth test section is equipped with several screens and meshes.

Figure 3 shows a cross-sectional view of the labyrinth seal test sections. Two parts form the labyrinth geometry, a lower part with fins representing the rotor and an upper part representing the stator. Different gap widths are adjusted by means of spacers. The

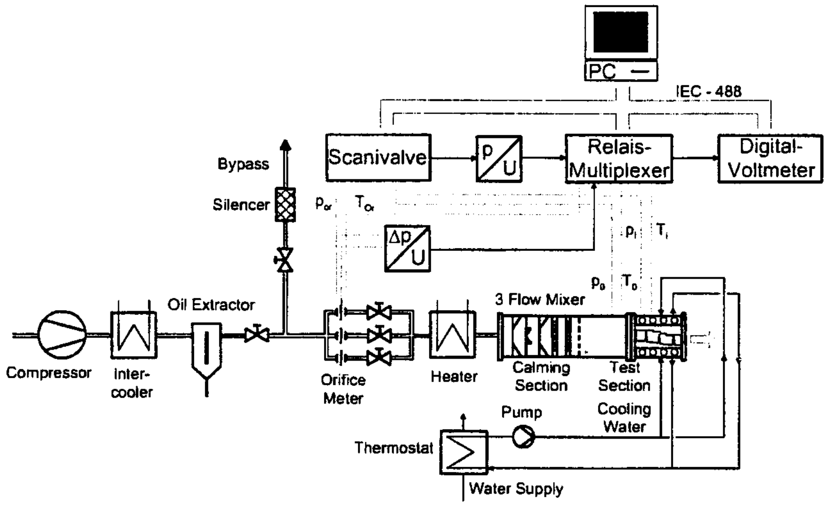

Fig. 2 Labyrinth seal test facility

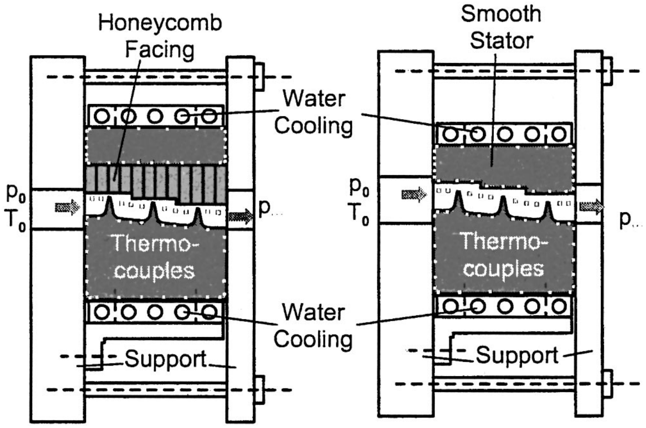

Fig. 3 Test sections with instrumentation

seal model is mounted directly to the settling chamber such that the flow enters the test section without swirl. In order to eliminate side effects, the test section is designed with a ratio of channel width to gap width greater than 90. For the heat transfer measurements, water-cooled plates mounted above and below the test section remove the heat with a sufficiently high-temperature gradient across the stator and the rotor.

Thermocouples (NiCr-Ni, Type K) with an outer diameter of 0.5 mm were used to measure the surface temperatures of the stator and the rotor. All thermocouples are positioned in one plane, approximately halfway of the width of the test section. In order to achieve a high thermal contact, the honeycomb structure is attached to the stator by means of a thin solder layer. Note that for this seal configuration, the thermocouples are positioned at the base of the honeycomb lining within the solder layer. Additional thermocouple probes were inserted horizontally from the side into the seal chambers and served to obtain the distribution of the gas temperature across labyrinth seal. A PC (Fig. 2) controls the data acquisition of all temperature and pressure signals.

In the heat transfer experiments, the inlet temperature was set to a typical value of 320°C. The cooling water was provided with a temperature of 15°C. This resulted in maximum temperatures of the surfaces facing the flow in the range from 50 to 160°C.

A modified two-dimensional set up of the LDV system that has been used in previous studies by Jakoby et al. [20] was employed for the velocity measurements. The light source is formed by an Argon-Ion laser in multimode operation. The optical components and signal processors are included in a commercial Dantec system which consists of a transmitter box, a two dimensional fiber probe, one photomultiplier tube and one burst spectrum analyzer (BSA) for each channel. Optical access to the labyrinth flow is gained from one side of the test section by replacing the solid sidewall with a glass window. The set up allowed acquiring the velocity components in the x-y plane (Fig. 1). The optical set up of the LDV system is characterized by a beam separation of 38 mm and a focal length of 400 mm. With wavelengths of 488 nm and 514.5 nm for the u and v velocity components, respectively, a measuring volume with a diameter of 0.2 mm and a length of approximately 4 mm is formed by the crossing laser beams. Due to the limited optical access from only one side of the test section, the backscatter mode was chosen for the measurements. $CaCO_3$ particles with a mean diameter of 1 μm were used for the seeding. Data rates in the range from 500 to 2000 Hz could be achieved in the present experiments. In order to eliminate sidewall effects the LDV traverses were conducted at z-positions sufficiently far away from the sidewall. Performing LDV traverses in planes located at several z-positions allowed the detection of a possibly occurring three-dimensional character of the flow field. Note that in order to simplify the experimental procedure and to match the conditions of the parallel numerical study ([21]) the LDV measurements have been conducted with unheated air, i.e., the inlet air temperature was ambient. Since the other parts of the test section were at the same temperature, adiabatic flow conditions were obtained.

Data Reduction. The Reynolds number is defined with the hydraulic diameter of the labyrinth gap as characteristic length scale. For the test section with a very large ratio of channel width to channel height the hydraulic diameter can be expressed as $2\cdot s$:

$$\mathrm{Re}=\frac{\rho c 2s}{\mu}=\frac{2\dot{m}}{\mathrm{B}\mu}. \tag{1}$$

The local heat transfer coefficient h is derived from the local heat flux, which is determined by the temperature gradient in the surface of rotor or stator:

$$h=\frac{-\lambda_W \left.\frac{\partial T_W}{\partial n}\right|_W}{T_G-T_W}. \tag{2}$$

The gas and wall temperatures were measured as described above. Finite element calculations with the measured surface temperatures as boundary conditions were performed to obtain the two-dimensional temperature distribution in the stator and the rotor. Therefore, the surface temperature on each boundary knot of the finite element mesh was interpolated from the measured temperature distributions utilizing rational spline functions. Since the labyrinth fins are not equipped with thermocouples, this region has not been resolved in the finite element mesh. However, the positioning of thermocouples on each side of the base ensures that the heat flux from the fins is taken into account in the finite element calculations. Thus the calculated heat transfer coefficients for the rotor represent fin heat transfer coefficients.

Mean heat transfer coefficients and global Nusselt numbers for the stator and the rotor have been obtained by averaging the local values:

$$\overline{h}=\frac{\dot{Q}w,\text{total}}{A(\overline{T}_G-\overline{T}_W)}. \tag{3}$$

For the rotor, the mean heat transfer coefficients were computed with the total heat flux normalized to the rotor surface without fins. The reference temperatures of gas and wall have also been averaged from local values. Analogous to the heat flux, the reference temperature for the rotor was computed without considering the fin surface. Nusselt numbers are derived from the mean heat transfer coefficients, analogous to the Reynolds number with the hydraulic diameter of the labyrinth gap $(2\cdot s)$ as characteristic length:

$$\mathrm{Nu}=\frac{\overline{h}2s}{\lambda_G}. \tag{4}$$

The overall pressure ratio π across the seal is defined as the ratio of inlet pressure to outlet pressure:

$$\pi=\frac{p_0}{p_\infty}. \tag{5}$$

An ideal velocity representative for isentropic expansion has been chosen to normalize all velocity data obtained in the LDV measurements:

$$c_s=\sqrt{2RT_0\frac{\kappa}{\kappa-1}(1-\pi^{(1-\kappa)/\kappa})}. \tag{6}$$

The uncertainty of the heat transfer coefficients obtained by the finite element method is determined mainly by the thermal conductivity and the thickness of the parts forming the stator and the rotor. According to a one-dimensional error analysis, the geometrical dimensions of the stator and the rotor have been optimized and the most suitable material was chosen in order to minimize the measuring inaccuracies of the heat transfer coefficients. The uncertainty of the local heat transfer coefficients was computed to be in the range from 12–25 percent. The largest inaccuracies occur for low heat transfer coefficients and small differences in gas and wall temperature. Since the mean heat transfer coefficients are derived by averaging the local values the uncertainty in the global Nusselt numbers are distinctly below the maximum uncertainty in the local heat transfer coefficients.

The statistical convergence of the velocity values has been checked and was found acceptable. Typically, more than 15,000 single data points were available for computing the mean velocity.

Results and Discussions

Comprehensive investigations have been conducted in the scope of the study reported here. In the following paragraphs, sample results of the LDV measurements characterizing the structure of the flow field are shown and are compared to the distributions of the local heat transfer coefficients. Following the discussion of the local heat transfer coefficients, global Nusselt numbers and appropriate correlations are presented.

Velocity Field. As mentioned above, LDV measurements have been conducted for the gap widths s1 and s3 for two pressure ratios. The results from LDV traverses in several planes at different *z*-positions showed the three-dimensional development of the flow field for the honeycomb configuration. As a sample, the velocity data for two gap widths and one pressure ratio are compared in Figs. 4–7 for the two seal configurations. LDV data acquired in two planes at different *z*-positions is presented for the honeycomb seal in order to illustrate the three-dimensional character of the flow-field induced by the honeycombs. Further detailed information regarding the local flow field is presented by Schramm et al. [21] who compared the experimental data with comprehensive numerical calculations.

The velocity distributions for the smooth configuration obtained by the LDV measurements are presented in Figs. 4 and 5. All velocity data are displayed in a nondimensional manner with the flow speed for isentropic expansion as reference (Eq. (6)).

The flow is accelerated above the fins and the highest flow speeds occur downstream of the labyrinth gap. For the smallest gap width (Fig. 4), the strong deflection at the forward facing step of the stator results in an almost normal impingement of the flow on the rotor in the center of the labyrinth chamber. Two counter-rotating vortices of equal size develop in the labyrinth chamber.

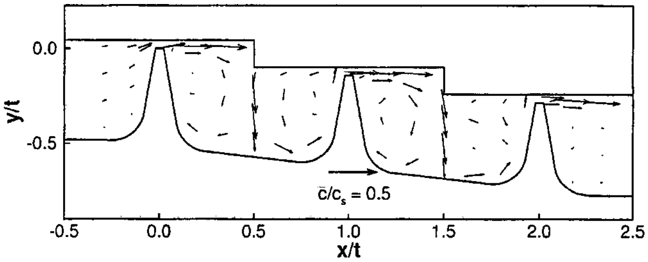

Fig. 4 Velocity field, smooth configuration, $\pi=1.1$, s1

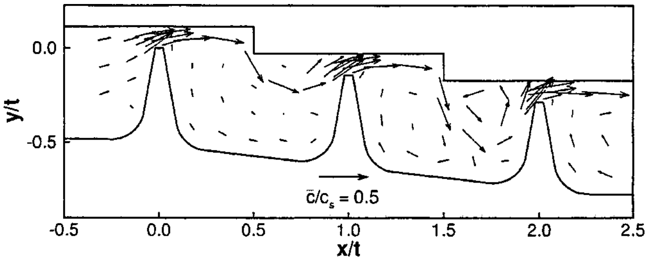

Fig. 5 Velocity field, smooth configuration, $\pi=1.1$, s3

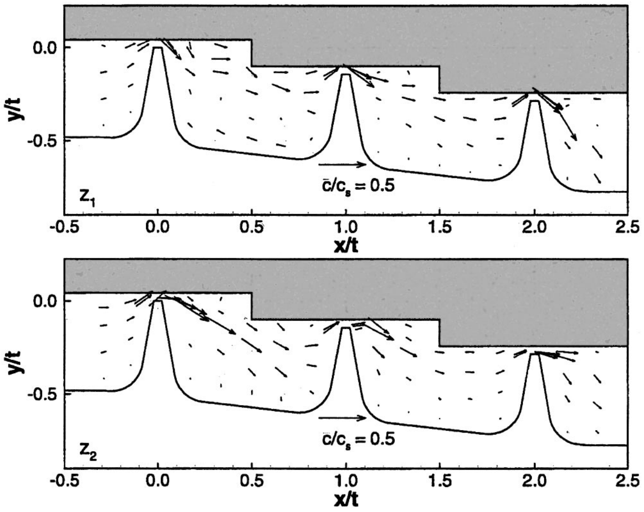

Fig. 6 Velocity field, honeycomb, $\pi=1.1$, s1

As visible in Fig. 5, the deflection of the main flow at the step of the stator is significantly reduced for the larger gap width s3. The two equally shaped vortices are replaced by one larger and deformed vortex at the bottom of the labyrinth chamber and a smaller structure located downstream of the stator step. Again, the highest flow velocities occur downstream of the labyrinth gap. For the two gap widths, the maximum normalized flow speeds are approximately the same.

The results show that the global flow structure differs significantly with the gap width. Measurements for further pressure ratios showed that the influence of the overall pressure ratio on the structure of the normalized velocity field is negligible.

In Figs. 6 and 7, the results of LDV traverses in two planes at different lateral positions of the honeycomb seal are shown for a fixed pressure ratio. Due to the not perfectly manufactured honeycomb structure, the relative position of the honeycomb cells to the traverse plane varies slightly along the seal. The distance between the measurement planes z1 and z2 is approximately one cell diameter.

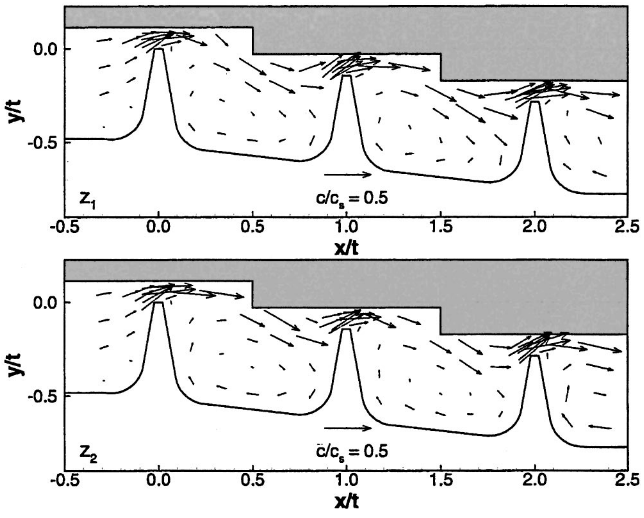

Fig. 7 Velocity field, honeycomb, $\pi=1.1$, s3

Figure 6 shows the velocity distribution of the honeycomb seal for the gap width s1. Compared to the smooth stator the deflection at the stator step is significantly reduced. A distinct three-dimensional character of the velocity field is observed. Different flow patterns are visible for the two lateral positions z1 and z2. Depending on the relative geometry at the seal clearance and the stator step the deflection angle varies between z1 and z2.

The velocity data for the larger gap width s3 are given in Fig. 7. Again, the deflection of the flow at the forward facing step of the stator is reduced compared to the smooth labyrinth seal. However, the differences between the velocity fields for smooth and honeycomb stator are less pronounced compared to the smaller gap width. Similar to the situation in the smooth seal, one larger deformed vortex develops in the labyrinth chamber. In addition the gap width s3 shows a three-dimensional flow structure, but significantly less pronounced than for the smaller clearance s1.

In the following subsection, the different structures of the velocity field are compared with the distributions of the local heat transfer coefficients.

Local Heat Transfer Coefficients. In Figs. 8 and 9 local heat transfer coefficients are compared for the smooth and the honeycomb configuration for a pressure ratio of $\pi = 1.5$. Compatible with the development of the flow-field, the overall pressure ratio showed no influence on the qualitative distribution of the heat transfer coefficients. The absolute values of the heat transfer coefficients increase with increasing pressure ratio.

At the smooth stator (Fig. 8, SM) the local heat transfer coefficients show a distinctly nonuniform distribution. Values from 80 to 1450 W/m^{2}K have been obtained. The highest heat transfer coefficients are reached between the labyrinth gap and the forward facing step. In this region, the highest flow speeds occur and the stator surface is directly exposed to the hot air flow.

In agreement with the results of previous investigations ([4]), a distinct minimum in the distribution of the local heat transfer coefficients is observed at the steps. A recirculation zone in front of the step is suspected to be responsible for this phenomenon as reported by Wittig et al. [4]. However, such a recirculation zone could not be resolved by the experimentally obtained velocity data of the present study. Due to the limited spatial resolution of the LDV system, the presence of a very small vortex structure at the step cannot be precluded. No definite dependence of the local heat transfer coefficient on the gap width can be identified for the smooth stator.

As visible in Fig. 8, the employment of the honeycomb structure (HC) results in a drastic decrease of the local heat transfer coefficients. For the stator lined with honeycombs, values reduced by a factor of five have been obtained. Compared to the smooth stator, a fairly uniform distribution ($h \approx 200\,\mathrm{W/m^2\,K}$) occurred. This decrease can be explained by the fluid enclosed in the honeycomb structure. The fluid separated from the main flow acts as an additional thermal insulation and reduces the convective transport of heat to the stator surface. In the region above the fins, the increased exchange of momentum between the main flow and the fluid inside the honeycombs results in a slightly enhanced convective heat transfer. For the honeycomb configuration, the local heat transfer coefficients increase with increasing gap width.

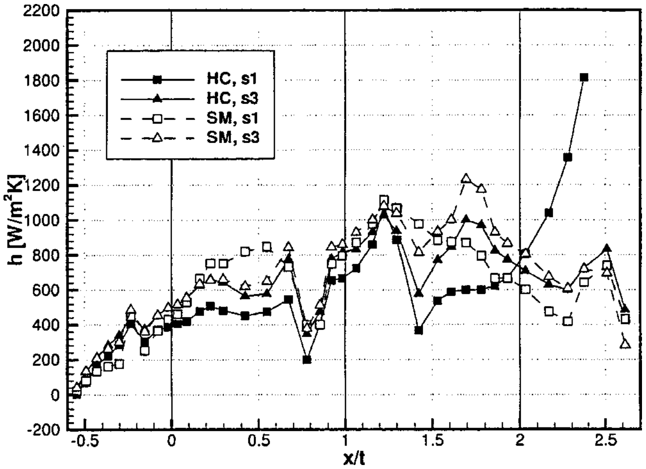

Fig. 9 Local heat transfer coefficients at the rotor, $\pi = 1.5$

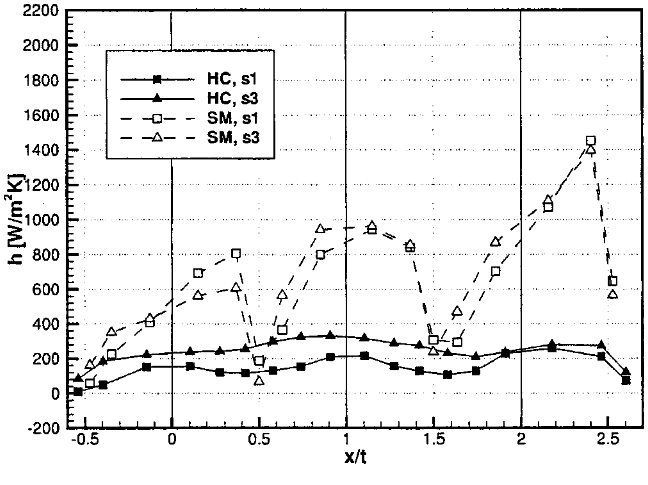

Fig. 8 Local heat transfer coefficients at the stator $\pi = 1.5$

Figure 9 shows the distributions of the local heat transfer coefficients at the rotor. For the labyrinth seal with the smooth stator, local heat transfer coefficients have been obtained in the range from 20–1250 W/m^2 K. Here (SM), the different structures of the velocity fields depending on the gap width are reflected in the distributions of the local heat transfer coefficients. The strong deflection of the flow at the forward-facing step of the stator and the resulting impingement of the flow on the stator in the center of the chamber for the gap width s1 agrees well with the maximum of the local heat transfer coefficients at this position in the first labyrinth chamber. For the larger gap width, this maximum is shifted downstream to the base of the following fin according to the reduced deflection of the flow. For the gap width s3, the distribution of the local heat transfer coefficients in the second chamber corresponds to the observed velocity field. The highest heat transfer coefficients are found at the base of the third fin where the main flow hits the rotor. However, for the gap width s1, no distinct increase in the heat transfer occurs in the center of the second labyrinth chamber, as it would be expected by the velocity field (Fig. 4).

Compared to the stator, the heat transfer coefficient distributions of the two seal configuration differ less distinctly at the rotor. The values of the local heat transfer coefficients are slightly lower for the honeycomb seal. Compatible with the relatively similar velocity fields in the labyrinth chambers for the two gap widths as shown in Figs. 6 and 7, the qualitative distributions of the local heat transfer coefficients for the honeycomb configuration agree fairly well. At the labyrinth exit, the heat transfer coefficients at the rotor of the two gap widths differ notably. Due to the stronger deflection by the honeycomb structure above the last fin at the gap width s1, the impingement of the flow on the stator results in a significantly increased heat transfer at this position.

Global Nusselt Numbers. In Figs. 10 and 11 global Nusselt numbers which have been computed from the local heat transfer coefficients are presented. The Nusselt numbers have been correlated with the Reynolds number and the gap width using an equation known from earlier investigations ([4]):

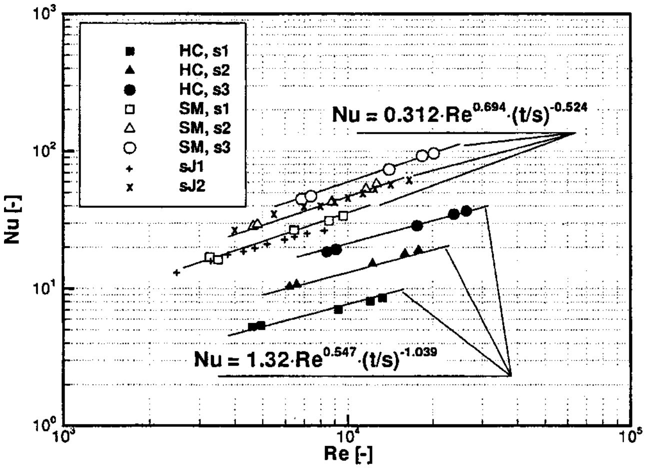

Fig. 10 Nusselt numbers for the stator

$$\mathrm{Nu} = C \cdot \mathrm{Re}^n \cdot \left(\frac{t}{s}\right)^m. \tag{7}$$

The functional dependence obtained for each configuration is included in the plots. For comparison the results obtained by Wittig et al. [4] who investigated a smooth design of a stepped labyrinth seal with comparable geometrical dimensions of the labyrinth chamber are also shown in the figures. The seal clearances sJ1 ($s/t = 0.028$) and sJ2 ($s/t = 0.060$) of the previous study represent values below the gap width s1 and between s1 and s2, respectively. In contrast to the present study, the labyrinth seal investigated by Wittig et al. ([4]) was equipped with five fins.

In the log-log scale of Fig. 10 a linear relationship between Nu and Re for each gap width is observed. As expected from the distribution of the local heat transfer coefficients, for a given gap width the Nu number increases with the Re number. The distributions of the Nu numbers show a strong dependence on the gap width with increasing Nu numbers as the gap width increases. Note that for a given Re number the dimensional mean heat transfer coefficient h decreases with increasing seal clearance. In agreement with the distribution of the local heat transfer coefficients, the heat transfer is distinctly reduced with the employment of the honeycomb facing. Compared to the smooth stator the honeycomb configuration shows a weaker impact of the Reynolds number as indicated by the lower exponent of the Re number.

Similar relations are observed for the rotor (Fig. 11). Again, the Nusselt number increases with increasing gap width. The difference in the level of the Nusselt numbers for the two configurations is less pronounced. In contrast to the stator, the slope of the correlation curves remains approximately the same. The reduced heat transfer at the rotor for the labyrinth configuration with honeycomb facing can be explained by the changed structure of the flow field. The direct impingement of the flow on the rotor as observed for the smooth configuration especially for the gap width s1 vanishes for the configuration with honeycombs. Furthermore, the reduced flow velocities at the bottom of the labyrinth chamber contribute to the decreased heat transfer.

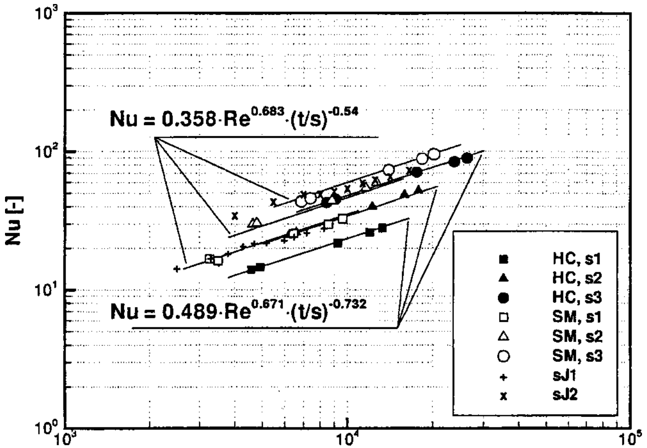

Fig. 11 Nusselt numbers for the rotor

Conclusions

In the present paper, the results of experimental investigations regarding the influence of a honeycomb facing on the heat transfer of a plain stepped labyrinth seal have been presented. Heat transfer coefficients as well as global Nusselt numbers have been obtained in the reported experiments. In addition, LDV measurements were performed to resolve the velocity field in the labyrinth geometry.

For the smooth seal configuration, the results of the LDV measurements show a distinct gap-size dependence of the structure of the velocity field. With the employment of the honeycomb facing, this dependence of the flow field is significantly less pronounced. Compared to the smooth design, the deflection of the flow at the forward facing step is reduced which means an also reduced direct impingement of the flow on the rotor. A three-dimensional character of the velocity field is induced by the honeycombs. With changing positions of the honeycomb cells relative to the fins and the stator step across the width of the seal the direction of the velocity vectors varies with the lateral position and crossover in the flow structures occur. This three-dimensional character is pronounced the most for the smaller gap width with a large ratio of cell diameter to seal clearance. Thus, the influence of the honeycomb lands on the flow field is dominated by geometrical effects.

The flow features observed from the LDV measurements are reflected in the distributions of the local heat transfer coefficients. The altered impingement of the flow on the rotor with increasing gap width for the smooth configuration was identified in the distributions of the local heat transfer coefficients. In agreement with the more similar velocity fields, the distributions of the local heat transfer coefficients of the honeycomb configuration differ only little. Compared to the smooth seal, distinctly lower values have been obtained.

For all configurations, the level of the Nusselt numbers depends strongly on the seal clearance. With increasing gap width, increasing Nusselt numbers have been obtained. The honeycomb facing causes a drastic decrease of the heat transfer at the stator. The fluid enclosed in the honeycomb structure prevents the convective heat exchange between the hot air flow and the stator surface and thus represents an additional thermal insulation of the stator. Due to the changed global flow field, the heat transfer is also reduced for the rotor. Compared to the stator the decrease is less pronounced. Correlations of the functional dependence of Nusselt number, Reynolds number and gap width (Eq. (7)) have been derived from the experimental data and include the influence of the honeycomb facing on the heat transfer.

Acknowledgment

The authors greatly acknowledge support for this work by the German BMWi. The work presented here was part of the German Luftfahrtforschungsprogramm 1995–1998. Special thanks are due to Dr. W. Waschka for intensive technical discussions and the coordination of the program.

Nomenclature

B = width of the test section [m]
b = fin tip thickness [m]
c = velocity [m/s]

C, m, n = correlation coefficients
H = height [m]
h = heat transfer coefficient [W/m^2 K]
L = honeycomb diameter [m]
$\dot{m}$ = mass flow rate [kg/s]
n = vector normal to the wall
$\mathrm{Nu}=\overline{h}2s/\lambda$ = Nusselt number
p = pressure [N/m^2]
R = specific gas constant [kJ/kg K]
$\mathrm{Re}=2\dot{m}/B\mu$ = Reynolds number
s = gap width [m]
t = pitch [m]
T = temperature [K]
x, y, z = Cartesian coordinates [m]
κ = ratio of specific heats
λ = thermal conductivity [W/mK]
μ = dynamic viscosity [kg/ms]
$\pi=p_0/p_\infty$ = pressure ratio
ρ = density [kg/m^3]

Subscripts

G = gas
HC = configuration with honeycombs
SM = smooth configuration
s = isentropic
total = total
W = wall
0 = inlet
∞ = outlet

Superscript

$-$ = mean value

References

[1] Komotori, K., and Miyake, K., 1977, ''Leakage Characteristics of Labyrinth Seals With High Rotating Speed,'' 1977 Tokyo Joint Gas Turbine Congress.
[2] Morrison, G. L., and Daesung, Chi, 1985, ''Incompressible Flow in Stepped Labyrinth Seals,'' ASME Paper 85-FE-4.
[3] Morrison, G. L., Johnson, M. C., and Tatterson, G. B., 1991, ''3-D Laser Anemometer Measurements in a Labyrinth Seal,'' ASME J. Eng. Gas Turbines Power, **113**, pp. 119–125.
[4] Wittig, S., Jacobsen, K., Schelling, U., and Kim, S., 1988, ''Heat Transfer in Stepped Labyrinth Seals,'' ASME J. Eng. Gas Turbines Power, **110**, pp. 63–69.
[5] Wittig, S., Schelling U., Jacobsen, K., and Kim, S., 1987 ''Numerical Predictions and Measurements of Discharge Coefficients in Labyrinth Seals,'' ASME Paper 87-GT-188.
[6] Rhode, D. L., and Hibbs, R. I., 1989 ''A Comparative Investigation of Corresponding Annular and Labyrinth Seal Flowfields,'' ASME Paper 89-GT-195.
[7] Rhode, D. L., Johnson, J. W., and Broussard, D. H., 1997, ''Flow Visualization and Leakage Measurements of Stepped Labyrinth Seals, Parts 1 and 2,'' ASME J. Turbomach., **119**, pp. 839–848.
[8] Prasad, B. V. S. S., Sethu Manavalan, D. L., Nanjunda Rao, N. V., 1997, ''Computational and Experimental Investigations of Straight-Through Labyrinth Seals,'' ASME Paper 97-GT-326.
[9] Stocker, H. L., 1978, ''Determining and Improving Labyrinth Seal Performance in Current and Advanced High Performance Gas Turbines,'' *AGARD-CP-237 Conference Proceedings*, pp. 13/1–13/22.
[10] Zimmermann, H., and Wolff, K. H., 1998, ''Air System Correlations, Part 1: Labyrinth Seals,'' ASME Paper 98-GT-206.
[11] Brownell, J. B., Millward, J. A., and Parker, R. J., 1989, ''Non-Intrusive Investigations Into Life-Size Labyrinth Seal Flow Fields,'' ASME J. Eng. Gas Turbines Power, **111**, pp. 335–342.
[12] Childs, D., Elrod, D., and Hale, K. 1989, ''Annular Honeycomb Seals: Test Results for Leakage and Rotordynamic Coefficients; Comparison to Labyrinth and Smooth Configurations,'' ASME J. Tribol., **111**, pp. 293–301.
[13] Ha, T. W., Morrison, G. L., and Childs, D. W., 1992, ''Friction-Factor Characteristics for Narrow Channels With Honeycomb Surfaces,'' ASME J. Tribol., **114**, pp. 714–721.
[14] Ha, T. W., and Childs, D. W., 1992, ''Friction-Factor Data for Flat-Plate Tests of Smooth and Honeycomb Surfaces,'' ASME J. Tribol., **114**, pp. 722–730.
[15] Millward, J. A., and Edwards, M. F., 1994, ''Windage Heating of Air Passing Through Labyrinth Seals,'' ASME J. Turbomach., **118**, pp. 415–419.
[16] Kapinos, V. M., and Gura, L. A., 1970, ''Investigation of Heat Transfer in Labyrinth Glands on Static Models,'' Therm. Eng., **17**, No. 11, pp. 54–56.
[17] Kapinos, V. M., and Gura, L. A., 1973, ''Heat Transfer of a Stepped Labyrinth Seal,'' Therm. Eng., **20**, No. 6, pp. 28–32.
[18] Waschka, W., Wittig, S., and Kim, S., 1992, ''Influence of High Rotational Speeds on the Heat Transfer and Discharge Coefficients in Labyrinth Seals,'' ASME J. Turbomach., **114**, pp. 462–468.
[19] Waschka, W., Wittig, S., Kim, S., and Scherer, T., 1993, ''Heat Transfer and Leakage in High-Speed Rotating Stepped Labyrinth Seals,'' AGARD-CP-527, pp. 26/1–26/10.
[20] Jakoby, R., Maeng, D. J., Kim, S., and Wittig, S., 1997, ''3D LDA-Measurements in Rotating Turbine Disk Systems,'' *Laser Anemometry Advanced Applications*, Proceedings of the 7th International Conference, Karlsruhe, Sept. 8–11.
[21] Schramm, V., Willenborg, K., Kim, S., and Wittig, S., 2002, ''Influence of a Honeycomb Facing on the Flow Field and Discharge Behavior of a Stepped Labyrinth Seal,'' ASME J. Eng. Gas Turbines Power, **124**, pp. 140–146.

V. Schramm

K. Willenborg

S. Kim

S. Wittig

Lehrstuhl und Institut für Thermische
Strömungsmaschinen,
Universität Karlsruhe,
Kaiserstr. 12,
D-76128 Karlsruhe, Germany

Influence of a Honeycomb Facing on the Flow Through a Stepped Labyrinth Seal

This paper reports numerical predictions and measurements of the flow field in a stepped labyrinth seal. The theoretical work and the experimental investigations were successfully combined to gain a comprehensive understanding of the flow patterns existing in such elements. In order to identify the influence of the honeycomb structure, a smooth stator as well as a seal configuration with a honeycomb facing mounted on the stator wall were investigated. The seal geometry is representative of typical three-step labyrinth seals of modern aero engines. The flow field was predicted using a commercial finite volume code with the standard k-ϵ turbulence model. The computational grid includes the basic seal geometry as well as the three-dimensional honeycomb structures.

[DOI: 10.1115/1.1403460]

Introduction

Labyrinth seals represent an elementary component of the internal air system of gas turbines. The flow characteristics of these elements have been investigated using manifold experimental and numerical techniques (e.g., [1–8]). Nevertheless, no detailed information is available for the flow case where honeycomb facings are present. In addition, only few publications deal with the influence of honeycomb facings on the leakage losses.

Stocker [9] studied the influence of abradable and honeycomb lands on the leakage through a four-knife straight-through labyrinth seal. For his investigations, he employed a planar two-dimensional and a rotating three-dimensional test rig. Stocker varied the seal clearance and the honeycomb diameter. He observed a significant influence on the honeycomb lands on the leakage, strongly dependent on the geometrical configuration. At large seal clearances in the planar test rig the honeycombs caused a leakage reduction up to 21 percent compared to the smooth configuration. However, with decreasing clearance the sealing performance deteriorated. At the smallest seal clearance and the largest honeycomb diameter investigated, the leakage was 96 percent higher than the leakage of the configuration with a smooth stator wall.

Brownell and Parker [10] investigated the leakage and the flow field of several straight-through and stepped-labyrinth seals. In their experiments, they used a holographic technique to visualize the isodensity contours of the flow field. In one configuration, honeycomb lands were attached to a five-stage straight-through labyrinth seal. Compared to the other cases, the holographic visualization showed a significant change in the isodensity contours. This change was explained to a direct consequence of a much lower carryover velocity, i.e., a better sealing performance.

To obtain a more detailed insight into the flow mechanisms that are responsible for the discharge behavior, the present study applies both experimental and computational techniques. In order to demonstrate the influence of the honeycomb land, the investigations have been conducted for a nonrotating labyrinth with a smooth stator, as well as for a labyrinth with honeycombs. The objective of this work is to point out the flow phenomena associated with such three-dimensional elements. The better understanding of the physics of the flow will allow a more efficient employment of honeycomb facings in future applications.

Figure 1 shows a cross-sectional view of the investigated seal geometry. A 4:1 scaled-up planar model of typical engine seal was chosen to obtain better spatial resolution of the LDV measurements. The scaled-up model was employed to obtain detailed information on the flow field. The investigations have been carried out for three gap widths $s1/t=0.043$, $s2/t=0.071$, and $s3/t=0.114$. For the smooth configuration, these gap widths have been covered in the experiments as well as in the numerical calculations. For the seal with honeycombs, the numerical investigations have been focused on the largest gap width. To match typical engine operating conditions, the overall pressure ratio has been varied from $\pi=1.03$ to 1.6. The honeycombs were aligned with the first labyrinth tip.

Experimental Setup

The present experiments were carried out in the test facility which has been used in previous studies of leakage loss and heat transfer in labyrinth seals ([3,11,13]). A schematic diagram of a test facility is shown in Fig. 2. Air can be supplied to the test section at variable temperatures and pressures. A maximum air flow rate of 0.5 kg/s can be achieved at a pressure ratio of 2 across the test section. A bypass valve serves to keep the pressure at the three parallel orifice meters at a constant value of 3 bar. Depending on the desired flow rate, one of the three orifice meters is chosen for the accurate measurement of the mass flow of air. A high precision differential pressure transducer is used to determine the pressure drop at the respective orifice meter. An error analysis yielded an uncertainty in the discharge coefficients of three percent. The intercooler and the heater serve to adjust the temperature of the air flow. Temperatures up to 400°C can be achieved. Hot air was used only in the parallel experimental heat transfer investigations ([14]). For the present adiabatic flow experiments, the inlet air temperature was typically 300 K. In order to generate a uniform velocity and temperature distribution, a calming section equipped with several screens and meshes is positioned upstream of the labyrinth test section.

The labyrinth model contains two main parts. The lower component carries the fins and represents the rotor of the labyrinth seal. The upper part represents the stator and is equipped with or without a honeycomb structure. Different gap widths are adjusted by means of spacers. The seal model is mounted directly to the settling chamber. In order to minimize side effects, the ratio of channel width to gap width was chosen to be greater than 90.

Contributed by the International Gas Turbine Institute (IGTI) of THE AMERICAN SOCIETY OF MECHANICAL ENGINEERS for publication in the JOURNAL OF ENGINEERING FOR GAS TURBINES AND POWER. Paper presented at the International Gas Turbine and Aeroengine Congress and Exhibition, Munich, Germany, May 8–11, 2000; Paper 00-GT-291. Manuscript received by IGTI Nov. 1999; final revision received by ASME Headquarters Feb. 2000. Associate Editor: D. R. Ballal.

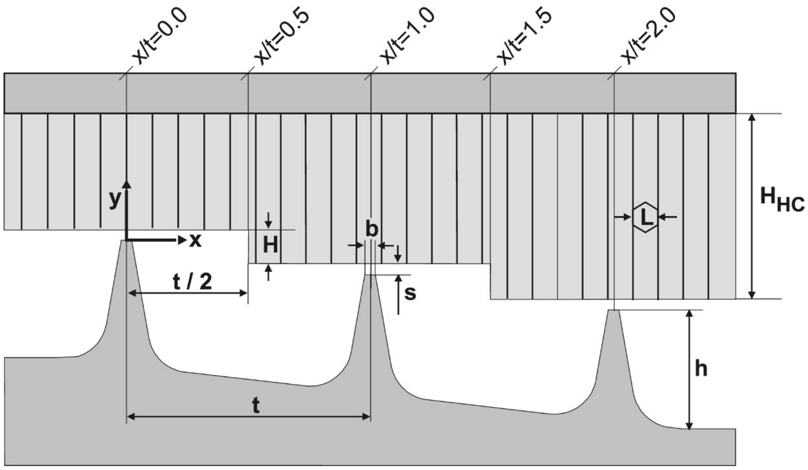

Fig. 1 Geometry of labyrinth seal: $h/t=0.46$, $H/t=0.14$, $b/t=0.047$, $HC/t=0.86$, $L/t=0.23$, $s/t=0.043,\ldots,0.114$, $t=28$ mm

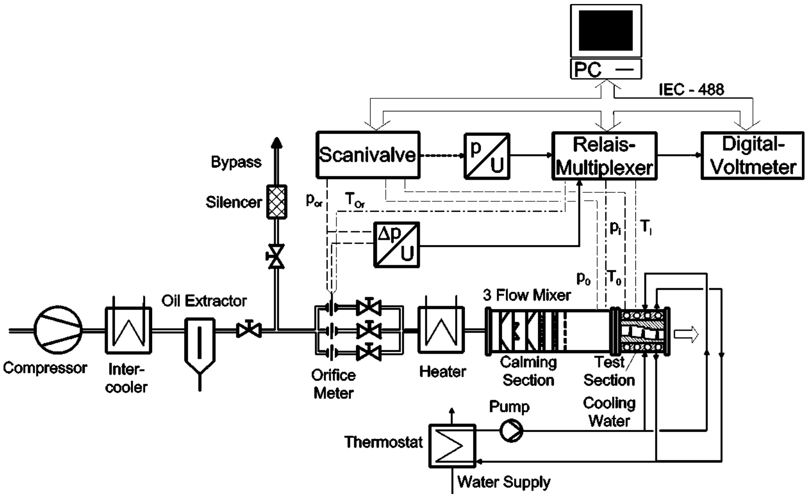

Fig. 2 Labyrinth seal test facility

For the velocity measurements, a two-dimensional LDV system was utilized. Optical access to the labyrinth flow was accomplished from one side of the test section by means of a glass window. The set up allowed the acquisition of velocity components in the x-y plane. The LDV traverses were conducted in several planes at sufficiently large distances from the window. Hence, a potential three-dimensional character of the flow field could be detected. A more detailed description of the experimental setup is given in Willenborg et al. [14].

Numerical Approach

For the numerical simulation of the labyrinth seal flow, the commercial finite volume code, TASCflow3D is used. This software solves the compressible time-averaged Navier-Stokes equations on a nonorthogonal, body-fitted structured grid. A second-order discretization scheme, the so-called linear profile scheme, combined with physical advection correction terms is used ([15]). The turbulence characteristics of the flow are modeled by the standard k-ϵ equations. The logarithmic wall function is used to describe the near-wall velocity. The y^+ criterion is met over almost the entire wall region. Critical locations for applying the logarithmic law are the regions of stagnation points and the regions inside the honeycomb cells, where minimum y^+ has relatively low values. However, as shown in earlier publications ([4,12,16]), this turbulence model is capable of simulating the labyrinth flow.

Due to the different geometrical topologies of the actual labyrinth and the honeycombs, the spatial discretization with a structured grid is critical. A grid adapting the labyrinth-grid topology to the honeycomb-grid topology results in massively distorted control volumes in the transition region between the labyrinth tip and the facing. Consequently, the convergence behavior deteriorates and the accuracy of discretization is reduced. In some cases, it is even impossible to obtain a converged solution. To avoid this difficulty, a “general grid interface” implemented in TASCFlow3D is used ([15]). This feature allows the connection of two grids with nonfitting nodal points. In the present study, it serves to connect the labyrinth with the honeycomb geometry.

A computational grid following this approach is shown in Fig. 3. Since only axial flow is admitted, the grid takes advantage of the symmetric properties of the seal geometry respective to the x-y plane. Hence, only half honeycombs are modeled. The grid consists of 34 blocks with a total number of 92,000 grid nodes. In case of the smooth configuration, only the lower part of the presented grid is used in the computations and the “general grid interface” is replaced by a wall boundary condition. For the

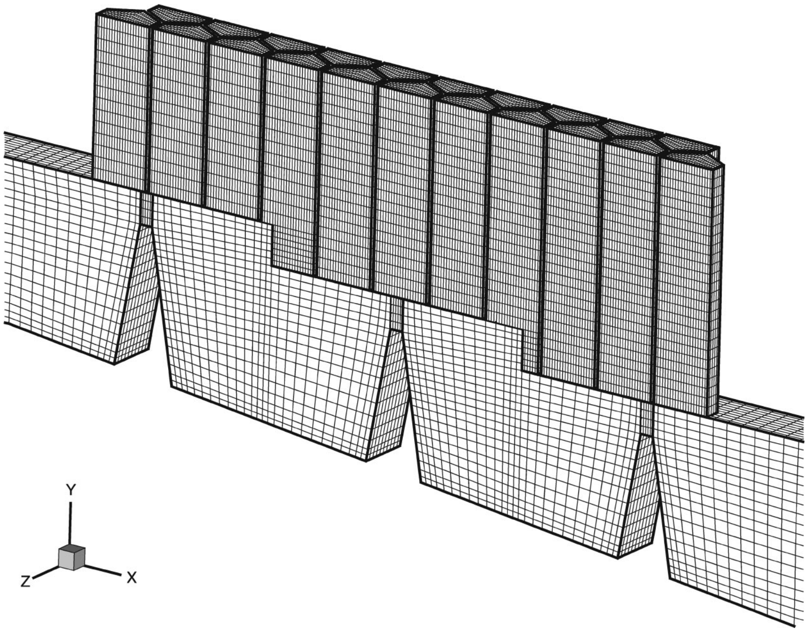

Fig. 3 Computational grid, configuration with honeycombs

smooth configuration, studies on refined computational grids showed the grid independence of the computational results. Velocity, temperature, and turbulence quantities are defined at the inlet of the seal. In addition, the walls are defined to be adiabatic and the outlet pressure is chosen to be ambient, in agreement with the experimental conditions.

Geometrical Considerations

Besides preventing mechanical failure, another purpose of the honeycomb facing is to reduce leakage through the seal. Pursuing this task, it has to be kept in mind that the honeycomb facing changes the boundary conditions near the tip of the fin. This is a region where the discharge behavior is extremely sensitive to small geometrical variations. A first step in estimating the influence of a honeycomb facing on the leakage is to describe the change of the gap width. In this context, Zimmermann [17] mentions an enlarged effective gap width, especially at small clearances. In Fig. 4, it is shown that the effective gap width, s_{eff}, can be substantially larger than the nominal clearance, s_{nom}, in the presence of honeycombs. If the tip thickness, b, is smaller than the honeycomb diameter, L, the effective gap width, s_{eff}, for a tip centered below the honeycomb opening becomes

$$s_{\mathrm{eff}}=\sqrt{\left(\frac{L-b}{2}\right)^2+s_{\mathrm{nom}}^2}. \tag{1}$$

For b larger than L, the effective gap width, s_{eff}, is equal to s_{nom}. Equation (1) is valid for the case, where the tip is centered below the opening of the honeycomb. For positions with the tip aligned to a web of the honeycombs, the nominal gap width, s_{nom}, takes effect. A simple geometrical consideration finally leads to an averaged gap width, s_{mean}.

$$\zeta_{\mathrm{geom}}=\frac{s_{\mathrm{mean}}}{s_{\mathrm{nom}}}=\frac{\frac{1}{2}s_{\mathrm{eff}}+\frac{1}{2}s_{\mathrm{nom}}}{s_{\mathrm{nom}}} \tag{2}$$

The parameter ζ_{geom} describes the averaged change of the cross-sectional area available for the through flow and gives an estimate for the increase of leakage. However, additional effects like a changed flow field or an increased roughness caused by the honeycomb facing are not considered by Eq. (2). In Fig. 5, ζ_{geom} is plotted for different ratios of b/L and s_{nom}/L. For increasing values of s_{nom}/L, the parameter ζ_{geom} shows an asymptotic trend towards a value of 1. In turn, ζ_{geom} diverges for decreasing ratios of s_{nom}/L. This behavior agrees well with the observations made

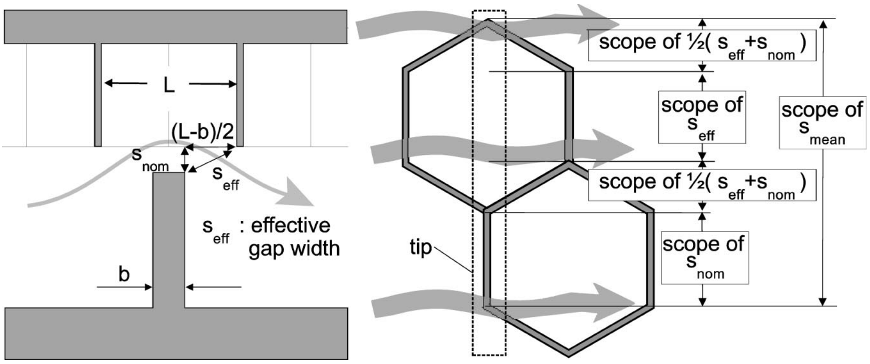

Fig. 4 Geometric situation near the gap, configuration with honeycombs

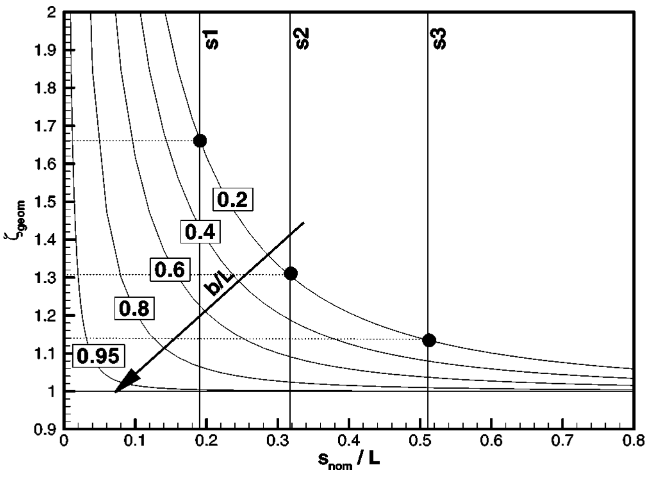

Fig. 5 Estimated influence of honeycomb facing on seal leakage

by Stocker [9] for straight-through labyrinth seals with smooth and honeycomb stator. Stocker recommended that honeycomb lands should be selected carefully for applications with small seal clearances. While the smooth configuration performed better in this situation, the roughness of the honeycomb lands became predominant at large clearances. Here Stocker observed a leakage reduction. To minimize the leakage through labyrinth seals with honeycomb facing, preferably values of $b/L \approx 1$ or $b/L > 1$ should be chosen. For such ratios, the values of ζ_{geom} are approximately 1 for a wide range of nominal gap clearances. For the geometry employed in the present investigation, b/L is fixed at 0.19 and s_{nom}/L is varied between 0.19 and 0.52. Hence, using Eqs. (1) and (2), the maximum relative increase of leakage is estimated to be 66 percent. In the results section, ζ_{geom} will be used for comparison with the leakage change due to the honeycombs.

Results: Smooth Configuration

Flow Field. Figure 6 shows the flow field obtained for the smooth configuration for two gap widths, $s1$ and $s3$. For clarity, every second velocity vector in each direction is omitted for the CFD data. The overall pressure ratio was set to $\pi = 1.1$. All velocity data have been normalized by an ideal velocity, c_s, which can be derived assuming isentropic expansion:

$$c_s = \sqrt{2RT_0 \frac{\kappa}{\kappa - 1}\left(1 - \pi^{(1-\kappa)/\kappa}\right)}. \tag{3}$$

The flow patterns show a distinct dependence on the gap width. In the first case (gap width $s1$, Fig. 6(*a*)), the fluid passes the labyrinth gap and impinges on the step. The jet is then deflected by almost 90 deg and directed towards the bottom of the labyrinth chamber beneath the step. Inside the cavity the jet separates two counter-rotating equally sized recirculation zones. The results for gap width $s2$ (not displayed in Fig. 6) show a flow field similar to the one obtained for gap width $s1$. Note that the stagnation point below the step has shifted slightly downstream (positive x-direction) compared to gap width $s1$. In case of gap width $s3$ (Fig. 6(*b*)), the shape of the flow field has changed distinctly. Due to the lower ratio of H/s, the flow deflection at the step is reduced. The position of the jet impingement zone on the rotor has moved from the position below the step to the flank of the downstream labyrinth fin. For the adjusted overall pressure ratios, sufficiently away from choking conditions, the influence of the pressure ratio on the shape of the flow field was observed to be very small.

Discharge Coefficients. A dimensionless discharge coefficient is defined to quantify the leakage behavior:

$$C_D = \frac{\dot{m}}{\dot{m}_{\text{ideal}}}. \tag{4}$$

In Eq. (4), the leakage mass flow rate $\dot{m}$ is taken from experiments or the CFD analysis. $\dot{m}_{\text{ideal}}$ stands for a theoretical mass flow for isentropic conditions:

$$\dot{m}_{\text{ideal}} = \frac{p_0 A}{\sqrt{T_0}} \sqrt{\frac{2\kappa}{R(\kappa - 1)}\left[\left(\frac{1}{\pi}\right)^{2/\kappa} - \left(\frac{1}{\pi}\right)^{(\kappa+1)/\kappa}\right]}. \tag{5}$$

In this formula, π represents the ratio of the inlet and outlet pressure ($\pi = p_0/p_\infty$). The cross-sectional area of the gap is calculated as $A = B \cdot s_{\text{nom}}$.

Figure 7 shows experimental and numerical results for the smooth configuration. Like the shape of the flow field, the leakage behavior depends strongly on the gap width, s. The discharge

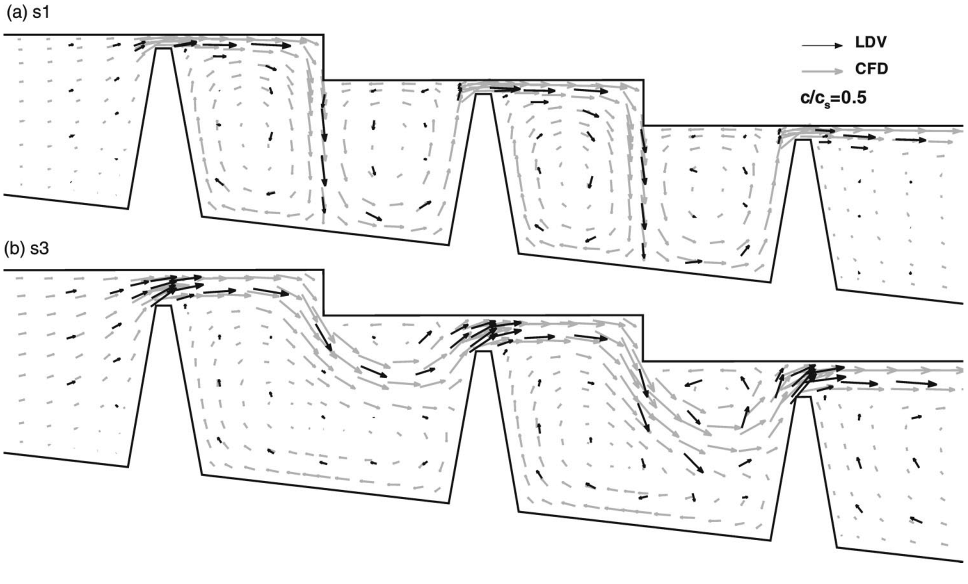

Fig. 6 Flow field, smooth configuration, π=1.1

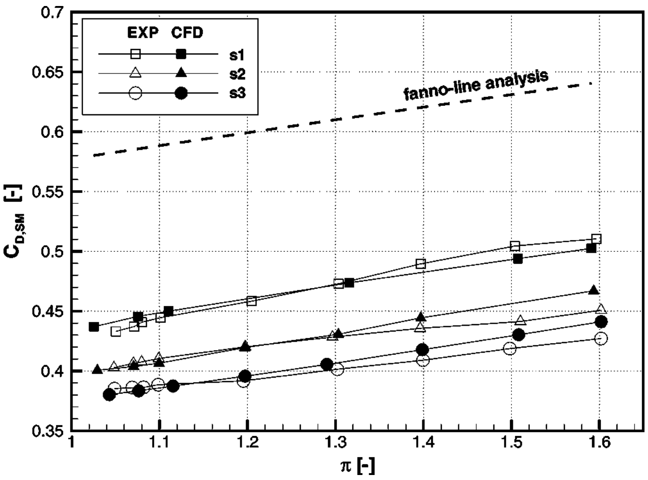

Fig. 7 Discharge coefficients, smooth configuration

coefficients decrease with increasing gap width. The linear rise of C_D with increasing pressure ratio can be reproduced by a simple Fanno-line analysis, which assumes an isentropic expansion across the fins and an isobaric dissipation within the labyrinth cavities. For a given overall pressure ratio and a given number of fins, the cavity pressure and the leakage flow rate of this ideal labyrinth can be calculated. The same linear and progressive behavior of the discharge coefficients with pressure ratio is shown for the present experimental and numerical results. For pressure ratios up to $\pi=1.3$, the measured discharge coefficients and the numerically obtained values agree very well. With increasing π, the CFD results deviate slightly from those obtained experimentally. The averaged relative deviation $((C_{D,CFD} - C_{D,EXP})/C_{D,EXP})$ approximates to 1.4 percent, the maximum relative deviation is 3.6 percent.

Results: Configuration With Honeycomb Facing

Flow Field. Figure 8 shows the computed flow field for the configuration with honeycombs at two lateral positions $z1$ and $z2$. The gap width is fixed for $s3$. For clarity, every second velocity vector in each direction is omitted. The shape of the flow field is similar to the smooth configuration at $s3$. Inside the honeycombs, recirculation zones occur that are driven by the viscous shear layer at the opening of the honeycombs. The intensity and the shape of these recirculation zones change with the position of the honeycombs relative to the labyrinth tips and the step on the stator. The flow pattern inside the honeycombs is further influenced by the height of these elements. A more detailed illustration of the flow field in the vicinity of the first tip is given in Fig. 9. At the lateral position $z1$ where the tip is centered beneath the opening of a honeycomb cell, part of the air uses the additional area provided by the honeycomb cell to overflow the fin. The main flow is slightly deflected towards the bottom of the labyrinth cavity. At the lateral position $z2$, the flow direction is distinctly less affected by the honeycombs. The air passes the gap similar to the flow case with a smooth stator.

The flow field from the LDV-measurements is shown in Fig. 10 (gap width $s3$) and Fig. 11 (gap width $s1$) for the two lateral positions, $z1$ and $z2$, respectively. Although the planes $z1$ and $z2$ of the experimental investigations do not exactly match the planes displayed in Figs. 8 and 9 due to a not perfectly manufactured honeycomb facing, the experimental results agree well with the numerical predictions (compare Fig. 10 with Fig. 8). Compared to the smooth configuration, the flow field changes substantially at the gap width $s1$ (see Fig. 6 and Fig. 11). Near the tip, the influence of the honeycomb land becomes most predominant. The local variation of geometry provokes a shift of the flow path into the honeycombs, as it has been already shown for the gap width $s3$ (Fig. 9).

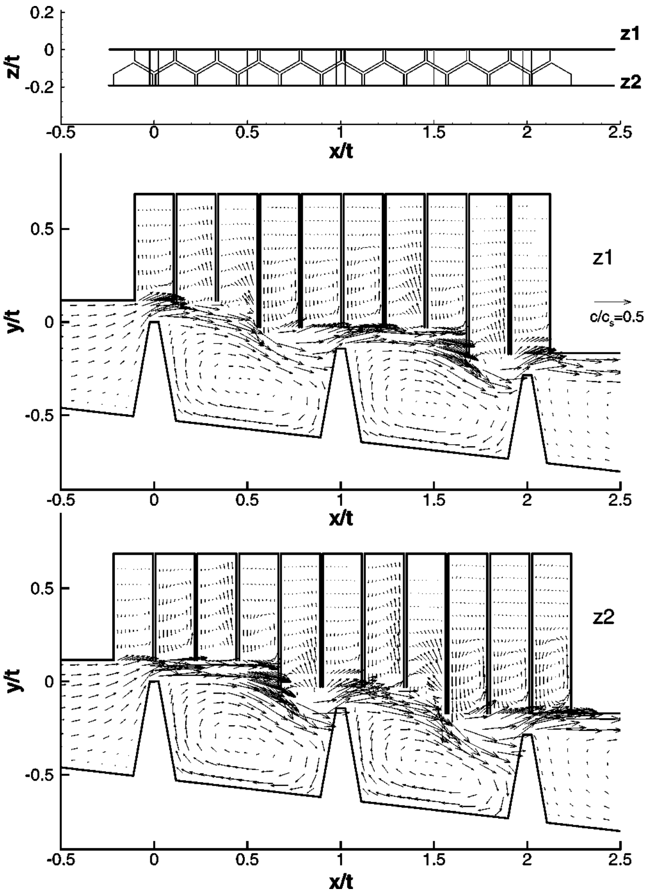

Fig. 8 Computed flow field, $\pi=1.1$, $s3$

For the smallest gap width, $s1$, the angle of the velocity vectors towards and away from the honeycomb land (Fig. 11) is greater than for gap width $s3$ (Fig. 10). This results in a more distinct deflection of the flow towards the bottom of the labyrinth chamber directly downstream of the fin tip. Hence, for the present configuration, the honeycombs do not act as an additional roughness element but change the global structure of the flow field by a macroscopic variation of the geometry.

Discharge Coefficients. The influence of the honeycombs on the discharge behavior is described by the ratio of the discharge coefficient for the configuration with honeycombs to the value for the smooth configuration.

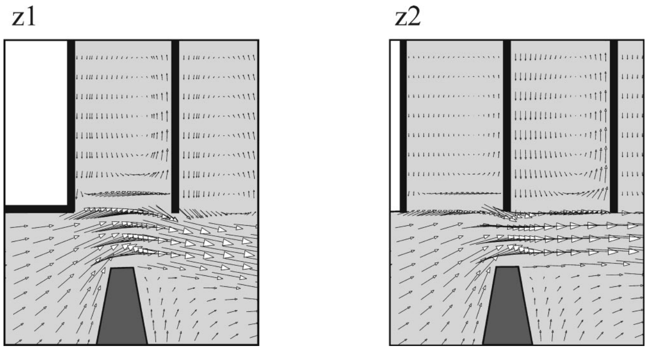

Fig. 9 Flow field detail (CFD)

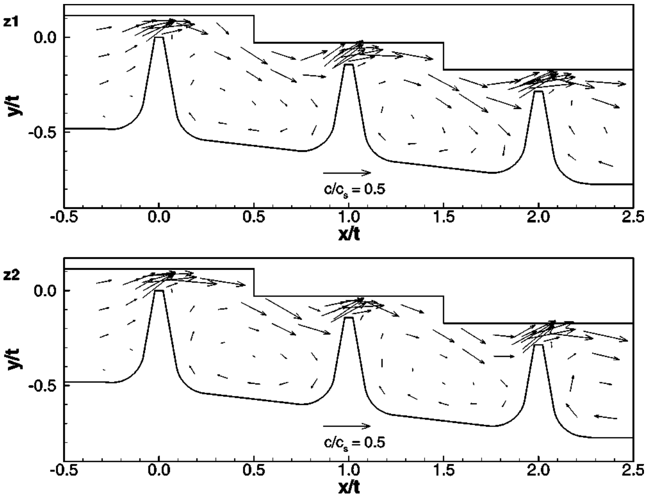

Fig. 10 Flow field with honeycombs (LDV), $s3$, π=1.1

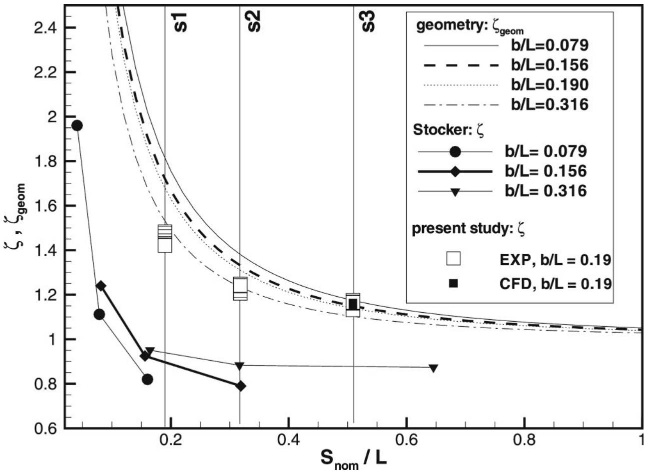

Fig. 12 Influence of honeycomb-lands on discharge characteristics

$$\zeta = \frac{C_{D,HC}}{C_{D,\mathrm{SMOOTH}}} \tag{6}$$

Both $C_{D,HC}$ and $C_{D,\mathrm{SMOOTH}}$ are calculated using the nominal gap width to describe the cross-sectional area at the tip ($A = B \cdot s_{\mathrm{nom}}$). The parameter ζ, determined in the present study, and the data presented by Stocker [9] are compared in Fig. 12. The geometrical parameter ζ_{geom} is also plotted in this diagram. The experimental data acquired in the present study show a behavior similar to the results reported by Stocker for a straight-through labyrinth seal. The comparison made between ζ and ζ_{geom} shows that ζ_{geom} is an appropriate parameter to qualitatively describe the effect of a local variation of the seal geometry. The geometrical change near the gap caused by the attachment of a honeycomb land dominates the discharge behavior for the present seal configuration as well as for the smaller clearances investigated by Stocker. The numerical flow simulation for the gap width $s3$ had a maximum relative deviation from the measured discharge coefficients of 6.8 percent. Considering the geometrical complexity of the investigated flow problem, the agreement between the experimental discharge data and numerical simulation results is excellent. As shown in Fig. 12, the predicted leakage increase parameter ζ is in good agreement with the measured data. The differences of the values for ζ for the straight-through labyrinth and the stepped labyrinth in Fig. 12 can be attributed to the different flow fields. In case of the straight-through labyrinth, the main flow is in direct contact with the honeycomb structure at the stator over the whole length of the seal. This direct contact and hence the interaction of the main flow with the honeycomb structure is significantly reduced for the stepped labyrinth seal because of the strong deflection of the main flow at the steps of the stator. Therefore, roughness effects are expected to have a stronger leakage reducing impact on the flow for straight-through labyrinth seals.

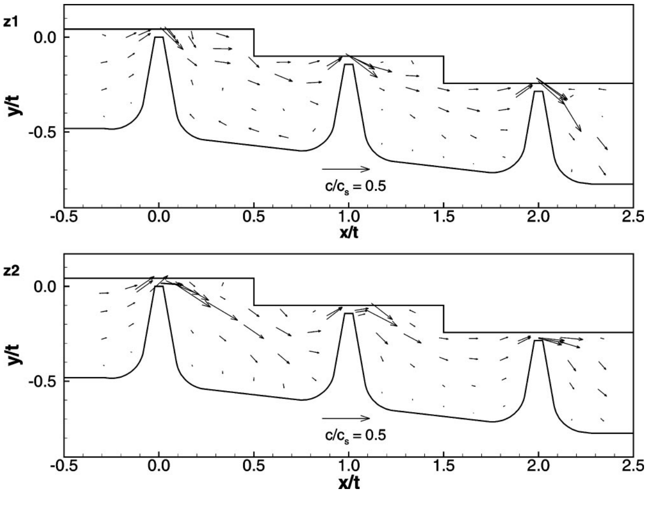

Fig. 11 Flow field with honeycombs (LDV), $s1$, π1.1

To completely describe the influence of honeycombs on the discharge behavior, the combination of geometrical effects and roughness effects have to be considered. Geometrical effects can occur from the honeycomb structure as well as from the stepped or straight-through labyrinth seal geometry. Whereas the former includes changes in the effective seal clearance, the latter describes the dependence of the flow pattern on the basic seal design (e.g., stepped straight-through). In the present study, a strategy to describe the effective gap width depending on seal and honeycomb geometry has been developed. A possible approach to consider roughness effects may be based on friction factors as provided by Ha and Childs [18,19]. For a complete understanding of the influence of honeycombs on the flow through labyrinth seals, further investigations including more geometrical variations are needed.

Conclusions

Results of a combined experimental and numerical investigation have been presented. The numerical results give insight into the flow patterns inside the labyrinth seal and agree well with the velocity data that have been obtained using LDV. For the smooth wall configuration, the flow pattern showed a distinct dependence on the gap width. This dependence is well reflected by the discharge coefficients, which continuously increase with decreasing seal clearance. The influence of the overall pressure ratio on the qualitative structure of the flow field is negligible while the discharge coefficients show a linear increase with increasing pressure ratio. A significant influence of the honeycomb structure on the flow field and the discharge characteristics has been observed. The honeycomb facing provides an enlarged effective gap width and results in an increased leakage mass-flow rate. Compared to the smooth configuration, the dependence of the flow field on the gap width is significantly reduced. The numerical results show details of the flow above the seal fin into the honeycomb structure. Both the numerical simulation results and the LDV data show the development of a three-dimensional velocity field due to the three-dimensional geometry of the honeycomb structure. The characteristic influence of honeycomb facings on the discharge behavior that was observed in the present study qualitatively agrees with the investigations conducted by Stocker [14]. The observed trend of an increased leakage for honeycomb seals at small gap widths has been qualitatively described by means of simple geometrical considerations. This indicates that, in the present study, the geometrical changes near the gap caused by the honeycombs have a dominating influence on the discharge behavior of the labyrinth seal.

Acknowledgment

The authors gratefully acknowledge support for this work by the German BMWi. The work presented here was part of the German Lufthahrtforschungsprogramme 1995–1998. Special thanks are due to Dr. W. Waschka for the coordination of this program.

A = area (m^2)
B = width of the test section (m)
b = fin tip thickness (m)
c = velocity (m/s)
c_s = isentropic velocity (m/s)
C_D = discharge coefficient
H = step height (m)
H_{HC} = height of the honeycombs (m)
HC = configuration with honeycombs
L = honeycomb diameter (m)
$\dot{m}$ = mass flow rate (kg/s)
$\dot{m}_{\text{ideal}}$ = ideal mass flow rate (kg/s)
p_0 = inlet pressure (N/m^2)
p_∞ = outlet pressure (N/m^2)
R = specific gas constant (kJ/kg K)
s_{eff} = effective seal clearance or gap width (m)
s_{nom} = nominal seal clearance or gap width (m)
s_{mean} = mean seal clearance or gap width (m)
SM = smooth configuration
t = pitch (m)
T_0 = inlet temperature (T)
ζ = leakage increase parameter
ζ_{geom} = geometrical leakage increase parameter
π = pressure ratio (p_0/p_∞)
κ = ratio of specific heats

References

[1] Wittig, S., Dörr, L., and Kim, S., 1983, ''Scaling Effects on Leakage Losses in Labyrinth Seals,'' ASME J. Eng. Gas Turbines Power, **105**, pp. 305–309.
[2] McGreehan, W. F., and Ko, S. H., 1989, ''Power Dissipation in Smooth and Honeycomb Seals,'' ASME Paper 89-GT-220.
[3] Waschka, W., Wittig, S., and Kim, S., 1990, ''Influence of High Rotational Speeds on the Heat Transfer and Discharge Coefficients in Labyrinth Seals,'' ASME J. Turbomach., **114**, pp. 462–468.
[4] Rhode, D., Ko, S., and Morrison, G., 1994, ''Leakage Optimization of Labyrinth Seals Using a Navier-Stokes Code,'' Tribol. Trans., **37**, No. 1, pp. 105–110.
[5] Rhode, D., Ko, S., and Morrison, G. L., 1994, ''Experimental and Numerical Assessment of an Advanced Labyrinth Seal,'' Tribol. Trans., **37**, No. 4, pp. 743–750.
[6] Rhode, D. L., and Allen, B. F., 2001, ''Measurement and Visualization of Leakage Effects of Rounded Teeth Tips and Rub-Grooves on Stepped Labyrinth,'' ASME J. Eng. Gas Turbines Power, **123**, pp. 604–611.
[7] Prassad, B., Sethu Manavalan, V., and Nanjunda Rao, N., 1997, ''Computational and Experimental Investigations of Straight-Through Labyrinth Seal,'' ASME Paper 97-GT-326.
[8] Komotori, K., and Miyake, K., 1977, ''Leakage Characteristics of Labyrinth Seals With High Rotating Speed,'' 1977 Tokyo Joint Gas Turbine Congress.
[9] Stocker, H. L., 1978, ''Determining and Improving Labyrinth Seal Performance in Current and Advanced High Performance Gas Turbines,'' AGARD CP273.
[10] Brownell, J. B., Millward, J. A., and Parker, R. J., 1989, ''Non-Intrusive Investigations Into Life-Size Labyrinth Seal Flow Fields,'' ASME J. Eng. Gas Turbines Power, **111**, pp. 335–342.
[11] Wittig, S., Jacobsen, K., Schelling, U., and Kim, S., 1988, ''Heat Transfer in Stepped Labyrinth Seals,'' ASME Eng. Gas Turbines Power, **110**, pp. 63–69.
[12] Wittig, S., Jacobsen, K., Schelling, U., and Kim, S., 1987, ''Numerical Predictions and Measurements of Discharge Coefficients in Labyrinth Seals,'' ASME Paper 87-GT-188.
[13] Waschka, W., Wittig, S., Kim, S., and Scherer, T., 1993, ''Heat Transfer and Leakage in High-Speed Rotating Stepped Labyrinth Seals,'' AGARD Conference Proceedings 527, paper 26.
[14] Willenborg, K., Schramm, V., Kim, S., and Wittig, S., 2000, ''Influence of a Honeycomb Facing on the Heat Transfer in a Stepped Labyrinth Seal,'' ASME Paper 2000-GT-0290.
[15] TASCflow User Documentation, 1996, Advanced Scientific Computing Ltd.
[16] Benim, A. C., and Arnal, M., 1994, ''A Numerical Analysis of the Labyrinth Seal Flow,'' *Computational Fluid Dynamics 94*, John Wiley and Sons, Ltd., London.
[17] Zimmermann, H., and Wolff, K. H., 1998, ''Air System Correlations, Part 1: Labyrinth Seals,'' ASME Paper 98-GT-206.
[18] Ha, T. W., and Childs, D. W., 1992, ''Friction-Factor Data for Flat Plate Tests of Smooth and Honeycomb Surfaces,'' ASME J. Tribol., **114**, pp. 722–730.
[19] Ha, T. W., and Childs, D. W., 1994, ''Annular Honeycomb-Stator Turbulent Gas Seal Analysis Using a New Friction-Factor Model Based on Flat Plate Tests,'' ASME J. Tribol., **116**, pp. 352–360.

Thermo-Economic Analysis of an Intercooled, Reheat and Recuperated Gas Turbine for Cogeneration Applications—Part I: Base Load Operation

R. Bhargava
Universal Ensco, Inc.
1811 Bering Drive
Houston, TX 77057

M. Bianchi

G. Negri di Montenegro

A. Peretto

DIEM–University of Bologna,
Viale Risorgimento, 2,
Bologna 40136, Italy

This paper presents a thermo-economic analysis of an intercooled, reheat (ICRH) gas turbine, with and without recuperation, for cogeneration applications. The optimization analyses of thermodynamic parameters have permitted to calculate variables, such as low-pressure compressor pressure ratio, high-pressure turbine pressure ratio and gas temperature at the waste heat recovery unit inlet while maximizing electric efficiency and "Energy Saving Index." Subsequently, the economic analyses have allowed to evaluate return on the investment, and the minimum value of gross payout period, for the cycle configurations of highest thermodynamic performance. In the present study three sizes (100 MW, 20 MW, and 5 MW) of gas turbines have been examined. The performed investigation reveals that the maximum value of electric efficiency and "Energy Saving Index" is achieved for a large size (100 MW) recuperated ICRH gas turbine based cogeneration system. However, a nonrecuperated ICRH gas turbine (of 100 MW) based cogeneration system provides maximum value of return on the investment and the minimum value of gross payout period compared to the other gas turbine cycles, of the same size and with same power to heat ratio, investigated in the present study. A comprehensive thermo-economic analysis methodology, presented in this paper, should provide useful guidelines for preliminary sizing and selection of gas turbine cycle for cogeneration applications. [DOI: 10.1115/1.1413463]

Introduction

In recent years concerted efforts have been made in different areas of gas turbine technologies with the one main objective of improving cycle efficiency of the gas turbine engines. In this pursuit, particularly in the last 15 years, gas turbine industry has seen phenomenal advancements particularly in the fields of aerodynamics, materials, blade cooling, and fabrication technologies. With these advanced technologies implemented, gas turbines have been developed with the TiT value approaching 1500°C (2732°F) and simple cycle efficiency 40 percent and more ([1,2]). Another approach for improving cycle efficiency of the gas turbine engine is to modify the Brayton cycle.

The modifications (some of them have also been implemented) to the Brayton cycle, which have been studied in the past include regeneration, intercooled compression, reheat expansion, and their combination ([3–9]). It may be noted that these modified Brayton cycles have been sometimes referred in the literature as ''complex gas turbine cycles.'' The available literature, in general, presents thermodynamic performance of a modified Brayton cycle in noncogeneration applications with the exception of few studies ([4,7]). It is evident that the Brayton cycle when combined with intercooling, reheat, and recuperation can significantly improve cycle efficiency provided high value of overall cycle pressure ratio is used ([7]).

A limited amount of work has been done on the evaluation of intercooled, reheat, and recuperated gas turbine in cogeneration applications, particularly thermo-economic performance evaluation. A recent study on economic investigation of the recuperated ICRH gas turbine, in a noncogeneration application, showed that the minimum power generation cost coincides with the maximum cycle efficiency at a high value of the overall cycle pressure ratio ([10]).

The main objective of the study undertaken has been to conduct thermo-economic evaluation of recuperated and nonrecuperated ICRH cycles in cogeneration applications. The stated objective is achieved by optimizing thermodynamic parameters for the nonrecuperated and recuperated ICRH cycles at three design-load conditions, namely large (100 MW), medium (20 MW), and small (5 MW), and to apply the developed economic model to the highest performance GT (100 MW) considered. The results obtained for the simple and recuperated Brayton cycles are also included for comparison purposes.

It may be noted that the present study has concentrated on the evaluation of nonrecuperated and recuperated ICRH gas turbine based cogeneration systems under base-load operation.

Prospects of Simple and Complex Gas Turbine Cycles in Cogeneration Applications. Focusing on cogeneration applications, some gas turbine cycles (simple or complex Brayton cycles) with high cycle efficiency may not necessarily be thermo-economically suitable because of incompatibility between the gas turbine exhaust gas temperature and requirements of process heat for the thermal utility. It is important, therefore, to note that in a cogeneration application the value of exhaust gas temperature plays a major role.

To give an idea of the exhaust gas temperature values obtainable by simple or complex gas turbine cycles, a comprehensive

---

Contributed by the International Gas Turbine Institute (IGTI) of THE AMERICAN SOCIETY OF MECHANICAL ENGINEERS for publication in the ASME JOURNAL OF ENGINEERING FOR GAS TURBINES AND POWER. Paper presented at the International Gas Turbine and Aeroengine Congress and Exhibition, Munich, Germany, May 8–11, 2000; Paper 00-GT-316. Manuscript received by IGTI Nov. 1999; final revision received by ASME Headquarters Feb. 2000. Associate Editor: D. R. Ballal.

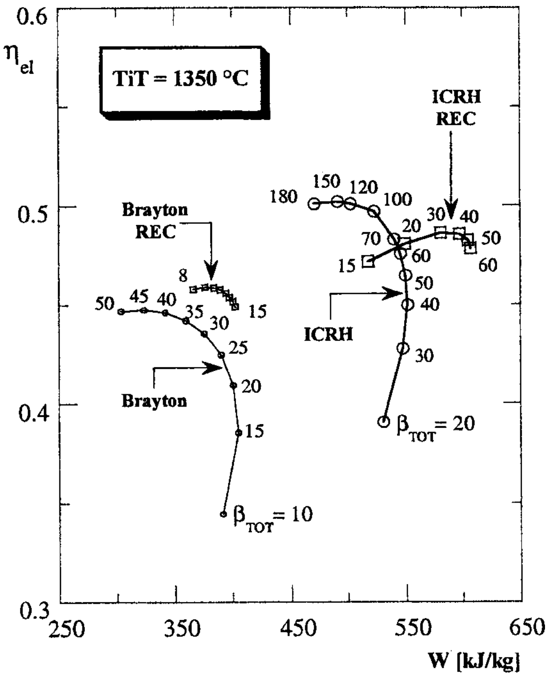

Fig. 1 η_{el} **versus** W **for recuperated and nonrecuperated ICRH and Brayton cycles (**β_{TOT} **values are reported)**

thermodynamic analysis was conducted for the cycles under investigation. The thermodynamic performances of the cycles, at the state-of-the-art value of TiT (1350°C), for different overall cycle pressure ratio are shown in Figs. 1 and 2. It must be noted that the results for simple and recuperated Brayton cycles are also included in Figs. 1 and 2 for comparison purposes.

Each point on the performance curves in Figs. 1 and 2 was determined, for a given value of overall cycle pressure ratio, by finding the low-pressure compressor (LPC) pressure ratio and the high-pressure turbine (HPT) pressure ratio while maximizing the value of cycle's electric efficiency. The optimum values of overall cycle pressure ratio, corresponding to maximum electric efficiency are 45 and 150 for the simple Brayton cycle and nonrecuperated ICRH cycle, respectively. It should be observed that, for nonrecuperated ICRH cycle, the results for the high values of overall cycle pressure ratios are included in Figs. 1 and 2 to show maximum achievable electric efficiency of the cycle at TiT of 1350°C.

For recuperated Brayton cycle and recuperated ICRH cycle, the optimum values of overall cycle pressure ratio are 10 and 30, respectively (see Fig. 1). The results, obtained in the present investigation, are found in good agreement with those available in the literature ([7]).

Figure 2 shows the same performance parameters as in Fig. 1 for the same cycles and emphasizing that there exists a specific value of the exhaust gas temperature corresponding to a given value of the overall cycle pressure ratio. In Fig. 2, as is in Fig. 1, the thermodynamic performance results for simple and recuperated Brayton cycles are included for the comparison purposes only.

For a nonrecuperated cycle (simple Brayton or ICRH cycle), the maximum value of cycle efficiency is achieved at a high overall cycle pressure ratio, but with approximately the lowest value of exhaust gas temperature (see Figs. 1 and 2). Also, for the recuperated cycles, the exhaust gas temperature varied relatively by a small amount, compared to the nonrecuperated cycles, in the overall cycle pressure ratio range considered as seen in Fig. 2. Furthermore, the maximum value of exhaust gas temperature achievable with recuperated cycles, as expected, reduces considerably compared to the nonrecuperated cycles (see Fig. 2).

For a cogeneration system, in addition to evaluating net electric efficiency and thermal efficiency, the important thermodynamic parameter of interest is the "Energy Saving Index" (ESI), which is a direct measure of savings in fuel consumption.

It is important to note that the amount of fuel saving has major impact on the economics of a cogeneration plant, since 80 percent of the operating cost can be attributed to the cost of fuel in a gas turbine based cogeneration plant.

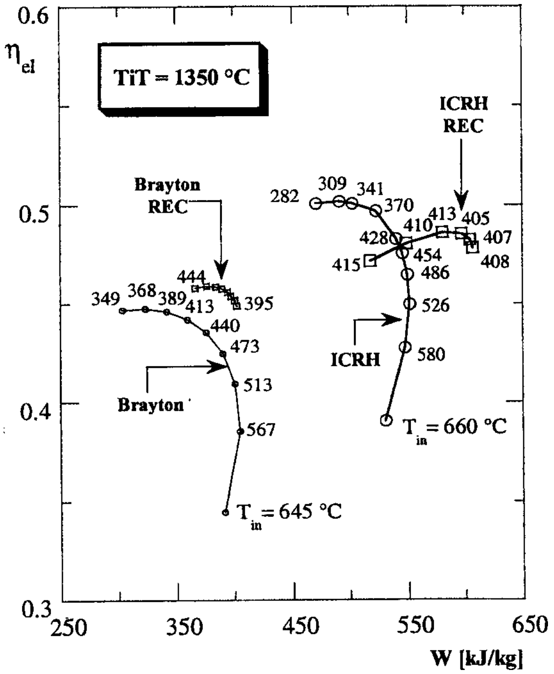

Fig. 2 η_{el} **versus** W **for recuperated and nonrecuperated ICRH and Brayton cycles (**T_{in} **values are reported)**

Thermodynamic Analysis — Cogeneration System

The Considered Performance Parameters. For evaluating cogeneration plant performance, the following performance parameters have been considered:

- electric efficiency, defined as a ratio between the net electric power output and the supplied thermal power associated with fuel;

$$\eta_{el}=\frac{P_{el}}{F}. \tag{1}$$

- thermal efficiency, defined as a ratio between the thermal power requested for cogeneration purposes and the supplied thermal power associated with fuel;

$$\eta_{th}=\frac{Q_{th}}{F}. \tag{2}$$

Note, in the case of intercooled compression, Q_{th} also takes into account the thermal power exchanged by the intercooler (IC), which is considered as a thermal source producing hot water at low temperature (100°C to 150°C) and available for the thermal utility.

- specific work (W), defined as a ratio between the electric power output and the air mass flow rate at LPC inlet;
- specific thermal power, defined as a ratio between the net thermal power requested for cogeneration purposes and the air mass flow rate at LPC inlet;

- ESI (Energy Saving Index) expresses the relative variation of the fuel power consumption in two separate plants producing the same electric and thermal power output of the cogeneration plant, and the fuel power consumption in the process plant:

$$\mathrm{ESI}=\frac{F^{*}-F}{F^{*}}=1-\frac{1}{\dfrac{\eta_{el}}{\eta_{el}^{*}}+\dfrac{\eta_{th}}{\eta_{th}^{*}}}. \tag{3}$$

The variables with the superscript "*" refer to values for η_{th} and η_{el} taken equal to 0.8 and 0.37, respectively. They may represent the reference scenario relative to average values for fossil fuel boiler efficiency (η_{th}) and for fossil fuel power plant efficiency (η_{el}) in a power generation system.

Modeling Technique. Figure 3 shows a schematic layout of the recuperated single-spool ICRH gas turbine cycle in cogenerative application. The thermodynamic analyses of cogeneration plants utilizing nonrecuperated and recuperated ICRH gas turbines, including similar cycles studied in noncogeneration mode and discussed earlier in this paper, have been performed using a commercial software package ([11]).

In the thermodynamic analyses performed, specific heat at constant pressure is considered function of the gas composition and its temperature and include pressure losses in the heat exchangers, at the compressor inlet, in the combustors and at the gas turbine discharge.

The amounts of cooling air flows required, for hot gas path and the most stressed components, have been evaluated using the procedures described by Benvenuti et al. [12] and El-Masri [5]. In these procedures, the amounts of cooling air flows are adjusted on the basis of temperatures of the cooling air and the hot gas at the inlet of each cascade. In the present analysis, as also commonly employed in many existing engines, it is assumed to cool the one stage HPT with the cooling air bled from the HPC discharge, and the four-stage LPT is cooled with two streams of bleed cooling air taken from the HPC intermediate stages (see Fig. 3).

The LPT stage expansion ratio is determined by assuming a realistic value of the aerodynamic loading parameter ($\Delta h/u^2$) for each stage ([12]). In the present study, the assumed values of aerodynamic loading parameter ($\Delta h/u^2$) for the LPT are 1.3, 1.15, 1.05, and 1.05 from the first to the fourth stage, respectively. The amount of cooling air flow rate necessary to cool the low pressure combustor, taken from one of the cooling streams bled from the HPC intermediate stages (see Fig. 3), is assumed six percent of the LPC inlet mass flow rate.

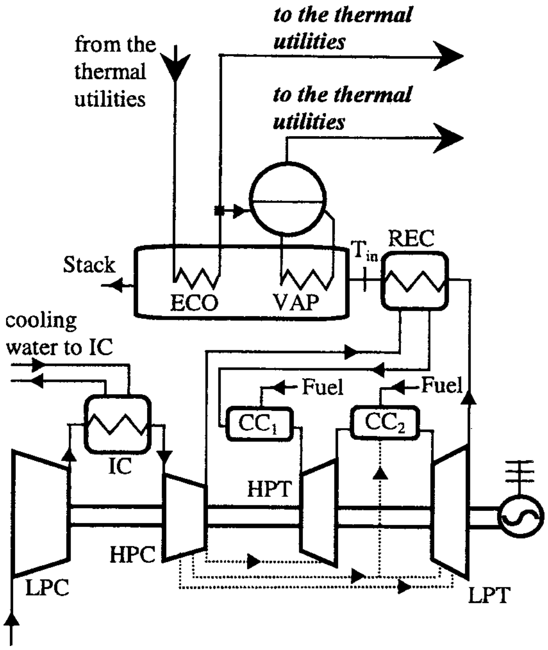

Fig. 3 Schematic layout of the recuperated ICRH gas turbine in cogenerative application (dotted lines represent GT cooling flow streams)

Table 1 Key design parameters for the three gas turbine sizes investigated

Size [MW]	TiT [°C]	η_{pc}	η_{pe}
5	1050	0.88	0.87
20	1200	0.90	0.89
100	1350	0.91	0.90

The pressure loss across each combustor is assumed 2.5 percent of its inlet pressure. For each heat exchanger, the internal pressure loss of the gas stream is assumed equal to two percent of its inlet pressure. The heat exchange surface areas of IC, REC, and HRSG exchangers (economizer and evaporator) are evaluated utilizing the most commonly used NTU method, once the overall heat exchanger coefficients have been set. The HPC inlet temperature is evaluated by assuming a value of 0.9 for the IC exchanger's effectiveness.

The thermodynamic analyses have been performed for three gas turbine sizes of 5, 20, and 100 MW electric power output: Each of the gas turbine is defined by the value of key design parameters as reported in Table 1. The values of polytropic efficiency for compressors and turbines, given in Table 1, are representative of the selected gas turbine sizes based on the current technology. It must be noted that, for a given size gas turbine, the polytropic efficiencies are assumed independent of the overall cycle pressure ratio, because all the performance calculations have been conducted corresponding to the design-load condition.

Methodology

For a given cogeneration system, the implemented numerical procedure allows to evaluate and optimize the desired thermodynamic performance including flow pressures and temperatures at inlet and exit of different components of the cycle and surface areas of different heat exchangers involved. It may be noted that the aforesaid methodology has been implemented for the three gas turbine sizes mentioned earlier. However, the results of the methodology are illustrated with charts for a large size (100 MW) gas turbine. For the other two gas turbine sizes, a summary of results obtained are tabulated in this paper.

These optimum thermodynamic parameters are subsequently used for the economic analysis, providing values of DCRR and GPO.

Nonrecuperated ICRH Gas Turbine Cycle. For the nonrecuperated ICRH gas turbine in a cogeneration application, the starting point of the analysis is to set a value of exhaust gas temperature (T_{in}) at the inlet of HRSG. The second step is to obtain, for an assigned overall cycle pressure ratio (β_{TOT}) and for the set T_{in}, the values of electric efficiency and ESI versus specific power. In this case, for every LPC pressure ratio the corresponding value of HPT pressure ratio is found within the bound of the imposed β_{TOT} and T_{in}. For a given value of T_{in}, the values of electric efficiency and ESI are then evaluated for different values of overall cycle pressure ratio.

The results for T_{in} of 420°C, with TiT of 1350°C are presented in Fig. 4. For the evaluation of η_{th} (which is necessary to estimate the value of ESI) the stack temperature of 90°C has been assumed in the present investigation (supposing to fuel the GT with the natural gas). The performance parameters for the cycle with the values of β_{TOT} and T_{in} of 70 and 420°C, respectively, are summarized in Table 2. It is evident from Fig. 4 and Table 2 that, for an assigned value of β_{TOT} and T_{in}, the values of β_{LPC} and β_{HPT}

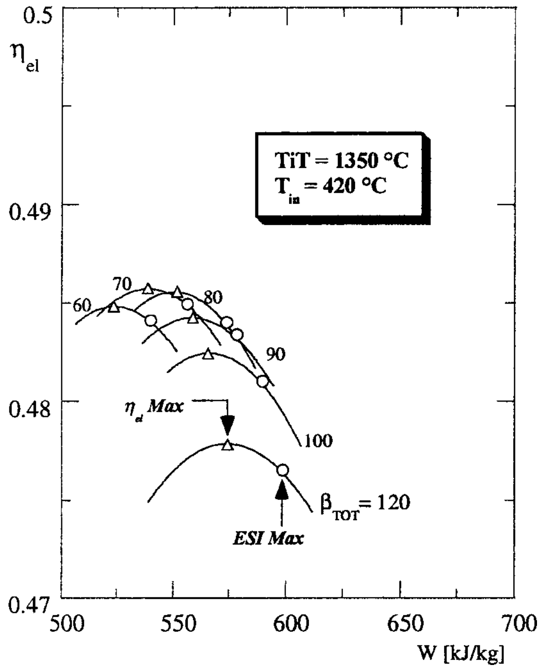

Fig. 4 η_{el} versus W for nonrecuperated ICRH gas turbine for different β_{TOT} (markers of η_{el} Max and ESI Max are identified)

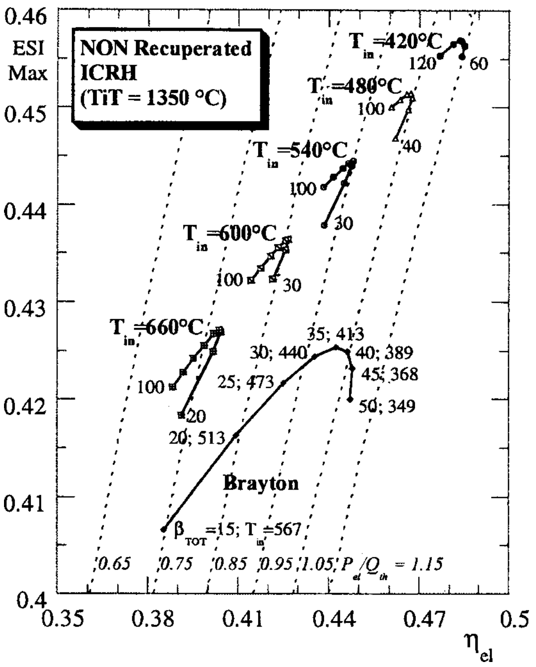

Fig. 5 ESI max versus η_{el} for different β_{TOT} as a function of T_{in} for nonrecuperated ICRH gas turbine based cogeneration systems

corresponding to maximum electric efficiency (white triangles) and maximum ESI (white balls) are different, even though the differences are small.

Based on the above discussed procedure, for an assigned T_{in} value, it is possible to get all the possible cycle configurations (for different β_{TOT} values) corresponding to maximum values of η_{el} and ESI.

For a cogeneration system, however, it would be important to consider configurations corresponding to the maximum value of ESI for each combination of β_{TOT} and T_{in}. The variations of maximum value of ESI versus electric efficiency as a function of β_{TOT} and T_{in} with TiT of 1350°C for the nonrecuperated ICRH gas turbine based cogeneration systems are shown in Fig. 5. The curves of constant electric power to thermal power ratio are also reported (shown as dotted lines) in Fig. 5.

For the nonrecuperated ICRH gas turbine based cogeneration system with TiT of 1350°C, the maximum value of ESI is achieved at T_{in} of 420°C and cycle overall pressure ratio of 90 as shown in Fig. 5. This aforesaid optimum configuration also realizes an electric efficiency close to its maximum achievable value.

The maximum values of ESI achievable with the simple Brayton cycle based cogeneration systems at TiT of 1350°C for different combinations of β_{TOT} and T_{in} are also included in Fig. 5 for comparison purposes. A combination of β_{TOT} and T_{in} of 35 and 413°C, respectively, provides the maximum value of ESI for the simple Brayton cycle based cogeneration system as is evident from Fig. 5.

A good amount (approximately three percent maximum) of increase in the value of ESI for nonrecuperated ICRH gas turbine based cogeneration system, compared to simple Brayton cycle is worth noting in Fig. 5.

Table 2 A summary of performance for nonrecuperated ICRH gas turbine at a given value of β_{TOT} and T_{in}

	β_{TOT}	T_{in} [°C]	β_{LPC}	β_{HPT}	η_{el} [%]	W [kJ/kg]	ESI [%]
η_{el} Max	70	420	3.6	1.89	48.57	543.6	45.60
ESI Max	70	420	4.0	1.87	48.50	556.2	45.64

Recuperated ICRH Gas Turbine Cycle. For the analysis of recuperated ICRH cycle, it was necessary to set a value of the recuperator effectiveness. This value was set to 0.9, since it was found, by the authors, that a lower value of the recuperator effectiveness leads to lower electric efficiency and ESI. A methodology, similar to that used for the nonrecuperated ICRH gas turbine cycle and described above, has been also used to identify the optimum configuration and performance parameters for the recuperated ICRH gas turbine cycle.

For the recuperated ICRH gas turbine based cogeneration systems with TiT and T_{in} values of 1350°C and 420°C, respectively, electric efficiency versus specific power output for different overall cycle pressure ratios, is presented in Fig. 6. As evident from Fig. 6, the optimum value of overall cycle pressure ratio, for the recuperated ICRH gas turbine based cogeneration system has a value of 30 for T_{in} of 420°C. The reason for using T_{in} of 420°C, in Fig. 6, will become clear in the discussion to follow.

Similar to the nonrecuperated ICRH cycle case, for an assigned β_{TOT} and T_{in}, the cycle configurations (β_{HPT} and β_{LPC}) relative to maximum electric efficiency (white triangles) and maximum ESI (white balls) are different even if the relative values of β_{HPT} and β_{LPC} are not far from each other (see Table 3).

Here again, for an assigned value of T_{in}, it is possible to get all the configurations (for different β_{TOT} values) corresponding to maximum values of ESI. The variations of maximum value of ESI versus electric efficiency as a function of β_{TOT} for different T_{in} values are shown in Fig. 7.

For the recuperated ICRH gas turbine based cogeneration system with TiT of 1350°C, maximum value of ESI is achieved at an optimum overall cycle pressure ratio of 40 and T_{in} of 420°C.

Furthermore, the values of ESI Max are observed to decrease at T_{in} of less than 400°C as is evident from Fig. 7. In this case also, as was the case with the nonrecuperated ICRH gas turbine based system, this optimum configuration permits to obtain an electric efficiency close to its maximum value.

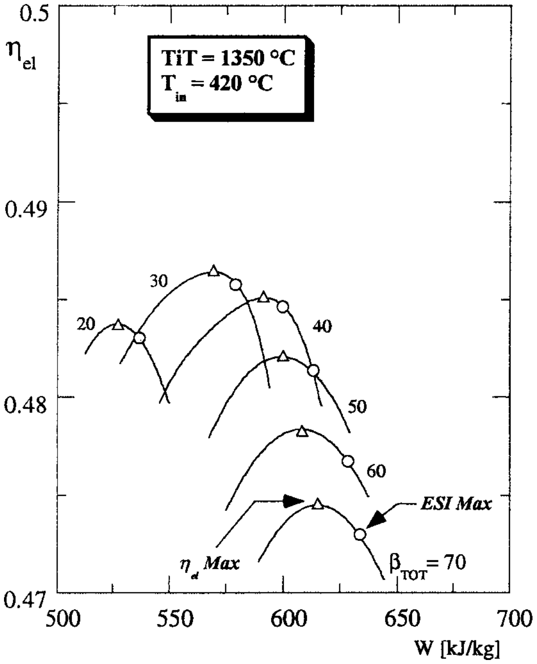

Fig. 6 η_{el} **versus** W **for recuperated ICRH gas turbine for different** β_{TOT} **(markers of** η_{el} **Max and ESI Max are identified)**

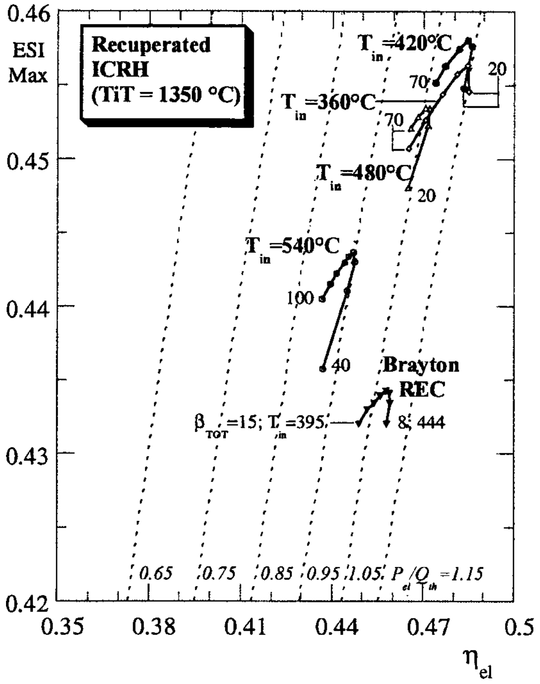

Fig. 7 ESI Max versus η_{el} **for different** β_{TOT} **as a function of** T_{in} **for recuperated ICRH gas turbine based cogeneration systems**

The above discussed results of maximum ESI clearly show that an optimum value of the overall cycle pressure ratio for the recuperated ICRH gas turbine based cogeneration system is considerably smaller compared to the nonrecuperated ICRH gas turbine based system. This implies that, for a given size (power rating) gas turbine, a smaller size compressor can be utilized in a recuperated ICRH gas turbine based system compared to the nonrecuperated ICRH gas turbine based system. Also, more specific power, with higher value of ESI, can be generated with the recuperated ICRH system compared to the nonrecuperated ICRH system at an optimum overall cycle pressure ratio (see Fig. 4 and Fig. 6).

It is interesting to note that at TiT of 1350°C, the optimum value of T_{in} is 420°C for both the cycles analyzed. For the recuperated ICRH gas turbine based cogeneration system, as was the case with nonrecuperated ICRH gas turbine based cogeneration system, a significant amount (approximately 2.5 percent maximum) of increase in the value of ESI can be achieved compared to the recuperated Brayton cycle system (see Fig. 7).

Moreover, the results presented in Figs. 5 and 7 show that for the considered overall cycle pressure ratio, it may not be possible to achieve the desired value of the electric to thermal power ratio (P_{el}/Q_{th}) corresponding to all the values of T_{in}. This observation is true for both the nonrecuperated and recuperated ICRH gas turbine based cogeneration systems.

To compare different gas turbine cycles in cogeneration applications, and also from the economic analysis point of view, it is more appropriate to consider the gas turbine cycles for the same value of electric to thermal power ratio. For this purpose, the previous numerical procedure, used in obtaining Figs. 5 and 7, was iterated until an appropriate value of T_{in} could be obtained, and consequently the value of β_{TOT}, which provides the desired values of electric power to heat ratio and the maximum ESI.

Table 3 A summary of performance for recuperated ICRH gas turbine at a given value of β_{TOT} **and** T_{in}

	β_{TOT}	T_{in} [°C]	β_{LPC}	β_{HPT}	η_{el} [%]	W [kJ/kg]	ESI [%]
η_{el} Max	30	420	3.8	1.77	48.65	567.1	45.74
ESI Max	30	420	4.2	2.02	48.58	578.8	45.77

To avoid a too small blade size in the last stages of a high pressure compressor and a particularly complex design phase in this procedure, an overall cycle pressure ratio was limited to a value of 50 for recuperated and nonrecuperated ICRH gas turbines.

To evaluate the overall exchanger surface area, the bottoming cycle layout chosen is schematically shown in Fig. 3.

In particular, it was assumed that the bottoming cycle makes available two thermal streams (1.7 MPa) with different enthalpy contents: the first, at the economizer outlet as a hot water, and the second, at the vaporizer outlet as a saturated steam. (Note, the values of pinch point temperature and approach point temperature assumed are 15°C and 5°C, respectively.) As mentioned before, the temperature of the hot gas at the bottoming cycle outlet (to the stack) is considered 90°C for all the analyses.

Following the above discussed methodology optimization of thermodynamic parameters are conducted for a given power rating plant at a constant value of P_{el}/Q_{th} and various cycles. The results obtained for large, medium, and small size cogeneration plants are summarized in Tables 4, 5, and 6, respectively.

For a cogeneration system with 100 MW power generation capacity, recuperated ICRH gas turbine provides the maximum value of ESI compared to the other cycles examined (see Table 4). However, for medium and small size cogeneration systems, the thermodynamic performance parameters (ESI and η_{el}) are observed comparable for recuperated and nonrecuperated ICRH gas turbine based systems (see Tables 5 and 6).

For three sizes of gas turbine systems evaluated in the present study, the calculated values of pressure ratio for HPT suggest a need for multiple stages in high pressure turbine section.

Economic Analysis

For a gas turbine based cogeneration plant, the selection of a gas turbine depends not only on its net electric efficiency but on the other parameters such as electric power to thermal load ratio

Table 4 Performance characteristics for a large size cogeneration system (P_{el}=100 MW and P_{el}/Q_{th}=1.05)

Type of Cycle	η_{el}	ESI	W [kJ/kg$_{air}$]	T_{in} [°C]	m_a [kg/sec]	β_{HPT}	β_{LPC}	β_{TOT}	Surface [m^2]				
									IC	ECO	VAP	REC	Total
Brayton	0.447	0.425	339	386	295	-	-	40.8	-	37477	18040	-	**55517**
Brayton REC	0.453	0.433	398	433	251	-	-	13.2	-	32058	17010	25951	**75019**
ICRH	0.466	0.445	568	480	176	1.90	3.2	50.0	12566	22892	13108	-	**48566**
ICRH REC	0.470	0.453	611	482	164	3.36	4.2	50.0	11435	21505	12303	11384	**56627**

Table 5 Performance characteristics for a medium size cogeneration system (P_{el}=20 MW and P_{el}/Q_{th}=0.95)

Type of Cycle	η_{el}	ESI	W [kJ/kg$_{air}$]	T_{in} [°C]	m_a [kg/sec]	β_{HPT}	β_{LPC}	β_{TOT}	Surface [m^2]				
									IC	ECO	VAP	REC	Total
Brayton	0.412	0.397	250.6	336	80	-	-	44.1	-	10073	4190	-	**14263**
Brayton REC	0.426	0.416	331.7	409	60	-	-	12.8	-	7649	3860	6991	**18500**
ICRH	0.442	0.437	495.7	450	40	2.17	3.6	50.0	2757	5202	2829	-	**10788**
ICRH REC	0.445	0.440	527.5	455	38	3.68	4.4	50.0	2590	4939	2719	3140	**13388**

Table 6 Performance characteristics for a small size cogeneration system (P_{el}=5 MW and P_{el}/Q_{th}=0.70)

Type of Cycle	η_{el}	ESI	W [kJ/kg$_{air}$]	T_{in} [°C]	m_a [kg/sec]	β_{HPT}	β_{LPC}	β_{TOT}	Surface [m^2]				
									IC	ECO	VAP	REC	Total
Brayton	0.354	0.371	237.5	402	21	-	-	21.8	-	2693	1323	-	**4016**
Brayton REC	0.357	0.376	253.6	422	20	-	-	15.4	-	2558	1313	2877	**6748**
ICRH	0.375	0.406	423.7	495	12	4.02	4.4	50.0	813	1554	907	-	**3274**
ICRH REC	0.373	0.403	392.7	495	13	5.13	3.2	50.0	901	1693	977	1272	**4843**

(P_{el}/Q_{th}), Energy Saving Index (ESI), utility avoided cost, fuel cost, etc. To evaluate suitability and meaningful comparison of different gas turbines for a given cogeneration system, it is essential that the value of P_{el}/Q_{th} should be the same. In the present study, once the optimum configurations for nonrecuperated and recuperated ICRH gas turbines were evaluated as discussed earlier in the paper, the economic parameters were then evaluated.

The economic parameters evaluated in the present study include discount cash flow rate of return (DCRR) and gross payout period (GPO), two terms commonly employed in engineering economic analysis.

The various parameters required for economic analysis, with their values used in the present study, are provided in Table 7. The cost data for various equipment used in a given cogeneration system including the fuel cost are based on 1999 U.S. Dollar value. As mentioned earlier in the case of thermodynamic analysis, the economic analyses were also conducted for cogeneration systems utilizing simple Brayton and recuperated Brayton cycles for comparison purposes

The economic model, developed in-house and utilized in the present investigation, has been realized by using an Excel Worksheet. This model has considerable amount of flexibility and takes into consideration equipment installed cost, operation and maintenance cost, financing cost during the construction phase, plant utilization factor, escalation rate, and financing and loan payment schedule in estimating values of DCRR and GPO.

The developed economic model has been applied to the highest performance gas turbine considered (100 MW). It must be highlighted that the application of the model to a limited extent of this case has allowed to quantify the required economic parameters, and it does not represent a limitation to the developed methodology or to the applicability of the economic analysis code.

Table 7 Parameters used for economic analysis

Parameter	Selected Value
Plant Utilization Factor, %	85
Plant Economic Life, Years	20
Loan Term, Years	20
Debt Interest Rate, APR	15
Depreciation Period, Years	10
Construction Period, Years	1.5
Escalation Rate, %	5
Fuel Gas Cost, $/MSCF	3.0
Utility avoided Cost, Cents/kWh	4.5
Local Taxes & Insurance (% of Total Investment Cost)	2.5
Auxiliary Power Consumption, % of Gross Power Generated	1.5
Income Taxes (Flat Rate, % of Net Revenues)	45

The results of the economic investigation, for the 100 MW cogeneration plant based on a nonrecuperated and recuperated ICRH gas turbine, are summarized in Tables 8(*a*) and 8(*b*). It must be noted that the results for cogeneration plants utilizing simple Brayton cycle and recuperated Brayton cycle are also included in Tables 8(*a*) and 8(*b*) for comparison purposes.

The economic analyses of cogeneration systems for a given value of electric sale price or fuel purchase price, utilizing different gas turbine cycles, show that the value of DCRR, even though quite attractive, is the lowest for a cogeneration plant utilizing recuperated ICRH gas turbine in comparison to the other gas turbines examined in the present study (see Tables 8(*a*) and 8(*b*)).

The main reasons for the observed decrease in the value of DCRR for the recuperated ICRH gas turbine based cogeneration system, in comparison to the simple Brayton and nonrecuperated ICRH gas turbine based cogeneration systems, can be attributed to two factors: a comparative increase in its investment cost and the lost revenues due to decrease in the amount of steam generated. However, in comparison to the recuperated Brayton cycle based cogeneration system, the observed decrease in the DCRR value for the recuperated ICRH gas turbine based cogeneration system is mainly caused due to the lost revenues associated with the decrease in the amount of generated steam.

It may be noted that the economic analysis results, presented in Table 8(*b*), are obtained using the electric sale price of 5 cents/kWh.

It is also noted that the cogeneration plant based on the nonrecuperated ICRH gas turbine provides highest value of DCRR as is evident from Tables 8(*a*) and 8(*b*). Furthermore, the value of GPO is found lowest for the nonrecuperated ICRH gas turbine based cogeneration system.

The aforesaid observations imply that a cogeneration system, with $P_{el}=100\,\mathrm{MW}$ and $P_{el}/Q_{th}=1.05$, using nonrecuperated ICRH gas turbine will be more economically viable compared to the other cycles investigated.

Concluding Remarks

Based on the thermo-economic analysis of an intercooled reheat gas turbine, with and without recuperation, in cogeneration applications, the following observations can be made:

1 An optimization study of the most expressive cogenerative parameters showed that, for a large-size (100 MW Capacity) gas

Table 8 (*a*) Economic performance for a large size cogeneration system ($P_{el}=100$ MW and $P_{el}/Q_{th}=1.05$) — effects of electric sale price (*b*) Economic performance for a large size cogeneration system ($P_{el}=100$ MW and $P_{el}/Q_{th}=1.05$) — effects of fuel purchase price

			Effect of Electric Sale Price on DCRR					Effect of Electric Sale Price on GPO			
	Total Investment Cost, $/kW	Electric Sale Price, Cents/kWh	4.50	5.0	5.50	6.00		4.50	5.0	5.50	6.00
			DCRR (%)					GPO (Years)			
Brayton	471		31.93	36.48	40.97	45.53		3.4	3.0	2.6	2.3
Brayton REC	519		30.42	34.56	38.64	42.70		3.6	3.2	2.8	2.5
ICRH	485		33.40	37.79	42.13	46.45		3.3	2.9	2.5	2.3
ICRH REC	506		29.48	33.74	37.94	42.10		3.7	3.2	2.9	2.5

(a)

	Effect of Fuel Purchase Price on DCRR					Effect of Fuel Purchase Price on GPO			
Fuel Purchase Price, $/MSCF	3.00	3.25	3.50	4.00		3.00	3.25	3.50	4.00
	DCRR (%)					GPO (Years)			
Brayton	36.48	34.72	32.96	29.39		3.0	3.1	3.3	3.75
Brayton REC	34.56	32.98	31.39	28.17		3.2	3.3	3.5	3.9
ICRH	37.79	36.16	34.52	31.22		2.9	3.0	3.2	3.5
ICRH REC	33.74	32.18	30.60	27.41		3.2	3.4	3.6	4.0

(b)

turbine and for a given power to heat ratio, maximum electric efficiency (47 percent) can be achieved with recuperated ICRH gas turbine based cogeneration system.

2 For medium (20 MW) and small (5 MW) size cogeneration plants, systems using ICRH gas turbine with and without recuperation are found to have almost the same electric efficiency (44.5 and 37.5, respectively). Similar observations are true if gas turbines are compared based on the value of ESI.

3 An economic evaluation of the cogeneration system (100 MW capacity and electric power to thermal load ratio of 1.05), showed that with electric sale price and fuel purchase price of 4.5 Cents/kWh and 3 $/MSCF, respectively the nonrecuperated ICRH gas turbine based system provides maximum (approximately 33.5 percent) return on the investment and minimum (3.3 years) gross payout period compared to the other cycles investigated.

4 The poor economic performance of the recuperated ICRH gas turbine based cogeneration system can be attributed to the increased value of the investment cost and/or the lost revenues associated with the decrease in the amount of generated steam.

5 In comparison to the other cycles investigated in the present study, recuperated ICRH gas turbine based cogeneration system showed maximum specific work capacity for all the sizes except for the smallest size unit studied.

Acknowledgment

The first author would like to thank Bob Pate, VP Engineering Universal Ensco, Inc., for his encouragement and continued support for the professional growth.

Nomenclature

ESI = Energy Saving Index (Eq. (3))
F = LHV fuel power supplied
m_a = air mass flow rate at the gas turbine inlet
P_{el} = electric power output
Q_{th} = thermal power to the utilities
T = temperature
T_{in} = temperature at inlet to the HRSG (Fig. 3)
TiT = Inlet temperature to the first stage nozzle
W = specific power (P_{el}/m_a)
$\Delta h/u^2$ = aerodynamic loading parameter (Δh, stage specific enthalpy drop; u peripheral speed)
β_{TOT} = overall cycle pressure ratio
β_{HPT} = HPT pressure ratio
β_{LPC} = LPC pressure ratio
η_{el} = LHV electric efficiency (Eq. (1))
η_{th} = LHV thermal efficiency (Eq. (2))
η_{pc} = polytropic compression efficiency
η_{pe} = polytropic expansion efficiency

Superscript

$*$ = reference

Acronyms

APR = annual percentage rate
CC_1 = high pressure combustor
CC_2 = low pressure combustor
DCRR = discount cash flow rate of return
ECO = economizer
GPO = gross payout period
GT = gas turbine
HPC = high pressure compressor
HPT = high pressure turbine
HRSG = heat recovery steam generator
ICRH = inter-cooled re-heat
IC = inter-cooler
LHV = lower heating value
LPC = low pressure compressor
LPT = low pressure turbine
REC = recuperator
MSCF = 1000 standard cubic foot
VAP = vaporizer

References

[1] Smith, D., 1999, ''First H System Gas Turbine Planned for Baglan,'' Modern Power System, May, pp. 37–42.
[2] Casper, R. L., 1993, ''Application of the LM-6000 for Power Generation and Cogeneration,'' ASME Paper No. 93-GT-278.
[3] Rice, I. G., 1980, ''The Combined Reheat Gas Turbine/Steam Turbine Cycle, Part I—A Critical Analysis of the Combined Reheat Gas Turbine Steam Turbine Cycle,'' ASME J. Eng. Gas Turbines Power, **102**, pp. 35–41.
[4] Rice, I. G., 1987, ''Thermodynamic Evaluation of Gas Turbine Cogeneration Cycles, Part II—Complex Cycle Analysis,'' ASME J. Eng. Gas Turbines Power, **109**, pp. 8–15.
[5] El-Masri, M. A., 1986, ''On Thermodynamics of Gas Turbine Cycles, part 2—A Model for Expansion in Cooled Turbines,'' ASME J. Eng. Gas Turbines Power, **108**, pp. 151–159.
[6] El-Masri, M. A., 1987, ''Thermodynamics and Performance Projections for Intercooled/Reheat/Recuperated Gas Turbine Systems,'' Paper No. 87-GT-108.
[7] Macchi, E., Bombarda, P., Chiesa, P., Consonni, S., and Lozza, G., 1991, ''Gas Turbine Based Advanced Cycles for Power Generation. Part B: Performance Analysis of Selected Configurations,'' International Gas Turbine Congress, Yokohama, Oct.
[8] Farmer, R., 1993, ''Reheat GTs Boost 250 and 365 MW Combined Cycle Efficiency to 58 percent,'' Gas Turbine World Sept.–Oct.
[9] Negri di Montenegro, G., Gambini, M., and Peretto, A., 1995, ''Reheat and Regenerative Gas Turbines for Feed Water Repowering of Steam Power Plant,'' ASME Turbo Expo. Houston, June 5–8.
[10] Massardo, A. F., and Scialo, M., 1999, ''Thermoeconomic Analysis of Gas Turbine Based Cycles,'' ASME Paper No. 99-GT-312.
[11] Gate Cycle, Computational Code, Release 5.22, 1998, Enter Software, Inc., Menlo Park, CA 94025, USA.
[12] Benvenuti, E., Bettocchi, R., Cantore, G., Negri di Montenegro, G., and Spina, P. R., 1993, ''Gas Turbine Cycle Modeling Oriented to Component Performance Evaluation From Limited Design or Test Data,'' ASME Cogen Turbo, Bournemouth, UK, Sept. 21–23.

Gas Turbine Field Performance Determination: Sources of Uncertainties

M. Pinelli
Dipartimento di Ingegneria,
University of Ferrara,
Ferrara, Italy

P. R. Spina
DIEM-University of Bologna,
Bologna, Italy

This paper presents an analysis of the uncertainties in the determination of gas turbine health, which arise by using a method of gas path analysis. This method uses field measurements to estimate, through a mathematical model of the gas turbine thermodynamic cycle, the characteristic geometric and performance parameters, which are indices of gas turbine health. The investigated sources of uncertainties are the influence of measurement accuracy and the a priori selection of the characteristic parameters that have to be considered constant during the calculation. This fact implies that variations occurring on these parameters in the actual gas turbine cause an estimation error on the characteristic parameters used as problem variables. The analysis leads to the selection of the appropriate measurements to be used in the gas turbine health determination and to the identification of both the most critical measurements and parameters.

[DOI: 10.1115/1.1413464]

Introduction

Gas turbines often have a critical task in industrial applications. Therefore, any unscheduled maintenance or outages can induce great additional costs and lost revenues. These costs are not only caused by maintenance or repairs but also by the standstill of industrial production. For this reason, in many critical applications, standby gas turbines are installed but used only during emergency; thus, a more considerable investment is needed.

The maximization of machine availability, optimizing its management and maintenance, can substantially reduce money loss due to gas turbine stops.

To achieve an increase of gas turbine availability, up-to-date knowledge of the gas turbine operating state is required to diagnose the causes of performance degradation ([1]). So, it is possible to plan in advance maintenance stops and, in some cases, to change the gas turbine control logic to adapt it to the actual machine operating state.

Among the various techniques that can be used for the determination of the gas turbine operating state, the gas path analysis often permits the achievement of good results. This method uses field measurements to estimate, through a mathematical model of the gas turbine thermodynamic cycle, the characteristic geometric and performance parameters (i.e., characteristic flow passage areas and efficiencies of the compressor and turbine, combustor efficiency, pressure drops in the gas path, etc). The calculation of the characteristic parameters is performed by solving in inverse mode linear or nonlinear models of the gas turbine thermodynamic cycle ([2–8]).

Bettocchi and Spina [8] developed a method based on gas path analysis that make use of the program for gas turbine cycle calculation and of the measurements taken from the standard machine instrumentation. The gas turbine operating condition analysis is performed adapting the characteristic geometric and performance parameters, used as inputs by the cycle program, until the real measurements are reproduced. The method can use, for the gas turbine cycle calculation, either an in-house program or a cycle deck developed by the manufacturer.

The determination of the operating state with this method could be uncertain because of some factors, such as

- measurement accuracy
- a priori selection of the geometric and performance characteristic parameters that have to be investigated.

This a priori selection is necessary because the particular method used permits the evaluation of a number of characteristic parameters equal to the number of available gas path measurements. So, some characteristic parameters have to be considered constant during the calculation. The second source of uncertainty becomes now evident if it is considered that the characteristic parameters kept constant may be changing in the actual machine due to deterioration or faults.

It has been shown ([2,7,9]) that when using techniques for the determination of gas turbine operating state, the uncertainties listed above play a significant role. In fact, these uncertainties may alter the estimated parameter as much as the alteration due to an actual loss in gas turbine performance.

In this paper, an analysis of the influence of measurement accuracy and a priori fixed parameter variations on the estimated parameters for gas turbine health determination is presented. This analysis can lead to (i) the selection of the appropriate measurements to be used in the operating state determination, and (ii) the identification of both the most critical measurements and parameters.

Evaluation of the Influence of Uncertainties

The gas turbine health determination requires the evaluation of the actual values of characteristic geometric and performance parameters, which are indices of the machine operating state. The comparison between the actual parameter values and the ones in the ‘‘new and clean’’ conditions allows the evaluation of the shifts between the actual gas turbine operating state and the expected one.

The evaluation of the characteristic parameters is performed utilizing the method developed by Bettocchi and Spina [8], which uses the program for gas turbine cycle calculation and the measurements taken by means of the standard machine instrumentation. The gas turbine operating condition analysis is performed ‘‘adapting’’ the characteristic geometric and performance parameters used as inputs by the cycle program, until the computed estimates of the measurable parameters agree with the values

---

Contributed by the International Gas Turbine Institute (IGTI) of THE AMERICAN SOCIETY OF MECHANICAL ENGINEERS for publication in the ASME JOURNAL OF ENGINEERING FOR GAS TURBINES AND POWER. Paper presented at the International Gas Turbine and Aeroengine Congress and Exhibition, Munich, Germany, May 8–11, 2000; Paper 00-GT-311. Manuscript received by IGTI Nov. 1999; final revision received by ASME Headquarters Feb. 2000. Associate Editor: D. R. Ballal.

measured on the gas turbine. The analysis of the variations between computed and expected values of the characteristic parameters allows the localization of inefficient operations due to deterioration and faults.

The measurable parameters $\mathbf{Q}_m$ computed by the cycle program are a function of the nondimensional machine characteristic parameters ($\mathbf{X}$) and of the parameters that unequivocally determine the actual point at which the gas turbine is operating ($\mathbf{Q}_{WP}$):

$$\mathbf{Q}_m = \mathbf{f}(\mathbf{X}, \mathbf{Q}_{WP}) \tag{1}$$

where $\mathbf{f}$ is a nonlinear function that represents the mathematical model of the system. Inverting Eq. (1), it is possible to calculate the characteristic parameters starting from the measurements, that is

$$\mathbf{X} = \mathbf{f}^{-1}(\mathbf{Q}_m, \mathbf{Q}_{WP}). \tag{2}$$

This calculation is performed by solving the system of equations obtained by equating to zero the residual between the values measured on the machine and computed by the cycle program. The solution algorithm repeatedly calls the cycle program and modifies the characteristic parameters $\mathbf{X}$ until the system of equations is satisfied ([8]).

It is possible to notice that the measurement accuracy affects the solution of Eq. (2), resulting in an uncertain determination of parameters $\mathbf{X}$. Moreover, there could be another source of uncertainty. It has been seen in a previous paper ([8]) that the number and type of gas turbine characteristic parameters which can be determined, depend on the number and type of the available measurements. In particular, the number of characteristic parameters which can be determined is generally equal to the number of available measurements, without considering the $\mathbf{Q}_{WP}$ measurements, which are used for defining the machine working point. Excluding the latter, the standard instrumentation of a gas turbine permits few gas path measurements (maximum six to eight). So, if the number of the characteristic parameters to be estimated is greater than the available measurements, some of them have to be kept constant. If we split the vector $\mathbf{X}$ representing the parameters into two parts, a constant one ($\mathbf{X}_f$) and a variable one ($\mathbf{X}_v$), Eq. (2) can be written

$$\mathbf{X}_v = \mathbf{f}^{-1}(\mathbf{Q}_m, \mathbf{Q}_{WP}, \mathbf{X}_f). \tag{3}$$

As can be seen from Eq. (3), a variation due to aging or deterioration that occurs on a characteristic parameter which was considered as a fixed parameter, causes an estimation error on the characteristic parameters that have to be estimated.

Finally, two sources of uncertainty are recognized: the first deriving from measurement uncertainty due to the bias and precision errors of the sensors and the second caused by the reduced number of available measurements that force some parameters, which otherwise may vary, to be kept constant.

The calculation procedures of the influence of the two sources of uncertainty on the estimated parameters are dealt with separately.

Measurement Accuracy. The procedure for determining the influence of the *i*th measurement accuracy on the *j*th parameter is presented.

Let X_j be the parameter for which we want to calculate the influence of a given measurement Q_{mi}. If this measurement is altered by a small percentage amount ε

$$Q^*_{mi} = Q_{mi} + \varepsilon \tag{4}$$

it is possible to evaluate the variation δQ_{mi} of the *i*th measurement as

$$\delta Q_{mi} = Q^*_{mi} - Q_{mi}. \tag{5}$$

Applying Eq. (3) for the parameter considered, the following is obtained:

$$X^*_j = f_j^{-1}(Q_{m1}, \ldots, Q^*_{mi}, \ldots, Q_{mn}, \mathbf{Q}_{WP}, \mathbf{X}_f). \tag{6}$$

Finally, the sensitivity of the *j*th parameter to the *i*th measurement can be obtained:

$$\delta X_j = X^*_j - X_j. \tag{7}$$

In the case in which the measurement accuracy does not coincide with ε, the sensitivity can be obtained multiplying the real accuracy, ΔQ_{mi}, by the ratio $\delta X_j / \delta Q_{mi}$ that represents the numerical partial derivative of the *j*th parameter on the *i*th measurement:

$$\Delta X_{ji} = \Delta Q_{mi} \left(\frac{\delta X_j}{\delta Q_{mi}} \right). \tag{8}$$

This is possible under the hypothesis that the partial derivative can be considered constant in the range defined by ΔQ_{mi} (i.e., the mathematical model of the system can be linearized in the range defined by ΔQ_{mi}).

It could be useful to define also a quantity that can represent the weighting factor of the *i*th measurement on the *j*th parameter:

$$W_{Qji} = \frac{\delta X_j}{(\delta Q_{mi}/Q_{mi})}. \tag{9}$$

This quantity can give qualitatively and quantitatively information on the relationship between the *j*th parameter and the *i*th measurement and also give the possibility of evaluating which measurements exert the strong influence on each parameter, independent of sensor accuracy.

Applying this procedure it is also possible to evaluate the influence of the accuracy of measurements defining the working point.

The total error on the variable parameters deriving from the uncertainties on all the measurements are estimated using the root-sum-square formula (RSS), that can be written

$$\Delta X_j = \sqrt{\sum_{i=1}^{n} \left(\Delta Q_{mi} \frac{\delta X_j}{\delta Q_{mi}} \right)^2 + \sum_{i=1}^{t} \left(\Delta Q_{WPi} \frac{\delta X_j}{\delta Q_{WPi}} \right)^2}, \quad j = 1, \ldots, s. \tag{10}$$

Error Due to Fixed Parameters. In this case the procedure is slightly different from the previous. In fact, having split the $\mathbf{X}$ vector into two parts, from Eq. (1) results

$$\mathbf{Q}_m = \mathbf{f}(\mathbf{X}_v, \mathbf{X}_f, \mathbf{Q}_{WP}). \tag{11}$$

Now, altering of a small amount one of the fixed parameter $\mathbf{X}_f$, a set of calculated measurements corresponding to the variation of the considered parameter is obtained from Eq. (11). Then, using Eq. (3), it is possible to evaluate how the algorithm interprets the change of the fixed parameter in terms of the estimated ones. Also in this case it is possible to define the weighting factor of the *i*th fixed parameter on the *j*th variable parameter through the relation

$$W_{Xji} = \frac{(\delta X_v)_j}{(\delta X_f / X_f)_i}. \tag{12}$$

The variation of the *j*th parameter is then

$$\Delta X_{ji} = W_{Xji} \left(\frac{\Delta X_f}{X_f} \right)_i. \tag{13}$$

Application of the Method

The analysis of error propagation due to the uncertainties described above was applied to a model of a 10 MW two shaft heavy-duty industrial gas turbine with variable power turbine nozzle.

For this machine configuration, three independent operating parameters, in addition to the boundary conditions p_a, T_a and RH, are needed to unequivocally determine the actual point at which

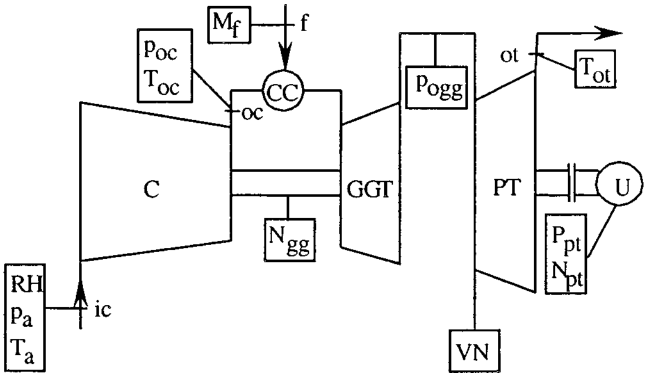

Fig. 1 Layout of the gas turbine with the measurements considered

the gas turbine is operating: in the analysis performed below, the measured values of the gas generator (N_{gg}) and power turbine (N_{pt}) rotational speeds and of the shaft power (P_{pt}) were used. All these measurements ($\mathbf{Q}_{WP}$) define the working point of the machine.

The standard instrumentation of a gas turbine generally allows five or six measurements, in addition to the ones already used for defining the working point. These measurements ($\mathbf{Q}_m$) are used to calculate the characteristic parameters which define the operating state of the gas turbine. The measurements which were considered to be available for calculating the characteristic parameters are: the pressure and temperature at the compressor outlet (p_{oc}, T_{oc}), the fuel mass flow rate (M_f), the turbine outlet temperature (T_{ot}), the variable turbine nozzle angular position (VN), and the pressure (p_{ogg}) at the gas generator outlet. Figure 1 shows the layout of the gas turbine with the measurements considered.

The characteristic parameters, which were considered as indices of gas turbine health, are the compressor and turbines mass flow functions and efficiencies, the combustor efficiency and pressure drop and the leaking and cooling mass flow rates.

Two sets of calculations were performed:

1 First, the case in which six measurements are available for the determination of gas turbine operating state was considered. The influence on the estimated parameters of the accuracy of all measurements was calculated. The assumed values of measurement errors are listed in Table 1. These values were chosen with respect to the ISO 2314 International Standard [10] and considering that the measurements were taken on the field with the standard instrumentation of the machine during normal operation and not when conducting an acceptance test ([11]). For this reason some errors were considered higher than that reported in the ISO 2314. As estimated parameters, the six most important indices for the gas turbine health determination were chosen; they are the efficiency and the mass flow function of the compressor (η_c, μ_c), the efficiency and the mass flow function of the gas generator turbine (η_{ggt}, μ_{ggt}) and the efficiency and the mass flow function of the power turbine (η_{pt}, μ_{pt}) ([8,9]). The influence on the estimated parameters of a one percent variation of the remaining parameters η_{cc}, Δp_{cc} and of the cooling mass flow rate having the highest influence on the thermodynamic cycle (M_{cool}) was then evaluated.

2 Secondly, the case in which the pressure at the gas generator outlet (p_{ogg}) is not available was considered. This measurement is not usually present in a practical situation. In this case, one more parameter must be fixed. Two different situations were then considered, in which the additional fixed parameter was alternatively the efficiency (η_{pt}) and the mass flow function of the power turbine (μ_{pt}). So, in addition to the same calculation performed for the first case, the influence on the estimated parameters of a one percent variation of these two parameters was considered.

Table 1 Typical measurement errors in percent of the reference value and reference values

Measured Quantities	Measurement Errors (percent of reference value)	Reference Values
p_a	0.10	101.3 (kPa)
$T_a{}^1$	0.35	288 (K)
RH	3.00	60 %
p_{oc}	0.40	1439.9 (kPa)
$T_{oc}{}^1$	0.50	669.1 (K)
p_{ogg}	0.40	306.0 (kPa)
$T_{ot}{}^1$	0.60	712.6 (K)
M_f	2.00	0.645 (kg/s)
VN	1.00	1.127 area ratio
P_{ot}	0.50	10000 (kW)
N_{gg}	0.25	10800 (rpm)
N_{pt}	0.25	7900 (rpm)

[1] Percent values of temperature measurements correspond to an error of ±1K, ±3K, and ±4K on T_a, T_{oc}, and T_{ot}, respectively.

Results and Discussion

The results of the calculations related to different sets of measurements are described below.

Case 1—Six Measurements. The influence of measurement accuracy was first considered. In addition to the measurements necessary to define the working point ($N_{gg}, N_{pt}, P_{pt}, p_a, T_a, RH$), the whole set of $\mathbf{Q}_m$ measurements ($p_{oc}, T_{oc}, p_{ogg}, T_{ot}, VN, M_f$) reported above was considered to be available. As a consequence, six of the nine characteristic parameters were considered as problem variables ($\eta_c, \eta_{ggt}, \eta_{pt}, \mu_c, \mu_{ggt}, \mu_{pt}$) and the other three as fixed ($\eta_{cc}, \Delta p_{cc}, M_{\text{cool}}$).

In Fig. 2, the error on the estimated parameters due to the error on the 12 measurements ($\mathbf{Q}_m$ and $\mathbf{Q}_{WP}$) is presented. As can be seen, the flow functions are the parameters most sensitive to measurement accuracy. The maximum error calculated with the RSS formula is of about three percent. It can be noticed also that, while the flow functions exhibit a comparable amount of error among them, the power turbine efficiency error is much higher than the errors on the compressor and gas generator turbine efficiencies.

The reason for this can be deduced from the analysis of Figs. 3 and 4, where the absolute values of the weights of $\mathbf{Q}_m$ and $\mathbf{Q}_{WP}$ measurements on the six estimated parameters are reported. Here it is possible to see how each measurement affects the estimation of each parameter. Analyzing these figures and observing Table 1, it is possible to notice that

- the outlet compressor temperature affects remarkably the estimation of the compressor and the gas generator efficiency, while the ambient temperature affects all the estimated parameters and

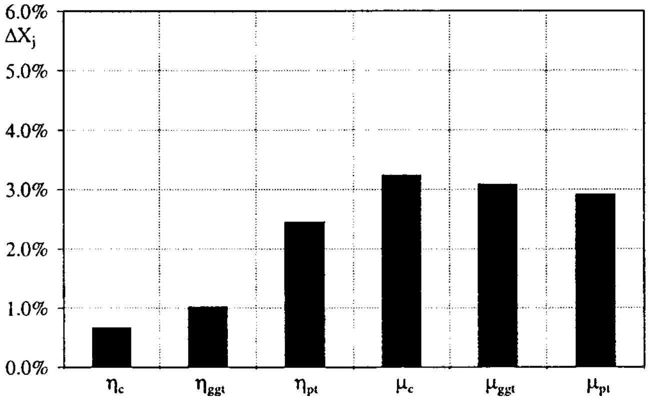

Fig. 2 Error on the estimated parameters due to the error on the measurements Q_m and Q_{WP} (Case 1a)

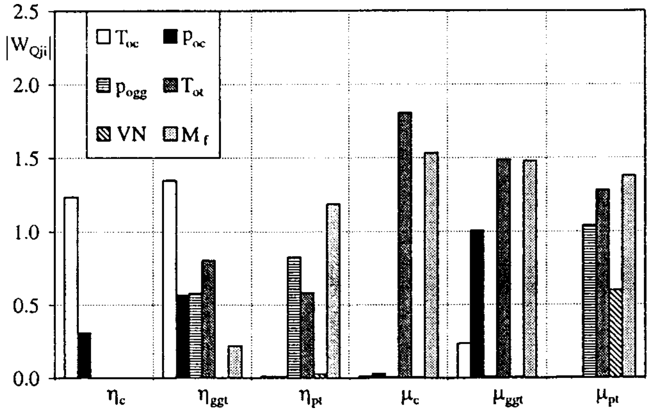

Fig. 3 Absolute value of the weighting factors of the Q_m measurements on the estimated parameters (Case 1)

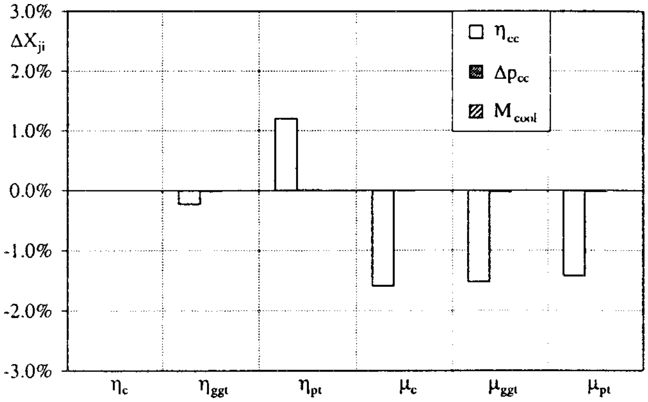

Fig. 5 Contribution ΔX_{ji} due to a one percent variation on the fixed parameters η_{cc}, Δp_{cc}, and M_{cool} (Case 1)

particularly the compressor flow function. These two measurements, however, present a good accuracy: Their contribution to the error evaluated with the RSS formula is only of limited relevance.

- the exhaust gas temperature and the fuel mass flow rate influence the estimation of all the parameters, excluding the compressor efficiency. But, while the first contributes only a little to the parameter total errors thanks to the good accuracy ΔQ_m of its measuring sensor (see Table 1), the second affects remarkably the total errors, since the accuracy of its measuring sensor is very low. In particular, focusing on gas generator and power turbine efficiencies, it can be noticed from Fig 3 that η_{ggt} is less influenced than η_{pt} by the fuel flow measurement. This can be regarded as the main reason of the remarkable difference between the estimation errors on these two parameters (Fig. 2).

The influence on the estimated variable parameters of a variation that may occur on one of the three fixed parameters η_{cc}, Δp_{cc}, and M_{cool} was considered. Figure 5 shows the influence ΔX_{ji} on the six variable parameters due to a one percent variation. As can be seen, the combustor efficiency is the only fixed parameter that has a relevant influence on the estimation of the variable parameters. On the contrary, the influence on the estimated variable parameters of one percent variation on Δp_{cc} and M_{cool} is negligible. In particular, the cooling mass flow rate begins to influence the estimated parameters for variations higher than ten percent.

Case 2a—Five Measurements (η_{pt}=const). In this case, a reduced set of Q_m measurements was considered. In particular, it was taken into account the case in which the measurement of the pressure at the gas generator turbine outlet (p_{ogg}) was not available. As a consequence, only five of the nine characteristic parameters can be used as problem variables. The choice of the additional parameter to be fixed is determined by

1 the necessity of having univocally determinate the system of equations that relate the variable parameters to the available measurements; this defines the set of parameters that can be additionally fixed;

2 the field experience, that determines the parameters having less probability to be subjected to variation due to aging or deterioration. In this way, fixing a parameter that does not vary frequently, it is possible to considerably reduce the probable error due to variations on fixed parameters.

For the two-shaft industrial gas turbine considered, among the parameters determined by the first condition ($\eta_{ggt}, \eta_{pt}, \mu_{pt}$), the efficiency and the mass flow function of the power turbine are the parameters that are less susceptible to variations.

In this first case, the power turbine efficiency was considered as the additional fixed parameter.

Figure 6 shows the error on the estimated parameters due to the error on the 11 measurements ($\mathbf{Q}_m$ and $\mathbf{Q}_{WP}$). Comparing with the results shown in Fig. 2 (case of six $\mathbf{Q}_m$ measurements), it can be noticed that the lack of p_{ogg} measurement determines a remarkable increment of the error on the power turbine mass flow function, while the other parameters remains almost the same as in Fig. 2. This is mainly due to an increment of the weight of the fuel flow measurement only on the power turbine mass flow function.

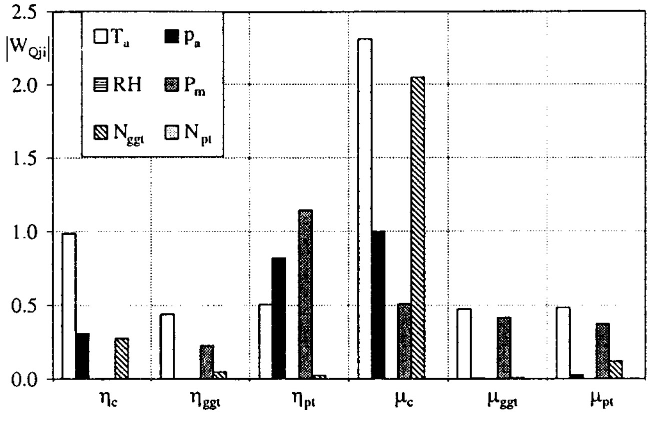

Fig. 4 Absolute value of the weighting factors of the Q_{WP} measurements on the estimated parameters (Case 1)

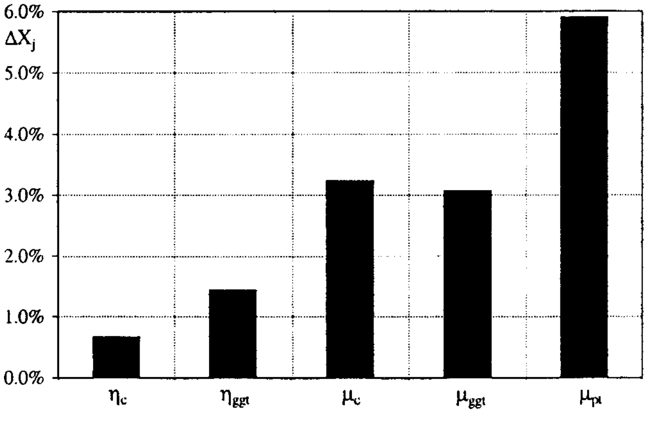

Fig. 6 Error on the estimated parameters due to the error on the measurements Q_m and Q_{WP} (Case 2a)

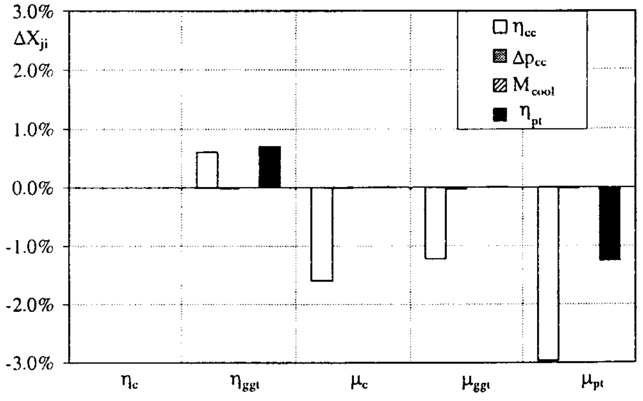

Fig. 7 Contribution ΔX_{ji} due to a one percent variation on the fixed parameters η_{cc}, Δp_{cc}, M_{cool}, and η_{pt} (Case 2a)

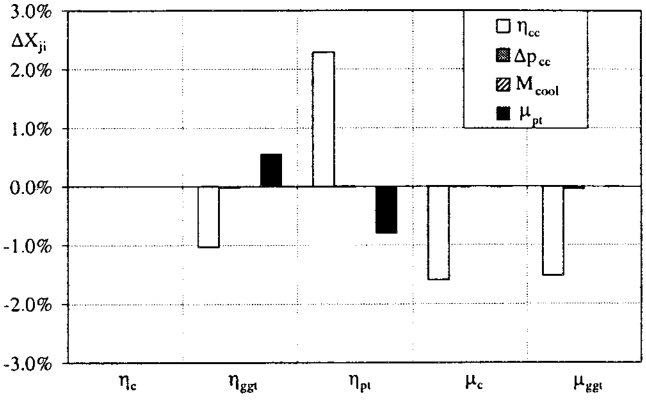

Fig. 9 Contribution ΔX_{ji} due to a one percent variation on the fixed parameters η_{cc}, Δp_{cc}, M_{cool}, and μ_{pt} (Case 2b)

Figure 7 shows the influence on the estimated variable parameters of a one percent variation on the three fixed parameters considered above (η_{cc},Δp_{cc},M_{cool}) and on the additional fixed parameter η_{pt}.

In this case, in addition to the combustor efficiency, also the power turbine efficiency presents a relevant influence on the estimation of the variable parameters.

Case 2b—Five Measurements (μ_{pt}=const). This case is similar to the previous one but the power turbine mass flow function μ_{pt} was considered as additional fixed parameter.

Figure 8 shows the error on the estimated parameters due to the error on the 11 measurements ($\mathbf{Q}_m$ and $\mathbf{Q}_{WP}$). Comparing these results with the case of six measurements available (Case 1), it can be noticed that an increment on the total error is recognizable both on the power turbine and gas generator turbine efficiencies.

Figure 9 shows the influence on the estimated variable parameters of a one percent variation on the three fixed parameters η_{cc}, Δp_{cc}, M_{cool} and on the additional fixed parameter μ_{pt}. Also in this case, in addition to the combustor efficiency, the additional fixed parameter μ_{pt} is the one which exerts a more relevant influence on the estimation of the variable parameters.

Comparing the calculations in Cases 2a and 2b, it can be seen that

- the maximum total error concerns a characteristic parameter of the power turbine, the mass flow function μ_{pt} in the first case, and the efficiency η_{pt} in the second;
- the error on μ_{pt} in Case 2a is higher than error on η_{pt} in 2b;
- the influence of the fixed parameter η_{cc} on the estimated parameters is in Case 2a higher than in Case 2b.

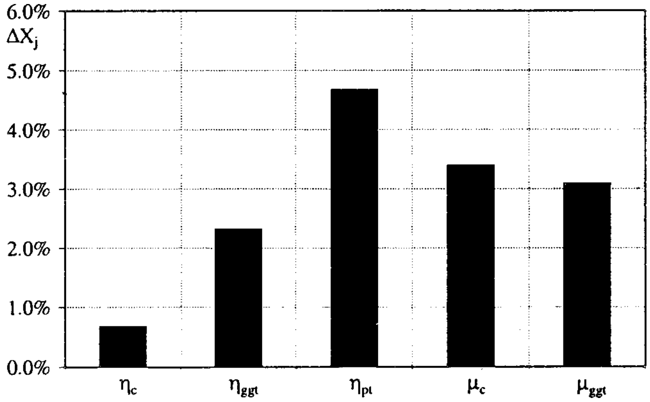

Fig. 8 Error on the estimated parameters due to the error on the measurements Q_m and Q_{WP} (Case 2b)

Conclusions

The analysis performed in this paper permitted the evaluation of the influence of measurement accuracy and a priori fixed parameter variations on the estimated characteristic parameters. The measurement accuracy was considered in the range of a typical industrial instrumentation.

This analysis shows that the error on the estimated parameters due to these uncertainties can hide a real variation of the characteristic parameter due to actual component deterioration or faults. When six measurements are available for the determination of the gas turbine operating state, the maximum total errors on the estimated parameters due to $\mathbf{Q}_m$ and $\mathbf{Q}_{WP}$ measurement accuracy (evaluated with the RSS formula) are close to three percent. Further, the combustor efficiency is the only fixed parameter that has a relevant influence on the variable parameter estimation. Then, the effect on the estimation error of a reduced set of available measurements was analyzed.

The calculations performed put into light that the lack of p_{ogg} measurement results in an increase of the estimation error on the gas generator efficiency and on one between the power turbine efficiency and the power turbine mass flow function, depending on the additional fixed parameter. Moreover, there is a significant influence of the additional fixed parameter on the variable parameter estimation. Finally, in the case of five measurements available, with respect to the total errors, it seems more convenient to fix the mass flow function instead of the efficiency of the power turbine.

The present analysis shows the criticality of two measurements: the exhaust gas temperature and the fuel mass flow rate. But, while the former does not affect remarkably the total error due to the good accuracy of the sensor, the latter has the highest influence on all the parameter estimations. The reason for this can be seen in the high uncertainty of its determination.

A remarkable improvement in the diagnostic reliability can be reached increasing the accuracy of a critical measurement such as the fuel mass flow rate and augmenting the number of available measurements. Further, improvements in the obtained results may be reached considering that gas path analysis method for gas turbine health determination is based on the evaluation of the shifts between computed and reference values of characteristic parameters. Therefore, the evaluation of the reference values on each particular gas turbine unit (custom baseline) allows the reduction, or the elimination, of the bias error. In this manner, only the precision error, remains to influence the estimation of desired parameters.

Acknowledgments

The work was carried out with the support of the M.U.R.S.T. (Italian Ministry of University and Scientific & Technological Research).

The authors gratefully acknowledge Prof. Roberto Bettocchi for the suggestions provided during the work.

Nomenclature

c_p = specific heat at constant pressure
c_v = specific heat at constant volume
k = c_p/c_v
M = mass flow rate
N = rotational speed
n = number of gas path measurements
P = power
p = pressure
$\mathbf{Q}_m$ = vector of measured parameters
$\mathbf{Q}_{WP}$ = vector of measurements necessary to define the working point
R = gas constant
RH = relative humidity
s = number of characteristic parameters
t = number of working point measurements
T = temperature
VN = variable nozzle angular position
W_{Qji} = weight of the ith measure on the jth parameter
W_{Xji} = weight of the ith fixed parameter on the jth variable parameter
$\mathbf{X}$ = vector of nondimensional characteristic parameters
ε = small measurement perturbation
η = efficiency
μ = $M\sqrt{kRT}/p$ mass flow function

Subscripts and Superscripts

$*$ = altered measurement/parameter
a = ambient
c = compressor
cc = combustor
cool = cooling
f = fuel, fixed parameter
gg = gas generator
i = inlet section
o = outlet section
ot = power turbine outlet section
pt = power turbine
t = turbine
v = variable parameter

Acronyms

C = compressor
CC = combustor
GGT = gas generator turbine
PT = power turbine
U = user

References

[1] Madej, J., Longtin, K., and Smith, D. P., 1996, ''Monitoring Service Delivery System and Diagnostics,'' *Proceedings, 39th GE Turbine State-of-the-Art Technology Seminar*, General Electric Company, Schenectady, NY, GER-3956.
[2] Urban, L. A., 1972, ''Gas Path Analysis Applied to Turbine Engine Condition Monitoring,'' AIAA Paper 72-1082, AIAA, New York.
[3] Stamatis, A., Mathioudakis, K., and Papailiou, K. D., 1990, ''Adaptive Simulation of Gas Turbine Performance,'' ASME J. Eng. Gas Turbines Power, **112**, pp. 168–175.
[4] Benvenuti, E., Bettocchi, R., Cantore, G., Negri di Montenegro, G., and Spina, P. R., 1993, ''Gas Turbine Cycle Modeling Oriented to Component Performance Evaluation From Limited Design or Test Data,'' *Proceedings, 7th ASME COGEN—TURBO*, Bournemouth, UK, IGTI Vol. 8, ASME, New York, pp. 327–337.
[5] Benvenuti, E., Bettocchi, R., Cantore, G., Negri di Montenegro, G., and Spina, P. R., 1994, ''Experimental Validation of a Gas Turbine Cycle Model Based on a Simultaneous Solution Method,'' *Proceedings, 8th ASME COGEN—TURBO*, Portland, OE, IGTI Vol. 9, ASME, New York, pp. 245–255.
[6] Doel, D. L., 1994a, ''TEMPER—A Gas-Path Analysis Tool for Commercial Jet Engines,'' ASME J. Eng. Gas Turbines Power, **116**, pp. 82–89.
[7] Doel, D. L., 1994b, ''An Assessment of Weighted-Least-Squares Based Gas Path Analysis,'' ASME J. Eng. Gas Turbines Power, **116**, pp. 366–373.
[8] Bettocchi, R., and Spina, P. R., 1999, ''Diagnosis of Gas Turbine Operating Conditions by Means of the Inverse Cycle Calculation,'' ASME Paper 99-GT-185.
[9] Stamatis, A., Mathioudakis, K., and Papailiou, K., 1992, ''Optimal Measurement and Health Index selection for Gas Turbine Performance Status and Fault Diagnosis,'' ASME J. Eng. Gas Turbines Power, **114**, pp. 209–216.
[10] ISO 2314, 1989, ''Gas Turbine—Acceptance Tests,'' International Standard.
[11] Brun, K., and Kurz, R., 1998, ''Measurement Uncertainties Encountered During Gas Turbine Driven Compressor Field Testing,'' ASME Paper 98-GT-001.

Effect of Crystal Orientation on Fatigue Failure of Single Crystal Nickel Base Turbine Blade Superalloys

N. K. Arakere
Associate Professor,
Mechanical Engineering Department,
University of Florida,
Gainesville, FL 32611-6300
e-mail: nagaraj@ufl.edu

G. Swanson
NASA Marshall Space Flight Center,
ED22/Strength Analysis Group,
MSFC, AL 35812

High cycle fatigue (HCF) induced failures in aircraft gas turbine and rocket engine turbopump blades is a pervasive problem. Single crystal nickel turbine blades are being utilized in rocket engine turbopumps and jet engines throughout industry because of their superior creep, stress rupture, melt resistance, and thermomechanical fatigue capabilities over polycrystalline alloys. Currently the most widely used single crystal turbine blade superalloys are PWA 1480/1493, PWA 1484, RENE' N-5 and CMSX-4. These alloys play an important role in commercial, military and space propulsion systems. Single crystal materials have highly orthotropic properties making the position of the crystal lattice relative to the part geometry a significant factor in the overall analysis. The failure modes of single crystal turbine blades are complicated to predict due to the material orthotropy and variations in crystal orientations. Fatigue life estimation of single crystal turbine blades represents an important aspect of durability assessment. It is therefore of practical interest to develop effective fatigue failure criteria for single crystal nickel alloys and to investigate the effects of variation of primary and secondary crystal orientation on fatigue life. A fatigue failure criterion based on the maximum shear stress amplitude [$\Delta\tau_{\max}$] on the 24 octahedral and 6 cube slip systems, is presented for single crystal nickel superalloys (FCC crystal). This criterion reduces the scatter in uniaxial LCF test data considerably for PWA 1493 at 1200°F in air. Additionally, single crystal turbine blades used in the alternate advanced high-pressure fuel turbopump (AHPFTP/AT) are modeled using a large-scale three-dimensional finite element model. This finite element model is capable of accounting for material orthotrophy and variation in primary and secondary crystal orientation. Effects of variation in crystal orientation on blade stress response are studied based on 297 finite element model runs. Fatigue lives at critical points in the blade are computed using finite element stress results and the failure criterion developed. Stress analysis results in the blade attachment region are also presented. Results presented demonstrates that control of secondary and primary crystallographic orientation has the potential to significantly increase a component's resistance to fatigue crack growth without adding additional weight or cost. [DOI: 10.1115/1.1413767]

1 Introduction

High cycle fatigue (HCF) induced failures in aircraft gas turbine engines is a pervasive problem affecting a wide range of components and materials. HCF is currently the primary cause of component failures in gas turbine aircraft engines ([1]). Turbine blades in high performance aircraft and rocket engines are increasingly being made of single crystal nickel superalloys. Single crystal nickel base superalloys were developed to provide superior creep, stress rupture, melt resistance, and thermomechanical fatigue capabilities over polycrystalline alloys previously used in the production of turbine blades and vanes. Currently the most widely used single crystal turbine blade superalloys are PWA 1480/1493 and PWA 1484. These alloys play an important role in commercial, military and space propulsion systems. PWA 1493, identical to PWA 1480, but with tighter chemical constituent control, is used in the NASA SSME alternate turbopump, a liquid hydrogen fueled rocket engine.

Single crystal materials differ significantly from polycrystalline alloys in that they have highly orthotropic properties making the position of the crystal lattice relative to the part geometry a significant factor in the overall analysis ([2]). The modified Goodman approach currently used for component design does not address important factors that affect HCF such as fretting and/or galling surface damage, and interaction with LCF ([1]). Rocket engine service presents another set of requirements that shifts emphasis to low temperature fatigue and fracture capability with particular attention given to thermal, cryogenic and high pressure hydrogen gas exposure ([3]). To address HCF induced component failures, the gas turbine industry, NASA, the U.S. Air Force, and the U.S. Navy have made significant efforts in understanding fatigue in single crystal turbine blade superalloys. Understanding fatigue initiation, threshold, and Region II fatigue crack growth are of primary importance and there is great need for improvements in fracture mechanics properties of turbine blade alloys. While a large amount of data has been collected there currently exists no simple method for applying this knowledge toward the design of more robust single crystal gas turbine engine components. It is therefore essential to develop failure criteria for single crystals, based on available fatigue and fracture test data that will permit a designer to utilize the lessons learned.

Objectives for this paper are motivated by the need for developing failure criteria and fatigue life evaluation procedures for high-temperature single crystal components, using available fa-

---

Contributed by the International Gas Turbine Institute (IGTI) of THE AMERICAN SOCIETY OF MECHANICAL ENGINEERS for publication in the ASME JOURNAL OF ENGINEERING FOR GAS TURBINES AND POWER. Paper presented at the International Gas Turbine and Aeroengine Congress and Exhibition, Munich, Germany, May 8–11, 2000; Paper 00-GT-334. Manuscript received by IGTI November 1999; final revision received by ASME Headquarters February 2000. Associate Editor: D. R. Ballal.

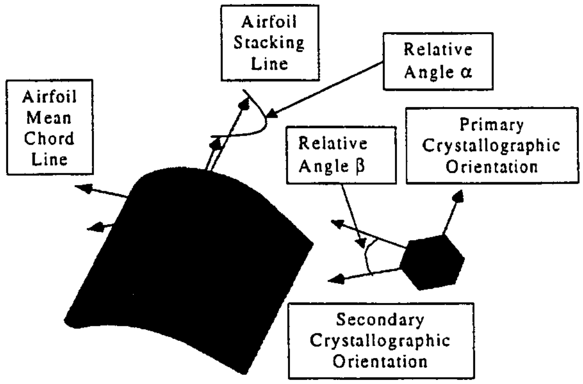

Fig. 1 Convention for defining crystal orientation in turbine blades ([2])

tigue data and finite element modeling of turbine blades. Fatigue failure criteria are developed for single crystal material by suitably modifying failure criteria for polycrystalline material. The proposed criteria are applied for uniaxial LCF test data, to determine the most effective failure parameter. A fatigue life equation is developed based on the curve fit of the failure parameter with LCF test data. Single crystal turbine blades used in the alternate advanced high-pressure fuel turbopump (AHPFTP/AT) are modeled using a large-scale three dimensional finite element model capable of accounting for material orthotrophy and variation in primary and secondary crystal orientation. Using the finite element stress analysis results and the fatigue life relations developed, the effect of variation of primary and secondary crystal orientations on life is determined, at critical blade locations. The most advantageous crystal orientation for a given blade design is determined. Results presented demonstrates that control of secondary and primary crystallographic orientation has the potential to optimize blade design by increasing its resistance to fatigue crack growth without adding additional weight or cost.

2 Crystal Orientation

Nickel-based single crystal superalloys are precipitation strengthened cast mono grain superalloys based on the Ni-Cr-Al system. The microstructure consists of approximately 60 percent to 70 percent by volume of γ' precipitates in a γ matrix. The γ' precipitate, based on the intermetallic compound Ni_3Al, is the strengthening phase in nickel-base superalloys and is a face centered cubic (FCC) structure. The γ' precipitate is suspended within the γ matrix, which is also of FCC structure and comprised of nickel with cobalt, chromium, tungsten and tantalum in solution. Single crystal superalloys have highly orthotropic material properties that vary significantly with direction relative to the crystal lattice. Primary crystallographic orientation of a turbine blade, commonly referred to as α, is defined as the relative angle between the airfoil stacking line and the $\langle 001\rangle$ direction, as shown in Fig. 1. Current manufacturing capability permits control of α to within 5 deg of the stacking line. Secondary orientation β defines the angle of the $\langle 100\rangle$ orientation relative to the blade geometry. In most turbine blade castings the secondary orientation β is neither specified nor controlled during the manufacturing process. The β orientation for a given blade casting therefore becomes a random variable. Usually, however, the β orientation for each blade is recorded after the casting process is complete.

3 Fatigue in Single Crystal Nickel Superalloys

Slip in metal crystals often occurs on planes of high atomic density in closely packed directions. The four octahedral planes corresponding to the high-density planes in the FCC crystal are shown in Fig. 2. The four octahedral slip planes have three primary slip directions (easy-slip) resulting in 12 independent primary $\langle 110\rangle\{111\}$ slip systems. The four octahedral slip planes also have three secondary slip directions resulting in 12 independent secondary $\langle 112\rangle\{111\}$ slip systems. Thus there are 12 primary and 12 secondary slip systems associated with the four octahedral planes ([4]). In addition, the three cube slip planes have two slip directions resulting in six independent $\langle 110\rangle\{100\}$ cube slip systems, as shown in Fig. 3. Deformation mechanisms operative in

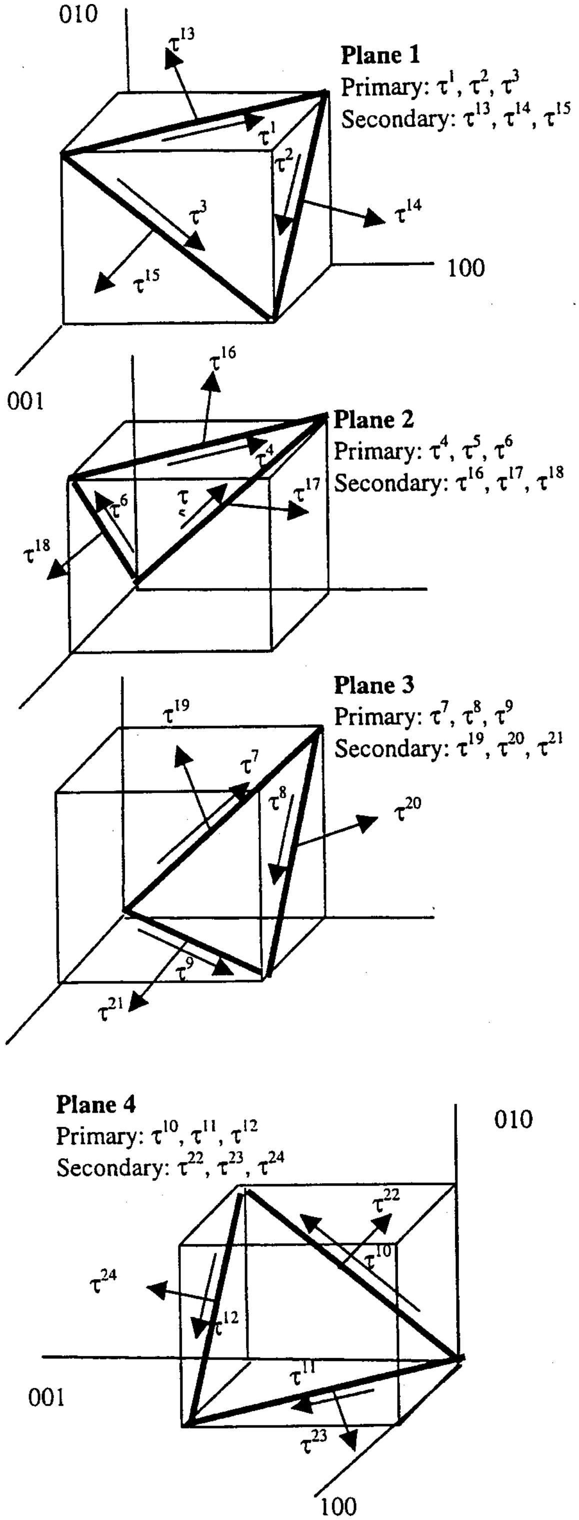

Fig. 2 Primary (close-packed) and secondary (non-close-packed) slip directions on the octahedral planes for a FCC crystal ([4])

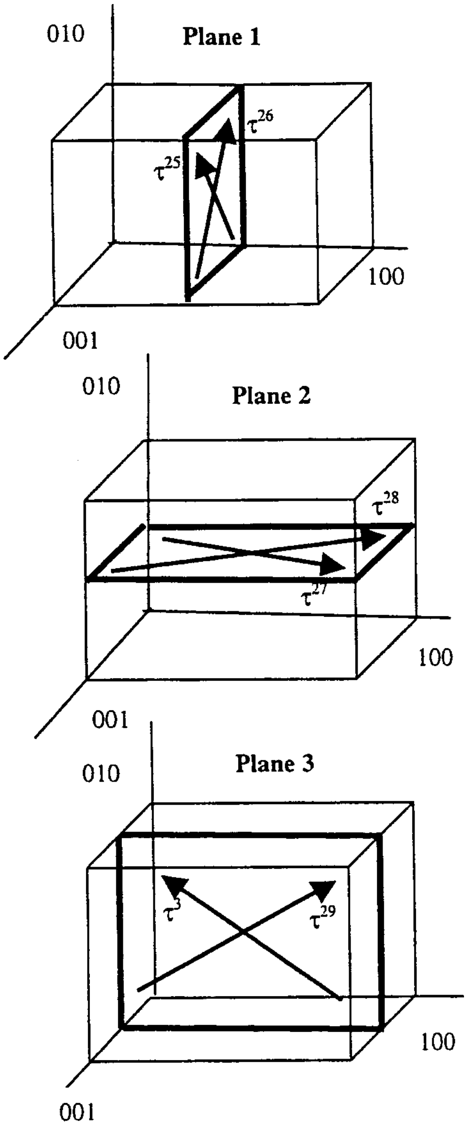

Fig. 3 Cube slip planes and slip directions for a FCC crystal ([4])

PWA 1480/1493 are divided into three-temperature regions ([5]). In the low-temperature regime (26°C to 427°C, 79°F to 800°F) the principal deformation mechanism is by (111)/⟨110⟩ slip, and hence fractures produced at these temperatures exhibit (111) facets. Above 427°C (800°F) thermally activated cube cross slip is observed which is manifested by an increasing yield strength up to 871°C (1600°F) and a proportionate increase in (111) dislocations that have cross slipped to (001) planes. Thus nickel-based FCC single crystal superalloys slip primarily on the octahedral and cube planes in specific slip directions. At low temperature and stress conditions crystallographic initiation appears to be the most prevalent mode. This mode warrants special consideration since this mode of cracking has been observed in many turbine blade failures ([3]). The operative deformation mechanism has a strong influence on the nature of fracture. As a result of the two phase microstructure present in single crystal nickel alloys a complex set of fracture mode exists based on the dislocation motion in the matrix (γ) and precipitate phase (γ'). Telesman and Ghosn ([6]) have observed the transition of fracture mode as a function of stress intensity (K) in PWA 1480 at room temperature. Deluca and Cowles ([7]) have observed the fracture mode transition that is environmentally dependent.

Fatigue life estimation of single crystal blade components represents an important aspect of durability assessment. Turbine blade material is subjected to large mean stresses from the centrifugal stress field. High-frequency alternating fatigue stresses are a function of the vibratory characteristics of the blade. Any fatigue failure criteria chosen must have the ability to account for high mean stress effects. Towards identifying fatigue failure criteria for single crystal material we consider four fatigue failure theories used for polycrystalline material subjected to multiaxial states of fatigue stress. Kandil et al. [8] presented a shear and normal strain based model, shown in Eq. (1), based on the critical plane approach which postulates that cracks initiate and grow on certain planes and that the normal strains to those planes assist in the fatigue crack growth process. In Eq. (1) $\gamma_{\max}$ is the max shear strain on the critical plane, ε_n the normal strain on the same plane, S is a constant, and N is the cycles to initiation.

$$\gamma_{\max}+S\varepsilon_n=f(N). \tag{1}$$

Socie et al. [9] presented a modified version of this theory shown in Eq. (2), to include mean stress effects. Here the maximum shear strain amplitude ($\Delta\gamma$) is modified by the normal strain amplitude ($\Delta\varepsilon$) and the mean stress normal to the maximum shear strain amplitude (σ_{no}).

$$\frac{\Delta\gamma}{2}+\frac{\Delta\varepsilon_n}{2}+\frac{\sigma_{no}}{E}=f(N) \tag{2}$$

Fatemi and Socie [10] have presented an alternate shear based model for multiaxial mean-stress loading that exhibits substantial out-of-phase hardening, shown in Eq. (3). This model indicates that no shear direction crack growth occurs if there is no shear alternation.

$$\frac{\Delta\gamma}{2}\left(1+k\frac{\sigma_n^{\max}}{\sigma_y}\right)=f(N) \tag{3}$$

Smith et al. ([11]) proposed a uniaxial parameter to account for mean stress effects which was modified for multiaxial loading, shown in Eq. (4), by Bannantine and Socie ([12]). Here the maximum principal strain amplitude is modified by the maximum stress in the direction of maximum principal strain amplitude that occurs over one cycle.

$$\frac{\Delta\varepsilon_1}{2}(\sigma^{\max})=f(N) \tag{4}$$

4 Application of Failure Criteria to Uniaxial LCF Test Data

The polycrystalline failure parameters described by Eqs. (1)–(4) will be applied for single crystal uniaxial strain controlled LCF test data. Transformation of the stress and strain tensors between the material and specimen coordinate systems (Fig. 4) is necessary for implementing the failure theories outlined. The components of stresses and strains in the (x',y',z') system in terms of the (x, y, z) system is given by ([13])

$$\{\sigma'\}=[Q']\{\sigma\}; \quad \{\varepsilon'\}=[Q'_\varepsilon]\{\varepsilon\} \tag{5}$$

$$\{\sigma\}=[Q']^{-1}\{\sigma'\}=[Q]\{\sigma'\}$$

$$\{\varepsilon\}=[Q'_\varepsilon]^{-1}\{\varepsilon'\}=[Q_\varepsilon]\{\varepsilon'\} \tag{6}$$

where

$$\{\sigma'\}=\begin{Bmatrix}\sigma_x'\\ \sigma_y'\\ \sigma_z'\\ \tau_{yz}'\\ \tau_{zx}'\\ \tau_{xy}'\end{Bmatrix},\quad \{\sigma\}=\begin{Bmatrix}\sigma_x\\ \sigma_y\\ \sigma_z\\ \tau_{yz}\\ \tau_{zx}\\ \tau_{xy}\end{Bmatrix};\quad \{\varepsilon'\}=\begin{Bmatrix}\varepsilon_x'\\ \varepsilon_y'\\ \varepsilon_z'\\ \gamma_{yz}'\\ \gamma_{zx}'\\ \gamma_{xy}'\end{Bmatrix}\ \text{and}\ \{\varepsilon\}=\begin{Bmatrix}\varepsilon_x\\ \varepsilon_y\\ \varepsilon_z\\ \gamma_{yz}\\ \gamma_{zx}\\ \gamma_{xy}\end{Bmatrix} \tag{7}$$

$$[Q]=\begin{bmatrix}\alpha_1^2 & \alpha_2^2 & \alpha_3^2 & 2\alpha_3\alpha_2 & 2\alpha_1\alpha_3 & 2\alpha_2\alpha_1\\ \beta_1^2 & \beta_2^2 & \beta_3^2 & 2\beta_3\beta_2 & 2\beta_1\beta_3 & 2\beta_1\beta_1\\ \gamma_1^2 & \gamma_2^2 & \gamma_3^2 & 2\gamma_3\gamma_2 & 2\gamma_1\gamma_3 & 2\gamma_2\gamma_1\\ \beta_1\gamma_1 & \beta_2\gamma_2 & \beta_3\gamma_3 & \beta_2\gamma_3+\beta_3\gamma_2 & \beta_1\gamma_3+\beta_3\gamma_1 & \beta_1\gamma_2+\beta_2\gamma_1\\ \gamma_1\alpha_1 & \gamma_2\alpha_2 & \gamma_3\alpha_3 & \gamma_2\alpha_3+\gamma_3\alpha_2 & \gamma_1\alpha_3+\gamma_3\alpha_1 & \gamma_1\alpha_2+\gamma_2\alpha_1\\ \alpha_1\beta_1 & \alpha_2\beta_2 & \alpha_3\beta_3 & \alpha_2\beta_3+\alpha_3\beta_2 & \alpha_1\beta_3+\alpha_3\beta_1 & \alpha_1\beta_2+\alpha_2\beta_1\end{bmatrix} \tag{8}$$

and

$$[Q_\varepsilon]=\begin{bmatrix}\alpha_1^2 & \alpha_2^2 & \alpha_3^2 & \alpha_3\alpha_2 & \alpha_1\alpha_3 & \alpha_2\alpha_1\\ \beta_1^2 & \beta_2^2 & \beta_3^2 & \beta_3\beta_2 & \beta_1\beta_3 & \beta_2\beta_1\\ \gamma_1^2 & \gamma_2^2 & \gamma_3^2 & \gamma_3\gamma_2 & \gamma_1\gamma_3 & \gamma_2\gamma_1\\ 2\beta_1\gamma_1 & 2\beta_2\gamma_2 & 2\beta_3\gamma_3 & \beta_2\gamma_3+\beta_3\gamma_2 & \beta_1\gamma_3+\beta_3\gamma_1 & \beta_1\gamma_2+\beta_2\gamma_1\\ 2\gamma_1\alpha_1 & 2\gamma_2\alpha_2 & 2\gamma_3\alpha_3 & \gamma_2\alpha_3+\gamma_3\alpha_2 & \gamma_1\alpha_3+\gamma_3\alpha_1 & \gamma_1\alpha_2+\gamma_2\alpha_1\\ 2\alpha_1\beta_1 & 2\alpha_2\beta_2 & 2\alpha_3\beta_3 & \alpha_2\beta_3+\alpha_3\beta_2 & \alpha_1\beta_3+\alpha_3\beta_1 & \alpha_1\beta_2+\alpha_2\beta_1\end{bmatrix}. \tag{9}$$

Table 1 shows the direction cosines between the (x, y, z) and (x', y', z') coordinate axes. The transformation matrix $[\mathbf{Q}]$ is orthogonal and hence $[\mathbf{Q}]^{-1}=[\mathbf{Q}]^T=[\mathbf{Q}']$. The generalized Hooke's law for a homogeneous anisotropic body in Cartesian coordinates (x, y, z) is given by Eq. (10) ([13])

$$\{\boldsymbol{\varepsilon}\}=\lfloor a_{ij}\rfloor\{\boldsymbol{\sigma}\} \tag{10}$$

$[\mathbf{a}_{ij}]$ is the matrix of 36 elastic coefficients, of which only 21 are independent, since $[\mathbf{a}_{ij}]=[\mathbf{a}_{ji}]$. The elastic properties of FCC crystals exhibit cubic symmetry, also described as cubic syngony. Materials with cubic symmetry have only three independent elastic constants designated as the elastic modulus, shear modulus, and Poisson ratio ([4]) and hence $[\mathbf{a}_{ij}]$ has only three independent elastic constants, as given below.

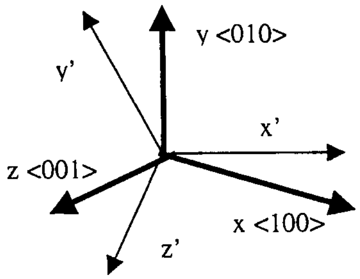

Fig. 4 Material (x,y,z) and specimen (x',y',z') coordinate systems

Table 1 Direction cosines

	x	y	z
x\`	α_1	β_1	γ_1
y\`	α_2	β_2	γ_2
z\`	α_3	β_3	γ_3

$$[\mathbf{a}_{ij}]=\begin{bmatrix}a_{11} & a_{12} & a_{12} & 0 & 0 & 0\\ a_{12} & a_{11} & a_{12} & 0 & 0 & 0\\ a_{12} & a_{12} & a_{11} & 0 & 0 & 0\\ 0 & 0 & 0 & a_{44} & 0 & 0\\ 0 & 0 & 0 & 0 & a_{44} & 0\\ 0 & 0 & 0 & 0 & 0 & a_{44}\end{bmatrix} \tag{11}$$

The elastic constants are

$$a_{11}=\frac{1}{E_{xx}},\quad a_{44}=\frac{1}{G_{yz}},\quad a_{12}=-\frac{\nu_{yx}}{E_{xx}}=-\frac{\nu_{xy}}{E_{yy}}. \tag{12}$$

The elastic constants in the generalized Hooke's law of an anisotropic body, $[\mathbf{a}_{ij}]$, vary with the direction of the coordinate axes. In the case of an isotropic body the constants are invariant in any orthogonal coordinate system. The elastic constant matrix $[\mathbf{a}_{ij}']$ in the (x', y', z') coordinate system that relates $\{\boldsymbol{\varepsilon}'\}$ and $\{\boldsymbol{\sigma}'\}$ is given by the following transformation ([13]).

$$\begin{aligned}[\mathbf{a}_{ij}']&=[\mathbf{Q}]^T[\mathbf{a}_{ij}][\mathbf{Q}]\\ &=\sum_{m=1}^{6}\sum_{n=1}^{6}a_{mn}Q_{mi}Q_{nj}\quad (i,j=1,2,\ldots\ldots,6).\end{aligned} \tag{13}$$

Shear stresses in the 30 slip systems shown in Figs. 1 and 2 are denoted by $\tau^1, \tau^2, \ldots, \tau^{30}$. The shear stresses on the 24 octahedral slip systems are ([4])

$$\begin{Bmatrix} \tau^1 \\ \tau^2 \\ \tau^3 \\ \tau^4 \\ \tau^5 \\ \tau^6 \\ \tau^7 \\ \tau^8 \\ \tau^9 \\ \tau^{10} \\ \tau^{11} \\ \tau^{12} \end{Bmatrix} = \frac{1}{\sqrt{6}} \begin{bmatrix} 1 & 0 & -1 & 1 & 0 & -1 \\ 0 & -1 & 1 & -1 & 1 & 0 \\ 1 & -1 & 0 & 0 & 1 & -1 \\ -1 & 0 & 1 & 1 & 0 & -1 \\ -1 & 1 & 0 & 0 & -1 & -1 \\ 0 & 1 & -1 & -1 & -1 & 0 \\ 1 & -1 & 0 & 0 & -1 & -1 \\ 0 & 1 & -1 & -1 & 1 & 0 \\ 1 & 0 & -1 & -1 & 0 & -1 \\ 0 & -1 & 1 & -1 & -1 & 0 \\ -1 & 0 & 1 & -1 & 0 & -1 \\ -1 & 1 & 0 & 0 & 1 & -1 \end{bmatrix} \begin{Bmatrix} \sigma_{xx} \\ \sigma_{yy} \\ \sigma_{zz} \\ \sigma_{xy} \\ \sigma_{zx} \\ \sigma_{yz} \end{Bmatrix} \tag{14}$$

$$\begin{Bmatrix} \tau^{13} \\ \tau^{14} \\ \tau^{15} \\ \tau^{16} \\ \tau^{17} \\ \tau^{18} \\ \tau^{19} \\ \tau^{20} \\ \tau^{21} \\ \tau^{22} \\ \tau^{23} \\ \tau^{24} \end{Bmatrix} = \frac{1}{3\sqrt{2}} \begin{bmatrix} -1 & 2 & -1 & 1 & -2 & 1 \\ 2 & -1 & -1 & 1 & 1 & -2 \\ -1 & -1 & 2 & -2 & 1 & 1 \\ -1 & 2 & -1 & -1 & -2 & -1 \\ -1 & -1 & 2 & 2 & 1 & -1 \\ 2 & -1 & -1 & -1 & 1 & 2 \\ -1 & -1 & 2 & 2 & -1 & 1 \\ 2 & -1 & -1 & -1 & -1 & -2 \\ -1 & 2 & -1 & -1 & 2 & 1 \\ 2 & -1 & -1 & 1 & -1 & 2 \\ -1 & 2 & -1 & 1 & 2 & -1 \\ -1 & -1 & 2 & -2 & -1 & -1 \end{bmatrix} \begin{Bmatrix} \sigma_{xx} \\ \sigma_{yy} \\ \sigma_{zz} \\ \sigma_{xy} \\ \sigma_{zx} \\ \sigma_{yz} \end{Bmatrix} \tag{15}$$

Table 2 Direction cosines

	x	y	z
x`	$\alpha_1=0.5445$	$\beta_1=0.2673$	$\gamma_1=0.8018$
y`	$\alpha_2=-0.8320$	$\beta_2=0.0$	$\gamma_2=0.5547$
z`	$\alpha_3=0.1482$	$\beta_3=-0.9636$	$\gamma_3=0.2223$

and the shear stresses on the six cube slip systems are

$$\begin{Bmatrix} \tau^{25} \\ \tau^{26} \\ \tau^{27} \\ \tau^{28} \\ \tau^{29} \\ \tau^{30} \end{Bmatrix} = \frac{1}{\sqrt{2}} \begin{bmatrix} 0 & 0 & 0 & 1 & 1 & 0 \\ 0 & 0 & 0 & 1 & -1 & 0 \\ 0 & 0 & 0 & 1 & 0 & 1 \\ 0 & 0 & 0 & 1 & 0 & -1 \\ 0 & 0 & 0 & 0 & 1 & 1 \\ 0 & 0 & 0 & 0 & -1 & 1 \end{bmatrix} \begin{Bmatrix} \sigma_{xx} \\ \sigma_{yy} \\ \sigma_{zz} \\ \sigma_{xy} \\ \sigma_{zx} \\ \sigma_{yz} \end{Bmatrix}. \tag{16}$$

Shear strains (engineering) on the 30 slip systems are calculated using similar kinematic relations.

As an example problem we consider a uniaxial test specimen loaded in the [213] direction (chosen as the x'-axis in Fig. 4) under strain control. The applied strain for the specimen is 1.212 percent. We wish to calculate the stresses and strains in the material coordinate system and the shear stresses on the 30 slip systems. The x'-axis is aligned along the [213] direction. The required direction cosines are shown in Table 2. The stress-strain relationship in the specimen coordinate system is given by

$$\{\boldsymbol{\varepsilon}'\} = \lfloor \mathbf{a}'_{ij} \rfloor \{\boldsymbol{\sigma}'\}. \tag{17}$$

The $[\mathbf{a}'_{ij}]$ matrix is calculated using Eq. (13) as

$$\lfloor \mathbf{a}'_{ij} \rfloor = \begin{bmatrix} 3.537E-8 & -2.644E-9 & -1.986E-8 & 5.209E-9 & 1.405E-8 & 1.878E-8 \\ -2.644E-9 & 3.975E-8 & -2.423E-8 & -5.61E-9 & 1.297E-8 & -2.023E-8 \\ -1.986E-8 & -2.423E-8 & 5.696E-8 & 4.007E-10 & -2.703E-8 & 1.445E-9 \\ 5.209E-9 & -5.61E-9 & 4.007E-10 & 7.089E-8 & 2.889E-9 & 2.595E-8 \\ 1.405E-8 & 1.297E-8 & -2.703E-8 & 2.889E-9 & 8.838E-8 & 1.042E-8 \\ 1.878E-8 & -2.023E-8 & 1.445E-9 & 2.595E-8 & 1.042E-8 & 1.572E-7 \end{bmatrix} \tag{18}$$

Since σ'_x is the only nonzero stress in the specimen coordinate system, we have

$$\sigma'_x = \frac{\varepsilon'_x}{a'_{11}} = \frac{0.01212}{3.537E-8} = 342{,}663\,\text{psi}. \tag{19}$$

Knowing $\{\boldsymbol{\sigma}'\}$ we can now calculate $\{\boldsymbol{\varepsilon}'\}$ as

$$\{\boldsymbol{\varepsilon}'\} = \begin{Bmatrix} \varepsilon'_x \\ \varepsilon'_y \\ \varepsilon'_z \\ \gamma'_{yz} \\ \gamma'_{zx} \\ \gamma'_{xy} \end{Bmatrix} = [\mathbf{a}'_{ij}] \begin{Bmatrix} 342{,}663 \\ 0 \\ 0 \\ 0 \\ 0 \\ 0 \end{Bmatrix} = \begin{Bmatrix} 0.01212 \\ -9.059E-4 \\ -6.805E-3 \\ 1.785E-3 \\ 4.815E-3 \\ 6.435E-3 \end{Bmatrix}. \tag{20}$$

The stresses and strains in the material coordinate system can be calculated using Eqs. (6) as

$$\begin{Bmatrix} \varepsilon_x \\ \varepsilon_y \\ \varepsilon_z \\ \gamma_{yz} \\ \gamma_{zx} \\ \gamma_{xy} \end{Bmatrix} = \begin{Bmatrix} -1.43E-5 \\ -6.693E-3 \\ 0.011 \\ 4.676E-3 \\ 9.353E-3 \\ 3.118E-3 \end{Bmatrix}, \quad \begin{Bmatrix} \sigma_x \\ \sigma_y \\ \sigma_z \\ \tau_{yz} \\ \tau_{zx} \\ \tau_{xy} \end{Bmatrix} = \begin{Bmatrix} 9.789E+4 \\ 2.447E+4 \\ 2.203E+5 \\ 7.342E+4 \\ 1.468E+5 \\ 4.895E+4 \end{Bmatrix}. \tag{21}$$

The shear stresses on the 30 slip planes are calculated using Eqs. (15)–(16) as

Table 3 Strain-controlled LCF test data for PWA1493 at 1200°F for four specimen orientations

Specimen Orientation	Max Test Strain	Min Test Strain	R Ratio	Strain Range	Cycles to Failure
<001>	.01509	.00014	0.01	.01495	1326
<001>	.0174	.0027	0.16	0.0147	1593
<001>	.0112	.0002	0.02	0.011	4414
<001>	.01202	.00008	0.01	0.0119	5673
<001>	.00891	.00018	0.02	.00873	29516
<111>	.01219	-0.006	-0.49	.01819	26
<111>	.0096	.0015	0.16	0.0081	843
<111>	.00809	.00008	0.01	.00801	1016
<111>	.006	0.0	0.0	0.006	3410
<111>	.00291	-0.00284	-0.98	.00575	7101
<111>	.00591	.00015	0.03	.00576	7356
<111>	.01205	0.00625	0.52	0.0058	7904
<213>	.01212	0.0	0.0	.01212	79
<213>	.00795	.00013	0.02	.00782	4175
<213>	.00601	.00005	0.01	.00596	34676
<213>	.006	0.0	0.0	0.006	114789
<011>	.0092	.0004	0.04	0.0088	2672
<011>	.00896	.00013	0.01	.00883	7532
<011>	.00695	.00019	0.03	.00676	30220

$$\left\{\begin{array}{c}\tau^{1}\\\tau^{2}\\\tau^{3}\\\tau^{4}\\\tau^{5}\\\tau^{6}\\\tau^{7}\\\tau^{8}\\\tau^{9}\\\tau^{10}\\\tau^{11}\\\tau^{12}\end{array}\right\}=\left\{\begin{array}{c}-5.995E+4\\1.199E+5\\5.995E+5\\3.996E+4\\-1.199E+5\\-1.599E+5\\-5.995E+4\\-3.996E+4\\-9.991E+4\\0\\0\\0\end{array}\right\},\quad\left\{\begin{array}{c}\tau^{13}\\\tau^{14}\\\tau^{15}\\\tau^{16}\\\tau^{17}\\\tau^{18}\\\tau^{19}\\\tau^{20}\\\tau^{21}\\\tau^{22}\\\tau^{23}\\\tau^{24}\end{array}\right\}=\left\{\begin{array}{c}-1.038E+5\\0\\1.038E+5\\-1.615E+5\\1.154E+5\\4.615E+4\\8.076E+4\\-9.229E+4\\1.154E+4\\0\\0\end{array}\right\}\tag{22a}$$

$$\left\{\begin{array}{c}\tau^{25}\\\tau^{26}\\\tau^{27}\\\tau^{28}\\\tau^{29}\\\tau^{30}\end{array}\right\}=\left\{\begin{array}{c}1.384E+5\\-6.922E+4\\8.652E+4\\-1.73E+4\\1.557E+5\\-5.191E+4\end{array}\right\}.\tag{22b}$$

The engineering shear strains on the 30 slip planes are

$$\left\{\begin{array}{c}\gamma^{1}\\\gamma^{2}\\\gamma^{3}\\\gamma^{4}\\\gamma^{5}\\\gamma^{6}\\\gamma^{7}\\\gamma^{8}\\\gamma^{9}\\\gamma^{10}\\\gamma^{11}\\\gamma^{12}\end{array}\right\}=\left\{\begin{array}{c}-9.725E-3\\0.017\\7.362E-3\\8.452E-3\\-0.011\\-0.02\\-2.745E-4\\-0.012\\-0.012\\9.451E-3\\5.907E-3\\-3.544E-3\end{array}\right\},\quad\left\{\begin{array}{c}\gamma^{13}\\\gamma^{14}\\\gamma^{15}\\\gamma^{16}\\\gamma^{17}\\\gamma^{18}\\\gamma^{19}\\\gamma^{20}\\\gamma^{21}\\\gamma^{22}\\\gamma^{23}\\\gamma^{24}\end{array}\right\}=\left\{\begin{array}{c}-0.014\\-1.364E-3\\0.015\\-0.018\\0.016\\1.575E-3\\0.014\\-7.243E-3\\-6.768E-3\\-1.364E-3\\-7.502E-3\\8.867E-3\end{array}\right\}\tag{23a}$$

$$\left\{\begin{array}{c}\gamma^{25}\\\gamma^{26}\\\gamma^{27}\\\gamma^{28}\\\gamma^{29}\\\gamma^{30}\end{array}\right\}=\left\{\begin{array}{c}8.818E-3\\-4.409E-3\\5.511E-3\\-1.102E-3\\9.92E-3\\-3.307E-3\end{array}\right\}.\tag{23b}$$

The normal stresses and strains on the principal and secondary octahedral planes are

$$\left\{\begin{array}{c}\sigma_1^n\\\sigma_2^n\\\sigma_3^n\\\sigma_4^n\end{array}\right\}=\left\{\begin{array}{c}293{,}700\\130{,}500\\32{,}630\\0\end{array}\right\},\quad\left\{\begin{array}{c}\varepsilon_1^n\\\varepsilon_2^n\\\varepsilon_3^n\\\varepsilon_4^n\end{array}\right\}=\left\{\begin{array}{c}0.007185\\0.001989\\-0.001128\\-0.002167\end{array}\right\}.\tag{24}$$

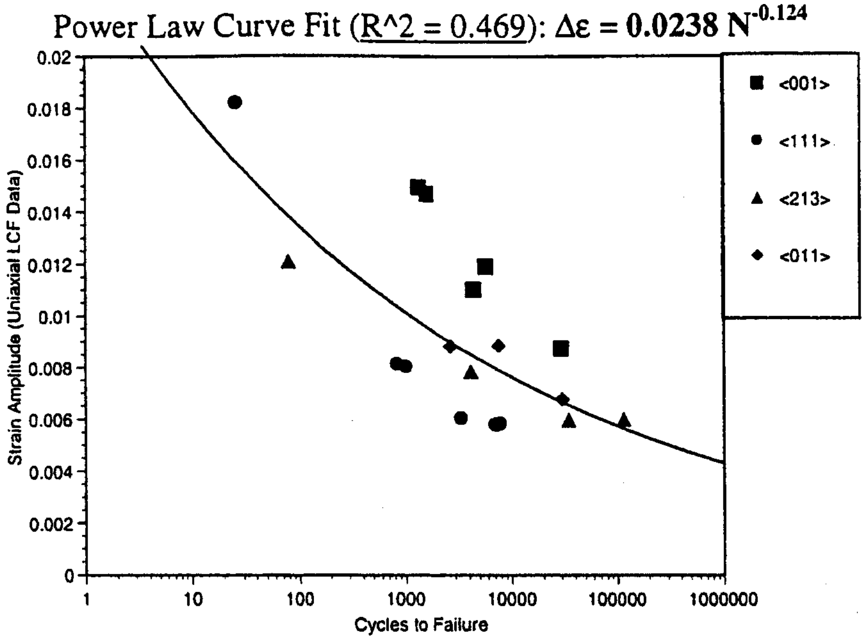

Fig. 5 Strain range versus cycles to failure for LCF test data (PWA 1493 at 1200°F)

Table 4 Maximum values of shear stress and shear strain on the slip systems and normal stress and strain values on the same planes

γ_{max} = Max shear strain of 30 slip systems for max specimen test strain value
γ_{min} = Max shear strain of 30 slip systems for min specimen test strain value
τ_{max} = Max shear stress of 30 slip systems for max specimen test strain value
τ_{min} = Max shear stress of 30 slip systems for min specimen test strain value

Specimen Orientation	γ_{max}	γ_{min}	$\Delta\gamma/2$	ε_{max}	ε_{min}	$\Delta\varepsilon/2$	τ_{max} psi	τ_{min} psi	$\Delta\tau$ psi	σ_{max} psi	σ_{min} psi	$\Delta\sigma$ psi	Cycles to Failure
<001>	0.02	0.000185	0.0099075	0.00097	9.25E-06	0.0004804	1.10E+05	1016	1.08E+05	7.75E+04	719	7.68E+04	1326
	0.023	0.0036	0.0097	0.0015	1.78E-04	0.000661	1.26E+05	1.96E+04	1.06E+05	8.93E+04	1.39E+04	7.54E+04	1593
$\tau_{max}=\tau^{14}$	0.015	2.64E-04	0.007368	7.34E-04	1.32E-05	0.0003604	8.13E+04	1452	7.98E+04	5.75E+04	1027	5.65E+04	4414
$\gamma_{max}=\gamma^{14}$	0.016	0	0.008	7.94E-04	0	0.000397	8.73E+04	0	8.73E+04	6.17E+04	0	6.17E+04	5673
	0.012	0	0.006	5.89E-04	0	0.0002945	6.47E+04	0	6.47E+04	4.57E+04	0	4.57E+04	29516
<111>	0.014	-7.06E-03	0.01053	2.05E-03	-1.01E-03	0.00153	2.25E+05	-1.10E+05	3.35E+05	1.59E+05	-7.80E+04	2.37E+05	26
	0.011	0.00176	0.00462	0.0016	0.00025	0.000675	1.77E+05	2.77E+04	1.49E+05	1.25E+05	1.96E+04	1.05E+05	843
$\tau_{max}=\tau^{25}$	.0095	9.40E-05	0.004703	0.00136	1.34E-05	0.0006733	1.49E+05	1478	1.48E+05	1.06E+05	1045	1.05E+05	1016
$\gamma_{max}=\gamma^{25}$	.0076	0	0.0038	0.001	0	0.0005	1.10E+05	0	1.10E+05	7.84E+04	0	7.84E+04	3410
	.0034	-0.0033	0.00335	0.00049	-0.00048	0.000485	5.40E+04	-5.30E+04	1.07E+05	3.80E+04	-3.70E+04	7.50E+04	7101
	.0069	1.76E-04	0.003362	9.90E-04	2.50E-05	0.0004825	1.09E+05	2771	1.06E+05	7.70E+04	1959	7.50E+04	7356
	0.014	0.007	0.0035	0.002	0.001	0.0005	2.25E+05	1.10E+05	1.15E+05	1.60E+05	7.80E+04	8.20E+04	7904
<213>	0.018	0	0.009	0.002	0	0.001	1.60E+05	0	1.60E+05	1.30E+05	0	1.30E+05	79
	0.012	1.90E-04	0.005905	0.0013	2.10E-05	0.0006395	1.06E+05	1732	1.04E+05	8.60E+04	1400	8.46E+04	4175
$\tau_{max}=\tau^{29}$	.0088	0	0.0044	0.00098	0	0.00049	8.00E+04	0	8.00E+04	6.50E+04	0	6.50E+04	34676
$\gamma_{max}=\gamma^{29}$	.0088	0	0.0044	0.00098	0	0.00049	8.00E+04	0	8.00E+04	6.50E+04	0	6.50E+04	114789
<011>	0.015	6.50E-04	0.007175	0.0039	1.68E-04	0.001866	1.23E+05	5333	1.18E+05	1.73E+05	7538	1.65E+05	2672
$\tau_{max}=\tau^{15}$	0.015	0	0.0075	0.0039	0	0.00195	1.23E+05	0	1.23E+05	1.70E+05	0	1.70E+05	7532
$\gamma_{max}=\gamma^{15}$	0.011	3.10E-04	0.005345	0.0029	8.00E-05	0.00141	9.30E+04	2532	9.05E+04	1.31E+05	3581	1.27E+05	30220

The normal stresses and strains on the cube slip planes are simply the normal stresses and strains in the material coordinate system along (100), (010), and (001) axes. This procedure is used to compute normal and shear stresses and strains in the material coordinate system, for uniaxial test specimens loaded in strain control, in different orientations.

Strain controlled LCF tests conducted at 1200°F in air for PWA1480/1493 uniaxial smooth specimens, for four different orientations, is shown in Table 3. The four specimen orientations are ⟨001⟩ (five data points), ⟨111⟩ (seven data points), ⟨213⟩ (four data points), and ⟨011⟩ (three data points), for a total of 19 data points. Figure 5 shows the plot of strain range versus cycles to failure. A wide scatter is observed in the data with poor correlation for a power-law fit. The first step towards applying the failure criteria discussed earlier is to compute the shear and normal stresses and strains on all the 30 slip systems, for each data point, for maximum and minimum test strain values, as outlined in the example problem. The maximum shear stress and strain for each data point, for min and max test strain values, is selected from the 30 values corresponding to the 30 slip systems. The maximum normal stress and strain value on the planes where the shear stress is maximum is also noted. These values are tabulated in Table 4. Both the maximum shear stress and maximum shear strain occur on the same slip system, for the four different configurations examined. For the ⟨001⟩ and ⟨011⟩ configurations the max shear stress and strain occur on the secondary slip system (τ^{14}, γ^{14} and τ^{15}, γ^{15} respectively). The slip direction for τ^{14} is $[2\ -1\ -1]$ and for ε^{15} is $[-1\ -1\ 2]$. For the ⟨111⟩ and ⟨213⟩ configurations max shear stress and strain occur on the cube slip system (τ^{25}, γ^{25} and τ^{29}, γ^{29}, respectively). The slip direction for τ^{25} is $[\ 0\ 1\ 1]$ and for τ^{29} is $[1\ 1\ 0]$. Using Table 4 the composite failure parameters highlighted in Eqs. (1)–(4) can be calculated and plotted as a function of cycles to failure. In addition to the four failure parameters discussed, some other composite parameters are also plotted as a function of cycles to failure (N).

Figures 6–9 show that the four parameters based on polycrystalline fatigue failure parameters do not correlate well with the test data. The application of these parameters for single crystal material is somewhat different since they are evaluated on the slip systems that are thought to be the critical planes. The parameters that collapse the failure data well and give the best correlation with a power-law fit are the maximum shear stress amplitude $[\Delta\tau_{max}]$ shown in Fig. 10, the composite parameter $[(\Delta\tau_{max})\times(\Delta\gamma_{max}/2)]$ shown in Figs. 11 and 12, and the max principal shear stress amplitude (Tresca theory) shown in Fig. 13. The parameter $\Delta\tau_{max}$ is appealing to use for its simplicity, and its power-law curve fit is shown in Eq. (25). It must be remembered that these curve fits are only valid for 1200°F.

$$\Delta\tau_{max}=397{,}758\ \mathrm{N}^{-0.1598} \tag{25}$$

One data point for $\Delta\tau_{max}$ in Fig. 10 is calculated at 335 ksi, well above the yield point for the material, and is not very realistic. The problem stems from the fact that testing was conducted under strain control and specimen load values were not recorded. The specimen stresses were calculated from measured strain values based on linear elastic assumptions, as outlined in Section 4. The peak $\Delta\tau_{max}$ values would clearly be lower if effects of inelasticity are accounted for. The correlation for $[\Delta\tau_{max}]$ would also be better if the stress data above the yield point are corrected for inelastic effects. Since the deformation mechanisms in single crystals are controlled by the propagation of dislocations driven by shear the $[\Delta\tau_{max}]$ might indeed be a good fatigue failure parameter to use. This parameter must be verified for a wider range of R-values and specimen orientations, and also at different temperatures and environmental conditions. Equation (25) will be used to calculate fatigue life at a critical blade tip location for the SSME turbine blade.

5 Application of Fatigue Failure Criteria to Finite Element Stress Analysis Results of Single Crystal Nickel Turbine Blades

Turbine blades used in the advanced high-pressure fuel turbopump (AHPFTP) are fabricated from single crystal nickel base PWA1480/1493 material. Many of these blades have failed during operation due to the initiation and propagation of fatigue cracks from an area of high concentrated stress at the blade-tip leading edge. Inspection of blades from other units in the test program revealed the presence of similar cracks in the turbine blades. During the course of the investigation an interesting development was

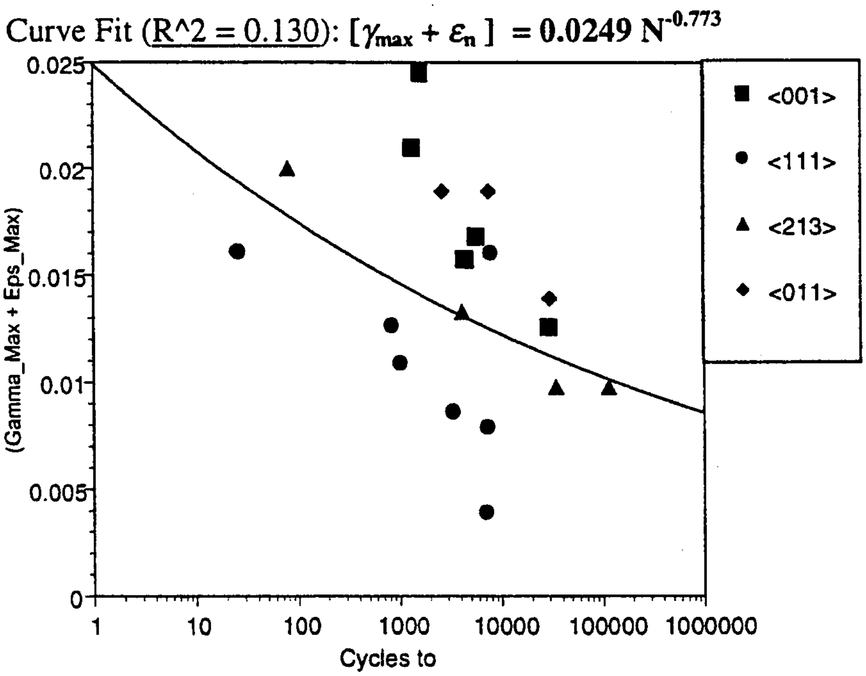

Fig. 6 [$\gamma_{\max}+\varepsilon_n$] (Eq. (1)) versus *N*

brought to light. When the size of the fatigue cracks for the population of blades inspected was compared with the secondary crystallographic orientation β a definite relationship was apparent as shown in Fig. 14 ([2,14]). Secondary orientation does appear to have some influence over whether a crack will initiate and arrest or continue to grow until failure of the blade airfoil occurs. Figure 14 reveals that for $\beta = 45 + / - 15$ deg tip cracks arrested after some growth or did-not initiate at all. This suggests that perhaps there are preferential β orientations for which crack growth is minimized at the blade tip.

In an attempt to understand the effect of crystal orientation on blade stress response a three-dimensional finite element model

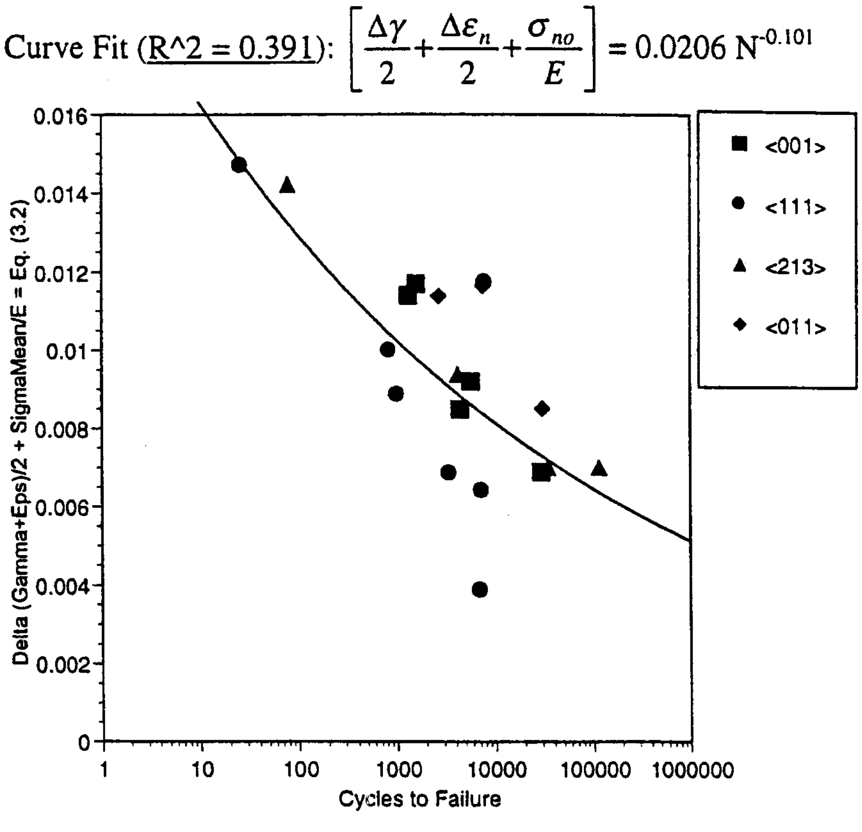

Fig. 7 [$\Delta\gamma/2+\Delta\varepsilon_n/2+\sigma_{no}/E$] (Eq. (2)) versus *N*

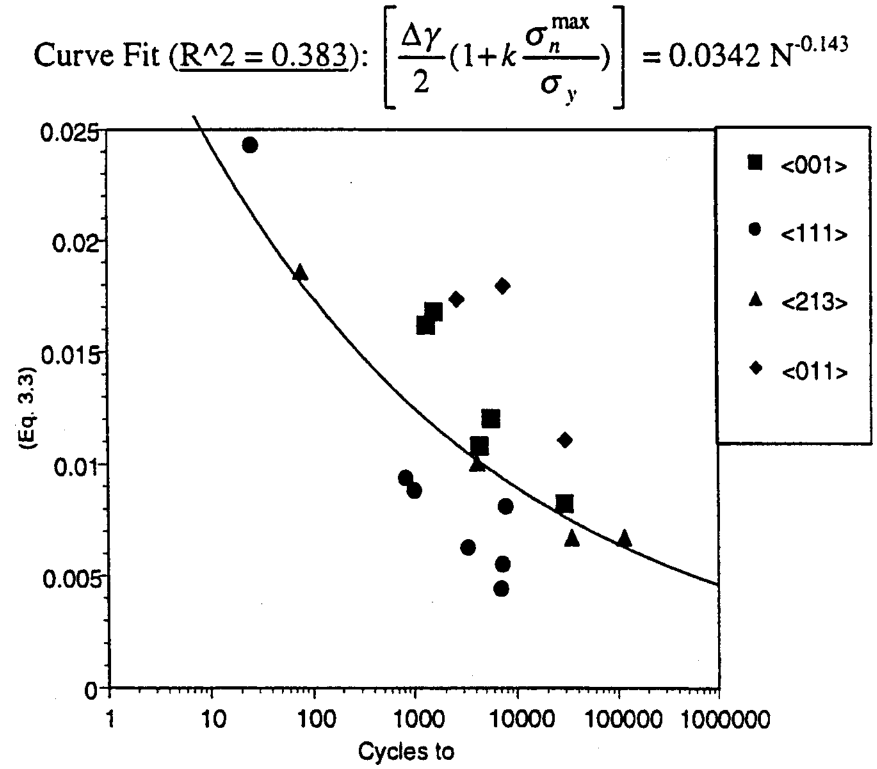

Fig. 8 $[\Delta\gamma/2(1+k(\sigma_n^{\max}/\sigma_y))]$ (Eq. (3)) versus N

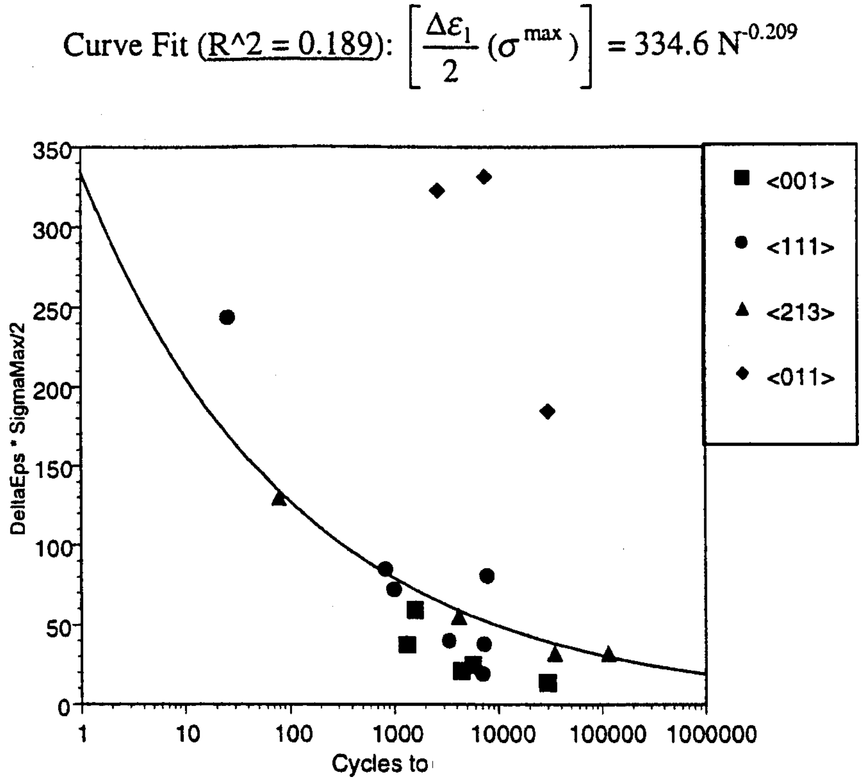

Fig. 9 $[\Delta\varepsilon_1/2(\sigma^{\max})]$ (Eq. (4)) versus N

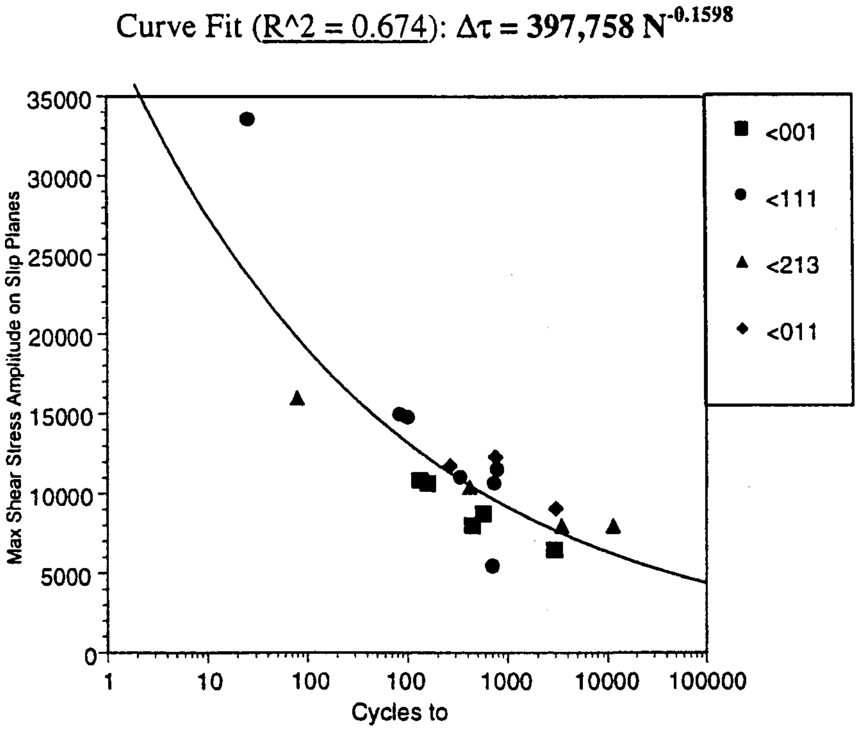

Fig. 10 Shear stress amplitude $[\Delta\tau_{\max}]$ versus N

capable of accounting for primary and secondary crystal orientation variation was constructed. The alternate high pressure fuel turbo pump (HPFTP/AT) first stage blade ANSYS finite element model was cut from a large three-dimensional cyclic symmetry model that includes the first and second stage blades and retainers, interstage spacer, disk and shaft, and the disk covers (Fig. 15). The blade dampers are represented with forces applied to the blade platforms at the damper contact locations. The models are geometrically nonlinear due to the contact surfaces between the separate components. The element type used for the blade mate-

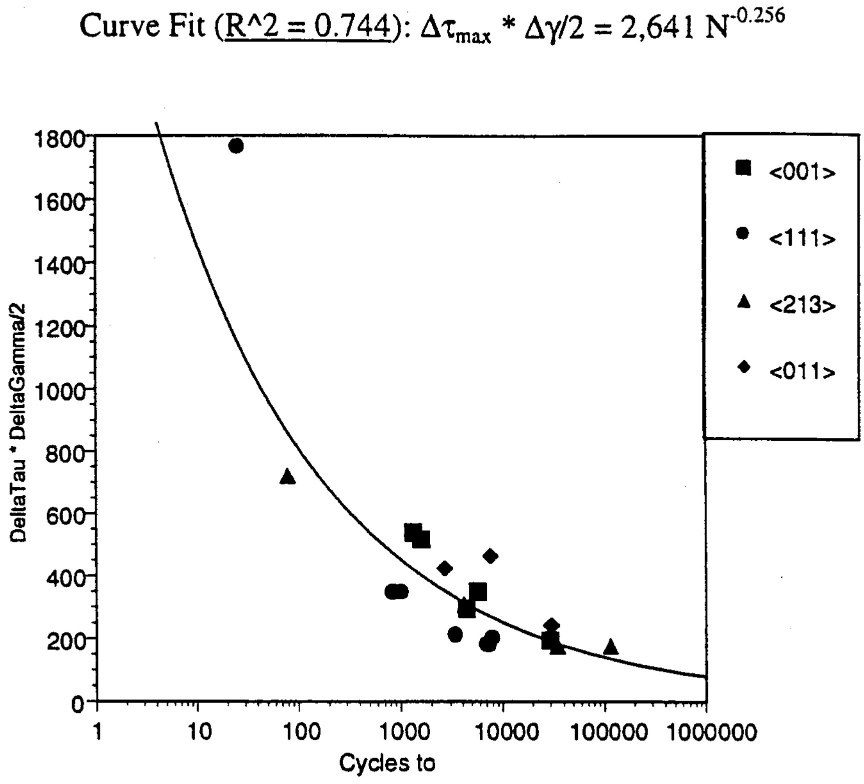

Fig. 11 $[\Delta\tau_{\max}(\Delta\gamma_{\max}/2)]$ versus N

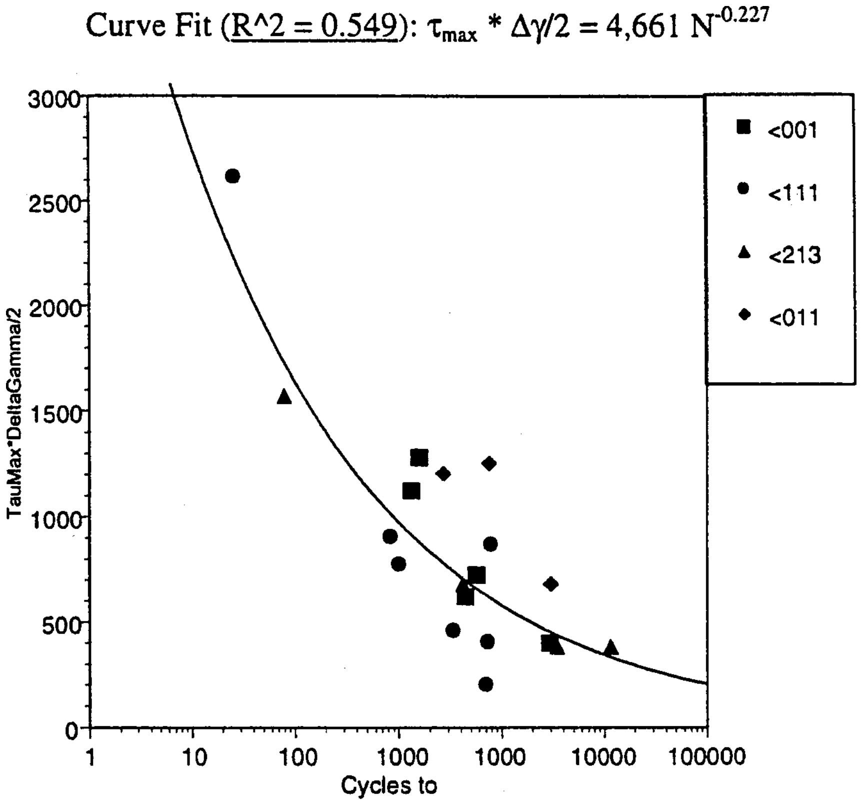

Fig. 12 $[\tau_{max}(\Delta\gamma_{max}/2)]$ versus N

rial is the ANSYS SOLID45, an eight-noded three-dimensional solid isoparametric element. Anisotropic material properties are allowed with this element type. ANSYS aligns the material coordinate system with the element coordinate system.

The effect of crystal orientation on blade stress response was studied by running 297 separate finite element models to cover the complete range of primary and secondary crystal orientation variation. To generate the 297 material coordinate systems used for this study local coordinate systems were generated and the element coordinate systems aligned with them [[15]]. The material coordinate system is referenced to the blade casting coordinate system, shown in Fig. 16. Two angles, Δ and Γ, locate the primary material axis relative to the casting axis, and are shown in Fig. 17 as rotations about the X and Y casting axis. The third angle, β, is the clocking of the secondary material axis about the primary material axis, as shown in Fig. 1. Figure 17 and Table 5 show the

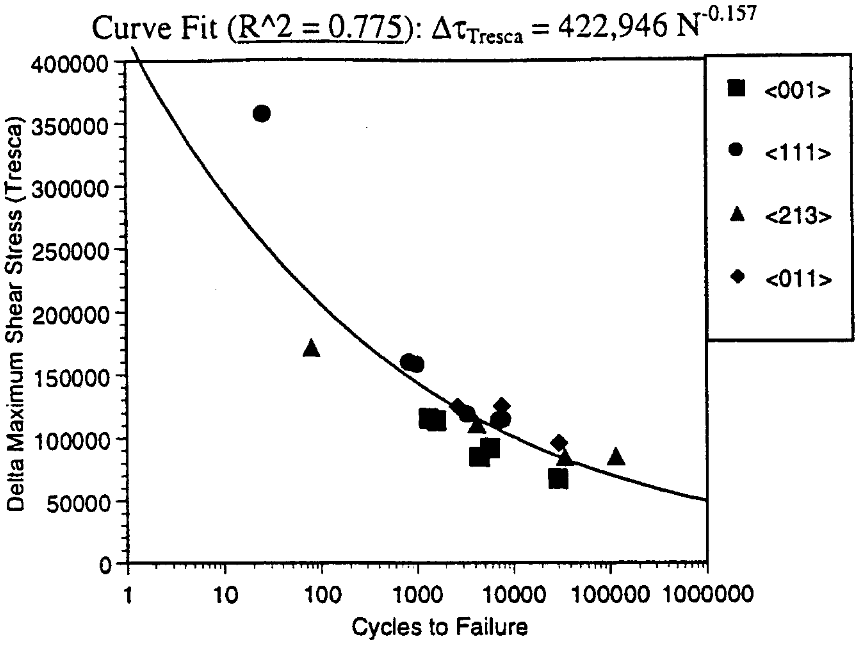

Fig. 13 $\Delta\tau_{Tresca}$ versus N

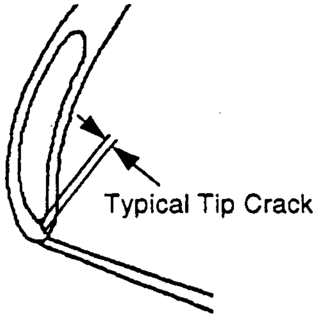

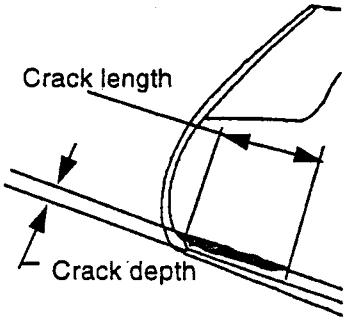

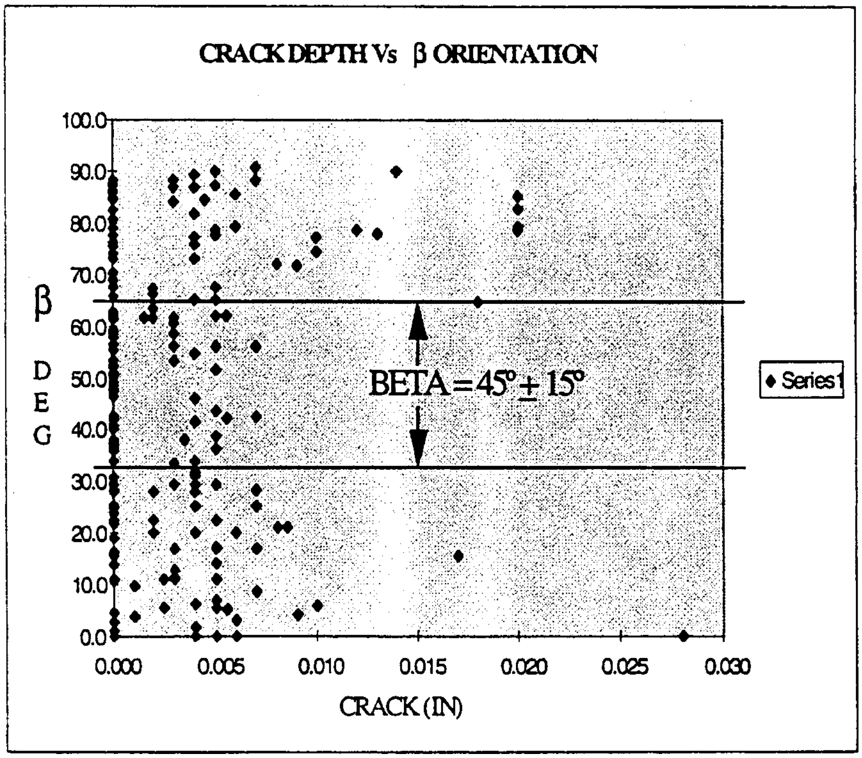

Fig. 14 Secondary crystallographic orientation, β, versus crack depth for the SSME AHPFTP first stage turbine blade ([2])

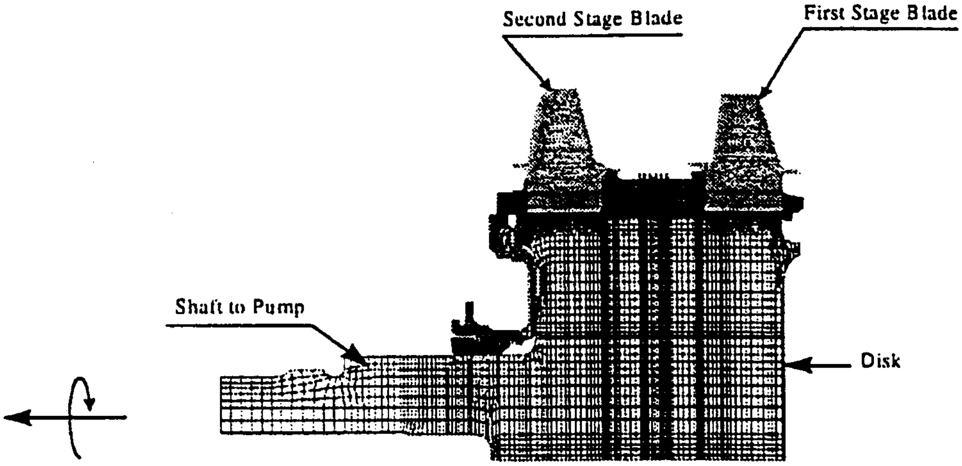

Fig. 15 Three-dimensional ANSYS model of HPFTP/AT rotating turbine components

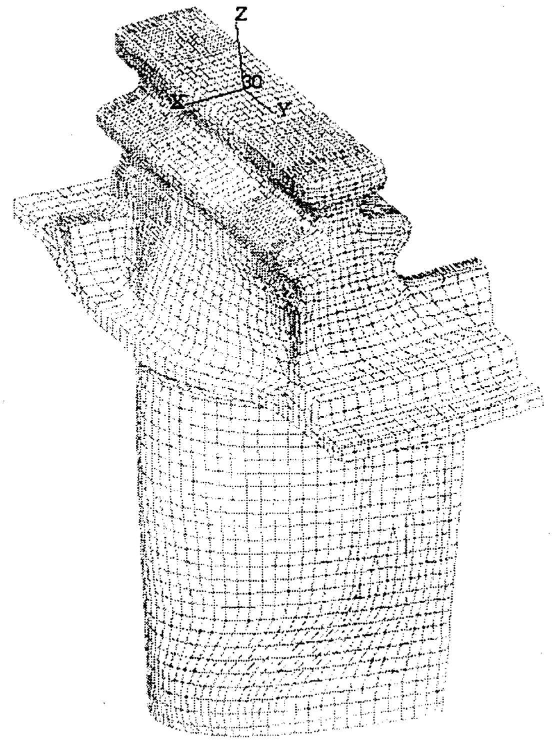

First Stage Blade Casting Coordinate System

Z axis along stacking axis pointing radially inward.

X axis pointing away from the pressure side.

Y axis pointing towards the second stage blade.

Fig. 16 First-stage bla1de finite element model and casting coordinate system

Table 5 33 primary axis cases with nine secondary cases each, for a total of 297 material orientations

Case	Delta	Gamma	Beta
0	0.00	0.00	0,10,20,30,40,50,60,70,80
1	7.50	0.00	0,10,20,30,40,50,60,70,80
2	6.93	2.87	0,10,20,30,40,50,60,70,80
3	5.30	5.30	0,10,20,30,40,50,60,70,80
4	2.87	6.93	0,10,20,30,40,50,60,70,80
5	0.00	7.50	0,10,20,30,40,50,60,70,80
6	-2.87	6.93	0,10,20,30,40,50,60,70,80
7	-5.30	5.30	0,10,20,30,40,50,60,70,80
8	-6.93	2.87	0,10,20,30,40,50,60,70,80
9	-7.50	0.00	0,10,20,30,40,50,60,70,80
10	-6.93	-2.87	0,10,20,30,40,50,60,70,80
11	-5.30	-5.30	0,10,20,30,40,50,60,70,80
12	-2.87	-6.93	0,10,20,30,40,50,60,70,80
13	0.00	-7.50	0,10,20,30,40,50,60,70,80
14	2.87	-6.93	0,10,20,30,40,50,60,70,80
15	5.30	-5.30	0,10,20,30,40,50,60,70,80
16	6.93	-2.87	0,10,20,30,40,50,60,70,80
17	15.00	0.00	0,10,20,30,40,50,60,70,80
18	13.86	5.74	0,10,20,30,40,50,60,70,80
19	10.61	10.61	0,10,20,30,40,50,60,70,80
20	5.74	13.86	0,10,20,30,40,50,60,70,80
21	0.00	15.00	0,10,20,30,40,50,60,70,80
22	-5.74	13.86	0,10,20,30,40,50,60,70,80
23	-10.61	10.61	0,10,20,30,40,50,60,70,80
24	-13.86	5.74	0,10,20,30,40,50,60,70,80
25	-15.00	0.00	0,10,20,30,40,50,60,70,80
26	-13.86	-5.74	0,10,20,30,40,50,60,70,80
27	-10.61	-10.61	0,10,20,30,40,50,60,70,80
28	-5.74	-13.86	0,10,20,30,40,50,60,70,80
29	0.00	-15.00	0,10,20,30,40,50,60,70,80
30	5.74	-13.86	0,10,20,30,40,50,60,70,80
31	10.61	-10.61	0,10,20,30,40,50,60,70,80
32	13.86	-5.74	0,10,20,30,40,50,60,70,80

distribution of the 297 different material coordinate systems within the allowed 15-deg maximum deviation from the casting axis. The secondary repeats after 90 deg, so only 0 to 80 deg needs to be modeled.

The load conditions represent full power mainstage operation of the Space Shuttle Main Engine, referred to as 109 percent RPL SL

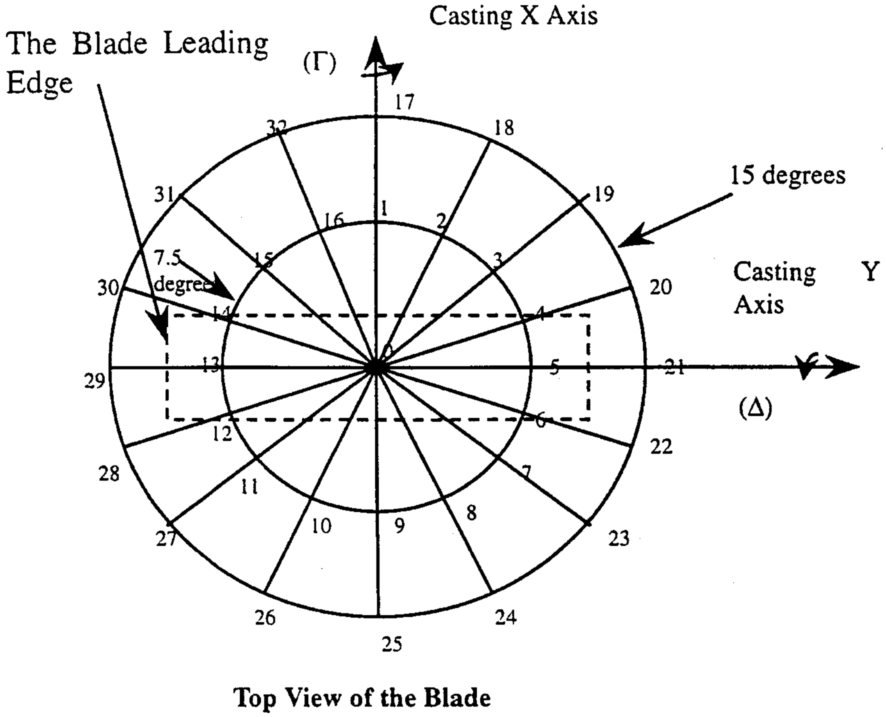

Fig. 17 33 primary axis cases (Γ and Δ variations shown in Table 5) with nine secondary axis cases (β or θ values) each, for a total of 297 material orientations

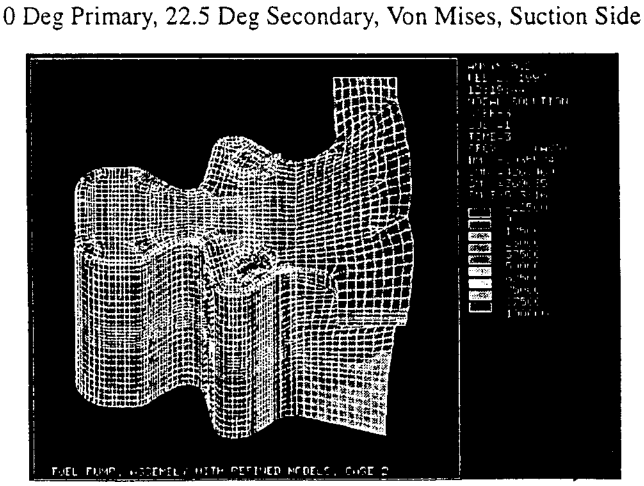
0 Deg Primary, 22.5 Deg Secondary, Von Mises, Suction Side

Fig. 18 Representative von Mises stress distribution results in the blade attachment region

(rated power level service life). The shaft speed is 37,355 rpm, the airfoil temperature is approximately 1200°F, forces representing the blade damper radial sling load are applied to the blade platform, and aerodynamic pressure loads are applied to the blade surfaces and internal core.

Postprocessing of the 297 finite element results files presented a fairly difficult challenge, and represents a considerable amount of

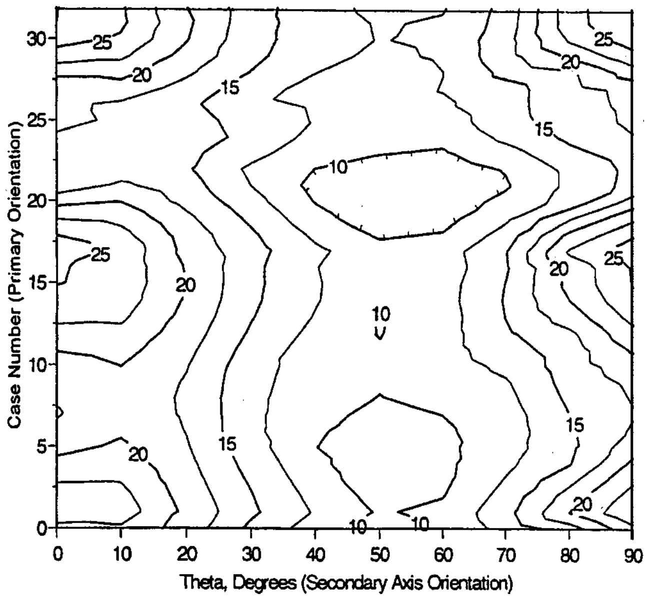

Fig. 19 Maximum shear stress amplitude ($\Delta\tau_{max}$, ksi) contour plot at the blade-tip critical point

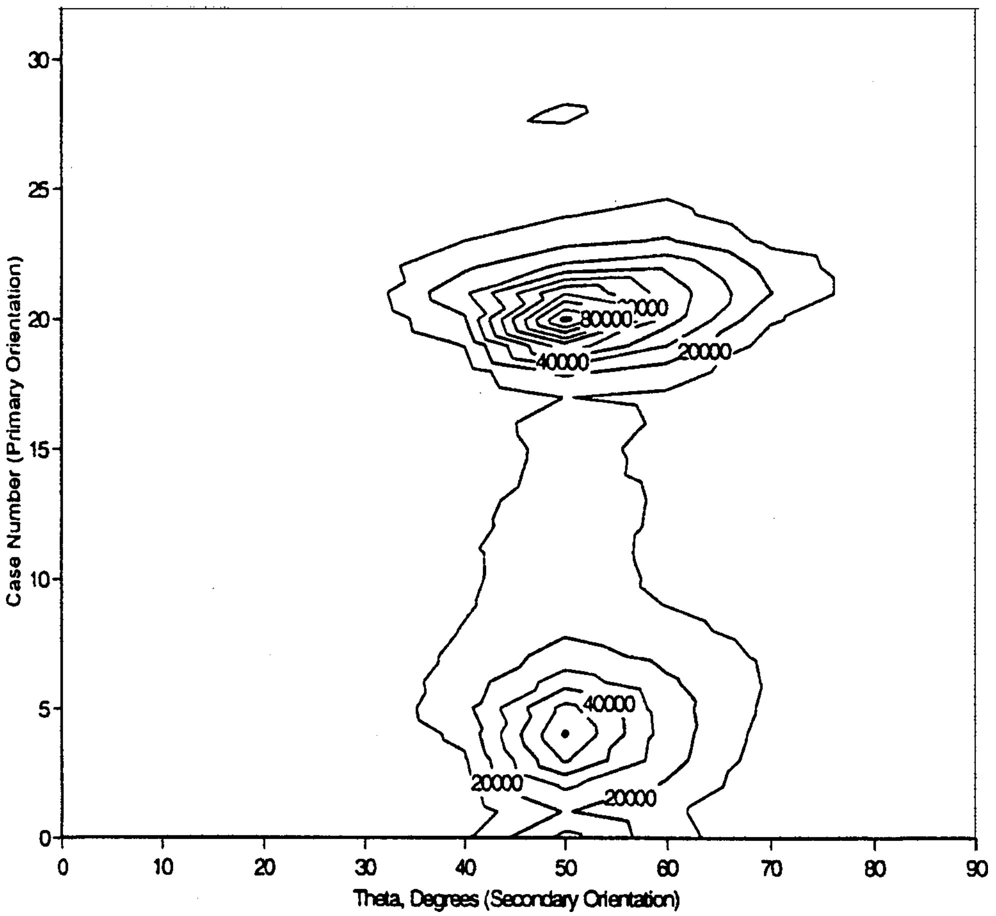

Fig. 20 Normalized HCF life (contour plot) at the blade-tip critical point, as a function of primary and secondary orientation

effort. Two FORTRAN programs were employed for the postprocessing work. The first selects the element results from the coded binary output files and places them into ASCII text files. The second program processes the ASCII files to calculate averaged nodal results, the resolved shear stresses and strains and the normal stresses and strains on the 30 slip systems, in the single crystal material coordinate system. It then calculates the parameters chosen for study and sorts them based on user set criteria.

The connection between the blade and disk are modeled with ANSYS COMBIN40 elements. These elements have one degree-of-freedom at each node. The nodal motion in that degree-of-freedom sets the separation or contact of these elements only. This element does not have the capability for friction tangent to the contact surface. For this model the nodal coordinate systems on the contacting surface of the blade firtree attachment were rotated so that one axis is normal to the surface. This is the degree of freedom used in the COMBIN40 element. The nodal coordinate systems on the disk contact surfaces were similarly oriented. An interesting feature of the ADAPCO model is that the blade is next to a cyclic symmetry section of the disk (a 1 of 50 piece) so that only the pressure side of the blade attachment contact surface nodes are nearly coincident to the disk. The suction side of the blade is clocked 7.2 deg about the shaft from the mating surface on the disk. The blade and disk nodal coordinate systems for the suction side attachment are 7.2 deg out of parallel to each other to account for this. Since the COMBIN40 element only acts on the one degree-of-freedom normal to the contact surfaces the 7.2 deg offset in physical location and orientation is properly accounted for. To run the blade model separate from the global model the nodal displacements of the disk nodes attached to the COMBIN40 elements were taken from a run of the global model and used as enforced displacements for what would become free ends of the contact elements.

Figure 18 shows representative Von Mises stress distribution plot for the turbine blade in the attachment region. The crack location and orientation at the critical blade tip location is shown in Fig. 14.

6 Effect of Secondary Crystal Orientation on Blade-Tip Stress Response

Variation of secondary crystal orientation on stress response at the blade tip critical point prone to cracking (tip point on inside radius) was examined by analyzing the results from the 297 finite element model runs. The finite element node at the critical point was isolated and critical failure parameter value ($\Delta\tau_{\max}$) computed on the 30 slip systems. A contour plot of $\Delta\tau_{\max}$ was generated as a function of primary and secondary orientation, shown in Fig. 19. The contour plot clearly shows a minimum value for $\Delta\tau_{\max}$ for secondary orientation of $\beta = 50$ deg and primary orientation designated by cases 5 and 20. From Table 5 we see that case 5 corresponds to a primary orientation of $\Delta = 0$ deg and $\Gamma = 7.5$ deg. Case 20 corresponds to a primary orientation of $\Delta = 5.74$ deg and $\Gamma = 13.86$ deg. Using the fatigue life equation based on the $\Delta\tau_{\max}$ curve fit of LCF test data, Eq. (25), we can obtain a contour plot of normalized HCF life at the critical point as a function of primary and secondary orientation, as shown in Fig. 20. The maximum life is again obtained for $\beta = 50$ deg, and $\Delta = 0$ deg and $\Gamma = 7.5$ deg, and $\Delta = 5.74$ deg and $\Gamma = 13.86$ deg. The optimum value of secondary orientation $\beta = 50$ deg, corresponds very closely to the optimum value of β indicated in Fig. 14. This demonstrates that control of secondary and primary crystallographic orientation has the potential to significantly increase a component's resistance to fatigue crack growth without adding additional weight or cost.

7 Conclusions

Fatigue failure in PWA1480/1493, a single crystal nickel base turbine blade superalloy, is investigated using a combination of experimental LCF fatigue data and three-dimensional finite element modeling of HPFTP/AT SSME turbine blades. Several failure criteria, based on the normal and shear stresses and strains on the 24 octahedral and six cube slip systems for a FCC crystal, are evaluated for strain controlled uniaxial LCF data (1200°F in air). The maximum shear stress amplitude $[\Delta\tau_{\max}]$ on the 30 slip systems was found to be an effective fatigue failure criterion, based on the curve fit between $\Delta\tau_{\max}$ and cycles to failure. Since deformation mechanisms in single crystals are controlled by the propagation of dislocations driven by shear, $\Delta\tau_{\max}$ might indeed be a good fatigue failure parameter to use. However, this parameter must be verified for a wider range of *R*-values and specimen orientations, and also at different temperatures and environmental conditions.

Investigation of leading edge tip cracks in operational SSME turbine blades had revealed that secondary crystal orientation appeared to influence whether a crack initiated and arrested or continued to grow until failure of the blade airfoil. The turbine blade was modeled using three-dimensional FEA that is capable of accounting for material orthotrophy and variation in primary and secondary crystal orientation. Effects of variation in crystal orientation on blade stress response were studied based on 297 finite element model runs. Fatigue life at the critical locations in blade was computed using finite element stress results and failure criterion developed. Detailed analysis of the results revealed that secondary crystal orientation had a pronounced effect on fatigue life. The optimum value of secondary orientation $\beta = 50$deg computed corresponds very closely to the optimum value of β indicated in the failed population of blades. Control of secondary and primary crystallographic orientation has the potential to significantly increase a component's resistance to fatigue crack growth without adding additional weight or cost. "Seeding" techniques developed by single crystal casters over the last ten years can readily achieve these degrees of primary and secondary crystallographic orientation control with economic resultant airfoil casting yields.

Acknowledgments

The authors would like to gratefully acknowledge the NASA/ASEE Summer Faculty Fellowship Program. The support from this program, administered by the University of Alabama in Huntsville, enabled the first author to complete this work between June 1–Aug 20, 1999 at the NASA Marshall Space Flight Center, Huntsville, AL.

References

[1] Cowles, B. A., 1996, "High Cycle Fatigue Failure in Aircraft Gas Turbines: An Industry Perspective," Int. J. Fract., **80**, pp. 147–163.

[2] Moroso, J., 1999, "Effect of Secondary Crystal Orientation on Fatigue Crack Growth in Single Crystal Nickel Turbine Blade Superalloys," M. S. thesis, Mechanical Engineering Department, University of Florida, Gainesville, FL, May.

[3] Deluca, D., and Annis, C., 1995, "Fatigue in Single Crystal Nickel Superalloys," Office of Naval Research, Department of the Navy FR23800, Aug.

[4] Stouffer, D. C., and Dame, L. T., 1996, *Inelastic Deformation of Metals*, John Wiley and Sons, New York.

[5] Milligan, W. W., and Antolovich, S. D., 1985, "Deformation Modeling and Constitutive Modeling for Anisotropic Superalloys," NASA Contractor Report 4215, Feb.

[6] Telesman, J., and Ghosn, L., 1989, "The Unusual Near Threshold FCG Behavior of a Single Crystal Superalloy and the Resolved Shear Stress as the Crack Driving Force," Eng. Fract. Mech., **34**, No. 5–6, pp. 1183–1196.

[7] Deluca, D. P., and Cowles, B. A., 1989, "Fatigue and Fracture of Single Crystal Nickel in High Pressure Hydrogen," *Hydrogen Effects on Material Behavior*, By N. R. Moody and A. W. Thomson, eds., TMS., Warrendale, PA.

[8] Kandil, F. A., Brown, M. W., and Miller, K. J., 1982, *Biaxial Low Cycle Fatigue of 316 Stainless Steel at Elevated Temperatures*, Metals Soc., London. pp. 203–210.

[9] Socie, D. F., Kurath, P., and Koch, J., 1985, "A Multiaxial Fatigue Damage Parameter," presented at the Second International Symposium on Multiaxial Fatigue, Sheffield, U.K.

[10] Fatemi, A., and Socie, D., 1998, "A Critical Plane Approach to Multiaxial Fatigue Damage Including Out-of-Phase Loading," Fatigue Fracture in Engineering Materials, **11**, No. 3, pp. 149–165.

[11] Smith, K. N., Watson, P., and Topper, T. M., 1970, ''A Stress-Strain Function for the Fatigue of Metals,'' J. Mater., **5**, No. 4 pp 767–778.
[12] Banantine, J. A., and Socie, D. F., 1985, ''Observations of Cracking Behavior in Tension and Torsion Low Cycle Fatigue,'' presented at ASTM Symposium on Low Cycle Fatigue—Directions for the Future, Philadelphia, PA.
[13] Lekhnitskii, S. G., 1963, ''*Theory of Elasticity of an Anisotropic Elastic Body*,'' Holden-Day, San Francisco, pp. 1–40.
[14] Pratt and Whitney, 1996, ''SSME Alternate Turbopump Development Program HPFTP Critical Design Review.'' P&W FR24581-1 Dec. 23, NASA Contract NAS8-36801.
[15] Sayyah, T., 1999, ''Alternate Turbopump Development Single Crystal Failure Criterion for High Pressure Fuel Turbopump First Stage Blades,'' Report No.: 621-025-99-001, NASA Contract NAS 8-40836, May 27.

A Study on Five Flank Machining of Centrifugal Compressor Impellers

D. M. Tsay
Professor

H. C. Chen
Graduate Student

M. J. Her
Research Engineer

Department of Mechanical Engineering,
National Sun Yat Sen University,
Kaohsiung 80424, Taiwan

Referring to machining technologies used for turbomachinery components, generally there are two cutting strategies: point cutting and flank cutting. Based on considerations of the cost, efficiency, and surface roughness, flank cutting by using a five-axis machining tool is a promising way to machine blade surfaces of turbomachinery components constructed by ruled surfaces. In this article, a flank cutting technology for centrifugal compressor impellers is developed by using the B-spline curve interpolation, ruled surface construction, and coordinate transformations. Also, an impeller with 12 blades is actually machined to verify the proposed approach by using a five-axis machining center. [DOI: 10.1115/1.1413768]

Introduction

Centrifugal compressor impellers, axial compressors, and fans composed of complex blades are important parts in the field of aerospace and power industries. Traditionally, to manufacture such tubomachinery components, investment casting, and machining procedures may be considered. Both methods have advantages and disadvantages, respectively. In order to obtain a dimensional accuracy within a desired tolerance for blade surfaces, machining is usually performed to effectively achieve the specified requirements. However, due to the complex geometries of such components, it is a challenging problem to precisely machine the blade surfaces.

Though, in the design of blade surfaces of turbomachinery parts, two types of surfaces including sculptured and ruled surfaces may be considered. A ruled surface is covered by straight lines, called rulings or rectilinear generators which form a family with one parameter [1,2]. Owing to this characteristic, ruled surfaces are more frequently utilized to simplify the blade surfaces design when compared with free form, sculptured surfaces.

In the machining of turbomachinery components with complex, overlapping geometries of ruled blade surfaces, five-axis numerically controlled NC machines possessing two more degrees-of-freedom than traditional three-axis machines are necessarily utilized. More importantly, before cutting a turbomachinery component, proper machining processes must first be schemed. And, the cutter paths for five-axis milling must be carefully generated in consideration of the used tools. Otherwise, the desired surfaces of blades may be cut and/or improper cutter paths may result in the fracture of the cutter and the damage of the machine tool. In milling ruled surfaces, techniques including point cutting and flank milling can be selected. By the use of the point cutting method, typical articles [3–7] focused on the efficiency in material-removal rate, machining time, avoidance of global interference and local gouging, surface finish, and scallop heights were reported. More recently, with practical application examples, a procedure [8] can be reliably used to generate collision-free tool paths for five-axis machining of centrifugal compressor impellers with general types of blade surfaces.

Compared to point cutting, flank milling is a much less common approach. However, it has advantages over point cutting. For example, the material-removal rate can be significantly increased and the surface finish can be efficiently improved. Even the flank milling method possesses advantages over the point cutting approach, flank milling a blade surface usually incurs undercutting due to the twist property of ruled surfaces [9]. Owing to the twist of ruled blade surfaces, there are discrepancies between the desired surfaces and machined surfaces. In order to reduce the error to within a specified tolerance, it is possible to position the cutter axis with respect to a ruling along a prescribed direction by selecting an appropriate cutter size free of global interference. Without giving the detailed derivations for undercutting, some rules were specified to analyze undercutting incurred in flank milling and to decide the optimal cutter location [10]. Rehsteiner [11] investigated the collision-free milling strategies of cylindrical cutters applied to twisted ruled surfaces. Wu [12] applied an arbitrary surface flank milling system to flank mill axial bladed rotors and centrifugal compressor impellers. Recently, based on cylindrical cutters, undercutting incurred in flank milling ruled surfaces is identified with detailed derivations [13].

As mentioned above, to machine a turbomachinery part, given a set of the preliminary design data, a manufacturing engineer faces to construct the blade surfaces and to scheme the tool paths. In this study, for flanking centrifugal compressor impellers, a complete and ependable procedure is developed. It is composed of the techniques of the B-spline curve interpolation, ruled surface construction, and coordinate transformations for five-axis flank milling. By using these methods, a practical example for flank milling a centrifugal compressor impeller by a five-axis machine shown in

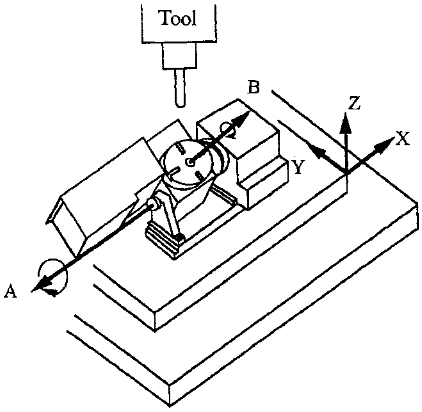

Fig. 1 Five-axis milling machine

Contributed by the International Gas Turbine Institute (IGTI) of THE AMERICAN SOCIETY OF MECHANICAL ENGINEERS for publication in the ASME JOURNAL OF ENGINEERING FOR GAS TURBINES AND POWER. Paper presented at the International Gas Turbine and Aeroengine Congress and Exhibition, Munich, Germany, May 8–11, 2000; Paper 00-GT-342. Manuscript received by IGTI Nov. 1999; final revision received by ASME Headquarters Feb. 2000. Associate Editor: D. R. Ballal.

Fig. 1 is given to illustrate the proposed procedure. The developed algorithms can also be modified without difficulty by adjusting the coordinate transformations if different types of five-axis machine tools are selected.

Background

Before introducing the five-axis flank milling procedure to mill a centrifugal compressor impeller, it is important to know the geometric features of centrifugal compressor impellers so that the construction of the blade surfaces can be done without difficulty. In addition, during the process of generating cutter paths, it is helpful to clear the necessary coordinate transformations to fit the prescribed cutter position for a specific five-axis machine.

Basically, a centrifugal compressor impeller is made up of one or two sets of blades with the same geometry and angular spacing around the centerline of the impeller. A ruled blade surface is twisted more or less to achieve a good compression performance. However, the geometry of an impeller can be divided into two main portions: blade surface and hub surface. And, both sides of a blade surface are the suction surface and the pressure surface. They are generated by offsetting an equal distance along the opposite normal direction of a camber surface bounded in a region by curves of a shroud camberline and a hub camberline. Hence, once a camber surface is constructed by a family of rulings between the shroud camberline and the hub camberline, the resulting geometry of its blade is with ruled surfaces. Meanwhile, the hub surface is formed by revolving the hub camberline around the centerline of the impeller.

When a set of discrete data points is obtained from the aerodynamic analysis, generally, it is in the form of a cylindrical coordinate system as shown in Fig. 2 to define the camber surface. For creating a camber surface, the original data points defined in a cylindrical coordinate system can be transformed into the Cartesian coordinate system. Then, they will be used to generate curves of the shroud camberline and the hub camberline.

Generation of Shroud and Hub Camberlines

To obtain complete shroud and hub camberlines, the discrete data points received from the aerodynamic analysis can be further interpolated to create these two smooth space curves as shown in Fig. 3. In this report, the B-spline curve interpolation method is adopted. A parametric B-spline curve [14] can be written as follows:

$$P(t)=\sum_{i=1}^{n} B_i N_{i,k}(t) \tag{1}$$

where P is the point on the curve, n is the number of data point, B_i are constant coefficients, and $N_{i,k}$ are B-splines of order k (degree$=k-1$).

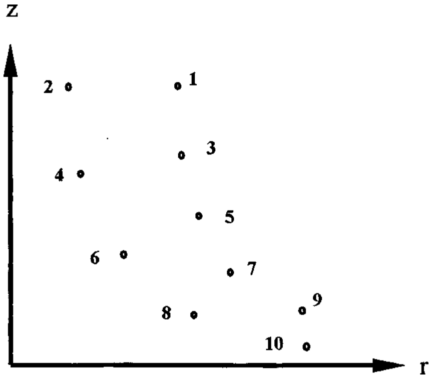

Fig. 2 Basic design data points

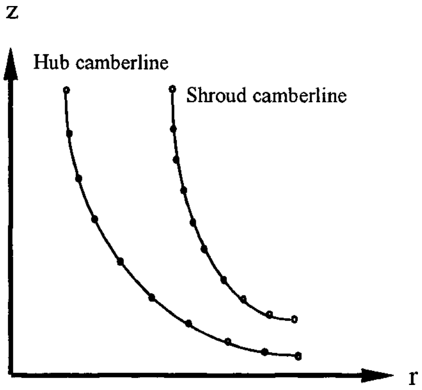

Fig. 3 Curve interpolation

The recursion formula of B-splines of order k with knot sequence T is defined as below ([15]):

$$N_{i,1}(t)=\begin{cases}1 & \text{if } T_i \leq t < T_{i+1} \\ 0 & \text{otherwise}\end{cases} \tag{2}$$

$$N_{i,k}(t)=\frac{(t-T_i)N_{i,k-1}(t)}{T_{i+k-1}-T_i}+\frac{(T_{i+k}-t)N_{i+1,k-1}(t)}{T_{i+k}-T_{i+1}}. \tag{3}$$

Note, to interpolate n discrete data points, the required n number of B-splines are established on knot sequence T. A single B-spline of order k is constructed on $k+1$ knots. As a result, the $n+k$ knots constitute a nondecreasing sequence with real values on the interval $[0,n-k+1]$ of the parameter t. Also, knots at both ends of the interval $[0,n-k+1]$ are repeated k times. For interpolating, usually cubic $(k=4)$ B-splines are smoothly sufficient and parameters corresponding to the chord lengths ([14,16]) between the original data points defined in the Cartesian coordinate system can be taken to compute values of B-splines.

When a set of n data points is given, we can substitute the points into Eq. (1) to form a set of equations

$$\begin{cases} P(t_1)=N_{1,k}(t_1)B_1+N_{2,k}(t_1)B_2+\cdots+N_{n,k}(t_1)B_n \\ P(t_2)=N_{1,k}(t_2)B_1+N_{2,k}(t_2)B_2+\cdots+N_{n,k}(t_2)B_n \\ \qquad\vdots \\ P(t_n)=N_{1,k}(t_n)B_1+N_{2,k}(t_n)B_2+\cdots+N_{n,k}(t_n)B_n \end{cases}. \tag{4}$$

Equation (4) can be rewritten in a matrix form as

$$[P]=[N][B] \tag{5}$$

and the solution of the linear system for the constant coefficients can be obtained as

$$[B]=[N]^{-1}[P]. \tag{6}$$

Since $[B]$ is found, we can substitute $[B]$ into Eq. (1) to find more interpolated data points if different parameters t are given. By this way, the shroud camberline can be described by the B-spline curve to produce more data points. In a similar way, we can also represent the hub camberline by Eq. (1).

Generation of Camber and Blade Surfaces

For an impeller with ruled blade surfaces, first, its camber surface must be defined by a ruled surface. The ruled surface is a surface formed by a family of straight lines passing through corresponding points on the shroud camberline and the hub camberline as $\mathbf{P}(u)$ and $\mathbf{Q}(u)$ shown in Fig. 4. As described above, here the shroud camberline and the hub camberline can be written as parametric B-spline curves. To obtain the parametric equation of a ruled surface for the camber surface, consider the ruling $u=u_i$ joining points $\mathbf{P}_i$ and $\mathbf{Q}_i$ on $\mathbf{P}(u)$ and $\mathbf{Q}(u)$, respectively. The equation of the ruling can be expressed as ([1,2])

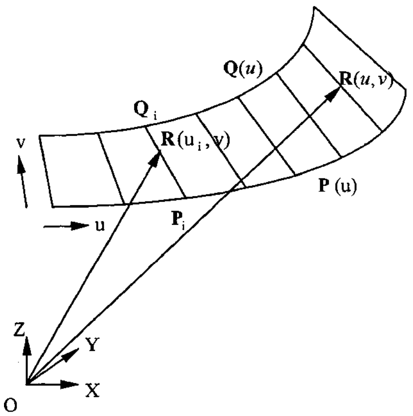

Fig. 4 Ruled surface

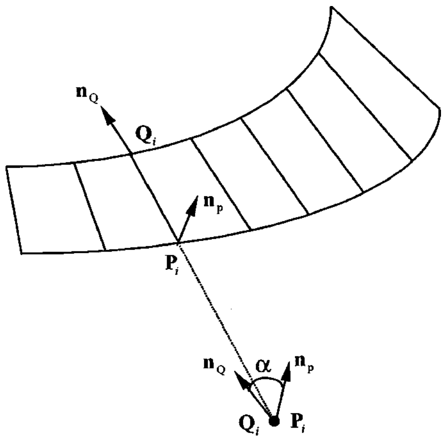

Fig. 5 Normal direction and twist angle

$$\mathbf{R}(u_i,v)=\mathbf{P}_i+v(\mathbf{Q}_i-\mathbf{P}_i) \tag{7}$$

where v is the parameter along the ruling. The one-parameter trajectory traced by $\mathbf{R}(u_i,v)$, denoted as $\mathbf{R}(u,v)$, is a ruled surface defined by the equation

$$\mathbf{R}(u,v)=\mathbf{P}(u)+v[\mathbf{Q}(u)-\mathbf{P}(u)]=(1-v)\mathbf{P}(u)+v\mathbf{Q}(u) \tag{8}$$

where $0\leqslant u\leqslant 1$, $0\leqslant v\leqslant 1$. By using curve interpolation and ruled surface construction, it is possible to establish a smooth ruled surface for the camber surface.

Once the camber surface is defined, the suction and pressure surfaces can be easily produced by describing the offset surfaces of the camber surfaces. To obtain offset surfaces, the unit normal vector of the camber surface must first be calculated. It can be expressed as

$$\mathbf{n}=\left[\frac{\partial\mathbf{R}(u,v)}{\partial u}\times\frac{\partial\mathbf{R}(u,v)}{\partial v}\right]\Big/\left|\frac{\partial\mathbf{R}(u,v)}{\partial u}\times\frac{\partial\mathbf{R}(u,v)}{\partial v}\right|. \tag{9}$$

Given the desired thickness of the blade, d, the suction surface and the pressure surface can be written as

$$\mathbf{O}(u,v)=\mathbf{R}(u,v)\pm(0.5d)^{*}\mathbf{n}. \tag{10}$$

Since both of the suction and the pressure surfaces are two curved surfaces parallel to the camber surface, they can also be represented in a form of Eq. (8) in consideration of flank milling for convenience.

Twist of Blade Surface and Cutter Axis

Using Eq. (9), we can find the directions of the unit normal vectors at both end points along a ruling on the blade surface. Because of the twist of the blade surface, the directions of the two unit normal vectors at both ends of a ruling are not coincident with each other when view down along the ruling. That is to say that these two normal vectors will form a twist angle α as shown in Fig. 5. Due to this twist, proper tool positions cannot be easily determined for flank milling. In flank milling, a cylindrical cutter properly located at one end will undercut the ruled surface near the other end and vice versa. Generally, flank milling a blade surface of a centrifugal compressor impeller with a finite cutter size can never generate the true geometry unless the size of the cutter is infinitely reduced to a line.

In order to reduce the differences between the designed and flank milled surfaces, the cutter size and the projected angle between the ruling and the axis of the cutter must be further analyzed. To improve the accuracy of the machined blade surfaces, the result obtained from the investigation [13] is applied here. To analyze the amount of undercutting incurred in flank milling a twisted ruled surface, the distance between the cutter axis and the ruling as well as the projected angle between the cutter axis and the ruling can be determined when the length of the ruling and the cutter size are given. When these two main variables for the attitude of a cutter axis are decided, by appropriate coordinate transformations, this prescribed position of the tool axis must be moved to coincide with the cutter axis of a specific machine. Then, flank milling the suction surface and the pressure surface on corresponding rulings can proceed, respectively.

Coordinate Transformations

In this section, the postprocessor will be discussed based on the type of a five-axis machine shown in Fig. 1. To flank mill a centrifugal compressor impeller with complex, overlapping geometries, a simultaneous five-axis milling machine with two more degrees-of-freedom in rotating and tilting axes must be utilized. Depending on the configuration of a machine, it may have different rotational axes either on the spindle or on the working table. As a result, the complexity of five-axis flank milling increases with the flexibility of used equipment even an improved attitude of a cylindrical cutter can be found. Hence, the remaining process of preparing the cutter paths for a specific type of a five-axis machine is still a challenging problem to be overcome.

Referring to Fig. 1, the cutter is located on the Z-axis that can just be moved up and down along the Z-axis while the blank is clamped on the working table. In order to machine the ruled blade surface, we can simultaneously rotate and tilt the prescribed position of the cutter axis decided in the last section to become parallel to the Z-axis by the coordinate transformations introduced below.

To perform appropriate coordinate transformations, the corresponding rotating and tilting angles for each prescribed cutter axis $\overline{\mathbf{PQ}}$ mentioned in the previous section must be calculated. First, with reference to Fig. 6, end points, $\mathbf{P}$ and $\mathbf{Q}$, of the cutter axis are rotated by an angle ϕ_z with respect to the B-axis so that the coordinates of the two ends, $\mathbf{P}'$ and $\mathbf{Q}'$, on the X-axis will be the same. This transformation can be described in matrices as follows:

$$\mathbf{P}'=\mathbf{P}[\mathbf{R}_{-x}][\mathbf{R}_z][\mathbf{R}_x];\quad \mathbf{Q}'=\mathbf{Q}[\mathbf{R}_{-x}][\mathbf{R}_z][\mathbf{R}_x] \tag{11}$$

where

$$[\mathbf{R}_z]=\begin{bmatrix}\cos\phi_z & \sin\phi_z & 0 & 0\\ -\sin\phi_z & \cos\phi_z & 0 & 0\\ 0 & 0 & 1 & 0\\ 0 & 0 & 0 & 1\end{bmatrix} \tag{12}$$

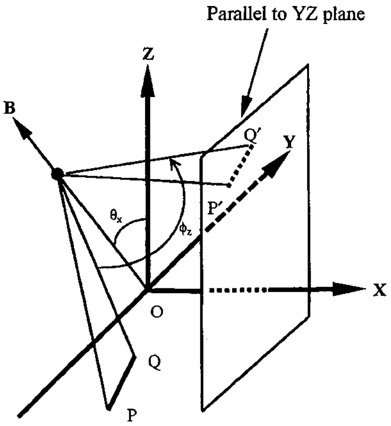

Fig. 6 Coordinate transformation for rotating axis

$$[\mathbf{R}_x]=\begin{bmatrix} 1 & 0 & 0 & 0 \\ 0 & \cos\theta_x & \sin\theta_x & 0 \\ 0 & -\sin\theta_x & \cos\theta_x & 0 \\ 0 & 0 & 0 & 1 \end{bmatrix}. \tag{13}$$

Because the coordinate components of points $\mathbf{P}'$ and $\mathbf{Q}'$ on the X-axis are equal, we can calculate the corresponding rotating angle ϕ_z. Note that θ_x is the angle between the Z-axis and the B-axis.

Secondly, since the coordinate components of points $\mathbf{P}'$ and $\mathbf{Q}'$ on the X-axis are equal, points $\mathbf{P}'$ and $\mathbf{Q}'$ can be tilted an angle ψ_x so that the Y-axis coordinates of both $\mathbf{P}'$ and $\mathbf{Q}'$ will be the same as shown in Fig. 7. Using the relationship that the Y-axis components of points $\mathbf{P}''$ and $\mathbf{Q}''$ are equal, we can formulate the following relationship:

$$|\mathbf{r}_1|\cos(\alpha_1+\psi_x)=|\mathbf{r}_2|\cos(\alpha_2+\psi_x) \tag{14}$$

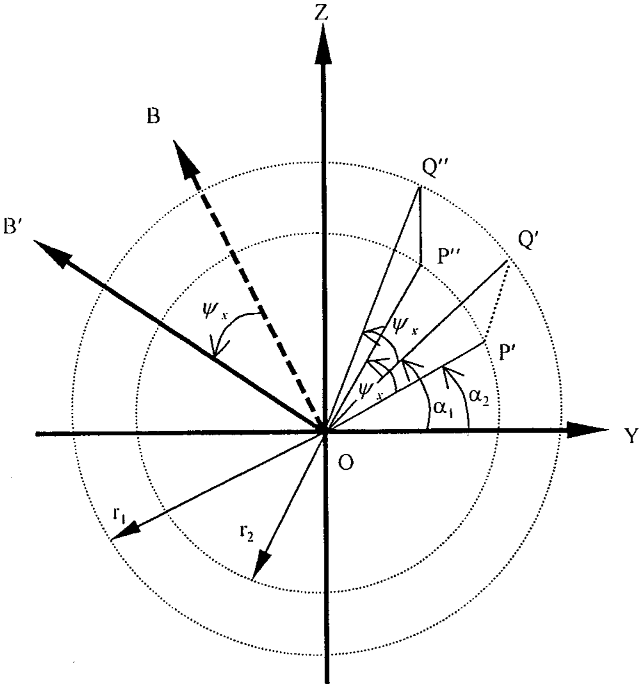

Fig. 7 Coordinate transformation for tilting axis

where $\mathbf{r}_1$ and $\mathbf{r}_2$ are the position vectors of $\mathbf{Q}'$ and $\mathbf{P}'$, respectively.

From Eq. (14), tilting angle ψ_x can be solved for the A-axis. After the coordinate transformations for rotating and tilting angles, the prescribed attitude of the cutter axis, $\overline{\mathbf{PQ}}$, will be parallel to the Z-axis of the five-axis milling machine. From the geometric relationship between the initial and the final positions of the cutter axis, $\overline{\mathbf{P''Q''}}$ can be further translated to coincide with the cutter axis of the used five-axis machine tool. Therefore, the coordinates of the both ends of the found cutter axis in the last section together with the rotating and tilting angles will form the cutter location data of the five-axis flank cutting.

Application Example

Based on the developed five-axis flank milling technology for centrifugal compressor impellers proposed here, a practical application example is illustrated to demonstrate its reliability and usefulness. An interactive computer code in C language is developed and run on a personal computer to implement the processes for the B-spline interpolation, ruled surface construction, determination of the attitude of cutter axis, and postprocessing based on the type of a five-axis machine shown in Fig. 1. As shown in Fig. 8, the geometries of the hub surface and blade surfaces for an impeller with 12 blades are first generated for this application.

The size of the blank (7075T6) of the impeller is 118 mm and 32 mm for its diameter and thickness, respectively. In this study, to save machining time, a numerically controlled lathe is em-

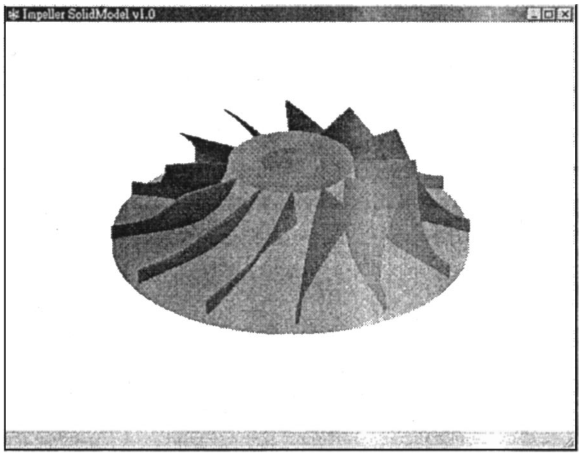

Fig. 8 Centrifugal compressor impeller with 12 blades

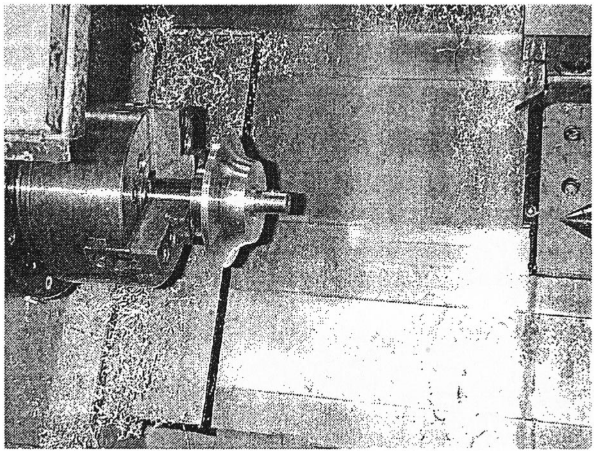

Fig. 9 Cutting exterior contour

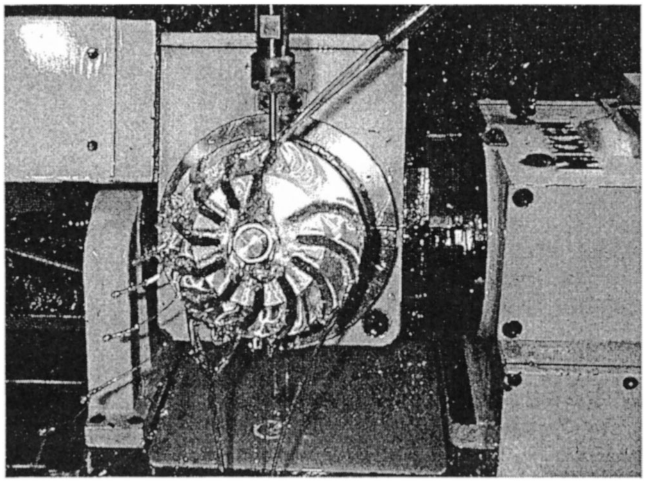

Fig. 10 Rough flank milling

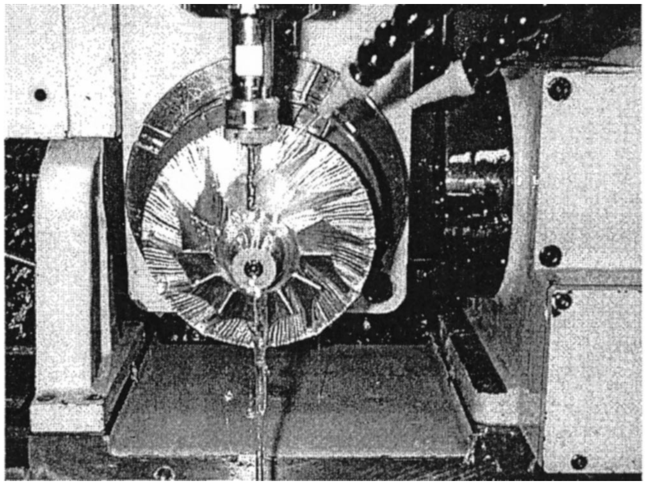

Fig. 11 Finish flank milling

ployed to cut the blank for the exterior contour (shown in Fig. 9) by using the interpolated shroud camberline. Photographed in Fig. 10, for rough flank milling, the diameter of 6 mm of a cylindrical ball-end cutter is applied in consideration of the maximum allowable cutter size between two neighboring blades. After the previous two steps, finish flank milling is performed to mill the suction and pressure surfaces, respectively. In this step, the diameter of the cutter is 4 mm. In this process, blending surfaces required between the blade surfaces and the camber surface are also obtained by controlling the depth of the cylindrical ball-end cutter. The finish flank milling is photographed in Fig. 11.

Discussion and Conclusion

A flank cutting technology that can be applied to generate five-axis cutter paths for machining centrifugal compressor impellers is developed. As has been demonstrated by a practical example, the usefulness of this approach is verified. Though, this procedure is illustrated by a popular type of a five-axis machining center, it can be modified without difficulties if other types of five-axis machining tools are used.

In this article, only the type of cylindrical ball-end cutters is applied in the machining process. For flank milling general turbomachinery components, different shapes of cutters may also be used. It is expected to include them in the approach. And the cutter location data should be regenerated if different types of cutters are utilized.

Acknowledgments

This study is being supported by the National Science Council of Taiwan under grants of NSC 86-2212-E-110-012 and NSC 89-2212-E-110-024. The authors are grateful to Yi Tay Liu who developed the algorithm to produce the basic geometric data from the preliminary design of the impeller.

References

[1] Goetz, A., 1970, *Introduction to Differential Geometry*, Addison-Wesley, Reading, MA.

[2] do Carmo, M. P., 1976, *Differential Geometry of Curves and Surfaces*, Prentice-Hall, Englewood Cliffs, NJ.

[3] Marciniak, K., 1987, ''Influence Of surface Shape on Admissible Tool Positions in 5-Axis Face Milling,'' Comput.-Aided Des., **19**, No. 5, pp. 233–236.

[4] Vickers, G. W., and Quan, K. W., 1989, ''Ball-Mills Versus End-Mills for Curved Surface Machining,'' ASME J. Eng. Ind., **111**, pp. 22–26.

[5] Takeuchi, Y., and Watanable, T., 1992, ''Generation of 5-Axis Control Collision-Free Tool Path and Post-Processing for NC Data,'' CIRP Ann., **41**, pp. 539–542.

[6] Oliver, J. H., Wysocki, D. A., and Goodman, E. D., 1993, ''Gauge Detection Algorithms for Sculptured Surface NC Generation,'' ASME J. Eng. Ind., **115**, pp. 139–144.

[7] Suresh, K. H., and Yang, D. C. H., 1994, ''Constant Scallop-Height Machining of Free-Form Surfaces,'' ASME J. Eng. Ind., **116**, pp. 253–259.

[8] Tsay, D. M., Yan, W. F., and Ho, H. C., 2001, ''Generation of Five-Axis Cutter Paths for Turbomachinery Components,'' ASME J. Eng. Gas Turbines Power, **123**, pp. 50–56.

[9] Ravani, B., and Ku, T. S., 1991, ''Bertrand Offsets of Ruled and Developable Surfaces,'' Comput.-Aided Des., **23**, No. 2, pp. 145–152.

[10] Stute, G., Storr, A., and Sielaff, W., 1979, ''NC Programming of Ruled Surfaces for Five-Axis Machining,'' CIRP Ann., **28**, No. 1, pp. 267–271.

[11] Rehsteiner, F., 1993, ''Collision-Free Five-Axis Milling of Twisted Ruled Surfaces,'' CIRP Ann., **42**, No. 1, pp. 457–461.

[12] Wu, C. Y., 1995, ''Arbitrary Surface Flank Milling of Fan, Compressor, and Impeller Blades,'' ASME J. Eng. Gas Turbines Power, **117**, pp. 534–539.

[13] Tsay, D. M., and Her, M. J., 2001, ''Identification of Undercutting and Machining of Twisted Ruled Surfaces,'' ASME J. Manuf. Sci. Eng., **123**.

[14] Rogers, D. F., and Adams, J. A., 1989, *Mathematical Elements for Computer Graphics*, McGraw-Hill, New York.

[15] de Boor, C., 1978, *A Practical Guide to Splines*, Springer-Verlag, New York.

[16] Lee, E. T. Y., 1989, ''Choosing Nodes in Parametric Curve Interpolation,'' Comput. Aided Des., **21**, pp. 363–370.

G. B. Sinclair
Department of Mechanical Engineering,
Louisiana State University,
Baton Rouge, LA 70803-6413

N. G. Cormier
General Electric Aircraft Engines,
Cinncinati, OH 45215

J. H. Griffin
Department of Mechanical Engineering,
Carnegie Mellon University,
Pittsburgh, PA 15213-3890

G. Meda
Science and Technology Division,
Corning, Inc.,
Corning, NY 14831

Contact Stresses in Dovetail Attachments: Finite Element Modeling

The stress analysis of dovetail attachments presents some challenges. These challenges stem from the high stress gradients near the edges of contact and from the nonlinearities attending conforming contact with friction. To meet these challenges with a finite element analysis, refined grids are needed with mesh sizes near the edges of contact of the order of one percent of the local radii of curvature there. A submodeling procedure is described which can provide grids of sufficient resolution in return for moderate computational effort. This procedure furnishes peak stresses near contact edges which are converging on a sequence of three submodel grids, and which typically do converge to within about five percent. [DOI: 10.1115/1.1391429]

1 Introduction

1.1 Background and Motivation.

Single tooth attachments or ‘‘dovetails’’ are used to secure fan and compressor blades to disks in gas turbines. A section through a typical dovetail is shown in Fig. 1(*a*). Herein the base of the blade is pulled as a result of the centripetal acceleration of its remainder, while it is restrained by contact with the disk on two flats (e.g., $C-C'$ in Fig. 1(*a*)). At the edges of these contact regions, fretting can occur when loads vary. This fretting can lead to fatigue crack initiation and ultimately to failures (e.g., in the disk at *C*, the blade at C'). In order to understand the failure mechanisms involved, an appreciation of the stresses occurring in these critical regions is required. The primary intent of this work is to assist in achieving such an appreciation.

The stress analysis of dovetail attachments like that in Fig. 1(*a*) is not without challenges. To start with, these challenges stem from resolving the *stress gradients* present. Some idea of the nature of these gradients can be obtained from classical elasticity solutions for contact by various frictionless rigid indentors. Sketched in Fig. 2(*a*) are sections through a cylindrical roller, a polynomial profile indentor,[1] and a flat punch with sharp corners. These indentors share a common contact extent of $2a$. Companion stresses for frictionless contact are given in Hertz [1], Steuermann [2], and Sadowsky [3], respectively. These are plotted in Fig. 2(*b*) wherein σ_c is the contact stress and is positive when compressive (Fig. 1(*b*), (*c*)), while $\overline{\sigma_c}$ is its mean value throughout the contact region. Evident in Fig. 2(*b*) are the increases in stress gradients that attend smaller radii of curvature at the edges of contact. If *R* is the local radius of curvature (as in Fig. 1(*b*)), then $R/a>1$ for the roller, $R/a\approx 1$ for the polynomial profile, and $R/a=0$ for the flat sharp indentor. For dovetail attachments like that of Fig. 1(*a*), typically $1/4<R/a<1$ (the left-hand side of a dovetail with $R/a=1/2$ is shown as a broken line in Fig. 2(*a*)). Hence stress gradients for dovetail attachments can be expected to be between that of the polynomial profile indentor and that of the flat punch with sharp edges. The first of these has a stress concentration factor of 1.5 in Fig. 2(*b*), the second, with its stress singularity, an infinite stress concentration factor. Thus dovetail attachments cannot only have high stress concentration factors, but there is also a wide range of values such factors can take on.

There are further sources of challenge in the stress analysis of dovetail attachments. These stem from the *nonlinearities* present. The first of these is the geometric nonlinearity associated with expanding contact regions when contact is conforming (as at *C*, C' in Fig. 1(*a*)). Tracking the extent of contact is essential if accurate finite stresses are to result. The second of these stems from the conditional nature of boundary conditions under an Amonton’s law for friction (also referred to as Coulomb’s law). Complying with this law is vital since associated contact shears τ_c largely govern values of the hoop stress σ_h (Fig. 1(*c*)), and it is the hoop stress that can be expected to be a major contributor to fatigue failure at the edge of contact.

1.2 Literature Search.

The stress analysis of dovetail attachments belongs to a class of problems in solid mechanics commonly termed *contact problems*. A good description of the analysis of such problems, especially via complex variable techniques, is given in Gladwell [4]. A first-rate description of their analysis and physics is given in Johnson [5] (see, in particular, Chapter 13 which describes when Amonton’s law is physically applicable). A well-organized review of research in the area through 1975 is given in Kalker [6]. Further contributions to the literature through 1984 can be obtained from the extensive list of references in Johnson [5]. Papers since 1984 treating conforming contact/numerical analysis of contact problems may be found in Meda and Sinclair [7].

Turning to the literature which specifically addresses the stress analysis of dovetail attachments, we focus on those using finite element analysis. This is because the complexity of such configurations dictates the use of numerical methods, and because, of the numerical methods available, the finite element method is arguably the most adaptable and the most widely used in industry.

There are several papers which describe finite element analysis of dovetail attachments. An early contribution is Boddington et al. [8] which considers two-dimensional elastic analysis. This paper explores the feasibility of implementing Amonton’s law with finite elements and is successful in devising an approach for doing this. Such a capability is now available in standard codes (e.g., ANSYS, [9]). Other papers which include two-dimensional elastic finite element analysis are Kenny et al. [10], Papanikos and Meguid [11], and Meguid et al. [12]. The ambitious task of a three-dimensional elastic analysis is included in Papanikos et al. [13]. While these analyses seem to be capable of computing general trends, it is questionable whether or not they have sufficient mesh refinement near the edge of contact to capture crucial local stresses in this vicinity. More precisely in this regard, if *h* is the

---

[1] In terms of the rectangular coordinates of Fig. 2(*a*), the particular polynomial profile shown therein has $y/a=[(x/a)^8-1]/16$.

Contributed by the International Gas Turbine Institute (IGTI) of THE AMERICAN SOCIETY OF MECHANICAL ENGINEERS for publication in the ASME JOURNAL OF ENGINEERING FOR GAS TURBINES AND POWER. Paper presented at the International Gas Turbine and Aeroengine Congress and Exhibition, Indianapolis, IN, June 7–10, 1999; ASME Paper 99-GT-387. Manuscript received by IGTI, Oct. 1998; final revision received by the ASME Headquarters, Mar. 1999. Associate Editor: D. Wisler.

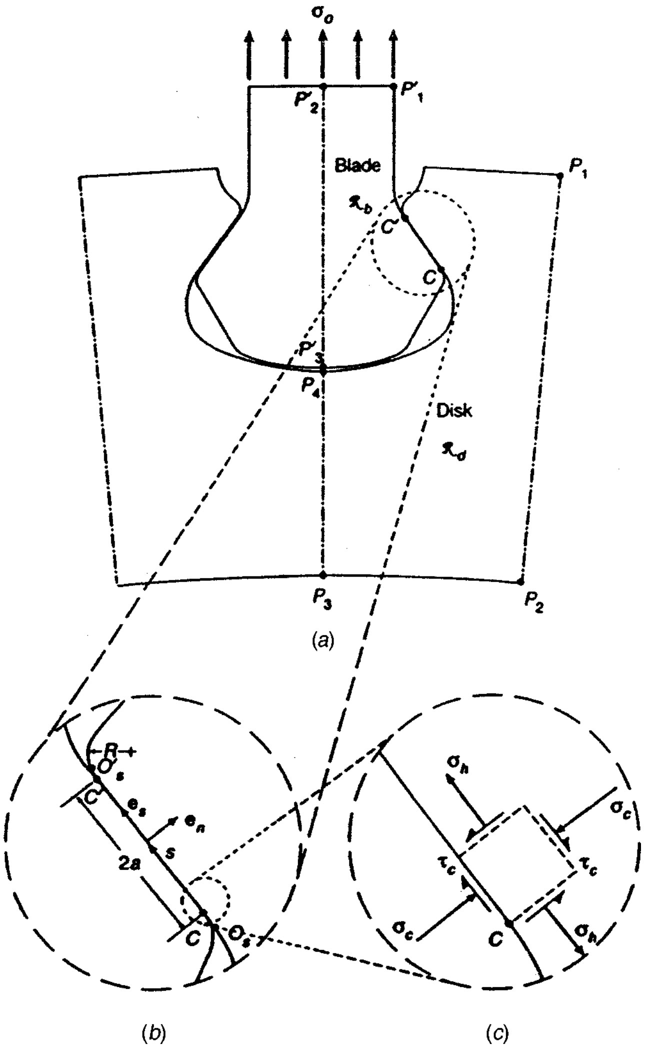

(*b*) (*c*)

Fig. 1 Dovetail attachment configuration: (*a*) overall attachment, (*b*) close-up of contact region with local coordinates, (*c*) close-up of disk near lower contact point with stresses acting

length between nodes of elements used in this vicinity, then these studies have $1/6<h/R<1/2$, where R continues as the local radius of curvature. It remains to be seen if such h are small enough to obtain key local stresses.

1.3 Objective and Scope. Here, then, we seek to develop an approach for obtaining the *local*, two-dimensional, elastic stresses occurring near the *edges of contact* in dovetail attachments. While a two-dimensional elastic treatment represents a simplification of the actual configuration, it is a first step in analyzing more complex models entailing three-dimensional effects and elastoplastic flow. Further, even though simplified, two-dimensional elastic stresses can furnish a basis for understanding physics if the stresses are sufficiently accurately determined.

Critical in obtaining reasonable stress estimates is the policing of the constraints accompanying conforming contact. Only then are stresses guaranteed to be nonsingular. Thus next, in Section 2, we begin with a recap of the asymptotic arguments that establish that, properly analyzed, the conforming contact stresses of interest here are nonsingular. We summarize these arguments not only for completeness, but also because we have been given to understand that there is a diversity of opinion in the gas turbine community as to whether or not stresses in dovetail attachments are nonsingular.

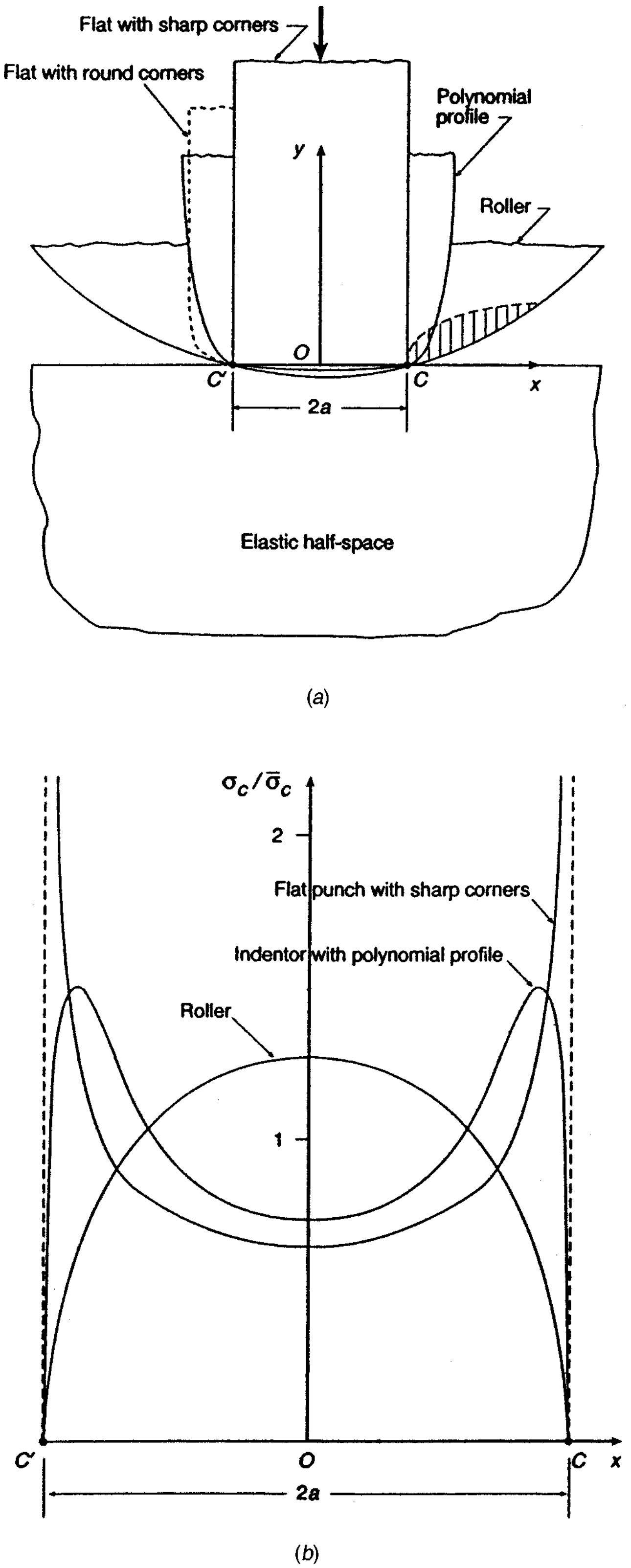

(*a*)

(*b*)

Fig. 2 Examples of contact problems: (*a*) indentor profiles, (*b*) contact stresses

In addition, we wish to include a somewhat subtle but not insignificant point that is missing from these arguments in the literature.

The remainder of the paper is organized as follows. In Section 3, we describe a finite element analysis of a dovetail attachment.

This finite element analysis features a submodeling procedure which enables mesh sizes to be employed which are up to two orders of magnitude smaller than those reported in the literature. Then, in Section 4, we check that the contact stresses actually obtained comply with being nonsingular by systematically examining their convergence in some detail. We also check the policing of the friction law. We close by offering some concluding remarks in Section 5 in the light of results found.

2 Conforming Contact Stresses

2.1 Conforming Contact Without Friction. Here by "conforming" is meant contact which, from no load to full load, has the indentor and indented material share a common tangent as the contact region's boundary is approached from outside. An example is the roller of Fig. 2(*a*). Initially, before any loading, the contact region for this configuration consists of a line through a single contact point. Subsequently, under loading, this point splits into C and C' as the contact region spreads (Fig. 2(*a*)). Throughout, contact is conforming at C (or C') in the above sense. A further example is the polynomial profile indentor of Fig. 2(*a*). In contrast is the sharp-edged flat punch of Fig. 2(*a*): This is an example of nonconforming contact at both C and C'.

In addition to assuming conforming contact to be frictionless in this subsection, we further simplify the exposition by initially considering just the rigid roller of Fig. 2(*a*). The local boundary conditions at C therefore take the form

$$\begin{gathered}\sigma_y=\tau_{xy}=0 \quad \text{on} \quad y=0, \quad x>a, \\ \nu=-\nu_0, \quad \tau_{xy}=0, \quad \text{on} \quad y=0, \quad x<a,\end{gathered} \tag{1}$$

where σ_y, τ_{xy} are stress components in rectangular Cartesian coordinates (x,y), and v is the displacement in the y-direction. The first of (1) are the stress-free conditions external to the contact region. The second reflects local indentation by an amount $\nu_0=\nu_0(x)$ without any friction within the contact region. The local fields for (1) admit to being supplemented by their fully homogeneous counterparts, namely those for (1) with $\nu_0=0$. Then we recover the classical boundary conditions for a crack, so that inverse-square-root stress singularities are possible ([14]). To remove this possibility, we add physically sensible constraints. These insist that *within the contact region* there can be *no tensile contact stresses*, while *without* there can be *no interpenetration or contact* between the indentor and the indented material. Thus we require

$$\begin{gathered}\sigma_y\leqslant 0 \quad \text{on} \quad y=0, \quad x<a, \\ \nu<\sqrt{[R^2-a^2]}-\sqrt{[R^2-x^2]} \quad \text{on} \quad y=0, \quad x>a.\end{gathered} \tag{2}$$

Given compliance with these added restrictions, singular response is no longer possible.

To see this, consider what happens otherwise. There are two cases.

(i) Singular stresses participate with a positive stress intensity factor.

(ii) Singular stresses participate with a negative stress intensity factor.

Under (i), the singular stress field must dominate all others as C is approached from within the contact region, so that the contact stresses must become tensile. This is in violation of the first of (2). Under (ii), the displaced shape of the indented material just outside C is vertically upwards and consequently interpenetrates the indentor (indicated by the hatched area on the right-hand side of Fig. 2(*a*)). This is in violation of the second of (2). Hence the classical singular fields associated with a crack cannot participate in the conforming contact configuration of the rigid frictionless roller if the inequality constraints of (2) are enforced.

The point that is omitted consideration in the literature is whether we can, in actuality, enforce the inequality constraints of (2) and so remove singularities. The fact that (2) would seem to be physically sensible and therefore desirable does not necessarily mean they can be enforced within classical elasticity. After all, singularities in general are nonphysical so it would be physically sensible and desirable if we could simply legislate them out of elastic solutions. Unfortunately, such legislation typically leads to the posing of a problem that has no solution, the local regular elastic fields being incomplete without their singular counterparts. For conforming contact, however, we have an additional degree of freedom of which we can take advantage. This is the extent of the contact region (i.e., the length between C and C' that $2a$ denotes in Fig. 2(*a*)). By suitably adjusting this extent, the inverse-square-root stress singularity can be removed. Then, since there are no other singular fields within elasticity satisfying the local boundary conditions (1) or their homogeneous counterparts, the configuration is rendered singularity free. The fact that there are no other singularities follows first from the corresponding eigenvalue equation given in Williams [14], then from the completeness of the Williams' eigenfunctions for this configuration established in Gregory [15].

Implicitly this adjustment of contact extent so as to remove the inverse-square-root singularity is what Hertz did ([1]). His solution features a contact stress which is nonsingular and, in fact, goes to zero at the edges of the contact region. Stress gradients, on the other hand, are infinite there. To exemplify, for the roller of Fig. 2(*a*), this Hertzian contact stress is

$$\sigma_c=\frac{4\overline{\sigma}_c}{\pi a}\sqrt{a^2-x^2}, \tag{3}$$

for $-a\leqslant x\leqslant a$.

The same situation applies for frictionless conforming contact by rigid indentors in general. That is, the extent of the contact region can be adjusted so that only compressive tractions occur within it and there is no interpenetration outside of it. Given compliance with these constraints, stresses are nonsingular. Examples for more extensive conforming contact than that of the roller on the half-space are given in Steuermann [2] and Persson [16].

2.2 Conforming Contact With Friction. To obtain a bound on these effects to complement that of frictionless conditions, we can assume that there is no slipping whatsoever while continuing to consider a rigid roller for the time being. The resulting stick conditions within the contact region take the form

$$\nu=-\nu_0, \quad u=0, \quad \text{on} \quad y=0, \quad x<a. \tag{4}$$

In (4), u is the displacement in the x-direction which is set to zero by virtue of the indented material completely sticking to the rigid indentor. Again the homogeneous counterpart of (4), taken together with the stress-free condition in (1), admits the possibility of stress singularities. From Williams [14], these are of $\text{ord}(r^{-1/2}\cos(\eta\ln r))$ and $\text{ord}(r^{-1/2}\sin(\eta\ln r))$ as $r\to 0$, where $r=|x-a|$ and $\eta=(1/2\pi)\ln(3-4\nu)$, ν being Poisson's ratio. These two singularities occur in combination in *two* distinct local fields which can participate independently of each other (unless $\nu=1/2$). Thus adjusting the *one* parameter we have available to us, the contact extent, is not sufficient to remove both of them in general. Accordingly, now it can be impossible to find elastic solutions in compliance with (2), and singular stresses can occur. For example, for the rigid roller of Fig. 2(*a*) but now with stick conditions as in (4), the contact stress becomes

$$\begin{aligned}\sigma_c=\frac{4\overline{\sigma}_c}{\pi a}\Bigg[&\sqrt{a^2-x^2}\cos\left(\eta\ln\left(\frac{a-x}{a+x}\right)\right) \\ &+\frac{2\eta a x}{\sqrt{a^2-x^2}}\sin\left(\eta\ln\left(\frac{a-x}{a+x}\right)\right)\Bigg],\end{aligned} \tag{5}$$

for $-a<x<a$.[2] The contact shear is similarly singular. Hence under these conditions, conforming contact does have a stress singularity.

To alleviate the singular response of direct conforming contact with no slip, one can allow some lateral displacement. This can be done by applying the load incrementally so that surface material outside the contact region is at least allowed to move laterally prior to coming into contact. Mossakovskii [17] describes the implementation of such a physically more realistic approach. Results are nonsingular and comply with the constraints of (2). Indeed, for the contact stress, σ_c is as in (5) but with $\eta=0$, so that the Hertzian contact stress of (3) is recovered. However, in the limit as the edge of the contact region is approached from within, the ratio of the shear contact stress divided by the normal approaches infinity. This implies an infinite coefficient of friction is needed if no slip is to occur once contact is made. This in turn suggests that we entertain the possibility of slip in the outer portions of the contact region itself.

For such slip under a rigid indentor up to the contact limit at C in Fig. 2(a), the boundary conditions under Amonton's law take the form

$$v=-v_0, \quad \tau_{xy}=\mu\sigma_y, \quad \text{on} \quad y=0, \quad x<a. \tag{6}$$

In (6), μ is the coefficient of friction. The condition in (6) with the first of (1) prescribe local boundary conditions for a *slip-to-free* transition: when taken abutting the displacement requirements in (4) if $\tau_{xy}<\mu\sigma_y$, they prescribe local boundary conditions for a *slip-to-stick* transition. For both transition configurations it is possible to show only a single singularity exists (the analysis is similar to that in Williams [14], and relies on completeness implied in Gregory [15]. Accordingly, by appropriately adjusting the positions of these two transitions, both singularities can be removed. To capture the physics better, the loading needs to continue to be applied incrementally (or effectively so via similarity arguments). Such an analysis may be found in Spence [18] and produces singularity-free stresses.

In closing this section, we consider deformation of the indentor, previously taken as rigid. Results remain essentially the same. For conforming contact without friction, or with friction but allowing for slip, physically reasonable inequalities can be complied with by adjusting boundary region extents and configurations thereby rendered free of singularities. Dundurs and Comninou [19] furnishes asymptotic arguments that obeying such inequality constraints removes singular behavior, while there are a number of examples showing that one can actually adjust extents to do this (see, e.g., Johnson [5]).

In sum, therefore, when sufficient degrees-of-freedom are available to enable compliance with the pertinent inequalities, stress singularities can be removed from conforming contact problems. The resulting nonsingular stress distributions have been found to be generally supported by experiments (see Johnson [5], Chapter 4). Consequently, in these circumstances the stress analyst should make every effort to comply with the inequality conditions. Furthermore, these are the circumstances that apply in dovetail attachments. The key, then, to gauging that one has in fact complied with contact inequalities in numerical solutions is *spatial convergence* (i.e., convergence with grid refinement).

3 Finite Element Analysis

3.1 Problem Description. We exploit the symmetry of the configuration to consider only half of the attachment. We denote the two regions within this half by $\mathfrak{R}_b$ and $\mathfrak{R}_d$ for the blade and disk, respectively (Fig. 1(a)). We take the boundary of $\mathfrak{R}_b$, $\partial_b\mathfrak{R}$, to be comprised of the points $P_1'-P_3'$ and C, C', and the boundary of $\mathfrak{R}_d$, $\partial_d\mathfrak{R}$, to be comprised of the points P_1-P_4 and C, C' (Fig. 1(a)). We use local coordinates (s,n) with origin O_s in the contact region to state the key contact conditions and to present results. For this system, s is the arc length along the surface of the disk starting from a point just outside of the contact region at maximum load and has a corresponding unit vector $\mathbf{e}_s$, while n is the distance locally perpendicular to s and has a unit vector $\mathbf{e}_n$ (Fig. 1(b)). With these geometric preliminaries in place, we can formulate the problem as follows.

In general, we seek the plane-strain stresses, σ_s, σ_n, τ_{sn}, and their associated displacements u_s, u_n, throughout $\mathfrak{R}_b$ and $\mathfrak{R}_d$ satisfying: the stress equations of equilibrium including the body force field produced by the centripetal acceleration of the components; the stress-displacement relations for a homogeneous and isotropic, linear elastic solid in a state of plane strain; the symmetry conditions on the centerline P_3-P_2' prohibiting transverse displacement and setting the shear stress to zero there; the periodic conditions on the line P_1-P_2 which also prohibit transverse displacement and set shear to zero; an applied radial displacement and zero shear stress on the line P_2-P_3 reflecting the expansion of the disk due to rotation; the applied stress conditions on the end of the blade between points $P_1'-P_2'$ which apply a tension σ_0 in the absence of shear, where σ_0 represents the pull of the unmodelled section of the blade due to its rotation; the stress-free conditions on $\partial_b\mathfrak{R}$ between the points P_1' and C' and between C and P_3'; the stress-free conditions on $\partial_d\mathfrak{R}$ between the points P_1 and C' and between C and P_4; the *contact conditions* on $C-C'$ matching normal and shear contact stresses on the blade and the disk, σ_n^b and σ_n^d as well as τ_{ns}^b and τ_{ns}^d, matching normal displacements, u_n^b and u_n^d, and applying Amonton's law,

$$\begin{gathered}\sigma_n^b=\sigma_n^d=\sigma_c, \quad \tau_{ns}^b=\tau_{ns}^d=\tau_c, \\ u_n^b=u_n^d, \\ u_s^b=u_s^d \quad \text{if} \quad \tau_c<\mu\sigma_c, \quad \tau_c=\mu\sigma_c \quad \text{otherwise;}\end{gathered} \tag{7}$$

and finally the *contact constraints* requiring that the contact stress be nowhere tensile and prohibiting interpenetration

$$\begin{gathered}\sigma_c\leqslant 0 \quad \text{for} \quad s_c<s<s_c+2a, \\ u_n^b<u_n^d+\frac{(s-s_c)^2}{2R} \quad \text{for} \quad s<s_c, \\ u_n^b<u_n^d+\frac{(s-s_c-2a)^2}{2R} \quad \text{for} \quad s>s_c+2a,\end{gathered} \tag{8}$$

where s_c is the s coordinate of C (Fig. 1(b)). In particular, we seek the peak stresses occurring at the edge of contact.

Actual input values for the foregoing problem are as follows. The maximum applied stress σ_0 is about 1/6 GPa. The angular velocity is approximately 900 rad/sec at maximum load. This increases the effective applied stress by about ten percent. It is this increased applied stress, $\sigma_0'=1.1\sigma_0$, that is used to normalize stress results subsequently. Material constants used are for density. Young's modulus, and Poisson's ratio. Both the disk and the blade are made of a titanium alloy so that these material constants are taken accordingly (see, e.g., Gere and Timoshenko [20] Appendix H). To provide bounds on the effects of friction we take $\mu=0$ and $\mu=0.4$, the latter being suggested in Hamdy and Waterhouse [21] as a likely upper bound for dovetail attachments made of titanium alloys.

3.2 Global Finite Element Analysis. To police (8), we use the point-to-surface contact elements of ANSYS [9], CONTAC 48. Following ANSYS [9] recommendations for the analysis of contact problems, these are used in conjunction with ANSYS four-node quadrilateral elements, PLANE 42.

There are some input parameters required to run CONTAC 48 elements. Here we take these to be

---

[2] The derivation of (5) is straightforward using complex potential methods as in Gladwell [4], Chapter 4.

$$h/100 \leqslant \mathrm{TOLN} \leqslant h/50, \qquad (9)$$

$$\mathrm{KN}=E, \quad \mathrm{KT}=E/100,$$

where E is the Young's modulus of the titanium alloy and h continues as the mesh size in the contact region. The parameters in (9) let the iterative scheme for the contact elements converge fairly quickly, thereby policing the contact inequalities (8). Typically results are reasonable (free of interpenetration, one-element stress spikes, segments wherein the contact shear is zero when it should not be, etc.). On the few occasions in which the iterative scheme did not converge to sensible results, decreasing TOLN and increasing KN and KT all by a factor of ten completely removed any such problems, albeit at the expense of longer run times. For the number of load substeps required, we take 10, 20, and 40 to check for any sensitivity. We find no differences between results for 20 and 40 for a number of analyses and so take 20 throughout the remainder of the analysis.

To address the issue of *spatial convergence*, we begin with a series of three global grids: a coarse grid (C), a medium (M), and a fine (F). Each of these grids has a boundary layer in the contact region in which we have a uniform mesh (see, e.g., Fig. 3(*a*), (*b*)). We take the depth of this boundary layer to be one-fourth of the radius of curvature, this value being found to be adequate in numerical experiments on Hertz-like contact problems. Within this boundary layer, grid refinement is systematic with element edge lengths being successively halved to produce refined grids. Outside of the boundary layer, we approximately systematically refine our grids. We do this by specifying refined element edge lengths at a few locations in the far field and then use the AMESH command of ANSYS [9] to automatically mesh the rest of the region.

For these first three grids, the actual mesh sizes in the contact region together with the numbers of spatial and contact elements are given in the upper half of Table 1. The mesh size for the coarse grid is as small as any we could discern in the literature reporting finite element analysis of dovetail attachments cited earlier. For the medium and fine grids it is reduced by factors of two and four. Element numbers increase consequently, though not as systematically because of the use of the AMESH automatic mesh generator away from the contact region, and because of some economies made in the use of contact elements in going from the medium to the fine grid.

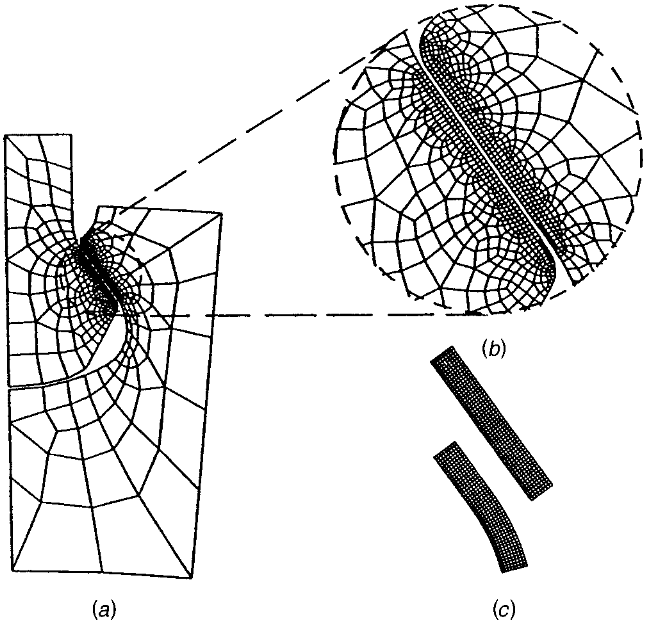

Fig. 3 Finite element grids: (*a*) coarse global grid, (*b*) close-up of coarse global grid with submodel region shown shaded, (*c*) coarse submodel grid

For this fairly systematically refined sequence of three grids, we take as our criterion for any peak contact stress component $\sigma_{\max}$ to be *converging* that

$$|\sigma_{\max}^{\mathrm{C}} - \sigma_{\max}^{\mathrm{M}}| > |\sigma_{\max}^{\mathrm{M}} - \sigma_{\max}^{\mathrm{F}}|, \qquad (10)$$

where the superscripts distinguish grids used. Some justification for convergence checks of this genre is given in Sinclair [22].

If (10) is not satisfied, we can proceed with a yet further refined grid to see if we can obtain converging stresses. Specifics of such a superfine grid (S) are also included in Table 1. Again h is halved. Then (10) can be checked for the upgraded set of grids, M, F, and S. This is not an attractive option, however, in terms of computational effort. While the coarse grid runs in under half an hour and even the fine grid runs in about eight hours, the superfine typically takes over 40.[3] Instead, therefore, we turn to submodeling when (10) is not satisfied on our initial three-grid sequence.

3.3 Submodel Finite Element Analysis.

We view global results in deciding where peak contact stresses occur and pick a submodel region which includes these stresses. This results in the shaded submodel region shown in Fig. 3(*b*). Within this region, grids are uniformly meshed (Fig. 3(*c*)), and consequently can be fully systematically refined. The first submodel grid (CS) has elements sized the same as for the superfine global grid in this region. Successively halving element sides then produces a medium submodel grid (MS) and a fine (FS). Other specifics of the three-grid sequence for the submodel region are given in the lower half of Table 1.

Computational savings with the submodeling are significant. Run times for the coarse submodel grid are two orders of magnitude less than for the superfine global grid, even though they share a common mesh size in the contact region. Run times for the fine submodel grid are somewhat shorter than those for the fine global grid, and consequently quite manageable. This is in marked contrast to the run times to be expected with a global grid of the same resolution in the contact region.

In running submodel grids, some of the boundary conditions applied must use values drawn from the global analysis. To ensure that the submodel analysis actually is converging to the correct response for the original global problem, any errors in such boundary conditions must effectively be zero. The steps taken to realize this goal in the submodeling procedure used here are described in Cormier et al. [23]. In brief they are as follows.

First, *displacements* are chosen as the quantities to be taken from global grids for use in boundary conditions for submodel grids. This is because they converge more rapidly than stresses. For four-node quadrilateral elements, Strang and Fix [24] has

$$e_u = O(h^2), \quad e_\sigma = O(h), \quad \text{as } h \to 0, \qquad (11)$$

where e_u, e_σ are the errors in displacements and stresses, respectively.

Table 1 Summary of finite element grids

Grid	Mesh Size in Contact Region, h/R	No. of Spatial Elements	No. of Contacts Elements
Coarse global (C)	0.156	915	2,048
Medium global (M)	0.078	2,604	8,462
Fine global (F)	0.039	8,314	11,711
Superfine global (S)	0.020	22,812	40,667
Coarse submodel (CS)	0.020	768	3,181
Medium submodel (MS)	0.010	3,072	12,697
Fine submodel (FS)	0.005	12,288	50,368

---

[3] Run times are for an HP 780 workstation with 720 MB of RAM.

Second, *nodal* values of displacements are taken from global grids. This is because experience with finite element analysis on test problems demonstrates that typically these displacements are more accurately determined than displacements between nodes (see, e.g., [23]).

Third, a *cubic spline* is fitted through nodal displacements from global grids to furnish the intervening displacement values needed to run submodel grids. This is because cubic splines are once continuously differentiable throughout their lengths in common with the elastic displacement fields they are trying to replicate.[4]

Fourth, the so-fitted displacements are submitted to a three-grid check analogous to (10). This is to see if these displacement boundary conditions are *converging.*

Fifth and last, a single submodel grid is run with displacement boundary conditions from two successive global grids and peak stresses compared to see that effectively there are no differences between the two evaluations. This is to see if these displacement boundary conditions have *converged*. We provide the results of such a check next in Section 4, after we examine the spatial convergence issue.

4 Verification of Finite Element Analysis

4.1 Spatial Convergence Checks. Here we examine the convergence of the contact stress σ_c, the contact shear τ_c, and the hoop stress σ_h. We do this initially with a series of plots of stress distributions at maximum load (Figs. 4, 5). In these plots, stresses are normalized by σ_0', the total applied stress, while arc length s is normalized by s', the distance between O_s and O_s' in Fig. 1(*b*). This distance slightly exceeds $2a$, the length of the attachment flats and initial contact region. This is so that, when s/s' ranges from 0 to 1, it encompasses the entire contact region, even with the expanded contact present at maximum load. In addition, we tabulate peak stress values for various grids at maximum load (Table 2).

The highest magnitudes of σ_c at maximum load occur under frictionless conditions. We view their convergence in Fig. 4. In Fig. 4(*a*), global grid results are presented. These are converging in the interior of the contact region, results from different grids being indistinguishable there. They are not converging, though, near the edges of contact. This is more clearly shown in Fig. 4(*b*) which shows peak σ_c for the three global grids. It shows peak σ_c for the three submodel grids as well. These last are converging. This can be confirmed by substituting results from the first column of stresses in Table 2 into checks like (10). Similar results apply for σ_c when there is friction (see the third column of stress results in Table 2).

Similar results also apply for τ_c. That is, contact shears converge on global grids in the interior of the contact region, but not at the edges of contact. Here submodel results are needed to achieve convergence. This is illustrated in Fig. 5(*a*) and confirmed by the fourth column of stress results in Table 2.

Without friction, σ_h values are actually converging on the global grid sequence, albeit slowly (see second column of stress results in Table 2). With friction, though, convergence of σ_h is more difficult to achieve. In fact, σ_h for the grid sequence M, F, CS does not satisfy its version of (10) (see Fig. 5(*b*) and the last column of Table 2). However, σ_h on the grid sequence F, CS, MS is converging, as it is on the sequence CS, MS, FS. Hence, provided submodel results are used, *all* peak stresses at the edge of contact are *spatially converging.*

To begin to assess the level of accuracy peak stresses have converged to, we adopt the error estimate e calculated by

$$e=|\sigma_{\max}^{\mathrm{MS}}-\sigma_{\max}^{\mathrm{FS}}|/|\sigma_{\max}^{\mathrm{FS}}|, \tag{12}$$

and expressed as a percentage. In (12), $\sigma_{\max}$ continues as the peak value of any one of the stresses σ_c, τ_c, σ_h, and the superscript identifies the grid used to compute it.

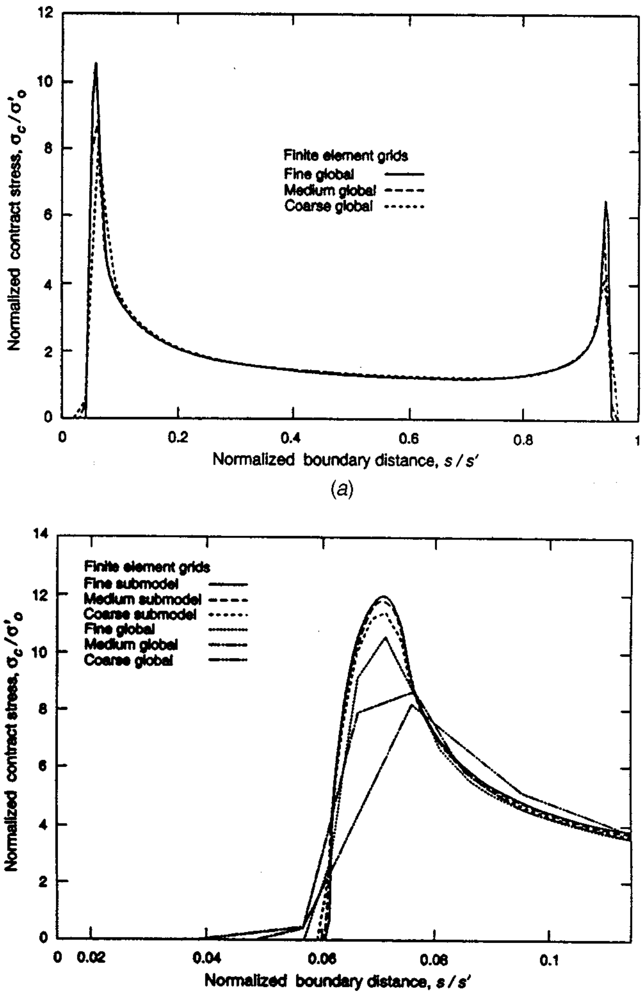

(*a*)

(*b*)

Fig. 4 Converge of contact stress (μ=0): (*a*) global distributions (from global grids), (*b*) local distributions (including submodel results)

Given stresses converging linearly with h as in (11), e of (12) is the appropriate error estimate. Here, however, stresses do not uniformly comply with (11). This is because, in addition to resolving the stress gradients present, the finite element analysis is attempting to resolve the extent of the contact region. The latter activity can result in somewhat erratic convergence. The situation is skin to finding a root of an equation with a bisection algorithm: While this algorithm must ultimately converge if the root is not repeated, successive estimates of the root themselves do not have to move monotonically closer to the true answer.

Typically convergence difficulties associated with determining the extent of contact diminish with increasing grid refinement. This is illustrated on the s/s' axes in Figs. 4(*b*), 5(*b*). It is also reflected in the stresses in Table 2. Eventual compliance with (11) implies differences between CS and MS stresses are twice those between MS and FS stresses. For the most part in Table 2, this halving of differences holds at least approximately.

The stress that deviates the most from ultimately complying with (11) is σ_h when μ=0.4. This is because there is an abrupt change in the slope of the hoop stress at the edge of contact in the presence of friction (see Poritsky [26]). Consequently the finite element analysis has the further task of positioning this sharp peak

---

[4] This is in contrast to the practice in some standard finite element analysis codes. They use element shape functions which are not, in general, continuously differentiable at nodes. Such discontinuities can be shown to lead to spurious logarithmic stress singularities on submodel boundaries ([25]).

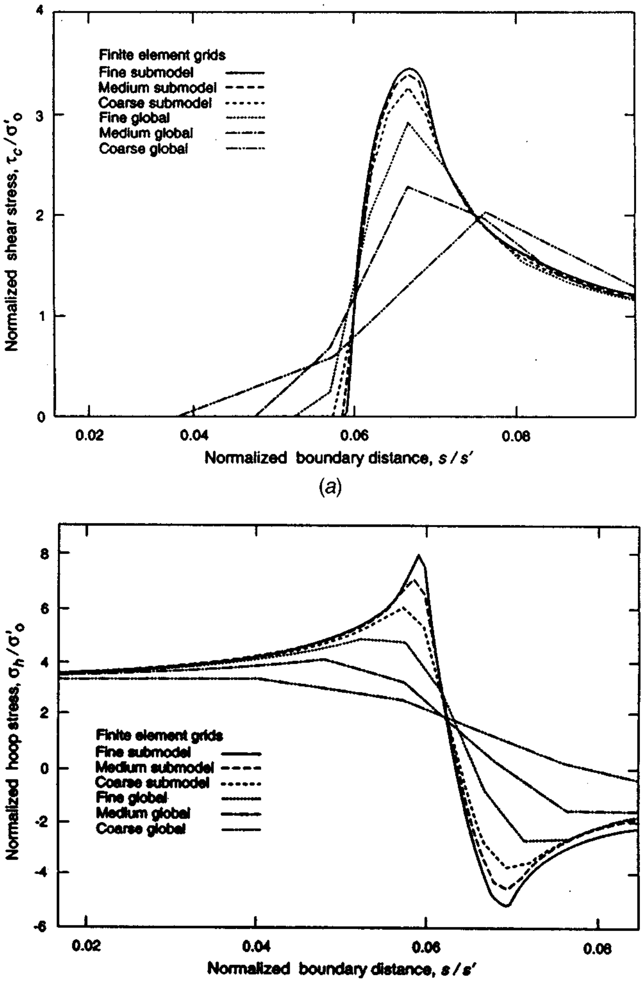

(*a*)

(*b*)

Fig. 5 Convergence of other stress components (μ=0.4); (*a*) local shear stresses, (*b*) local hoop stresses

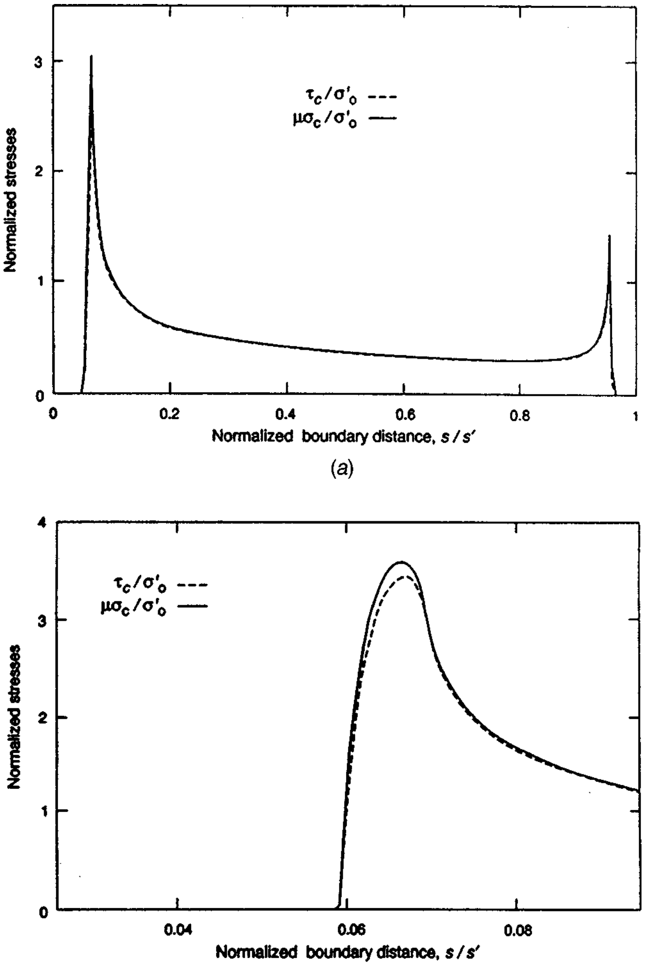

(*a*)

(*b*)

Fig. 6 Comparison of shear stress with limiting value (τ_c cf. $\mu\sigma_c$, μ=0.4): (*a*) global comparison (from fine global grid), (*b*) local comparison (from fine submodel grid)

in σ_h (see Fig. 5(*b*)). This positioning slows convergence and compliance with (11). However, in lieu of anything obviously superior, we continue to use *e* of (12) for our error estimate.

Applying (12) to Table 2 results in the following error estimates: for σ_c and $\mu=0$ or 0.4, $e=1.7$(percent); for τ_c, $e=2.0$(percent); for σ_h ($\mu=0$), $e=3.5$(percent); and for σ_h ($\mu=0.4$), $e=10$(percent). Hence for the most part, *spatial convergence* to good levels of accuracy is realized (<5 percent). To improve the one instance of merely satisfactory convergence (10 percent), a further submodel within our subregion is needed. We do not undertake this in the present study. Cormier et al. [23] describes how to effect such successive submodeling, and demonstrates on a test problem the sort of improved accuracy that can be so realized.

Table 2 Normalized peak stresses at the edge of contact

Grid	Stresses Without Friction		Stresses With Friction (μ=0.4)		
	σ_c/σ'_0	σ_h/σ'_0	σ_c/σ'_0	τ_c/σ'_0	σ_h/σ'_0
C	8.26	−5.24	5.22	2.00	3.41
M	8.63	−7.12	5.93	2.26	4.10
F	10.6	−8.93	7.66	2.93	4.88
CS	11.4	−10.4	8.52	3.26	6.05
MS	11.8	−11.0	8.85	3.41	7.13
FS	12.0	−11.4	9.00	3.48	7.95

4.2 Other Checks. Here we summarize checks on submodel boundary conditions, compliance with Amonton's law, and convergence with unloading.

For the *check on submodel boundary conditions*, the medium submodel grid is used to calculate peak contact stresses when displacements are taken from the medium, fine and superfine global grids. To keep computation down, this is only done for the frictionless case. Results for peak σ_c/σ'_0 with these respective grids furnishing boundary conditions are: 12.5, 11.8, 11.5. Here differences between successive σ_c/σ'_0 are approximately halving, so that it is reasonable to take the difference between the first two as a measure of the error in results reported here from this source. This yields an estimate of 5.9 percent, higher than what one would want for a good level of accuracy. However, this error is associated with an overestimate of σ_c/σ'_0, whereas the earlier error estimate *e* is associated with an underestimate. Consequently the two cancel to a degree and give an overall error estimate within the five percent limit for a good level of accuracy. The same sort of cancellation occurs for the hoop stress under frictionless conditions and is expected to occur for results when friction is present, thereby effectively leaving accuracy levels unimpaired by errors in submodel boundary conditions.

To *check on Amonton's law*, we first observe that a flag in the ANSYS code indicates that all nodes in the contact region should be slipping during loading up. Therefore the contact conditions (8) have $\tau_c=\mu\sigma_c$ throughout contact. To see if this is so, Fig. 6 plots

τ_c and $\mu\sigma_c$. For most of the global distributions, the two are indistinguishable (Fig. 6(*a*)). At the edge of contact, there are some differences (Fig. 6(*b*)). For the peak values, τ_c is 3.3 percent low (Table 2). This underestimate of τ_c may well be offset in large part by an overestimate resulting from submodel boundary conditions, so that it seems likely that the error remains fairly close to the corresponding e of Section 4.1 (2.0 percent), and that overall accuracy levels for τ_c are still good.

For *checks on unloading*, we consider two loading histories. The first completely unloads the attachment under frictionless conditions. Theoretically, response at any load level under these conditions should be independent of whether one is loading up or down. The finite element analysis results for all grids agree with this prediction to within 0.5 percent. The second loading history cycles the loading down then back up after reaching maximum load. Friction is present for these load cycles. For a fixed unload increment, a steady-state response can be expected to be realized under these circumstances. The finite element analysis results stabilized after two cycles to three significant figures.

In sum, therefore, the finite element analysis described here is in good agreement with all additional checks.

5 Concluding Remarks

The conforming contact occurring in dovetail attachments does *not* lead to *singular* stresses. This is so with or without friction effects being present. That stresses are finite can be shown via asymptotic analysis (Section 2). It follows that finite element analysis of dovetail attachments should produce converging stresses. In fact, converging stresses can be realized if *contact elements police* the required *contact constraints*. The point-to-surface contact elements used here (CONTAC 48 of ANSYS, 1995) are quite capable of the requisite policing. This is demonstrated in this study with and without friction (Table 2).

Although the contact stresses in dovetail attachments are finite, they are large near the edges of contact and do possess *high stress gradients* there. Furthermore, it is necessary to *position* the *edges of contact* themselves with some precision if contact constraints are to be satisfied. Consequently if one is to accurately capture stresses near the edges of contact in dovetail attachments with finite elements, one can expect to need a *highly refined mesh* in this vicinity ($h \sim R/100$). The submodeling procedure described here (Section 3.3) appears ultimately to provide a mesh of sufficient resolution, and to do so in return for moderate computational effort. To achieve good levels of accuracy for peak stresses near the edges of contact, the mesh sizes required are considerably smaller than those in cited earlier analyses.

Two final observations are in order. First we observe that the somewhat erratic convergence which can occur initially in conforming contact problems can mislead a stress analyst into thinking stresses have converged when they have not. To see this, suppose one adopted a two-grid convergence check and viewed a change of five percent as acceptable. Then from the first two global grids used to analyze the dovetail here, one would conclude that the peak normalized contact stress is 8.63 under frictionless conditions (Table 2). In fact this estimate is low by about 40 percent of its value. While the three-grid check used in this paper does not guarantee that one could not make such a nonconservative estimate, it does prevent it happening here and can be expected to make it less likely for other conforming contact configurations.

Second we observe that it should not be thought that the smoothing of stress gradients which accompanies plastic flow obviates the stress analyst from accurately resolving elastic stress fields if accurate elasto-plastic stresses are sought. Basically this is because elastic response physically precedes and triggers elasto-plastic. To explain further, using the fine submodel grid, local first yielding for the dovetail without friction is predicted to occur when loads attain 58 percent of the maximum value used here (based on a Tresca yield criterion). Using just the coarse global grid, this event is not predicted to occur until loads reach 84 percent of their maximum value. Clearly a significant erroneous delay results from using a finite element mesh of insufficient refinement.

Acknowledgments

We are pleased to acknowledge the benefit of technical discussions with engineers at General Electric Incorporated. We are also grateful for the financial support of this work by General Electric Aircraft Engines.

References

[1] Hertz, H., 1882, ''On the Contact of Elastic Solids,'' J. Reine Agnew. Math., **92**, pp. 156–171 (in German: for an account in English, see Johnson, [5], Chapter 4).

[2] Steuermann, E., 1939, ''To Hertz's Theory of Local Deformations in Compressed Elastic Bodies,'' C. R. (Dokl.) Acad. Sci. URSS, **25**, pp. 359–361.

[3] Sadowsky, M. A., 1928, ''Two-Dimensional Problems of Elasticity Theory,'' Z. Angew. Math. Mech., **8**, pp. 107–121 (in German).

[4] Gladwell, G. M. L., 1980, *Contact Problems in the Classical Theory of Elasticity*, Sijthoff and Noordhoff International Publishers, Alphen aan den Rijn, The Netherlands.

[5] Johnson, K. L., 1985, *Contact Mechanics*, Cambridge University Press, Cambridge, UK.

[6] Kalker, J. J., 1977, ''A Survey of the Mechanics of Contact Between Solid Bodies,'' Z. Angew. Math. Mech., **57**, pp. T3–T17.

[7] Meda, G., and Sinclair, G. B., 1996, ''A Survey of Some Recent Papers in Contact Mechanics,'' Report SM 96-7, Department of Mechanical Engineering, Carnegie Mellon University, Pittsburgh, PA.

[8] Boddington, P. H. B., Chen, K., and Ruiz, C., 1985, ''The Numerical Analysis of Dovetail Joints,'' Comput. Struct., **20**, pp. 731–735.

[9] ANSYS personnel, 1995, *ANSYS User's Manual*, Revision 5.2, Vol. I, ANSYS Inc., Canonsburg, PA.

[10] Kenny, B., Patterson, E. A., Said, M., and Aradhya, K. S. S., 1991, ''Contact Stress Distributions in a Turbine Disk Dovetail Type Joint—A Comparison of Photoelastic and Finite Element Results,'' Strain, **27**, pp. 21–24.

[11] Papanikos, P., and Meguid, S. A., 1994, ''Theoretical and Experimental Studies of Fretting-Initiated Fatigue Failure of Aeroengine Compressor Discs,'' Fatigue Fract. Eng. Mater. Struct., **17**, pp. 539–550.

[12] Meguid, S. A., Refaat, M. H., and Papanikos, P., 1996, ''Theoretical and Experimental Studies of Structural Integrity of Dovetail Joints in Aeroengine Discs,'' J. Mater. Process. Technol., **56**, pp. 668–677.

[13] Papanikos, P., Meguid, S. A., and Stjepanovic, Z., 1998, ''Three-Dimensional Nonlinear Finite Element Analysis of Dovetail Joints in Aeroengine Discs,'' Finite Elem. Anal. Design, **29**, pp. 173–186.

[14] Williams, M. L., 1952, ''Stress Singularities Resulting from Various Boundary Conditions in Angular Corners of Plates in Extension,'' ASME J. Appl. Mech., **19**, pp. 526–528.

[15] Gregory, R. D., 1979, ''Green's Functions, Bi-Linear Forms, and Completeness of the Eigenfunctions for the Elastostatic Strip and Wedge,'' J. Elast., **9**, pp. 283–309.

[16] Persson, A., 1964, ''On the Stress Distribution of Cylindrical Elastic Bodies in Contact,'' Doctoral dissertation, Chalmers University of Technology, Göteborg, Sweden.

[17] Mossakovskii, V. I., 1954, ''The Fundamental Mixed Problem of the Theory of Elasticity for a Half-Space With a Circular Line Separating the Boundary Conditions,'' Prikl. Mat. Mekh., **18**, pp. 187–196 (in Russian).

[18] Spence, D. A., 1975, ''The Hertz Contact Problem with Finite Friction,'' J. Elast., **5**, pp. 297–319.

[19] Dundurs, J., and Comninou, M., 1979, ''Some Consequences of the Inequality Conditions in Contact and Crack Problems,'' J. Elast., **9**, pp. 71–82.

[20] Gere, J. M., and Timoshenko, S. P., 1991, *Mechanics of Materials*, 3rd SI ed., Chapman & Hall, London.

[21] Hamdy, M. M., and Waterhouse, R. B., 1981, ''The Fretting Wear of Ti-6A1-4V and Aged Inconel 718 at Elevated Temperatures,'' Wear, **71**, pp. 237–248.

[22] Sinclair, G. B., 1998, ''Finite Element Analysis of Singular Elasticity Problems,'' *Proceedings of the Eighth International ANSYS Conference*, Vol. 1, ANSYS Inc., Canonsburg, PA, pp. 225–236.

[23] Cormier, N. G., Smallwood, B. S., Sinclair, G. B., and Meda, G., 1999, ''Aggressive Submodelling of Stress Concentrations,'' Int. J. Numer. Methods Eng., **46**, pp. 889–909.

[24] Strang, G., and Fix, G. J., 1973, *An Analysis of the Finite Element Method*, Prentice-Hall, Englewood Cliffs, NJ.

[25] Sinclair, G. B., 1998, ''On the Logarithmic Stress Singularities Induced by the Use of Displacement Interpolants as Boundary Conditions in Submodelling,'' Report SM 98-5, Department of Mechanical Engineering, Carnegie Mellon University, Pittsburgh, PA.

[26] Poritsky, H., 1950, ''Stresses and Deflections of Cylindrical Bodies in Contact,'' ASME J. Appl. Mech., **17**, pp. 191–196.

A Scientific Approach to the Process Development Bonded Attachments for High-Speed Rotor Application

R. R. Cairo[1]
Pratt and Whitney
P.O. Box 109600, M/S 714-03,
West Palm Beach, FL 33410-9600

K. A. Sargent
Air Force Research Laboratory
AFRL/PRTC
1950 Fifth Street,
Wright-Patterson AFB, OH 45433-7251

The quest for increased work per stage of compression to reduce overall gas turbine engine system cost has placed extreme demands on the high-pressure turbine (HPT) system. As an example, the HPT is required to operate at unprecedented levels of AN^2 *(the product of turbine annulus area and mechanical speed squared) to enable compressor performance goals to be met. The typical approach of mechanically attaching blades via firtree or dovetail configured mechanical attachments, limits rotor speed because of the life limiting broach slots (stress concentrators) in the disk rim. Exacerbating this problem is the fact that the disk lugs, which react the blade loading, impose a dead load. Higher disk speed results in higher blade loading requiring a deeper or wider lug to support the blade. This in turn results in a wider disk bore to support the deeper, dead load lug region. The dilemma is that higher speed results in larger stress concentrations at the rim and a wider disk bore to support the added parasitic rim load. The answer to this dilemma lies in creating an integrally bladed rotor (IBR) in which the blades are integral with the disk. Since typically, for an HPT, the blades are single crystal and the disk equiaxed nickel alloys, the IBR design suggested precludes absolute machining as the fabrication approach. A solution lies in metallurgically bonding the blades to the disk rim. Bonded airfoil attachments have the potential to increase* AN^2 *and component life by 9–10 percent by eliminating broach induced stress concentrations as noted. Moreover, bonded attachments can reduce external rim loading by upward of 15 percent with a corresponding reduction in disk weight. The key to the solution is a controlled, economical process to concurrently join a full complement of HPT blades in a repeatable manner. This paper discusses how a scientific approach and creative design practice can lead to such a process. Three alternative tooling concepts, and one universal tool that allows independent use of two of these concepts, were developed. Tool stresses and deflections, tool load paths, and bond pressure profiles were all quantified through ANSYS finite element analyses and closed-form analytical solutions. Prior experience has shown that joint strength is sensitive to the bond pressure level. Therefore, the tool materials and geometry were iterated upon until the pressure applied to the blade bond plane was as uniform as possible. Since absolute uniformity is elusive when deformable bodies are part of the bond load train, accurately determining the maximum and minimum bond plane pressure is absolutely essential for subsequent joint characterization and design allowable determination. This allows localized working stresses in the designed attachment to be compared to specific, bond pressure driven, allowable strengths rather than an average strength. This paper will show how applying a scientific approach to the development of a critical technology process can reduce both the cost and risk of process development.*

[DOI: 10.1115/1.1414131]

Introduction

The emphasis in the gas turbine engine industry today is reduced cost: in procurement and operation. Although bonded airfoil attachments in the HPT have the potential to enable higher levels of AN^2, reduce weight, and improve rotor system life, the fabrication process may render their first cost prohibitive. A fabrication process that metallurgically joins a full complement of single crystal blades to an equiaxed nickel disk in a concurrent manner is needed. The feasibility of metallurgically joining dissimilar alloys has been demonstrated with coupon joining, Fig. 1. Not only must the process produce concurrent bonds, but it must also do so with minimal material deformation (upset) to minimize the amount, hence cost, of post bond machining to blend laterally deformed material or notched boundaries. These constraints on the bond process are necessary to keep the cost of fabricating an HPT IBR to a minimum. The conundrum then focuses on processes that lend themselves to effecting simultaneous and precise bonds at upwards of 50–60 locations (blade sites). Precise is a key word here because the resulting complement of blades must be precisely aligned with respect to a prescribed incidence angle and present a smoothly contoured inner and outer radial flowpath for optimal aerodynamic performance. Moreover, since the blades must be cooled in service, the bonding process must append them in the prescribed orientation to allow full ingress of air to cool the interior of the blade. These constraints eliminate (1) forge bonding

---

[1] Currently at GE Power Systems, Gas Turbine Technology Center, 300 Garlington Road, Greenville, SC 29602.

Contributed by the International Gas Turbine Institute (IGTI) of THE AMERICAN SOCIETY OF MECHANICAL ENGINEERS for publication in the ASME JOURNAL OF ENGINEERING FOR GAS TURBINES AND POWER. Paper presented at the International Gas Turbine and Aeroengine Congress and Exhibition, Munich, Germany, May 8–11, 2000; Paper 00-GT-355. Manuscript received by IGTI November 1999; final revision received by ASME Headquarters February 2000. Associate Editor: D. R. Ballal.

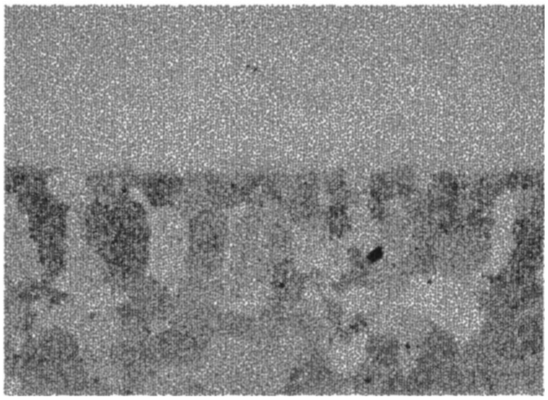

Fig. 1 Microstructure of metallurgical bond between single crystal and equiaxed nickel

because of the extent of material deformation; (2) diffusion bonding because of the duration of the bond cycle time (cost inefficient); and (3) transient liquid phase bonding due to insufficient property retention for highly stressed joints. This leaves the activated forge joining (AFJ) process ([1]) as the prime contender because of its combination of low material deformation, relatively short bond cycle time, and excellent property retention ([2]). The strategy for applying the AFJ process for IBR fabrication relies on the differential thermal expansion between the bond tool (fixture) and the blade and disk components being bonded. This is commonly referred to as the ''delta alpha'' tooling approach. Applying this strategy in an isothermal environment became the focus of this IBR development project and the thesis of this paper.

Barriers to be Overcome

Although the delta alpha tooling approach has been used extensively to produce high-quality polymeric matrix composite components (where the process is also referred to as elastomeric tooling), it has not been used extensively for high-temperature (2000+°F(1093+°C)) fabrication. The tooling is used to generate a bond pressure by the mutual interaction of deformable bodies in a contained environment. The deformable bodies in this case are the tool and the components being bonded. The preliminary tooling concept employed a full-annular containment ring (the bull ring) and radial ''blocks'' or ''shuttles,'' both of molybdenum. These shuttles reacted against both the blade platforms and bull ring to generate pressure at the disk/blade root neck interface, as shown in the ANSYS model in Fig. 2. The large change in temperature in going from room temperature to bond temperature (roughly 2000+°F(1093+°C)), coupled with the difference in expansion rates of the blade/disk assembly and bull ring, resulted in greater than yield strength stresses in the bull ring, which was unacceptable. Essentially, a small change in radial dimension produces a large change in bull ring hoop stress, which is one reason this approach has not been used extensively at temperatures in the 2000+°F(1093+°C) range. Attempts to desensitize the system by introducing compliance in the form of Belleville springs, leaf springs or features machined in the bull ring (Figs. 3(*a*) and 3(*b*)) proved futile. The dilemma for compliance is shown in Fig. 4 in which generated bond pressure is plotted against coefficient of thermal expansion with spring elastic modulus as parameter. As can be seen, dropping below a bond pressure of 65,000 psi (448 Mpa) to a goal of less than 1000 psi (6.9 Mpa) cannot be accomplished even with a leaf spring modulus of 0.5 Msi (3447 Mpa)! In addition to desensitization, another key barrier is control of the spatial positioning and orientation of the blades, especially with respect to their inner and outer flowpath boundaries.

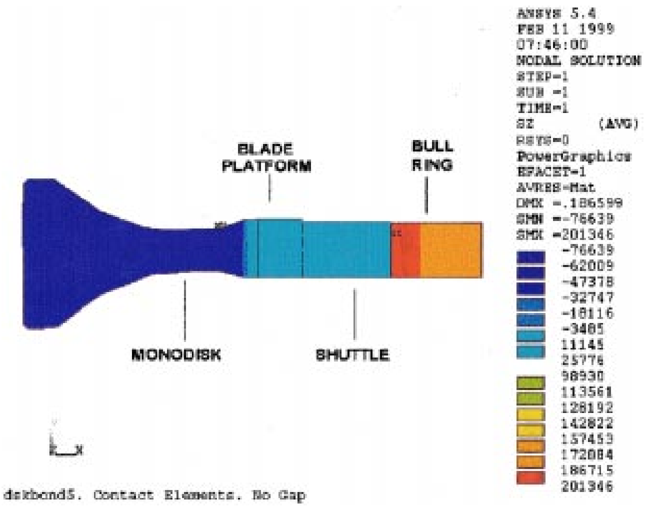

Fig. 2 Line-on-line contact results in unacceptably high stresses in delta-alpha tooling

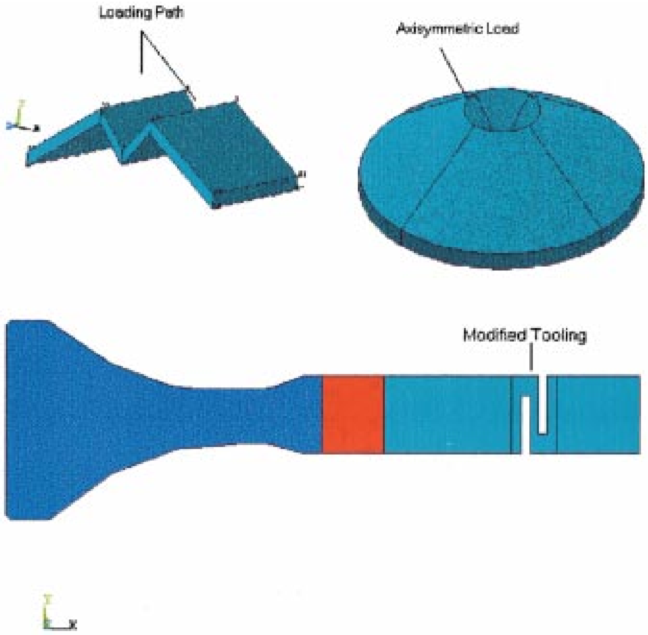

Fig. 3 Attempts to desensitize tooling with geometric compliance

Candidate Solutions

In an effort to desensitize the bond tool system and control spatial positioning of the bonded blades, four alternative approaches were developed and evaluated: (1) blade shuttle; (2) platform hook and spring; (3) neck/pedestal fork; and (4) combined spring and wedge loaded neck/pedestal fork. Each approach utilizes the delta alpha concept and employs the massive, molybdenum bull ring to react the loads induced by thermal expansion. These approaches are listed in the order of which they were conceived, which also coincides with the order of increasing innovation. ANSYS finite element models were built for each approach to identify the uniformity of the bond pressure distribution at the blade/disk interface and to identify shortcomings and undesirable deformations/stresses.

1 Blade Shuttle Concept. The blade shuttle approach, shown in Fig. 5, utilizes a shuttle to position the blade and apply the reaction load that is imparted when the shuttle outer diameter (OD) contacts the bull ring and transfers load to the blade plat

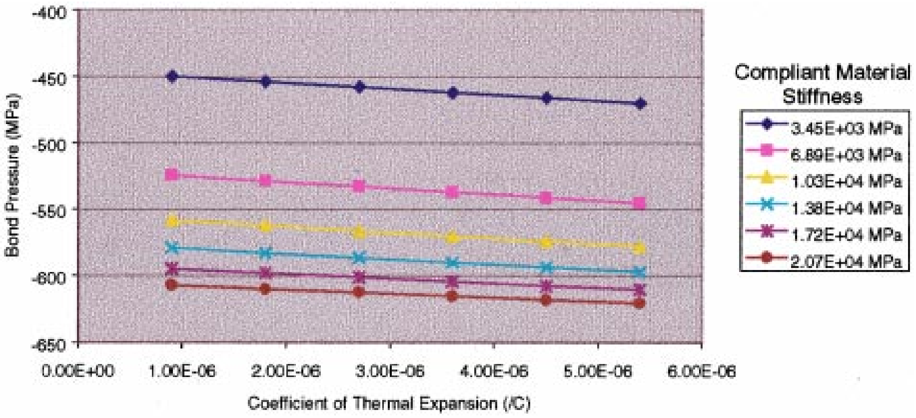

Fig. 4 The sensitivity of bond pressure to material compliance

form. As can be seen, the shuttle reacts the load through four pedestals; two to the fore and two to the aft platform regions. Available platform surface area dictates load application points. This approach was discounted because (a) it is complex to fabricate; (b) it lacked blade-to-blade positioning control; and (c) it resulted in extremely nonuniform bond pressures that peaked at the fore and aft locations and were near zero at the center.

2 Platform Hook and Spring Concept. Figure 6 shows the platform hook approach, which addresses a few of the deficiencies of the shuttle approach relative to positioning control and fabrication complexity. Unlike the blade shuttle, this concept utilizes an open structure consisting of fore and aft rods attached to load application blocks. The blocks also position two adjacent platforms to control the platform (inner flow path) uniformity. Also present are ceramic coil springs to desensitize the system. Coil springs allow more axial travel than leaf springs, hence enabling the desired degree of desensitization for the system. Ceramics were selected because of the high temperatures the entire load train will be subjected to during bonding. Once again, the outer bull ring provides all reaction forces and the springs are key to maintaining ring hoop stresses below the yield point of the molybdenum. Although the platform hook and spring solves a few of the blade shuttle problems, it was discounted because (a) it still produced an extremely nonuniform bond pressures that peaked at the fore and aft locations and were near zero at the center and (b) the many critical engagement points for load application added risk to assembly operations. It did, however, highlight the fact that the platforms were simply too thin and flexible for effective load transfer to the bond plane.

3 Neck/Pedestal Fork Concept. This innovative approach utilizes the best features of the platform hook and spring concept, eliminating the platform locating slots. It applies the load, very close to the bond plane, on a solid foundation instead of a cantilevered platform edge. The approach, shown in Fig. 7, utilizes fore and aft rods with ceramic springs to apply the load to load-application blocks. These, in turn, apply load to the fore and aft ends of a fork that reacts against a step that is machined near the root of the attachment. Notches in the load application blocks control adjacent platform alignment without imparting significant load to them. Also visible in Fig. 7 is a vertical ridge in the left load application block that engages a slot in a base plate to guide the motion of the spring/blade/load application block assembly in the radial direction. This helps to control the blade alignment. Imparting the bond load to a step that is more rigid than a blade platform has the potential for more uniform pressure distribution

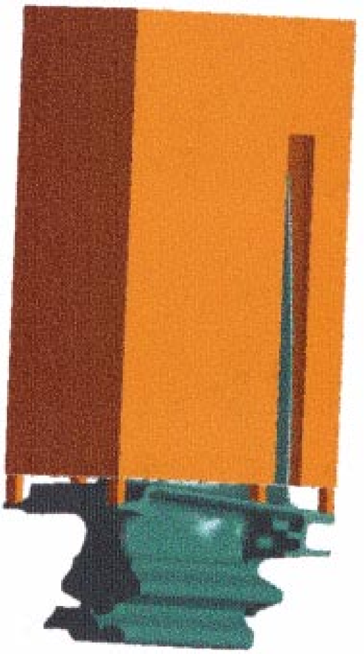

Fig. 5 Shuttle concept

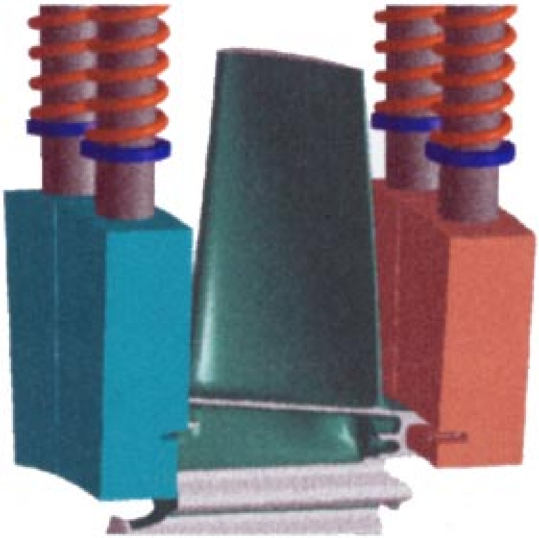

Fig. 6 Platform hook and spring concept

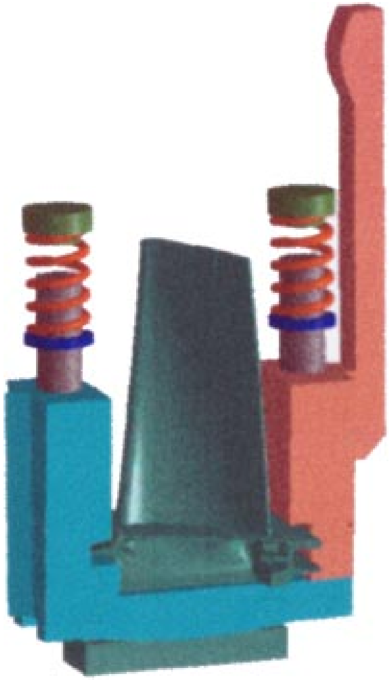

Fig. 7 Neck/pedestal fork concept

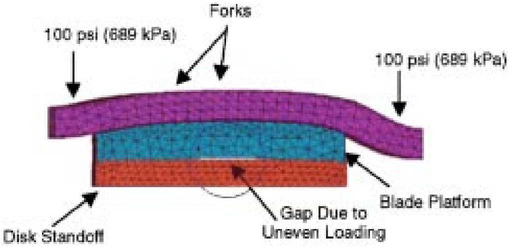

Fig. 8 Fork bending

on the bond plane. However, the bending flexibility of the fork caused the fore and aft regions of the step to receive higher load than the central third. This effect was examined using the ANSYS model shown in Fig. 8. Contact elements were used to model the interaction of the fork and blade root. As can be seen, there is actually a tendency for the central third zone of the bond plane to ''lift.'' This effect underscores the need to address tool design using the principles of mechanics for deformable bodies and using either closed form or finite element analyses.

This tooling concept had enough merit to warrant continued refinement to improve the bond stress distribution. The approach taken was geometric stiffening. The depth of the fork cross section was increased (increasing section modulus) and cylindrical camber was introduced in the central third of the fork, to force contact in that region. This created high Hertzian contact pressures in the center of the bond plane (Fig. 9) and very minimal contact pressure outside the middle third region.

The next iteration involved the introduction of a flat spot in the center of the cylindrically cambered region. This reduced the peak pressure as shown in Fig. 10. A map was generated, seen in Fig. 11, to determine the status of contact. The regions of contact, sliding, and no contact are labeled in the figure. Subsequent iterations to fine-tune the length of the flat spot enabled the goal bond pressure to be achieved with an acceptable pressure distribution. Given the nature of deformable bodies, uniform bond pressure is unattainable, but tuning to an acceptable level by geometric manipulation is economically possible when a scientific approach is utilized.

4 Wedge Loaded Neck/Pedestal Fork Concept and Combined Spring and Wedge Loaded Neck/Pedestal Fork Concept. In principle, the spring loaded neck/pedestal fork concept will work but there is a risk using the brittle ceramic springs. As an alternative to pure delta alpha loading, an approach relying on external, hydraulic loading was developed. The tooling concept shown in Fig. 12, loads the bond plane with the same load application rod and fork arrangement described previously, but does so by wedge rather than spring action. The wedges are loaded axially by an external hydraulic ram. The wedge travels along a mating surface on the inner boundary of the bull ring generating a radially inward component of load to the load application block/fork arrangement. Spacer bumps, integral to the radial sides of the wedges, ensure parallel movement for consistent bond pressure

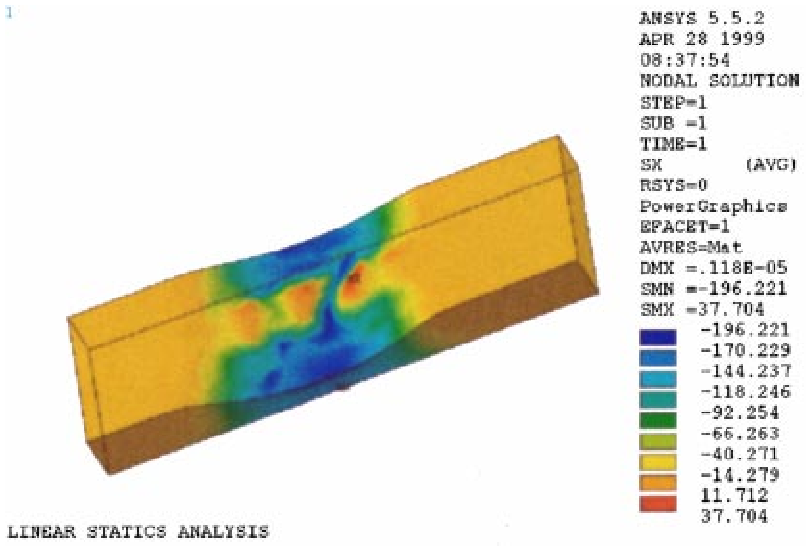

Fig. 9 Bond pressure distribution due to fork stiffening and cylindrical curvature

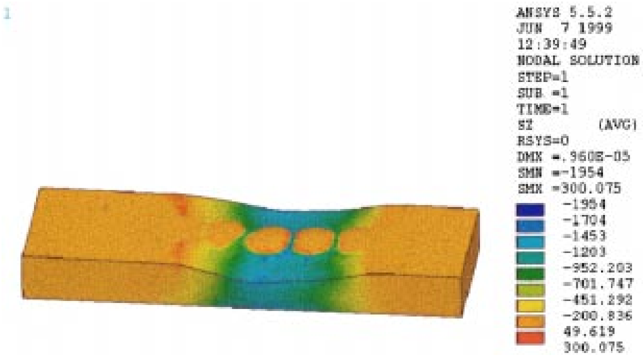

Fig. 10 Bond pressure distribution due to geometric realignment in center region of fork

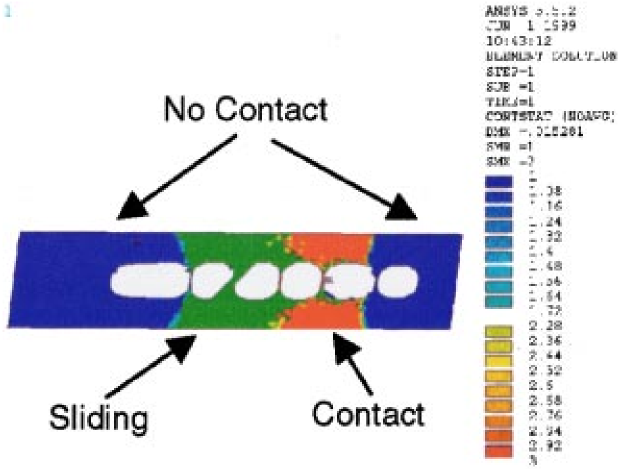

Fig. 11 Contact zones on bond plane

profiles at each bond site. Again, in principle, the wedge loaded neck/pedestal fork approach will work but there is a risk that the wedges will bind due to excessive friction.

To mitigate the risk of committing to either approach too early in the component development effort, a combined tool design (Fig. 13) was conceived that could load the bond plane with the previously described spring loaded approach or, should the springs prove problematic, be converted to the wedge loaded approach. The tool would have a wedge shaped insert piece with a right circular cylinder outer contour and a conical interior boundary to match the conical contour of the bull ring. For pure delta alpha tooling, the springs react against the conical surface of the bull ring insert. For hydraulic load augmentation, the springs are removed and radially deeper wedges are installed. A hydraulic ram presses on the axial face of the wedges which move along the conical surface of the bull ring insert imparting a radially inward load to the loading block fork assembly. Spacer bumps integral to the radial sides of the wedges, ensure parallel movement for consistent bond pressure profiles on at each bond site. The bond tool assembly for the spring and wedge loaded neck/pedestal fork approach is shown in Fig. 14. This also shows a closure ring to hold the wedges in place under thermal growth.

Fig. 12 Wedge loaded neck/pedestal

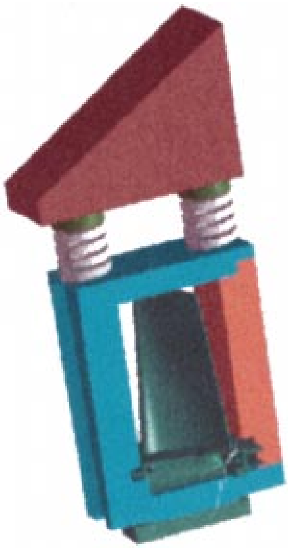

Fig. 13 Combined spring and wedge loaded neck/pedestal

Fig. 14 Universal tool assembly allowing the spring or wedge approach

Summary

IBRs utilizing bonded attachments are an enabling technology to achieve the higher rotational speeds of advanced high-pressure turbine systems. Metallurgically bonding the blades to the disk rim can increase AN^2 and component life by 9–10 percent. The key to the solution is a controlled, economical process to concurrently join a full complement of HPT blades in a repeatable manner. The process must be capable of the accurate spatial positioning of the blades with respect to their angle of attack and their inner and outer flowpath boundaries.

This study showed that applying finite element analyses and creative design practice to tool design is very beneficial. It demonstrated that modifying the tooling geometry, based on finite element results, produced a bonding pressure that was within acceptable, defined limits across the entire bond area. Prior experience has shown that joint strength is sensitive to the bond pressure level. Since absolute uniformity is elusive when deformable bodies are part of the bond load train, accurately determining the maximum and minimum bond plane pressure is absolutely essential for subsequent joint characterization and design allowable determination. Taking this approach towards tool design allows these pressures to be determined, thus providing the actual allowable attachment strengths. A process that precisely controls blade position and imparts the required material response cannot be efficiently developed by trial and error, and shouldn't be. The blade and disk components are too expensive, the variables are too vast, and the design requirements are too unique for an empirical approach. This paper has demonstrated how the use of the scientific approach to process development and tool design cannot only lead to such a process but is absolutely essential in today's fiscal environment.

Acknowledgment

The authors wish to thank Advanced Rotor System Team members David Cunningham, Chad Garner, Johnny Wang, and Beatriz Suarez-Crosse for their input of ideas, figures, and ANSYS analyses.

References

[1] Cairo, R. R., 1999, ''Composite Ring Reinforced Turbine Program Final Report,'' Contract F33615-92-C-2201, Report Number AFRL-PR-WP-TR-1999-2050.
[2] Cairo, R. R. and Sargent, K. A., 1998, ''Twin Web Disk—A Step Beyond Convention,'' ASME Paper No. 88-GT-505.

C. Bréard
e-mail: c.breard@ic.ac.uk

M. Vahdati

A. I. Sayma

M. Imregun

Mechanical Engineering Department,
Center of Vibration Engineering,
Imperial College of Science,
Technology & Medicine,
Exhibition Road
London SW7 2BX, UK

An Integrated Time-Domain Aeroelasticity Model for the Prediction of Fan Forced Response due to Inlet Distortion

The forced response of a low aspect-ratio transonic fan due to different inlet distortions was predicted using an integrated time-domain aeroelasticity model. A time-accurate, nonlinear viscous, unsteady flow representation was coupled to a linear modal model obtained from a standard finite element formulation. The predictions were checked against the results obtained from a previous experimental program known as "Augmented Damping of Low-aspect-ratio Fans" (ADLARF). Unsteady blade surface pressures, due to inlet distortions created by screens mounted in the intake inlet duct, were measured along a streamline at 85 percent blade span. Three resonant conditions, namely 1F/3EO, 1T & 2F/8EO and 2S/8EO, were considered. Both the amplitude and the phase of the unsteady pressure fluctuations were predicted with and without the blade flexibility. The actual blade displacements and the amount of aerodynamic damping were also computed for the former case. A whole-assembly mesh with about 2,000,000 points was used in some of the computations. Although there were some uncertainties about the aerodynamic boundary conditions, the overall agreement between the experimental and predicted results was found to be reasonably good. The inclusion of the blade motion was shown to have an effect on the unsteady pressure distribution, especially for the 2F/1T case. It was concluded that a full representation of the blade forced response phenomenon should include this feature. [DOI: 10.1115/1.1416151]

1 Nature of the Problem

The forced response of bladed disks is a very common vibration problem during the development phase of new aeroengines. A primary mechanism of blade failure is high-cycle fatigue (HCF) which is caused by vibrations at levels exceeding material endurance limits. For axial flow machines, forced-response problems are often associated with turbine blades but the development fan assemblies may suffer from the same phenomenon due to their special geometry. In a fan forced-response context, periodic upstream obstacles such as variable-angle inlet guide vanes (VIGVs) and struts give rise to blade passing frequency (BPF) forced response, and flow distortions due to nonsymmetric intake duct geometries give rise to low-engine order (LEO) forced response. The former type is relatively easy to deal with because the order of the excitation can be deduced from the number of blades. There are no straightforward methods for the latter type since the determination of low-order harmonics requires a detailed knowledge of the inlet flow. In any case, both types of excitation co-exist in modern fans and, from a design viewpoint, the requirement is the prediction of absolute vibration levels under their combined effect so that appropriate fatigue life calculations can be undertaken. The actual vibration levels depend on two quantities: unsteady aerodynamic loading and total damping in the mode of interest, the determination of both of which is fraught with major difficulties. First, the modeling of the unsteady aerodynamic loading is a formidable challenge when dealing with high-speed transonic viscous flows. Second, there are no established methods for accurate structural damping predictions under operating conditions, especially for the higher modes of vibration. The problem is further complicated by the fact that, for some cases, the aerodynamic damping may interact in a nonlinear fashion with the structural motion, a case that can only be investigated using a integrated structural-fluid model.

2 Overview of the Aeroelasticity Model

There are many computational methods for the study of unsteady aerodynamic loads arising from rotor/stator interactions. Time accurate nonlinear analyses using Euler or Navier-Stokes equations have been reported by Giles [1], Rai [2] Dawes [3], Arnone [4], Denton [5], and He [6]. Because of the large computational effort required to deal with nonlinear time-accurate flow representations, models based on linearized unsteady aerodynamics have been developed by Hall and Clark [7,8].

Because of computational limitations, each bladerow is usually considered individually, such separate analyses being linked through inflow boundary conditions. The prediction of absolute blade vibration amplitudes is relatively rare and it is usually achieved by exporting the unsteady pressures into some external finite element code (Green and Marshall [9]).

A more realistic simulation of the aeroelasticity phenomena requires a three dimensional time-accurate viscous representation of the unsteady compressible flow and the inclusion of the blade's vibratory motion. Such an approach is described by Vahdati and Imregun [10] and it has the added benefit of using unstructured grids for increased modeling flexibility. Indeed, the use of unstructured grids may well be the only way to model complex geometries such as tip gaps, snubbered fan blades, fan assemblies with intake ducts, struts, and various other structural elements. Although tetrahedral grids, the choice of which appears obvious for generating unstructured meshes, are relatively easy to generate for inviscid flow calculations, the situation becomes more complicated in boundary layers, where large aspect ratio cells are required for computational efficiency. Such considerations led to the development of optimum semi-structured meshes with mixed elements [11]. The mesh is unstructured in the blade-to-blade plane and structured in the radial direction. Hexahedral cells are used in the boundary layers and tetrahedral and prismatic cells fill the

---

Contributed by the International Gas Turbine Institute (IGTI) of THE AMERICAN SOCIETY OF MECHANICAL ENGINEERS for publication in the ASME JOURNAL OF ENGINEERING FOR GAS TURBINES AND POWER. Paper presented at the International Gas Turbine and Aeroengine Congress and Exhibition, Munich, Germany, May 8–11, 2000; Paper 00-GT-373. Manuscript received by IGTI November 1999; final revision received by ASME Headquarters February 2000. Associate Editor: D. R. Ballal.

domain away from the walls. The forced response work described here will also use semi-structured meshes of mixed elements.

2.1 Flow Model. The governing equations of the flow are cast in their conservation form in a Cartesian coordinate system which is fixed to a rotating blade:

$$\frac{d}{dt}\int_{\Omega}\mathbf{U}d\Omega+\oint_{\partial\Omega}\mathbf{F}.nd\Gamma+\oint_{\partial\Omega}\mathbf{G}.nd\Gamma=\int_{\Omega}\mathbf{I}d\Omega \qquad (1)$$

where Ω refers to any piecewise smoothly bounded fixed volume with boundary Γ. $\mathbf{U}$ is the vector of conservative variables, $\mathbf{F}$ and $\mathbf{G}$ are the inviscid and viscous flux vectors, respectively, and $\mathbf{I}$ contains the terms due to the rotation of the coordinate system. These terms can explicitly be written as

$$\mathbf{U}=\begin{bmatrix}\rho\\ \rho u_i\\ \rho\varepsilon\end{bmatrix};\quad \mathbf{F}=\begin{bmatrix}\rho(u_j-w_j)\\ \rho u_i(u_j-w_j)+p\delta_{ij}\\ \rho\varepsilon(u_j-w_j)+Pu_j\end{bmatrix};$$

$$\mathbf{G}=\begin{bmatrix}0\\ \sigma_{ij}\\ u_k\sigma_{ik}+\kappa\dfrac{\partial T}{\partial x_i}\end{bmatrix}$$

where ρ is the density, ϵ is the specific total energy, u_i is the absolute velocity vector, w_j is the grid velocity relative to the rotating frame of reference, and κ is the effective thermal conductivity. The viscous stress tensor σ_{ij} is given by

$$\sigma_{ij}=\mu\left(\frac{\partial u_i}{\partial x_j}+\frac{\partial u_j}{\partial x_i}\right)-\frac{2}{3}\delta_{ij}\mu\frac{\partial u_k}{\partial x_k} \qquad (2)$$

where μ is the summation of the molecular and eddy viscosities.

The term $\mathbf{I}$ in (1) is given by

$$\mathbf{I}=[0\ \ 0\ \ \rho\omega u_3\ \rho\omega u_2\ \ 0]^T \qquad (3)$$

where ω is the rotational speed along the x-axis. The above system of equations is complemented by the perfect gas equation

$$p=(\gamma-1)\rho\left(\varepsilon-\frac{u^2}{2}\right) \qquad (4)$$

where γ denotes the ratio of the fluid specific heats. The Eddy viscosity is calculated using the one-equation turbulence model of Baldwin and Barth [12].

2.2 Discretization and Solution. The solution vector is stored at the vertices of the cells and an edge-base data structure is used for better computational efficiency. The edge weights which represent the intercell boundaries are computed in a separate preprocessor stage. Consequently, the solver has a unified data structure and the nature of the mixed-element mesh does not affect the main calculations loops.

For an edge-based scheme, the semi-discrete form at internal node I becomes

$$\frac{d(\Omega_I\mathbf{U}_I)}{dt}+\sum_{s=1}^{n_s}\frac{1}{2}|\boldsymbol{\eta}_{IJ_s}|(\mathcal{F}_{IJ_s}-\mathcal{G}_{IJ_s})+B_I=\Omega_I\mathbf{S}_I \qquad (5)$$

where Ω_I is the control volume, $\mathbf{U}_I$ is the solution vector at node I, n_s is the number of sides connected to node I, $\mathcal{F}_{IJ_s}$ and $\mathcal{G}_{IJ_s}$ are the numerical inviscid and viscous fluxes along side IJ_s, and B_I is the boundary integral. The side weight $\boldsymbol{\eta}_{IJ_s}$ represents the area summation within each cell sharing that side.

The inviscid fluxes in (5) are expressed using a central difference formulation with a suitable artificial dissipation coefficient which is required to stabilize the scheme. Thus, inviscid fluxes can be written as

$$\mathcal{F}_{IJ_s}=\frac{\boldsymbol{\eta}_{IJ_s}}{|\boldsymbol{\eta}_{IJ_s}|}\cdot(\mathbf{F}_I+\mathbf{F}_{J_s})-\mathcal{D}_{IJ_s} \qquad (6)$$

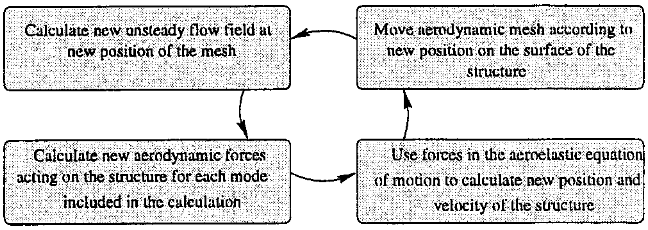

Fig. 1 Exchange of boundary conditions between the structural and fluid domains

where $\mathcal{D}_{IJ_s}$ is the artificial dissipation along the side IJ_s. The artificial dissipation is based on an upwind scheme developed by Swanson and Turkel [13] and Jorgenson and Turkel [14]. The scheme consists of a mixture of second and fourth-order artificial viscosity. The fourth-order terms ensure the stability of the scheme in smooth flow regions. The second-order terms are required to damp numerical oscillations in the vicinity of discontinuities where the scheme reverts to first order using a pressure-based sensor.

The viscous fluxes are treated within the same edge-based data structure framework, provided the gradients of the primitive variables are known at the mesh nodes. Using the edge weights, these gradients can be calculated from the formula

$$[\Omega\theta x_j]_I=\sum_{s=1}^{n_s}\frac{1}{2}\eta_{IJ_s}(\theta_I+\theta_{J_s})+B_I \qquad (7)$$

where θ represents a generic primitive variable and B_i is the boundary integral arising from the contributions of the boundary faces.

The system of equations is advanced in time using a second-order, point-implicit time integration technique. A point-relaxation procedure with Jacobi iterations is used for steady-state flows. Solution acceleration techniques, such as residual smoothing and local time stepping, are employed for faster convergence. A dual time-stepping procedure is used for unsteady flow computations. External Newton iterations are employed to ensure time accuracy. Within each Newton iteration, steady-state flow solution techniques are used to drive the solution to convergence.

2.3 Inclusion of Blade Vibration. The structural model is based on a linear modal representation obtained from a standard finite element formulation. It is implicitly assumed that the vibration amplitude remains within the bounds of linear behavior. The global aeroelasticity equations of motion can be written as

$$\mathbf{M}\ddot{\mathbf{q}}+\mathbf{C}\dot{\mathbf{q}}+\mathbf{K}\mathbf{q}=\mathbf{P}(t) \qquad (8)$$

where $\mathbf{q}$ is the displacement vector, $\mathbf{M}$, $\mathbf{C}$, and $\mathbf{K}$ are the mass, damping, and stiffness matrices, respectively, and $\mathbf{P}(t)$ is the aerodynamic load vector. A transformation into principal coordinates via $\mathbf{q}=\phi\eta$ yields

$$\ddot{\eta}_i+(2\zeta_i\omega_i)\dot{\eta}_i+(\omega_i^2)\eta_i=\phi_i^T\mathbf{P}(t)=\Theta_i(t)\quad i=1,N \qquad (9)$$

where i is the mode index, η_i is the modal deflection, ϕ_i is the mode shape vector, ω_i is the natural frequency, ζ_i is the nondimensional structural damping coefficient, N is the number of mode shapes retained in the analysis, and $\Theta_i(t)$ is the modal projection of the aerodynamic load vector $\mathbf{P}(t)$ onto the mode-shape ϕ_i. Having interpolated the mode shapes onto the aerodynamic mesh, the i-modal force can be obtained via the relationship

$$\Theta_i(t)=\sum_{j=1}^{\text{nodes}}i\phi_j(\delta A_j n_j)p_j(t) \qquad (10)$$

where $p_j(t)$ is the static pressure, n_j is the inward unit normal vector, and δA_j is the surface element area all considered at the surface boundary node j. The structural motion is computed via modal summation over the modes which are of interest in forced

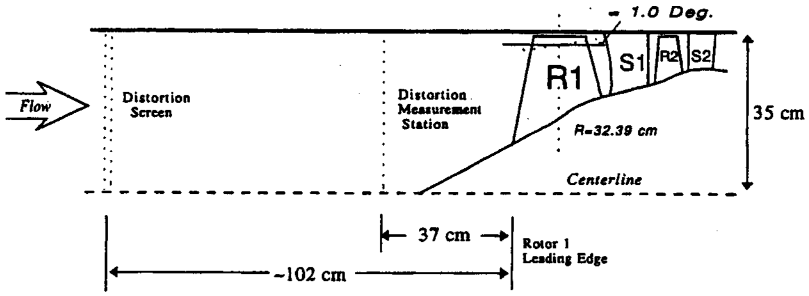

Fig. 2 Test configuration

response. It is important to note that the system of second-order coupled differential Eqs. (8) has been transformed into a much smaller number of uncoupled Eqs. (9). Each equation is advanced in time using the Newmark-β method. As shown in Fig. 1, the boundary conditions from the structural and aerodynamic domains are exchanged at each time-step (Marshall and Imregun [15]). The unsteady aerodynamic load vector $\mathbf{P}(t)$ is obtained at every time-step from the flow solution and imposed as a boundary condition to the structural model so that the new blade position can be computed. Using a spring analogy algorithm, the aerodynamic mesh is then moved to follow the structural motion. The final operation in the cycle is the determination of the new unsteady flow solution about the new position so that the unsteady pressures become available as boundary conditions for the next time-step. The origins of such an integrated methodology can be tracked back to wing flutter. For instance, Ballhaus et al. [16] studied the transonic wing flutter problem using a reduced modes model. A unified discretisation of the fluid and structural domains is described by Bendiksen [17] who studied both wing and turbomachinery blade flutter. Further contributions include those by Srivastava et al. [18] and Bakhle et al. [19].

3 Case Study

The numerical study is focused on a benchmark case, the so-called ADLARF fan, resulting from a collaborative research program between the US Air Force and the GE Aircraft Engines. The basic objective of the work was to evaluate the state of the art of HCF avoidance via the use of numerical models, involving both flow predictions and modification of structural properties, such as mode shapes and damping, to minimize the response levels. A large amount of unsteady pressure data was acquired for a range of inlet distortions so that advanced numerical tools could be validated [20,21].

The ADLARF fan, shown in Fig. 2, is a two-stage compressor and the analysis reported here is focused on the first-stage rotor blade. This rotor contains 16 low aspect ratio (LAR) blades. The first-stage rotor was instrumented to measure the unsteady blade surface pressures along the 85 percent span streamline. Total pressure distortions were created using screens of varying porosity mounted at 1.5 diameter upstream of Rotor 1. The distortions were measured using rakes mounted in the intake duct. Three resonant conditions, summarized in Table 1, were investigated.

Table 1 Resonant conditions (refer to Table 4 and Fig. 7 for a description of the mode shapes)

Distortion	Shaft Speed (RPM)	Aero. Speed (%)	Mode
3/Rev	8,700	66	1F
8/Rev	9,400	69	2F & 1T
8/Rev	13,700	100	2S

4 Steady Flow Analysis

A typical semi-structured mesh, containing about 180,000 points per passage, is shown in Fig. 3. Because of the blade untwist, a new grid was generated for each speed of interest. The basic blade mesh was extended to include the spinner and the intake. Ideally, the boundary conditions should correspond to the working line along which the unsteady flow measurements were recorded. Due to the lack of exact data, several cases were con-

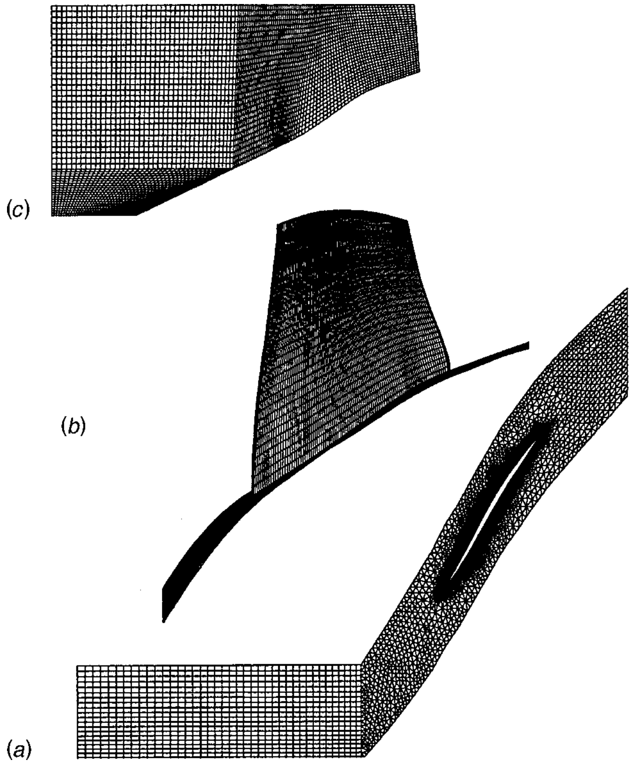

Fig. 3 Single passage mesh; (*a*) tip section, (*b*) blade and hub section, (*c*) periodic boundary

Table 2 Aerodynamic conditions at the three resonances of interest

Aero. Speed (%)	Mass Flow (kg/s/passage)	Pressure Ratio
66 (Case 1)	2.95	1.391
66 (Case 2)	2.55	1.458
69 (Case 1)	3.10	1.458
69 (Case 2)	2.61	1.583
69 (Case 3)	2.77	1.566
100	4.17	2.35

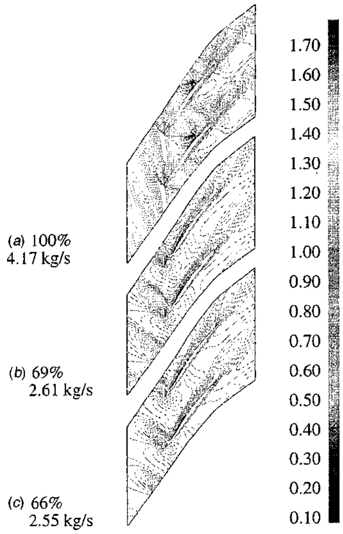

Fig. 4 Steady-state Mach number contours at 85 percent span

sidered at each speed (Table 2). Typical steady-state flow results are plotted in Figs. 4(*a*) to (*c*) for each speed considered. Using the mass flow boundary conditions from Rabe et al. [20], good agreement was obtained with the shock position prediction of Manwaring et al. [21], at 69 percent aerodynamic speed (2.61 kg/s). Moreover, the pressure ratio of 1.58 and the temperature ratio of 1.155 are very close to the measured data reported in Rabe et al. [20], the quoted values being 1.56 and 1.16, respectively.

5 The Structural Model

The mesh used for a cyclic symmetry structural analysis is shown in Fig. 5. The Campbell diagram in Fig. 6 shows features

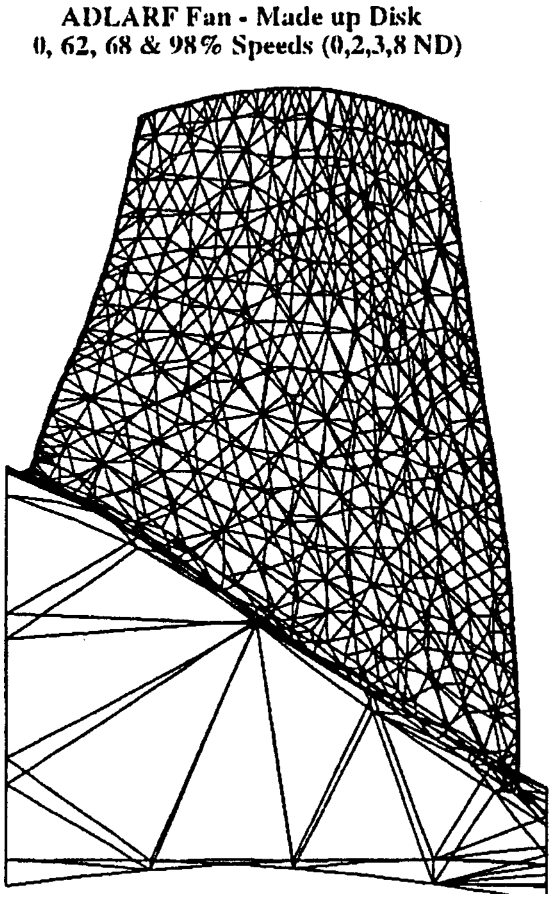

Fig. 5 Structural analysis mesh

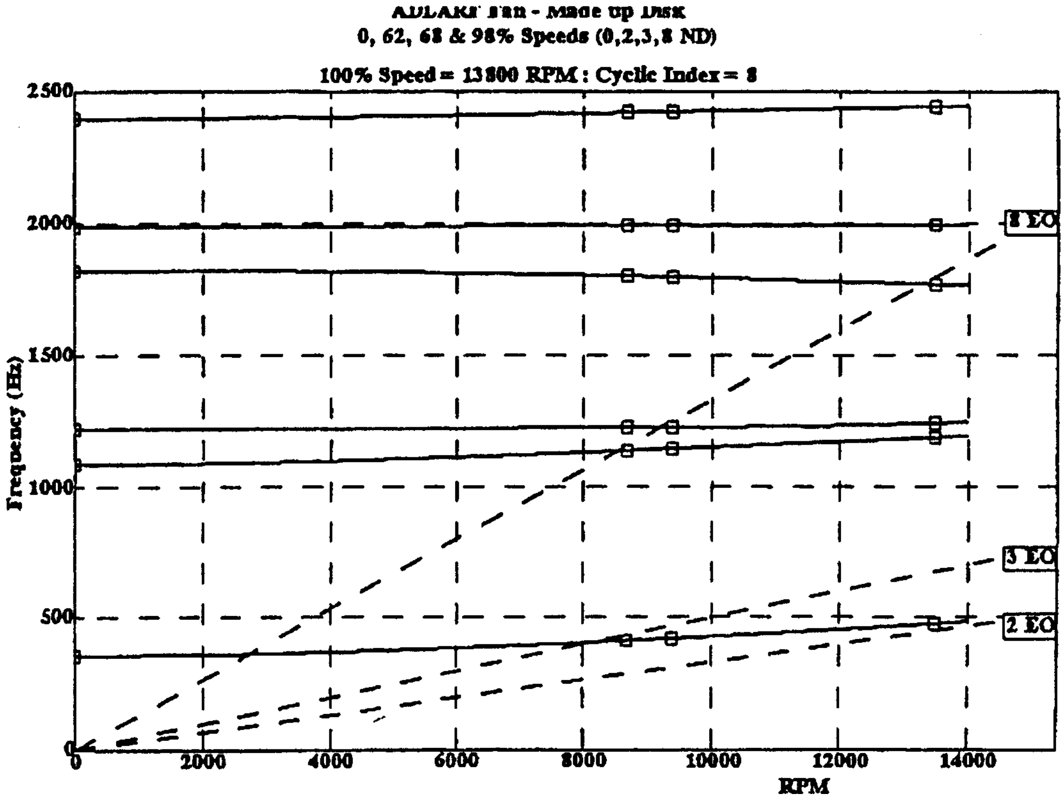

Fig. 6 Campbell diagram

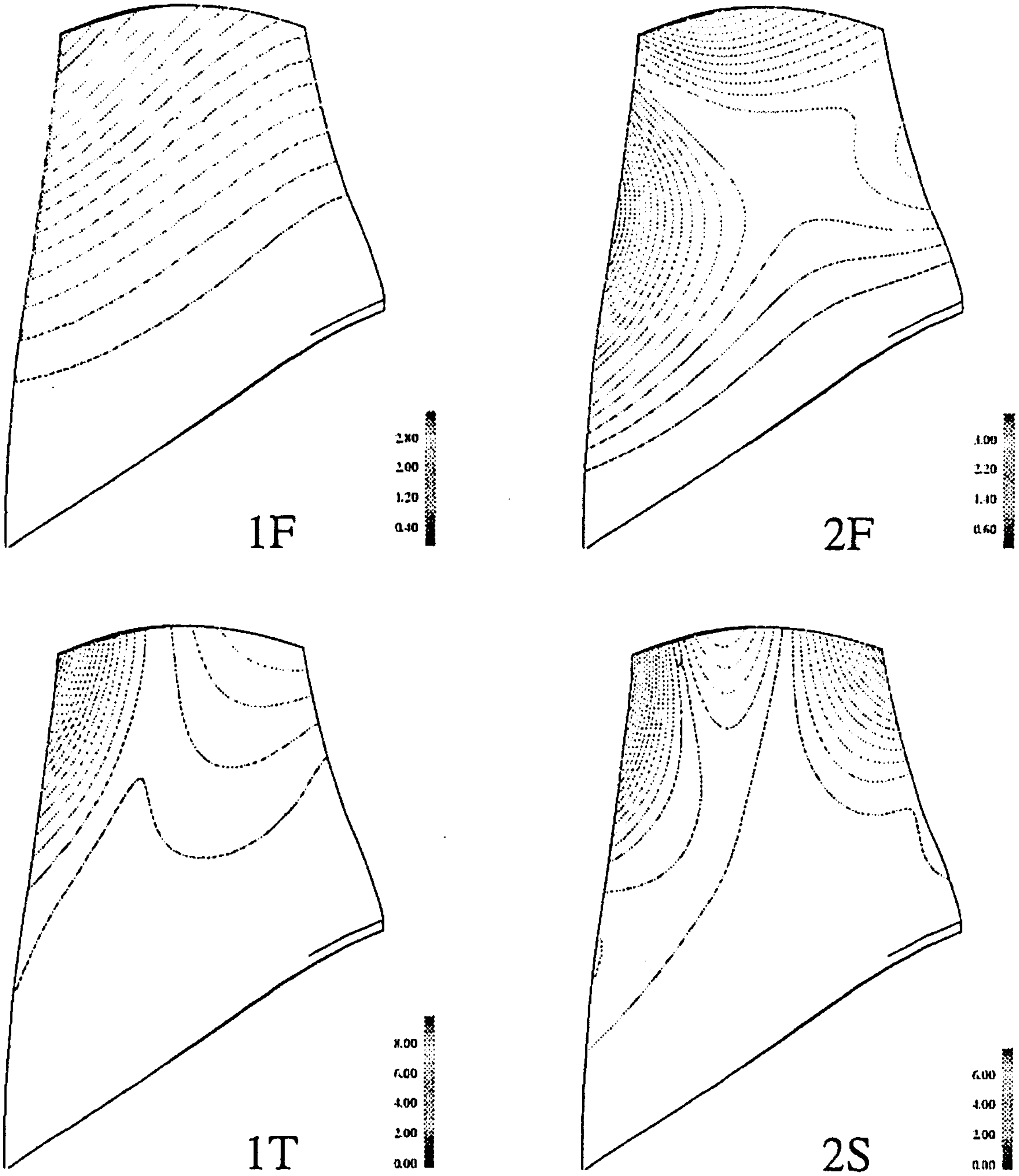

Fig. 7 Structural mode shapes

similar to those published in the literature ([21]), though it was not possible to obtain an exact match due to lack of data. The three resonances of interest correspond to the following four crossings: 1F/3EO, 1T/8EO, 2F/8EO, and 2S/8EO.

The corresponding mode shapes are shown in Fig. 7. Because of their close proximity, it was assumed that the 1T and the 2F modes were excited together and hence the natural frequencies were adjusted accordingly. Further frequency adjustments were made to ensure consistency with the available aerodynamic data (Table 3).

Table 3 Structural frequencies

Shaft Speed	Aero. Speed	Frequency (Hz)	Adjusted (Hz)	Mode
62%	66%	412.09	434.5 (+5.44%)	1F
68%	69%	1148.45	1251.7 (+9.03%)	2F
68%	69%	1227.86	1251.7 (+1.94%)	1T
98%	100%	1770.72	1800. (+1.65%)	2S

6 Forced Response Computations

The forced response computations were initiated by applying a prescribed total pressure variation to the steady-state solution. The modeling of the 3/Rev distortion requires a full assembly representation, while only two blade passages are necessary for an 8/Rev distortion. In order to assess the effects of blade flexibility, computations with and without the blade motion were undertaken. About 150 time-steps were used per cycle of vibration and mechanical damping was assumed to be zero.

The modal forces, modal displacements, aerodynamic Q-factors and maximum actual displacements are given in Table 4 for all

Table 4 Summary of results

Aero. Speed (%)	Mode	Modal Force (N.kg$^{1/2}$)	Aero. Q-factor	Max. Disp. Peak-Peak (mm)
66 (2.55 kg/s)	1F	70.0	60	4.00
69 (3.1 kg/s)	2F/1T	27.5/86.0	44/80	0.14/2.11
69 (2.61 kg/s)	2F/1T	41.0/87.0	52/98	0.25/2.58
100	2S	60	100	0.37

resonant conditions of interest. The aerodynamic Q-factor is obtained by matching the modal displacements from the computations with and without blade motion:

$$Q=\frac{\omega_o^2 A_o}{F_o}$$

where ω_o, A_o, and F_o represent the angular frequency of vibration, the modal displacement amplitude, and modal force amplitude, respectively. For the 69 percent speed case, the computation was done with both the 1T and 2F modes and hence the damping value is only an approximation since it includes contributions from both modes. The following sections present the distribution of the first harmonic of the pressure across the blade along the chord and at 85 percent blade span and compare these with the experimental data. The measured amplitude and phase are plotted for two values from the two adjacent blades with an error-bar format. When no errors-bars are present, only one measured value from measurement was available.

6.1 1F/3EO Crossing. The mesh and the corresponding steady-state Mach number contours are depicted in Figs. 8 and 9, respectively. The input total pressure distortion is shown in Fig. 10. The steady-state pressure distribution is given in Fig. 11 which shows the shock position at 14 percent chord. A periodic solution was obtained after about 20 cycles of vibration by checking the time history of the modal force. Figures 12 and 13 show the amplitude and the phase distribution. A good prediction of the phase distribution (Fig. 13) is obtained with blade motion, and the measurements show good repeatability between the two blades. The maximum computed blade vibration amplitude is about 4 mm. The computed damping (ζ) is estimated to be 0.0083 which is in good agreement with the measured damping which is estimated to be 0.008 for one blade and 0.01 for the adjacent blade.

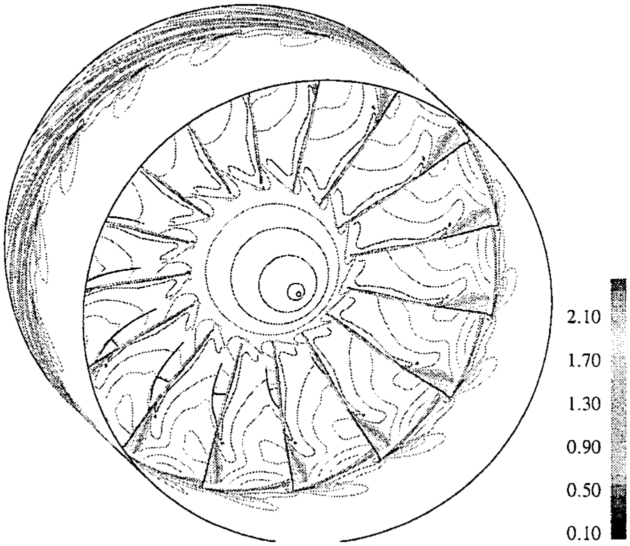

Fig. 9 Steady-state Mach number contour for the 1F/3EO crossing

The time history of the envelope of the modal displacement amplitude computed with and without the blade motion is shown in Fig. 14. The prediction without the blade motion yields better amplitude match but the phase comparison is poor. It shows clearly that the flexibility of the blades is important for this case. However, during the test, the resonance condition could not be kept during a long period for such large displacements. Further details of the blade flexibility effects are given in Figs. 15 and 16 where the first harmonic of the unsteady pressure is plotted for the pressure and suction surfaces for both with and without motion. The amplitude is about half for the case with motion, though the unsteady pressure amplitude remains very high at the shock position.

6.2 2F&1T/8EO Crossing. Because of the uncertainties in the aerodynamic conditions, the unsteady loads were predicted for three different mass flow rates for an imposed total pressure variation. Figures 17, 18, and 19 show the pressure amplitude distribution for the three cases. The result from the lowest mass flow rate (Fig. 18) shows a better agreement but the measurement point

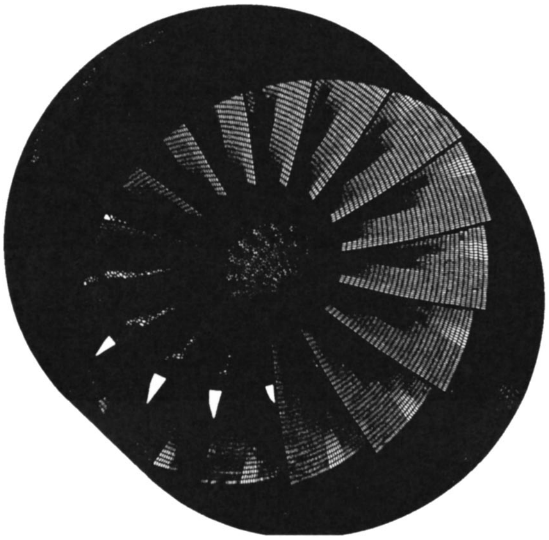

Fig. 8 Full assembly mesh for the 1F/3EO crossing case

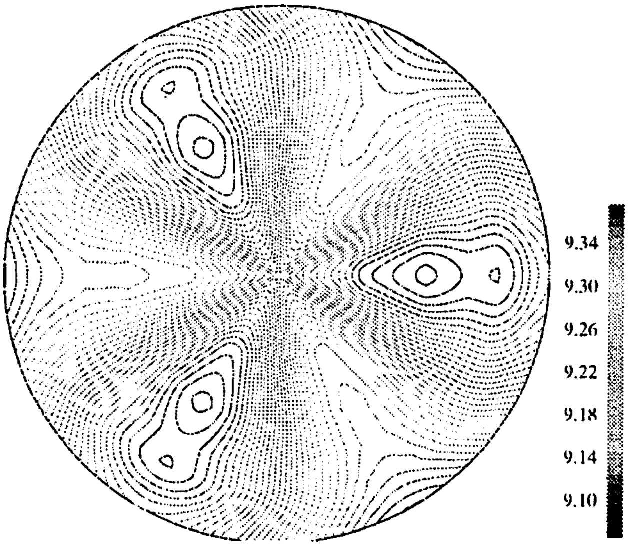

Fig. 10 Total pressure distortion—1F/3EO crossing

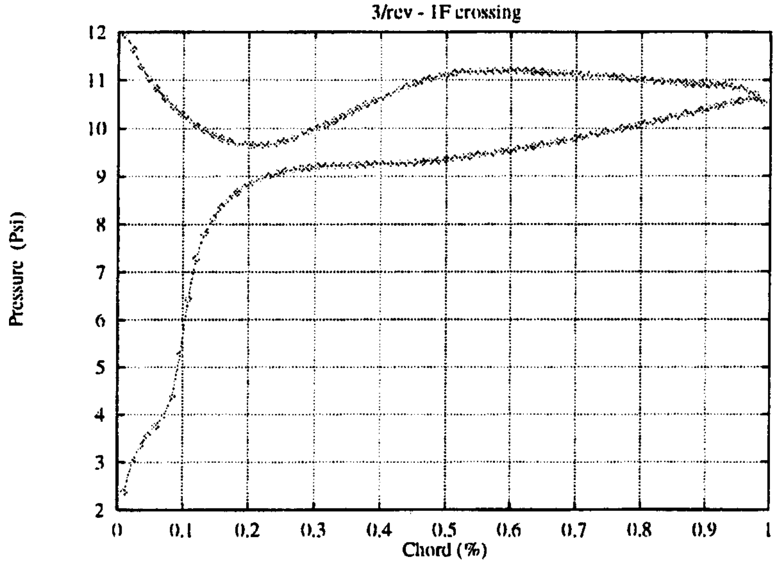

Fig. 11 Steady-state pressure profile at 85 percent span for 1F/3EO

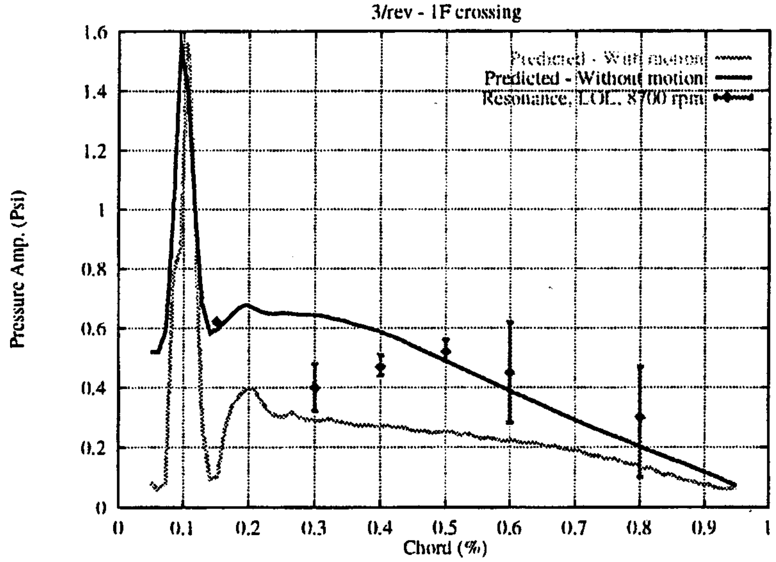

Fig. 12 Unsteady pressure amplitude for the 1F/3EO

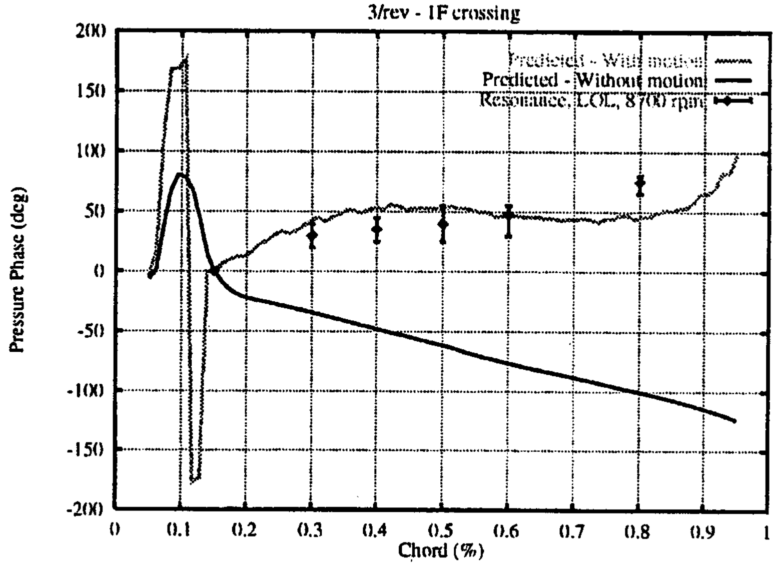

Fig. 13 Unsteady pressure phase for 1F/3EO

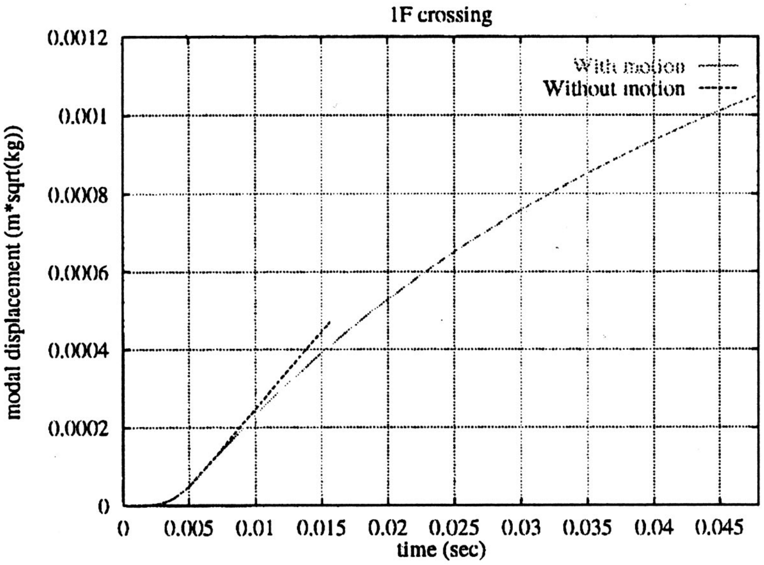

Fig. 14 Amplitude of the 1F modal displacement time history 1F/3EO

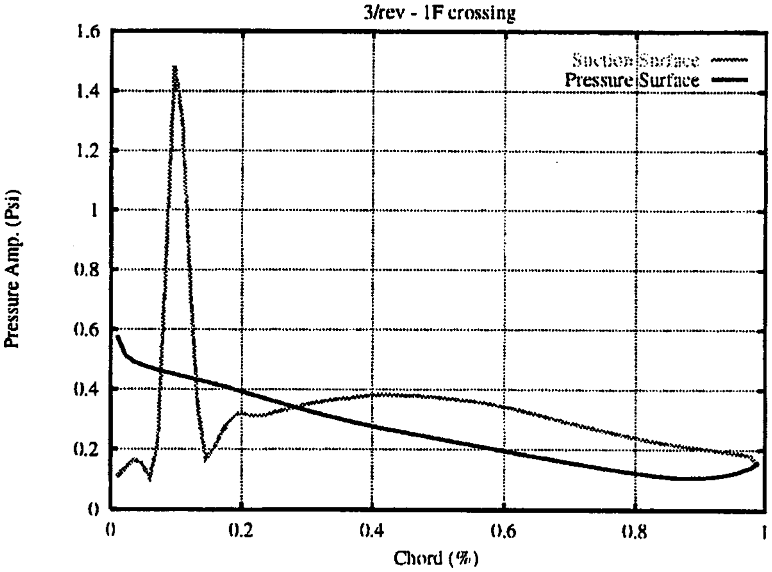

Fig. 15 Unsteady pressure amplitude for 1F/3EO without motion

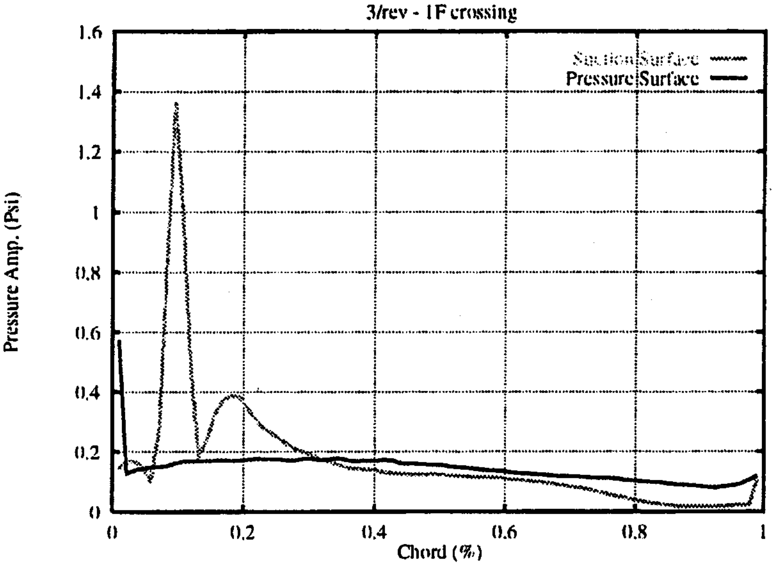

Fig. 16 Unsteady pressure amplitude for 1F/3EO with motion

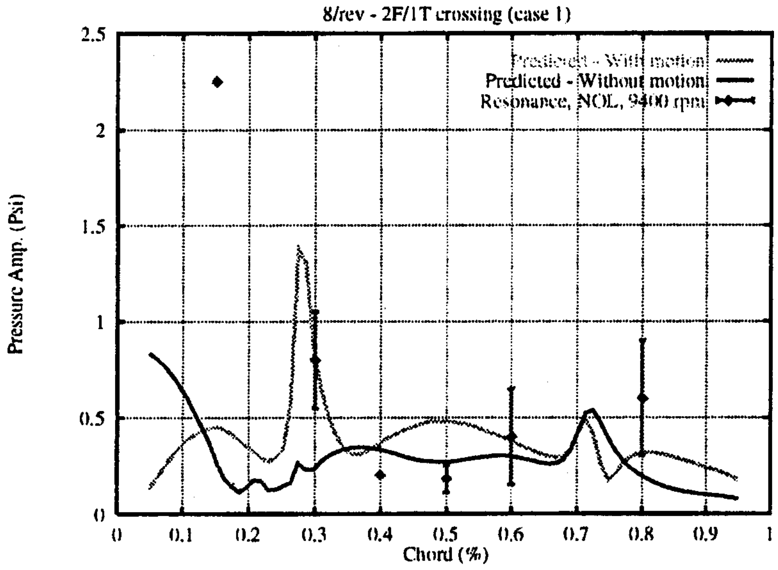

Fig. 17 Unsteady pressure amplitude—2F&T (Case 1)

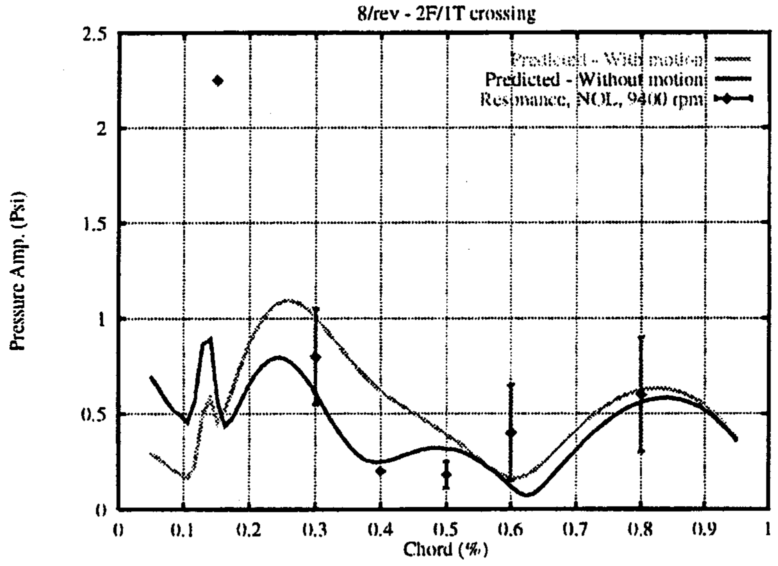

Fig. 18 Unsteady pressure amplitude—2F&1T (Case 2)

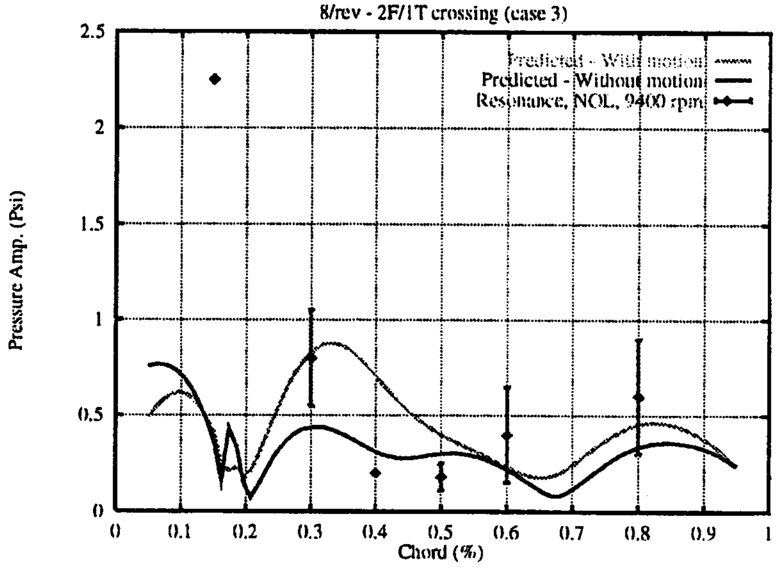

Fig. 19 Unsteady pressure amplitude—2F&1T (Case 3)

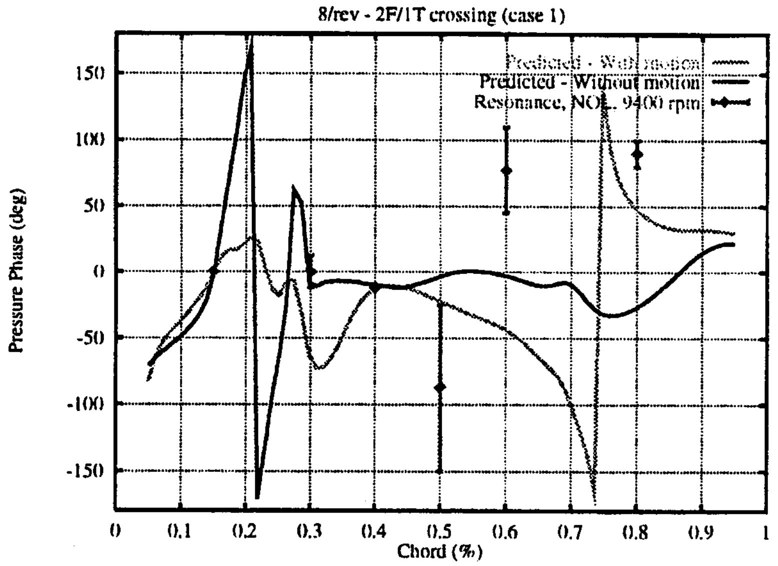

Fig. 20 Unsteady pressure phase—2F&1T (Case 1)

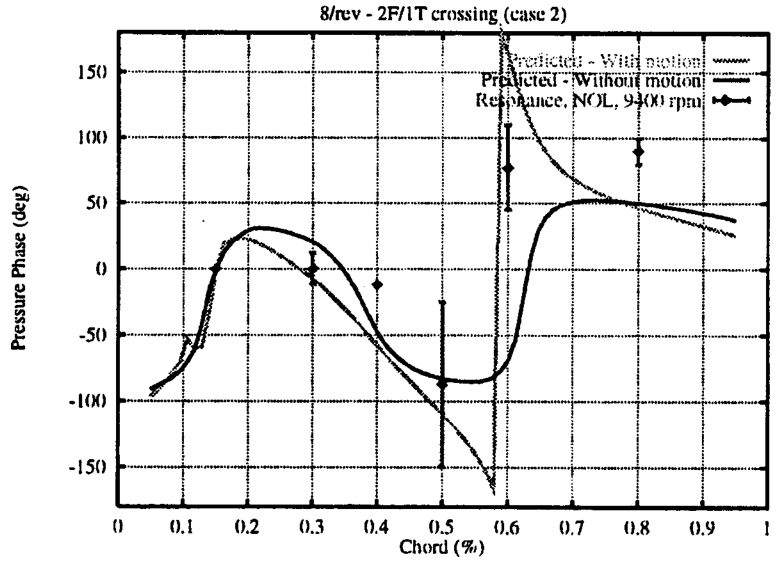

Fig. 21 Unsteady pressure phase—2F&1T (Case 2)

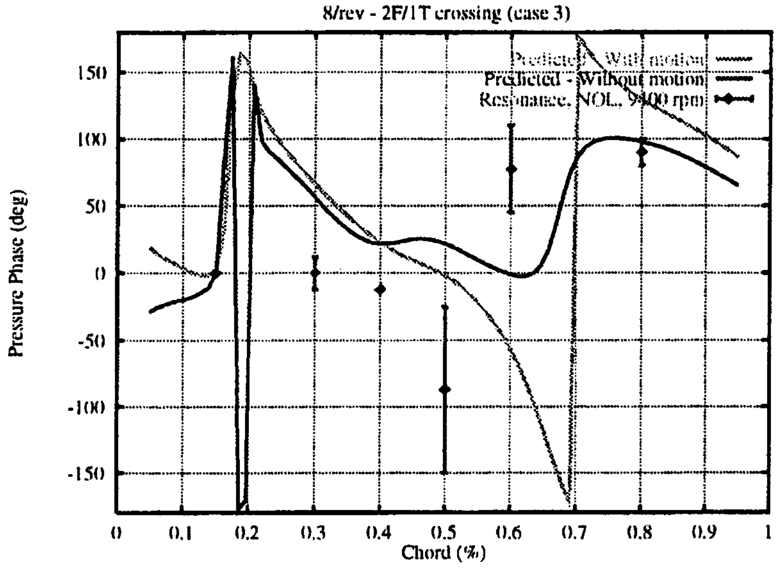

Fig. 22 Unsteady pressure phase—2F&1T (Case 3)

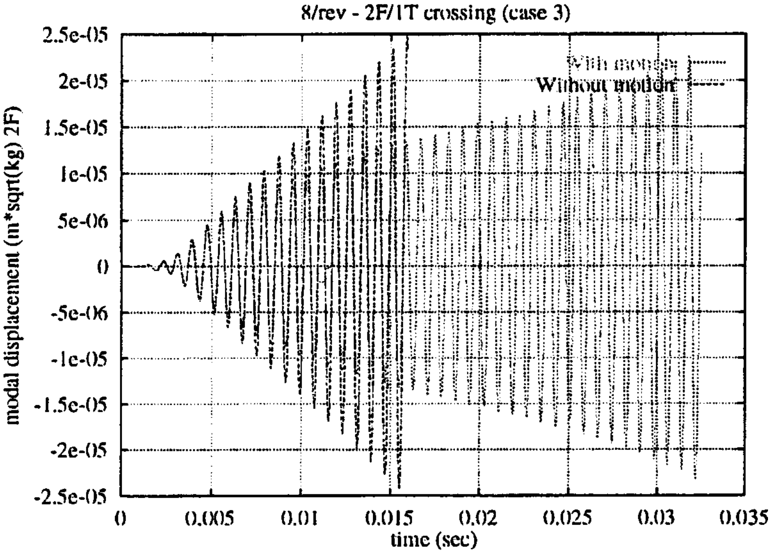

Fig. 23 2F modal displacement amplitude time history—2F&1T/8EO crossing—Case 3)

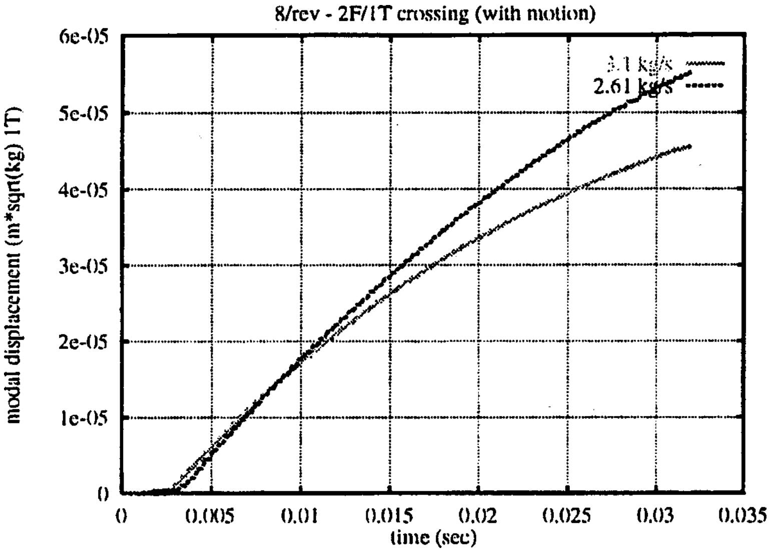

Fig. 24 1T modal displacement amplitude time history—2F&1T/8EO crossing with motion—Cases 1 and 2

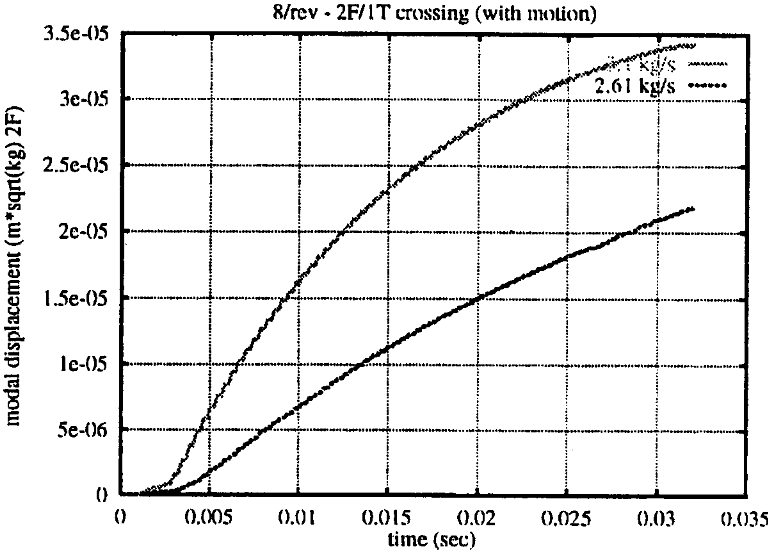

Fig. 25 2F modal displacement time history—2F&IT/8EO crossing with motion—Cases 1 and 2

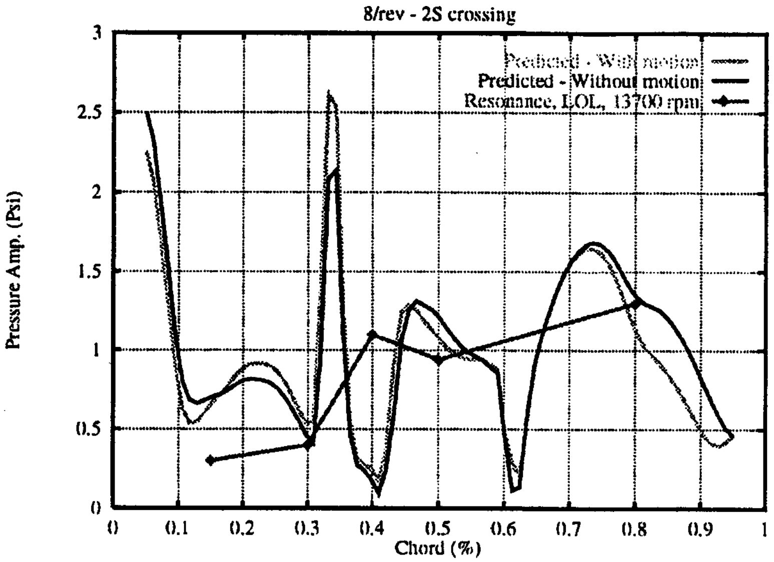

Fig. 26 Unsteady pressure amplitude—2S/8EO

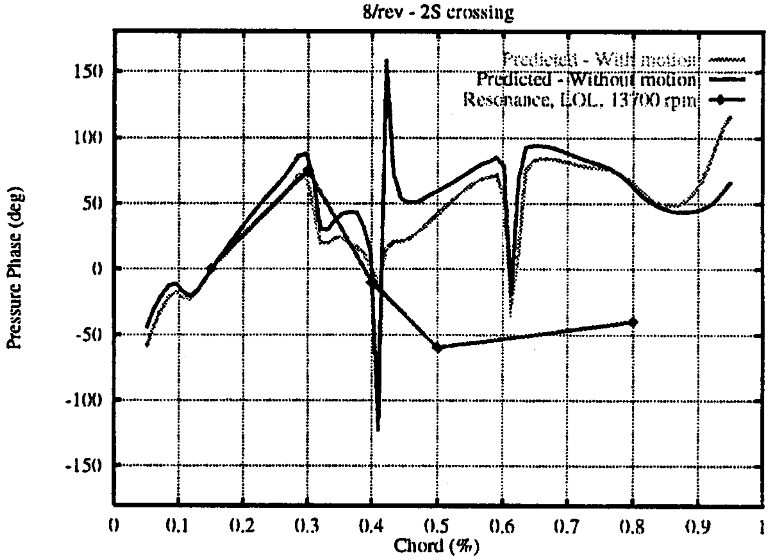

Fig. 27 Unsteady pressure phase—2S/8EO

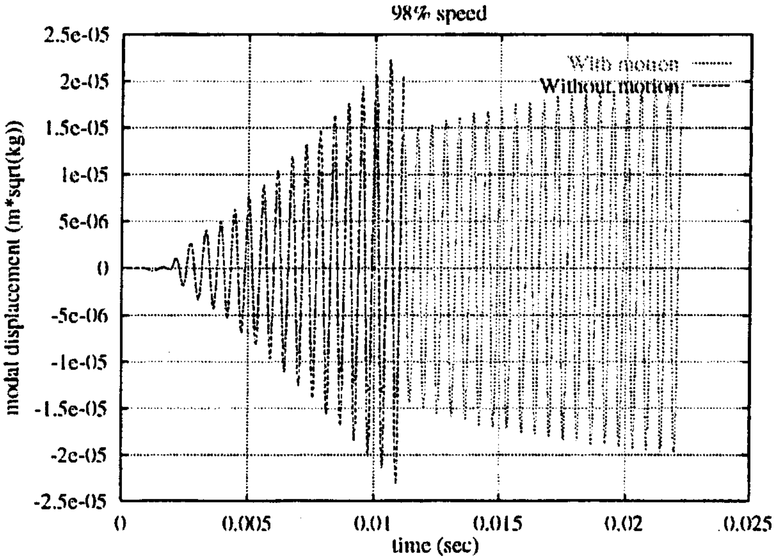

Fig. 28 2S modal displacement time history—2S/8EO crossing close to the leading edge is underestimated in all cases. The predicted phase shown in Figs. 20, 21, and 22 is again in reasonable agreement with the measured data.

The decrease of the mass flow rate will move the shock upstream, consequently the unsteady pressure amplitude close to the leading edge is predicted better. This can clearly be seen by comparing Figs. 18 and 19. In any case, the measurements show significant blade-to-blade differences for both the amplitude and phase, indicating a certain amount of mistuning. Figure 23 shows the time history of the modal displacements with and without blade motion for Case 3. Figures 24 and 25 compare the time history of the modal displacements amplitude for Cases 1 and 2. It is seen from these figures that, as the mass flow decreases, the amplitude of the forcing increases by about 50 percent for the 2F mode but it remains unchanged for the 1T mode. However, the aerodynamic damping decreases by about 20 percent for both modes. The computed maximum vibration amplitudes for the 2F and 1T modes were 0.14 mm and 2.11 mm for Case 1, and 0.25 mm and 2.58 mm for Case 2.

6.3 2S/8EO Crossing. The amplitude and the phase of the predicted and measured unsteady pressures are shown in Figs. 26 and 27, respectively. The phase values are well predicted over the first half of the blade but there is a sign discrepancy from midchord. For this case, the reference transducer on Blade 1 had failed and it is therefore very difficult to obtain the correct phase as no reference signal is available, but the overall shape along the chord can still be used. The predicted phase distribution shows that the phase is nearly constant over the second half of the blade. A comparison of the predictions with and without blade motion shows that the unsteady loading is very similar in both cases. The measurements seem to confirm this trend, the unsteady loading at resonance being very close to the unsteady loading off-resonance, though a small difference can be observed between 30 percent and 40 percent chord. Such a feature is due to the fact that the amplitude of the blade motion is very small, confirmed by the low-vibration signal from the strain gauges. The modal displacement time histories with and without blade motion are shown in Fig. 28. A significant difference is seen between these two cases in spite of the corresponding unsteady pressure variations being very small. No experimental data were available to check this finding.

7 Concluding Remarks

(i) The forced response of the ADLARF transonic fan due to inlet distortions was analyzed for three resonant conditions. The predicted unsteady loading was found to be in reasonable overall agreement with available measured data for all three cases. A number of uncertainties must be borne in mind when comparing the results. First, the measurements are thought to exhibit blade mistuning effects, probably due to instrumentation. Such effects are not taken into account in the numerical model. Second, there were some uncertainties about the aerodynamic boundary conditions and some geometric details. Third, it was assumed that one of the 8EO resonant conditions would involve two blade modes, namely 2F and 1T. The computations showed indeed coupling effects between the two modes.

(ii) The computations were performed both with and without blade motion. It was found that unsteady loading was sensitive to blade vibration for the 2F/1T case. Consequently, the vibration amplitude was also affected. For the 2S/8EO case, the unsteady loading was relatively unaffected by the blade motion but the actual vibration amplitude was sensitive to blade flexibility. Such numerical observations emphasise the need to include the flexibility in forced response calculations. Although some cases may well not be affected by this feature, the most straightforward way of identifying such instances is a full analysis.

Acknowledgments

The authors thank the UK Ministry of Defense and Rolls-Royce plc. for both funding the work and allowing its publication, the U.S. Air Force for supplying the measured data, and Drs. J. G. Marshall and R. M. Hall for coordinating the work as well as for many useful discussions.

References

[1] Giles, M. B., 1987, ''Calculation of Unsteady Wake/Rotor Interaction,'' AIAA Paper No. 87-0006.

[2] Rai, M. M., 1987, ''Navier-Stokes Simulations of Rotor/Stator Interaction Using Patched and Overlaid Grids,'' AIAA J. Propul. Power, **3**, pp. 387–396.

[3] Dawes, W. N., 1988, ''Development of a Three-Dimensional Navier-Stokes Solver for Application to all Types of Turbomachinery,'' ASME Paper 88-GT-70.

[4] Arnone, A., 1995, ''Multigrid Methods for Turbomachinery Navier-Stokes Calculations,'' *Solution Techniques for Large-Scale CFD Problems*, W. G. Habashi, ed., John Wiley and Sons, New York, pp. 293–332.

[5] Denton, J. D., 1990, ''The Calculation of 3D Viscous Flows Through Multistage Turbomachines.'' ASME Paper 90-GT-19.

[6] He, L., 1997, ''Computation of Unsteady Flow Through Steam Turbine Bladerows at Partial Admission,'' IMechE J of Power & Energy, **211**.

[7] Hall, K. C., and Clark, W. S., 1991, ''Calculation of Unsteady Linearized Euler Flows in Cascades Using Harmonically Deforming Grids,'' *6th international Symposium on UAATP*, Univ. of Notre Dame, Sept. 15–19.

[8] Hall, K. C., and Clark, W. S., 1999, ''A Time Linearised Navier-Stokes Analysis of Stall Flutter,'' ASME Paper 99-GT-389.

[9] Green, J. S., and Marshall, J. G., 1999, ''Forced Response Prediction Within the Design Process,'' 3rd European Conference on Turbomachinery, IMECHE Paper C557/121/99.

[10] Vahdati, M., and Imregun, M., 1996, ''A Non-linear Aeroelasticity Analysis of a Fan Blade Using Unstructured Dynamic Meshes.'' J. Mech. Eng. Sci., Part C **210**, pp. 549–563.

[11] Sbardella, L., Sayma, A. I., and Imregun, M., 1997, ''Semi-Unstructured Mesh Generator for Flow Calculations in Axial Turbomachinery Blading,'' *18th International Symposium on Unsteady Aerodynamics and Aeroelasticity of Turbomachines*, T. Franson, ed., Kluwer Academic Publishers, Dordrecht.

[12] Baldwin, B. S., and Barth, T. J., 1991, ''A One-Equation Turbulence Transport Model for High Reynolds Number Wall-Bounded Flows,'' Paper No. AIAA 91-0610.

[13] Swanson, R. C., and Turkel, E., 1992, ''On Central-Difference and Upwind Schemes,'' J. Comput. Phys., **101**, pp. 292–306.

[14] Jorgenson, P. C., and Turkel, E., 1993, ''Central Difference TVD Schemes for Time Dependent and Steady State Problems,'' J. Comput. Phys., **107**, pp. 297–308.

[15] Marshall, J. G., and Imregun, M., 1996, ''An Analysis of the Aeroelastic Behaviour of a Typical Fan Blade With Emphasis on Flutter Mechanisms,'' ASME Paper 96-GT-78.

[16] Ballhaus, W. F., and Goorjian, P. M., 1978, ''Computation of Unsteady Transonic Flows by the Indicial Method,'' AIAA J., **16**, pp. 117–124.

[17] Bendiksen, O. O., 1991, ''A New Approach to Computational Aeroelasticity,'' AIAA Paper 91-0939.

[18] Srivastava, R., Sankar, L. N., Reddy, T. S. R., and Huff, D. L., 1991, ''Application of an Efficient Hybrid Scheme for Aeroelastic Analysis of Advanced Propellers,'' Journal of Propulsion, **7**, pp. 767–775.

[19] Bakhle, M. A., Reddy, T. S. R., and Keith, T. G., 1992, ''Time Domain Flutter Analysis of Cascades Using a Full-Potential Solver,'' AIAA J., **30**, pp. 163–170.

[20] Rabe, D. C., Bolcs, A., and Russler, P., 1995, ''Influence of Inlet Distortion on Transonic Compressor Blades Loading,'' AIAA Paper 95-2461.

[21] Manwaring, S. R., Rabe, D. C., Lorence, C. B., and Wadia, A. R., 1996, ''Inlet Distortion Generated Forced Response of a Low Aspect Ratio Transonic Fan,'' ASME Paper 96-GT-376.

Evaluation of Acoustic Flutter Suppression for Cascade in Transonic Flow

P.-J. Lu

S.-K. Chen

Institute of Aeronautics and Astronautics,
National Cheng Kung University
Tainan, Taiwan R.O.C.

Flutter suppression via actively excited acoustic waves is a new idea proposed recently. The high flutter frequency (typically 50–500 Hz for a fan blade) and stringent space constraint make conventional mechanical type flutter suppression devices difficult to implement for turbomachines. Acoustic means arises as a new alternative which avoids the difficulties associated with the mechanical methods. The objective of this work is to evaluate numerically the transonic flutter suppression concept based on the application of sound waves to two-dimensional cascade configuration. This is performed using a high-resolution Euler code based on a dynamic mesh system. The concept has been tested to determine the effectiveness and limitations of this acoustic method. In a generic bending-torsion flutter study, trailing edge is found to be the optimal forcing location and the control gain phase is crucial for an effective suppression. The P&W fan rig cascade was used as the model to evaluate the acoustic flutter suppression technique. With an appropriate selection of the control logic the flutter margin can be enlarged. Analogous to what were concluded in the isolated airfoil study, for internal excitation, trailing-edge forcing was shown to be optimal since the trailing-edge receptivity still works as the dominant mechanism for generating the acoustically induced airloads. [DOI: 10.1115/1.1365933]

1 Introduction

Flutter suppression using active acoustic excitation is a new idea first realized in the laboratory ([1]). Contrary to the conventional mechanical type flutter suppression devices, the acoustic flutter suppression technique has the advantages of light weight, and most importantly, fast response and virtually unlimited frequency response range. Owing to the high flutter frequency (typically 50–500 Hz for a fan blade), and the stringent space constraint in turbomachines, the acoustic flutter suppression technique is considered in the present research as a prospective alternative. Whether or not this acoustic means can be applied in turbomachines has to be evaluated. The objective of the present research, therefore, is aimed at performing a two-dimensional investigation which can shed some light on the effectiveness and limitations of this acoustic method.

Acoustic control of flow instabilities recently arised as a new research area [2]. The idea of acoustic flutter suppression originates first from the external airfoil flow study. Huang [1] has first conducted a wind tunnel experiment to show that a fluttering airfoil can be suppressed by the application of an actively controlled loudspeaker system. Later Lu and Huang [3] performed a theoretical analysis for incompressible flow and pointed out that the trailing-edge receptivity, rather than the hydraulic analogy proposed ([1]), is the flutter suppression mechanism. The unsteady airloads generated arise mainly from the acoustic/vortical interaction that takes place around the sharp trailing edge. The emitted sound wave serves as a trigger to activate the process of acoustic/vortical wave conversion. These acoustically induced shedding vortices must be counterbalanced by a variation of bound circulation around the solid airfoil in accordance with the Kelvin's theorem. Flutter motion was then suppressed when an appropriate control phase was selected to make the acoustically induced airloads destructively interfere with the unsteady airloads produced by the structural oscillation.

In the incompressible flow analysis ([3]), the acoustic wave nature was masked since the sound speed is infinite. The induced unsteady circulatory airloads and their relative phase lags can be explained by way of Biot-Savart induction of the vorticity field. For transonic flow in which the flow compressibility is essential, the mechanism associated with the unsteady, acoustically generated airload needs to be readdressed. The questions of where the most effective excitation location is and how phase lags are related to the induced airloads are of particular importance for the present acoustic flutter suppression technique. This fundamental investigation was first performed in Section 3 to address the wake effect in a subsonic flow, and then a generic bending-torsion flutter analysis of a two-dimensional cascade follows, aiming at studying the difference in response between isolated airfoil and cascade when excited acoustically.

Owing to the high nonlinearity of transonic flutter, the present work adopts the time-domain approach. Airloads are evaluated by solving the Euler equations formulated on a dynamic mesh, which simulates a bending-torsion flutter model system. This generic aeroelastic system was then integrated to study various problems concerning the effectiveness of the present acoustic method. Suppression of a fluttering blade row in the transonic flow is successfully demonstrated as an appropriate control law is selected.

Subsequent to the fundamental flow investigation and generic flutter analysis, a cascade consisting of real engine fan blades was examined. This blade row consists of the near-tip sections of the P&W fan rig and the two given mean flow conditions are in the transonic region. Acoustic control of a single-degree-of-freedom torsional flutter was performed. Trailing-edge forcing was selected as the internal acoustic excitation. Based on these studies, critical comments on the key issues and limitations were given and some suggestions for the future work were made as well.

2 Numerical Method

2.1 Aerodynamic Flow Solver. The present problem is concerned with the acoustic/vortical wave interaction around a

---

Contributed by the International Gas Turbine Institute (IGTI) of THE AMERICAN SOCIETY OF MECHANICAL ENGINEERS for publication in the ASME JOURNAL OF ENGINEERING FOR GAS TURBINES AND POWER. Paper presented at the International Gas Turbine and Aeroengine Congress and Exhibition, Stockholm, Sweden, June 2–5, 1998; ASME Paper 98-GT-065. Manuscript received by the IGTI Division Feb. 1998; final revision received by the ASME Headquarters Nov. 2000. Associate Editor: R. Kielb.

solid moving surface. This acoustically induced vorticity production at the trailing edge might be taken as an inviscid result, since the role of viscosity can be accounted for via the satisfaction of Kutta condition. Based on these arguments, Euler equations are adopted as the governing equations to be solved. In the construction of the numerical flow solver, emphasis was placed upon the reduction of the numerical dissipation and dispersion effects, as well as the treatment of the boundary conditions. Special care involving the numerical procedure of discretizing the flux terms in a dynamic mesh system was also considered. For detailed explanations please see Lu et al. [4,5]. In the following only main features of the scheme are outlined.

2.1.1 Spatial Discretization and Time Marching. The unsteady, two-dimensional inviscid Euler equations are expressed in an integral conservation form,

$$\frac{\partial}{\partial t}\int_V U\,dV+\oint_S \mathbf{n}\cdot\mathbf{F}\,ds=0. \tag{1}$$

In Eq. (1) the set of conservative variables U and the normal flux vector $F_n=\mathbf{n}\cdot\mathbf{F}$ are given, respectively, by the column vectors:

$$U=\begin{bmatrix}\rho\\ \rho u\\ \rho v\\ \rho e\end{bmatrix},\quad F_n=\begin{bmatrix}\rho(u_n-v_n)\\ \rho u(u_n-v_n)+pn_x\\ \rho v(u_n-v_n)+pn_y\\ \rho e(u_n-v_n)+pu_n\end{bmatrix} \tag{2}$$

where $u_n=\mathbf{u}\cdot\mathbf{n}$ is the normal velocity component, and $v_n=\mathbf{v}_g\cdot\mathbf{n}$ is the normal grid velocity component with n_x and n_y defined as the projections of the unit normal $\mathbf{n}$ in the Cartesian x and y-directions. The variables p, ρ, u, v, and e denote the pressure, density, Cartesian velocity components, and specific total energy, respectively. In closing the above governing equations, the thermodynamic state equation of a perfect gas is required,

$$p=(\gamma-1)\left(\rho e-\frac{\rho}{2}\mathbf{u}\cdot\mathbf{u}\right), \tag{3}$$

in which the specific heat ratio is given by $\gamma=1.4$.

Applying finite-volume discretization, one can approximate the flux term by the use of an upwind flux-difference scheme ([6]) to result in a semi-discretized system of ordinary differential equations. This system of ordinary differential equations is then integrated in a time-accurate sense using the explicit three-stage Runge-Kutta time stepping method ([7]).

The spatial accuracy of this finite-volume discretization depends on the construction of the numerical flux function specified at the cell interface. In this study, Osher-Chakravarthy MUSCL type upwind scheme ([7]) based on the Roe splitting ([8]) is employed. Modification ([4,5]) has been made on the interpolation of cell interface values to improve the accuracy of the scheme. This modified MUSCL type upwind TVD scheme, which considers the grid nonuniformity effect, takes the following form:

$$\begin{aligned}U^-_{i+1/2}&=U_i+\chi_i\sum_m\left[(\zeta_i+2\phi\sigma_i)\tilde{\alpha}^m_{i+1/2}\right.\\&\qquad\left.+\frac{1}{\zeta_i}(1-2\phi\sigma_i)\tilde{\tilde{\alpha}}^m_{i-1/2}\right]r^m_i\\U^+_{i-1/2}&=U_i-\chi_i\sum_m\left[(\zeta_i-2\phi\sigma_i)\tilde{\alpha}^m_{i+1/2}\right.\\&\qquad\left.+\frac{1}{\zeta_i}(1+2\phi\sigma_i)\tilde{\tilde{\alpha}}^m_{i-1/2}\right]r^m_i.\end{aligned} \tag{4}$$

The notations appearing in Eq. (4) can be found in Lu et al. [5]. The magnitude of acoustic disturbance is usually so small that it is very easy to be contaminated. It has been shown ([5]) that the present improvement, Eq. (4), is meaningful for a time-accurate acoustic computation.

2.1.2 Surface Boundary Condition Treatment. Sound waves emitted from a solid surface can be taken as a monopole whose strength or volume flowrate is specified. For a cell-centered finite volume Euler method, the physical boundary condition specified on the surface, with or without blowing or suction, usually does not involve directly the static pressure. Static pressure required by the numerical method ought to be derived using momentum equations subject to the given nonpermeable or specified normal flux condition:

$$(\mathbf{u}-\mathbf{v}_g)\cdot\mathbf{n}=\begin{cases}0 & \text{for solid wall}\\ v_\omega & \text{for wall with blowing or suction}\end{cases} \tag{5}$$

in which v_w is the imposed surface normal velocity which characterizes the monopole strength. The density of the emitted volume flux can be extrapolated from the adjacent interior cell-averaged values. The determination of the surface pressure, however, must invoke the momentum equations which, as expressed in the computational domain (ξ,η,τ), take the form ([9])

$$\begin{aligned}\sqrt{\eta_x^2+\eta_y^2}\frac{\partial p}{\partial n}=\rho\Bigg[&\frac{\partial}{\partial\tau}\eta_t+u\frac{\partial}{\partial\tau}\eta_x+v\frac{\partial}{\partial\tau}\eta_y\\&-\overline{U}\left(\eta_x\frac{\partial u}{\partial\xi}+\eta_y\frac{\partial v}{\partial\xi}\right)-\Pi_\omega\Bigg]\end{aligned} \tag{6}$$

$$\Pi_\omega=\begin{cases}0 & \text{for solid wall}\\ \dfrac{\partial}{\partial t}\overline{V}_\omega+\overline{V}_\omega\left(\dfrac{\partial u}{\partial\eta}\eta_x+\dfrac{\partial v}{\partial\eta}\eta_x\right) & \text{for wall with blowing or suction}\end{cases} \tag{7}$$

where $\overline{U}[=(\mathbf{u}-\mathbf{v}_g)\cdot\nabla\xi]$ is the ξ-contravariant velocity, and $\overline{V}_\omega(=v_\omega\sqrt{\eta_x^2+\eta_y^2})$ is the given surface volume flux. With all the terms in Eqs. (6) and (7) being properly treated and differenced, $\partial p/\partial n$ can be calculated readily, and the wall pressure can thus be extrapolated using this gradient value and the adjacent cell-centered quantity.

2.1.3 Inflow/Outflow Boundary Condition Treatment. At the inflow and outflow boundaries nonreflective boundary condition ([10,11]) treatments are employed. Unlike the external flow simulations where the outer boundaries are situated far away from the solid surface, much delicated treatments must be devised for internal flow computations to assure that the nonphysical spurious waves would not contaminate the acoustic simulations. Both one-dimensional and two-dimensional inflow/outflow boundary condition treatments of Giles [12] were used for the present study. Usually one-dimensional treatment is sufficient should the boundaries are placed remote enough from the blade row.

2.1.4 Dynamics Grid Method. In the aeroelastic computation the grid system must be adapted to account for the body deformation and/or the vibrational motion. Care must therefore be exercised in the determination of the cell boundary velocity since the computation of the fluxes across the boundaries would be affected by this boundary movement. Thus, to avoid errors induced by the mesh movement, the geometric conservation law ([13]) needs to be incorporated in addition to the basic physical conservation laws used.

In the previous work ([4]), we have developed a finite volume scheme based on a dynamic grid system. The geometric and physical conservation laws are solved together using an explicit Runge-Kutta time marching scheme, with appropriate cell boundary velocity defined for each internal stage.

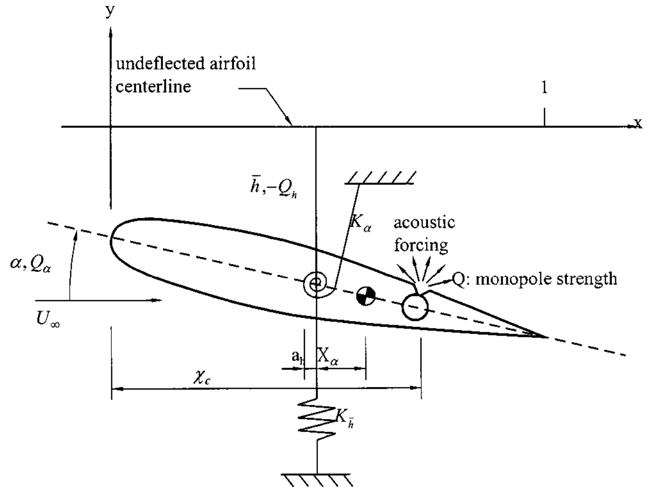

Fig. 1 Schematic of typical section model with acoustic excitation

2.2 Aeroelastic Time Marching. A typical section model (see Fig. 1) consisting of bending and torsion modes is used for the following investigation (see Section 4). The aeroelastic governing equations for each blade thus read

$$\begin{aligned} m\frac{d^2\bar{h}}{dt^2}+S_\alpha\frac{d^2\alpha}{dt^2}+K_{\bar{h}}\bar{h}&=Q_{\bar{h}} \\ S_\alpha\frac{d^2\bar{h}}{dt^2}+I_\alpha\frac{d^2\alpha}{dt^2}+K_\alpha\alpha&=Q_\alpha \end{aligned} \tag{8}$$

in which $\bar{h}$ and α are the bending and torsion displacements; m, S_α, and I_α are the mass, static mass moment, and mass moment of inertia of the typical section (per unit span), respectively; $K_{\bar{h}}$ and K_α are the spring constants for bending and torsion motions, and $Q_{\bar{h}}$ and Q_α are the generalized aerodynamic forces for bending and torsion modes. In this model problem, no structural damping is included, therefore, the damping of this dynamic system, positive or negative, comes entirely from the aerodynamic contribution. Sound waves are emitted from a slot near the trailing edge (see Fig. 1), with the monopole strength specified or actively actuated.

The governing equations, as appropriately nondimensionalized ([4,9]), can be put in a state-space form. This state-space system can be time marched using an aeroelastic time integrator proposed by Edwards et al. [14]. This integrator has been demonstrated accurate and robust since full advantage of the linearity of the structural operator has been taken.

3 Fundamental Wave Interaction Mechanism

3.1 Theoretical Background. In the previous analysis ([3]), the mechanism of acoustic/vortical interaction around a sharp trailing edge and the characteristics of the induced circulatory and noncirculatory airloads were explained. Since the flow analyzed was incompressible, the flow-field was therefore determined by Biot-Savart induction, leaving no actual acoustic characteristics in the construct of the physical mechanism. As transonic flow is of concern, the finite sound speed is by all means important. Important issues such as shock formation, shock movement, etc., are all centered around the acoustic wave propagation and interaction phenomenon. In fact, for the past decades the study of transonic aeroelasticity has been benefited by improved understanding of the shock motions ([15,16]), in which particular emphasis has been placed on the study of phase lag between the driving oscillation and the induced airloads. Legitimate questions may arise as how unsteady airloads are generated and by what mechanism can these instability-related relative phase lags be achieved as acoustic excitations are applied to the transonic flow.

The phenomenon of release of shedding vortices from the trailing edge has been an important acoustic/aerodynamic interaction problem in which the satisfaction of Kutta condition plays a critical role ([17,18]). Moreover, it has been shown in Lu and Huang [3] that the effectiveness of the present acoustic excitation method is also guaranteed by the satisfaction of Kutta condition at the trailing edge. For flows having supersonic trailing edges, the present acoustic excitation method no longer works ([9]). This is because that continuous smooth flow or the Kutta condition is not required in the supersonic trailing-edge flows. This basic mechanism of vortices released from trailing edge to avoid singularities occurring at the sharp edge is common for both incompressible and compressible subsonic flows. This so-called trailing-edge receptivity phenomenon has been understood for quite some time, and in many cases simulated we found that specifying forcing location closest to the trailing edge is always the best strategy, because it can exert the largest disturbances to the trailing edge, hence making the maximal induced unsteady airloads out of the acoustic excitation. Another problem of concern in transonic aeroelasticity is the phase-related upstream influence, or the role of the acoustically generated shedding vortices, to the original aerodynamic field. This problem has not yet been answered satisfactorily. This sound emission associated with the motion of vortical structures appears in many aeroacoustic problems which have been analyzed with fruitful achievements ([19–21]). In order not to get into great confusion at the beginning, we first ignore the presence of shock waves in the following compressible flow investigation, and focus our attention on the upstream influence provided by the shedding vortices ever since their inception from the trailing edge.

Goldstein adopted the concept of splitting the velocity field into a potential and a solenoidal part ([22,23]). The acoustic wave phenomenon in a free space is then assigned completely to the potential part, whereas the vorticity of the flow to the solenoidal part. By further utilizing the linearization of an initially potential flow assumption, Goldstein [24] derived a formula that explains the role of vortical disturbances to the acoustic field:

$$\mathbf{u}=\nabla\phi+\mathbf{v}, \quad \nabla\cdot\mathbf{v}=0 \tag{9a}$$

$$p'=-\rho_0\frac{D_0\phi}{Dt}, \quad \frac{D_0}{Dt}=\frac{\partial}{\partial t}+U\cdot\nabla \tag{9b}$$

$$\frac{D_0}{Dt}\left(\frac{1}{c_0^2}\frac{D_0\phi}{Dt}\right)-\frac{1}{\rho_0}\nabla\cdot(\rho_0\nabla\phi)=\frac{1}{\rho_0}\nabla\cdot\rho_0\mathbf{v}. \tag{9c}$$

Equation (9*c*) clearly indicates that the right-hand side rotational field works as a source term to the original irrotational mean flow. Explicit form of **v**, for instance, can be determined for problems of gust (or vortical wave) convecting from upstream. Equations (9*a*), (9*b*), and (9*c*) have been used to model the wake induced disturbances in turbomachines ([25]) and can now lend themselves to the present acoustic excitation problem. The difference between the in-flow distortion and the present problem lies in, first, the place to determine the vortical velocity **v** for the present problem is the trailing edge rather than the upstream; and, second, unlike the gust flow problem the strength of the present trailing-edge vorticity is not known *a priori*. Nonetheless, the source term of Eq. (9*c*) identifies the role of shedding vortices as sound sources that radiate acoustic waves to the upstream to influence the aerodynamic field around the airfoil surface. By this token, vorticities in the wake can be taken as downstream drifting sound sources whose current position and connection to the trailing edge (which determines the strength and phase of the shedding vortices to the bound circulation) are important elements that may contribute to the phase lag of the induced unsteady airloads.

Equations (9*a*), (9*b*), and (9*c*), when applied to model the present acoustic excitation problem, are much more difficult to

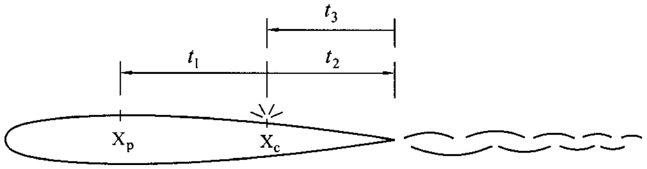

Fig. 2 A schematic illustrating the different time intervals characterizing the wave interaction phenomenon

solve than for the in-flow distortion problem. The reason has been illustrated before in the case of incompressible acoustic/vortical wave conversion around the trailing edge ([3]). The right-hand side forcing term of Eq. (9*c*) is no longer given, but behaving as a function dependent on the acoustic potential ϕ and closing back in a closed-loop manner with the left-hand side acoustic operator.

The present aeroacoustic field is to be solved by a numerical procedure directly dealing with the Euler equations. In other words, all the potential and vortical contents of the acoustically excited flow should be obtainable if the resolution of the numerical simulation is sufficient. Goldstein's model is used only as a conceptual guide to process and explain the data simulated, as shown in the following.

3.2 Numerical Investigation. As the sound wave is emitted from a source on the airfoil surface, there are two physical mechanisms that can contribute to the disturbances: one is the emitted acoustic wave and the other the vorticity wave shedding from the trailing edge. The simulated numerical results do not partition themselves into contributions associated either with the monopole on the surface or with the vortices in the wake. Therefore, special design must be used to split the disturbance content. An impulse forcing case described in the following is a designed test that can achieve this wave splitting and identification purpose.

The first numerical experiment performed is an impulse acoustic excitation case, in which the time instants characterizing acoustic wave fronts sent by the forcing monopole and the shedding vortices can be separated. The model considered is a NACA64A006 airfoil in a subsonic freestream of Mach number $M_\infty = 0.5$ held with zero angle of attack. The sound sources are symmetrically located at $X_C = 0.75$ on both sides of the airfoil, and the pressure history at $X_P = 0.25$ on the upper surface is recorded. The impulse forcing function selected is a half-period sine function with peak strength $Q_o = 5\times10^{-3}$ and a duration $\Delta t = 0.5$. In the following discussion we will use, respectively, ''symmetric'' and ''antisymmetric'' forcings to represent in-phase and out-of-phase harmonic excitations of the two monopole sources located on the two sides of the airfoil. The freestream Mach number ($M_\infty = 0.5$) is purposely chosen to reveal the compressibility effect, while avoiding the nonlinear behavior of shock formation.

In Fig. 2 sketched the idea of time intervals characterizing several key time periods that will be used in the following discussions. The time t_1 represents the elapsed time for an initial wave front to reach the pressure recording position X_P from the forcing monopole at X_C. Time t_2, however, indicates the instant when the downstream propagated acoustic wave first arrives at the trailing edge. Vorticity wave will be generated, via the acoustic/vortical wave conversion mechanism, ever since the instant t_2. According to the Goldstein's model, the upstream acoustic waves will be emitted spontaneously accompanying the occurrence of these shedding vortices. The first wavefront sent by this shedding vortex can be approximated by assuming that the vortex is located at the trailing edge. Hence, time t_3 represents the time interval for this vortex-induced sound to propagate upstream from the trailing edge to the forcing location. In the evaluation of these time intervals, the time duration for an acoustic wave to travel over a distance from X_1 to X_2 can be estimated by

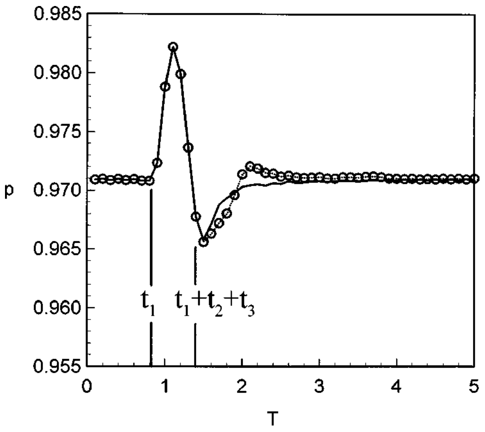

Fig. 3 Pressure histories induced by impulsive excitations on a NACA64A006 airfoil. ($M_\infty=0.5$, $\alpha=0$, $Q_o=5.0$E-3, $\Delta t=0.5$, $X_C=0.75$, $X_P=0.25$; ——: symmetric forcing, and ○: asymmetric forcing).

$$t = \int_{X_1}^{X_2} \frac{dx}{|\overline{u} \pm \overline{c}|} \tag{10}$$

where $\overline{u} \pm \overline{c}$ are the mean flow sound speeds and the "±" sign is selected depending on which direction the wave is propagated. Thus, for the present case the time t_1 for acoustic wave to travel upstream from X_C to X_P is approximately 0.83; the time for vorticity to start shedding from the trailing edge is $t_2 = 0.14$; and the time t_3 that the vortex-induced sound propagates upstream from the trailing edge to the forcing location is 0.42. It is seen that the vorticity shedding in response to the trailing-edge excitation occurs much earlier than the upstream propagated acoustic front to reach the receiving position X_P.

A symmetric forcing test is firstly performed, in which the vorticity wave is absent so that the pressure recorded is caused purely by the upstream propagated sound wave. Figure 3 shows this symmetrically forced pressure history (solid line). The pressure trace at X_P is seen starting varying at $t = t_1$, then reaching its maximum value around $t = 1.05$ when the peak pressure disturbance arrives at X_P. The recorded pressure then gradually returns to its original mean-flow value as sound waves leave the airfoil. The antisymmetric forcing result is also plotted in Fig. 3. The pressure history (open circle) is seen first coincident with that of the symmetric case, and then departs at $t = t_1 + t_2 + t_3 = 1.4$, reaches its second local maximum at $t = 2.1$, and returns to the mean value asymptotically.

In the antisymmetric forcing test, vorticity is shed from the trailing edge after the instance t_2, but the pressure recorded at X_P is seen nearly unchanged as compared to the symmetric forcing case until $t = 1.4$, the instant that the vortex-induced upstream propagated acoustic wave first reaches X_P. Thus, the way that vorticity disturbs the aerodynamic flow-field indeed follows the Goldstein's theoretical model.

The induced lift can better be presented using circulatory information. Figure 4 illustrates the lift coefficient and the bound circulation histories induced. Symmetric forcing yields no net loading nor circulation around the airfoil, contrary to the antisymmetric forcing case in which both airload and circulation are produced. Note that the peak circulation occurs around $t = 0.3$, but the upstream pressure recording point does not detect at this moment the downstream activity of vorticity production. This signifies the finite sound speed effect in the compressible flow and affirms that the upstream pressure disturbances are associated entirely with the acoustic waves.

The split of the two pressure traces (see Fig. 3) beyond $t = 1.4$ shows the effect contributed by the wake vorticity. Not only the magnitude differs but also the peak shifts. This peak shift phe-

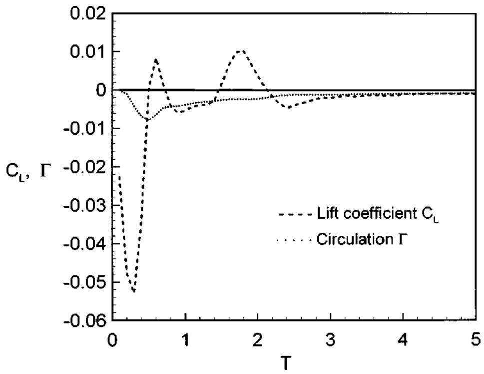

Fig. 4 Lift coefficient and circulation histories induced by asymmetric impulsive excitation on a NACA64A006 airfoil ($M_\infty=0.5$, $\alpha=0$, $Q_o=5.0\text{E-}3$, $\Delta t=0.5$, and $X_C=0.75$)

nomenon (around $t=2$) implies that the wake can alter the phase of the pressure and hence the resultant forces acting on the airfoil. This reaffirms the conclusions obtained in the incompressible analysis. Acoustic wave acts indeed as a trigger rather than a control force for the present acoustic control technique. Phase shift is attributed to the acoustically induced vorticity which, under appropriate manipulation, can result in destructive interference to suppress the flutter instability.

4 Optimal Forcing Location Study

The following numerical experiment is designed to find the optimal forcing location for the cascade blade row and the isolated airfoil. The acoustic forcing model is a surface harmonic monopole, with strength defined by $Q(t)=\sin(\omega t)$, $\omega=0.4$. The isolated airfoil case considers an externally unbounded NACA0006 airfoil in a freestream ($M_\infty=0.85$) with zero angle of attack, whereas the cascade case simulated is a nonstaggered NACA0006 blade row

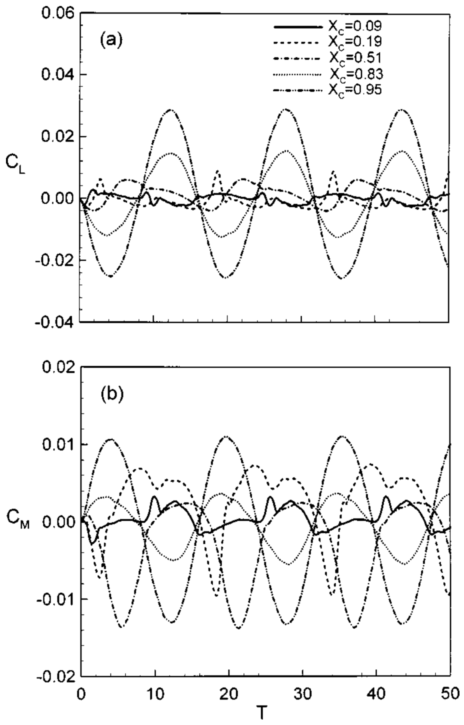

Fig. 7 Acoustically induced unsteady (*a*) life and (*b*) pitching moment coefficient histories on a NACA0006 cascade ($M_\infty=0.85$, $\alpha=0$, $p_e=1.10p_\infty$, $G=1.0$, $Q=Q_o\sin\omega t$, $Q_o=5.0\text{E-}3$, and $\omega=0.4$)

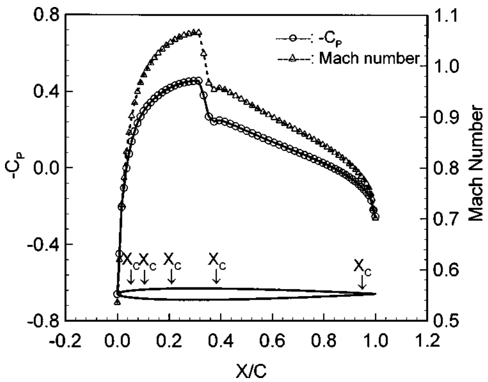

Fig. 5 Steady-state pressure and Mach number distributions on a NACA0006 airfoil ($M_\infty=0.85$, $\alpha=0$)

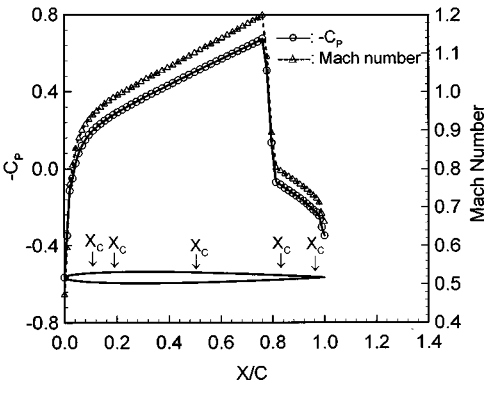

Fig. 6 Steady-state pressure and Mach number distributions on a NACA0006 cascade ($M_\infty=0.85$, $\alpha=0$, $p_e=1.10p_\infty$, $G=1.0$, and $\sigma=0$ deg)

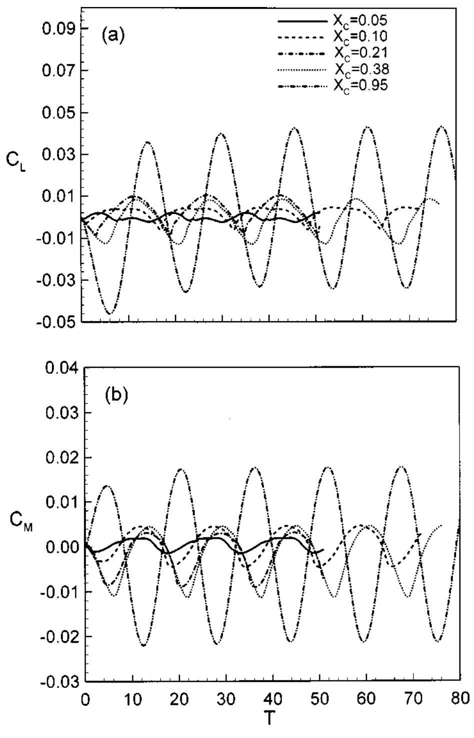

Fig. 8 Acoustically induced unsteady (*a*) lift and (*b*) pitching moment coefficient histories on a NACA0006 airfoil ($M_\infty=0.85$, $\alpha=0$, $Q=Q_o\sin\omega t$, $Q_o=5.0\text{E-}3$, and $\omega=0.4$)

subjected to the following conditions: $M_\infty=0.85$, solidity=1.0, zero incident angle, $p_e=1.10p_\infty$, in which p_e is the back static pressure specified at four chordlengths downstream from the trailing edge.

Figures 5 and 6 show the mean flow and wall pressure distributions associated with the isolated airfoil and the cascade, respectively. It can be seen that these two flow-fields are quite different, indicating the effects of blade row and the adverse pressure gradient existing in the turbomachine.

There are five locations that are selected for imposing acoustic excitations, as shown in Figs. 5 and 6. In the cascade case, these five excitation locations are $X_C=0.95$ (near trailing edge), $X_C=0.83$ (near shock root), $X_C=0.51$ (in between shock root and sonic point), $X_C=0.19$ (near sonic point), and $X_C=0.09$ (in between sonic point and leading edge). In the isolated airfoil case, however, the five locations selected for the zones as described in the cascade case are $X_C=0.95$, 0.38, 0.21, 0.10, and 0.05. In Figs. 7 and 8 illustrated the lift and pitching moment coefficient histories of the acoustically induced airloads for the cascade and the isolated blade, respectively. It is seen that trailing edge is the most effective forcing area and trailing-edge receptivity still holds true for both configurations.

5 Generic Flutter Control Investigation

5.1 Acoustic Flutter Suppression Test. Suppression of a flutter instability using active acoustic excitation has been shown possible for an isolated airfoil ([4]). As this acoustic technique is to be extended to the cascade flow, some modifications have to be considered. Conceptually, an internal cascade flow possesses much complex wave phenomena than does an externally unbounded isolated airfoil flow. Waves can be reflected back and forth in a cascade passage and the neighboring oscillating blades might act as additional sound sources. These extraneous sound sources are in general not synchronous when interblade phase angles are present.

To address these special problems regarding the suppression of a fluttering cascade, we use in the following a bending-torsion aeroelastic model. The readers may refer to Bendikson and Hsiao [26] for a detailed description of the structure model and the nonmenclacture involved. Here the fluttering cascade adopted for examination has no stagger angle, vibrating with 180-deg interblade phase angle in a mean flow as defined previously in Section 4. Figure 9 shows the responses when active acoustic excitation is applied. It is observed that although the flutter boundary has been exceeded for 20 percent, the instability can still be suppressed as an actively controlled acoustic excitation is applied.

Experiences gained previous ([4]) indicate that the feedback control logic design is very crucial. The present control logic is defined in relation to the torsional response:

$$Q(t)=G_a\cdot\alpha(t-\tau) \tag{11}$$

in which G_a is the control gain which determines the amplitude of the source strength. The time delay τ in Eq. (11) can be converted into phase angle in the frequency domain. The flutter frequency and damping ratio are determined using the model identification technique ([27])

$$X_i(t)=a_{i,0}+\sum_{j=1}^{m} e^{\sigma_i t}[a_{i,j}\cos(\omega_j t)+b_{i,j}\sin(\omega_j t)]$$
$$i=1,2,\ldots,m. \tag{12}$$

Figure 10 shows whether a fluttering cascade can be suppressed when varying the control gain phase. For the present case, the most effective control law is found with the in-phase feedback gain, $\phi=0$. A positive damping rate appearing between 90 deg$<\phi<$315 deg means that the original flutter instability is enhanced, indicating that a wrong choice of control gain phase will lead to a reversed and dangerous situation.

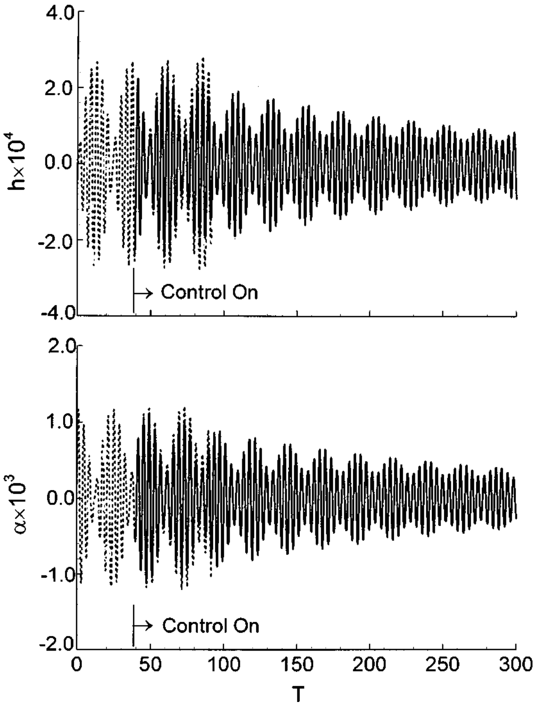

Fig. 9 Transient response for acoustically suppressed flutter at $M_\infty=0.85$, $\alpha_m=0.0$ deg, $p_e=1.10p_\infty$, $\sigma=180$ deg, $G=1.0$, $\mu=192.0$, $a_h=-0.24$, $\omega_h/\omega_\alpha=1.0$, $V^*=1.2V_F^*$, $r_\alpha=0.4735$, $X_\alpha=0.076$, $G_\alpha=0.5$, $\phi=0$, $X_C=0.95$; (*a*) plunging mode and (*b*) pitching mode (——:open-loop no-control solution, and ——: closed-loop acoustical-control solution)

5.2 Acoustic Energy Supply. How much acoustic energy ought to be supplied for flutter suppression is a problem concerned in the practical design of the acoustic actuator system. It was concluded in the previous investigation ([4]) that an effective suppression can only be achieved when the flutter amplitude is small. This constraint simply comes from the nature of the acoustics, namely, the pressure fluctuation of a sound wave is in general very small. Here we use the energy content to measure the power consumption of the acoustic device used:

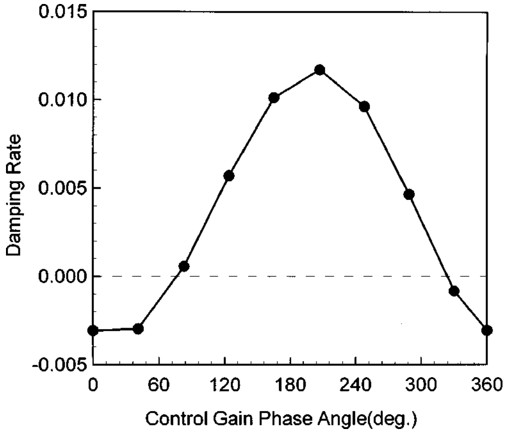

Fig. 10 Damping rate versus phase angle using close-loop feedback control on NACA0006 cascade ($M_\infty=0.85$, $\alpha_m=0$ deg, $p_e=1.10p_\infty$, $\sigma=180$ deg, $G=1.0$, $\mu=192.0$, $a_h=-0.24$, $\omega_h/\omega_\alpha=1.0$, $V^*=1.2V_F^*$, $r_\alpha=0.4735$, $X_\alpha=0.076$, $G_\alpha=0.5$, and $X_C=0.95$)

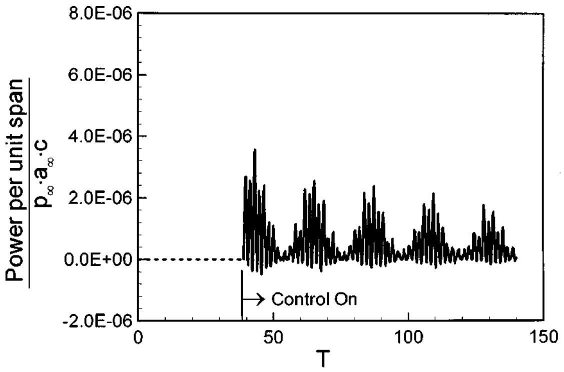

Fig. 11 Acoustic energy supply histories of an acoustically suppressed flutter motion (NACA0006 cascade, $M_\infty = 0.85$, $\alpha_m = 0.0$ deg, $p_e = 1.10 p_\infty$, $\sigma = 180$ deg, $G = 1.0$, $\mu = 192.0$, $a_h = -0.24$, $\omega_h/\omega_\alpha = 1.0$, $V^* = 1.1 V_F^*$, $r_\alpha = 0.4735$, $X_\alpha = 0.076$, $G_\alpha = 0.5$, $\phi = 0$, and $X_C = 0.95$)

$$\int_v \left(\frac{\partial E}{\partial \tau} + \nabla \cdot \mathbf{I} \right) dV = \sum_i p_i' Q_i \tag{13}$$

where E and $\mathbf{I}$ are the acoustic energy and acoustic flux vectors, respectively, ([22]). This relationship describes the energy contents of the stored acoustic energy in the control volume, $\int EdV$, the energy flux across the control surfaces, $\oint_S \mathbf{I} \cdot \mathbf{n} ds$, and the acoustic energy supplied from a monopole source located on the solid surface, $\Sigma_i p_i' Q_i$.

The case simulated is the same cascade studied in Section 5.1, except that the reduced velocity is ten percent above the flutter boundary. The power supplied as acoustic control is switched on is illustrated in Fig. 11. The maximum amplitude of the power required, as nondimensionalized by $p_\infty a_\infty c$ (a_∞ sound speed, c chord length), is around 3×10^{-6}. For a flight altitude of 10^4 m, a blade of 0.5 m in chord length demands a sound generator that can supply, approximately, 8-Watt power output per unit span (meter). This power consumption level is encouraging, however, it should be noted that the losses are not accounted for in this evaluation. To have a closer view of the sound source strength used, we can take a look of the averaged normal velocity $\overline{v_\omega}$ around the monopole. The maximum averaged velocity fluctuation found for the present case is about 3 m/s. This forcing amplitude is comparable to those applied in a low-speed wind tunnel investigation of separated flow control ([28]). Although this velocity fluctuation level was shown achievable using a loud speaker system in the laboratory, there still exist many difficult tasks in the practical actuator design when an internal turbomachinery environment is considered.

6 Internal Acoustic Excitations of a Fan Cascade

Based on the study performed in Section 4, and the intention to make the number of parameters to be investigated tractable, the numerical simulations carried out in the following will be done using trailing-edge excitation as the internal acoustic forcing. The coordinate system, the cascade flow configuration, and the mean flow and wave directions are illustrated in Fig. 12.

The test article is a linear cascade consisting of a row of blades whose profile is illustrated in Fig. 13. This is a near-tip section of a fan rig provided by Pratt and Whitney. Each blade is vibrating torsionally around a center of twist located 1.704 chord downstream from the blade trailing edge, as shown in Fig. 12. The blade is so rigid that it can be assumed that the flutter frequency is equal to the natural torsional vibration frequency of 180.8 Hz. Other geometrical parameters chosen are stagger angle $\Theta = 60.59$ deg and gap ratio $G = 0.736$. The torsional vibration angle α relative to the steady-state mean angle of incidence α_m is $\alpha = \alpha_m + \alpha_o \sin(\omega t)$, in which the amplitude α_o is assumed to be $\alpha_o = 0.005$ rad.

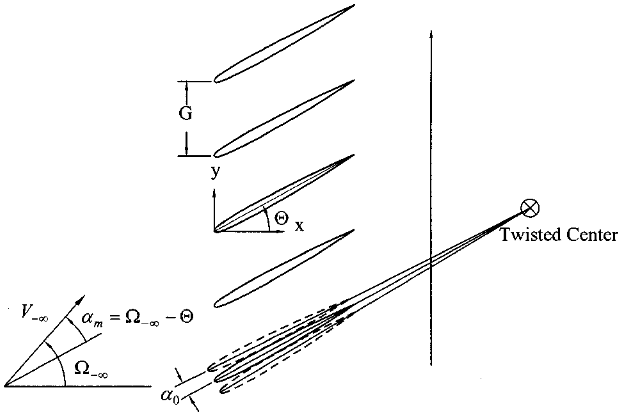

Fig. 12 Two-dimensional transonic cascade configuration

In the following there will be two mean flow conditions termed, respectively, Case A and Case B, that are to be investigated. The freestream Mach number M_∞, inflow stream angle $\Omega_{-\infty}$ and exit to freestream pressure ratio p_e/p_∞ are defined as follows:

	M_∞	$\Omega_{-\infty}$	p_e/p_∞
Case A	0.9848	68.54 deg	1.3408
Case B	0.7820	68.54 deg	1.164

6.1 Steady-State Mean Flow. Both Case A and Case B flow-fields were simulated using a grid system depicted in Fig. 14.

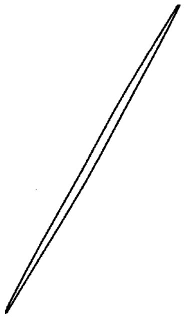

Fig. 13 P&W fan blade profile

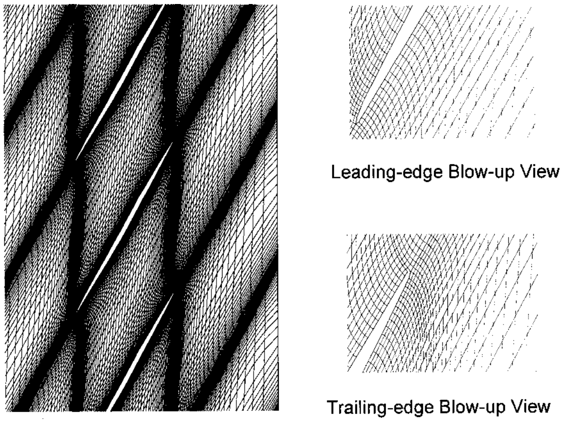

Leading-edge Blow-up View

Trailing-edge Blow-up View

Fig. 14 Grid system of P&W TS33 Cascade (120×40 cells per passage)

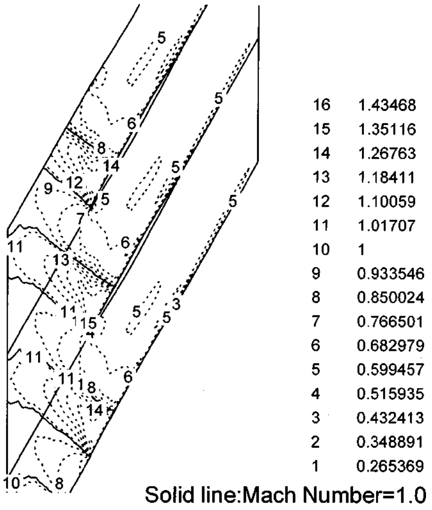

Fig. 15 Mach number contours of P&W TS33 Case A ($M_\infty = 0.9848$, $\Omega_{-\infty} = 68.54$ deg, $G = 0.736$, $\Theta = 60.59$ deg, and $p_e = 1.3408 p_\infty$)

The grid topology adopted is the H-type. There are totally 120×40 cells used per blade passage which extends one chordlength to the up and downstream, respectively.

The steady-state flow-fields are illustrated in Figs. 15 and 16. In both flows, a bubble-type supersonic zone is found embedded around the leading edge. The shock is weak and the trailing edge is subsonic which together make the flow-field susceptible to acoustic forcing, as inferred from the previous studies.

6.2 Internal Acoustic Forcing. First, we evaluate the forcing location effect by placing surface monopole at $X_C = 0.98$, 0.56 and 0.105, representing respectively forcing at trailing-edge, mid-cord, and leading-edge areas. The results of acoustically induced lift and pitching moment histories are shown in Figs. 17 and 18 for the two tested cases. In these simulations, the acoustic forcing is assumed in-phase for each blade while the blades were all held still. Therefore, only one blade passage is required for the computation and the periodic boundary condition was enforced along the corresponding cells distributed on the lateral boundaries. Analogous to the previous NACA0006 test cases, trailing edge stands out to be the best forcing location which indicates that trailing-edge receptivity is the mechanism responsible for generating acoustically induced bound circulation around the blade.

Shock excursion in transonic flow plays a central role for the nonlinear effect in transonic aerodynamics ([15]). Acoustic excitation was shown capable of moving the shock waves ([9]). To

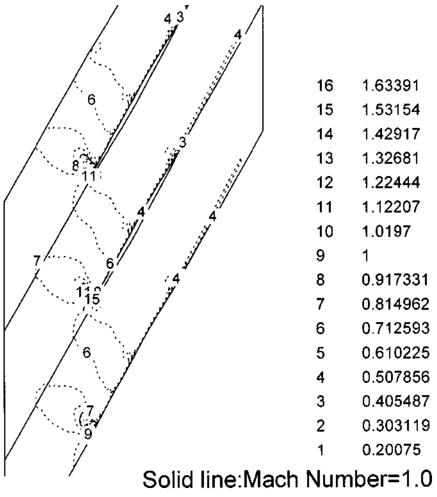

Fig. 16 Mach number contours of P&W TS33 Case B ($M_\infty = 0.782$, $\Omega_{-\infty} = 68.54$ deg, $G = 0.736$, $\Theta = 60.59$ deg, and $p_e = 1.1646 p_\infty$)

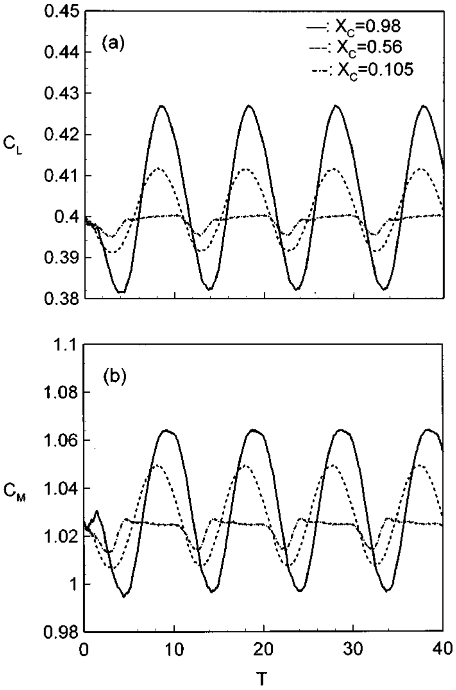

Fig. 17 Unsteady (*a*) lift and (*b*) pitching moment variations induced by acoustic excitation on P&W TS33 Case A cascade ($M_\infty = 0.9848$, $\Omega_{-\infty} = 68.54$ deg, $G = 0.736$, $\Theta = 60.59$ deg, $\sigma = 0$ deg, $p_e = 1.3408 p_\infty$, $Q(t) = Q_o \sin \omega t$, $Q_o = 5.E\text{-}3$, and $\omega = 0.64458$)

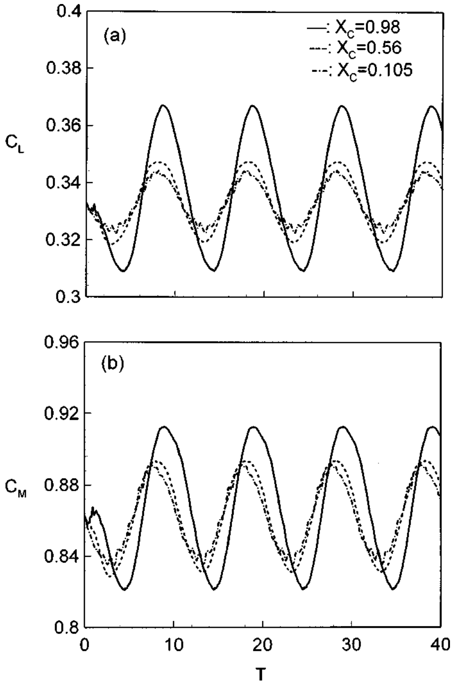

Fig. 18 Unsteady (*a*) lift and (*b*) pitching moment variations induced by acoustic excitation on P&W TS33 Case B cascade ($M_\infty = 0.782$, $\Omega_{-\infty} = 68.54$ deg, $G = 0.736$, $\Theta = 60.59$ deg, $\sigma = 0$ deg, $p_e = 1.1646 p_\infty$, $Q(t) = Q_o \sin \omega t$, $Q_o = 5.0E\text{-}3$, and $\omega = 0.62497$)

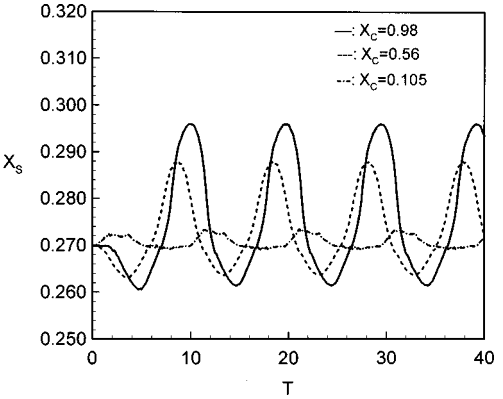

Fig. 19 Unsteady shock motion induced by acoustic excitation on P&W TS33 Case A cascade ($M_\infty=0.9848$, $\Omega_{-\infty}=68.54$ deg, $G=0.736$, $\Theta=60.59$ deg, $\sigma=0$ deg, $p_e=1.3408p_\infty$, $Q(t)=Q_o \sin \omega t$, $Q_o=5.0\text{E-}3$, and $\omega=0.64458$)

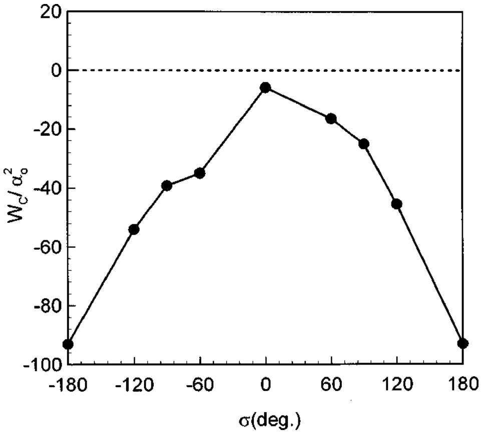

Fig. 21 Work per cycle versus interblade phase angle for a torsional vibrating cascade of P&W TS33 Case A ($M_\infty=0.9848$, $\alpha=\alpha_m+\alpha_o \sin \omega t$, $\alpha_m=0.1388$, $\alpha_o=0.005$ rad, and $\omega=0.64458$)

move the shock acoustically, it was found that there are two fundamental mechanisms that can lead to shock movement. The first is the acoustically induced circulation that rotates the whole flowfield including the displacement of the shock. The second is the modulation of the pressure ahead or behind the shock by a direct impingement of the acoustic wave on the shock. The shock excursion traces caused by acoustic forcing on the Case A and Case B cascades are shown in Figs. 19 and 20, respectively. In Fig. 19, trailing-edge forcing $X_C=0.98$ is most effective in moving the shock wave, while in Fig. 20 it shows that, for Case B cascade, forcing at $X_C=0.105$ is the best. The reason why forcing at $X_C=0.105$ in the Case A cascade is not as effective as in the Case B cascade is that, in the Case A excitation the forcing location is in the upstream of the shock root. Regarding moving shock wave by impinging acoustic wave from ahead or behind the shock root, downstream modulation of the back pressure is found comparatively much effective ([9]).

Trailing-edge forcing, in general, can produce the largest amount of acoustically induced airloads. No matter where the supersonic bubble may occur in the transonic flow, trailing-edge forcing and the mechanism of acoustic/vortical conversion is always the dominant factor. Due to the robustness of trailing-edge forcing which works well for a wide range of Mach number application, it is recommended that the optimal place for implementing internal acoustic excitation be the trailing edge of the airfoil or the blade row.

6.3 Flutter Analysis of P&W Fan Cascade. The effect of interblade phase angle σ is analyzed for the present vibrating cascade flow. The interblade phase angles simulated were 0 deg, ±180 deg, ±120 deg, ±90 deg, and ±60 deg. These interblade phase angle simulations call for a computational domain of 1, 2, 3, 4, and 6 blade passages, respectively. Periodic boundary condition implementation hence was enforced on the outmost lateral boundaries of the computational domain.

Flutter instability is examined by a forced-response type simulation. The blades were given with preassigned vibrational frequency and interblade phase angles. The turbomachinery blades are usually very rigid, so the flutter frequency can be assumed known and equal to the blade natural frequency. The torsion vibration is hence defined as a harmonic oscillation around the steady-state mean angle of incidence. The amplitude of oscillation was set to be $\alpha_o=0.005$ rad. Work per cycle done by unsteady airloads can thus be obtained which are shown in Figs. 21 and 22. Both Case A and Case B simulations predict a stable system as indicated by the negative work per cycle over the simulated interblade phase angle range. The more negative the work per cycle, the more stable the cascade is. The in-phase ($\sigma=0$) vibration is shown most prone to flutter instability due to the narrowest margin from the zero-work line.

6.4 Internal Acoustic Flutter Suppression. Since active control is considered in the present acoustic flutter suppression,

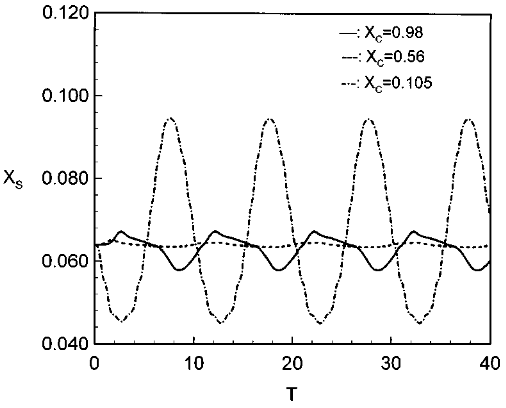

Fig. 20 Unsteady shock motion induced by acoustic excitation on P&W TS33 Case B cascade ($M_\infty=0.782$, $\Omega_{-\infty}=68.54$ deg, $G=0.736$, $\Theta=60.59$ deg, $\sigma=0$ deg, $p_e=1.1646p_\infty$, $Q(t)=Q_o \sin \omega t$, $Q_o=5.0\text{E-}3$, and $\omega=0.62497$)

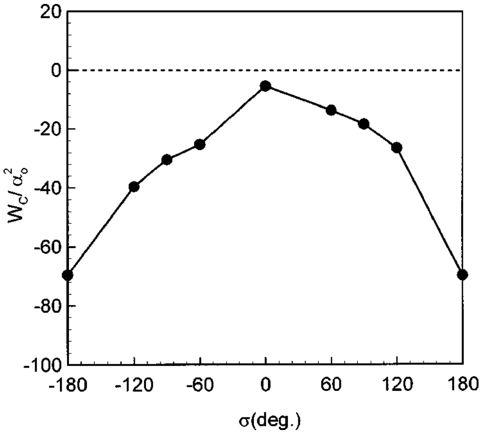

Fig. 22 Work per cycle versus interblade phase angle for a torsional vibrating cascade of P&W TS33 Case B ($M_\infty=0.782$, $\alpha=\alpha_m+\alpha_o \sin \omega t$, $\alpha_m=0.1388$, $\alpha_o=0.005$ rad, and $\omega=0.62497$)

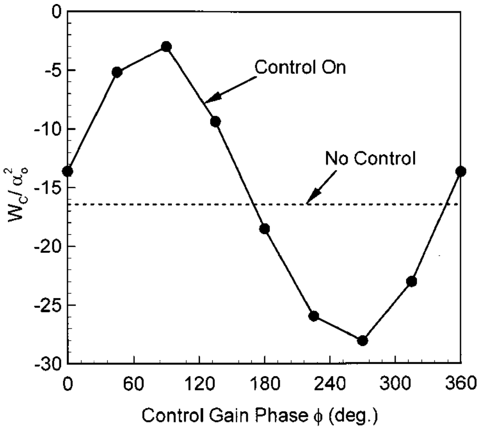

Fig. 23 Effect of control gain phase on the work per cycle for a torsional vibrating cascade of P&W Case A under actively controlled acoustic excitations ($M_\infty=0.9848$, $\sigma=60$ deg, $\alpha=\alpha_m+\alpha_o \sin \omega t$, $\alpha_m=0.1388$, $\alpha_o=0.005$ rad, $\omega=0.64458$, $X_C=0.95$, $Q(t)=G_\alpha[\alpha(\omega t+n\sigma+\phi)-\alpha_m]$, and $G_\alpha=0.5$)

the monopole strength should vary in response to the motion or states detected. For the present single-degree-of-freedom torsion oscillation, the control law assumed for a blade having $n\sigma$ interbalde phase angle is of the form

$$Q(t)=G_a[\alpha(\omega t+n\sigma+\phi)-\alpha_m] \quad n=0,1,2,3\ldots \tag{14}$$

in which G_a is the gain amplitude and ϕ the gain phase of the control logic. In the following acoustic control simulations we use $G_a=0.5$ which amounts to a forcing amplitude of $Q_o=2.5\times10^{-3}$. The interblade phase angle of the acoustically excited flow remains unchanged when this control logic is applied. Here we chose a 60 deg interblade phase angle as an example, and the simulated acoustic control results are shown in Figs. 23 and 24.

It was not surprising that the gain phase ϕ is very critical to the stability of the dynamic system. For both test cases, the stabilizing phase resides between 170 deg$<\phi<$350 deg. The most effective phase is around $\phi=270$ deg. From the data depicted in the illustrations, the flutter margin can be enlarged 70–80 percent suppose an optimal gain phase ($\phi\approx270$ deg) is selected. This observation basically agrees with what were found in the low-speed analysis ([3]). The gain phase controls the stability of the acoustically excited system, whereas the gain amplitude controls the decaying or growing rate of the response motion.

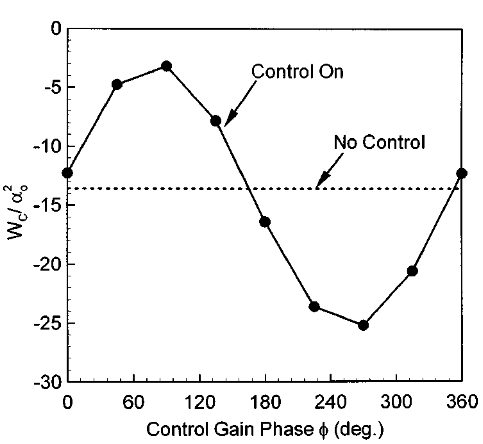

Fig. 24 Effect of control gain phase on the work per cycle for a torsional vibrating cascade of P&W Case B under actively controlled acoustic excitations ($M_\infty=0.782$, $\sigma=60$ deg, $\alpha=\alpha_m+\alpha_o \sin \omega t$, $\alpha_m=0.1388$, $\alpha_o=0.005$ rad, $\omega=0.62497$, $X_C=0.95$, $Q(t)=G_\alpha[\alpha(\omega t+n\sigma+\phi)-\alpha_m]$, and $G_\alpha=0.5$)

7 Conclusions

The phenomenon of acoustically excited transonic cascade flow and the use of acoustic wave to suppress flutter instability are investigated numerically. The generation of the acoustically induced airloads is found mainly governed by the trailing-edge receptivity mechanism, a phenomenon that has been well elucidated in the incompressible flow analysis. The role of the shedding vortices in compressible flow was first explained conceptually using Goldstein's model, and then quantitatively checked via a specially designed impulse forcing numerical experiment. Sound emitted by the wake vortices not only changes the magnitude but also modifies the phase lag of the induced airloads. With this fundamental understanding gained, a generic bending-torsion flutter test was conducted for a cascade having 180-deg interblade phase angle. Flutter instability is shown suppressed as actively controlled acoustic excitation is applied.

A real fan blade row was used to examine the feasibility and limitations pertaining to the present acoustic method. Trailing-edge forcing was taken as the representative internal excitation scheme. It is found that, as appropriate control phase is employed, internal acoustic excitations can stabilize the fluttering motion. Analogous to the isolated airfoil result, trailing edge is still the optimal internal forcing location for the cascade. The challenge posed on the internal excitations, therefore, lies in the hardware design and manufacturing of the sensor and actuator systems. The sensor must be very sensitive so as to capture the instability in the early stage. The actuator, on the other hand, must be fast responsive and small enough so that it can be housed within a narrow space around the trailing-edge area.

Acknowledgment

The authors would like to thank Dr. Ron-Ho Ni of Pratt & Whitney for many helpful technical suggestions and the supply of the P&W cascade profile.

References

[1] Huang, X.-Y., 1987, ''Active Control of Aerofoil Flutter,'' AIAA J., **25**, pp. 1126–1132.
[2] Ffowcs Williams, J. E., 1993, ''Acoustic Control of Flow Instabilities,'' *Unsteady Aerodynamics, Aeroacoustics, and Aeroelasticity of Turbomachines and Propellers*, H. M., Atassi, eds., Springer-Verlag, New York, pp. 643–653.
[3] Lu, P.-J., and Huang, L.-J., 1992, ''Flutter Suppression of Thin Airfoils Using Active Acoustic Excitations,'' AIAA J., **30**, No. 12, pp. 2973–2881.
[4] Lu, P.-J., Pan, D., and Yeh, D.-Y., 1995, ''Transonic Flutter Suppression Using Active Acoustic Excitation,'' AIAA J., **33**, No. 4, pp. 694–702.
[5] Lu, P.-J., Pan, D., and Yeh, D.-Y., 1995, ''Numerical Simulation of Trailing-Edge Acoustic/Vortical Interaction,'' AIAA J., **33**, No. 5, pp. 785–793.
[6] Chakravarthy, S. R., and Osher, S., 1985, ''A New Class of High Accuracy TVD Schemes for Hyperbolic Conservation Laws,'' AIAA paper 85-0363.
[7] Venkatakrishnan, V., and Jameson, A., 1988, ''Computation of Unsteady Transonic Flows by the Solution of Euler Equations,'' AIAA J., **26**, No. 8, pp. 974–981.
[8] Roe, P. L., 1981, ''Approximate Riemann Solvers, Parameter Vectors, and Difference Schemes,'' J. Comput. Phys., **43**, pp. 357–372.
[9] Yeh, D.-Y., 1992, ''Unsteady Aerodynamic and Aeroelastic Behaviors of Acoustically Excited Transonic Flow,'' Ph.D. thesis, Institute of Aeronautics and Astronautics, National Cheng Kung University, Taiwan, R.O.C.
[10] Hedstrom, G. W., 1979, ''Nonreflecting Boundary Conditions for Hyperbolic System,'' J. Comput. Phys., **30**, pp. 222–237.
[11] Thompson, K. W., 1987, ''Time Dependent Boundary Conditions for Hyperbolic Systems,'' J. Comput. Phys., **68**, pp. 1–24.
[12] Giles, M. B., 1990, ''Nonreflecting Boundary Conditions for Euler Equation *Calculations*,'' AIAA J., **28**, No. 12, pp. 2050–2058.
[13] Vinokur, M., 1989, ''Review Article: An Analysis of Finite-Difference and Finite-Volume Formulation of Conservation Law,'' J. Comput. Phys., **81**, pp. 1–52.
[14] Edwards, J. W., Bennett, R. M., Whitlow, W., Jr., and Seidel, D. A., 1993, ''Time-Marching Transonic Flutter Solutions Including Angle-of-Attack Effects,'' J. Aircr., **20**, No. 11, pp. 899–906.
[15] Tijdeman, H., and Seebass, R., 1980, ''Transonic Flow Past Oscillating Airfoils,'' Annu. Rev. Fluid Mech., **12**, pp. 181–222.

[16] Ashely, H., 1980, ‘‘Role of Shock in the ‘Sub-Transonic’ Flutter Phenomenon,’’ J. Aircr., **17**, No. 3, pp. 187–197.
[17] Crighton, D. G., 1981, ‘‘Acoustics as a Branch of Fluid Mechanics,’’ J. Fluid Mech., **106**, pp. 261–298.
[18] Daniels, P. G., 1978, ‘‘On the Unsteady Kutta Condition,’’ Q. J. Mech. Appl. Math., **31**, pp. 49–75.
[19] Lighthill, M. J., 1952, ‘‘On Sound Generated Aerodynamically. I. General Theory,’’ Proc. R. Soc. London, Ser. A, **211**, pp. 564–587.
[20] Lighthill, M. J., 1954, ‘‘On Sound Generated Aerodynamically. II. Turbulence as a Source of Sound,’’ Proc. R. Soc. London, **A222**, pp. 1–32.
[21] Crow, S. C., 1970, ‘‘Aerodynamic Sound Emission as a Singular Perturbation Problem,’’ Stud. Appl. Math., **49**, No. 1, pp. 21–44.
[22] Goldstein, M. E., 1976, *Aeroacoustics*, McGraw-Hill, New York.
[23] Chu, B.-T., and Kovasznay, L. S. G., 1958, ‘‘Nonlinear Interactions in a Viscous Heat-Conducting Compressible Gas,’’ J. Fluid Mech., **3**, pp. 494–514.
[24] Goldstein, M. E., 1978, ‘‘Unsteady Vortical and Entropic Distortions of Potential Flows Round Arbitrary Obstacles,’’ J. Fluid Mech., **89**, Part 3, pp. 433–468.
[25] Verdon, J. M., 1978, ‘‘Linearized Unsteady Aerodynamic Theory,’’ *Aeroelasticity in Axial-Flow Turbomachines*, *Vol. 1*, *Unsteady Turbomachinery Aerodynamics*, M. F. Platzer and F. O. Carta, eds., AGARDograph No. 298.
[26] Bendiksen, O. O., and Hsiao, C., 1993, ‘‘New Computational Method for Aeroelastic Problems in Turbomachines. Part II,’’ UCLA Report ENG-93-14.
[27] Bennett, R. M., and Desmarais, R. N., 1975, ‘‘Curve Fitting of Aeroelactic Transient Response Data With Exponential Functions,’’ *Flutter Testing Techniques*, NASA SP-415, pp. 43–58.
[28] Shyu, R.-N., 1991, ‘‘Improvement of Airfoil Stalling Performance by Internal Periodic Excitation at Leading Edge,’’ Ph.D. thesis, Institute of Aeronautics and Astronautics, National Cheng Kung University, Taiwan, R.O.C.

In-Cylinder Pressure Reconstruction Based on Instantaneous Engine Speed Signal

D. Moro

N. Cavina

F. Ponti

DIEM
University of Bologna,
Viale Risorgimento 2,
Bologna 40136, Italy

This paper presents an original methodology for the instantaneous in-cylinder pressure waveform reconstruction in a spark-ignited internal combustion engine. The methodology is based on the existence of a linear correlation, characterized by frequency response functions, between in-cylinder pressure and engine speed signals. This correlation is experimentally verified and evaluated by simultaneous measurements of the above-mentioned quantities. The evaluation of different frequency response functions, one for each steady-state condition investigated, allows recovering the pressure waveform even under other engine running conditions (i.e., transients). In this way, during on-board operation, the pressure waveform could be recovered using only the engine speed signal, already present in current production electronic control units. In this paper the signal processing methodology and some experimental results, obtained during transient tests, are presented. The methodology could be interesting for the development of advanced engine control strategies aimed at the management of the torque generated by the engine. As an example, traction control in drive-by-wire systems could be a possible challenging application. The in-cylinder pressure reconstruction performed using the frequency response functions, in fact, allows the evaluation of the indicated torque. An important characteristic of this methodology is, furthermore, the diagnostic capability for the combustion process, that is guaranteed by the linear correlation between in-cylinder pressure and instantaneous engine speed waveforms. Also in presence of a misfiring cylinder, when the instantaneous engine speed waveform is strongly affected by the absence of combustion, the reconstructed in-cylinder pressure shows a good agreement with the measured one. The experimental tests have been conducted in a test cell using a four-cylinder production engine. It has to be noted, anyway, that the same methodology can be applied to engines with a higher number of cylinders. [DOI: 10.1115/1.1391430]

Introduction

The cycle-by-cycle and cylinder-by-cylinder pressure waveform knowledge is a very important information that could have several applications both for engine control and diagnosis. Many researchers ([1–7]) have developed methodologies for the estimation of torques (indicated, load, friction, and accessories) acting on the engine shaft, in order to enhance a new class of engine control systems aimed at the optimal management of the engine torque. Other studies ([8]) demonstrate the possibility to estimate the air-fuel-ratio of the mixture introduced into the cylinder by analyzing the pressure waveform during combustion, thus allowing a finer mixture control. Another application is represented by the diagnosis of abnormal combustion (i.e., presence of misfire) that could be achieved simply by the analysis of the recovered pressure waveform in each cylinder.

The realization of these different control and diagnostic features is related to the quality and accuracy of the recovered pressure waveform, some of them requiring only the low-frequency content of the signal to be reconstructed. The methodology proposed in this paper allows the reconstruction of the pressure signal up to the 12th harmonic order with respect to the engine cycle. Such pressure reconstruction can be successfully used, as reported in the result section of this paper, to diagnose abnormal combustion or for misfire detection. In addition, the evaluation of the indicated torque produced by the engine can be performed with an accuracy that is sufficient for torque-based engine control systems. The authors are actually working on these control and diagnostic applications.

General Considerations for In-Cylinder Pressure Estimation

Several researchers have demonstrated the feasibility of the pressure waveform estimation using information based either on the engine block vibration or on the engine speed signals ([1–5]). The authors have presented some results using both the reconstruction methodologies. Anyway, it has been verified the impossibility of using the knock accelerometer, already present on board the vehicle, to measure the interesting frequency content of the engine block vibration signal. The frequency range of interest for knock detection (high frequencies) is, in fact, totally different from the one needed to perform the in-cylinder pressure reconstruction (low frequencies). The low-cost knock accelerometer sensor gives a low signal-to-noise ratio in the low-frequency range and, sometimes, its position is not optimized for the pressure reconstruction, thus requiring a specific sensor for this purpose. The need to reduce as much as possible the costs of the control instrumentation on board the vehicle forces the selection of the pressure reconstruction methodology based on the engine speed signal analysis, being this signal already available in a modern engine control unit.

Some considerations have to be done in order to understand how the methodology can recover the pressure waveform starting from the engine speed signal. These considerations are reported in

---

Contributed by the Internal Combustion Engine Division of THE AMERICAN SOCIETY OF MECHANICAL ENGINEERS for publication in the ASME JOURNAL OF ENGINEERING FOR GAS TURBINES AND POWER. Manuscript received by the ICE Division Sept. 2000; final revision received by the ASME Headquarters Mar. 2001. Editor: D. N. Assanis.

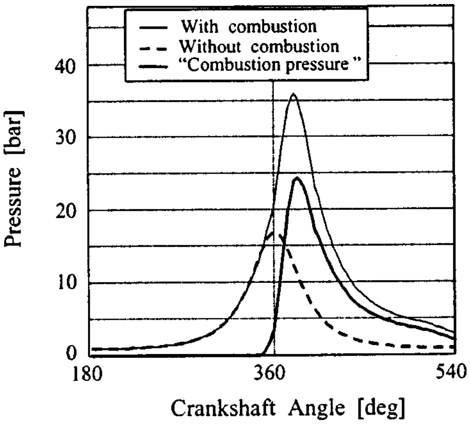

Fig. 1 In-cylinder pressure with and without combustion and "combustion pressure" when the engine is running at 2000 rpm at full load

the following and are related to a four-cylinder in-line 1.6-liter engine architecture, even if general considerations for engine with different number of cylinders can be extrapolated.

The in-cylinder pressure can be thought, in our approach, as the sum of two different contributions: the pressure variations due to the piston movement and the "combustion pressure" due to the combustion phenomenon. The first term is the pressure that could be measured inside the cylinder if the engine is motored, i.e., if there is no combustion. The second term could be evaluated, by definition, by computing the difference between the in-cylinder pressure measured during firing and motoring operating conditions: it represents what is added to the pressure waveform by the combustion process, with respect to the corresponding motoring operating condition. In Fig. 1 the in-cylinder pressure for a firing cycle and the corresponding two terms are reported.

A more detailed analysis can be done about these two terms focusing on the engine cycle portion when the compression, combustion and expansion occur (about one engine rotation). The first term, introduced in the preceding paragraph, is function of the actual engine operating conditions since it depends on the mass inside the cylinder and, thus, on the in-cylinder pressure and temperature at the beginning of the compression phase, when the intake valves close. Its waveform can be modeled as a polytropic process (pV^n=constant with $n=1.32$ during compression and $n=1.27$ during expansion ([9]) for each operating condition, using as starting point the in-cylinder pressure when the intake valves close. This pressure waveform can then be mapped over the engine operating range and stored in memory, allowing the evaluation of this first term under any engine operating condition. In order to perform the in-cylinder pressure reconstruction, the only unknown term is now the "combustion pressure," that, as it can be noted in Fig. 1, is different from zero, for each cylinder, only in a limited portion of the cycle. This portion lasts approximately 180 deg, corresponding roughly to the expansion phase, taking into account the presence of the spark-advance and the exhaust valves opening before the BDC.

In a multicylinder engine the sum of the indicated torques of the various cylinders is the main physical effect that determines the dynamic behavior of the engine crankshaft and, thus, of the instantaneous engine speed. For each cylinder the pressure waveform in a cycle determines the instantaneous indicated torque relative to that cylinder, taking into account the crank-slider mechanism kinematics. As an example, Fig. 2 reports the pressure and the corresponding indicated torque waveforms for cylinder number 1, during an engine cycle.

In Fig. 3 the overall instantaneous indicated torque during an engine cycle for the four-cylinder engine under study is reported. Because of the engine multicylinder architecture only in a partial interval of the engine cycle (in this case in the angular range 340 deg÷520 deg) the correspondence between the single cylinder indicated torque and the overall indicated torque is verified. The contribution of the other three cylinders in terms of indicated torque can be in fact considered negligible over this engine cycle portion. This observation is very important for our purposes, since the direct physical relationship between the instantaneous engine speed and the pressure waveform in one cylinder is limited to a partial angular sector of the engine cycle. The main consequence of the preceding considerations is that the reconstruction of the "combustion pressure" has to be limited to an angular sector of 180 deg (for a four-cylinder engine). If the engine has less than four cylinders, the angular sector used for the reconstruction is still 180 deg, since the "combustion pressure" to be recovered is defined only in that sector. If the engine has more than four cylinders, the angular sectors corresponding to the expansion phases in the various cylinders are superimposed, thus limiting the possibility to recover the whole "combustion pressure." In a six-cylinder engine, for example, the angular sector that can be used for each cylinder for the "combustion pressure" reconstruction is at most 120 deg. For higher number of cylinders a more detailed analysis is required.

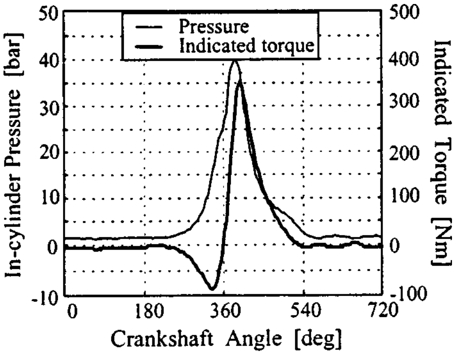

Fig. 2 Pressure and indicated torque waveforms in a cycle for a single cylinder

The second main consideration is related to the necessity of reducing the distortion on the instantaneous engine speed due to the reciprocating mass inertial torque. This effect is mainly evident at high engine speeds, because the inertial torque can be modeled as a function of the crank-slider mechanism kinematics, of the equivalent reciprocating mass (that takes into account the masses of pistons, piston rings, connecting rods) and of the square power of the engine speed. Some researchers ([10]) have pointed out the importance of taking into account the effects of this reciprocating inertial torque when the instantaneous dynamic behavior of an internal combustion engine is to be analyzed. In Fig. 4 the waveform of the instantaneous reciprocating mass inertial torque in a cycle due to all the four cylinders, when the engine is running at a mean speed of 2000, 3000, and 4000 rpm is reported. It is to

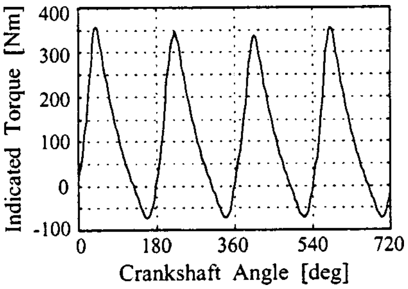

Fig. 3 Instantaneous indicated torque waveforms in a cycle in the four cylinder engine under study

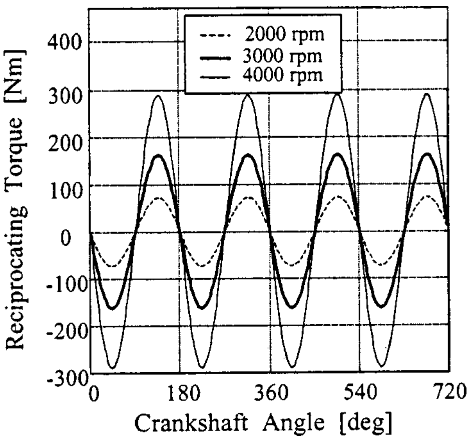

Fig. 4 Instantaneous reciprocating mass inertial torque waveforms in a cycle in the four-cylinder engine under study at 2000, 3000, and 4000 rpm

be noted that the mean value of this reciprocating torque is equal to zero: when the attention is devoted to the cycle mean value dynamic behavior of the engine it is then possible to neglect its influence.

The comparison between Figs. 3 and 4 is very interesting: It can be noted that the reciprocating mass inertial torque has positive values in correspondence of the final part of the compression stroke of each cylinder, when the indicated torque is negative. The sum of the indicated and reciprocating mass inertial torque in this angular range (for example, from about 300 deg to 360 deg) can assume positive values as the engine speed increases. In a similar way, during the first 90 deg of the expansion stroke, even if the indicated torque has a positive value, the sum of the indicated and reciprocating torques can yield a negative value, at high speed. The overall effect is that, when the engine is running at steady-state and low speed, the reciprocating mass inertial torque does not significantly influence the instantaneous engine speed variations, while at high engine speed its influence is so strong that the instantaneous engine speed variations are mainly due to it. Due to this influence, at high speed, the instantaneous engine speed presents fluctuations in the opposite direction with respect to the instantaneous indicated torque waveform. In Fig. 4 the quadratic relationship between the engine speed and the reciprocating mass inertial torque is very clear. The higher the engine speed, the lower the correlation between the instantaneous indicated torque and the instantaneous engine speed.

To assure a high correlation between these two signals an engine speed pre-processing technique is used ([10]) to remove from the measured instantaneous engine speed the effects of the reciprocating mass inertial torque, thus obtaining a "synthetic" engine speed that is strictly related to the indicated torque. Figure 5 shows some experimental data measured in a four-cylinder engine during a single cycle when the engine was running at a relatively high speed (4000 rpm). The thick line is the measured engine speed, while the thinner one is the "synthetic" speed. It is very clear the completely different waveform of the two speeds, and it is also evident that the "synthetic" waveform is physically correlated with the indicated torque, considering that the top dead centers (TDC) of the four cylinders are reported in Fig. 5.

The Combustion Pressure Recovery Methodology

As it has been shown in the preceding section, the correlation between pressure and "synthetic" engine speed for each cylinder is limited to an angular range of about 180 deg, corresponding roughly to the expansion phase, large enough to reconstruct the "combustion pressure." On the other hand it has been noted that a polytropic process model, using as starting point the in-cylinder pressure when the intake valve is closing, can very well describe the motored in-cylinder pressure waveform during compression and expansion phases. Analyzing the data acquired in a large number of engine tests with the engine running under different steady-state conditions, it has been noted that the in-cylinder pressure when the intake valve is closing is strictly dependent on the intake manifold pressure and the mean engine speed (see Fig. 6).

The mapping of this value on the engine operating range allows thus to recover the pressure waveform due to the piston motion for each engine operating condition. The "combustion pressure" has then to be added to this pressure waveform in order to obtain the whole in-cylinder pressure waveform.

The basic idea for the "combustion pressure" reconstruction is to evaluate a map of frequency response functions that represent the correlation between the instantaneous "synthetic" engine speed and the "combustion pressure" over the whole engine operating range. In order to highlight the "combustion pressure" information hidden in the "synthetic" speed signal an original signal processing procedure has been developed. The relationship between the "synthetic" speed and the torques acting on the engine crankshaft can be written as

$$T_i(t)-T_L(t)-T_f(t)=J\ddot{\theta}_s(t). \tag{1}$$

If there is no "combustion pressure," i.e., if a misfire occurs, for example in the cylinder number 1, the "synthetic" engine speed is affected by this malfunctioning condition:

$$T_{i\ \mathrm{misf}}(t)-T_L(t)-T_f(t)=J\ddot{\theta}_{s\ \mathrm{misf}}(t). \tag{2}$$

The difference between the torques acting on the shaft in these two situations is reported in Eq. (3). It is mainly due to the "combustion pressure" inside cylinder number 1, under the hypothesis

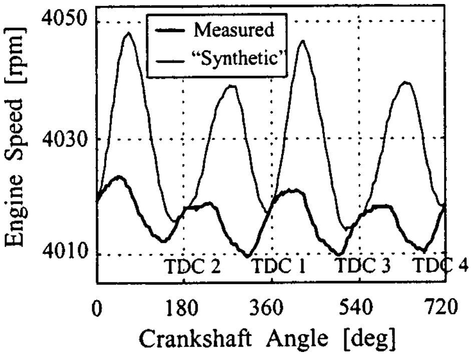

Fig. 5 Measured and "synthetic" engine speed at 4000 rpm and full load, for the four-cylinder in-line engine under study

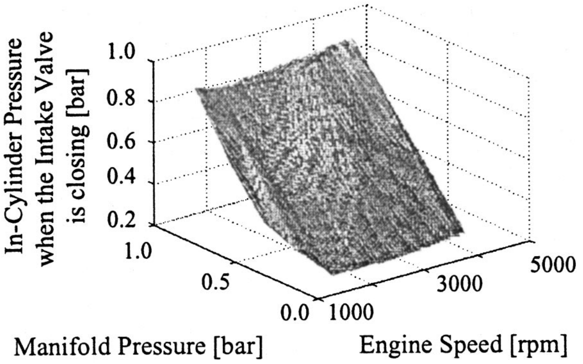

Fig. 6 Three-dimensional surface of the in-cylinder pressure when the intake valve is closing

that the difference in the friction torque due to the relative motion between piston and cylinder walls in these two situations can be neglected.

$$\Delta T_i(t) = T_i(t) - T_{i\ \mathrm{misf}}(t) = Ar(p(t) - p_{\mathrm{misf}}(t)) f_{\mathrm{crank}}(t) = Ar p_{\mathrm{comb}}(t) f_{\mathrm{crank}}(t) \quad (3)$$

Using Eqs. (1), (2), and (3) it is then possible to obtain an estimation of the effects of the "combustion pressure" on the "synthetic" speed:

$$Ar(p_{\mathrm{comb}}(t)) f_{\mathrm{crank}} = \Delta T(t)_i = J\ddot{\theta}_s(t) - J\ddot{\theta}_{s\ \mathrm{misf}}(t) = J\Delta\ddot{\theta}_s(t). \quad (4)$$

Equation (4) highlights that the "combustion pressure" is directly correlated to the quantity $\Delta\ddot{\theta}_s(t)$ that is related to the difference between the actual "synthetic" engine speed and the "synthetic" engine speed that would have been measured in case of misfire. It is evident that the knowledge of the "synthetic" speed in case of misfire is required to evaluate $\Delta\ddot{\theta}_s(t)$, that is necessary both to identify the frequency response functions and to recover the "combustion pressure." A possible procedure to determine the "synthetic" speed in case of misfire is to calculate it, once and for all, at each engine operating condition by the knowledge of the motored in-cylinder pressure (see Eq. (5)). The waveform obtained is then stored in memory for each engine running condition, to be used in the pressure reconstruction step.

$$\begin{aligned}\dot{\theta}_{s\ \mathrm{misf}}(\theta) &= \int d\dot{\theta}_{s\ \mathrm{misf}}(\theta) \\ &= \int (d\dot{\theta}_s(\theta) - d(\Delta\dot{\theta}(\theta))) \\ &= \dot{\theta}_s(\theta) - \int \frac{\Delta T(\theta)}{J\dot{\theta}} d\theta \\ &= \dot{\theta}_s(\theta) - \int \frac{Ar(p(\theta) - p_{\mathrm{misf}}(\theta)) f_{\mathrm{crank}}(\theta)}{J\dot{\theta}} d\theta \quad (5)\end{aligned}$$

Another possibility to evaluate the "synthetic" speed in case of misfire is to cause some misfires at each monitored engine running condition and to measure the engine speed. The waveforms obtained can then be stored in memory. The approach used in the present work is the first one, using Eq. (5), since it is simpler and quicker, requiring less experimental work.

In Figs. 7 and 8 the waveform of the measured in-cylinder pressure and the corresponding "synthetic" engine speed when the engine is running at 3000 rpm at full load are shown. In the same two figures the waveform of the pressure without combustion and the "synthetic" engine speed in this last situation have been calculated.

The correlation between the "combustion pressure" and the difference between the actual "synthetic" speed and the "synthetic" speed in case of misfire, has then been represented by means of frequency response functions.

Each frequency response function is experimentally evaluated via direct measurements of the engine speed and of the in-cylinder pressure. These signals are then pre-processed to obtain from the first one the difference between the actual "synthetic" engine speed and the "synthetic" speed in case of misfire, that has been stored in memory, and from the second one the "combustion pressure." For the in-cylinder pressure signal the pre-processing procedure has to take into account also the influence of the charge amplifier and of short and long thermal drift that affect in-cylinder pressure measurement realized, as in our case, with noncooled sensors.

In Fig. 9 the two signals that are used to evaluate the frequency response function in a specific engine running condition are reported.

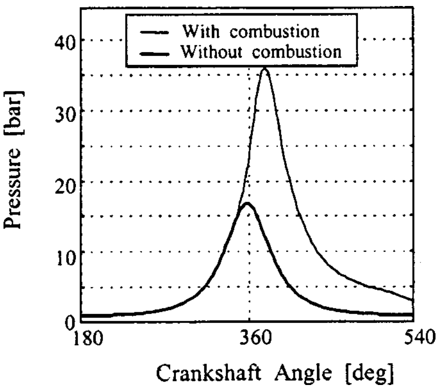

Fig. 7 In-cylinder pressure and pressure without combustion when the engine is running at 3000 rpm at full load

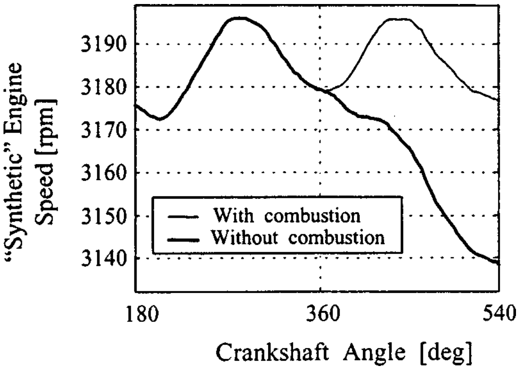

Fig. 8 "Synthetic" engine speed with normal combustion and misfire when the engine is running at 3000 rpm at full load

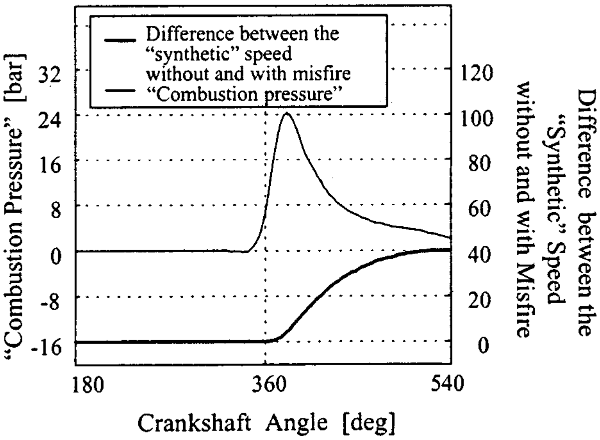

Fig. 9 "Combustion pressure" and the difference between the actual "synthetic" engine speed and the synthetic speed in case of misfire when the engine is running at 3000 rpm at full load

From Fig. 9 it can be noted that the "combustion pressure" signal is different from zero before the top dead center because of the spark ignition advance. For this reason it has been selected a "combustion pressure" reconstruction window that begins 15 deg before the compression TDC and finishes 20 deg before the end of the expansion stroke, when the exhaust valves open. The linear relationship between the low harmonic content of the "combustion pressure" signal and the difference between the actual "syn-

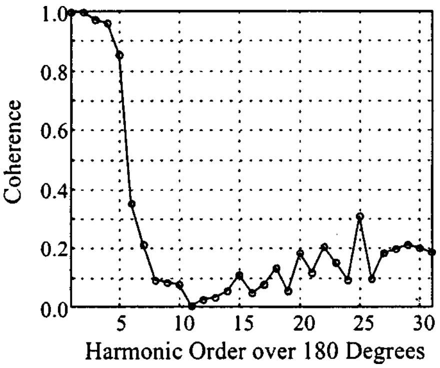

Fig. 10 Coherence function between the "combustion pressure" waveform and the difference between the actual "synthetic" engine speed and the one in case of misfire

thetic'' engine speed and the ''synthetic'' speed in case of misfire has been verified using the coherence function, as it can be seen in Fig. 10.

Experimental Results

The experimental validation of the pressure recovery methodology has been carried out using some transient tests. A previous step where the frequency response functions have been evaluated has been carried out with the engine running in a limited number of steady-state conditions in order to cover all the engine operating range. The engine used to perform the tests is a FIAT 1600, whose characteristics are reported in Table 1 together with the main characteristic of the sensors used. The tests have been carried out in a test cell with the engine coupled to an eddy-current brake.

In Fig. 11 the 38 steady-state conditions where the frequency response functions have been evaluated are reported on the intake manifold pressure versus engine speed plane. In the same figure the trace of a transient test used to validate the methodology is reported too.

During the transient test the actual frequency response function has been evaluated by means of an interpolation, for both real and imaginary harmonic components up to the third order, using the values previously determined from the 38 steady-state conditions.

In the following figures the results obtained for the pressure reconstruction at different functioning points during the transient reported in Fig. 11 can be seen. The pressure recovery related to the point A, where the engine is at low speed and low load, is reported in Fig. 12. The map of the basic waveform of the pressure (i.e., without combustion) assures a quite good reconstruction of the first part of the pressure waveform. During the expansion phase, the addition of the recovered ''combustion pressure'' introduces some oscillation on the instantaneous ''combustion pressure'' waveform since the reconstruction is performed with a limited number of harmonics. It can be seen that the contribution of the ''combustion pressure'' is quite small in this low load case.

The pressure recovery related to the point B in Fig. 11, where the engine is now at high speed and high load is reported in Fig. 13. In this case the high load determines quite large values of the ''combustion pressure,'' that is well recovered. In Fig. 14 the pressure recovery is related to point C in Fig. 11.

It can be seen that the pressure reconstruction methodology underestimates systematically the maximum pressure value. This is due to the limited number of harmonics used to recover the signal. In fact, the linear correlation between the ''combustion pressure'' and the ''synthetic'' engine speed is verified only in a limited (3) number of harmonics. This error is balanced by a systematic tendency to overestimate the last part of the ''combustion pressure.'' This phenomenon allows to obtain a good estimation of

Table 1 Engine and sensors characteristics

FIAT 1600
Displacement: 1581 cm^3
Cylinders: 4
Bore: 86.4 mm
Stroke: 67.4 mm
Compression ratio: 9.2
Maximum torque: 124 Nm at 3000 rpm
Maximum power: 57 kW at 6000 rpm
In-Cylinder Pressure Sensors
Type: Kistler 6117B
Range: 0–200 bar
Sensitivity: −15 pC/bar
Linearity: $\leq \pm 0.6$ FSO

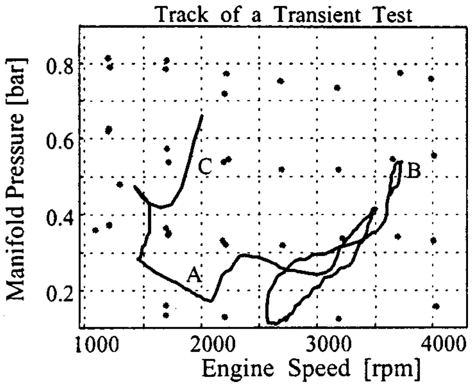

Fig. 11 Intake manifold pressure versus engine speed plane

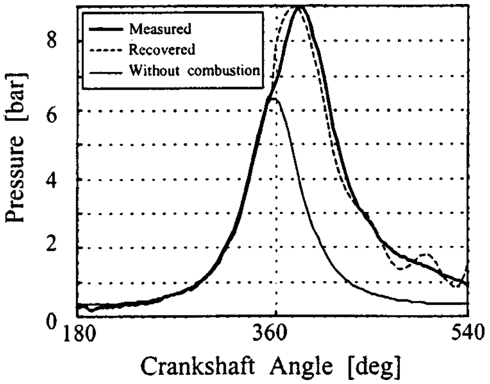

Fig. 12 Pressure recovery related to the point A in Fig. 11

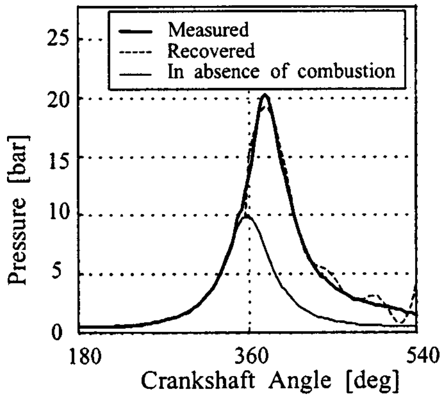

Fig. 13 Pressure recovery related to the point B in Fig. 11

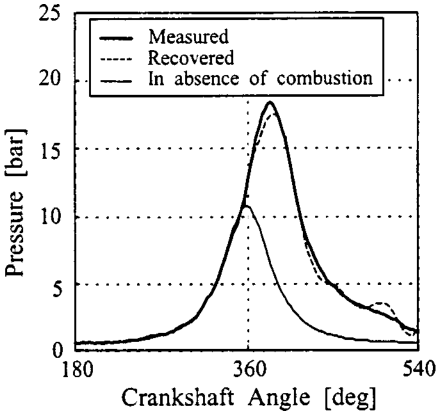

Fig. 14 Pressure recovery related to the point C in Fig. 11

the mean indicated torque since the error of the pressure waveform recovery at high values occurs when the piston is near the TDC position, where the indicated torque is still low, and it is compensated in the second part of the expansion stroke. Finally it has to be noted that the 3rd harmonic over an angular sector of 180 deg corresponds to the 12th harmonic over one cycle (720 deg). For this reason the whole pressure signal is recovered up to the 12th cycle harmonic (see Fig. 10).

In Fig. 15 it is shown the pressure reconstruction during a steady-state test in which some consecutive misfires were induced in the same cylinder. Both the recovered and measured in-cylinder pressure waveforms during one misfiring cycle have been reported for comparison. Thanks to the specific signal processing that has been developed, these waveforms show a good agreement; in presence of a misfire the frequency response function is in fact multiplied by a null signal since the actual "synthetic" engine speed is equal to the "synthetic" engine speed in presence of misfire. Therefore the developed procedure is able to diagnose if an abnormal combustion or a misfire occurs.

Conclusion

In this paper an original methodology for cycle-by-cycle and cylinder-by-cylinder in-cylinder pressure reconstruction has been presented. The main characteristics of this procedure are the sensitivity to malfunctioning situations (as abnormal combustion or misfire) and the ability to obtain a quite good pressure waveform recovery.

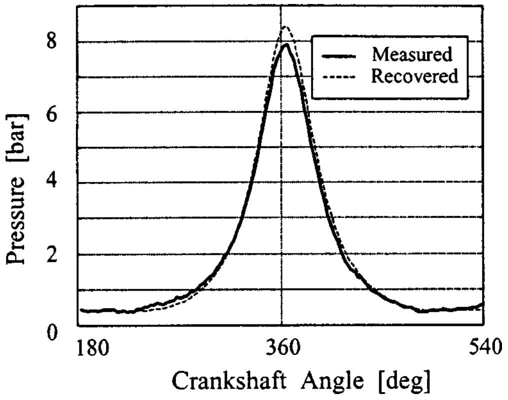

Fig. 15 Pressure recovery related to a steady-state test in presence of a misfire at partial load

The application of this pressure reconstruction methodology to develop new torque-based engine control algorithms is considered realistic by the authors.

Useful applications of this technique are in progress, especially for drive-by-wire engine control systems both for port and direct injection SI engines, and misfire diagnosis applications.

Acknowledgments

The authors would like to acknowledge Prof. Giorgio Minelli and Prof. Piero Azzoni for their support and technical suggestions in the development of this work.

Nomenclature

t = time (s)
p = in-cylinder pressure (bar)
p_{misf} = in-cylinder pressure in case of misfire (bar)
p_{comb} = "combustion pressure" (bar)
p_{man} = intake manifold pressure (bar)
T_i = indicated torque (Nm)
$T_{i\ \text{misf}}$ = indicated torque in case of misfire (Nm)
ΔT_i = difference between the indicated torque during firing and misfiring conditions (Nm)
T_L = load torque (Nm)
T_f = friction and accessories torque (Nm)
$\dot{\theta}_s$ = "synthetic" engine speed (rad/s)
$\dot{\theta}_{s\ \text{misf}}$ = "synthetic" engine speed in case of misfire (rad/s)
$\Delta\dot{\theta}_s$ = difference between the "synthetic" engine speed during firing and misfiring conditions (rad/s)
V = volume enclosed inside the cylinder (m^3)
n = polytropic process coefficient
J = moment of inertia ($kg\cdot m^2$)
A = piston area (m^2)
r = crank radius (m)
f_{crank} = crank-slider kinematics function, that relates the force acting on the piston due to the in-cylinder pressure to the corresponding force acting on the shaft

References

[1] Azzoni, P., Moro, D., Ponti, F., and Rizzoni, G., "Engine and Load Torque Estimation with Application to Electronic Throttle Control," SAE Technical Paper No. 980795.
[2] Citron, S. J., O'Higgins, J. E., and Chen, L. Y., "Cylinder by Cylinder Engine Pressure and Pressure Torque Waveform Determination Utilizing Speed Fluctuations," SAE Technical Paper No. 890486.
[3] Kao, M., and Moskwa, J. J., 1995, "Nonlinear Diesel Engine Control and Cylinder Pressure Estimation," ASME J. Dyn. Syst., Meas., Control, **117**, No. 2.
[4] Shiao, Y., and Moskwa, J. J., "Misfire Detection and Cylinder Pressure Reconstruction for SI Engines," SAE Technical Paper No. 940144.
[5] Cavina, N., Ponti, F., and Rizzoni, G., "Fast Algorithm for On-Board Torque Estimation," SAE Technical Paper No. 1999-01-0541.
[6] Wakuri, Y., Soejima, M., Ejima, Y., Hamatake, T., and Kitahara, T., "Studies on Friction Characteristics of Reciprocating Engines," SAE Technical Paper No. 952471.
[7] Arsie, I., Pianese, C., Rizzo, G., Flora, R., and Serra, G., "Development and Validation of a Model for Mechanical Efficiency in a Spark Ignition Engine," SAE Technical Paper 1999-01-0905.
[8] Gassenfeit, E. H., and Powell, J. D., "Algorithms for Air-Fuel Ratio Estimation Using Internal Combustion Engine Cylinder Pressure," SAE Technical Paper No. 890300.
[9] Randolph, A., "Methods of Processing Cylinder-Pressure Transducer Signals to Maximize Data Accuracy," Paper No. SAE 900170.
[10] Moskwa, J., Wang, W., and Bucheger, D. J., 1998, "A New Methodology for Engine Diagnostics and Control Utilizing "Synthetic" Engine Variables: Theoretical and Experimental Results, *Proceedings of the ASME, Dynamic Systems and Control Division*, DSC-Vol. 64, ASME, New York.